THE UNIVERSITY *of* EDINBURGH

This thesis has been submitted in fulfilment of the requirements for a postgraduate degree (e.g. PhD, MPhil, DClinPsychol) at the University of Edinburgh. Please note the following terms and conditions of use:

This work is protected by copyright and other intellectual property rights, which are retained by the thesis author, unless otherwise stated.
A copy can be downloaded for personal non-commercial research or study, without prior permission or charge.
This thesis cannot be reproduced or quoted extensively from without first obtaining permission in writing from the author.
The content must not be changed in any way or sold commercially in any format or medium without the formal permission of the author.
When referring to this work, full bibliographic details including the author, title, awarding institution and date of the thesis must be given.

The nature and dynamics of ice-stream beds: assessing their role in ice-sheet stability

Damon Davies

Thesis submitted in fulfilment of the requirement
for the degree of
Doctor of Philosophy
to
THE UNIVERSITY OF EDINBURGH

2017

"The commercial spirit of the present day can see no good in pure science: the English manufacturer is not interested in research which will not give him a financial return within one year: the city man sees in it only so much energy wasted on unproductive work: truly they are bound to the wheel of conventional life."

Apsley Cherry-Garrard, *The Worst Journey in the World, 1922.*

Abstract

Ice streams are fast flowing outlet glaciers through which over 90% of the ice stored within the Antarctic Ice Sheet drains. The dynamic behaviour of ice streams is therefore crucial in controlling the mass balance of the ice sheet.

Over the past few decades, Antarctica has been losing mass. Much of this mass loss has been focussed around coastal regions of the Antarctic Ice Sheet. Some of the most dramatic changes such as grounding-line retreat, acceleration and surface elevation change have been observed in Pine Island Glacier (PIG) and its neighbouring ice streams. This is of particular concern because these ice streams account for $\sim$10% of the discharge from the west Antarctic Ice Sheet and therefore have the potential to contribute significantly to global sea-level rise.

One of the key challenges in accurately forecasting this future sea-level rise is improving understanding of processes occurring at the beds of ice streams. This requires detailed knowledge of the properties and dynamics of the bed. This thesis aims to address this knowledge gap by investigating the spatial and temporal characteristics of the bed of PIG using high-resolution geophysical data acquired in its trunk and tributaries and beneath the ice shelf.

The thesis begins by analysing radar-derived high-resolution maps of subglacial topography. These data show a contrasting topography across the ice-bed interface. These diverse subglacial landscapes have an impact on ice flow through form drag, controlled by the size and orientation of bedrock undulations and protuberances.

The next chapter provides a quantitative analysis of these landscapes using Fast Fourier analysis of subglacial roughness. This analysis investigates the roughness signature of subglacial bedforms and the how the orientation and wavelength of roughness elements determine their correlation with ice dynamic parameters. The slow-flowing inter-tributary site is found to have a distinct signature comparable to "ribbed" patterns of modelled basal shear stress and transverse "mega rib" bedforms. Roughness oriented parallel to ice flow with wavelengths approaching mean ice thickness are found to have the highest correlation with ice dynamic parameters.

The temporal stability of PIG is analysed using repeat radar measurements. No significant change is observed over a period of 3-6 years with no evidence of rapid erosion or the evolution of subglacial bedforms as observed in previous repeat measurements of ice-stream beds elsewhere in Antarctica. This suggests that the widespread deforming till layer detected in extensive seismic reflection surveys is in steady state.

Lastly, the thesis explores geomorphological evidence of twentieth-century grounding-line retreat beneath PIG Ice Shelf using high-resolution geophysical data acquired from autonomous underwater vehicle surveys. Evidence of erosion, deposition, meltwater flow and post-glacial

modification is observed in fine detail. The observed distribution of sediment supported previous surveys indicating a geological transition coinciding with the ridge that acted as a former stable grounding-line location. Metre-scale resolution images of recently deglaciated ice stream beds were found to reveal bedforms that are not detectable with traditional offshore bathymetric surveys.

Together these findings reveal the role of short wavelength topography as both an influence on, and product of fast ice stream flow. It also highlights the spatial diversity of subglacial environments and the need to focus future research on tying detailed observations of ice-stream beds with knowledge of basal properties over time.

Lay Summary

Fast flowing outlet glaciers drain over 90% of the ice stored within the Antarctic Ice Sheet. The dynamic behaviour of ice streams is therefore crucial in controlling the mass balance of the ice sheet.

Over the past few decades, Antarctica has been experiencing ice loss at an ever increasing rate. Much of this loss has been focussed around coastal regions of the West Antarctic Ice Sheet. Some of the most dramatic changes such as rapid retreat, increased ice flow speeds and thinning of the ice have been observed in Pine Island Glacier. This is of particular concern because the region drains around $\sim$10% of the ice stored in the West Antarctic Ice Sheet. If this ice is released into the ocean where it can melt, it will lead to increases in sea-level that threaten coastal communities around the world.

One of the key challenges in accurately forecasting rates of future sea-level contributions from Antarctica is a poor understanding of processes occurring at the bed of the ice. This thesis aims to address this knowledge gap by investigating the spatial characteristics of the bed and how it changes over time. This is achieved by imaging the bed using radar to penetrate through the ice and acoustic soundings to investigate the seafloor beneath the floating ice shelf further downstream.

The thesis begins by analysing maps of the topography underlying Pine Island Glacier. A diverse landscape of smooth and mountainous surfaces buried beneath ice are revealed. These diverse landscapes affect the flow speed of the glacier by controlling the drag affecting the ice at its bed.

The next chapter calculates how rough is the landscape beneath the ice and investigates what characteristics of this roughness impose the greatest effect on how the glacier flows. Distinct characteristics of this roughness are observed between areas of fast and slow ice flow, corresponding to different topographic features at the bed.

Next, the thesis assesses whether the glacier bed has changed over a period of a few years by analysing repeat measurements from the same locations. No significant changes are observed, suggesting that the bed beneath Pine Island Glacier is stable.

Lastly, the thesis explores the characteristics of the landscape beneath the ice shelf at the front of the ice stream using measurements from an autonomous submarine (similar to Boaty McBoatface). These measurements yield evidence of erosion, deposition, meltwater flow and modification of the bed during a pervasive retreat of the ice during the twentieth century. A change in the geology of the bed is observed coinciding with a large ridge which used to act as a pinning point keeping the glacier stable. The images taken from the autonomous submarine

show clearer images of the bed than has been possible from similar measurements taken aboard ships.

Acknowledgements

Five years ago I made the decision to apply for this Ph.D. I almost didn't bother as I thought the competition would be too high. Looking back now I can honestly say it was the best decision I've ever made. The last 4 years have been a blast and have given me opportunities I could never have imagined when I started on this journey. The following pages are my feeble attempt at thanking the many people who have provided countless happy memories and helped me get to where I am today. I apologise to anyone I may have forgotten but my brain hurts and I want to sleep now...

First of all I would like to thank my supervisor Rob. It's difficult to express how grateful I am for his guidance, diligence and good humour. He has been an outstanding supervisor but more importantly a good friend. Spending the first few months of my Ph.D in one of the most remote regions on the planet with my boss could have been a nightmare, but it was an absolute joy and an experience I will never forget. I am very lucky to have worked with someone who shares the same passion for mountains and who encourages making the most of the temperamental Scottish weather, even if that means midweek absenteeism! Thank you Rob.

My co-supervisors Matteo and Ali have also been a pleasure to work with. Their knowledge of marine geology and glacial geomorphology have been instrumental to the success of this Ph.D and their tolerance for Skype ineptitude knows no bounds! I would also like to thank my colleagues at the British Antarctic Survey; Ed King for his endless patience teaching me geophysics for dummies; Andy Smith, David Vaughan and Rob Mulvaney for imparting their many pearls of wisdom on surviving an Antarctic field season (any fool can be uncomfortable); and Alex Brisbourne for many fruitful discussions about seismics and cycling.

I am forever indebted to everyone involved in the NERC iSTAR research programme including the many people who worked behind the scenes with planning and logistical support for making it such a success. Pierre Dutrieux and Adrian Jenkins made a valuable contribution to this thesis in sharing data obtained on the iSTAR B research cruise. I particularly want to thank my colleagues and friends in the field; Emma, Jan, Anna, Becky, Seb and Izzy who all shared with me the wild adventure of experiencing Antarctica for the first time and James, Tim, Mark, Jonny and Alex T. for putting up with the "beakers".

Numerous teachers and lecturers inspired and guided me in my formative years of education. Most notable are my secondary school geography teacher Paul Clark who made it fun to learn about the world and introduced me to the Talking Heads; Colin Whiteman who ignited my interest in the cryosphere during my undergraduate degree and Ian Candy, Adrian Palmer and John Lowe for their guidance at Royal Holloway.

I have benefited a huge amount from being part of a fun and supportive glaciology research group at Edinburgh. All have contributed to this thesis in discussions either in a formal environment or over a pint. I particularly want to thank Pete Nienow for being a constant reminder to not take yourself too seriously and David Sugden for just being David Sugden! Over the course of my Ph.D I have been fortunate to be involved in numerous tutoring and demonstrating opportunities and learnt from the best. Anthony Newton has supported and encouraged me throughout my Ph.D except when playing pool. The only 9am meetings I have ever looked forward to are the weekly ES&C tutor meetings with Caroline Lehmann. The Inchnadamph field trips produced many of the most memorable moments of my Ph.D courtesy of Hugh Sinclair and I have the utmost admiration and respect for Andy Dugmore after seeing his dedication and commitment to teaching on the Iceland field trip.

For all the mischief in Edinburgh and beyond, I thank my friends and fellow Drummond St cohort. I especially thank Donald, Andrew, and Tom for the climbing and hillwalking jollies (not forgetting the casual abuse), Lizzie for sharing many miles of pleasure and pain on two wheels, Ed for the cycling chat and weekends "a la campagne", Ben and Ruari for never failing to make me laugh and Frazer for being a relentless devil on my shoulder. I thank my climbing friends, Liam and Nick, for making me say yes before thinking about the consequences.

I have been fortunate to have shared homes with four exceptional women over the past four years. Kathleen and Emma who have an infectiously optimistic attitude to life and an unparalleled dedication to fancy dress; Mollie, whose modesty in light of her staggering achievements is an inspiration; and Jess, who has a never ending appetite for adventure, gin, red wine and the finest alpine catering skills on the planet! I am especially thankful to Jess and Mollie for keeping me sane and putting up with my zombie-like state over the past few months.

I am extremely grateful to my PhD examiners, Simon Mudd and Chris Clark, for taking time during the added pressure of University strikes and the imminent lambing season to read my thesis and provide an enjoyable and stimulating viva experience. I will always remember that loving a cat is not the same as loving a girlfriend!

I thank my brothers, for always being there and finally, I dedicate this thesis to my parents. They instilled in me the value of hard work and never expected anything of me other than to pursue what makes me happy. Their unwavering love and support has got me where I am today. This thesis is just as much their achievement as it is mine.

Declaration

I declare that this thesis was composed by myself, that the work contained herein is my own except where explicitly stated otherwise in the text, and that this work has not been submitted for any other degree or professional qualification except as specified.

Damon Davies

Contents

Abstract iii

Lay Summary v

Acknowledgements vii

Declaration ix

Figures and Tables xiv

1 Introduction 1

1.1 The "weak underbelly" of the Antarctic Ice Sheet . . . 1

1.2 Thesis aims and overview . . . 4

2 Background 7

2.1 Structure and properties of the Antarctic Ice Sheet . . . 7

2.1.1 Ice Streams . . . 7

2.1.2 Marine Ice Sheet Instability . . . 8

2.2 Rapid ice loss in the Amundsen Sea region . . . 10

2.2.1 Future projections of change . . . 13

2.3 The significance of bed topography and basal processes . . . 14

2.4 Investigations of contemporary ice stream beds . . . 16

2.4.1 Direct observations . . . 16

2.4.2 Geophysical surveys . . . 17

2.5 Offshore investigations of palaeo-ice stream beds in West Antarctica . . . 24

2.6 Key points and gaps in knowledge . . . 27

2.7 Thesis aims and objectives . . . 28

3 Methods 29

3.1 Study Area . . . 29

3.2 Dataset overview . . . 31

3.3 Radar data acquisition . . . 33

3.4 GPS processing . . . 35

3.5 Radar data processing . . . 38

3.5.1 Bed picking and DEM interpolation . . . 39

3.6 Repeat radar surveys . . . 40

3.6.1 Experimental strategy to recover absolute bed elevation change . . . 40

3.6.2 Recovering absolute bed elevation from internal radar stratigraphy . 45
3.7 AUV geophysical data acquisition and processing 49
3.7.1 Multibeam data processing 51
3.7.2 Geomorphological mapping and bedform metrics 52
3.7.3 Sub-bottom profiler data processing 53

4 Diverse landscapes beneath Pine Island Glacier influence ice flow 56
4.1 Abstract 56
4.2 Introduction 57
4.3 Methods 67
4.4 Results 67
4.4.1 High-resolution images of Pine Island Glacier bed 67
4.4.2 Implications for ice-sheet modelling projections 70
4.5 Discussion 72

5 Sub-kilometre roughness signature of the bed of Pine Island Glacier, West Antarctica: implications for subglacial landscape evolution and ice stream dynamics. 75
5.1 Introduction 75
5.2 Methods 77
5.2.1 Roughness analysis 77
5.3 Results 79
5.3.1 Characteristics of subglacial topography 79
5.3.2 Spatial distribution of basal roughness 80
5.3.3 Influence of DEM interpolation on along-flow roughness 81
5.3.4 Grid orientation and roughness length scale 82
5.3.5 Comparison to previous roughness analysis of Pine Island Glacier . 89
5.4 Discussion 89
5.4.1 Spatial distribution of basal roughness: implications for bed conditions and landscape evolution 89
5.4.2 What characteristics of bed roughness are important for ice dynamics? 95
5.5 Conclusion 96

6 How dynamic are ice-stream beds? 98
6.1 Abstract 98
6.2 Introduction 99
6.3 Methods 101
6.3.1 Data acquisition 103
6.3.2 Data processing 104
6.3.3 Errors 105

6.4 Results . . . 106
6.5 Discussion . . . 107
6.5.1 Are ice-stream beds dynamic? . . . 107
6.5.2 Implications for subglacial sediment transport and future surveys . . 115
6.6 Conclusion . . . 119

7 High-resolution sub-ice-shelf seafloor records of 20th-century ungrounding and retreat of Pine Island Glacier, West Antarctica 121
7.1 Abstract . . . 122
7.2 Introduction . . . 122
7.3 Study area and geological context . . . 123
7.4 Data and Methods . . . 125
7.4.1 Multibeam-swath bathymetry . . . 125
7.4.2 Sub-bottom profiling . . . 126
7.4.3 Mapping and metrics . . . 128
7.5 Results and Analysis . . . 128
7.5.1 Zone 1:Outer sub-ice-shelf seafloor . . . 130
7.5.2 Zone 2:PIG-distal flank of Jenkins Ridge . . . 131
7.5.3 Zone 3: Jenkins Ridge crest . . . 132
7.5.4 Zone 4:PIGIS submarine cavity . . . 133
7.6 Discussion . . . 133
7.6.1 Interpretation of bedforms and sediment properties . . . 133
7.6.2 Synthesis and implications . . . 142
7.7 Conclusions . . . 144

8 Conclusions 147
8.1 Summary of findings . . . 148
8.2 Synthesis of findings . . . 149
8.2.1 The nature of ice stream-beds: insights from Pine Island Glacier . . . 149
8.2.2 Bed dynamics of Pine Island Glacier and implications for ice-sheet stability . . . 153
8.3 Limitations and future research . . . 156
8.4 Concluding remarks . . . 158

References 159

Appendices

A Bingham *et al.* 2017 (Nature Communications) 184

B Davies *et al.* 2018 (The Cryosphere) 194

C Davies *et al.* 2017 (JGR-Earth Surface) 214

D Brisbourne *et al.* 2017 (JGR-Earth Surface) 229

E Morris *et al.,* 2017 (JGR-Earth Surface) 244

Figures and Tables

Figures

1.1 Maps of the Antarctic continent showing ice stream flow, bed elevation and recent ice loss and surface elevation change. . . . 3

2.1 Configuration of the Antarctic Ice Sheet. . . . 8
2.2 Bed elevation of the Antarctic Ice Sheet. . . . 9
2.3 Schematic representation of the marine ice sheet instability. . . . 10
2.4 Remote sensing observations of ice sheet thinning and grounding line retreat in the Amundsen Sea region. . . . 12
2.5 Simulated evolution of the Amundsen Sea sector of the WAIS 2015-2300 13
2.6 Radio-echo-sounding apparatus and imagery 18
2.7 Radar-derived bed roughness of Antarctica 19
2.8 Schematic diagram of seismic reflection apparatus 21
2.9 Seismic velocities of subglacial materials and schematic of bed conditions of Rutford Ice Stream 22
2.10 Schematic model of palaeo-ice stream landforms on the West Antarctic continental shelf 25

3.1 Overview of the study area 30
3.2 Data location map 32
3.3 DELORES radar system schematic and photos 34
3.4 Radar coverage of data acquired from Pine Island Glacier. . . . 36
3.5 Comparison of single-frequency and post-processed dual frequency surface elevation data. . . . 37
3.6 Radar data processing flow and DEM interpolation. . . . 41
3.7 Interpolated DEMs using isotropic and anisotropic interpolation methods. . . . 42
3.8 Plots of surface and bed elevation change from repeat radar surveys 44
3.9 Example of radar wave traces from the same profile for 2007/08 and 2013/14 data. 45
3.10 Radargrams showing a repeat survey with internal and basal reflectors. . . . 46
3.11 Results of apparent bed elevation change using internal reference horizons. . . 48
3.12 Comparison of absolute and relative bed elevation change methods for calculating bed elevation change. . . . 49
3.13 Correlation plots of horizontal bed alignment shifts 50
3.14 Autosub3 mission tracks 51
3.15 Comparison of unfiltered seafloor DEM with detrended seafloor surface DEMs . 52

3.16 Measurement of bedform metrics 53
3.17 Examples of raw and processed sub-bottom profiler data. 55

4.1 Map of study area and location of radar grids. 58
4.2 Perspective view of the bed beneath Pine Island Glacier for site iSTARt6, together with parameters of ice flow. Vertical exaggeration in the image = 10. τ_b and U_b are the mean basal shear stress (kPa) and mean basal ice velocity (m a^{-1}) from model inversion (*Arthern et al.*, 2015); P_r is the measured upstream propagation rate of ice thinning per ice-stream tributary from 1992 to 2015 using a thinning/non-thinning threshold of 1.0 m a^{-1} (*Konrad et al.*, 2017) and β is the inverted basal traction coefficient equal to τ_b/U_b. 59
4.3 Perspective view of the bed beneath Pine Island Glacier for site 2007t1, together with parameters of ice flow. Vertical exaggeration in the image = 10. τ_b and U_b are the mean basal shear stress (kPa) and mean basal ice velocity (m a^{-1}) from model inversion (*Arthern et al.*, 2015); P_r is the measured upstream propagation rate of ice thinning per ice-stream tributary from 1992 to 2015 using a thinning/non-thinning threshold of 1.0 m a^{-1} (*Konrad et al.*, 2017) and β is the inverted basal traction coefficient equal to τ_b/U_b. 60
4.4 Perspective view of the bed beneath Pine Island Glacier for site 2007t1, together with parameters of ice flow. Vertical exaggeration in the image = 10. τ_b and U_b are the mean basal shear stress (kPa) and mean basal ice velocity (m a^{-1}) from model inversion (*Arthern et al.*, 2015); P_r is the measured upstream propagation rate of ice thinning per ice-stream tributary from 1992 to 2015 using a thinning/non-thinning threshold of 1.0 m a^{-1} (*Konrad et al.*, 2017) and β is the inverted basal traction coefficient equal to τ_b/U_b. 61
4.5 Perspective view of the bed beneath Pine Island Glacier for site iSTARt5 , together with parameters of ice flow. Vertical exaggeration in the image = 10. τ_b and U_b are the mean basal shear stress (kPa) and mean basal ice velocity (m a^{-1}) from model inversion (*Arthern et al.*, 2015); P_r is the measured upstream propagation rate of ice thinning per ice-stream tributary from 1992 to 2015 using a thinning/non-thinning threshold of 1.0 m a^{-1} (*Konrad et al.*, 2017) and β is the inverted basal traction coefficient equal to τ_b/U_b. 62
4.6 Perspective view of the bed beneath Pine Island Glacier for **a** site 2010tr and **b** site 2007tr, together with parameters of ice flow. Vertical exaggeration in the image = 10. τ_b and U_b are the mean basal shear stress (kPa) and mean basal ice velocity (m a^{-1}) from model inversion (*Arthern et al.*, 2015); P_r is the measured upstream propagation rate of ice thinning per ice-stream tributary from 1992 to 2015 using a thinning/non-thinning threshold of 1.0 m a^{-1} (*Konrad et al.*, 2017) and β is the inverted basal traction coefficient equal to τ_b/U_b. 63

4.7 Perspective view of the bed beneath Pine Island Glacier for site iSTARt7, together with parameters of ice flow. Vertical exaggeration in the image = 10. τ_b and U_b are the mean basal shear stress (kPa) and mean basal ice velocity (m a^{-1}) from model inversion (*Arthern et al.*, 2015); P_r is the measured upstream propagation rate of ice thinning per ice-stream tributary from 1992 to 2015 using a thinning/non-thinning threshold of 1.0 m a^{-1} (*Konrad et al.*, 2017) and β is the inverted basal traction coefficient equal to τ_b/U_b. 64

4.8 Perspective view of the bed beneath Pine Island Glacier for site iSTARit, together with parameters of ice flow. Vertical exaggeration in the image = 10. τ_b and U_b are the mean basal shear stress (kPa) and mean basal ice velocity (m a^{-1}) from model inversion (*Arthern et al.*, 2015); P_r is the measured upstream propagation rate of ice thinning per ice-stream tributary from 1992 to 2015 using a thinning/non-thinning threshold of 1.0 m a^{-1} (*Konrad et al.*, 2017) and β is the inverted basal traction coefficient equal to τ_b/U_b. 65

4.9 Perspective view of the bed beneath Pine Island Glacier for site iSTARt9, together with parameters of ice flow. Vertical exaggeration in the image = 10. τ_b and U_b are the mean basal shear stress (kPa) and mean basal ice velocity (m a^{-1}) from model inversion (*Arthern et al.*, 2015); P_r is the measured upstream propagation rate of ice thinning per ice-stream tributary from 1992 to 2015 using a thinning/non-thinning threshold of 1.0 m a^{-1} (*Konrad et al.*, 2017) and β is the inverted basal traction coefficient equal to τ_b/U_b. 66

4.10 Comparison of surveyed beds beneath Pine Island Glacier with those used in ice-sheet modelling and imaged in selected palaeo-ice-streams. 71

4.11 Influence of bed roughness on inverted basal traction and inland propagation of ice-stream thinning. 72

5.1 Comparison of along-flow radar data against interpolated along-flow bed data. . 84

5.2 Location map of radar grid surveys and gridded maps of bed and surface elevation and across-flow and along-flow bed roughness. 85

5.3 Roughness analysis of radar profiles compared to bed elevation extracted from interpolated DEM. 86

5.4 Plots showing correlation between basal roughness and ice dynamic parameters for different moving-window lengths and grid orientation. 87

5.5 Comparison of along and across flow mean log roughness in this study with mean log roughness from *Rippin et al.* (2011). 89

5.6 Log-normal frequency distribution of across and along-flow roughness for each site 92

5.7 Roughness anisotropy histogram. 93

5.8 Similar patterns in basal roughness, basal shear stress and bedform morphology. 94

6.1 Location maps of the study area 102

6.2 Geophysical data and bed picks from PIG 108
6.3 Geophysical data and bed picks from PIG 109
6.4 Geophysical data and bed picks from RIS 110
6.5 Close-up view of change in bed morphology between 2007/08 and 2013/14 identified in survey R1 111
6.6 Mean erosion rates from previously published literature in a range of locations. . 118

7.1 Map and locations of Autosub3 sub-ice shelf missions beneath Pine Island Glacier Ice-Shelf (PIGIS). 127
7.2 Sub-ice-shelf multibeam-bathymetry data and geomorphological interpretation. . 129
7.3 Three-dimensional surfaces of multibeam seafloor bathymetry 134
7.4 Acoustic sub-bottom profiler data. 135
7.5 Landform metrics of Jenkins Ridge crest. 136
7.6 Comparison of offshore swath bathymetry and Autosub3 multibeam bathymetry. 145

8.1 Geophysical evidence supporting the subglacial bedform continuum hypothesis. 152

Tables

3.1 Radar system configuration for each acquisition season. 34
3.2 Mean elevation and difference between dual-frequency GPS and WorldView DEM elevation data. 37
3.3 Processing parameters used in ReflexW software to process radar data. 39

4.1 Parameters pertaining to ice flow and basal topography across each survey patch 69

5.1 Comparison of mean roughness values calculated for radar bed elevation data and interpolated DEM bed elevation. 82
5.2 Mean ice dynamic parameter values for each site used in correlation analysis. . 88

6.1 Mean velocities for each repeat radar survey profile 2007-2017. 103
6.2 Analysis of navigational divergence and associated variability in bed elevation. . 106

7.1 Summary statistics of lineations in Zone 3 compared to previously published metrics of mega-scale glacial lineations and flutes 138

Chapter 1

Introduction

Antarctica is revered for being the highest, driest, coldest and windiest continent on Earth. This reputation for extremes has set the stage for some of greatest feats of human exploration and endurance, capturing people's imagination for over two centuries.

When viewed from space, the surface of Antarctica appears barren and featureless. However, satellite observations of the speed of the Antarctic Ice Sheet reveal a complex pattern of arterial networks of fast flowing ice known as ice streams (Fig. 1.1a). These ice streams flow at speeds in excess of 1 km per year and drain >90% of ice from the interior of Antarctic Ice Sheet (*Bamber et al.*, 2000; *Bennett*, 2003). They play a crucial role in the mass balance of the Antarctic Ice Sheet and consequently its contribution to global sea level rise.

Understanding the dynamic behaviour of ice streams is crucial to accurate forecasting of future mass loss from the Antarctic continent. This requires the ability to look deep beneath the surface of the ice sheet to the subglacial environment.

1.1 The "weak underbelly" of the Antarctic Ice Sheet

The first insights into the nature of the bed beneath the Antarctic Ice Sheet arrived during a series of measurements of ice thickness across Antarctica as part of the International Geophysical Year between 1957 and 1958. It was during these field campaigns that glaciologists first discovered that much of the West Antarctic Ice Sheet (WAIS) rests on a bed that is largely below sea-level (*Bentley et al.*, 1960; *Bentley*, 1964b; *Drewry*, 1983) (Fig. 1.1b). This configuration became known as a "marine ice sheet,". During the mid 1970s, glaciologists investigating the dynamics of West Antarctic Ice Sheet theorised that marine ice sheets may be inherently

unstable (*Weertman*, 1974; *Thomas and Bentley*, 1978). It was thought that if inland retreat into deep subglacial basins were initiated, it could lead to a positive feedback mechanism causing collapse of the marine sectors of the WAIS (*Weertman*, 1974). This was due to a ice dynamic mechanism whereby the volume of ice discharged by ice streams is proportional to the thickness of ice at the boundary between grounded ice and floating ice shelves (known as the "grounding line") (*Weertman*, 1974; *Mercer*, 1978; *Schoof*, 2007a). *Mercer* (1978) further hypothesised that this process could be initiated by warming created by increases in CO_2 emissions by human activities.

Further research by *Hughes* (1981) identified a region of Antarctica that could be particularly sensitive to marine ice sheet instability. Two large ice streams, Pine Island and Thwaites Glaciers, draining to the Amundsen Sea, were singled out on account of deepening inland bedrock topography and relatively small ice shelves that have a relatively weak butressing effect on inland ice compared to the larger ice shelves of the Ross and Weddell Sea sectors. Furthermore, these ice streams , due to their volume and inland reach, hold the and potential to drain significant portions of the WAIS. Hughes referred to this region as the "weak underbelly" of West Antarctica.

Although the theories of Weertman, Mercer and Hughes provoked interesting questions surrounding ice-sheet stability and the potential for WAIS to contribute to sea-level rise, a lack of observational evidence for ice-sheet instability diminished the urgency of further research. Interest was not galvanised until the application of satellite remote-sensing techniques to cryospheric research in the 1990s. For the first time, changes in remote regions of Antarctica could be measured without the necessity for repeat field measurements in remote regions of the ice sheet. Pine Island and Thwaites Glaciers immediately stood out from early studies adopting these techniques, exhibiting dramatic lowering of the surface of the ice sheet and retreat of the grounding line (*Rignot*, 1998; *Wingham*, 1998). These studies promoted renewed interest in the weak underbelly and were followed by numerous investigations of this region detecting further changes in surface elevation (*Shepherd et al.*, 2001, 2002; *Pritchard et al.*, 2009; *McMillan et al.*, 2014; *Konrad et al.*, 2017), acceleration of ice flow (*Rignot et al.*, 2002; *Joughin*, 2003; *Scott et al.*, 2009), grounding-line retreat (*Park et al.*, 2013; *Rignot et al.*, 2014), ice-shelf

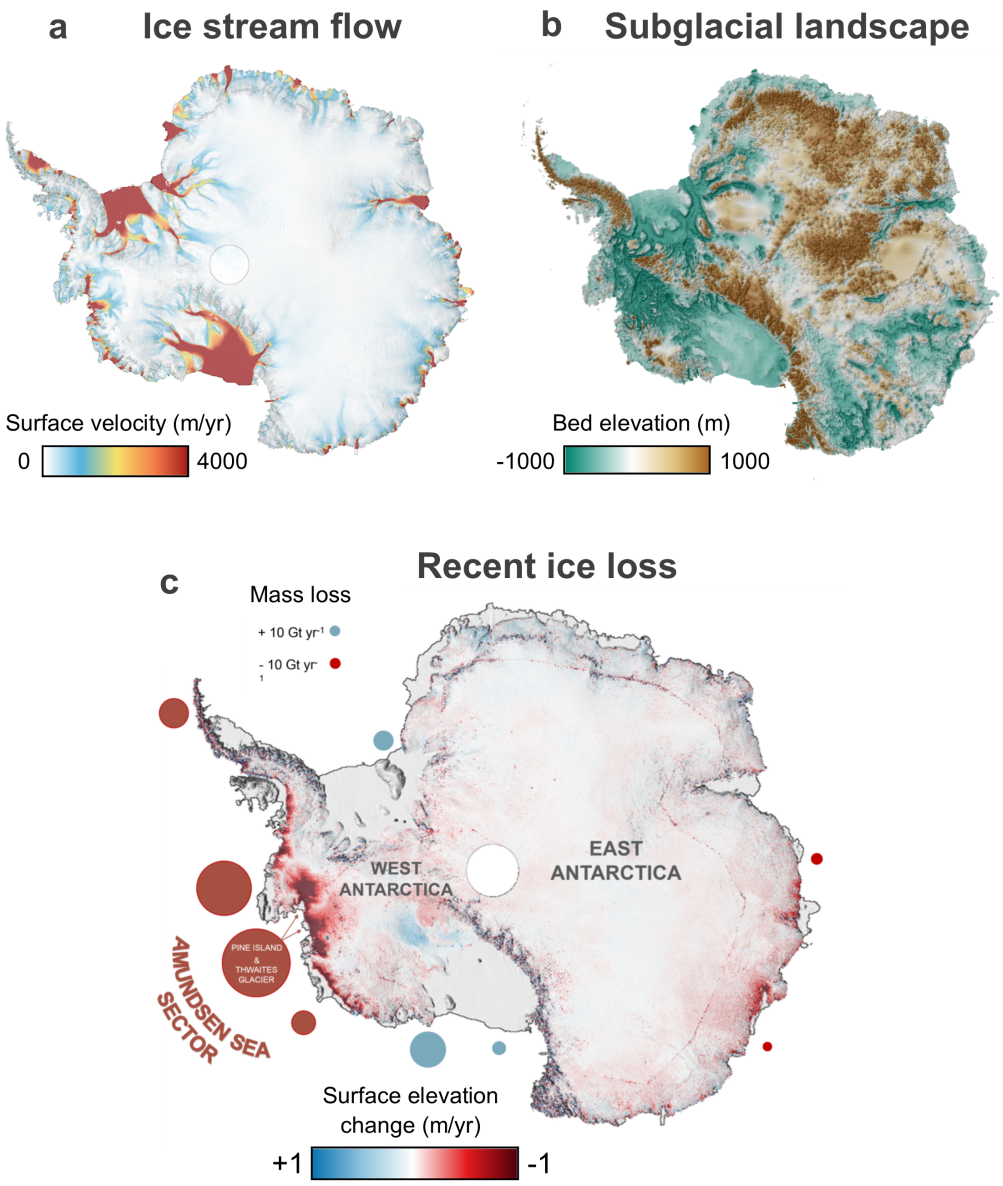

Figure 1.1: Maps of the Antarctic continent showing: **a** Surface velocity revealing ice stream flow networks (*Rignot et al.*, 2011a); **b** bed elevation revealing the subglacial landscape (*Fretwell et al.*, 2013) and **c** Ice mass loss from 1992-2006 (red and blue circles) (*Rignot et al.*, 2008) and surface elevation change from 2010-2013 (*McMillan et al.*, 2014).

thinning (*Bindschadler*, 2002; *Pritchard et al.*, 2012; *Rignot et al.*, 2013; *Mouginot et al.*, 2014) and mass loss (*Rignot*, 2008; *Shepherd et al.*, 2012) (Fig. 1.1c). In light of this research, new estimates suggested a potential 3.3 m rise in sea-level resulting from collapse of the WAIS (*Bamber et al.*, 2009b).

Despite increased research and advances in satellite remote sensing techniques, large uncertainties in the magnitude and rate of sea-level contributions from West Antarctica remain (*Church et al.*, 2013). A significant cause of these uncertainties results from uncertainties in bedrock topography and a lack of understanding about the interaction between the ice sheet and its underlying substrate (*Joughin et al.*, 2009; *Morlighem et al.*, 2010; *Durand et al.*, 2011; *Pollard and DeConto*, 2012; *Sun et al.*, 2014; *Ritz et al.*, 2015). Knowledge of time-dependent processes is also lacking, which critically inhibits the ability to understand how conditions beneath ice sheets evolve over time, either to enhance, or to stabilise the process of marine ice-sheet instability.

1.2 Thesis aims and overview

The previous section highlights the need for an improved understanding of the properties of ice-sheet beds and processes occurring at the interface between ice and its underlying substrate. Therefore the overall aim of this thesis is to examine the spatial and temporal characteristics of the bed of Pine Island Glacier and the effects this has on local and regional ice flow and stability.

Chapter 2 provides some background on the current state of knowledge with respect to Antarctica's ice stream flow and retreat patterns, and previous attempts to understand controls on this behaviour. It identifies the key knowledge gaps, and uses these as a basis to set out four key objectives for this thesis, which motivate and underpin the four main results chapters.

Chapter 3 outlines the datasets used in this thesis and describes the data acquisition, processing and analysis methodology. As that chapter describes, a significant component of the data acquisition was made during my participation in two traverses of Pine Island Glacier during

the 2013/14 and 2014/15 austral seasons as part of the U.K. Natural Environment Research Council Ice-Sheet Stability Research Programme (iSTAR).

The main results chapters 4-7 of this thesis have been written in in a format for publication in peer-reviewed journals. Chapters 4 and 6 have been published, chapter 6 is currently under review, and Chapter 5 is in preparation for submission. At the beginning of each results chapter, a summary of my personal contribution to the work is given. I include the publisher-typeset versions of Chapters 4, 6 and 7 as Appendices A, B and C respectively. In addition to these, I also contributed data acquisition and edits to two further peer-reviewed articles published during my Ph.D., which I include as Appendices D and E.

Chapter 4 investigates the characteristics of the bed topography of PIG and its effect on ice flow. It assesses the influence of short wavelength topography on form drag at the bed of PIG and its influence on ice dynamics. New insights into the basal topography at high-resolution are compared to previous knowledge of the bed at much coarser resolution. The value of these new insights for modelling projections of the future dynamic behaviour of Antarctic ice streams is evaluated.

Chapter 5 considers the high-resolution bed topography of PIG further, through the analysis of subglacial roughness. The chapter investigates the affect of grid orientation and varying moving window length on the relationship between bed roughness and ice dynamic parameters. It explores the roughness signature of subglacial geomorphology and its relationship to the flow dynamics of PIG.

Chapter 6 investigates temporal changes in basal topography through the analysis of repeat radar measurements. Processes of subglacial erosion, sediment transport and the interaction between subglacial hydrology are assessed. The subglacial properties of PIG are compared to other investigations of bed dynamics beneath ice streams in West Antarctica.

Chapter 7 explores the geomorphological signature of recent retreat of PIG. High-resolution images of the seabed surface and sub-surface beneath PIG are analysed to assess the distribution of bedforms and sediment. Processes associated with recent ungrounding and retreat of PIG from a submarine ridge are examined through the analysis of bedforms and seafloor sediment

distribution.

Chapter 8 summarises and synthesises the findings of the thesis, reviews some of the limitations of the research, and poses recommendations for future research.

Chapter 2

Background

2.1 Structure and properties of the Antarctic Ice Sheet

The Antarctic Ice Sheet is the Earth's largest store of freshwater and has a key role in controlling global sea level, hydrology, ocean chemistry and climate (*Siegert*, 2008). It is divided into two large ice sheets by the Transantarctic Mountains. The larger East Antarctic Ice Sheet (EAIS) has a grounded ice volume of 21.7 $\times$ 10^6 km^3, and the West Antarctic Ice Sheet (WAIS) 3.0 $\times$ 10^6 km^3 (*Benn and Evans*, 2010) (Fig.2.1a). Antarctica has been glaciated for $\sim$ 34 million years (*Zachos et al.*, 2001), but the volume of the ice sheets have fluctuated over time (*Siegert*, 2008).

2.1.1 Ice Streams

Around 90% of the Antarctic Ice Sheet is drained through relatively fast flowing corridors of ice known as "ice streams" (Fig.2.1b). Ice streams are warm-based and flow at speeds up to many hundreds of metres per year within surrounding cold-based, slow flowing ice (*Benn and Evans*, 2010). Although many ice streams occupy subglacial troughs, some, such as the Siple Coast Ice Streams in West Antarctica, are not significantly controlled by underlying bed topography, and other mechanisms can influence ice stream location (*Winsborrow et al.*, 2010, and references therein). However, one common property of ice streams is that they are typically underlain by a weak bed of dilatant, saturated sediment associated with low effective pressure at the ice-bed interface that promotes fast ice flow (*Alley et al.*, 1986; *Blankenship et al.*, 1986; *Alley et al.*, 1987a; *Blankenship et al.*, 1987; *Smith*, 1997c; *Brisbourne et al.*, 2017).

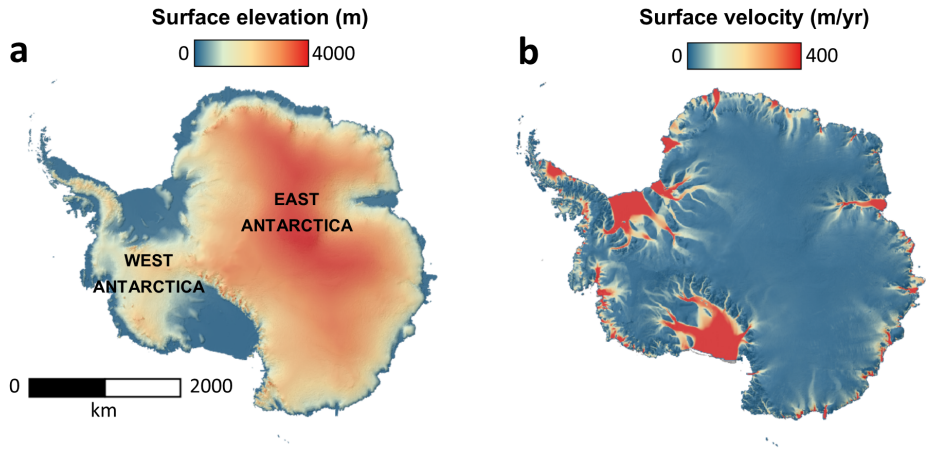

Figure 2.1: Configuration of the Antarctic Ice Sheet. **a** Surface elevation from *Bamber et al.* (2009a). **b** Surface velocity from *Rignot et al.* (2011a). Ice streams can be seen as dendritic fast flowing regions in red.

2.1.2 Marine Ice Sheet Instability

Traditionally, the EAIS has been conceptualised as being relatively stable compared to the WAIS (*Sugden et al.*, 1993). This is because much of the EAIS is grounded on bedrock above sea level. In contrast, the majority of the WAIS is grounded on bedrock below sea level, leading to the WAIS being termed as a so-called "marine ice sheet" (*Fretwell et al.*, 2013) (Fig. 2.2). This contrast was revealed in early radio-echo sounding surveys in West Antarctica and prompted glaciologists to hypothesise that this configuration was inherently unstable (*Hughes*, 1973; *Weertman*, 1974; *Vaughan*, 2008).

The process of Marine Ice Sheet Instability (MISI) occurs where an ice sheet is grounded on a bed below sea-level that deepens inland. A retreat in the position of the transition between grounded and floating ice (hereafter the "grounding line") will lead to an increase in ice thickness and ice discharge at the grounding line. A positive feedback ensues where an increase in ice discharge leads to further reduction in the ice sheet mass and grounding-line retreat and therefore further increases in ice discharge (Fig.2.3). The process would continue until the ice sheet completely collapses or stabilises on a seaward sloping bed (*Schoof*, 2007a).

A seminal paper by *Mercer* (1978) was the first to hypothesise that anthropogenic climate warming might trigger rapid deglaciation of the marine based WAIS, causing a rise in global

sea-level of 5 m. The MISI hypothesis highlights the importance of the buttressing effect of the WAIS' surrounding ice shelves and suggests that removal of these ice shelves would exacerbate the process of MISI (*Mercer*, 1978). The Pine Island and Thwaites Glacier basins were singled out as being potentially vulnerable to MISI owing to their deepening inland bed topography and relatively small ice shelves (*Mercer*, 1978) and were referred to by one author as the "weak underbelly" of the WAIS (*Hughes*, 1981).

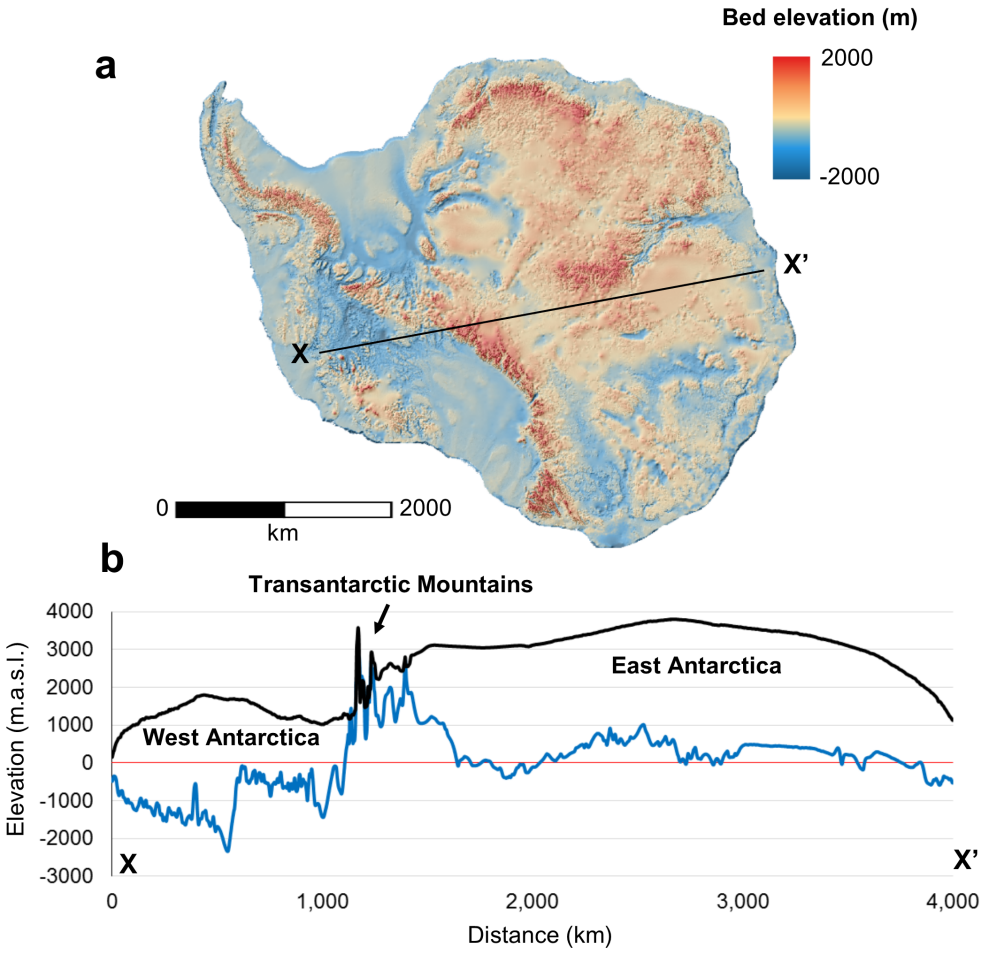

Figure 2.2: Bed elevation of the Antarctic Ice Sheet. **a** Map of Bedmap2 bed elevation (*Fretwell et al.*, 2013). Warm colours show areas of the bed above sea-level, cool colours show regions below sea-level. **b** Plot of bed and ice surface elevation of profile X-X'. Bed elevation is from Bedmap 2, surface elevation is extracted from *Bamber et al.* (2009a). The red line shows present sea-level.

These early studies established a strong theoretical basis for the plausibility of rapid collapse

of the WAIS. However there was little available observational evidence to assess if this process was currently in motion. However, there were tentative clues of a reduced WAIS during the last interglacial from an inferred greater ocean volume from oxygen-isotope records (*Shackleton and Opdyke*, 1973).

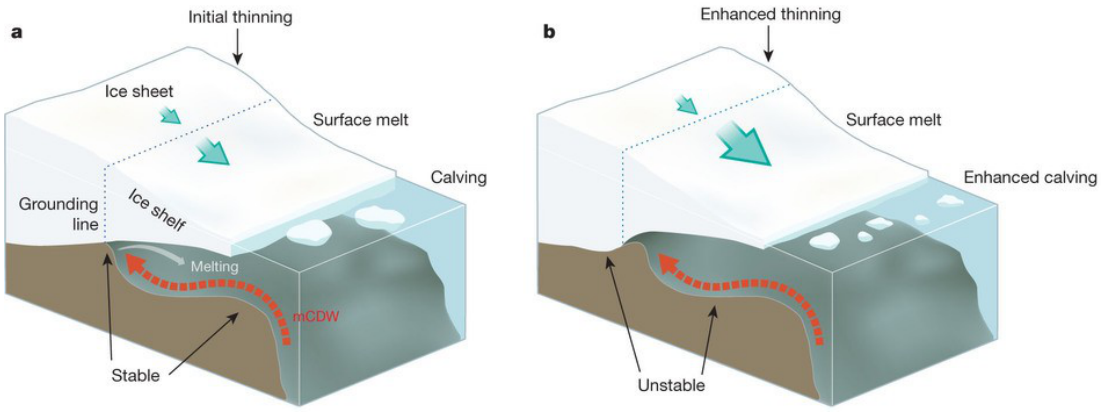

Figure 2.3: Schematic representation of the marine ice sheet instability. **a** Warm modified Circumpolar Deep Water (mCDW) leads to melting at the grounding line, leading to ice-shelf thinning, grounding-line retreat, and initial thinning. **b** Marine ice-sheet instability occurs when, in the absence of buttressing, the grounding line retreats on an upward-sloping (in the direction of the flow) bedrock (unstable): ice flux increases with thickness at the grounding line, leading to an increased out-flux to the ocean and enhanced thinning that may be compensated by further grounding-line retreat, until a new downward-sloping bed (pinning point) is reached (stable). Thinning of ice sheet and shelf can also be caused by surface melt and increased calving (Figure from *Hanna et al.*, 2013)

The MISI hypothesis provided an impetus for field campaigns throughout the 1980s and 1990s. Although these studies greatly expanded knowledge of ice streams, no clear evidence emerged that suggested the process of MISI was taking place in West Antarctica and logistical challenges left the Amundsen Sea ice streams largely unexplored (*Vaughan*, 2008).

2.2 Rapid ice loss in the Amundsen Sea region

The advent of remote sensing observations of the cryosphere in the late 1990s led to a reinvigoration of interest in the MISI. Over the past few decades, a growing body of evidence has emerged demonstrating rapid ice dynamic change occurring in coastal regions of the WAIS.

Much of this work has been made possible through the increased coverage of satellite data that provide observations across wide regions of the Antarctic continent.

The earliest of these studies were published in the late 1990s. Measurements of elevation change of the surface of Antarctica showed anomalously high thinning of the ice sheet in excess of 10 cm occurring in the Amundsen Sea region between 1992-1996 (*Wingham*, 1998). Similarly, satellite radar measurements of the location of the grounding line of Pine Island Glacier showed retreat rates of almost 1 km per year between 1992-1998 (*Rignot*, 1998). These changes were considered to be too rapid to be explained by regional fluctuations in accumulation and were therefore interpreted as a change in ice dynamics (*Shepherd et al.*, 2001).

Following these studies, more sophisticated satellites were launched providing more detailed observations, enabling further insights into the dynamic processes at play. Retreat of PIG's grounding line continued at a rate of almost 1 km per year from 1992-2011 (*Park et al.*, 2013). The flow speed of PIG had also undergone distinct periods of acceleration since at least the mid 1970s and into 21st-century (*Rignot et al.*, 2002; *Joughin*, 2003). This acceleration was observed as far as 250 km inland of the grounding line up to the drainage divides (*Rignot*, 2008; *McMillan et al.*, 2014; *Mouginot et al.*, 2014; *Konrad et al.*, 2017) and was associated with thinning rates in excess of 9 m yr^{-1} (*Pritchard et al.*, 2009). Collectively, these processes of thinning, acceleration and retreat became known as dynamic thinning (*Shepherd et al.*, 2001; *Pritchard et al.*, 2009).

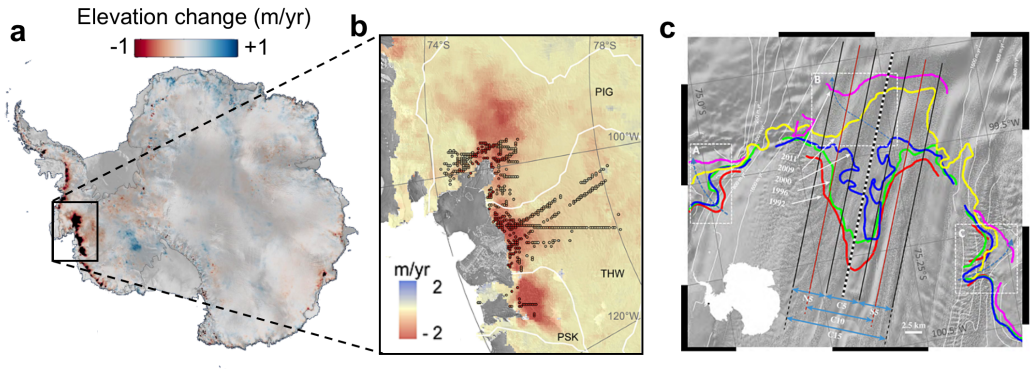

Figure 2.4: Remote sensing observations of ice sheet thinning and grounding line retreat in the Amundsen Sea region. **a** Rate of surface elevation change of the AIS from CryoSat2 between 2010 and 2013 (figure modified after *McMillan et al.*, 2014). **b** Close up of the PIG and Thwaites Glacier (THW) catchments showing inland thinning up to the drainage divides (white lines). Coloured dots show thinning rates from repeat airborne laser altimetry between 2009 and 2012 (Figure modified after *McMillan et al.*, 2014). **c** Inferred location of PIG grounding line between 1992 (red) and 2011 (magenta) from interferometric synthetic aperture radar (inSAR) measurements (Figure from *Park et al.*, 2013)

Widespread grounding-line retreat has now been observed on all ice streams draining into the Amundsen Sea (*Rignot et al.*, 2014) and along the adjacent Bellingshausen Sea coast (*Christie et al.*, 2016), indicating a common mechanism for dynamic change along the coastline of West Antarctica. Simultaneously, high basal melt rates have been measured beneath ice shelves along the Amundsen and Bellingshausen coasts, which have resulted in widespread ice-shelf thinning (*Jacobs et al.*, 1996; *Jenkins et al.*, 1997; *Rignot*, 1998; *Shepherd*, 2004; *Jacobs et al.*, 2011; *Pritchard et al.*, 2012). This ocean-driven basal melting of ice shelves results in reduced buttressing causing acceleration and inland thinning in ice stream catchments (*Pritchard et al.*, 2012). The key driving force of enhanced ice-shelf melting is strongly associated with wind-driven incursion of relatively warm Circumpolar Deep Water (CDW) onto the continental shelf of the ASE (*Jenkins et al.*, 1997; *Payne*, 2004; *Payne et al.*, 2007; *Jenkins et al.*, 2010; *Jacobs et al.*, 2011). This CDW incursion is steered along bathymetric troughs eroded by former ice flow, often along pre-existing geological rifts (*Rignot et al.*, 2008; *Bingham et al.*, 2012; *Pritchard et al.*, 2012).

Two decades of remote sensing studies have now identified the Amundsen Sea ice streams as currently being the greatest Antarctic contributors to global sea-level rise (*Shepherd and*

Wingham, 2007; *Shepherd et al.*, 2012). Between 1996-2006, mass loss from the Pine Island and Thwaites basins combined, more than doubled from 41 $\pm$ 27 Gt yr^{-1} to 90 $\pm$ 27 Gt yr^{-1} (*Rignot et al.*, 2008). Their contribution to sea-level rise was estimated at 0.28 $\pm$ 0.05 mm yr^{-1} between 2005 to 2010 (*Shepherd et al.*, 2012). The changes observed in West Antarctica have raised significant concern over the potential for continued and accelerating contribution to sea-level rise and have prompted some authors to suggest the WAIS may have passed a point of no return (*Joughin et al.*, 2014). Assessing the long-term stability of the WAIS is therefore the core aim of modelling studies of the WAIS.

2.2.1 Future projections of change

The WAIS, and Pine Island and Thwaites Glaciers especially, have been the focus of numerous numerical modelling studies aimed at understanding future contributions to sea-level rise and processes governing ice-stream dynamics. Recent modelling studies have suggested a potential contribution of over 1 m of sea-level rise from Antarctica by the year 2100 (*Pollard and Deconto*, 2016) and that the process of MISI may already be well under way in West Antarctica (*Favier et al.*, 2014; *Joughin et al.*, 2014). However, predicting the rate and magnitude of ice loss relies on improved knowledge of physical constraints on ice dynamics. For example, the rapid retreat projected by *Pollard and Deconto* (2016) relies on the assumption that processes such as ice cliff calving and surface melting will become more widespread over the next century.

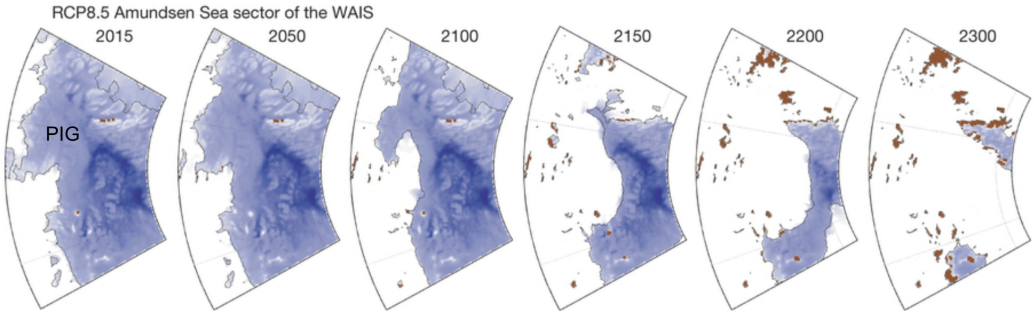

Figure 2.5: Simulated evolution of the Amundsen Sea sector of the WAIS under Representative Carbon Pathway emission scenario RCP8.5 (*Meinshausen et al.*, 2011) between 2015 and 2300 (Figure modified after *Pollard and Deconto*, 2016).

More focussed modelling studies of Amundsen Sea ice streams have highlighted some key processes that may determine the future contribution of this region to sea-level rise. The most important factors arising from these studies are ice-shelf melt rates and glacier specific factors such as grounding line configuration and bed topography. *Joughin et al.* (2010) found that recent observed accelerations and rapid retreat of PIG was associated with ice-plain ungrounding on a reverse bed slope. The magnitude of future retreat was highly dependent on the rate and distribution of ice-shelf melt rate. *Gladstone et al.* (2012) also found a highly variable upper limit of 21st Century sea-level contribution from PIG (7.6 - 19.9 cm) depending on which ocean model forcing was implemented.

Favier et al. (2014) tested a number of parameters using 3 models of PIG with all results demonstrating continued retreat 40 km inland on a retrograde slope upon which the current grounding line rests. A readvance was only possible where the ice shelf melt rate was reduced between 10 to 25% of the control. *Seroussi et al.* (2014a) found a more modest retreat of 10 km with a more conservative ice-shelf melt rate but demonstrated that temporary increases in melt rates can have a long-term impact on ice dynamics. However, the response of Amundsen Sea ice streams is not consistent.

The findings from these studies suggest that without a significant reduction in the transport of CDW permitting a reduction in ice-shelf melt rates, the process of MISI will lead to substantial sea-level rise contributions from the Amundsen Sea ice streams over the coming centuries. However, the range of projected contributions varies significantly depending on chosen model parameters. A key component of the accuracy of these predictions is detailed knowledge of basal topography and basal processes.

2.3 The significance of bed topography and basal processes

The accuracy of model projections relies upon detailed understanding of physical processes and realistic boundary conditions. A recurring theme in modelling studies is the desire for an improved understanding of bed topography and basal processes (*Durand et al.*, 2011; *Sun et al.*, 2014; *Gasson et al.*, 2015). Detailed knowledge of bed topography is important for the

parametrisation of basal traction. Ice-flow models of Antarctic ice streams typically utilise the BedMap2 dataset (*Fretwell et al.*, 2013) for the basal boundary. However, the accuracy of this dataset is limited by the density of geophysical measurements of ice thickness used in the interpolation of the bed DEM (typically >1 km). Ice-flow models can now resolve physical processes at sub-kilometre scales (e.g. *Cornford et al.*, 2013), therefore simulations may be sensitive to uncertainties in bed topography.

Modelling experiments by *Sun et al.* (2014) aimed to address these issues by exploring the impact of introducing high-frequency, small-amplitude noise to the BedMap2 DEM to assess how this affects model simulations of grounding-line retreat. They found that uncertainties in the amplitude of low-frequency bed features with length-scales of several kilometres were more significant than high frequency topographic features. For example, altering the amplitude of a submarine ridge beneath PIG by tens of metres caused the onset of grounding line retreat to vary by up to 35 years. *Nias et al.* (2016) also found a lower rate of sea-level rise from Amundsen Sea ice streams using a rougher bed geometry than BedMap2.

Whether a glacier flows over its bed by sliding or sediment deformation also depends upon bed substrate and hydrology. Observations and models have suggested that the coupled interaction between basal meltwater flow and sediment properties can lead to the shut-down and reactivation of ice streams (*Anandakrishnan and Alley*, 1997; *Bougamont et al.*, 2011). Understanding rheological properties of the basal substrate (i.e. viscous or plastic) can also have a significant influence on ice dynamics. This was illustrated by *Parizek et al.* (2013) who found that basal rheology has a significant effect on the simulated stability of Thwaites Glacier due to its influence on the distribution of stresses at the grounding line and the propagation of thinning upstream.

Another mechanism that affects the stability of ice streams but remains poorly constrained is sedimentation at the grounding line. Large bodies of sediments known as “grounding zone wedges” (GZW) have been observed on the seafloor on the Antarctic continental shelf formerly occupied by ice streams (*Jakobsson et al.*, 2012; *Batchelor and Dowdeswell*, 2015) and beneath the modern grounding line of a Whillans Ice Stream in West Antarctica (*Anandakrishnan et al.*, 2007; *Horgan et al.*, 2013). These features form at a stable margin through delivery

of subglacially transported sediments to the grounding line. (*Alley et al.*, 2007) suggest that GZW formation may provide a stabilising effect preventing grounding-line retreat forced by sea-level rise. Very little is known about the physical processes that determine where, and how quickly these features form. Therefore these stabilising mechanisms are not implemented in ice sheet models.

In order to assess the relative importance of bed topography and bed properties on ice stream dynamics, researchers have employed a range of observational methods to acquire a more detailed understanding of ice-stream beds. The following section outlines these approaches.

2.4 Investigations of contemporary ice stream beds

A variety of approaches and techniques are used to gain insights into ice-stream bed properties. This can be achieved either directly by accessing the bed or indirectly through remote sensing methods.

2.4.1 Direct observations

The foundations of our current understanding of the physical properties of ice stream beds were acquired in the 1980s and 1990s during field campaigns on Whillans Ice Stream (formerly named Ice Stream B) in the Siple Coast region of West Antarctica (*Alley et al.*, 1986, 1987a,b; *Blankenship et al.*, 1987; *Rooney et al.*, 1987; *Engelhardt et al.*, 1990; *Atre and Bentley*, 1993; *Engelhardt and Kamb*, 1998; *Tulaczyk et al.*, 2000). These studies combined geophysical surveys and direct observations from boreholes drilled to the bed (*Alley et al.*, 1986; *Rooney et al.*, 1987; *Engelhardt et al.*, 1990; *Engelhardt and Kamb*, 1998; *Blankenship et al.*, 1986).

A total of eight boreholes were drilled to the bed of Whillans Ice Stream using a hot water drill. The boreholes were used to monitor subglacial water pressure and obtain samples of subglacial sediments. A layer of till composed of unconsolidated marine sediments with a minimum thickness of 2 m (maximum penetration of drill), was sampled and found to have a high porosity, confirming interpretations of a coherent till layer from previous seismic surveys (*Blankenship et al.*, 1986). Basal water pressures were calculated to be close to overburden

pressure, with temperatures at pressure melting point, confirming conditions suitable for fast ice motion either by basal sliding or subglacial deformation (*Engelhardt et al.*, 1990). Ice motion was measured using a "tethered stake" instrument and found to be dominated by basal sliding with sediment deformation limited to a shallow (3-25 cm) shear zone (*Engelhardt and Kamb*, 1998). This contradicted previous theoretical assumptions of pervasive subglacial deformation distributed at a depth of several metres or more (*Boulton and Hindmarsh*, 1987; *Alley et al.*, 1987c; *Alley*, 1991).

2.4.2 Geophysical surveys

Various geophysical techniques have been developed to investigate the subsurface properties of the Antarctic Ice Sheet using ground-based and airborne platforms. The most commonly used method is radio-echo-sounding (RES). The key advantage of RES is that it is less labour intensive than other techniques; therefore data can be obtained over much wider geographical areas (*Bingham and Siegert*, 2007a). RES systems emit electromagnetic (EM) waves in the HF/VHF (megahertz) bands that can propagate through ice, reflecting off any surfaces that bear different dielectric properties. These reflections are recorded at a receiving antenna and can be converted to ice thickness based on the known EM wave speed through ice (*Siegert et al.*, 2005a; *Bingham and Siegert*, 2007a) (Fig. 2.6a).

Before the development of ice-penetrating radar systems in the 1950s and 1960s, very little was known about the subglacial topography of Antarctica. However they have been increasingly deployed over the past 40 years to provide continental and regional-scale insights into subglacial topography (*Robin et al.*, 1977; *Drewry*, 1983; *Lythe and Vaughan*, 2001; *Bingham et al.*, 2010; *Fretwell et al.*, 2013). These techniques made it possible to identify West Antarctica as a marine ice sheet (*Bentley*, 1964a; *Drewry*, 1975) and revealed alpine-scale mountain chains buried beneath East Antarctica that are thought to have been the seeding point for early formation of the EAIS (*Bo et al.*, 2009; *Jamieson et al.*, 2010). The subglacial topography revealed by RES surveys also attests to the role of geological processes in determining the location of modern ice streams that flow along troughs formed by pre-glacial rifting (*Bingham et al.*, 2012).

Over the last decade, more focussed ground-based RES surveys of Rutford Ice Stream have

provided images of active ice stream beds in unprecedented detail. High-density grids (<1 km line spacing), have revealed a suite of subglacial bedforms (*King et al.*, 2009, 2016). Bedforms associated with ice flow over deforming beds such as mega-scale glacial lineations (MSGL) (*Clark*, 1993; *Stokes and Clark*, 2001) and drumlins were observed (*King et al.*, 2007a, 2009) (Fig. 2.6b). The morphology (elongation) of these bedforms appear to be controlled by ice velocity as theorised by investigations of bedforms in palaeo-ice stream beds. These bedforms are discussed in more detail in section 2.10 of this chapter.

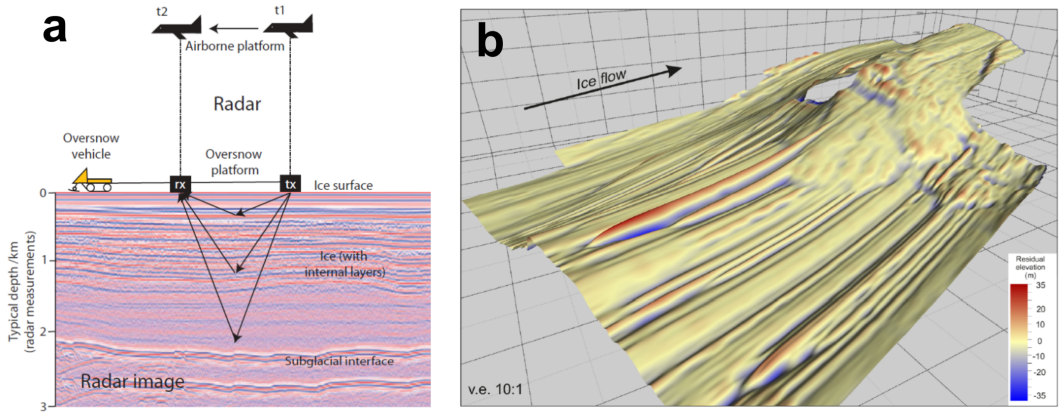

Figure 2.6: Radio-echo-sounding apparatus and imagery. **a** Schematic diagram showing the operation of RES systems. RES apparatus can be mounted on ground-based or airborne platforms. Arrows represent idealised propagation of EM waves. The background image shows a radargram displaying basal and internal reflectors (Figure modified after *Bingham et al.*, 2010). **b** Subglacial bedforms imaged using a high-density RES survey on Rutford Ice Stream, West Antarctica (Figure from *King et al.*, 2016).

As well as revealing the subglacial landscape, radar-derived topographic data can be used to assess the roughness of the bed (vertical change in bed elevation with horizontal distance) (*Taylor et al.*, 2004; *Bingham and Siegert*, 2009). Roughness metrics can provide information on subglacial landscape history and the distribution of subglacial sediments. Smooth beds are typically associated with erosion by warm-based ice stream flow or the presence of marine sediments (*Rippin et al.*, 2011), whereas rough beds indicate the preservation of pre-glacial landscapes due to lower subglacial erosion rates beneath cold-based ice (*Sugden and John*, 1976; *Bingham and Siegert*, 2007b, 2009; *Li et al.*, 2010). One might therefore expect that smoother beds should be found beneath ice streams (fast flow, warm beds) with rougher beds in

inter-stream ridges and the deep interior (slow flow, cold beds) (*Bingham and Siegert*, 2007b). However, this is not always the case. For example, smooth topography is found in the inter-stream regions of the Siple Coast, and in currently slow-flowing regions adjacent to Support Force Glacier; and in both cases lateral ice-stream migration has been implicated (*Siegert et al.*, 2004; *Bingham and Siegert*, 2007b).

RES systems are also capable of capturing information on basal properties through the interrogation of the reflection strength (brightness) of bed echoes. In early studies, bright reflections were used as qualitative indicators of the location of subglacial lakes (*Robin et al.*, 1977). Advances in RES systems and processing techniques led to a more quantitative approach to determining bed reflectivity known as "bed-returned power" (BRP). This method provides a numerical assessment of the amplitude of the bed echo to characterise the composition of the bed, such as the water content or geological properties (*Gades et al.*, 2000; *Catania et al.*, 2003). Higher values of BRP (brighter reflectors) are typically associated with higher water content or a more consolidated bed whereas the inverse is true of low BRP values (dimmer reflector) (*Bingham et al.*, 2010).

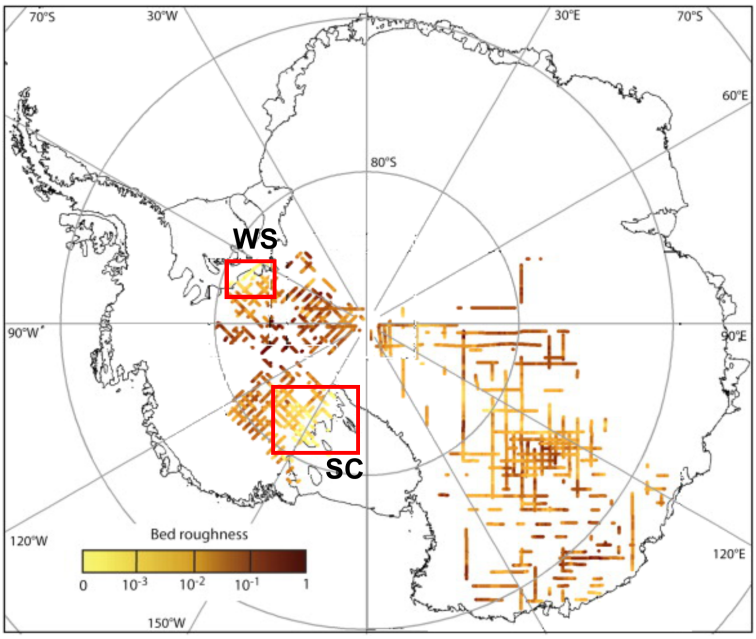

Figure 2.7: Radar-derived along-track bed roughness of Antarctica. Yellow shades denote smooth beds, dark brown denote rough beds. Red boxes outline smooth regions of the bed associated with the location of ice streams in the Weddell Sea (WS) and Siple Coast (SC) regions of West Antarctica (Figure modified after *Bingham and Siegert*, 2009).

BRP analysis conducted on the Siple Coast found high BRP values beneath ice streams compared to a decrease in BRP in an inter-ice stream regions (*Bentley et al.*, 1998; *Gades et al.*, 2000). This pattern was interpreted as representing the transition from a warm, wet bed to cold, frozen bed. Low BRP values also coincide with isolated regions of high basal drag known as "sticky spots" (*MacAyeal*, 1992; *Alley*, 1993; *Stokes et al.*, 2007) also associated with drier, frozen regions of the bed (*Jacobel et al.*, 2009; *Ashmore et al.*, 2014).

Seismology is another commonly used method to investigate the nature of ice-stream beds. Seismic methods exploit elastic rather than electromagnetic waves and can be used in the same way as RES to estimate ice thickness through the inversion of the travel time of bed reflections (*Bentley et al.*, 1960) (Fig. 2.8). The key advantage of seismic methods over RES is that elastic waves can penetrate through ice and the subsurface of the basal interface allowing properties beneath the bed to be determined. Normal-incidence seismic reflection is the most commonly adopted method used in Antarctica to determine subglacial properties (*Smith*, 2007) (Fig. 2.8). This method measures the reflection strength of an active source (typically explosives). The composition of the bed can be quantified by measuring the acoustic impedance of the bed and comparing values from known or modelled seismic velocities for a range of bed conditions (i.e. frozen or dilated sediment, bedrock, water) (Fig. 2.9a).

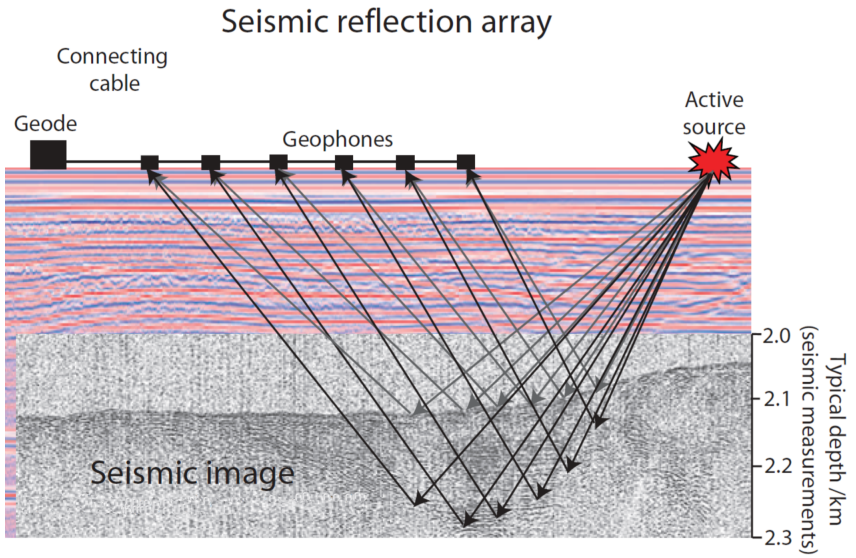

Figure 2.8: Schematic diagram showing normal-incidence seismic reflection apparatus. Black arrows represent idealised path of elastic waves between source and receiver (Figure from *Bingham et al.*, 2010)

The Siple Coast ice streams were again the location of some of the first studies using these methods. *Blankenship et al.* (1986) were the first to identify a distinct, highly porous and saturated sediment layer beneath an active ice stream, confirmed later by borehole observations (*Engelhardt et al.*, 1990, See section 2.4.1). This confirmed that ice stream flow is facilitated by sediment deformation (*Alley et al.*, 1986, 1987a,c) as hypothesised by *Boulton and Hindmarsh* (1987). Over the decades that followed, further seismic reflection surveys on the Siple Coast have shed light on the importance of basal properties on ice dynamics. The onset zones of ice streams on the Siple Coast have been found to coincide with deep sedimentary basins (*Anandakrishnan et al.*, 1998; *Bell et al.*, 1998; *Peters et al.*, 2006) and meltwater storage (*Peters et al.*, 2007) that act to lubricate ice flow.

Active seismic sounding was also deployed in the 1990s and 2000s on Rutford Ice Stream in West Antarctica to provide insights into basal controls on ice velocity. Acoustic impedance values there are predominantly typical of dilatant till with inferred ice motion by subglacial deformation. However, localised regions of the bed display values more typical of sedimentary rocks or lodged till associated with basal sliding over a rigid substrate (*Smith*, 1997c,a). No change in transverse velocity was detected in relation to variable basal conditions. However,

longitudinal velocities showed acceleration over regions of inferred basal sliding compared to no change in velocity in areas where deformation is dominant. This indicates variations in basal friction coupled to bed substrate (*Smith*, 1997a).

Surveys on Rutford Ice Stream were the first to provide information on the composition and properties of active subglacial bedforms. Analysis of acoustic impedance here revealed a "patchwork" of deforming and non-deforming sediment (Fig. 2.9b). Topographic features, including one prominent "bump" were found to coincide with locally-weak impedance and were interpreted as drumlins (*Smith*, 1997c).

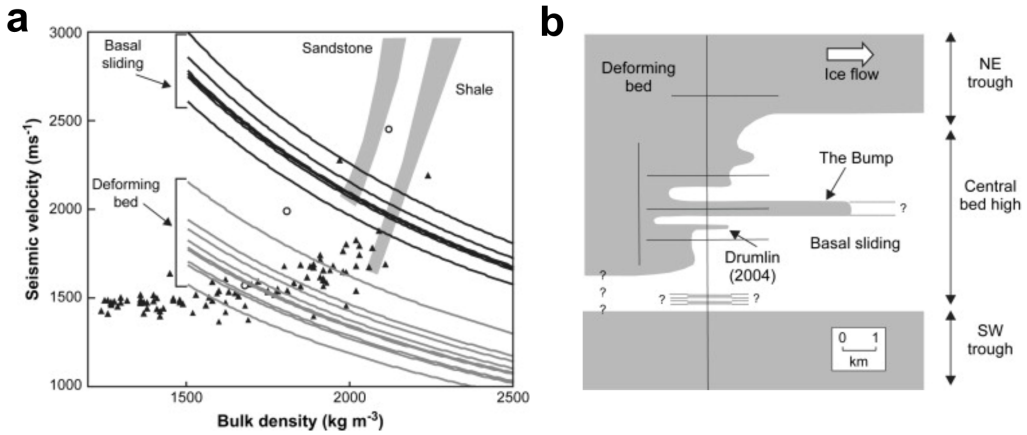

Figure 2.9: Seismic velocities of subglacial materials and schematic of bed conditions of Rutford Ice Stream. **a** Comparison of acoustic impedance data from RIS with measured seismic velocities of a range of subglacial materials. Black triangles represent water saturated sediments, circles are poorly lithified Cenozoic sedimentary rocks around McMurdo Sound, Antarctica. Shaded areas for sandstone and shale represent the lowest range of values typical for sedimentary rocks. **b** Schematic summarising interpreted basal conditions beneath the surveyed region on Rutford Ice Stream (Figure from *Smith and Murray*, 2009).

Surveys at this location were later repeated and expanded. Between 1991 and 1997, rapid erosion rates of 1 m a^{-1} were observed followed by the growth of a mound of sediment between 1997 to 2004 interpreted as a drumlin (*Smith et al.*, 2007). Seismic surveys upstream of the original surveys showed that many of the features first identified were continuous for >3 km (*Smith and Murray*, 2009). High-resolution imaging of bed topography was later achieved using ground based RES showing that these features were in fact mega-scale glacial lineations (MSGL) as opposed to drumlins as originally thought (*King et al.*, 2009) (Fig: 2.6b). This

provided the first identification of MSGL beneath a contemporary ice stream, supporting the hypothesis of *Stokes and Clark* (2002) that they are formed by fast-flowing ice. *Spagnolo et al.* (2014) found that MSGL beneath Rutford Ice Stream display high median amplitudes (8 m) compared to MSGL in observed in palaeo-ice streams (between 2 and 3 m).

High values of BRP were found to coincide with regions of dilated till interpreted from seismic lines suggesting the presence of free water at the bed. Further evidence for the presence of free water beneath active ice streams was identified in seismic data further upstream at the onset region of Rutford Ice Stream (*King et al.*, 2004). At this location, high amplitude wave anomalies indicated the presence of water at a depth of 0.4 to 0.6 m confined to an area >1 km long and <200 m in width (*King et al.*, 2004). These observations were interpreted as water flowing through channels cut into till, potentially playing a roll in the formation of MSGL.

A relationship between bedform morphology, inferred basal motion and substrate was also distinguished in these studies. RES revealed more subdued bed topography where basal sliding was dominant (*King et al.*, 2009) and transverse moraines were discovered in slow flowing regions in the onset region of Rutford Ice Stream with drumlins occurring downstream where velocity is higher (*King et al.*, 2004). This lends support to the hypothesis that bedform morphology is controlled by ice velocity, becoming more elongate with increasing ice velocity (*Rose*, 1987; *Stokes and Clark*, 2002).

On PIG, geophysical studies prior to those conducted as part of this thesis have revealed similar characteristics to those identified at Rutford Ice Stream. Airborne radar surveys of PIG found a strong inverse relationship between ice velocity and bed roughness (*Rippin et al.*, 2011). These authors suggest that basal roughness influences ice velocity by modifying surface slopes and associated driving stresses. They also hypothesise that variations in bed roughness should therefore affect how thinning at the ice shelf and grounding line is transmitted upstream (*Rippin et al.*, 2011). Seismic and airborne potential field data reveal that increases in bed roughness and decreases in ice velocity correspond to a geological transition from sedimentary basement to crystalline bedrock in the upstream catchment (*Smith et al.*, 2013). Varying thickness of soft dilated sediments at the bed has important implications for temporal changes in ice dynamics as one sediment layer could be removed by erosion exposing a different substrate that may have an

impact on flow dynamics (*Smith et al.*, 2013). This hypothesis is strengthened by an observed 32 m change in elevation over a 49 year period with no change in ice thickness indicating rapid erosion of the bed (*Smith et al.*, 2012). This demonstrates that beneath PIG, erosion is actively occurring and may lead to changes in basal conditions (*Smith et al.*, 2012).

2.5 Offshore investigations of palaeo-ice stream beds in West Antarctica

Due to the difficulty in accessing the beds of contemporary ice streams, researchers have sought to understand their basal environments by investigating deglaciated settings (*Stokes and Clark*, 2001). These studies provide information on wide spatial and temporal scales offering insights into the evolution of ice streams across glacial cycles (*Livingstone et al.*, 2012) and identifying landform assemblages thought to be representative of fast-flow regimes (*Clark*, 1993; *Stokes and Clark*, 1999, 2002).

In Antarctica, extensive marine geophysical surveys have produced high-resolution images of large swathes of the ocean floor, previously occupied by ice streams that have since retreated from their maximum extent at the last glacial maximum (LGM). The majority of these studies have surveyed offshore from the WAIS and Antarctic Peninsula and share common characteristics. The inner shelf is characterised by crystalline bedrock with thin sediment cover. Common features are erosional grooves, streamlined bedrock and incised channels. The outer shelf is characterised by a soft sediment bed with highly attenuated mega-scale glacial lineations (MSGL) (*Clark*, 1993), with elongation ratios >10:1, and drumlins are often present at the transition between these two geological units (*Livingstone et al.*, 2012). Streamlined bedforms indicative of fast-ice flow are confined to U-shaped troughs that are likely to have been overdeepened in pre-existing tectonic rifts by glacial erosion over successive glacial cycles (*Bingham et al.*, 2012). Bedforms typically become progressively more elongated with distance along these troughs with the highest elongation ratios (ratio of length to width) occurring in till on the outer sedimentary shelf.

Wellner et al. (2001) propose that 3 different flow regimes can be recognised, with slow flow on

the inner shelf where bedforms are less elongate, accelerating flow at the crystalline/sedimentary transition where drumlins occur and fast flow on the outer shelf where MSGL are dominant. However, *Ó Cofaigh et al.* (2002) argue that fast flow could also operate on the inner shelf due to the presence of meltwater at the bed allowing decoupling and enhanced basal sliding as evinced by the occurence of deeply incised meltwater channels in this region. *Graham et al.* (2009) suggest that bedforms on the inner shelf are likely to have experienced multiple phases of formation under varying basal conditions and ice flow regimes due to lower erosion rates of the crystalline bedrock. Therefore, the inner shelf can be viewed as a more complex, time-transgressive representation of past ice stream activity compared to the outer shelf that can be seen as the final 'footprint' of ice stream activity prior to deglaciation (Fig:2.10).

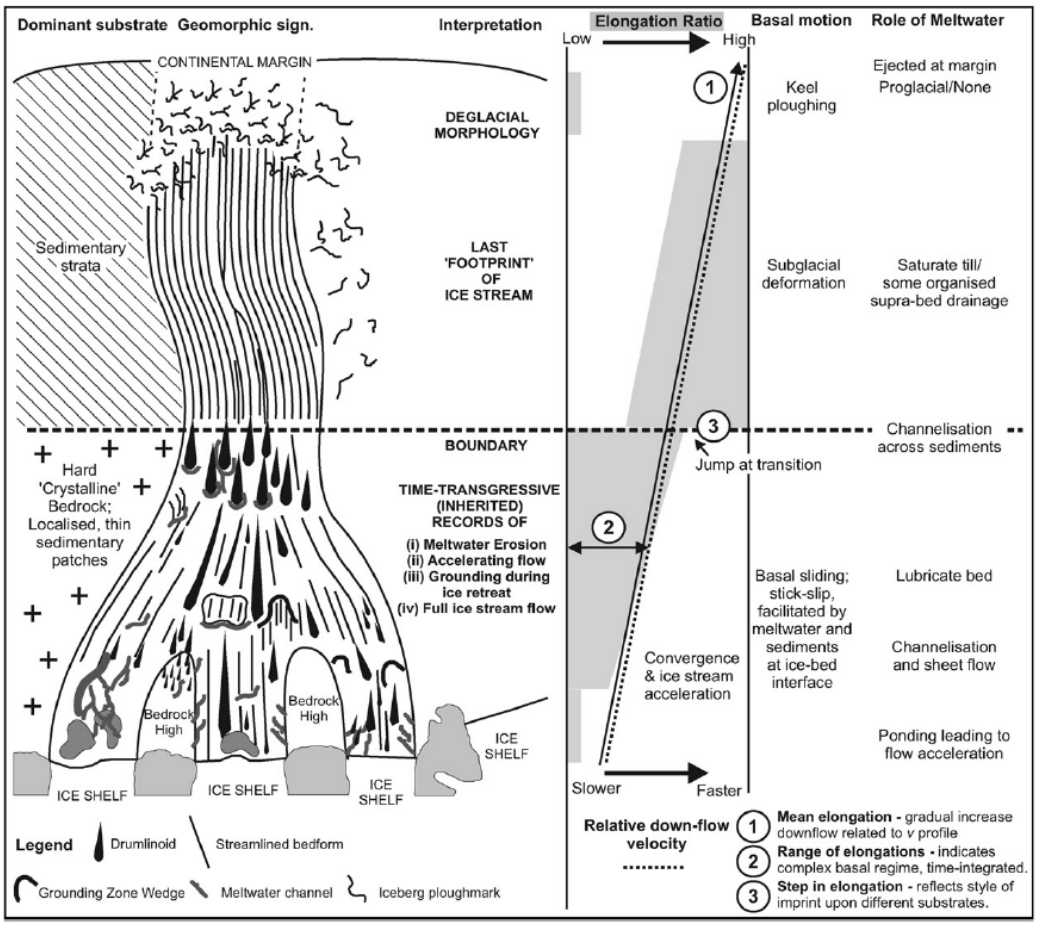

Figure 2.10: Schematic model of palaeo-ice stream landforms on the West Antarctic continental shelf. Schematic summarises interpreted landsystem assemblages alongside inferred LGM ice-stream velocity, bedform elongation and the role of basal motion and meltwater (Figure from *Graham et al.*, 2009).

In Pine Island Bay it is thought that the WAIS extended to the continental shelf break at the LGM. This is supported by MSGL that extend to the shelf edge and a radiocarbon age of 15,800 $\pm$ 3900 ^{14}C obtained from foraminifera shells on the inner shelf (*Lowe and Anderson*, 2002; *Evans et al.*, 2006). *Graham et al.* (2010) identified large accumulations of sediment on the sea bed termed 'Grounding Zone Wedges' (GZW), indicating stillstands of the grounding line during retreat from the LGM. These authors suggest the calculated volume of GZW in Pine Island Bay requires significant subglacial erosion beneath the main trunk of PIG. Substantial erosion has been observed by *Smith et al.* (2007) and *Smith et al.* (2012) and is discussed in Section 2.4.2.

Geomorphological evidence also indicates that rapid ice-shelf break-up took place in Pine Island Bay during a period of warming and sea-level rise around 12 ka. Regularly-spaced corrugated ridges were intepreted as tidally-modulated sediment squeezed at the trailing edge of large, broken ice shelf fragments (*Jakobsson et al.*, 2012). This implies that rapid ice shelf disintegration similar to the break-up of Larsen B and C has occurred in the past and may be possible again in the future. This mechanism could lead to rapid grounding line retreat due to reduced ice-shelf butressing of inland ice. *Jakobsson et al.* (2012) also observed cross-cutting MSGL on the outer shelf, indicating a switch in flow direction during a past readvance of PIG. This switch occurs in an area of dipping sedimentary strata offering greater bed resistance and a narrowing of the trough. Bedforms on the inner shelf just downstream of the present grounding line suggest a patchwork of crystalline and sedimentary beds. This implies greater spatial variability of basal friction resulting in heterogenous flow conditions (*Nitsche et al.*, 2013). This evidence suggests that subglacial bathymetry and geology has an important control on grounding-line retreat rates.

Studies of palaeo-ice streams indicate that ice-stream beds play a key role in modulating ice flow and grounding-line stability. This is likely to influence how changes at the ice shelf and grounding line are transmitted upstream. However this cannot be resolved without a better understanding of conditions beneath contemporary ice streams so that stronger links can be made between palaeo-ice stream bed morphology and ice dynamics.

2.6 Key points and gaps in knowledge

Section 2.2 summarised the evidence that rapid changes are occurring around the coastal WAIS, and may evince the onset of major retreat due to the marine ice sheet instability summarised in Section 2.1. Section 2.2 summarised Recent numerical model simulations suggesting these changes are being caused by mechanisms of MISI as first hypothesised by *Mercer* (1978) and that further mass loss is likely to continue unimpeded unless current ice-shelf melt rates are significantly reduced. However these studies acknowledge that forecasting how the WAIS may evolve in future requires a more detailed understanding of the mechanisms responsible for ice dynamic change and that a key component of this understanding is a more comprehensive understanding of basal properties and processes highlighted in Section 2.3.

Section 2.4 summarised previous geophysical studies conducted in West Antarctica and the wealth of information that can be gained from geophysical approaches to investigate ice-stream beds. More data of this kind are required to understand the environment of the ice-bed interface. In particular, there is a lack of high resolution observations from beneath contemporary ice-stream beds beneath dynamic ice streams such as PIG. Acquiring such data is necessary to understand the spatial scales at which subglacial topography may influence ice dynamics. Furthermore, studies of temporal change beneath ice streams are limited. Repeat surveys hint at a dynamic bed on sub-decadal timescales and offshore studies indicate high sediment flux indicating transport of high volumes of sediment. However, it remains difficult to assess how stable conditions beneath ice streams are and whether rapid change can alter ice stream behaviour.

Section 2.5 summarised knowledge gained from previous studies of palaeo-ice stream beds offshore of the WAIS. The geomorphology of Antarctic palaeo-ice stream beds indicates that ice stream motion and velocity are influenced by bedrock substrate. Past episodes of rapid grounding-line retreat and ice-shelf break-up are interrupted by prolonged pauses in retreat during the formation of GZW. These still-stands occur where bed slopes are shallow and where bed geology offers greater frictional resistance to ice flow. These insights allow us to understand how ice streams have behaved in the past. However, we lack the observations of more recent ice-stream stability and retreat to understand whether the dynamic behaviour observed in the

satellite era are exceptional or within the natural variability of ice stream behaviour.

2.7 Thesis aims and objectives

From the considerations set out throughout this chapter it can be seen that a more detailed understanding of basal conditions beneath contemporary ice streams is required to assess critically the future stability of ice streams in the ASE. To achieve this will require high-resolution images of bed topography over a wide spatial coverage. Repeat surveys with a greater spatial extent are also required to understand the temporal evolution of ice-stream beds. This thesis aims to address these issues and the broad aims outlined in Chapter 1 with the following key objectives:

1. Generate maps of high-resolution subglacial topography of PIG that can enable comparisons between contemporary and palaeo-ice stream beds.
2. To understand the extent to which subglacial topography affects local and regional ice dynamics and what aspects of topography are most influential.
3. To investigate sub-decadal dynamics of the bed of PIG to assess regional bed properties and processes associated with erosion, sediment transport and bedform evolution.
4. To investigate the geomorphological signature of contemporary ice-stream flow and recent grounding-line retreat.

Chapter 3

Methods

The research in this thesis utilises inland and offshore geophysical data collected in the Pine Island Glacier (PIG) region of the Amundsen Sea Sector of West Antarctica (Fig. 3.1). I acquired inland ground penetrating radar data used in chapters 4 and 6 during the 2013/14 austral field season on PIG (black lines in Fig. 3.2) and performed processing and analysis of offshore datasets obtained by other researchers used in chapter 5 (red and yellow lines in Fig. 3.2).

3.1 Study Area

Pine Island Glacier (75°,10'S, 100°,00'W) is a marine terminating ice stream located in the Amundsen Sea region of the West Antarctic Ice Sheet (Fig. 3.1). PIG has a catchment area of 175,000 km^2 and has the largest discharge (75 Gt $year^{-1}$) of any ice stream in West Antarctica (*Shepherd et al.*, 2001; *Vaughan et al.*, 2006). Ice flow close to the grounding line reaches speeds in excess of 2.5 km a^{-1} and is fed by a series of branching tributaries (*Stenoien and Bentley*, 2000; *Vaughan et al.*, 2006) (Fig.3.1a). The catchment area comprises a northern and southern drainage basin

, connected by a 150 km wide "neck" overlying Byrd Subglacial Basin. The southern basin contains slow-flowing ice characteristic of the ice-sheet interior, overlies Bentley Subglacial Trench (Fig.3.1b), and has not exhibited any clear response to climate and or ocean forcing over the era of satellite measurements (*Pritchard et al.*, 2009; *McMillan et al.*, 2014). It will not be considered further in this thesis. The northern basin, however, hosts the main ice stream and tributaries of PIG, rests on bedrock that deepens inland with regions up to 2300 m below

sea level (*Vaughan et al.*, 2006), and is a type example of an ice-stream catchment subject to the marine ice-sheet instability (*Bamber et al.*, 2009b, Section 2.1.2 in this thesis.). The northern basin of PIG therefore forms the focus of this study, and from this point forwards the term PIG will primarily be used as shorthand for the "actively changing" northern basin of PIG.

Between November 2013 and March 2015, two oceanographic and terrestrial field campaigns were conducted in the Amundsen Sea region as part of the UK Natural Environment Research Council (NERC) iSTAR (**i**ce **S**heet **Sta**bility **R**easearch) Programme. The majority of the data that form the basis of analyses in this thesis were acquired during these field campaigns. The following section provides an overview of the datasets used in this thesis.

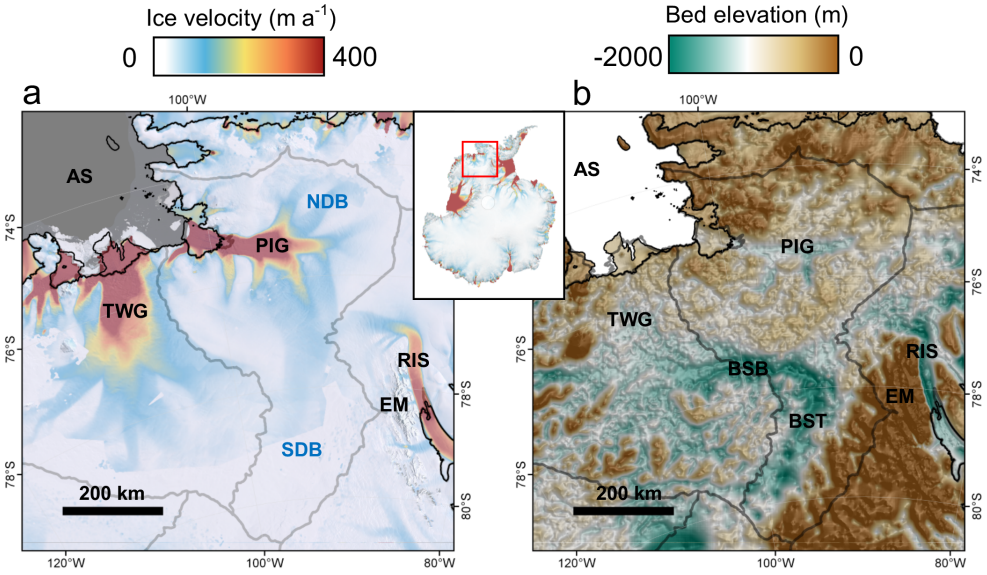

Figure 3.1: Overview of the study area. Black lines denote the coastline and grey lines the ice drainage areas (after *Zwally et al.*, 2012). AS = Amundsen Sea, PIG = Pine Island Glacier, TWG = Thwaites Glacier, RIS = Rutford Ice Stream, EM = Ellsworth Mountains. **a** Surface velocity of the study area (*Rignot et al.*, 2011a). NDB = Northern Drainage Basin, SDB = Southern Drainage Basin. Background image is a Landsat mosaic. **b** Bed topography of the study area from Bedmap2 dataset (*Fretwell et al.*, 2013). BST = Bentley Subglacial Trench, BSB = Byrd Subglacial Basin. Inset shows the location of the maps on the Antarctic Continent.

3.2 Dataset overview

An overview of the iSTAR traverse route and location of the main datasets used in this thesis are shown in Figure 3.2. There are three primary datasets used in this thesis:

- Ground penetrating radar (GPR) (Chapters 4-6).
- Acoustic multibeam echosounder (Chapter 7).
- Sub-bottom profiler (Chapter 7).

I acquired the majority of GPR data along with other iSTAR traverse participants during the 2013/14 iSTAR traverse of PIG (route and surveys shown in Fig. 3.2). Many of the data, and specifically those acquired in the six 10 km by 15 km "patches", were collected as a central objective of NERC grant NE/J005665. Bed DEMs for those data, and their influence on ice flow, are presented in Chapter 4 (*Bingham et al.*, 2017). I used the GPR processing flows described in this chapter to contribute datasets to that paper, which is included as Appendix A of this thesis. The same data also underpin the analyses presented in Chapter 5. Additional GPR data were acquired in 2013/14 specifically as part my NERC Training Grant NE/K011189, and underpin early analyses introduced in Section 3.6 below and Chapter 6. These parts of the thesis also analyse earlier GPR data collected in the austral seasons 2007/08 (by R.G. Bingham) and 2010/11 (by E.C. King).

Sub-bottom profiler data were acquired during autonomous underwater vehicle (AUV) surveys beneath PIG Ice Shelf during the 2014 iSTAR research cruise in the Amundsen Sea. Additional GPR data collected during radar surveys of PIG in 2007/08 and 2010/11 (*Bingham et al.*, 2017) were used in Chapter 6. Similarly, multibeam echosounder data used in Chapter 7 were recorded by AUV surveys during a research cruise prior to the iSTAR programme in 2009.

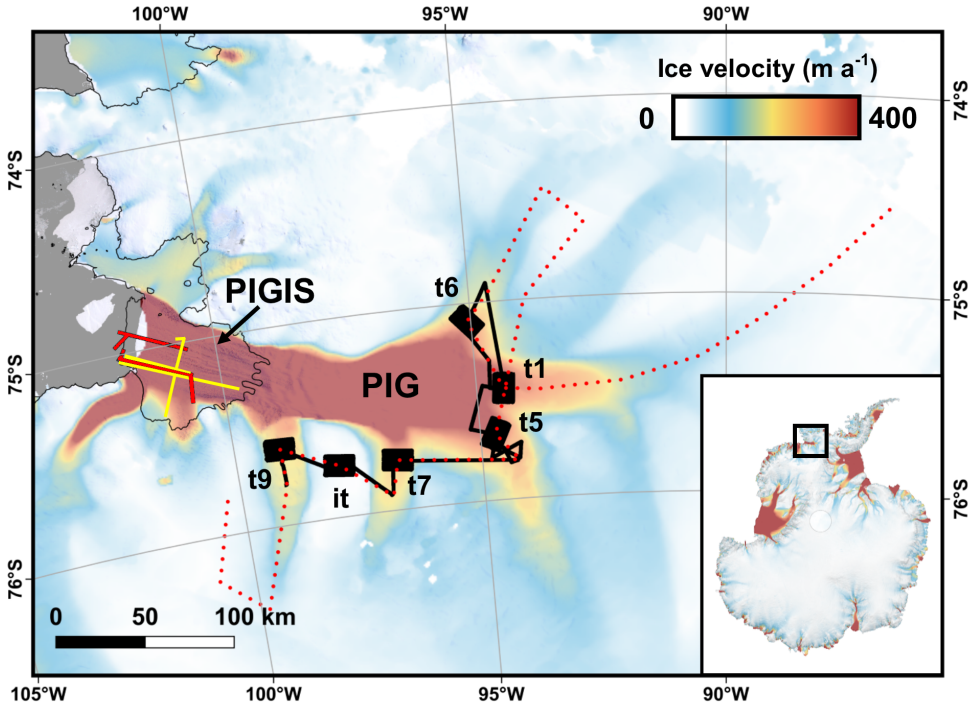

Figure 3.2: Map showing the location of geophysical data used in this thesis. Red dotted line shows the iSTAR traverse route. Black lines show the location of GPR data. Red and yellow lines show the location of marine geophysical data. Colour scale shows MEaSUREs ice surface velocity (*Rignot et al.*, 2011a). PIG = Pine Island Glacier, PIGIS = Pine Island Glacier Ice Shelf.

3.3 Radar data acquisition

Radar data were acquired with British Antarctic Survey **De**ep-**Lo**ok **R**adio **E**cho **S**ounder (DELORES) monopulse radar systems. The system is based on designs developed by the University of Washington (*Gades*, 1998) and St Olaf College (*Welch and Jacobel*, 2003). The systems were towed by snowmobiles, operated at a constant speed of 12 ± 2 km hr^{-1}. The total array length was $\sim$150 m, comprising 3 sleds for the transmitter (tx), receiver (rx) and chassis computer and GPS unit (Fig. 3.3). Data used in this thesis were obtained during two separate field seasons. The main dataset acquired for the purpose of this thesis was collected during the NERC iSTAR research programme traverse in 2013/14 (Fig. 3.4). Earlier datasets collected in the 2007/08 and 2010/11 austral summers (*King*, 2011; *Bingham et al.*, 2017) austral summer were also utilised and formed the basis for repeat surveys conducted in 2013/14 (see results Chapter 4). Details of the radar system configuration for the datasets are provided in Table 3.1. In each season, 1000 shots were stacked in the oscilloscope buffer to form each recorded trace to reduce the signal-to-noise ratio. A trigger pulse was transmitted between transmitter and receiver via a fibre-optic cable or via the airwave on occasions when the fibre-optic cable experienced damage.

Radar surveys were driven along pre-programmed lines driven orthogonal to the ice flow and spaced 500 m apart following the practice of previous surveys conducted in West Antarctica (*King et al.*, 2009, 2016) (Fig. 3.3c). Additional surveys were also acquired during transit between field sites and repeating surveys previously driven in 2007/08 (see Chapter 4). Navigation was achieved using single-frequency GPS units mounted to the snowmobiles. A dual-frequency GPS was located on a sledge between the rx and tx sledges to provide more accurate locations for data processing. A single-frequency GPS unit was also mounted to the radar array to provide backup positions in the event of dual-frequency GPS failure and to provide positions for data quality control checks in the field.

Table 3.1: Radar system configuration for each acquisition season.

Acquisition Season	Antenna Length (m)	Centre Frequency	Digitization Interval (ns)	System Bandwidth (MHz)	Tx pulse repetition rate (kHz)
2007/08	40	1.2	10	-	3
2010/11	20	3	4	50	1
2013/14	20	3	4	50	1

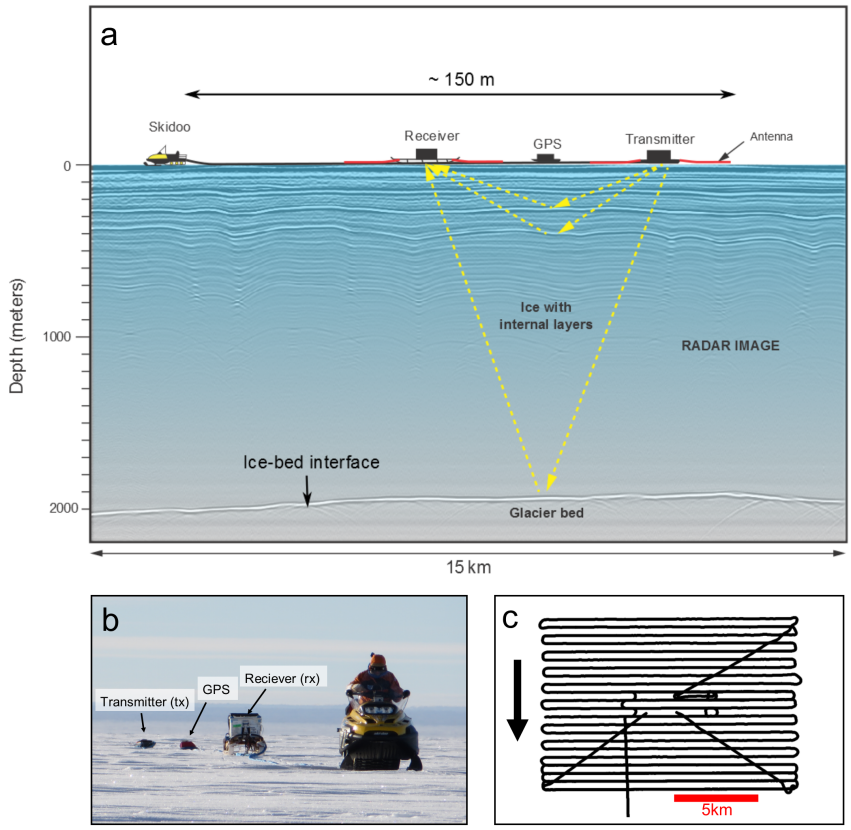

Figure 3.3: **a** Schematic of the DELORES radar system showing the radar array and idealised radar wave paths (yellow arrows). Background image shows a DELORES radargram with basal and internal reflectors (diagram modified after *Bingham and Siegert* (2007a)). **b** Photograph of the DELORES system deployed in the field (photo credit: A. Hogg). **c** GPS tracks of one of the survey grids acquired on PIG. Black arrow denotes broad ice flow direction.

3.4 GPS processing

GPS data were processed using the Canadian Spatial Reference System (CSRS) Precise Point Positioning (PPP) service (https://webapp.geod.nrcan.gc.ca/geod/tools-outils/ppp.php). This service uses the precise GNSS satellite orbit ephemerides to produce corrected *x,y,z* coordinates on a constant "absolute" accuracy. All data were submitted in RINEX format, and processed in kinematic mode in the International Terrestrial Reference Frame. Each output was provided in WGS84 coordinates, with *z* values given with respect to the WGS84 ellipsoid.

GPS data recording was unsuccessful for a limited portion of radar profiles acquired in 2013/14 for sites iSTARt1, iSTARt5 and iSTARt6 (Fig. 3.4). The possibility of substituting missing dual-frequency data with single-frequency data was explored for these profiles. Dual and single frequency data were cross-checked for profiles where both data were recorded concurrently. These comparisons show that *x,y* coordinates were broadly comparable with a difference of <1 m, but that the vertical accuracy was $\pm$10 m (Fig. 3.5). To overcome this issue, surface elevation was acquired from DigitalGlobe WorldView-1 and WorldView-2 image data (*Shean et al.*, 2016). Two DEMs were generated for each affected site (iSTARt1, iSTARt5 and iSTARt6):

- A weighted average of WorldView-generated DEMs from 2010 to 2015 (spanning the survey year of 2013/14).
- A 50 m resolution gridded output of the CSRS-PPP-processed surface elevation data generated from the radar profiles where the dual-frequency GPS had worked.

WorldView-generated DEMs for each site were extracted using the "extract by mask" tool in ArcGIS. A shapefile containing *x,y* coordinate points for each CSRS-PPP-processed GPS profile was then used to extract the elevation value from the WorldView DEMs to compare to the GPS elevation data. The difference between the datasets was calculated for each available GPS point. WorldView data were found to be slightly lower than GPS data (Table 3.2).

The difference was used to create a "difference" raster for each of the three affected sites using the "Topo to Raster" tool in ArcGIS. This difference raster was then extracted from the WorldView DEM for each site to create a new raster for sampling. Elevation was then sampled from this raster using the *x,y*, coordinates from the single-frequency GPS data where no dual-

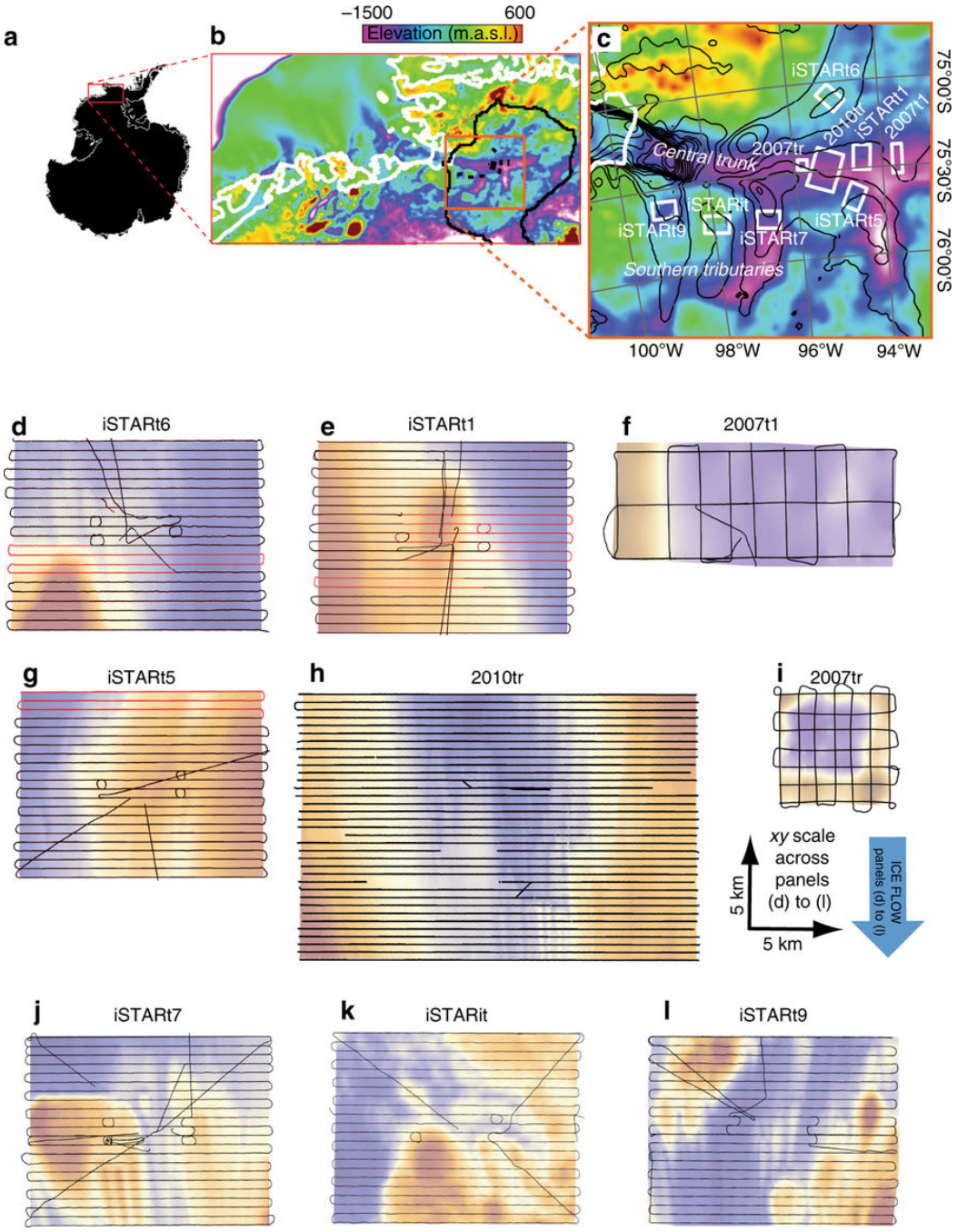

Figure 3.4: Radar coverage. **a** Location and context. In **b**, the colourmap shows regional bed topography from Bedmap2 (*Fretwell et al.*, 2013), the black line is the ice divide, the white line is the grounding line (*Bindschadler et al.*, 2011) and high-resolution survey patches are shown as black rectangles. **c** uses the same schema but demarcating survey patches with white rectangles, labelled by season of data acquisition (2007/08, 2010/11 and "iSTAR" = 2013/14) and an end label denoting the location (where "tr"= trunk; "it"= intertributary and "t1,t5..." denote tributaries numbered after *Stenoien and Bentley* (2000). Also shown are surface ice velocities (*Rignot et al.*, 2011a) contoured at 100 m intervals. **d-l** Plan views of each radar-survey patch across PIG. The colourmap shows bed elevation (scales in Fig. 4.1). Black lines depict radar tracks with dual-frequency GPS navigation. Red lines in **d, e, g** depict traverses where the dual-frequency GPS failed and navigation was recovered as described in the Methods summary

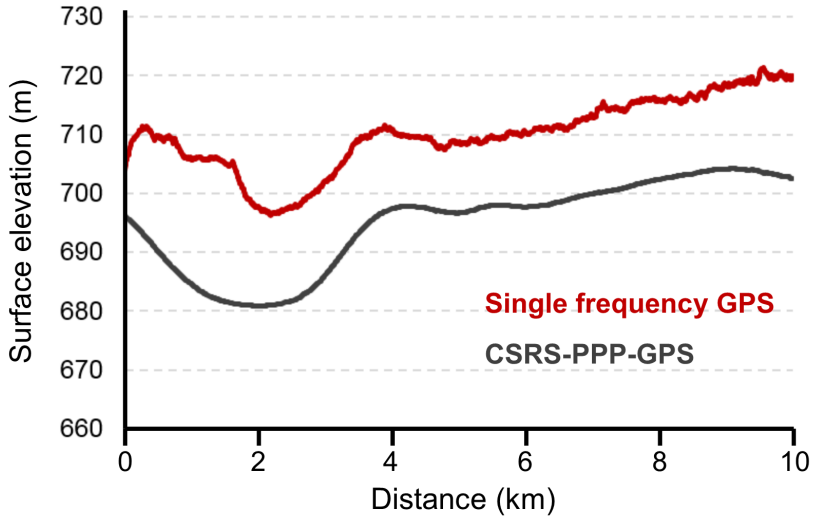

Figure 3.5: Comparison of single and dual frequency GPS data recorded simultaneously during the same survey. The single frequency data show greater variability in vertical elevation and a consistent offset of around 10 m.

Table 3.2: Mean elevation and difference between dual-frequency GPS and WorldView DEM elevation data.

Site	CSRS-PPP-GPS Mean Z (m)	WorldView Mean Z (m)	Min difference (m)	Max difference (m)	Mean difference (m)
iSTARt1	705.0	703.9	-0.24	-2.39	1.1
iSTARt5	693.8	691.1	-0.90	-3.03	2.7
iSTARt6	712.6	712.5	-0.96	-1.81	0.1

frequency data were recorded. These data could then be used to process radar data without any gaps in the grids.

3.5 Radar data processing

This section outlines the processing steps applied to the radar data. The aim of this processing is to improve the signal-to-noise ratio of the raw radar data in order to accurately pick the ice-bed interface. A flow diagram of the full processing flow is shown in Figure 3.6a and details of each step are listed below.

Radar data were processed in ReflexW software (Sandmeier Scientific Software) with the following steps:

- **Assign positioning information**. CSRS-PPP-processed, dual frequency GPS data and WorldView generated positional data were assigned to each recorded radar trace.
- **Suppress noise**. An average trace subtraction was applied to reduce noise introduced by the direct arrival of a high-amplitude pulse transmitted horizontally between the rx and tx antennae.
- **Increase signal-to-noise ratio**. A bandpass filter was applied to remove high and low-end frequencies. Traces were also stacked using a 6 x 6 trace ensemble. A divergence compensation was then applied to account for the attenuation of the radar wave with depth, thereby increasing the strength of the basal reflector (Fig. 3.6b).
- **Amplitude correction**. An amplitude scaling proportional to the two-way travel time of 0.168 m ns^{-1} was applied to compensate for the spherical spreading of the radar wave front with depth.
- **Migration**. Migration assigns the energy of the radar wave back to its source point. This has the effect of collapsing hyperbolae, correcting dipping events to true dip and improving horizontal resolution (Fig. 3.6d). A 2D Finite Difference migration was applied in this step.
- **Data export**. Processed radargrams were then exported in SEG-Y format for picking.

Table 3.3: Processing parameters used in ReflexW software to process radar data.

Processing step	Parameter
Move start-time (ns)	324
Trace resampling (ns)	12
Trace stacking	6 x 6
Make traces equidistant (m)	5
Bandpass frequency filter (MHz)	1,2,4,8
Divergence compensation	x 0.001
Finite-difference migration (MHz)	3
2nd Bandpass frequency filter (MHz)	1,2,4,8

Processing steps and parameters used in ReflexW software to process each radargram are shown in Table 3.3.

3.5.1 Bed picking and DEM interpolation

Bed picking and DEM interpolation were performed in Schlumberger^{TM}Petrel interpretation software package. The travel times of each reflection from the ice-bed interface were picked on the radar profiles at 5 m intervals using a semi-automatic picker that followed the onset of the bed-reflection wavelet from trace to trace (Fig.3.6e). The basal reflector can be seen as a bright reflector and high-amplitude wavelet which can be easily distinguished from surrounding internal reflectors (Fig.3.6e). The bed picks produced a raw dataset of *x,y,t* coordinates, where x and y were the coordinates in WGS84 Antarctic Polar Stereographic projection, and t the two-way travel time. t was converted to depth h using a single value of radar wave speed through ice of 0.168 m ns^{-1}. An additional 10 m was added to all depths to correct for the lower density/high-velocity firn layers as commonly applied in other radar soundings of ice-sheet beds (*King et al.*, 2009; *Fretwell et al.*, 2013; *King et al.*, 2016). Absolute elevation values for the bed were then calculated by subtracting h from the surface elevation.

Factors such as firn density, water content, englacial temperature and other dielectric properties are known to have an affect on radar wave speed (*Matsuoka et al.*, 2010; *Matsuoka*, 2011; *Matsuoka et al.*, 2012). However, this thesis is primarily concerned with examining subglacial bedforms. As such, precise determination of relative bed elevation is more important than absolute bed elevation. In this study area, firn properties are not likely to vary considerably

within areas surveyed. Therefore we are confident that the relative elevation of bedforms are well-represented.

When viewed in 3D in Petrel software, the raw dataset provides a "wire mesh" of bed topography to be used for interpolation of the bed DEM (Fig. 3.6f). The *x,y,z* bed picks were gridded onto a 40 m (across ice flow) x 100 m (along ice flow) grid oriented orthogonal to the profile lines using a natural neighbour algorithm (Fig. 3.6g). This anisotropic gridding preserves the continuity of linear bedforms oriented in the direction of ice flow while maintaining some of the high sampling resolution along the orthogonal radar profiles. Examples of DEM surfaces interpolated with isotropic and anisotropic gridding parameters are shown in Figure 3.7. This figure shows that when interpolated onto an isotropic grid, linear bedforms that are clearly visible in the radar bed picks (red lines in Fig. 3.7), are not reproduced as effectively in the DEM compared to anisotropic interpolation (Fig. 3.7b).

3.6 Repeat radar surveys

3.6.1 Experimental strategy to recover absolute bed elevation change

As stated in section 3.2, repeat measurements of radar surveys obtained in 2007/08 were carried out during the iSTAR field season in 2013/14. My initial strategy for analysing bed elevation change was to calculate absolute bed elevation for both datasets and compare the difference to measure change at the basal interface. This strategy applied steps 1-7 in Figure 3.6. This produced datasets comprising *x,y,h* points at 5 m intervals. I then calculated the difference in the absolute bed elevation (z) using a constant radar wave speed of 0.168 m ns^{-1} and plotted in an attempt to capture changes in bed elevation. The use of a single value of radar wave speed is an oversimplification and can vary due to factors such as firn density, temperature and water content (*Murray et al.*, 2007a). However, these changes are not likely to vary much with horizontal distance and therefore are unlikely to affect relative height of landforms (*King et al.*, 2016). An example of results from this initial strategy is shown in Figure 3.8.

It was apparent from these first results that the offset in the absolute bed elevation change was too high to be interpreted as a genuine change in bed elevation (e.g. around 40 m in 6 years; Fig.

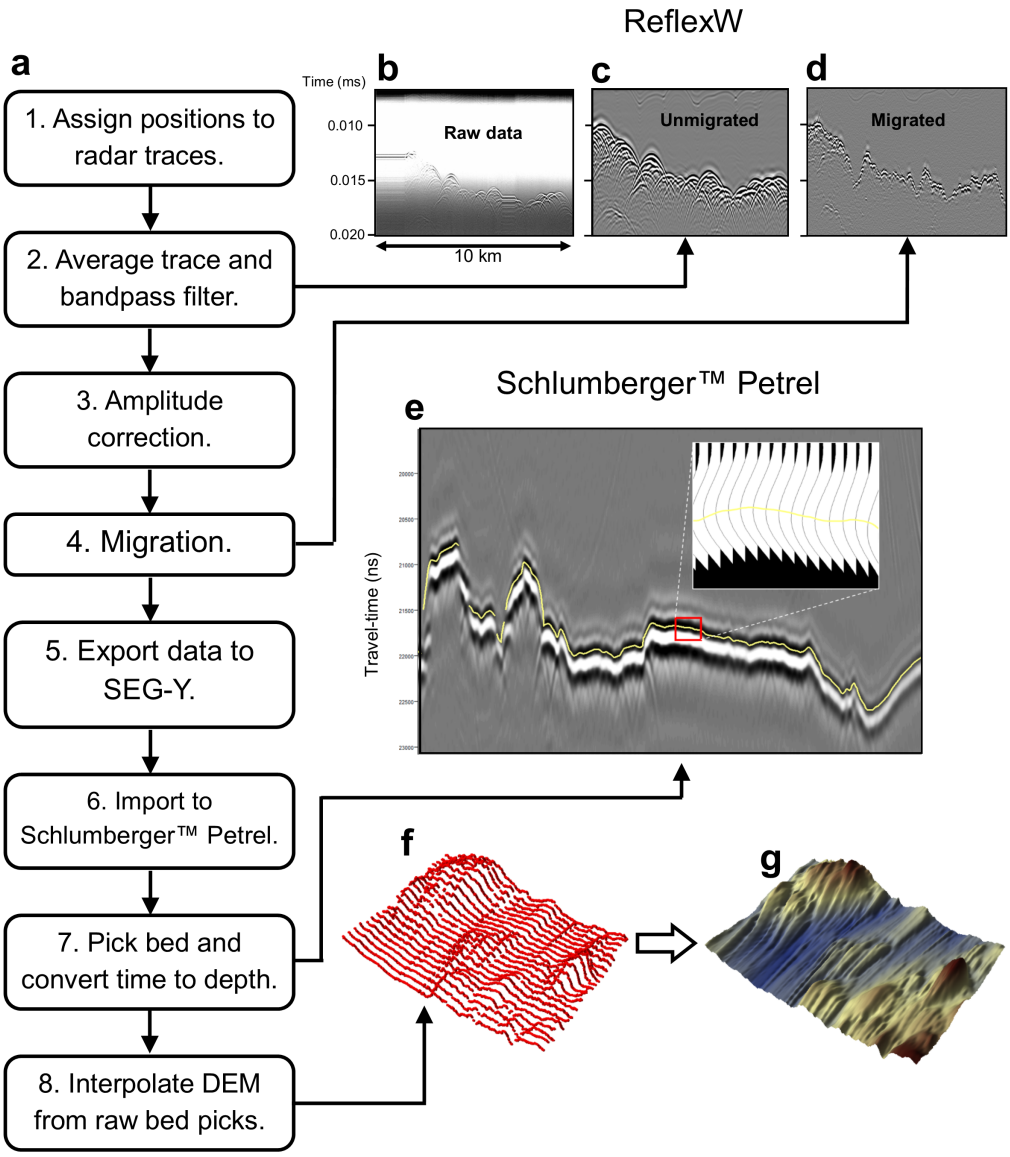

Figure 3.6: Radar data processing flow and DEM interpolation. **a** Flow chart of processing steps, **b** radargram showing unprocessed data, **c** radargram of data after noise reduction and bandpass filtering, **d** radargram after migration, **e** radargram with bed pick (yellow line) and trace view of the basal reflector (inset), **f** Wire mesh of all grid bed picks in 3D view, **g** final interpolated DEM.

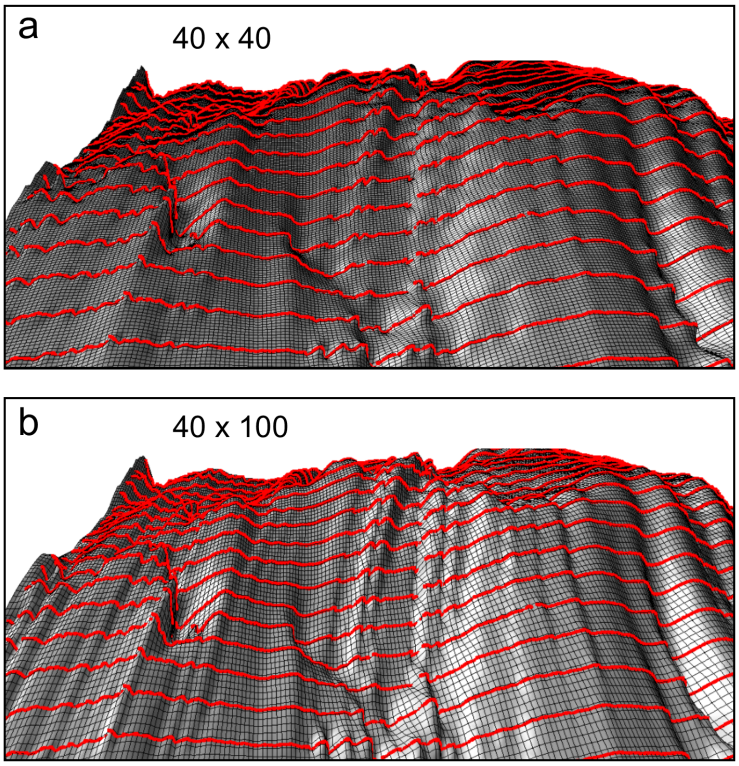

Figure 3.7: Interpolated DEMs using isotropic and anisotropic interpolation methods. **a** Isotropic interpolation using a 40 x 40 m grid. **b** Anisotropic interpolation using a 40 x 100 m grid with elongation along ice flow direction. Red lines denote radar bed picks. A 10x vertical exaggeration has been applied to both DEMs.

3.8a,b). Furthermore, this change far exceeded the observed surface elevation change calculated from dual-frequency GPS measurements (Fig. 3.8c, d). These results indicated that there were large errors in the estimated ice thickness from radar measurements. Potential causes of this error were the following:

- Changes in ice properties (temperature or density) leading to a change in the radar wave speed.
- Horizontal divergence in the survey profiles due to irregular driving.
- Ambiguity in the relative onset of the radar waveform (start-time) caused by differences in the radar system configuration in different survey years.

Although changes in the radar wave speed are possible due to changes in ice properties, the magnitude and consistency of the change in absolute bed elevation observed are too high to be explained by this factor. Similarly, although divergence in the radar profiles was registered, for the same reasons this factor could also not explain the observed change in bed elevation. Changes in the radar system configuration were therefore deemed the most likely cause and explored further.

I compared the onset of the radar wave form between the same profiles in both survey years (2007/08 and 2013/14). An example of these comparisons is shown in Figure 3.9 to illustrate the key differences. During the 2007/08 field season, data recording was triggered by the arrival of the radar wave travelling horizontally from the transmitter to the receiver. This resulted in truncation of the radar wavelet due to its delay arriving through the receiver antenna before being digitised (Fig. 3.9a). During the 2013/14 season, a pre-trigger recording period was set to capture the onset of the wavelet (Fig. 3.9b). I attempted to "wiggle match" waveforms to find a common reference point in wavelets from each survey. However, due to the different operating frequency, I could not identify similarities in the waveforms with enough precision to identify a common start-time.

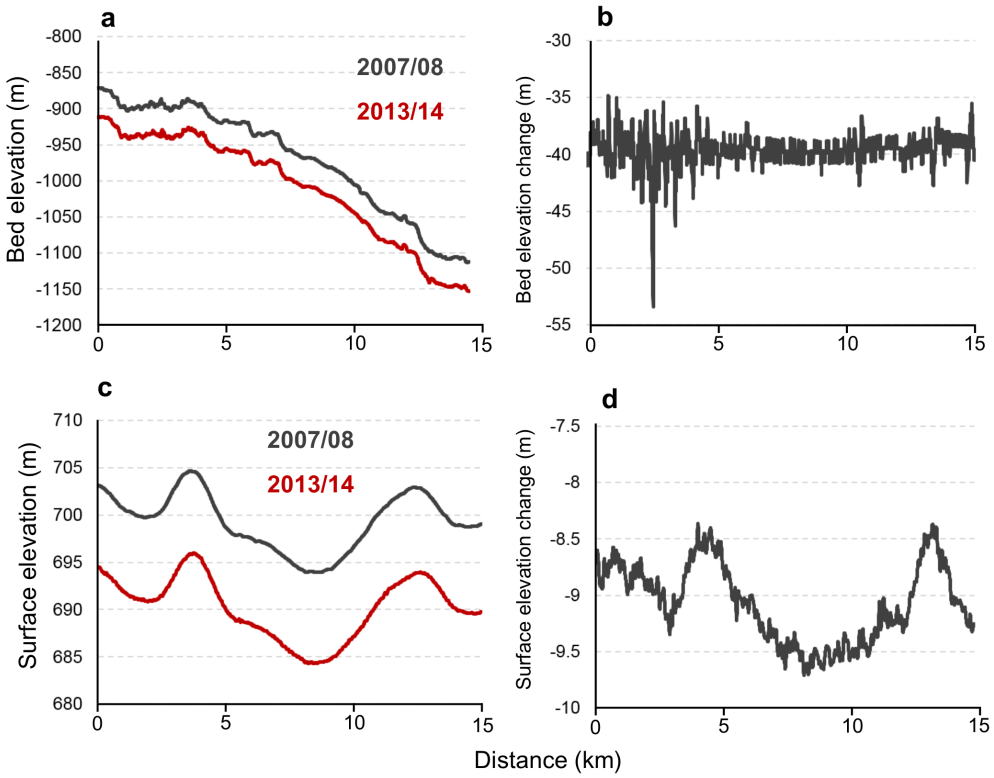

Figure 3.8: Example plots of surface and bed elevation change from repeat radar surveys. **a** Calculated bed elevation converted from radar-derived ice thickness measurements.**b** Bed elevation change between 2007/08 and 2013/14.**c** Surface elevation from dual-frequency GPS data. **d** Surface elevation change between 2007/08 and 2013/14.

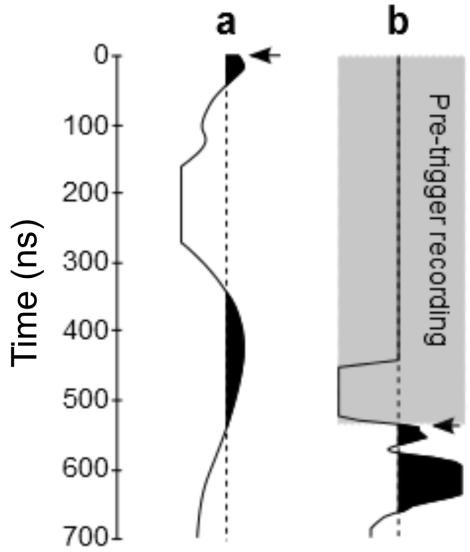

Figure 3.9: Example of radar wave traces from the same profile for **a** 2007/08 and **b** 2013/14 data. The onset of the recorded radar wave is marked by the arrows. The grey box marks the pre-trigger recording period.

3.6.2 Recovering absolute bed elevation from internal radar stratigraphy

Identifying a common start-time requires a more distinct reference point that could be easily identified in repeat surveys. I therefore adopted a strategy to recover absolute bed elevation by using internal radar stratigraphy to identify common "reference horizons" to act as a proxy surface to to calculate changes in bed elevation. The first step was to identify suitable reference horizons within the radar data. Figure 3.10 shows an example of a reference horizon that is clearly identifiable in a repeat survey.

Because data from three seasons (2007/08, 2010/11 and 2013/14) were used in the final repeat survey analysis presented as Chapter 6, in the following description of analysis I refer to the more recent data as T2 and earlier data as T1.

The first step was to pick the internal reference horizons and bed reflectors for T1 and T2. The proportion of ice column at which the T2 internal reflector lies was then calculated as:

$$x = 1 - \left(\frac{z_i}{h}\right) \tag{3.1}$$

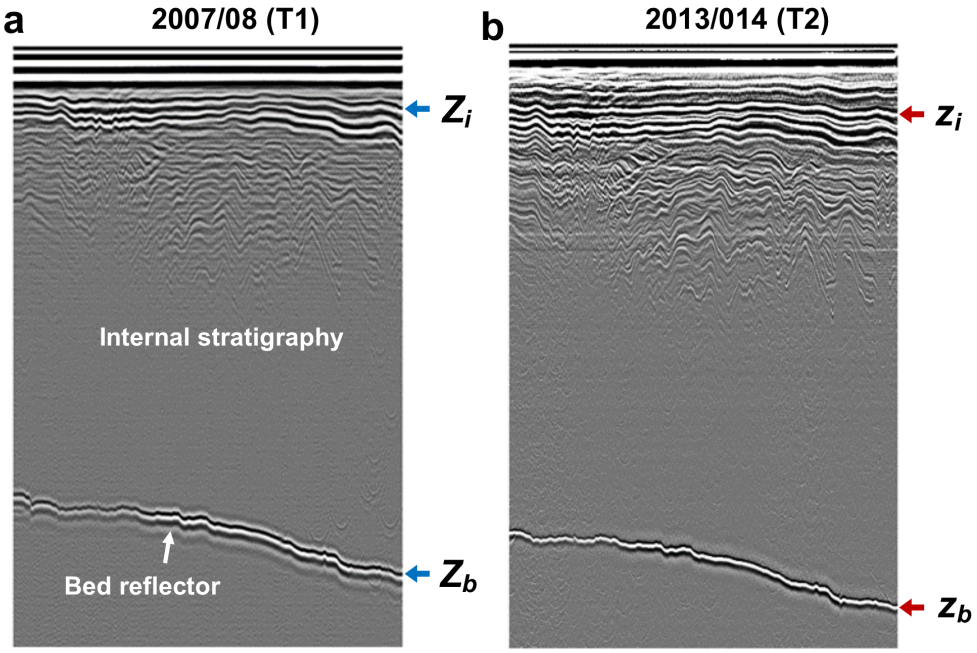

Figure 3.10: Radargrams showing a repeat survey with internal and basal reflectors acquired in **a** 2007/08 and **b** 2013/14. Annotations refer to internal and basal reflectors used in the calculation of bed elevation change described in text.

where z_i is the depth of the T2 internal reference horizon in metres, and h is the depth of the T2 bed reflector in metres. The expected elevation change of the T1 internal reference horizon is then calculated:

$$\Delta z_i = x\frac{\Delta h}{\Delta t} \tag{3.2}$$

where $\frac{\Delta h}{\Delta t}$ is the surface elevation change measured from the T1 and T2 GPS surface elevation measurements. The absolute elevation of the T1 internal horizon is then calculated:

$$Z_i = z_i + \Delta z_i \tag{3.3}$$

From this the absolute bed elevation for T1 is determined:

$$Z_b = Z_i - H \tag{3.4}$$

where H is the ice thickness from the T1 internal reference horizon to the bed reflector. The bed elevation change (ΔZ_b) is then calculated by subtracting z_b from Z_b. Results from this analysis are shown in Figure 3.11

Analyses using internal radar layers were performed on three repeat-radar datasets, which ultimately form the sites analysed in Chapter 6. The sites are introduced in detail in Section 6.3.1: here, for the purposes of discussion, it is only necessary to consider that there were three sites and they are named R1, R2 and R3. Results from these analyses showed significant change in bed elevation outside the vertical precision of the radar system for two of the three surveys analysed. Apparent bed lowering in excess of 5 m was calculated in the northern region of survey R1 and the southern region of survey R2.

In order to check the validity of the preliminary results in Figure 3.11, a comparison of relative bed change was performed. Bed picks for T1 and T2 were converted to relative height by removing the minimum bed depth in metres from all bed points. Bed picks were then plotted to check whether the change in absolute bed elevation was replicated in the comparison of relative bed elevation. As is shown in the example of repeat survey R2 in Figure 3.12, the change observed in this survey is not replicated. When relative bed height was plotted for all repeat surveys, change observed in absolute bed elevation was not replicated for any survey. The changes observed in the absolute bed elevation determined using internal reference horizons were therefore deemed to be an artefact of the reconstructed absolute bed elevation. This was likely caused by changes in the elevation of the internal reference horizon inherited from downstream advection of this internal layer in the period between repeat surveys.

Following the comparison of absolute and relative methods for repeat surveys, I decided that the absolute methods could not provide a reliable determination of bed change and, hence, instead, to focus on assessing relative changes in bed morphology between repeat surveys. This analysis underpins Chapter 6.

Changes in bed morphology were assessed by calculating the Pearson correlation coefficient (r) of the T1 and T2 bed reflector normalized to relative bed height across a 500 m moving window. The correlation of bed picks is sensitive to the horizontal alignment of the basal reflector. To

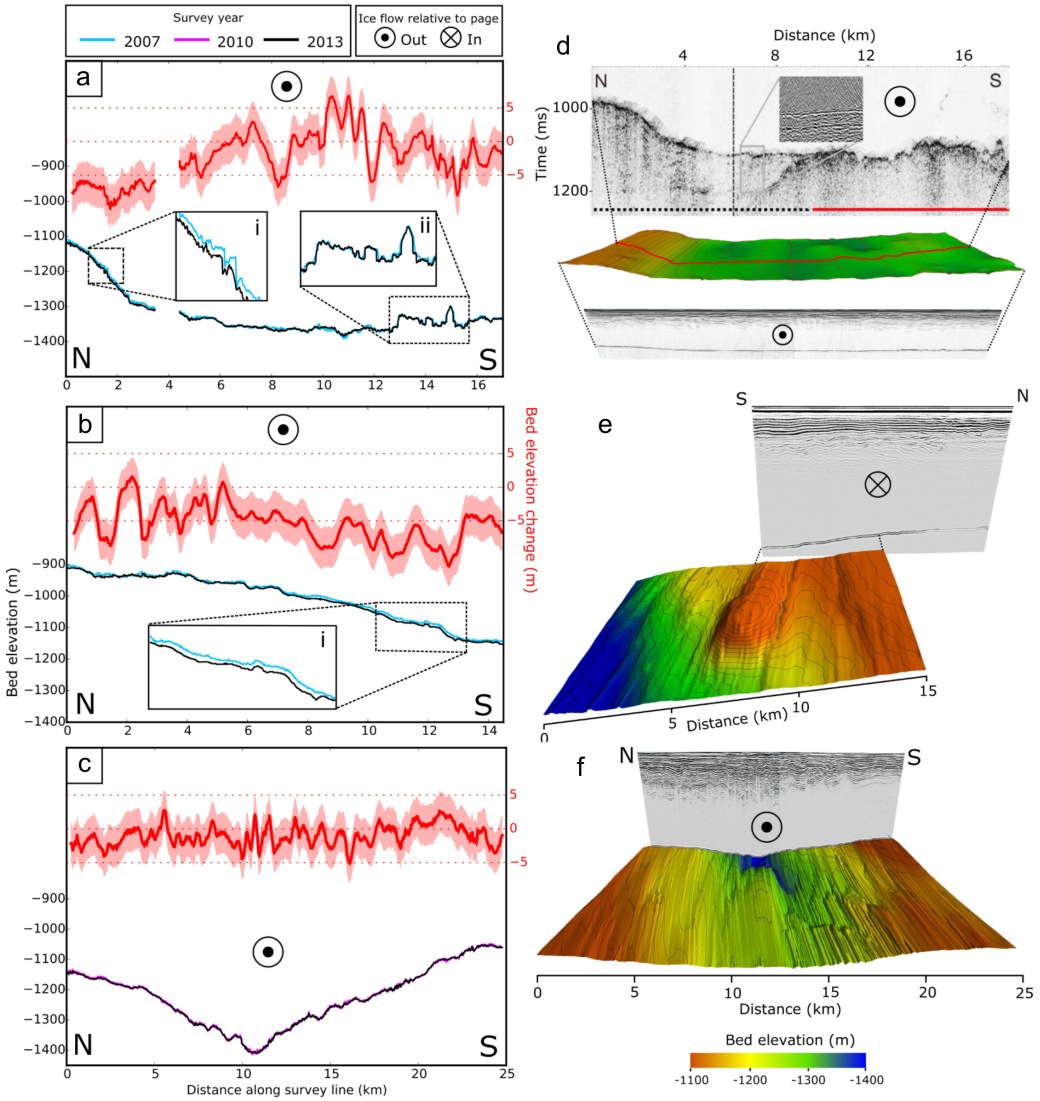

Figure 3.11: Results of apparent bed elevation change using internal reference horizons. Red line shows a 250 m moving average of bed elevation change. Error band shows the radar system vertical precision of ± 3 m. Black and coloured lines represent bed picks for each respective survey year (see key for details). **a** Survey R1 bed elevation; **i** close-up showing bed lowering; **ii** close-up showing absence of bed change. **b** Survey R2 bed elevation; i) close-up showing bed lowering. **c** Bed elevation for survey R3 **d** Top: Seismic survey from *Smith et al.* (2013) showing a basin of thick subglacial sediments in the North (black dashed line) and thin sediment drape over rough bedrock in the south (red solid line); Centre: Bed DEM interpolated from 2007 radar surveys. Red line indicates the location of the seismic survey; Bottom: Survey R1 radargram (2007/08). **e** iSTARt1 bed DEM interpolated from 2013/14 radar grid and survey R2 radargram (2007/08) located downstream of a "crag-and-tail" subglacial bedform. **f** Bed DEM interpolated from 2010/11 radar grid and R3 survey radargram.

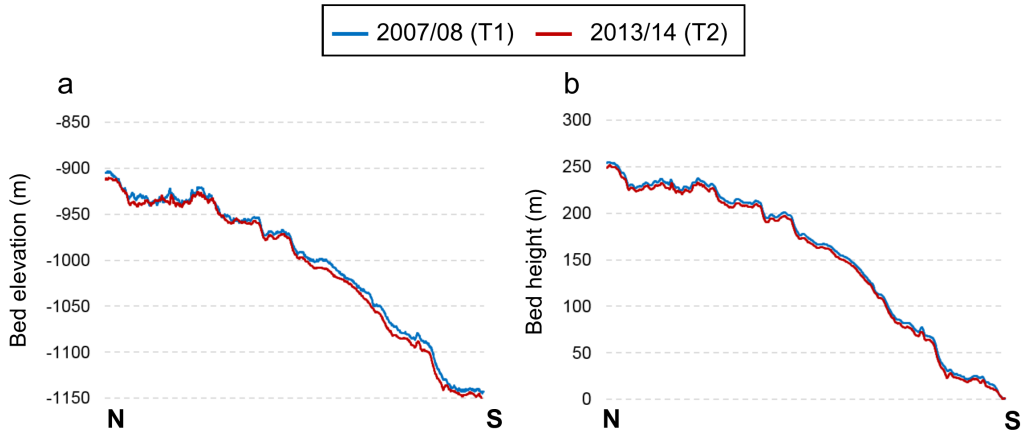

Figure 3.12: Comparison of absolute and relative methods for calculating bed elevation change. **a** Plots of absolute bed elevation for repeat survey R2 using internal reference horizons to reconstruct absolute bed elevation change. **b** Plots of relative bed height for the same survey. Note the absence of bed elevation change in the southern region of the bed.

ensure alignment of the bed before performing the moving correlation, r was calculated for the entire length of the T1 and T2 repeat surveys while performing a horizontal shift of the the T1 bed pick with respect to the T2 bed pick at 5 m intervals. A horizontal shift of the T1 bed pick based on the highest r for a given horizontal shift was then applied for the final moving correlation analysis of relative change in bed morphology. Results from these analyses are shown in Figure 3.13 and final results of the moving correlation are detailed in Chapter 4.

3.7 AUV geophysical data acquisition and processing

Marine geophysical data analysed in Chapter 5 were acquired during four AUV survey missions beneath PIG ice shelf (hereafter PIGIS). The data consist of acoustic multibeam echosounding recorded using a Kongsberg EM2000 swath bathymetry echosounder from two missions (M433 and M434) undertaken in January 2009 on research cruise NBP09-01 of the icebreaker *R/V Nathaniel B.Palmer*. An Edgetech 2-16 kHz sub-bottom profiler was deployed in two further AUV missions (M447 and M448) undertaken in February and March 2014 on the iSTAR research cruise JR294/295 of the *RRS James Clark Ross* (Fig. 3.14).

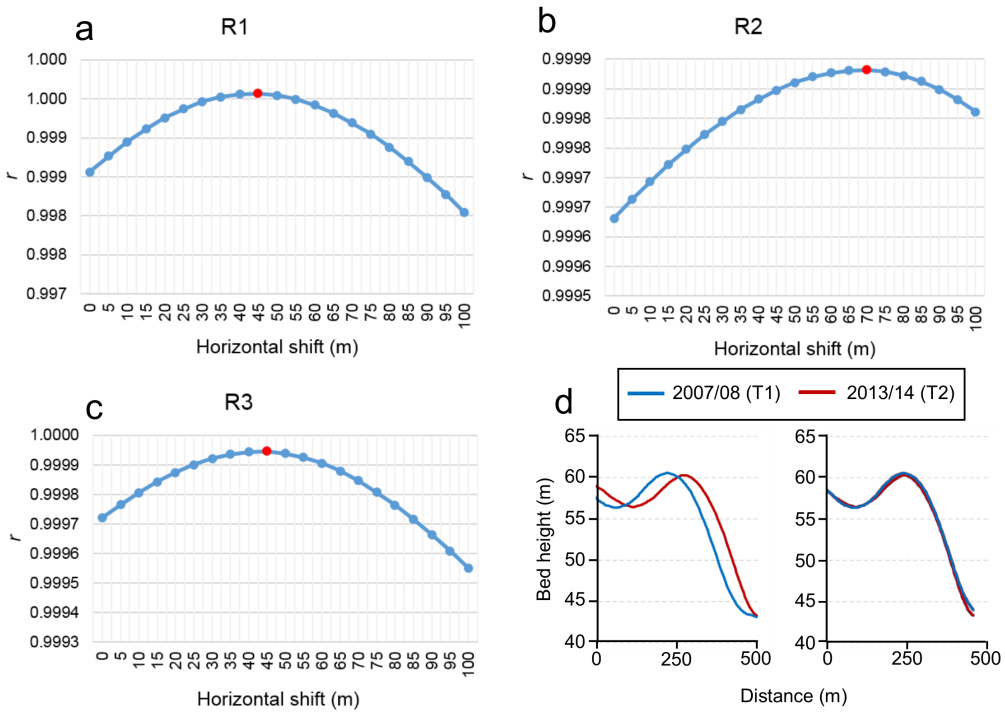

Figure 3.13: Correlation plots of horizontal bed alignment shifts for **a** repeat survey R1 **b** R2 and **c** R3. Red point indicates the horizontal shift with the highest *r* correlation. **d** example of a section of the basal reflector for survey R2 before and after a horizontal shift of 45 m was applied.

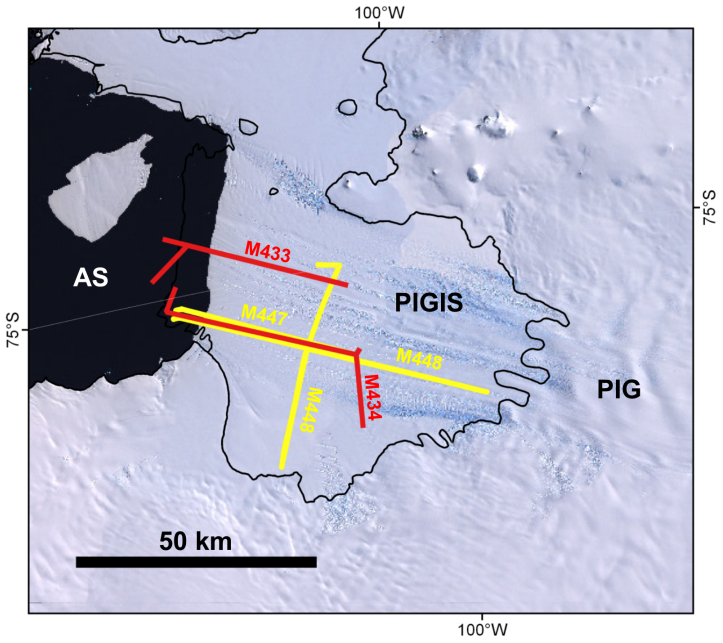

Figure 3.14: Autosub3 mission tracks. Red lines are multibeam swath bathymetry missions and yellow lines are sub-bottom profiler missions. Black line is the MODIS grounding line, background image is the LIMA Landsat image mosaic. PIG = Pine Island Glacier, PIGIS = Pine Island Glacier Ice Shelf, AS = Amundsen Sea.

3.7.1 Multibeam data processing

Multibeam swath bathymetry data were supplied by P. Dutrieux as raster files containing seafloor elevation. Prior to this, the raw data had been processed using MB-System Seafloor Mapping Software (*Caress and Chayes*, 1995) and interpolated onto a 2 m grid using a weighted near-neighbour algorithm (P. Dutrieux, pers. comm.) To aid detailed mapping of metre-scale geomorphology, I detrended the seafloor DEM by subtracting a fitted polynomial surface from the original DEM using an algorithm developed by *Hurst et al.* (2012) based on a 6-term quadratic function with the form:

$$f(x,y) - ax^2 + by^2 + cxy + dx + ey + f \tag{3.5}$$

The polynomial regression was applied to the DEM using an unweighted, square window of size L x L in which the cell of interest is at the centre. Experiments with different moving

window size were explored in order to find the optimum lengthscale to enhance subtle geomorphological features while minimizing short wavelength noise. A window size of 30 x 30 m was found to produce the best results for mapping (Fig. 3.15).

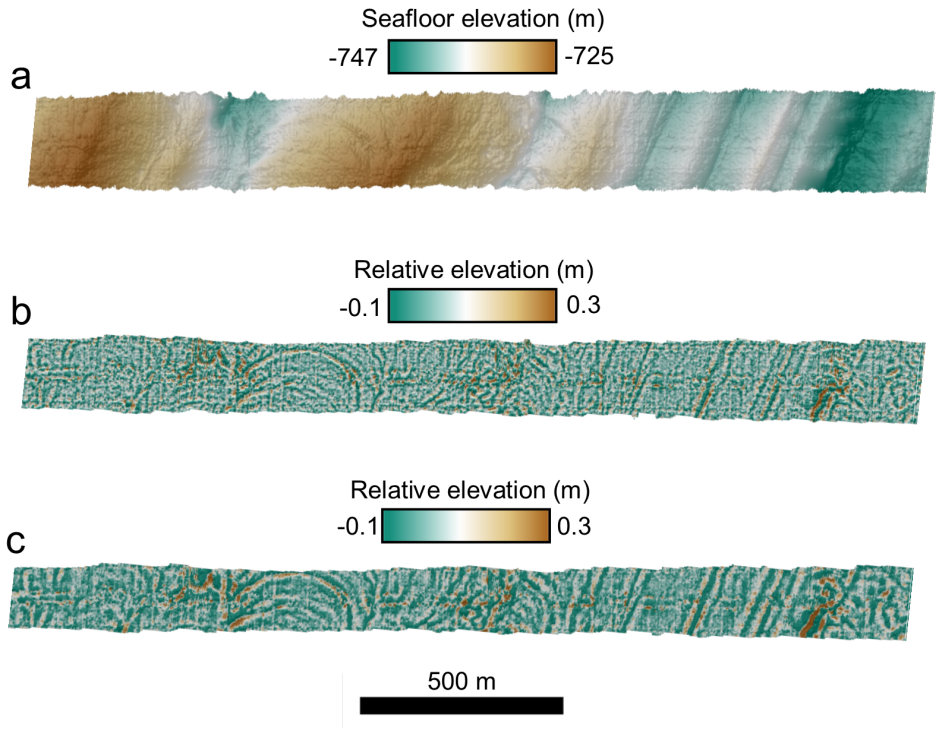

Figure 3.15: Comparison of **a** unfiltered seafloor DEM alongside detrended seafloor surface DEMs using a window size of **b** 20 m and **c** 30 m.

3.7.2 Geomorphological mapping and bedform metrics

Geomorphological mapping of multibeam DEMs was undertaken using ArcGIS v.10.1. Multiple-illumination azimuths and vertical exaggeration were applied to aid the visualisation of geomorphological features following methods of *Smith and Clark* (2005). Linear bedforms were digitized by drawing lines along the length of their crests (Fig. 3.16a) and other features were dilineated using freeform polyline and polygon shapefiles. The azimuth of lineations were extracted using the Field Calculator tool in ArcGIS. The azimuth of the polyline in degrees was determined as:

$$\alpha = \frac{180}{\pi} atan2(X_2 - X_1)(Y_2 - Y_1) \tag{3.6}$$

where X_1, Y_1 and X_2,Y_2 are the start and end points of each polyline. The spacing and amplitude of linear bedforms were calculated by extracting cross-sectional topographic profiles transverse to bedform crestlines. Following the method of *Spagnolo et al.* (2014), multiple profiles were extracted for each bedform. A mean lateral spacing was measured by averaging the crest-to-crest distance on either side of individual lineations. Only lineations with two adjacent neighbours were included in the analysis. Similarly, lineation amplitudes were measured by calculating the difference between the crestline and the lowest elevation in the troughs on either side of individual lineations and averaged to produce a single value (Fig. 3.16).

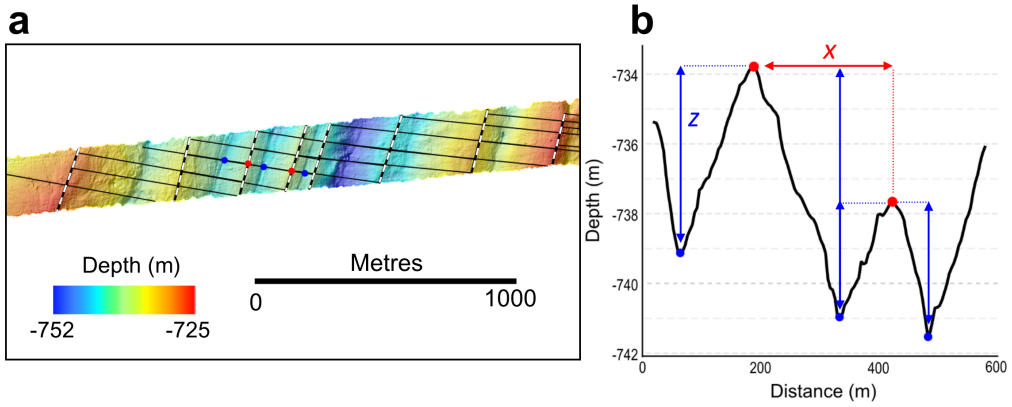

Figure 3.16: Measurement of bedform metrics. **a** Section of multibeam bathymetry from Autosub3 mission M434. Black and white dashed lines show the mapped crestlines of lineations, solid black lines show cross sectional profiles drawn for extraction of metrics. Blue dots show lineation troughs and crests are represented by red dots. **b** An example of a cross sectional profile showing the measurement of amplitude (z) and spacing x.

3.7.3 Sub-bottom profiler data processing

Sub-bottom profiler data were acquired by an Edgetech 2200 M instrument mounted on Autosub3. The system emits a chirp signal at 2-16kHz providing images of the seafloor subsurface with a vertical resolution of 6-10 cm. Navigation was achieved by dead-reckoning through an Inertial Navigation System (INS), integrated and mechanically coupled with a downward looking Acoustic Doppler Current Profiler (ADCP). Data for two missions were provided by

iSTAR project partners A. Jenkins and P. Dutrieux, involved in the ocean-based component of the iSTAR research programme. Mission M447 was flown along the direction of ice flow from seaward of the ice front into the sub-ice shelf cavity to ∼15 km seaward of the grounding line (Fig. 3.14). M448 was flown orthogonal to ice flow, along the sub-ice-shelf ridge and southern basin (Fig. 3.14). Sub-bottom profiler data were supplied as multiple raw data files for each mission (22 files for each mission). The first step taken was to concatenate these files to produce one file for each mission. Following this, data processing steps were taken with a similar approach to that described for GPR processing in section 3.5. The following processing steps were applied:

- **Assign navigation positions:** navigational data recorded by the INS were assigned to each trace.
- **Increase signal-to-noise ratio:** a band-pass Butterworth filter with lower and upper cutoffs of 1000 and 3500 kHz were was applied.
- **Correct seafloor topography:** a vertical correction was applied to account for the pitch of the AUV's flight.
- **Time-depth conversion:** data were converted from time to depth using an acoustic velocity of 1459 m s^{-1} in water. The absolute elevation was calculated by subtracting this depth from the flying height of Autosub3 recorded in the navigation data.

Figure 3.17 shows an example of raw and processed data.

This chapter has summarised the primary data acquisition and processing that underpins the analyses that now follow. I contributed significant processing to the development of 10 x 15 km bed DEMS collected for the iSTAR programme. These data are presented in Chapters 4 and 5. In Chapter 6 I use GPR data collected over three austral seasons to investigate temporal changes at the bed of PIG. Chapter 7 analyses multibeam and sub-bottom profiler data to investigate geomorphology of seafloor bedforms and sediment properties beneath PIGIS. Chapter 7 will synthesise these findings and identify the limitations of this research and recommend future work.

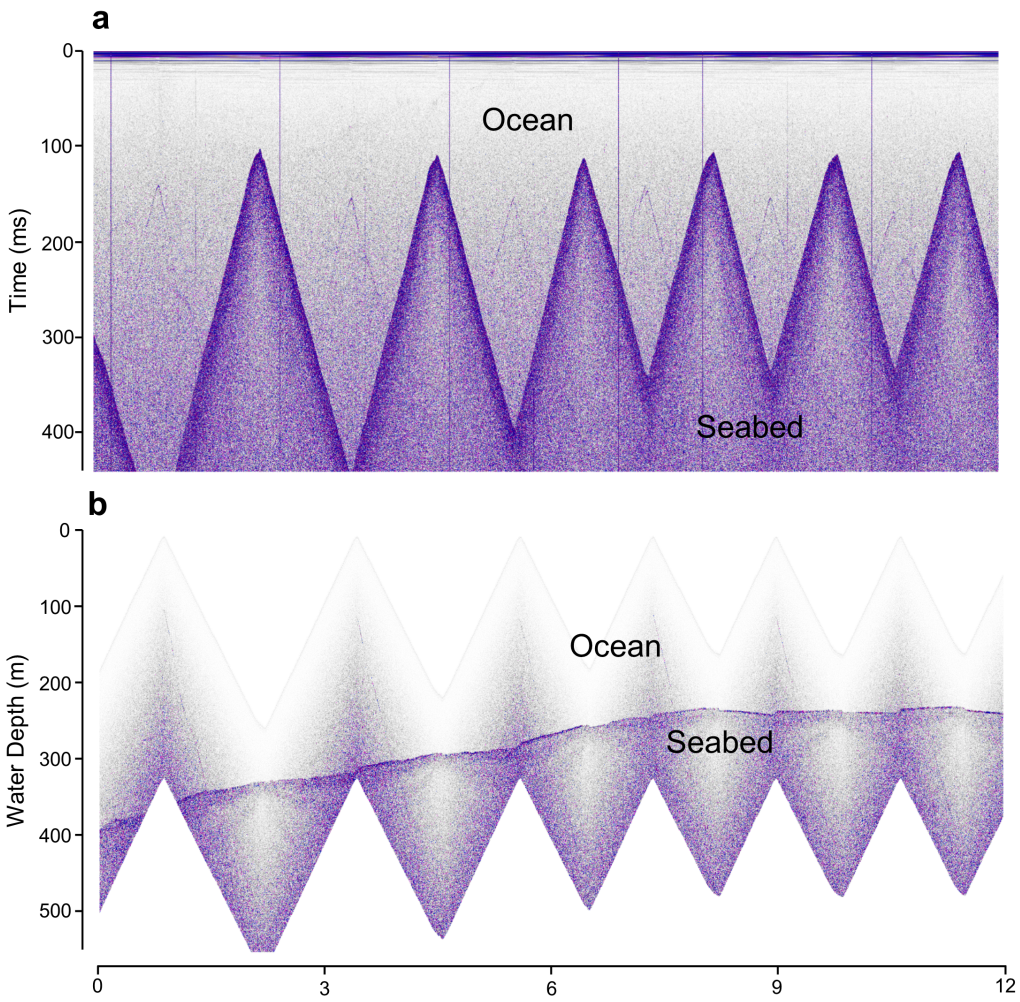

Figure 3.17: Examples of sub-bottom profiler data. **a** raw data and **b** processed data. Details of processing are provided in the text. The apparent spikes are caused by the ascending and descending flight of Autosub. The true seabed topography can be seen more clearly in **b** after correcting for Autosub's flying height.

Chapter 4

Diverse landscapes beneath Pine Island Glacier influence ice flow

A version of this chapter has been published in *Nature Communications* as:

Bingham, R.G., Vaughan, D.G., King, E.C., **Davies, D.**, Cornford, S.L., Smith, A.M., Arthern, R.J., Brisbourne, A.M., De Rydt, J., Graham, A.G., Spagnolo, M., Shean, D.E (2017). Diverse landscapes beneath Pine Island Glacier influence ice flow. *Nature communications*, 8(1), doi:10.1038/s41467-017-01597-y

I provided a major contribution to this work in data collection, processing and analysis described in the methods chapter (Chapter 3). This chapter also provides an overview of the main dataset and geographical context for the following chapters. The writing of this paper was led by my principal supervisor in collaboration with our co-authors. I contributed edits throughout the iterative writing process. A copy of the published paper is provided in Appendix A.

4.1 Abstract

The retreating Pine Island Glacier (PIG), West Antarctica, presently contributes ∼5-10% of global sea-level rise. PIG's retreat rate has increased in recent decades with associated thinning migrating upstream into tributaries feeding the main glacier trunk. To project future change requires modelling that includes robust parameterisation of basal traction, the resistance to ice flow at the bed. However, most ice-sheet models estimate basal traction from satellite-derived surface velocity, without a priori knowledge of the key processes from which it is derived, namely friction at the ice-bed interface and form drag, and the resistance to ice flow that arises

as ice deforms to negotiate bed topography. Here, we present high-resolution maps, acquired using ice-penetrating radar, of the bed topography across parts of PIG. Contrary to lower-resolution data currently used for ice-sheet models, these data show a contrasting topography across the ice-bed interface. We show that these diverse subglacial landscapes have an impact on ice flow, and present a challenge for modelling ice-sheet evolution and projecting global sea-level rise from ice-sheet loss.

4.2 Introduction

Over 40 years of satellite observations, the West Antarctic Ice Sheet (WAIS) has consistently lost ice and contributed up to a 10th of the observed rise in global sea levels (*Church et al.*, 2013; *Mouginot et al.*, 2014; *Rignot et al.*, 2014; *Christie et al.*, 2016; *Konrad et al.*, 2017; *Turner et al.*, 2017). The potential for this contribution to accelerate further as a consequence of the ice sheet's dynamical instability (*Alley et al.*, 2015; *Cornford et al.*, 2015) poses a threat to the long-term security and prosperity of the planet's coastal populations and infrastructure (*Church et al.*, 2013). However, despite advances in Earth-system modelling to constrain future change, recent projections of the Antarctic Ice Sheet's future global sea-level contribution still have a significant uncertainty (*Shepherd et al.*, 2012; *Bamber and Aspinall*, 2013). One of the greatest sources of this uncertainty is the parameterisation of basal boundary conditions in the ice-sheet models used for projection (*Joughin et al.*, 2009; *Ritz et al.*, 2015). This is most acute for the fast-flowing ice streams that discharge >90% of ice from Antarctica. A particular challenge for these models is the simulation of the basal traction generated by ice flow over its bed, which is the primary restraint on ice flow (*Joughin et al.*, 2009; *Morlighem et al.*, 2010; *Durand et al.*, 2011; *Pollard and DeConto*, 2012; *Ritz et al.*, 2015). Few observational data exist beneath Antarctic ice streams at the sub-km scale required to parameterise this complex, but crucial, interaction.

Here, we present high-resolution images of the topography underlying West Antarctica's Pine Island Glacier (PIG; Fig. 4.1-4.9). This glacier has undergone sustained retreat since at least the 1940s (*Smith et al.*, 2017b), with thinning having propagated progressively upstream from the

floating ice shelf, along the main trunk and into its tributaries over the interior basin (*Konrad et al.*, 2017). Several modelling studies have projected that the retreat and progressive upstream thinning of PIG will continue in the coming decades, potentially increasing its contributions to global sea-level rise (*Cornford et al.*, 2015; *Favier et al.*, 2014; *Seroussi et al.*, 2014b; *Nias et al.*, 2016; *Arthern and Williams*, 2017). However, the magnitude and rate of the projected contribution critically depend on the pace at which the retreat may propagate into the interior basin, which is largely controlled by the poorly constrained basal boundary conditions (*Durand et al.*, 2011; *Gasson et al.*, 2015; *Ritz et al.*, 2015; *Nias et al.*, 2016).

Our results reveal that PIG is underlain by a diverse landscape, and that the roughness of the landscape at the short wavelengths revealed by our observations impacts directly upon the ice flow. This demonstrates the predominance of form drag on ice flow, which presents a challenge for modelling the future retreat of the ice and, in turn, projecting global sea-level rise from ice-sheet loss.

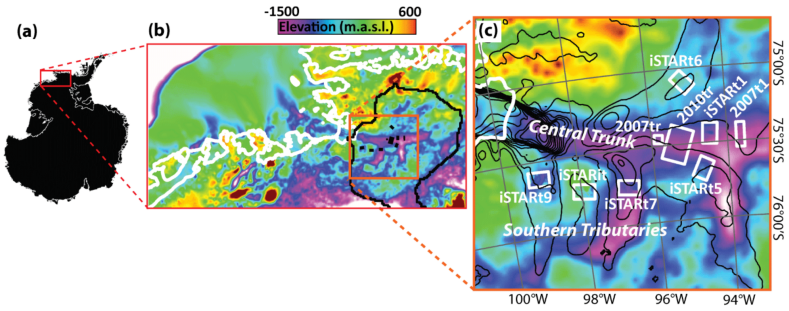

Figure 4.1: Map of study area and location of radar grids.**a** Location and context. In **b**, the colourmap shows regional bed topography from Bedmap2 (*Fretwell et al.*, 2013), the black line is the ice divide, the white line is the grounding line (*Bindschadler et al.*, 2011), and high-resolution survey patches are shown as black rectangles. Locations of offshore bathymetry shown in Fig. 4.10c, f are marked. **c** uses the same schema but demarcating survey patches with white rectangles, labelled by season of data acquisition (2007/08, 2010/11 and "iSTAR" = 2013/14) and an end label denoting the location (where "tr" = trunk; "it" = intertributary and "t1, t5..." denotes tributaries numbered after (*Stenoien and Bentley*, 2000). Surface ice velocities (*Rignot et al.*, 2011a) contoured at 100 m intervals are also shown.

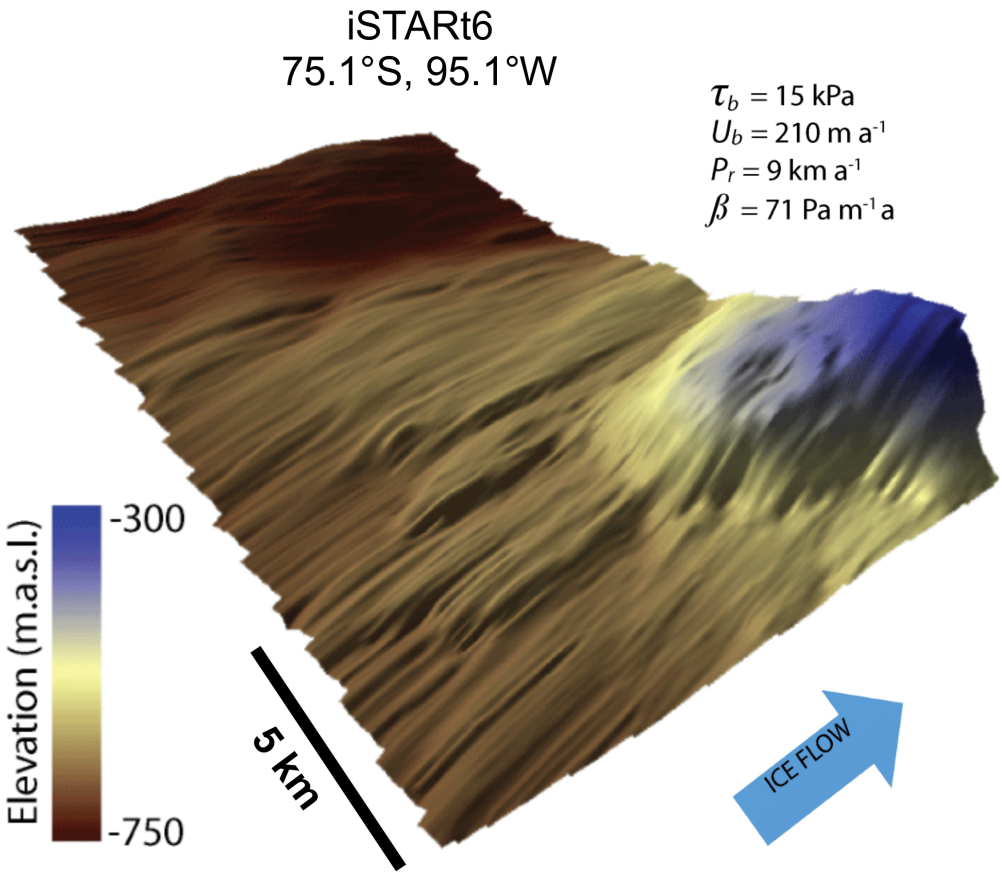

Figure 4.2: Perspective view of the bed beneath Pine Island Glacier for site iSTARt6, together with parameters of ice flow. Vertical exaggeration in the image = 10. τ_b and U_b are the mean basal shear stress (kPa) and mean basal ice velocity (m a^{-1}) from model inversion (*Arthern et al.*, 2015); P_r is the measured upstream propagation rate of ice thinning per ice-stream tributary from 1992 to 2015 using a thinning/non-thinning threshold of 1.0 m a^{-1} (*Konrad et al.*, 2017) and β is the inverted basal traction coefficient equal to τ_b/U_b.

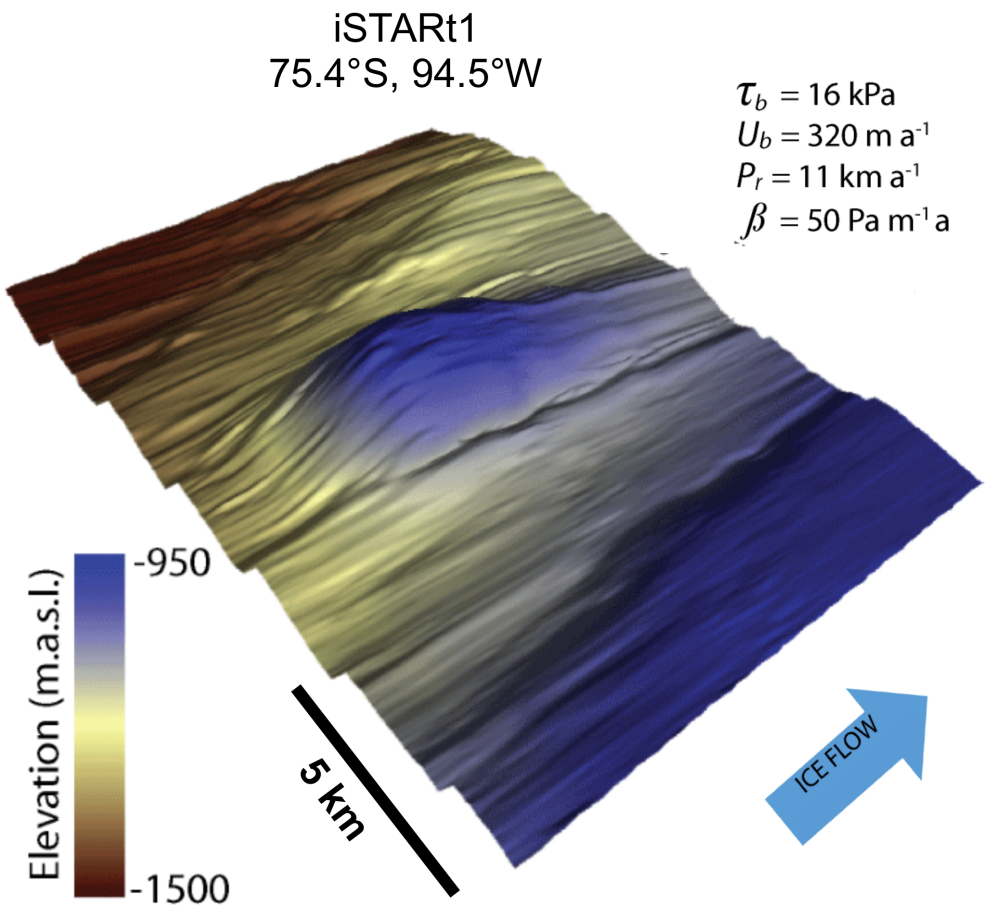

Figure 4.3: Perspective view of the bed beneath Pine Island Glacier for site 2007t1, together with parameters of ice flow. Vertical exaggeration in the image = 10. τ_b and U_b are the mean basal shear stress (kPa) and mean basal ice velocity (m a^{-1}) from model inversion (*Arthern et al.*, 2015); P_r is the measured upstream propagation rate of ice thinning per ice-stream tributary from 1992 to 2015 using a thinning/non-thinning threshold of 1.0 m a^{-1} (*Konrad et al.*, 2017) and β is the inverted basal traction coefficient equal to τ_b/U_b.

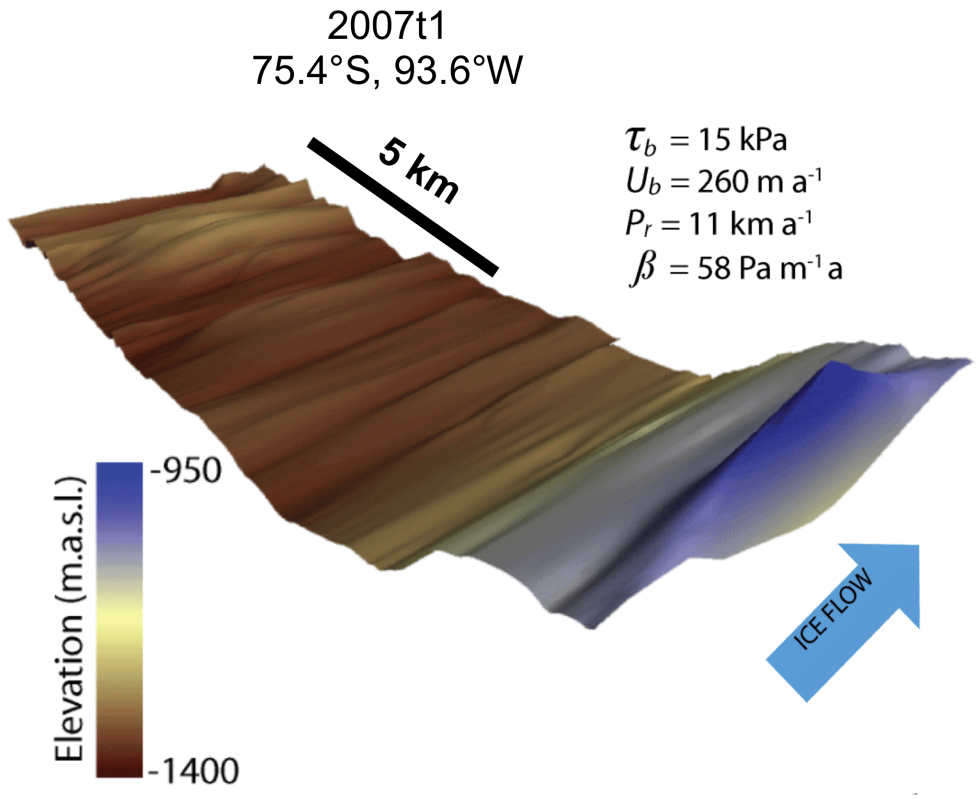

Figure 4.4: Perspective view of the bed beneath Pine Island Glacier for site 2007t1, together with parameters of ice flow. Vertical exaggeration in the image = 10. τ_b and U_b are the mean basal shear stress (kPa) and mean basal ice velocity (m a^{-1}) from model inversion (*Arthern et al.*, 2015); P_r is the measured upstream propagation rate of ice thinning per ice-stream tributary from 1992 to 2015 using a thinning/non-thinning threshold of 1.0 m a^{-1} (*Konrad et al.*, 2017) and β is the inverted basal traction coefficient equal to τ_b/U_b.

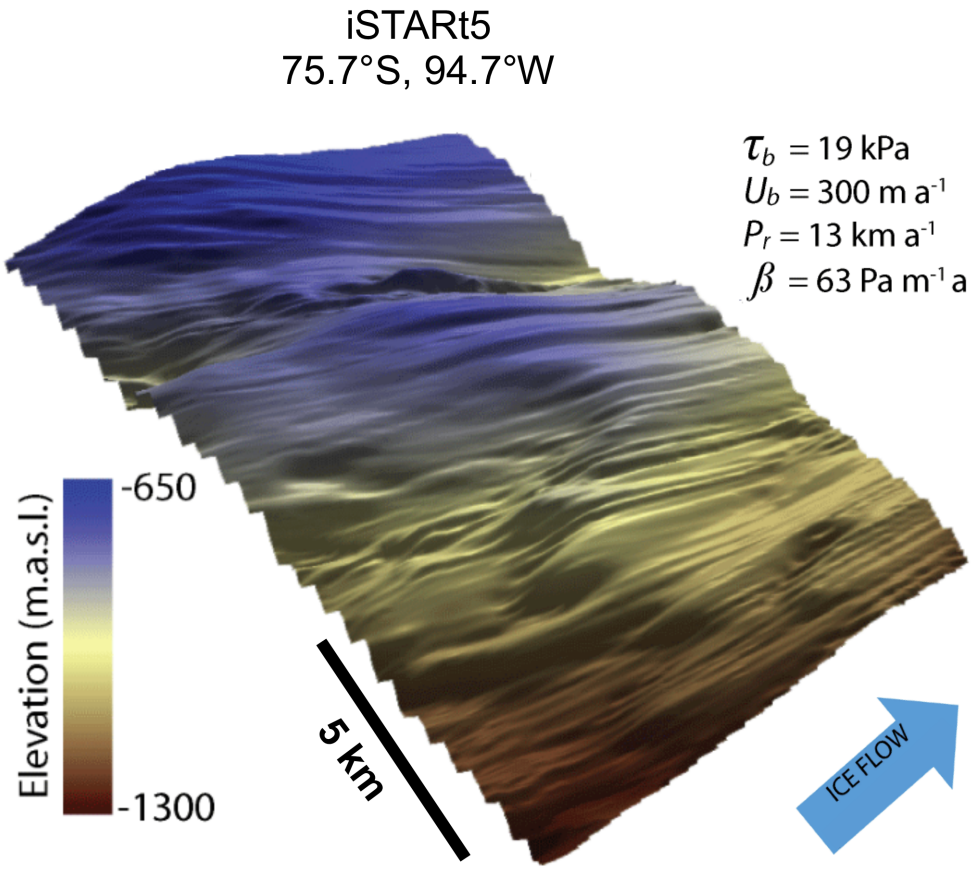

Figure 4.5: Perspective view of the bed beneath Pine Island Glacier for site iSTARt5 , together with parameters of ice flow. Vertical exaggeration in the image = 10. τ_b and U_b are the mean basal shear stress (kPa) and mean basal ice velocity (m a^{-1}) from model inversion (*Arthern et al.*, 2015); P_r is the measured upstream propagation rate of ice thinning per ice-stream tributary from 1992 to 2015 using a thinning/non-thinning threshold of 1.0 m a^{-1} (*Konrad et al.*, 2017) and β is the inverted basal traction coefficient equal to τ_b/U_b.

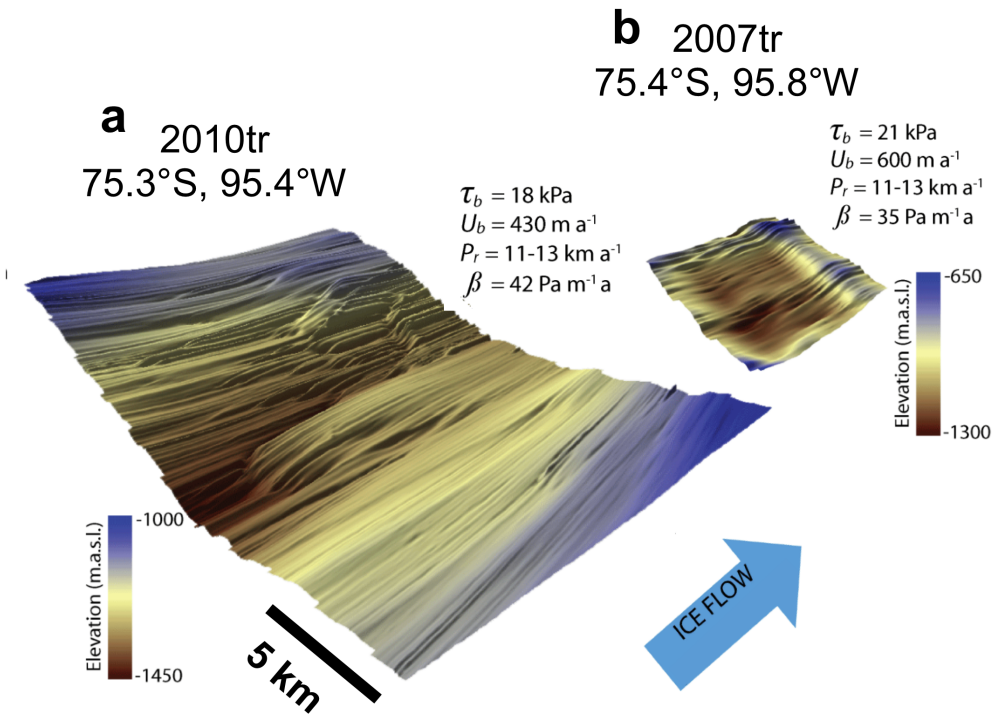

Figure 4.6: Perspective view of the bed beneath Pine Island Glacier for **a** site 2010tr and **b** site 2007tr, together with parameters of ice flow. Vertical exaggeration in the image = 10. τ_b and U_b are the mean basal shear stress (kPa) and mean basal ice velocity (m a^{-1}) from model inversion (*Arthern et al.*, 2015); P_r is the measured upstream propagation rate of ice thinning per ice-stream tributary from 1992 to 2015 using a thinning/non-thinning threshold of 1.0 m a^{-1} (*Konrad et al.*, 2017) and β is the inverted basal traction coefficient equal to τ_b/U_b.

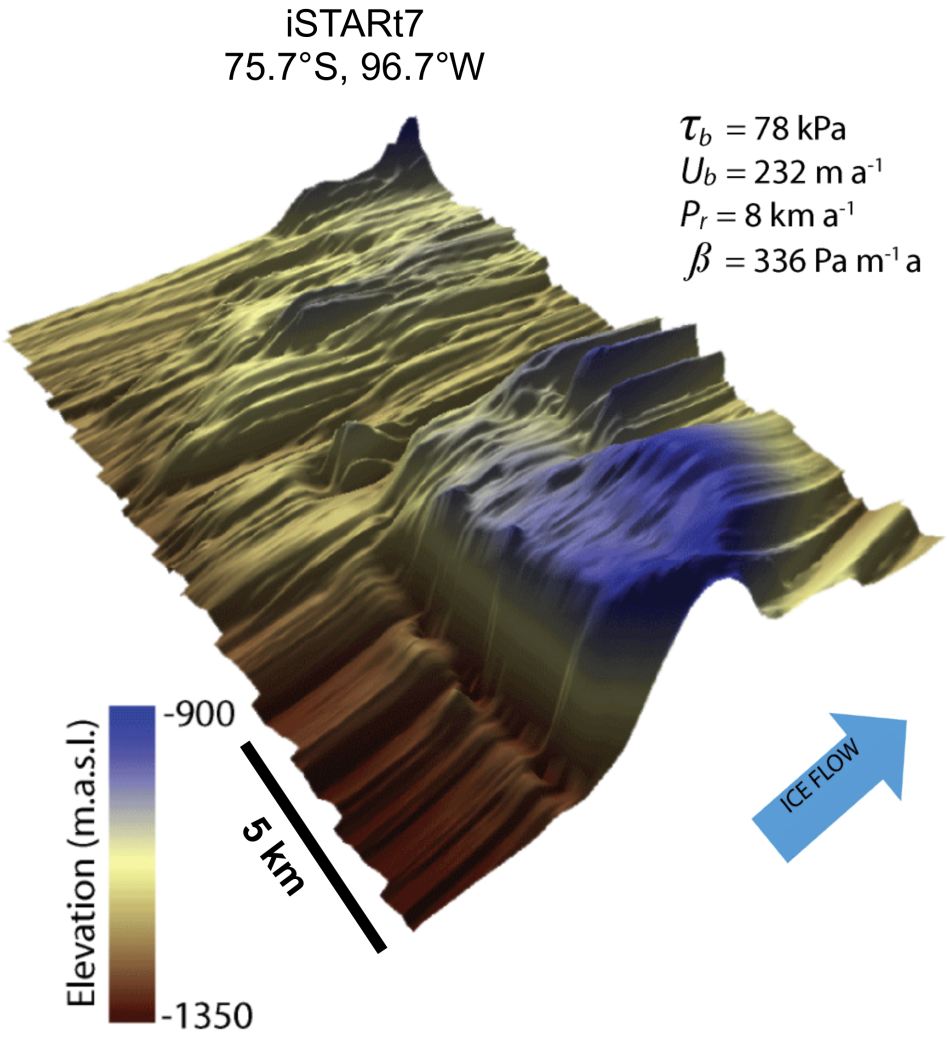

Figure 4.7: Perspective view of the bed beneath Pine Island Glacier for site iSTARt7, together with parameters of ice flow. Vertical exaggeration in the image = 10. τ_b and U_b are the mean basal shear stress (kPa) and mean basal ice velocity (m a^{-1}) from model inversion (*Arthern et al.*, 2015); P_r is the measured upstream propagation rate of ice thinning per ice-stream tributary from 1992 to 2015 using a thinning/non-thinning threshold of 1.0 m a^{-1} (*Konrad et al.*, 2017) and β is the inverted basal traction coefficient equal to τ_b/U_b.

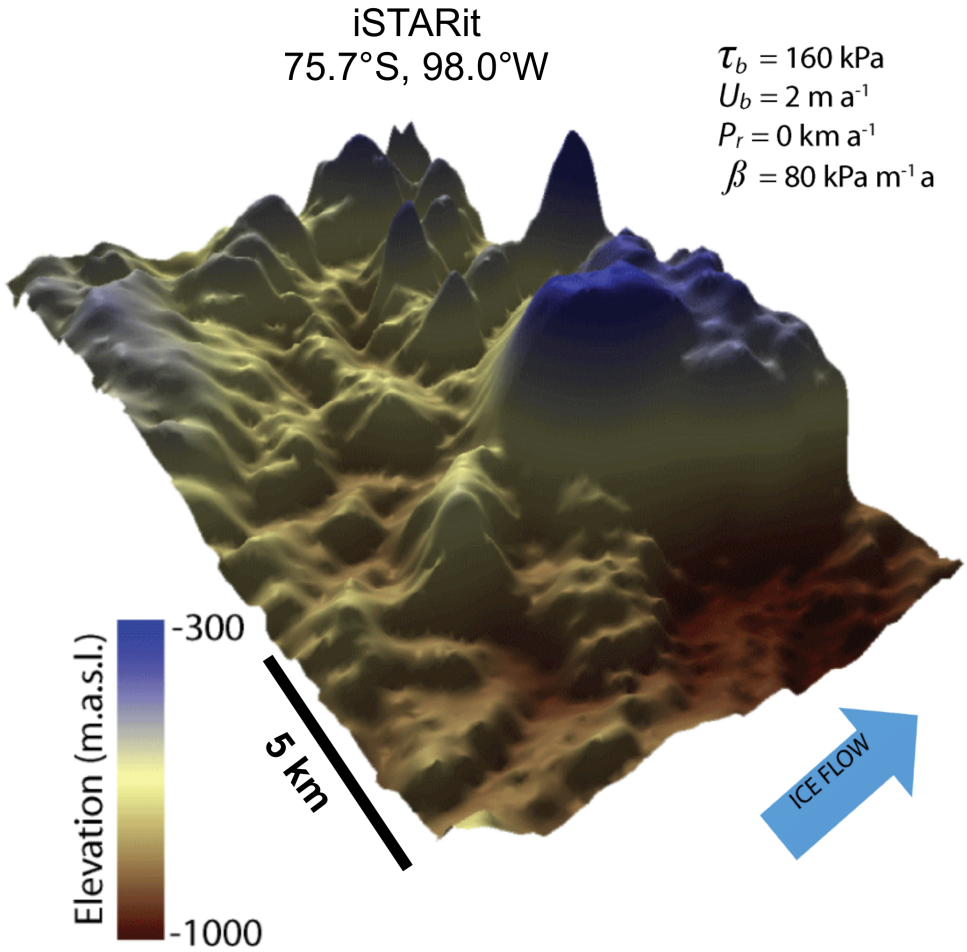

Figure 4.8: Perspective view of the bed beneath Pine Island Glacier for site iSTARit, together with parameters of ice flow. Vertical exaggeration in the image = 10. τ_b and U_b are the mean basal shear stress (kPa) and mean basal ice velocity (m a^{-1}) from model inversion (*Arthern et al.*, 2015); P_r is the measured upstream propagation rate of ice thinning per ice-stream tributary from 1992 to 2015 using a thinning/non-thinning threshold of 1.0 m a^{-1} (*Konrad et al.*, 2017) and β is the inverted basal traction coefficient equal to τ_b/U_b.

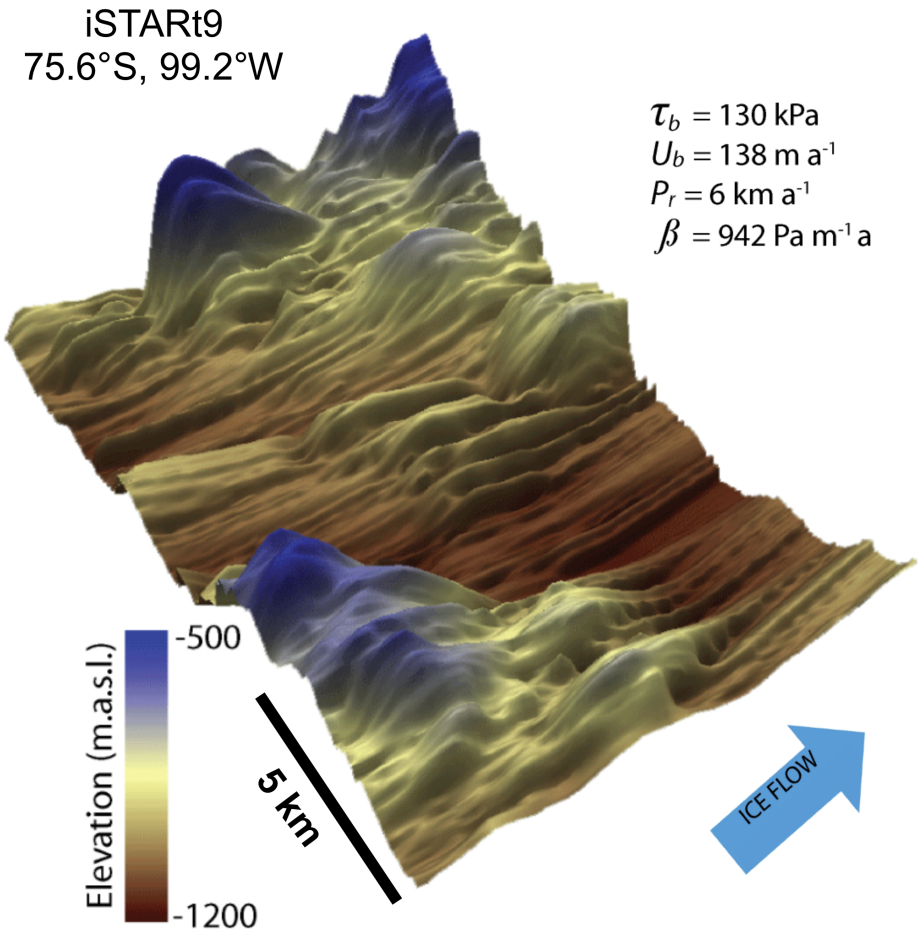

Figure 4.9: Perspective view of the bed beneath Pine Island Glacier for site iSTARt9, together with parameters of ice flow. Vertical exaggeration in the image = 10. τ_b and U_b are the mean basal shear stress (kPa) and mean basal ice velocity (m a^{-1}) from model inversion (*Arthern et al.*, 2015); P_r is the measured upstream propagation rate of ice thinning per ice-stream tributary from 1992 to 2015 using a thinning/non-thinning threshold of 1.0 m a^{-1} (*Konrad et al.*, 2017) and β is the inverted basal traction coefficient equal to τ_b/U_b.

4.3 Methods

Methods for producing digital elevation models (DEM) of the bed for this chapter are described in sections 3.3-3.5 of Chapter 3. Radar coverage for the datasets are shown in Figure 3.4. Bed roughness for Table 4.1 and Fig. 4.11 was calculated using a forward fast Fourier transform (FFT) technique described in *Bingham and Siegert* (2007b) and in Chapter 5.2.1. The code enables the derivation of roughness along 2D tracks using moving windows of predefined length. We applied the code along 2-km moving windows, which are sufficiently long to capture multiple streamlined landforms when applied across flow, yet small enough to capture roughness variability within each of the survey patches.

4.4 Results

4.4.1 High-resolution images of Pine Island Glacier bed

Our data comprise the first set of radar surveys that captures sub-kilometre-scale basal topography across an Antarctic glacial catchment, with a total coverage of $\sim$1500 km^2, or $\sim$15%, of PIG's main trunk and tributaries (defined as surface ice flow >200 m a^{-1}). The data, obtained by 1-3 MHz over-snow radar during three austral field seasons (2007/08, 2010/11 and 2013/14), were typically acquired in 10 x 15 km patches. The data comprise a total of nine patches imaged at 40 m (cross-flow) x 100 m (along-flow) grid resolution (Fig. 4.2-4.9) and, as a complete set, constitute by far the largest and most spatially detailed observational data set of a contemporary subglacial landscape ever acquired. Full details of the radar data acquisition and processing, and generation of these images, are given in Chapter 3.

The data reveal diverse subglacial environments across PIG that contrast with the smooth interpolated bed from prior airborne radar surveys (Fig. 4.2), and which has been used to define the boundary condition in most ice-sheet modelling of the last decade (*Vaughan et al.*, 2006; *Fretwell et al.*, 2013; *Pattyn et al.*, 2013; *Arthern and Williams*, 2017). All but one of the sites displays lineated bedforms aligned with the current ice flow, which are typical of features found on palaeo-ice-stream beds (*Clark*, 1993; *Stokes and Clark*, 2001; *Jakobsson*

et al., 2012; *Livingstone et al.*, 2012; *Nitsche et al.*, 2013; *Spagnolo et al.*, 2014) (Fig. 4.2). The exception is in the inter-tributary slow-flowing area (Fig. 4.8), where no streamlined topography is seen. Broadly, these observations confirm previous assertions that the pattern of PIG's ice-flow configuration has not changed significantly for thousands of years, despite variations in ice discharge (*Vaughan et al.*, 2006; *Karlsson et al.*, 2012). Between the different patches, however, the character and dimensions of the lineations vary (Table 4.1). Beneath the main trunk, subglacial lineations have vertical heights of ∼2-10 m (measured trough-to-crest) and typical widths of 2-400 m redolent of Mega-Scale Glacial Lineations (MSGL) moulded into subglacial sediments (*Clark*, 1993; *Stokes and Clark*, 2001; *Jakobsson et al.*, 2012; *Livingstone et al.*, 2012) (Figs. 4.2-4.6 and 4.10 b, c; Table 4.1). Beneath the southern tributaries, much larger lineated bedforms are present, with vertical heights of ∼25- 80 m and widths of 300-1000 m (Fig. 4.7 and 4.9; Table 4.1). In some locations, the smaller lineations are superimposed over larger basal features, for instance in the main trunk where an ∼5-km-wide, ∼400-m-high subglacial protuberance projects upwards from an otherwise flat bed (Fig. 4.3) and in the southeastern tributary t5 where ∼1-km-wavelength MSGL are superimposed over, and sometimes oblique to, a set of along-flow lineations with an ∼5-km spacing (Fig. 4.5).

Table 4.1: Parameters pertaining to ice flow and basal topography across each survey patch

Site	Mean basal shear stress τ_b (kPa)	Mean basal ice velocity U_b (m a^{-1})	Measured upstream propagation of thinning P_r (km a^{-1})	Inverted basal traction coefficient β	Dominant vertical height of topography (m)	Typical width of streamlined features (m)	Normalised across-flow roughness using a 2-km moving window	Normalised along-flow roughness using a 2-km moving window
iSTARt6	15	210	9	71	2-6	450-550	0.08 (new) 0.10 (BM2)	0.001 (new) 0.04 (BM2)
iSTARt1	16	320	11	50	2-3	100-300	0.77 (new) 0.24 (BM2)	0.72 (new) 0.04 (BM2)
2007t1	15	260	11	58	2-6	200-400	0.28 (new) 0.09 (BM2)	0.04 (new) 0.002 (BM2)
iSTARt5	19	300	13	63	3-6 (MSGL)100 (larger features)	500-800 (MSGL)5000 (larger features)	0.43 (new) 0.24 (BM2)	0.07 (new) 0.16 (BM2)
2010tr	18	430	12	42	5-10	300-400	0.18 (new) 0.14 (BM2)	0.04 (new) 0.08 (BM2)
2007tr	21	600	12	35	2-6	200-300	0.05 (new) 0.08 (BM2)	0.04 (new) 0 (BM2)

The observed heterogeneity in sub-kilometre subglacial topography likely results from a combination of glacial activity and the inherited underlying geology. Seismic surveys have revealed that soft, deformed subglacial sediments are ubiquitous beneath the ice in all of our surveyed regions (*Smith et al.*, 2013; *Brisbourne et al.*, 2017, Appendix D), regardless of the amplitude of the radar-imaged subglacial features. The vertically subtle MSGL present in most of our patches have dimensions consistent with MSGLs from other settings that have been interpreted as the topographic expression of ice flow over deformable beds (*King et al.*, 2009; *Jakobsson et al.*, 2012; *Spagnolo et al.*, 2014, 2016) (Fig. 4.2). The larger features in the subglacial landscape, such as the ∼400-m-high protuberance within the central trunk (Fig. 4.3), the >300-m cliff which basal ice overrides in one southern tributary (Fig. 4.7) and the >100-m-high ridges that are seen within both southern tributaries (Fig. 4.7 and 4.9), all have amplitudes far exceeding those of MSGL recorded from any deglaciated setting (*Spagnolo et al.*, 2014), and probably express components of the underlying geology, draped by deforming sediments a few 10 s of metres thick (*Brisbourne et al.*, 2017, Appendix D). PIG's trunk is bounded to the south by gravity anomalies indicative of a thicker crust, often associated with a harder subglacial bedrock (*Jordan et al.*, 2009), and one explanation for the rougher basal topography observed in PIG's southern tributaries (Fig. 4.7-4.9) is that the substrate here is substantially tougher to erode and the subglacial landscape is less mature.

4.4.2 Implications for ice-sheet modelling projections

The magnitude of ice flow through much of PIG dictates that the major component must result from basal motion, being a combination of sliding of ice over its bed, and deformation of the uppermost layers of that bed (*Arthern et al.*, 2015). Under such conditions, the resistive force exerted by the bed on the overlying ice sheet involves two processes: basal friction at the ice/bed interface and/or in a layer of deforming basal sediments (*Iverson and Zoet*, 2015); and form drag, the resistance to ice flow as ice deforms across and around basal obstacles (*MacAyeal*, 1987). A fully three-dimensional ice-sheet model might naturally simulate form drag arising from basal features longer than its horizontal resolution, but cannot be expected to simulate form drag not represented in the subglacial topographic model on which it rests

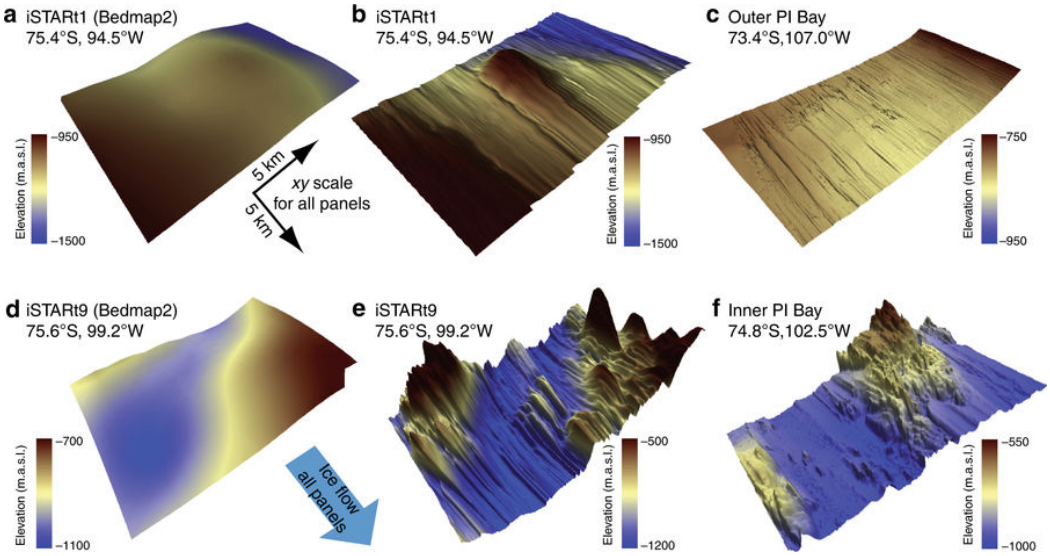

Figure 4.10: Comparison of surveyed beds beneath Pine Island Glacier with those used in ice-sheet modelling and imaged in selected palaeo-ice-streams. **a** Bed topography at site iSTARt1 (location in Fig. 4.1) from previous knowledge (*Fretwell et al.*, 2013). **b** New bed topography (alternative perspective view to Fig. 4.3). **c** Analogous subsample of bed topography from outer Pine Island Bay imaged from data presented in *Jakobsson et al.* (2012); patch location marked on Fig. 4.1b. **d** Bed topography at site iSTARt9 (location in Fig. 4.1) from previous knowledge (*Fretwell et al.*, 2013). **e** New bed topography (alternative perspective view to Fig. 4.9). **f** Analogous subsample of bed topography from inner Pine Island Bay imaged from data presented in *Nitsche et al.* (2013); patch location marked in Fig. 4.1b

nor, indeed, due to features of wavelengths shorter than it can resolve. Since neither basal friction nor form drag can currently be predicted from observable parameters, most models are initialised by an inversion which yields a field of basal traction (a.k.a. slipperiness) that allows the model to match the observed ice-surface velocity and/or elevation changes (*Joughin et al.*, 2009; *Morlighem et al.*, 2010; *Durand et al.*, 2011; *Pollard and DeConto*, 2012; *Pattyn et al.*, 2013; *Arthern et al.*, 2015; *Ritz et al.*, 2015). It is clear that the short-wavelength bed roughness shown in our data can explain much of the variability in the traction coefficient (β in Fig.4.2-4.9; Table 4.1 derived by the initialisation inversion in one model (*Arthern et al.*, 2015) (Fig. 4.11). Given that seismic data indicate broadly similar properties in subglacial sediments across the PIG catchment (*Smith et al.*, 2013; *Brisbourne et al.*, 2017), we conclude that much of the variability in the basal traction must be related to unresolved bed topography.

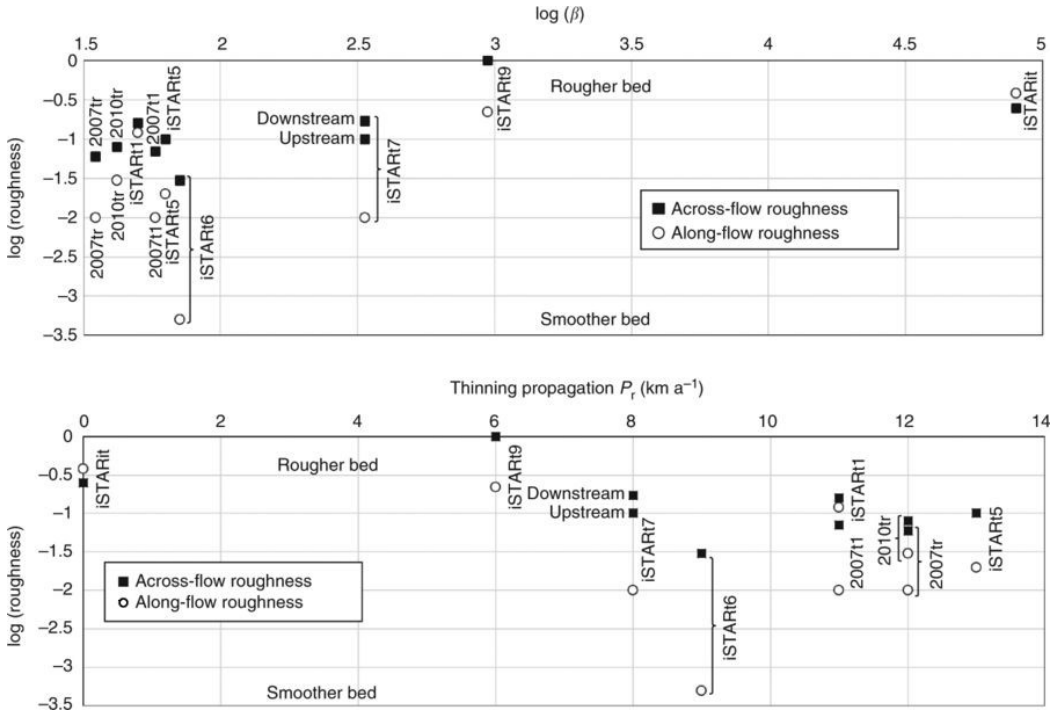

Figure 4.11: Influence of bed roughness on inverted basal traction and inland propagation of ice-stream thinning. Table 4.1 caption describes the derivation of basal traction β and inland propagation of thinning P_r. Basal roughness has been measured across and along flow at each patch in 2-km moving windows. In all cases except site iSTARit, the along-flow profiles are smoother than across-flow profiles, as expected in locations of streamlining

4.5 Discussion

Many state-of-the-art Antarctic ice-sheet models use the "Bedmap2" basal topography (*Fretwell et al.*, 2013) or derivations thereof (*Rignot et al.*, 2014). This topography was derived from unevenly distributed ice-bed elevation measurements spaced between tracks by many ice thicknesses, and interpolated onto a regular 5-km grid and, although supplied at 1-km resolution, only 17% of 5-km cells in Bedmap2 contained measurements (*Fretwell et al.*, 2013). Thus, Bedmap2 contains limited information on bed roughness, even for length scales >10 times the ice thickness. Our data thus show that significant, and potentially influential, bed topography occurs throughout PIG (and presumably other ice streams) on length scales of ∼5-50% of the ice thickness.

The issue of the degree to which basal traction arises from friction or form drag becomes more significant when models are used for projection. To achieve projections, most models

are run from the initialised condition with an unchanging field of traction coefficient varying according to a heuristic parameterisation of bed rheology, ranging from linear viscous to plastic. The choice of this parameterisation has a substantial impact on the timing and magnitude of ice loss (*Ritz et al.*, 2015). However, while basal friction is likely to be a highly dynamic field, evolving as water melts, flows and refreezes, and subglacial till is mobilised and refrozen (*Christoffersen and Tulaczyk*, 2003), form drag is likely to be considerably more static, defined primarily by the size and orientation of bedrock undulations and protuberances. Recent changes in PIG already indicate the potential importance of this factor, in as much as satellite data have shown that the rate of upstream propagation of ice thinning on PIG varies considerably between the tributaries, the southerly tributaries with rough beds showing 2-3 times slower propagation than the smoother tributaries (*Konrad et al.*, 2017) (Table 4.1; Fig. 4.11b). In summary, the new data show that the basal traction (hence ice flow) of Pine Island Glacier is much more heavily influenced by form drag, i.e., as opposed to basal friction, than has previously been shown to be the case.

Our data provide insight into the topographic diversity that exists even within one subglacial basin, let alone the entire ice sheet, which cannot adequately be represented in ice-sheet models. Given that the basal boundary is already identified as a major source of uncertainty in model projections (*Gasson et al.*, 2015; *Nias et al.*, 2016), they expose an urgent need to develop techniques for efficient measurement or more intelligent indirect estimation of short-wavelength subglacial topography beneath other vulnerable ice streams. One prospect for recovering short-wavelength subglacial topography may be provided by airborne swath-radar techniques that are currently under development (*Wang et al.*, 2016). Until such independent evaluation of form drag and basal friction is integrated into models, the current generation of ice-sheet models will be hampered in establishing projections of ice loss and sea-level rise. As an immediate step, the new data now make it possible to run data-informed experiments to develop adequate parameterisations of short-wave form drag on large outlet glaciers and ice streams, and in doing so expand our theoretical knowledge of its effects on ice flow, building upon existing idealised treatments (*Fowler*, 1979; *Schoof*, 2002).

The issues that we highlight will be particularly acute in PIG's neighbour, Thwaites Glacier,

which holds the potential for rapid and irreversible retreat, and a considerable contribution to sea-level rise (*Alley et al.*, 2015). Thwaites Glacier's lower reaches appear to exhibit a similarly high basal traction to the roughest of our patches (*Joughin et al.*, 2009; *Arthern et al.*, 2015), and may thus contain a similarly dramatic basal topography, but apparently already show a more rapid inland propagation of thinning than even the smoothest tributaries on PIG (*Konrad et al.*, 2017). Here, the significance of the interplays between basal topography, which may be sufficient to pause the retreat of the grounding line, and the static and dynamic contributions to basal traction, have yet to be explored.

Chapter 5

Sub-kilometre roughness signature of the bed of Pine Island Glacier, West Antarctica: implications for subglacial landscape evolution and ice stream dynamics.

The previous chapter introduced the topographic datasets and provided a first impression of the influence of subglacial roughness with respect to ice flow. In this chapter I investigate the role of roughness in much greater detail, exploring the orientation and wavelength with respect to ice flow and landscape evolution.

5.1 Introduction

Investigating the basal properties of ice streams is a key component for improving knowledge of the present and future flow dynamics of ice streams. This motive has driven the acquisition of large geophysical datasets that reveal the topography beneath ice sheets. Characterising the basal roughness (vertical variation with horizontal distance) is a common approach used to quantify the topographic signature of the basal interface, to improve the understanding of subglacial landscape evolution and ice-stream bed properties.

In Antarctica, basal roughness has been extracted from aerogeophysical survey data at at regional and continental scales (e.g. *Siegert et al.*, 2004; *Taylor et al.*, 2004; *Rippin et al.*, 2006; *Bingham and Siegert*, 2009; *Rippin et al.*, 2011). From these studies, a broad picture

of rough beds beneath slow-flowing ice sheet interiors and smooth beds beneath ice streams has emerged. This distribution of bed roughness is considered to reflect contrasts in basal conditions indicative of warm-based flow over smooth, deforming sediments or cold-based ice frozen to rough bedrock (*Siegert et al.*, 2005b; *Bingham and Siegert*, 2007b; *Rippin et al.*, 2014). A more detailed understanding of the relationship between bed roughness, basal conditions and ice dynamics has been restricted by the spatial resolution at which roughness can be analysed. This is largely a consequence of the resolution and density of data available from aerogeophysical surveys. However, the methods applied to subglacial environments were originally developed to investigate deglaciated terrain at much finer spatial scales (*McCarroll and Nesje*, 1996; *Hubbard et al.*, 2000). More recent work has focussed on investigating bed roughness at sub-kilometre scales using offshore bathymetric data and terrestrial Lidar data, providing an opportunity to investigate basal roughness at higher resolution. By applying Fourier spectral analysis of glaciated and non-glaciated terrains to high-resolution DEMs, *Spagnolo et al.* (2017) revealed a periodic signature indicative of instability-driven formation of mega-scale glacial lineations. *Spagnolo et al.* (2017) and *Gudlaugsson et al.* (2013) also find that roughness is highly anisotropic, with the lowest roughness found in the inferred direction of palaeo-ice flow. Analysis of bed roughness at similarly high resolution has not yet been applied to contemporary ice-stream beds. Such analyses are important for understanding the relationships between subglacial landscape evolution, bedform genesis and ice dynamics.

Another key aspect of subglacial roughness which is important to future projections of glacier dynamics its role in creating resistance to ice flow as ice deforms around subglacial obstacles (form drag) (*MacAyeal*, 1987). In the absence of high-resolution bed data, ice-sheet models typically adopt an inversion method to calculate basal traction that matches observations of ice-surface velocity or elevation change (*Joughin et al.*, 2009; *Morlighem et al.*, 2010; *Durand et al.*, 2011; *Pollard and DeConto*, 2012; *Arthern et al.*, 2015). Using the same high-resolution data presented in this chapter, Chapter 4 found that much of the variability in basal traction estimated by this approach could be explained by short-wavelength bed roughness not represented in lower resolution bed datasets. However, it is not clear what aspects of this roughness (e.g. orientation and wavelength) are most critical for impeding ice flow.

In this chapter, I address these issues by utilising high-resolution bed topography acquired from ground-based radar surveys from Pine Island Glacier (PIG), West Antarctica (Fig. 5.2a). In Section 5.3.2 I first explore the spatial distribution of bed roughness in relation to subglacial bedforms. Section 5.3.3 assess how interpolation of bed data affects calculated bed roughness. Section 5.3.4 then assess how varying the orientation of bed profiles and moving window length alters calculated roughness. Section 5.3.5 compares these results to previous roughness analysis conducted for PIG. Section 5.4 then discusses the implications of these results for landscape evolution and ice flow.

5.2 Methods

The methods used to generate digital elevation models of the bed are described in sections 3.3-3.5. 3-dimensional images of basal topography are shown in Figs 4.2-4.9 in the previous chapter.

5.2.1 Roughness analysis

To perform roughness analysis, the first step was to extract bed elevation data. In order to address the question of how grid orientation affects roughness, data were extracted from across-flow and along-flow profiles. For across-flow profiles I used the bed elevation data extracted from radar bed picks. These consisted of 22 lines, 15 km in length with a spacing of 500 m and a sampling interval of 5 m (see Fig. 3.4). Because no along-flow radar profiles were acquired, for along-flow roughness analysis I extracted bed elevation from interpolated bed DEMs. This was achieved in QGIS software by constructing a vector grid with the same dimensions and sampling interval as across-flow radar survey grids (22 line with a 500 m spacing sampled at 5 m intervals).

There are many ways to measure the roughness of surfaces (*Shepard et al.*, 2001; *Smith*, 2014). The most common method applied to the investigation of subglacial terrain is by spectral analysis using the Fast Fourier Transform (FFT) (e.g. *Taylor et al.*, 2004; *Bingham and Siegert*, 2007b, 2009; *Li et al.*, 2010; *Rippin et al.*, 2011). Prior to this thesis, *Rippin et al.* (2011) used

the FFT method to investigate the basal roughness of PIG and was the first roughness analysis performed in this region. However, their study used airborne data where along-track soundings of the bed were sampled at 15-30 m intervals along flightlines with a spacing of 30 km (data coverage presented in *Vaughan et al.*, 2006). The novelty of the data presented here is the ability to calculate subglacial roughness at significantly higher resolution than in all previous studies of Antarctic bed roughness and to analyse the results where we have high resolution data of the bed in three dimensions (see Fig. 5.2b).

To test the viability of using bed elevation extracted from the interpolated bed elevation DEM I compared the bed elevation of additional, along-flow radar surveys driven during transit between study sites. Figure 5.1 shows a comparison between the processed radar data from these additional along-flow transit lines (Fig. 5.1a) compared to bed elevation extracted from the interpolated DEM from the same profiles (Fig. 5.1b). This analysis shows that the interpolated bed data generally reflects the genuine bed elevation. This suggests that in the absence of along-flow radar data, the along-flow bed elevation from interpolated data provides a viable substitute for roughness analysis. However, there are some differences particularly for sites iSTARt1 and t9. This is investigated further in section 5.3.3.

FFT analysis is performed on moving windows of 2^N data points that track along the radar-sounded bed reflector. Previous studies have adopted a minimum recommended value of N=5, providing a window of 32 data points (*Oran Brigham*, 1988; *Taylor et al.*, 2004; *Bingham and Siegert*, 2007a; *Rippin et al.*, 2014). The sample interval of 5 m in this study therefore provides a minimum window length of 160 m. The mean ice thickness of all radar grids presented here is 1584 m. Therefore I am able to resolve basal roughness at a minimum of 10% of mean ice thickness. The minimum window length analysed in previous roughness investigations of Pine Island Glacier was 320 m (*Rippin et al.*, 2011).

Here I follow the approach of *Li et al.* (2010) to calculate the single-parameter roughness index (ξ). The first step of the FFT analysis is to detrend the bed elevation profile of length $(-l/2, l/2)$ (in this case the moving window length of 160 m) by removing the mean bed elevation $\langle Z(x) \rangle$ from $Z(x)$:

$$Z_0(x) = Z(x) - \langle Z(x) \rangle, \tag{5.1}$$

where x is the horizontal location and Z is the bed elevation. A Fast Fourier Transform is then applied to derive the spectral power density, $S(k)$:

$$S(k) = \frac{1}{l} \mid \bar{Z}_0(k) \mid^2, \tag{5.2}$$

where k is the wave number, $\bar{Z}_0(k)$ is the Fast Fourier Transform of $Z_0(x)$ and l is the moving window length. Finally, the roughness index, ξ, is obtained by integrating $S(k)$ over a specified wavelength,(k_1, k_2):

$$\xi = \int_{k_1}^{k_2} S(k) dk \tag{5.3}$$

When k_1 is zero and k_2 is infinity, I obtain the roughness index, ξ.

Maps of bed roughness presented in section 6.4 were generated in QGIS using a Triangulation interpolation gridded with a 50 m cell size.

5.3 Results

5.3.1 Characteristics of subglacial topography

The high-resolution radar data presented here allow the characteristics of subglacial roughness to be investigated in unprecedented detail. I will first provide a qualitative overview of the spatial distribution of bed roughness before exploring quantitative relationships between roughness and ice dynamics.

The subglacial landscape revealed by the six radar grids acquired on PIG is diverse. Bed elevation is highly varied with a host of subglacial bedforms (Fig. 5.2b). Kilometre-scale bed topography of upstream sites in the eastern tributaries (iSTARt1, iSTARt5 and iSTARt6; Fig. 5.2a) is noticeably smoother than the downstream, southern tributary sites in all horizontal

directions. In all sites with the exception of iSTARt5, a number of subglacial hills are observed, protruding from more gently sloping terrain. Most notably these comprise the following:

- iSTARt1: a 250 m high crag-and-tail (centre of Fig.5.2b, row 1).
- iSTARt6: a 300 m high spherical hill that extends off the survey patch (lower-left corner of Fig.5.2b, row 3).
- iSTARt7: a tapering, 400 m high outcrop with a steep, upstream, transverse cliff-face (centre-left of Fig.5.2b, row 4).
- iSTARit: a 400 m high outcrop (lower-centre of Fig.5.2b, row 5).
- iSTARt9: two regions of streamlined hills up to 500 m in height (upper-left and lower-right of Fig.5.2b, row 6).

With the exception of the inter-tributary site, iSTARit, these topographic features are expressed in ice surface topography (Fig. 5.2c). The ice surface rises on the upstream, stoss flank and is depressed in the downstream, lee of these subglacial landforms on the order of tens of metres (<10% of the height of the features they drape over).

At sub-kilometre scale, lineations interpreted as mega-scale glacial lineations (MSGL) (*Clark*, 1993) are the most abundant bedforms. They have amplitudes of 2-10 m and widths of 100-600 m and are observed in every site, with the exception of the slow-flowing (<10 m a^{-1}), inter-tributary site iSTARit (Fig. 5.2b, row 5). Bedforms present in this site lack the elongation of fast-flowing tributary sites and are more reminiscent of drumlins.

5.3.2 Spatial distribution of basal roughness

Maps of log across-flow (ξ_x) and along-flow (ξ_y) subglacial roughness are shown in figure 5.2d and e respectively. These maps show that the spatial distribution of roughness varies considerably between ξ_x and ξ_y. Significantly, many of the kilometre-scale subglacial landforms described in the previous section are not registered as regions of high ξ_x. However, variations in the relative amplitudes of MSGL are accentuated. In contrast, large-scale landforms are clearly demarcated by regions of high ξ_y. This is clearly demonstrated at the stoss face of the crag-and-tail landform in iSTARt1 and the transverse “cliff-face” in iSTARt7 (Fig.5.2b).

The inter-tributary site iSTARit displays unique patterns of roughness distribution. The pattern

of ξ_x has a speckled appearance, reflecting the absence of streamlined bedforms. Furthermore, iSTARit is the only site that exhibits regular patterns in ξ_y (Fig.5.2e, row 5). These patterns are comparable to regular patterns in inverted basal shear stress beneath ice stream beds (*Sergienko and Hindmarsh*, 2013; *Sergienko et al.*, 2014) and the morphology of "ribbed moraines" observed in palaeo-ice stream beds (*Dunlop and Clark*, 2006; *Stokes et al.*, 2008, 2016).

5.3.3 Influence of DEM interpolation on along-flow roughness

As mentioned in section 5.2.1, additional radar profiles were aqcuired between study sites (Fig. 5.1). These additional data provide an opportunity to assess how interpolated bed elevation extracted from along-flow profiles affects derived roughness compared to raw bed elevation from radar surveys. Comparisons of interpolated and raw bed elevation and roughness extracted from the same profiles are shown in Figure 5.3b and c respectively.

For three of the five sites analysed (iSTARt5, t6 and t7), there is very little difference between raw and interpolated bed elevation profiles (Fig.5.3b). Profiles of log ξ for these sites are also broadly comparable (Fig. 5.3c). However, there are notable differences in bed elevation profiles for sites iSTARt1 and t9. Interpolated bed elevation for iSTARt1 is more variable than the raw bed elevation (Fig.5.3b). This demonstrates that artefacts have been introduced in the DEM interpolation for this site. These artefacts are likely to be related to problems encountered with the GPS elevation data in at this site affecting the surface elevation data. The corresponding log ξ profile also exhibits greater variability (Fig.5.3c). In iSTARt9, the DEM interpolation changes a convex bed slope to a concave profile (Fig.5.3b). This appears to introduce a lower log ξ coincident with this feature (Fig.5.3c).

Mean ξ values for each of the profiles in 5.3 are shown in Table 5.1. The mean ξ values show that DEM interpolation increases ξ_y for sites with smoother beds (low overall ξ). However the difference is not significant compared to the overall variability in roughness for the entire grid as shown by the standard deviation of ξ_x (σ Grid ξ_x). For rougher sites (iSTARt7 and t9), DEM interpolation reduces ξ_y. However, this is even less significant in the context of the overall variability in roughness for the grid.

Table 5.1: Comparison of mean ξ values calculated for radar bed elevation data and interpolated DEM bed elevation.

Site	Mean ξ (GPR)	Mean ξ (DEM)	GPR-DEM	σ Grid ξ_x
iSTARt1	2.7	5.1	-2.4	6.9
iSTARt5	4.5	5.2	-0.7	9.0
iSTARt6	2.3	2.4	-0.2	5.0
iSTARt7	6.3	5.2	1.2	15.2
iSTARt9	14.9	14.2	0.7	24.6

5.3.4 Grid orientation and roughness length scale

Having assessed the spatial distribution and influence of DEM interpolation on basal roughness, this section will explore the relationship between basal roughness and ice dynamic parameters at different length-scales and grid orientations. Mean roughness values are compared to mean values of ice dynamic parameters shown in Table 5.1. Basal shear stress values are derived from a surface-to-bed 3D Stokes inversion (*Kyrke-Smith et al.*, 2017). These inversions produced two sets of values using iSTAR and BedMap2 bed elevation (*Fretwell et al.*, 2013) respectively. Ice surface velocity u is extracted from the MEaSUREs dataset (*Rignot et al.*, 2011a). Ice surface lowering propagation rates are taken from *Konrad et al.* (2017) from radar altimeter observations between 1992 and 2015. Both the 0.5 km and 1 km threshold for propagation rates are compared. Analysis of correlation between mean ξ_x, ξ_y and ice-dynamic parameters was performed by increasing the moving window length of the FFT from N=5 (160 m) to N=10 (5,120 m). These results are shown in Figure 5.4.

When comparing the results for across-flow and along-flow grid orientations, both ξ_x and ξ_y are more strongly correlated with basal shear stress derived from Bedmap2 (max R^2 = 0.86 and 0.98 respectively) than they are with basal shear stress derived from iSTAR (max R^2 = 0.63 and 0.92 respectively) (Fig.5.4). For ξ_x, the strongest correlation with basal shear stress is 0.64 km (below mean ice thickness) for basal shear stress derived from both iSTAR and Bedmap2 bed elevation. The same trend in correlation is also observed. For ξ_y, the strongest correlation with basal shear stress derived from iSTAR data is 1.28 km (below mean ice thickness). However, when comparing ξ_y with basal shear stress derived from Bedmap2 bed elevation, the correlation is consistently strong regardless of the moving window size. Although R^2 values are lower for

ξ_x, the same positive linear trend between basal roughness and basal shear stress is observed. Sites iSTAR t1, t5 and t6 display low ξ and low τ_b, iSTARit and t9 have high ξ and τ_b with iSTARt7 intermediate between these end members (Fig. 5.4 b,d).

Correlation between roughness and ice surface velocity is lower than for basal shear stress (Fig. 5.4e-h). The highest R^2 values are 0.22 and 0.66 for ξ_x and ξ_y respectively (Fig. 5.4e,g). R^2 is again higher for ξ_y than ξ_x suggesting that variability in ξ_x does not exert as strong an influence on ice flow as ξ_y (5.4f,h).

The final parameter explored is the inland spreading rate of ice surface lowering (*Konrad et al.*, 2017). As with all other parameters explored, correlation is greater for ξ_y than ξ_x (highest R^2 of 0.44 and 0.76 respectively) (Fig.5.4i-l). The same trends are observed for both 0.5 and 1.0 km threshold spreading rates, however, R^2 is higher for the 1.0 km spreading rate. A broad trend of low roughness and high spreading rates is observed. However, there is variability, particularly between sites iSTARt1, t5 and t6 that suggests basal roughness may not be the dominant control on spreading rates (Fig. 5.4j,l).

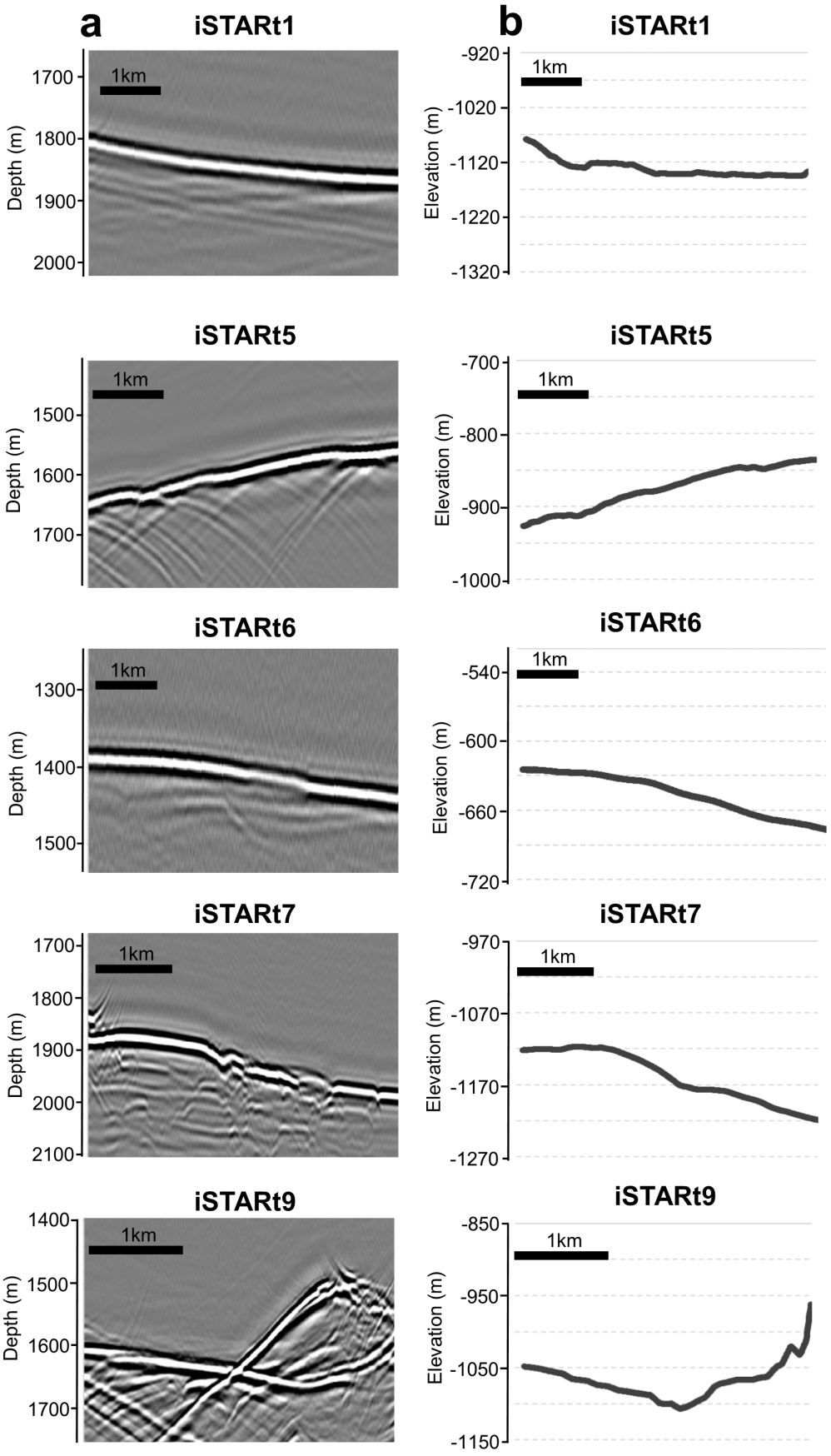

Figure 5.1: Comparison of along-flow radar data against interpolated along-flow bed data. **a** radargrams of along-flow radar surveys. **b** Plots of interpolated bed elevation extracted from the interpolated grid DEM along the same profiles as the radargrams shown in **a**.

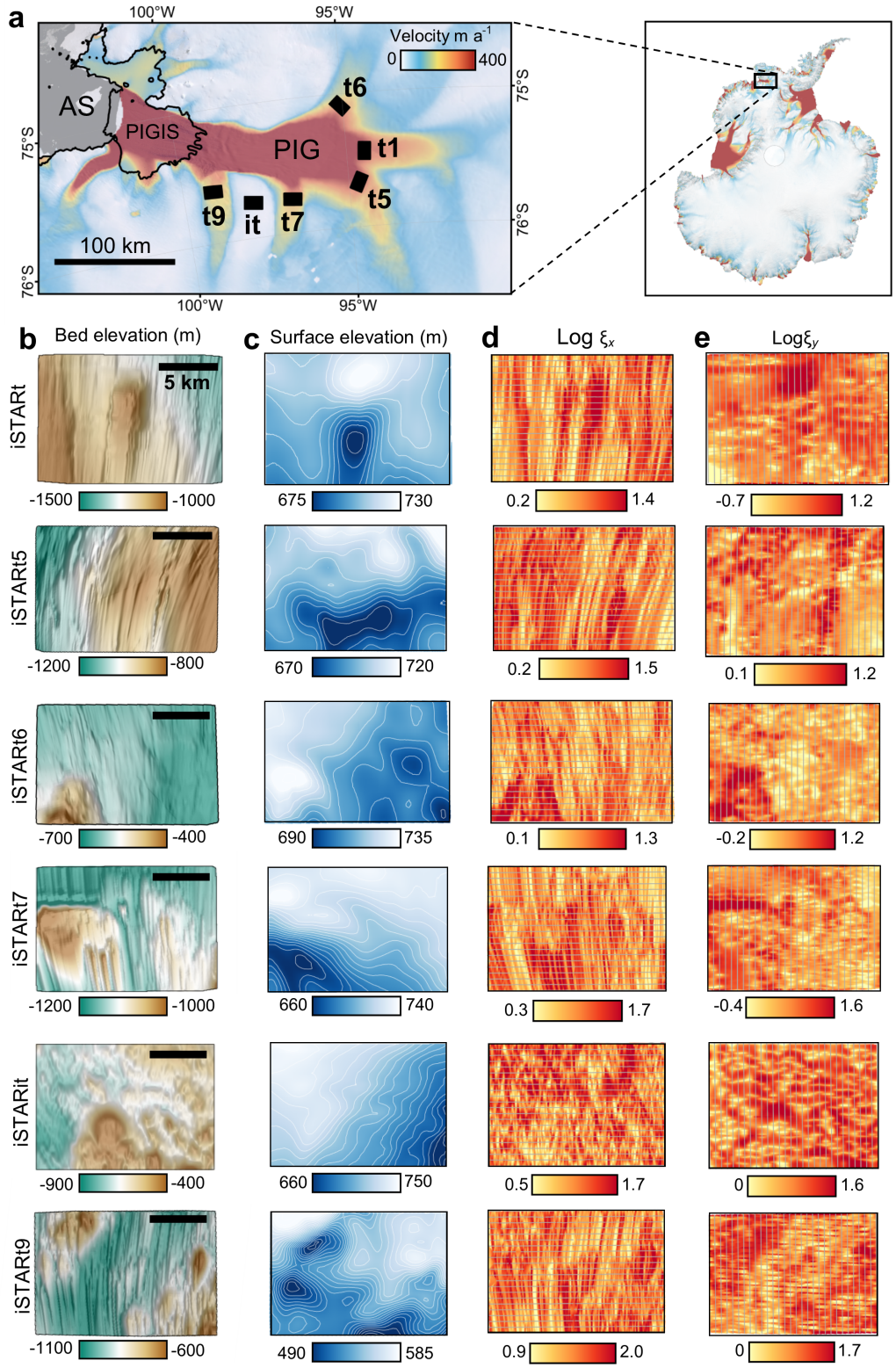

Figure 5.2: a Location map of radar grid surveys and inset map showing the location of the study area. PIG = Pine Island Glacier, PIGIS = Pine Island Glacier Ice Shelf, AS = Amundsen Sea. Gridded maps interpolated at 50 m resolution showing; **b** bed elevation overlaying multi-directional relief shaded topography; **c** ice-surface elevation with 10 m elevation contours (white lines); **d** log across-flow roughness index derived from radar survey (grey lines) and **e** log along-flow roughness index from interpolated bed elevation data (grey lines). General ice-flow direction is from top to bottom of the page in **b-e**.

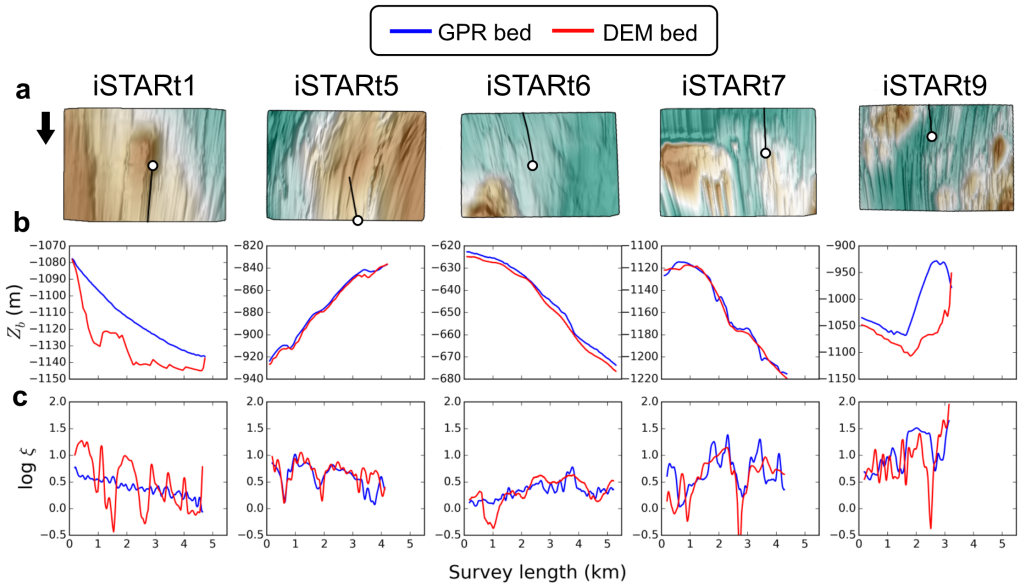

Figure 5.3: Roughness analysis of flow parallel radar profiles compared to bed elevation extracted from interpolated DEM. **a** bed elevation DEMs interpolated from GPR grids. Colour scale shows bed elevation as in Fig. 5.3. Black lines are radar profiles. White circles represent the start of profiles shown in **b**. Black arrow shows general ice flow vector. **b** Bed elevation extracted from radar profiles (blue lines) and interpolated bed DEM (red lines). **c** Log roughness of the bed from profiles in **b**. Lines have been smoothed with a 20 point moving window to improve readability. Comparison between the raw GPR bed picks and bed elevation extracted from the interpolated DEM show discrepencies in sites iSTARt1 and iSTARt9 caused by DEM interpolation errors.

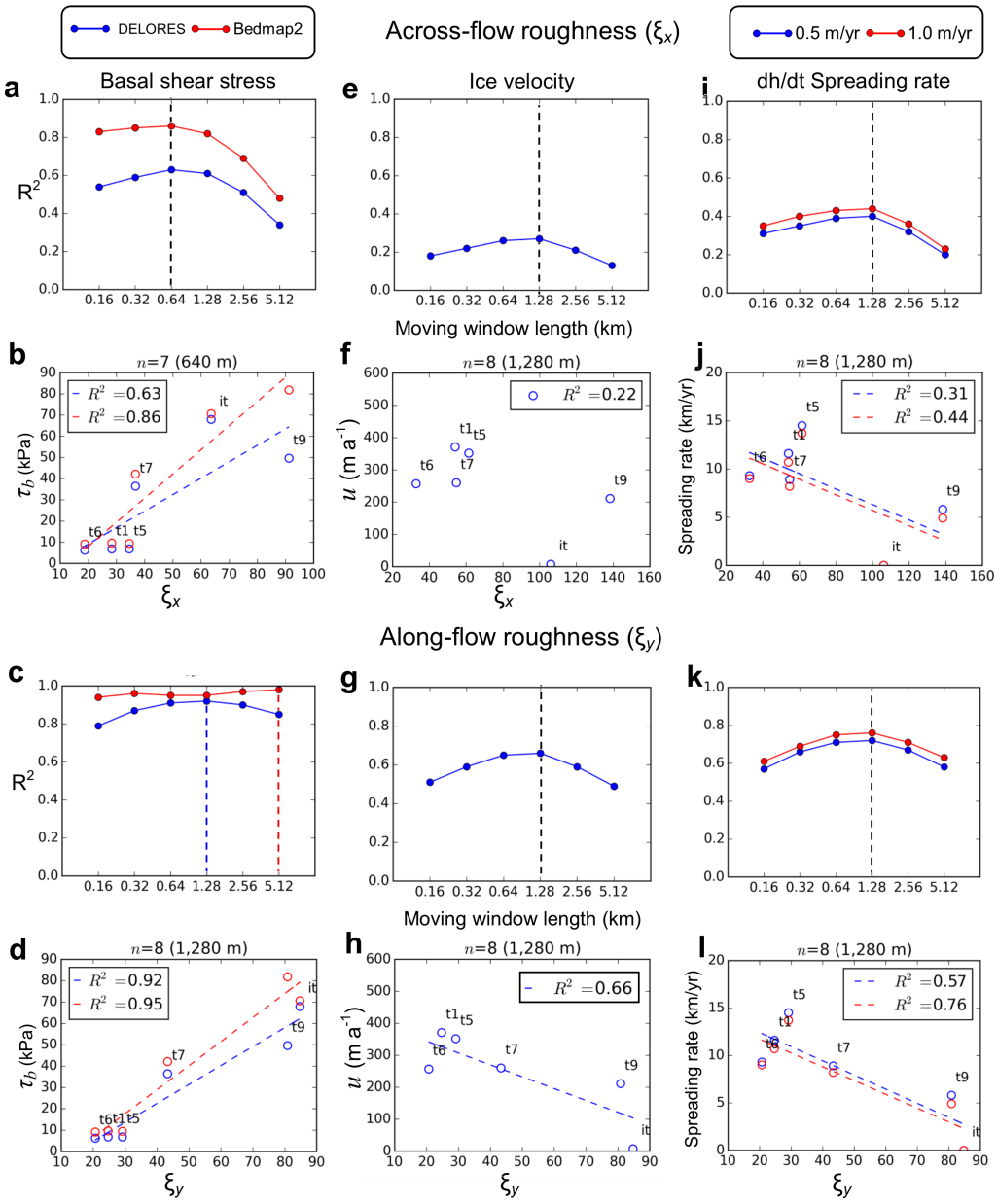

Figure 5.4: Plots showing correlation between basal roughness and ice dynamic parameters for different moving-window lengths and grid orientation. **a** R^2 plots of mean ξ_x for ice dynamic parameters at different moving-window lengths. **b** Scatter plots of mean ξ_x for each site against ice dynamic parameters. Moving window lengths correspond to highest observed R^2 represented by the dashed line in row a. **c** R^2 plots of mean ξ_y for ice dynamic parameters at different moving-window lengths. **d** Scatter plots of mean ξ_y for each site against ice dynamic parameters. Moving window lengths correspond to highest observed R^2 represented by the dashed line in row **c**.

Table 5.2: Mean ice dynamic parameter values for each site used in correlation analysis.

	Mean τ_b (kPa)	**Mean τ_b (kPa)**	**Mean ice velocity (m a^{-1})**	**0.5 km spreading rate (km a^{-1})**	**1 km spreading rate (km a^{-1})**
Data source	Kyrke Smith et al., (2017) (iSTAR bed elevation)	Kyrke Smith et al., (2017) (Bedmap2 bed elevation)	MEAsUREs (Rignot et al., 2011)	Konrad et al., (2017)	Konrad et al., (2017)
Data resolution (km)	0.05	1.0	0.9	5.0	5.0
Site name					
iSTARt1	6.8	9.6	370.8	11.6	10.7
iSTARt5	6.8	9.4	351.6	14.5	13.7
iSTARt6	6.2	9.1	256.7	9.3	9.0
iSTARt7	36.4	42.1	259.8	8.9	8.2
iSTARit	67.9	70.6	7.3	0	0
iSTARt9	49.6	81.8	211.0	5.8	4.9

5.3.5 Comparison to previous roughness analysis of Pine Island Glacier

Comparisons between DELORES roughness calculated using a moving window length of 0.16 km and roughness derived by *Rippin et al.* (2011) using a window length of 1.08 km are shown in Figure 5.5. For the most part, the results show a good correlation for both ξ_x and ξ_y. Sites iSTARit and t9 are consistent in being the sites with the highest roughness for ξ_x and ξ_y. However there is more variability between ξ_x and ξ_y for the other sites which is not captured in the data of (*Rippin et al.*, 2011). This is reflected in the lower correlation between ξ_x (R^2 = 0.78) compared to ξ_y (R^2=0.94).

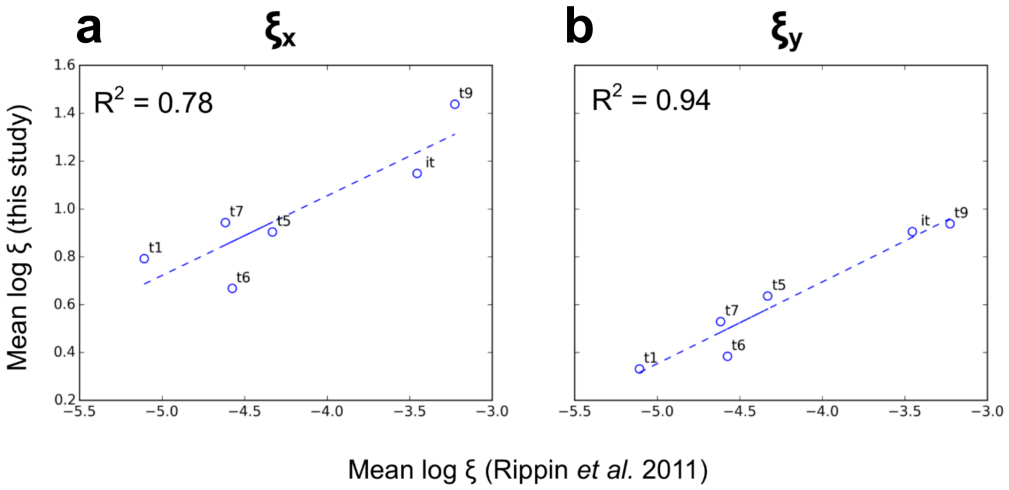

Figure 5.5: Comparison of along and across flow mean log roughness in this study with mean log roughness from *Rippin et al.* (2011). **a** Across-flow roughness (ξ_x) plotted against Rippin et al's mean log roughness for each site. **b** Along-flow roughness (ξ_y) plotted against Rippin et al's mean log roughness for each site

5.4 Discussion

5.4.1 Spatial distribution of basal roughness: implications for bed conditions and landscape evolution

I begin this section by discussing the broad trends in roughness identified in the grid surveys across the PIG catchment. I then consider how kilometre-scale roughness is influenced by

subglacial bedforms and the implications of the distribution of roughness for landscape and bedform evolution.

The general picture that has emerged from previous investigations of subglacial roughness in Antarctica is that fast, warm-based ice flow over deforming sediments is associated with smooth beds and slow-cold based ice in the interior of the ice sheet is associated with rough beds (*Siegert et al.*, 2004; *Rippin et al.*, 2006; *Bingham and Siegert*, 2009; *Rippin et al.*, 2011, 2014). The data presented in this chapter provide a range of both fast (> 100 m a^{-1}) and slow (< 10 m a^{-1}) flow settings to test whether this relationship holds true.

Both along-flow and across-flow roughness was found to be lower in the eastern, upstream tributary sites (iSTARt1, t5 and t6) and progressively higher towards the coast in the western tributaries and inter-tributary site (iSTARt7, it and t9) (Fig. 5.4). This is contrary to the trend of decreasing roughness with distance downstream in both sub-ice stream and inter-ice stream regions observed elsewhere in Antarctica (*Bingham and Siegert*, 2009). iSTARt9 has the highest bed roughness both along and across flow , comparable to the inter-tributary site (iSTARt9) despite being the site closest to the grounding line (Fig. 5.4). This suggests that other factors, such as the broad subglacial topographic trough underlying the tributary, and/or the potential presence of subglacial sediments overlying rough subglacial topography (*Brisbourne et al.*, 2017, Appendix D), may promote high driving stresses sufficient to overcome rough basal topography. *Rippin et al.* (2011) suggested that roughness beneath PIG is indirectly related to velocity whereby it reduces the driving stress required to achieve the balance flux. The relatively weak correlation between velocity and roughness observed in this chapter (Fig. 5.4) also supports a more complex relationship between roughness and ice velocity.

Previous investigations of the subglacial roughness of the Siple Coast and Institute and Möller Ice Streams (*Siegert et al.*, 2004; *Bingham and Siegert*, 2009) have shown that smooth subglacial topography exists beneath slow-flowing inter-ice stream regions of the bed and the now stagnant Kamb Ice Stream. This is interpreted as supporting evidence from disruption of internal radar layers that Kamb Ice Stream has previously undergone fast ice flow (*Anandakrishnan et al.*, 2001; *Ng and Conway*, 2004; *Catania et al.*, 2006). The data presented in this chapter demonstrate that fast ice flow is also possible in areas of rough subglacial topography

(e.g. iSTARt9; Fig. 5.2a). Using subglacial roughness alone as a diagnostic of regions of bed characterised by previous or present fast or slow flow is therefore not straightforward. However, it is evident in the subglacial geomorphology that there are clear differences in the elongation of bedforms between the rough ice stream site iSTARt9 and equally rough inter-stream site iSTARit.

To explore these differences further, I explore the log-frequency distributions of roughness (Fig. 5.6). These results show that roughness is higher across-flow than along flow. I explored this further by calculating the roughness anisotropy ratio of each grid site (Fig. 5.7) following the method of *Smith et al.* (2006). The roughness anisotropy ratio (Ω) is defined as:

$$\Omega = \frac{\xi_y - \xi_x}{\xi_y + \xi_x} \tag{5.4}$$

where ξ_x and ξ_y are the mean across and along-flow roughness respectively. For isotropic surfaces, $\Omega = 0$; Ω tends towards 1 where $\xi_y > \xi_x$, and tends towards -1 where $\xi_y < \xi_x$. Results showing Ω for each site are shown in Figure 5.7. The results show that all sites have negative Ω values, indicating that all sites, even the intertributary site iSTARit, are anisotropic with greater across-flow compared to along-flow roughness (Fig. 5.7). Sites iSTARt1 and t9 have the lowest and most comparable Ω (-0.42 and -0.41 respectively) despite having the greatest difference in mean ice velocity excluding the inter-tributary site (iSTARit) (Table 5.2). iSTARit is the least isotropic of all sites, which is consistent with the lack of apparent streamlining observed in the geomorphology of the bed (Fig. 5.2b, row 5). iSTARit is also the only site where the peak in the maximum frequency of log roughness for ξ_x and ξ_y is centred around the same value. For all other sites, the peak in maximum frequency is higher for ξ_x than ξ_y.

The markedly low anisotropy ratio and distinct frequency distribution of iSTARit are consistent with geomorphological theory of a continuum of bedform elongation associated with basal ice velocity (*Stokes and Clark*, 2002; *Ely et al.*, 2016a). It also suggests that basal conditions of consolidated, non-deforming and potentially frozen sediments detected in seismic reflection surveys at iSTARit (*Brisbourne et al.*, 2017, Appendix D) have likely persisted for a prolonged period of time. Combined, these observations confirm previous assertions that the confined,

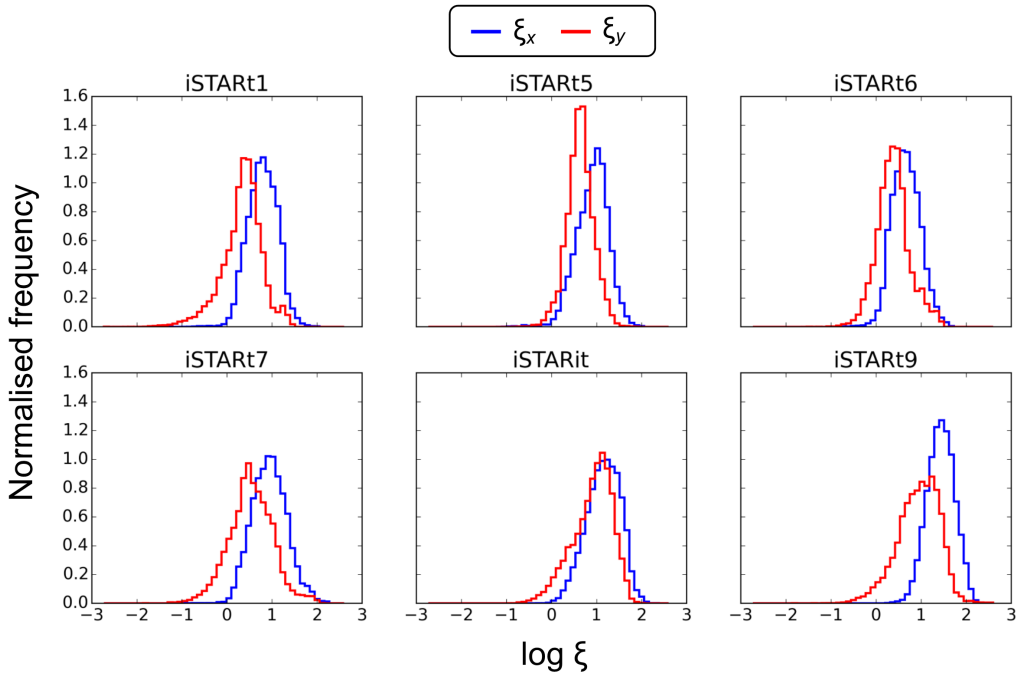

Figure 5.6: Log normal frequency distribution of ξ_x (blue lines) and ξ_y (red lines) for each site

subglacial troughs of PIG dictate its current flow configuration and would likely prohibit collapse of the WAIS into elevated, rough inter-tributary regions of PIG (*Vaughan et al.*, 2006; *Rippin et al.*, 2011).

Turning to the local, kilometre-scale distribution of roughness, the spatial distribution of roughness shown in Figure 5.2 exhibits clear differences in the spatial pattern of roughness for ξ_x (Fig. 5.2d) and ξ_y (Fig. 5.2e). Regions of high ξ_x are more evenly distributed within individual grids, reflecting the ubiquity of linear bedforms with a high frequency and short wavelength transverse to flow. Conversely, regions of high ξ_y exhibit a more discrete distribution around high-amplitude, long-wavelength features. These differences highlight the clear influence that subglacial geomorphology has on the signature of roughness and the directionality of these bedforms. Regions of low elevation that are smooth along-flow, and large bedrock obstacles such as the "cliff" feature in iSTARt7 and the stoss face of the crag and tail in iSTARt1, are not easily distinguished in maps of ξ_x. This highlights that ξ_y is more effective than ξ_x for distinguishing between hard and soft regions of the bed at kilometre-scale resolution.

As previously highlighted in section 5.3.2, the spatial pattern of ξ_y in site iSTARit resembles

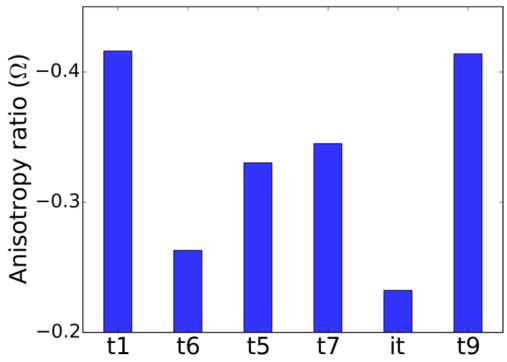

Figure 5.7: Roughness anisotropy ratio (Ω) for each site.

ribbed patterns of basal shear stress from model inversions (Fig. 5.8a). Numerous modelling studies have now detected organised patterns of high basal stress perpendicular to ice-stream flow (*MacAyeal*, 1992; *Macayeal et al.*, 1995; *Joughin et al.*, 2004; *Sergienko and Hindmarsh*, 2013; *Sergienko et al.*, 2014, Fig. 5.8b). These features have been interpreted as being caused by alternations between areas of weak bed and localised "sticky spots" possibly related to heterogeneous bed properties or topographic features (*Joughin et al.*, 2004). More recently, *Sergienko and Hindmarsh* (2013) identified similarities in the pattern of basal shear stress and large transverse bedforms known as "mega-ribs" or "ribbed moraine" (*Dunlop and Clark*, 2006; *Greenwood and Kleman*, 2010). *Stokes et al.* (2016) also highlighted the similarity in the pattern of ribbed bedforms observed in palaeo-ice stream beds in western Canada and basal shear stress patterns observed by *Sergienko and Hindmarsh* (2013) and *Sergienko et al.* (2014) (Fig. 5.8c).

The bands of high ξ_y we observe are of a similar scale to the bedforms observed by *Stokes et al.* (2016) and basal shear stress modelled by *Sergienko and Hindmarsh* (2013) (Fig. 5.8). These bands of high ξ_y correspond to ridges trending oblique and transverse to flow at the bed of iSTARit (Fig. 5.8d). These are the first bedforms analogous to mega-ribs to be observed beneath a contemporary ice-sheet bed. Given the similarity between the observed pattern of ξ_y and basal shear stress observed in model inversions, it is likely that some of the regular patterns of basal shear stress observed in model inversions are created by ice flowing over transverse ridges as hypothesised by *Joughin et al.* (2004).

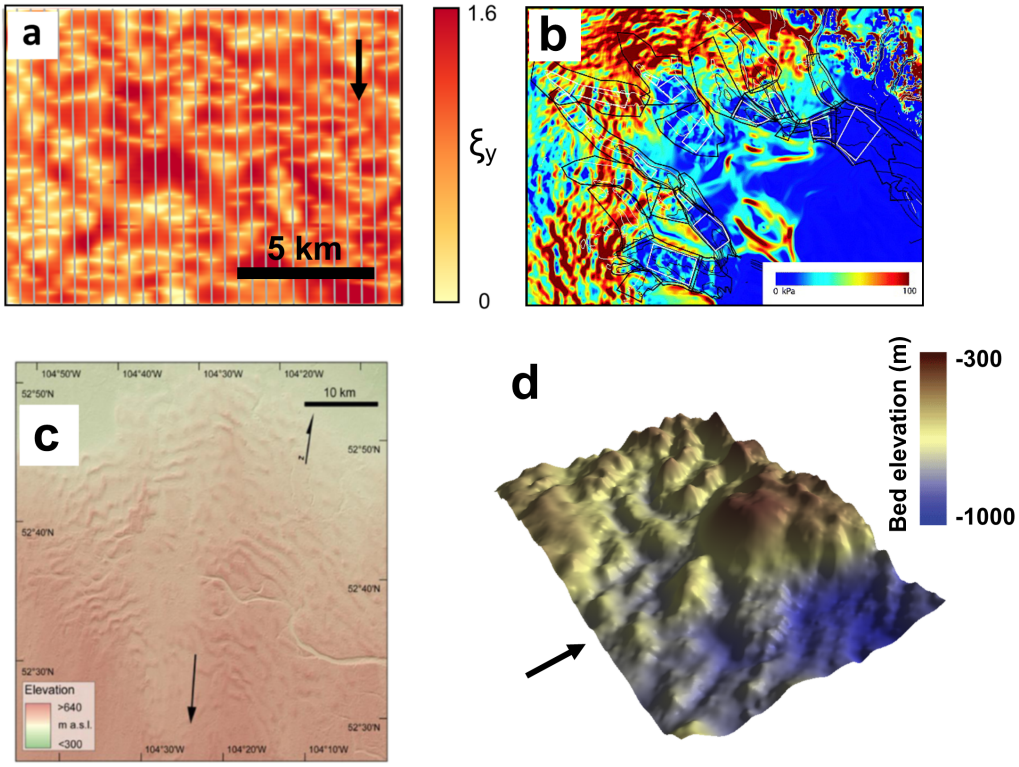

Figure 5.8: Similar patterns in basal roughness, basal shear stress and bedform morphology. **a** Log basal roughness (this study) beneath iSTARit. **b** Spatial patterns of basal shear stress from model inversion of the Siple Coast Ice Streams (Figure from *Joughin et al.*, 2004). **c** low-amplitude rib-like ridges aligned transverse to palaeo-ice flow from a DEM of the Buffalo palaeo-ice stream in Saskatchewan (Figure from *Stokes et al.*, 2016). **d** 3-dimensional oblique view of iSTARit bed DEM showing high-resolution subglacial topography with a 5x vertical exaggeration (Chapter 4). Black arrows show broad (palaeo)ice-flow direction.

Roughness frequency distributions shown in Figure 5.6 exhibit a unimodal log-normal distribution. Previous studies analysing the size-frequency distribution of drumlins and mega-scale glacial lineations find the same distribution (*Clark et al.*, 2009; *Fowler et al.*, 2013; *Hillier et al.*, 2013; *Spagnolo et al.*, 2014). This distribution is considered to arise from random incremental growth and decay through a large number of independent events (*Limpert et al.*, 2001). This has been taken to suggest that subglacial bedforms similarly arise through random periods of growth and decay (*Fowler et al.*, 2013; *Hillier et al.*, 2013; *Spagnolo et al.*, 2014). The occurrence of this distribution across all sites despite the diverse nature of the subglacial topography beneath PIG may indicate that this randomness occurs through the stochastic dynamics of ice-sediment-water interaction as suggested by *Hillier et al.* (2013). This would explain the

equifinality of linear bedforms observed in sediment (smooth beds, e.g iSTARt1) and bedrock (rough beds, e.g. iSTARt9).

5.4.2 What characteristics of bed roughness are important for ice dynamics?

I now consider what role subglacial roughness plays in influencing ice dynamics. Comparisons between ξ_x and ξ_y analysed at different length-scales with ice dynamic parameters (Fig. 5.4) have provided some insights into the interaction between basal topography and ice dynamics. ξ_y has a stronger correlation with modelled basal shear stress, ice velocity and dh/dt spreading rates. This is likely due to the anisotropic nature of bedforms discussed in the previous section. ξ_x is higher than ξ_y due to the high-frequency, short-wavelength amplitude of MSGL transverse to flow. However, this roughness has little influence on form drag compared to longitudinal roughness. When comparing these results to previous analysis of roughness beneath PIG by *Rippin et al.* (2011) (Fig. 5.3.5), the lower correlation between ξ_x compared to ξ_y suggests that the shorter wavelength across-flow roughness elements are not detected in *Rippin et al's* data due to the lower resolution of airborne data.

In experiments with the moving window length, correlations between ξ_y and ice dynamic parameters was found to be strongest using a window length of 1280 m that is closest to the mean ice thickness for all sites (1584 m). This indicates that there is potentially a threshold length-scale approximately equivalent to ice thickness at which bedforms exert an influence on basal drag. This agrees with numerical modelling experiments that suggest that basal perturbations of wavelengths comparable to ice thickness are sufficient to limit glacier sliding velocities and create surface expressions (*Gudmundsson et al.*, 1998; *Schoof*, 2002; *Raymond and Gudmundsson*, 2005; *Rydt et al.*, 2013). Features with this length-scale appear to have the strongest influence on ice surface topography derived from GPS surface measurements in this study (Fig. 5.2c). The strong correlation between ξ_y using a window length of 0.16 km and the *Rippin et al* roughness also demonstrates that the relative smoothness of along-flow bed topography (see radargrams in Fig. 5.1) does not require high-resolution data to resolve.

However, as demonstrated in the analysis of the along-flow transit profile in iSTARt9 (Fig. 5.3.3), it is possible for roughness to be underestimated due to poor interpolation of along-flow

bed topography. This would potentially have greater implications close to the grounding-line where modelling experiments have shown that variability in the amplitude of bedrock on the order of tens of metres can have a significant effect on the rate of projected grounding-line retreat (*Sun et al.*, 2014).

In comparisons between roughness and dh/dt spreading rates (*Konrad et al.*, 2017), correlation was highest when comparing ξ_y with the 1.0 m/yr threshold (Fig. 5.4l). Sites with low roughness (iSTARt1, t5 and t6) had the highest spreading rates with rates decreasing with increasing bed roughness. These results support the hypothesis that inland transmission of imbalance in PIG would occur at different rates in different tributaries depending on their basal resistance (*Rippin et al.*, 2011). If the current oceanic perturbation affecting PIG in recent decades continues, it is likely that inland thinning and flow acceleration will continue to progress further inland via the eastern tributaries (iSTARt1, t5 and t6).

5.5 Conclusion

In this chapter I have performed roughness analysis using Fast Fourier methods to analyse the subglacial roughness of Pine Island Glacier at sub-kilometre resolution. This is the first analysis of subglacial roughness in Antarctica at such high resolution where roughness can be mapped and analysed alongside images of the subglacial geomorphology at comparable resolution.

The spatial pattern and magnitude of subglacial roughness varies depending on the orientation of radar survey profiles. Roughness extracted from along-flow radar lines and interpolated basal topography is found to be lower than across-flow roughness. This is fundamentally controlled by the anisotropy of linear subglacial bedforms (MSGL) created by fast ice stream flow. Across-flow roughness was found to be weakly correlated to ice dynamics parameters compared to along-flow roughness, demonstrating that the orientation of bedforms dictates how form drag at the bed impacts ice flow.

Correlation between roughness and ice dynamic parameters was found to be highest where a moving window size closest to the mean ice thickness was used. These experiments suggest that bedforms with along-flow wavelengths on the order of ice thickness have the greatest impact on

impeding ice flow. This length-scale is reflected in the surface expression of basal topography as predicted in modelling experiments investigating the surface expression of form drag.

The spatial distribution of along-flow roughness in the inter-tributary site bears remarkable resemblance to "ribbed" patterns of modelled basal shear stress observed in the onset zones of ice streams in Antarctica. This pattern corresponds to transverse bedforms analogous to mega-ribs and ribbed moraines observed in palaeo-ice stream beds and is the first observation of such bedforms beneath a modern ice sheet. Future research assessing along-flow basal properties and topography associated with ribbed patterns of modelled basal shear stress may shed light on the interaction between basal properties, ice flow and emergent subglacial bedforms. Such observations may provide valuable insights to test instability theories of subglacial bedform evolution.

The anomalously low roughness anisotropy ratio observed in the inter-tributary site demonstrates the potential for this parameter as a tool for identifying regions of the bed that have not experienced prolonged high erosion beneath warm-based ice stream flow. Conversely, these analyses also show that hard ice-stream beds with high roughness (e.g. iSTARt9) and soft ice-stream beds with low roughness (e.g. iSTARt1) display similar roughness anisotropy ratios. Therefore, caution should be taken when assessing whether inland regions of Antarctica have formerly experienced erosion under warm-based ice, particularly when radar lines are oriented transverse to (palaeo)ice flow.

Chapter 6

How dynamic are ice-stream beds?

The previous chapters have presented an overview of the key characteristics and properties of the bed of PIG and assessed the influence of subglacial roughness on ice-stream flow. This chapter now turns to investigating the dynamics of ice-stream beds. A version of this chapter is published in The Cryosphere as:

Davies, D., Bingham, R. G., King, E. C., Smith, A. M., Brisbourne, A. M., Spagnolo, M., Graham, A. G. C., Hogg, A. E., and Vaughan, D. G. (2017). How dynamic are ice-stream beds?, *The Cryosphere*, 12, pp.1615-1628 https://doi.org/10.5194/tc-12-1615-2018.

I acquired data in the field, performed the data analysis and processing and wrote the manuscript. My co-authors also assisted with data acquisition and contributed to edits in the writing process. Data from Rutford ice stream also included in this chapter were acquired and processed by my co-authors and presented in *Smith et al.* (2007), *Smith et al.* (2013) and *King et al.* (2016).

6.1 Abstract

Projections of sea-level rise contributions from West Antarctica's dynamically thinning ice streams contain high uncertainty because some of the key processes involved are extremely challenging to observe. An especially poorly observed parameter is sub-decadal stability of ice-stream beds, which may be important for subglacial traction, till continuity and landform development. Only two previous studies have made repeated geophysical measurements of ice-stream beds at the same locations in different years, but both studies were limited in spatial extent. Here, we present the results from repeat radar measurements of the bed of Pine Island Glacier, West Antarctica, conducted 3-6 years apart, along a cumulative $\sim$ 60 km of profiles.

Analysis of the correlation of bed picks between repeat surveys shows that 90% of the bed displays no significant change despite the glacier increasing in speed by up to 40% over the last decade. We attribute the negligible detection of morphological change at the bed of Pine Island Glacier to the ubiquitous presence of a deforming till layer, wherein sediment transport is in steady state, such that sediment is transported along the basal interface without inducing morphological change to the radar-sounded basal interface. Given the precision of our measurements, the upper limit of subglacial erosion observed here is 500 mm a^{-1}, far exceeding erosion rates reported for glacial settings from proglacial sediment yields, but substantially below subglacial erosion rates of 1.0 m a^{-1}previously reported from repeat geophysical surveys in West Antarctica.

6.2 Introduction

Glaciological studies over the past three decades have revealed that the West Antarctic Ice Sheet (WAIS) is losing mass at an accelerating rate, raising concerns over its potential future contribution to global sea level (*Shepherd et al.*, 2012; *Pollard and Deconto*, 2016). Between 2010 and 2013, around 33% of the ice sheet's net mass loss came from Pine Island Glacier (hereafter PIG), a major ice stream draining to the Amundsen Sea Embayment (*McMillan et al.*, 2014). There, from satellite altimetry observations, mass loss was first expressed at the grounding zone in the mid-1990s, and has now propagated all the way up to the divides (*McMillan et al.*, 2014) by a set of processes broadly termed dynamic thinning (*Shepherd et al.*, 2001; *Pritchard et al.*, 2009). At PIG the dynamic thinning has incorporated an upstream expansion of regions both of accelerating ice (e.g. *Scott et al.*, 2009; *Mouginot et al.*, 2014) and ice-surface lowering (e.g. Konrad et al., 2017), and upstream migration, by several 10s of km, of the grounding line (e.g. *Park et al.*, 2013; *Rignot et al.*, 2014), prompting suggestions that PIG is in runaway retreat (*Joughin et al.*, 2014). However, the detailed processes by which dynamic thinning works, especially upstream from the grounding zone, are not well constrained. Particularly unclear is how the coupling between basal ice and the bed may evolve or vary over time and whether this needs to be accounted for in models projecting future ice response. For example, previous studies have theorised that high subglacial till fluxes can lead

to the rapid formation of grounding-zone wedges, potentially stabilising ice streams against sea-level rise (e.g. *Alley*, 1989; *Alley et al.*, 2003; *Alley*, 1989; *Alley et al.*, 2007).

Monitoring the beds of ice streams is also important for understanding processes of erosion and sediment transport that can provide information on landscape evolution (e.g. *Jamieson et al.*, 2010; *Herman et al.*, 2011), basal processes (*Cuffey and Alley*, 1996; *Alley et al.*, 1997; **?**) and the supply of nutrients to polar oceans (*Raiswell et al.*, 2006). Furthermore, knowledge of till flux and associated till properties is key to an improved understanding of glacier physics and ice-stream stability (*Blankenship et al.*, 1986; *Boulton and Hindmarsh*, 1987; *Alley*, 1989; *Jenson et al.*, 1995; *Engelhardt and Kamb*, 1998; *Truffer et al.*, 2000; *Iverson and Iverson*, 2001; **?**; *Damsgaard et al.*, 2013, 2016). A review of previously published erosion rates for hard-bedded glaciers (*Hallet et al.*, 1996) indicates low erosion rates in polar settings (0.01 mm a^{-1}) contrasting with relatively high rates beneath temperate alpine glaciers (10-100 mm a^{-1}). However, more recent studies have identified far more rapid erosion rates of 4.8 mm a^{-1} in Greenland (*Cowton et al.*, 2012) and as much as 1 m a^{-1} or more in soft-bedded glaciers in Alaska (*Motyka et al.*, 2006) and Antarctica (*Smith et al.*, 2007, 2012). Critically, measurements of erosion rates in Antarctica are limited both temporally and spatially, making it difficult to assess whether such high rates of erosion are typical or exceptional.

A significant difficulty in assessing temporal changes to the beds of WAIS ice streams is lack of direct access. Theoretical and geophysical constraints have shown that ice streams typically achieve fast flow by overriding dilated till that provides low basal drag (*Alley et al.*, 1986; *Bentley et al.*, 1998). It has been inferred that even relatively small fluctuations to hydrological conditions in these locations can induce significant changes to basal drag, in the most extreme circumstances causing ice streams to switch on or off (e.g. *Anandakrishnan and Alley*, 1997; *Conway et al.*, 2002; *Vaughan et al.*, 2008). However, to our knowledge, only two studies have attempted directly to capture temporal changes to ice-stream bed conditions over decadal to sub-decadal timescales commensurate with available satellite records of surface elevation and velocity change. The first was a single-location repeat measurement of ice thickness and surface elevation on PIG (location, Fig. 6.1) made firstly in 1960 and remeasured in 2009 (*Smith et al.*, 2012). That study found surface lowering with no significant change in ice thickness,

suggesting that mean erosion of the ice-stream bed of up to 1 m a^{-1} took place during the study period (*Smith et al.*, 2012). This rate is well above the range reported elsewhere (*Hallet et al.*, 1996). The second, more detailed study, consisted of three repeat seismic surveys of the bed of Rutford Ice Stream (hereafter RIS; Fig. 6.1c) obtained in 1991, 1997 and 2004 (*Smith et al.*, 2007). There, across a ∼0.5 km width of the bed, 6 m of sediment were removed from the ice bed between 1991 and 1997 followed by the appearance of a drumlin 10 m high and 100 m wide between 1997 and 2004. Both of the studies from West Antarctica therefore implied that active sediment erosion or deposition at rates ∼ 1-1.4 m a^{-1}, and landform evolution, are possible beneath ice streams on decadal to sub-decadal timescales.

In this paper, we present and analyse results from three repeat surveys of the bed of PIG, whereby we geophysically surveyed co-located profiles of PIG's bed in different years along a cumulative ∼60 km of traverses. Our principal aim was to ascertain whether erosion or deposition, and any morphological changes, were detectable at the bed of PIG over intervals of 3-7 years, periods over which PIG (from satellite monitoring) has undergone considerable ice-surface lowering and ice acceleration (*McMillan et al.*, 2014; *Mouginot et al.*, 2014).

6.3 Methods

Our data consist of three repeat radar surveys of PIG's bed acquired with a low frequency ice-penetrating radar system in austral seasons 2007/2008 and 2013/2014 (two profiles of 18 and 16 km long separated by ∼6 years) and 2010/2011 and 2013/2014 (one 25 km profile separated by ∼ 3 years) (Fig. 6.1a, b). The 18 km profile, R1, was acquired 3 km downstream and parallel to an 18 km seismic survey acquired in austral season 2007/2008 (Smith et al., 2013), 5 km of which was resurveyed in austral season 2014/2015 (Brisbourne et al., 2017) (profiles $S1_{2007}$ and $S1_{2014}$ on Fig. 6.1b respectively). Each of the repeat survey locations on PIG experienced significant ice-surface lowering and acceleration over the encompassing period (Table 6.1). In our analysis we consider our findings from PIG against the results from Smith et al.'s (2007) repeat seismic surveys of the bed of RIS (profile C1 in Fig. 6.1c), where ice flow has remained relatively stable over decadal timescales and negligible surface lowering has been observed

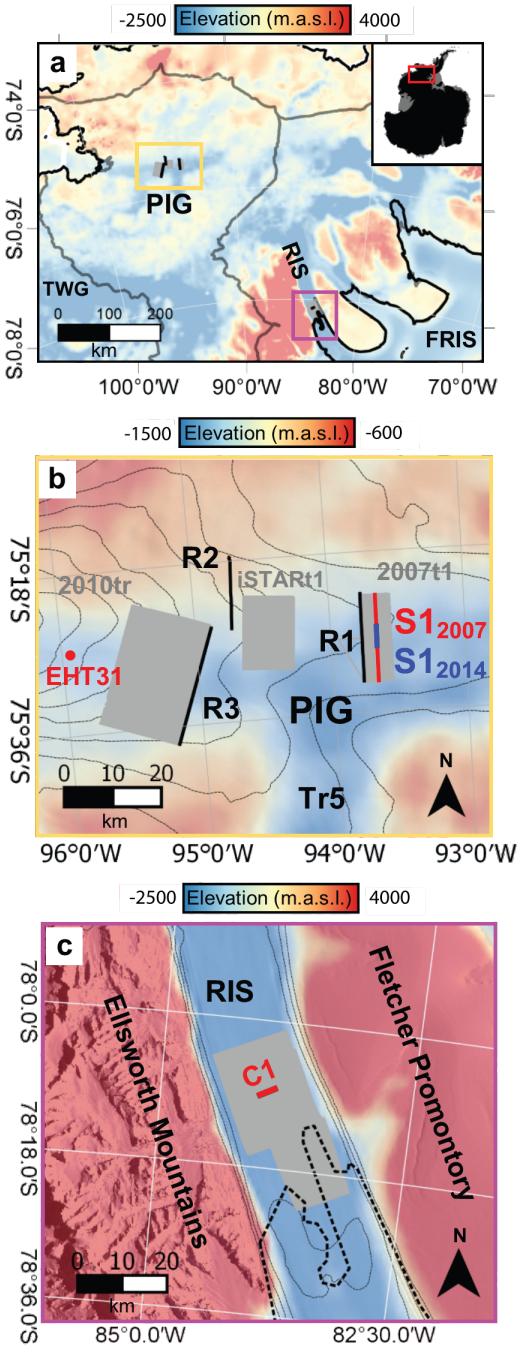

Figure 6.1: Location maps of the study area. Colourscale shows BEDMAP2 bed elevation (*Fretwell et al.*, 2013). **a** Map of the Pine Island Glacier (PIG) and Rutford Ice Stream (RIS) catchments. Grey lines show drainage boundaries (*Zwally et al.*, 2012). **b** Location of PIG surveys. Grey contours are 100 m a^{-1} ice surface velocity contours (*Rignot et al.*, 2011a). Grey shaded boxes show the locations of radar grid DEMs in Fig 6.2a, 6.3a,f., black lines are repeat radar surveys. $S1_{2007}$ is a seismic survey presented in *Smith et al.* (2013) and $S1_{2014}$ is a section of this profile resurveyed in 2014 (presented in *Brisbourne et al.*, 2017). EHT31 is a single point repeat survey presented in *Smith et al.* (2012). **c** Location of RIS surveys. Thick dashed line represents the MODIS grounding line. Grey contours are 100 m a^{-1} velocity contours (*Rignot et al.*, 2011a). Grey shaded box is the area of the radar grid DEM in Fig. 6.5a.

Table 6.1: Mean velocities for each repeat radar survey profile 2007-2017.

Survey	Velocity (m a $^{-1}$) 2007-2009 (MEaSUREs)	Velocity (m a^{-1}) 2017[a]	Velocity change (m a $^{-1}$)	Mean surface elevation change (m)[b]
C1 (RIS)	370	407	37	-
R1 (PIG)	287	361	74	-8.2
R2 (PIG)	384	523	139	-8.0
R3 (PIG)	435	609	174	-

[a]Velocities derived from Sentinel-1 image pairs obtained in April 2017. Details of processing methodology are provided in *Hogg et al.* (2017). [b] Surface elevation change derived from differential GPS measurements. No GPS data were available for surveys C1 and R3.

(Table 6.1).

6.3.1 Data acquisition

All radar profiles were acquired with the British Antarctic Survey's "DELORES" (Deep-Look Radio-Echo Sounder) system, a skidoo-towed monopulse array (see *King et al.*, 2016, , for general specifications). During the 2007/2008 field season, the system operated using 40 m half-dipole antennae, resulting in a centre frequency of 1.2 MHz. In 2010/2011 and 2013/2014, 20 m half-dipole antennae were used, giving a centre frequency of 3 MHz. Along-track traces were sampled at <1m intervals, stacked for noise reduction to produce data points at $\sim$5 m spacing, and georeferenced with a dual-frequency differential GPS mounted on the radar system.

The repeat radar surveys on PIG were each acquired approximately orthogonal to ice flow at sites 150, 120 and 115 km upstream from the 2011 grounding line (*Park et al.*, 2013) (R1, R2 and R3 respectively in Fig. 6.1b), in each case close to, or forming part of, more extensive radar surveys of patches of the ice bed conducted in the three field seasons (*Bingham et al.*, 2017). Repeat radar profile R1 comprises a traverse $\sim$18 km in length, first surveyed in January 2008 and then again in December 2013. The January 2008 profile also represents the most downstream traverse of a more extensive set of radar profiles used to image a 108 km^2 patch of PIG's bed in January 2008 surrounding the 18 km seismic profile acquired in the same season (patch 2007t1 and seismic profile $S1_{2007}$in Fig. 6.1b). Profile R2 is derived from a 16 km traverse first driven in December 2007 and then again in December 2013; this profile lies

$\sim$2 km downstream of an extensive survey of 150 km^2 of PIG's bed also surveyed in December 2013 (patch iSTARt1 in Fig. 6.1b). Profile R3, $\sim$25 km in length, was first surveyed in January 2011 as the upstream profile of multiple transects used to image a 425 km^2 patch of PIG's bed (patch 2010tr in Fig. 6.1b), and then again in December 2013 to yield a survey gap of $\sim$3 years.

6.3.2 Data processing

Radar data were processed using ReflexW seismic processing software (Sandmeier Scientific Software). A data processing flow was applied which included a gain function to improve the strength of reflections at greater depth, and bandpass and 2-D median filters to reduce data noise. Finite-difference (FD) migration was used to contract diffraction hyperbolae and to recover the correct locations of individual reflectors. The onset time of the bed reflector was determined at 5 m horizontal intervals at the peak in the amplitude of the bed reflector using a semi-automated "phase follower" picking procedure that allows automatic assignment of picks to a selected phase. These picks were checked and edited using manual picking where necessary. Bed picks were then converted to depth using a radar wave speed of 0.168 m ns^{-1} and no additional firn correction. We smoothed bed picks by applying a moving average over a 50 m window to all bed picks to remove high-frequency noise.

To assess changes at the bed, we focus on comparing the morphological character of the picked bed along repeat profiles rather than deriving changes in absolute bed elevation between surveys. This is for two reasons. Firstly, we do not have the data to assess whether firn properties, that impact upon radar wave speed, changed over the periods between repeat surveys. However we do not expect firn properties to have varied spatially on the scale of our surveys. For this reason we make no firn correction to our derived ice thicknesses. Secondly, differences in the triggering mechanism of the radar system between survey years meant that we could not directly match the onset waveforms between repeat surveys. In both cases, the effects preclude recovery of absolute ice thickness or bed elevation. Therefore we compare relative bed profiles by applying a static correction to a common bed datum (0 m) for both surveys.

The seismic surveys $S1_{2007}$ and $S1_{2014}$ in the vicinity of R1 were processed and analysed by *Smith et al.* (2013, 2007/2008 profile only) and *Brisbourne et al.* (2017, both profiles).

Brisbourne et al. (2017) primarily report on the calculation of acoustic impedance at the bed from both profiles, which we will consider in our discussion below. For this paper, we also investigated the possibility of directly picking the bed for the repeated 5 km section in an analogous manner to the radar picking described above. However, low signal-noise ratios along large parts of the bed, resulting from the similarity of ice and bed acoustic impedance (*Brisbourne et al.*, 2017), precluded the recovery of results with sufficiently low picking errors to have confidence in identifying any change or lack thereof.

6.3.3 Errors

For each profile R1-R3, the ability to detect changes in bed morphology is largely determined by the precision with which the bed reflector can be picked, and the degree to which the second radar profile of a repeat survey follows or diverges slightly from the path driven by the first profile.

The signal-to-noise ratio in all our radar profiles is high and the strength of the basal reflector produces a clearly discernible, high-amplitude wavelet (e.g. radargrams in Figs. 6.2-6.5) that requires little user interaction during the semi-automatic picking procedure. With such clear data, the uncertainty with which the bed reflection can be picked is determined primarily by the system rise-time of 250 V ns^{-1}, the recording-system bandwidth of 50 MHz and the digitisation interval of 10 ns. Also, considering the uncertainty in our GPS-derived elevations, we estimate that our radar data have a vertical range precision of $\pm$3 m.

As we are unable to recover absolute elevation change, in this study the horizontal resolution is more important than the vertical range precision. Differences in the morphology of the basal reflector need to be considered along with consideration of the different frequencies used in repeat surveys (1.2 and 3 MHz). This is best illustrated using commonly adopted resolution limits. For a circular wavefront, features at the bed with a width less than $\sqrt{2d\lambda + \frac{\lambda^2}{4}}$ will appear as point diffractors. For a bed at a depth of 2000 m, a 1.2 MHz (λ_{ice} = 250 m) wavelet will image features with a width <634 m. These differences may affect the appearance of the basal reflector depending on the roughness of the bed. For these reasons we express caution when considering subtle changes in basal morphology.

Table 6.2: Analysis of navigational divergence and associated variability in bed elevation.

Repeat survey	**R1**	**R2**	**R3**
Repeat survey divergence			
Maximum	45.1	54.0	35.0
Mean	23.7	13.7	20.0
Standard Deviation	$\pm$10.3	$\pm$12.0	$\pm$8.0

Survey lines were repeated by following a route programmed into a dashboard GPS unit mounted on the radar skidoo. Due to the higher accuracy and precision of the dual-frequency GPS compared to the dashboard units, and the challenges of navigating in featureless terrain, navigational divergences were registered. These divergences were mostly <50 m (Table 6.2); however, where bed topography is rough, even small navigational divergences may lead to incorrect interpretation of bed change. In order to visually assess whether navigational divergence affects observed bed change we have provided plots of minimum horizontal distance between repeat surveys alongside bed elevation profiles in Figs. 6.2 and 6.3.

6.4 Results

Bed picks for the repeat geophysical surveys from PIG are shown in Figs. 6.2 and 6.3 alongside associated geophysical images. A visual inspection of the radar/seismic images and bed picks (Figs. 6.2 and 6.3) shows that there is remarkable consistency in the morphology of the bed at all three of the repeat survey sites. This qualitative impression is confirmed by calculating the Pearson correlation coefficient (r) of each repeat profile's bed picks across 500 m moving windows (Figs. 6.2 and 6.3). For 90% of the repeat radar tracks r >0.9, underscoring that there has been negligible morphological change for much of the surveys. For context, we performed the same correlation routine for the bed picks of repeat seismic survey data acquired in 1991, 1997 and 2004 along the 3.5 km profile C1 of RIS previously reported by *Smith et al.* (2007) (these results are shown in Fig. 6.4e). At C1, the $\sim$0.5 km section of track for which *Smith et al.* (2007) reported basal erosion between 1991 and 1997 yields $r > 0.5$, and the $\sim$100 m length of profile interpreted as hosting the growth of a drumlin between 1997 and 2004 returns

$r \sim$-0.2.

There is only one location on PIG where r is considerably lower than 0.9; this occurs between 8.5 and 9 km along profile R1 where r spikes around a value of -0.2 (Fig.6.2). Closer inspection of this location reveals a subtle change in the morphology of the bed picks between 2007/2008 and 2013/2014 (Fig. 6.5). At this site two bumps of $\sim$1-2 m height in 2007/2008 are replaced in 2013/2014 by a central ridge with two troughs $\sim$3 m in depth. However, it is possible that this change is caused by the aforementioned differences in horizontal resolution of the radar systems between surveys. We are therefore cautious to interpret this as a genuine change in bed morphology resulting from erosion and deposition.

6.5 Discussion

The prevailing picture that emerges from our 58 km of repeat surveys of PIG's bed is one of little measurable change having been effected to the ice stream's basal topography and morphology over the 3-7 year timescale. This is despite significant changes occurring to ice-flow speeds and ice-surface elevations over the same periods (Table 6.1), and the observations of active erosion and deposition made over similar timescales at RIS (Fig. 6.4); at RIS ice has experienced little to no dynamic thinning and ice flow is essentially stable (Table 6.1). In the following discussion we firstly consider how these apparently different behaviours between the ice beds of PIG and RIS can be reconciled (Sect. 6.5.1). We then turn to the implications of our results for the understanding of processes of sediment erosion, transport and deposition beneath ice streams and implications for future monitoring of the bed (Sect. 6.5.2).

6.5.1 Are ice-stream beds dynamic?

The only precedent for the measurements obtained here from PIG in terms of repeat geophysical survey over comparable timescales is that from RIS where erosion and deposition on the order of $\sim$1 m a^{-1} were observed in association with morphological changes at the bed (*Smith et al.*, 2007). Here we assess whether the lack of comparable changes observed at PIG can be explained by contrasting glaciological, hydrological and basal characteristics to the RIS survey

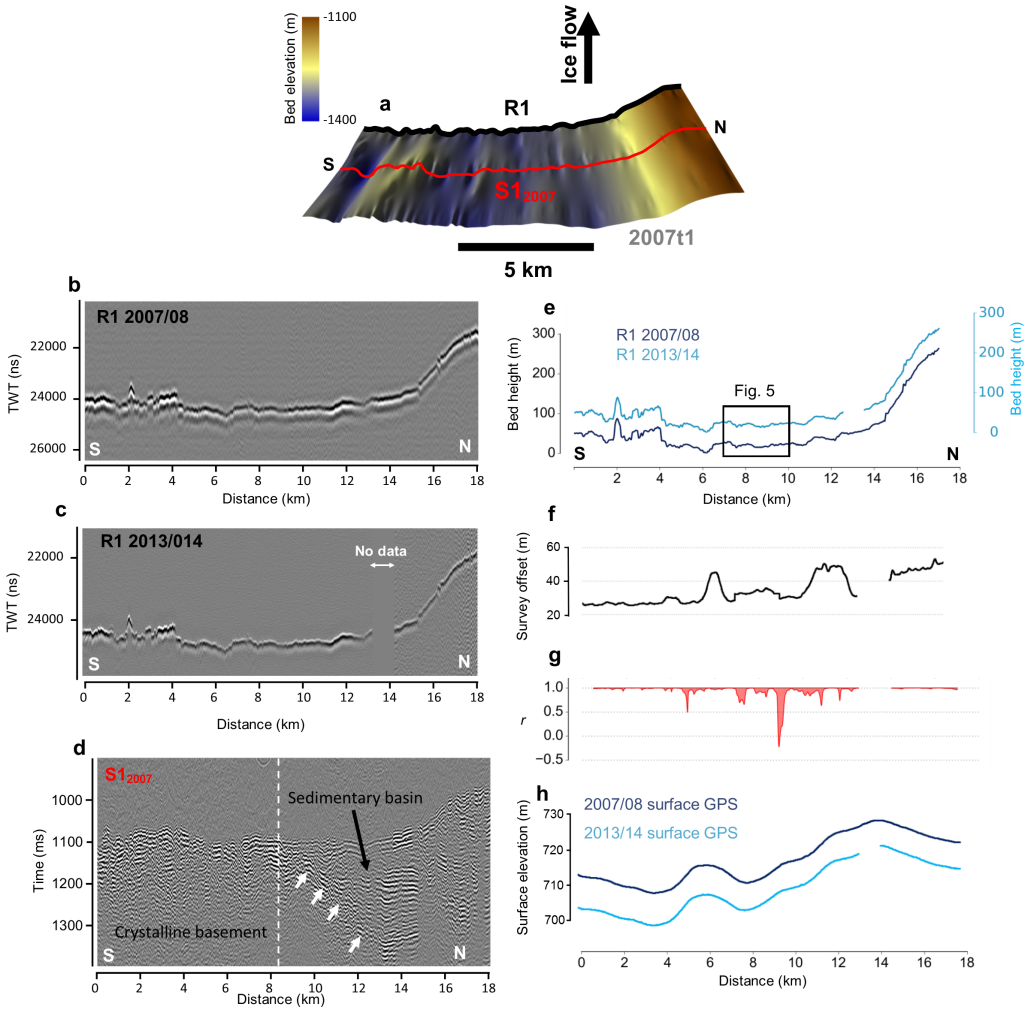

Figure 6.2: Geophysical data and bed picks from PIG. **a** Radar derived DEM from PIG showing the location of radar (black line) and seismic survey (red line). **b, c**, processed radargrams of repeat radar surveys. **d** Processed seismic section of S1 (*Smith et al.*, 2013). White arrows denote a dipping reflector demarcating a sedimentary basin. **e** Bed picks from repeat radar survey R1. **f** Plot showing the divergence between radar profiles in 2007/2008 and 2013/2014. **g** Correlation coefficient of repeat bed picks between 2008/09 and 2013/14 across a 500 m moving window. **h** Plot of surface elevation profiles derived from differential GPS measurements.

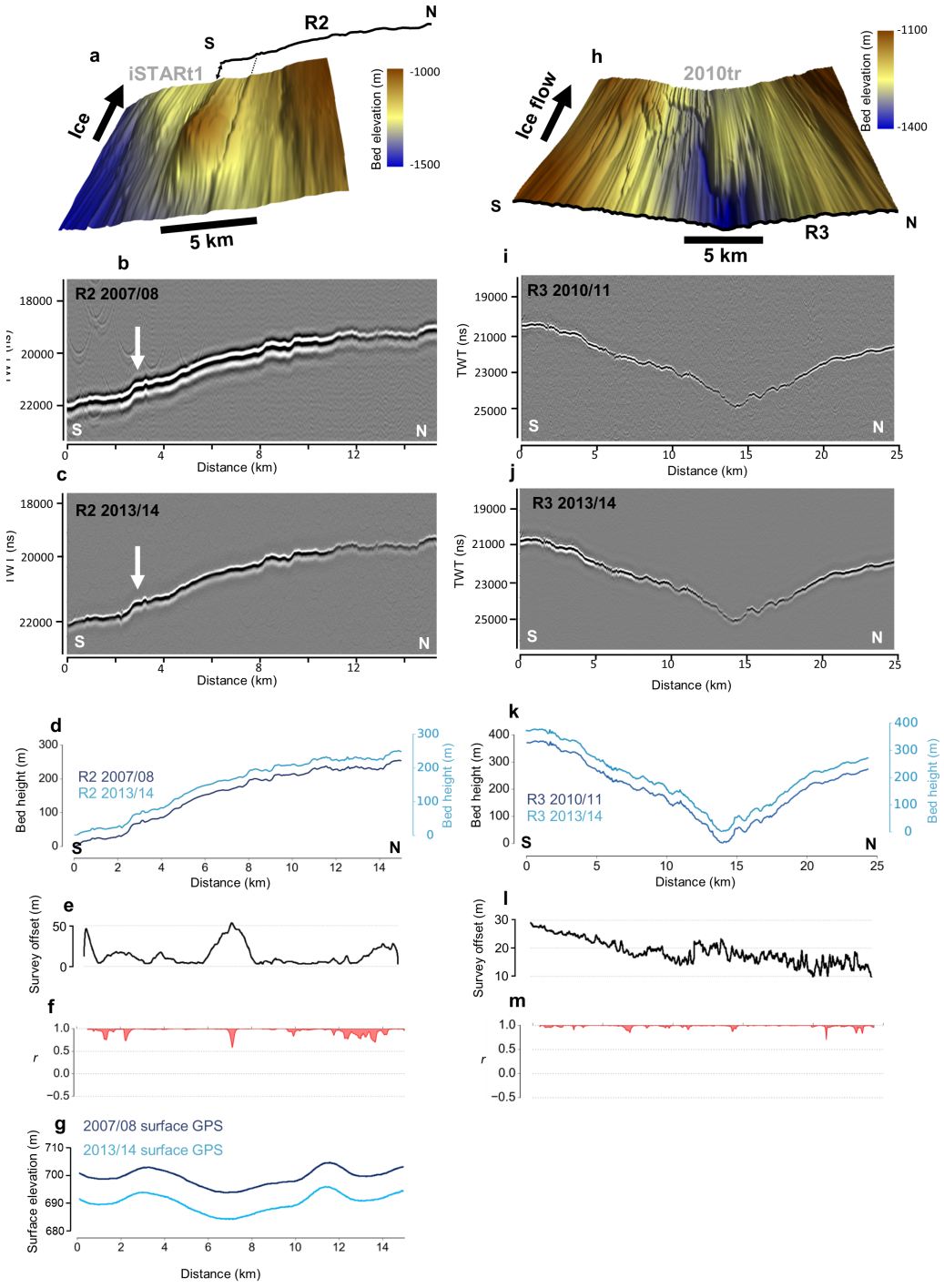

Figure 6.3: Geophysical data and bed picks from PIG. **a** radar derived bed DEM (*Bingham et al.*, 2017) showing the location of survey R2 2 km downstream. **b,c** processed radargrams of repeat radar surveys. **d** bed picks from repeat radar survey R2. **e** Plot showing the divergence between radar profiles in 2007/2008 and 2013/2014. **f** Correlation coefficient of repeat bed picks between 2008/09 and 2013/14 across a 500 m moving window. **g**Plot of surface elevation profiles derived from differential GPS measurements. **h** radar derived bed DEM (*Bingham et al.*, 2017) showing the location of survey R3 at the upstream limit of the radar grid. **i,j** processed radargrams of repeat radar surveys. **k** bed picks from repeat radar survey R3. **l** Plot showing the divergence between radar profiles in 2007/2008 and 2013/2014. **m** Correlation coefficient of repeat bed picks between 2010/11 and 2013/14 across a 500 m moving window.

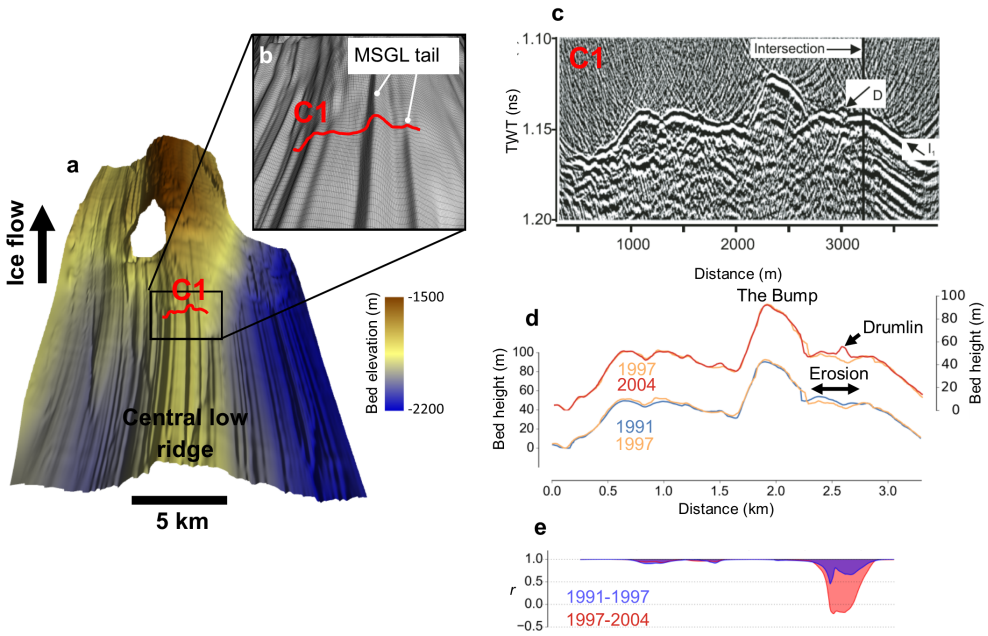

Figure 6.4: Geophysical data and bed picks from RIS **a** radar derived bed DEM for RIS (*King et al.*, 2016) showing geomorphology of the bed and the location of survey C1. **b** close-up of the location of survey C1 showing the 3-dimensional character of the bed. **c** Processed seismic section of survey C1. **d** bed picks from repeat seismic surveys showing erosion and drumlin formation between 1991 and 2004 (*Smith et al.*, 2007). **e** Correlation coefficient of repeat bed picks between 1991 and 2004 across a 500 m moving window.

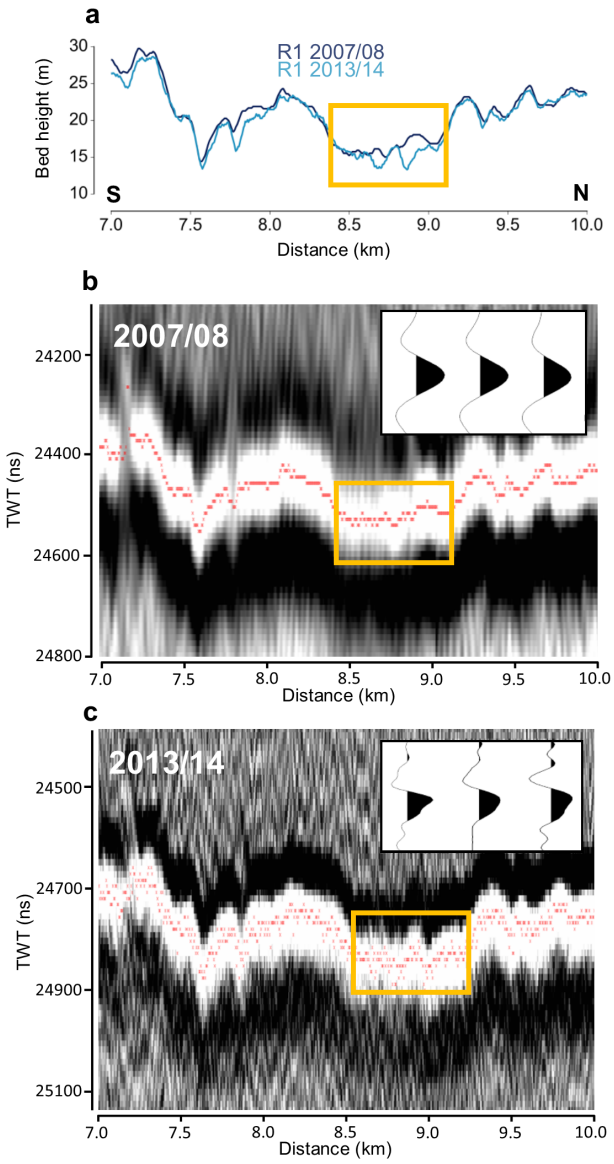

Figure 6.5: Close-up view of change in bed morphology between 2007/08 and 2013/14 identified in survey R1. Yellow boxes outline the area of change identified as having a low correlation (r = -0.2) **a** smoothed bed picks from radar data. **b, c** raw bed picks (red dots) of the basal reflector in 2007/08 and 2013/14. Inset plots show representative traces sampled from the bed reflector.

site, and whether either is likely to be more representative of wider changes occurring at the beds of Antarctic ice streams.

The first notable difference between PIG and RIS is the broad subglacial topography. Each of the repeat surveys on PIG was conducted across the 30 km-wide, ∼2000 m deep, main ice-stream trunk where, at the multi-km wavelength, the bed is largely flat along and across flow (*Vaughan et al.*, 2006). By contrast, the repeat survey location on RIS, though also traversing the ice-stream trunk, overlies a notable topographic ridge ("Central low ridge") that abuts ∼350 m vertically upwards into the central ∼5 km width of the ∼30 km-wide, ∼2000 m deep ice-stream trunk (Fig. 6.4a). There is, therefore, a clear contrast in the gross topographic shape of the cross-sectional bed profile between the PIG and RIS repeat survey sites; and we note that the flat-bedded trough of PIG is more characteristic of the majority of ice streams in West Antarctica (*Fretwell et al.*, 2013). Turning to the finer, sub-km morphological character of each site, detailed ground-based radar surveys of PIG's trunk (Figs. 6.2 and 6.3, and see further imagery in Bingham et al., 2017) have depicted ubiquitous mega-scale glacial lineations (MSGL) across all regions of PIG's trunk, indicative of the widespread presence of deforming sediment (*Clark*, 1993; *Stokes and Clark*, 2001; *Spagnolo et al.*, 2016) MSGL with mean amplitudes ∼ 10 m and a mode spacing of 300-400 m are also pervasive surrounding the RIS repeat survey site (Fig. 6.4a) but, unlike PIG, within the MSGL themselves linear features with much higher amplitudes (up to 70 m) are observed; *King et al.* (2016) termed these features "tapering drumlins".

The physical properties of the bed between PIG and RIS also differ. Seismic reflection surveying of several sites along PIG's trunk, including upstream and downstream of our repeat survey sites, has confirmed that the bed immediately below the ice pervasively consists of dilated sediments, which are at least several metres thick (*Smith et al.*, 2013; *Brisbourne et al.*, 2017). Along seismic profile $S1_{2007}$ potential-field data indicate that a transition from sedimentary to crystalline bedrock lies beneath the cap of deformable sediments (at position 9 km on Fig. 6.2d) (*Smith et al.*, 2013), but the repeat survey of S1 in 2014/2015 ($S1_{2014}$) exhibited no change to acoustic impedance anywhere along this profile (*Brisbourne et al.*, 2017), reinforcing the notion of a relatively stable basal environment despite the transition in geology below the

deforming till layer. By contrast, the bed around RIS profile site C1 is characterised by a "patchwork" of soft, deforming sediments contrasting with regions of basal sliding indicative of more consolidated sediments (*Smith and Murray*, 2009; *Smith et al.*, 2015). Notably, the areas of deforming sediment coincide with topographic highs such as the feature known as "The Bump" (*Smith*, 1997b) (Fig. 6.4c). Changes in acoustic impedance were detected for parts of the RIS repeat profile between 1997 and 2004, and were interpreted as changes in hydrological conditions within subglacial sediments affecting till porosity (*Smith et al.*, 2007).

A third key difference between the PIG and RIS repeat survey sites is the degree to which the survey sites are affected by tidal influences, and the potential effects this can have on subglacial hydrology. High temporal resolution GPS monitoring of ice motion at RIS site C1, 10 km upstream of the grounding line, has shown that horizontal ice velocity varies by $\sim$20% on fortnightly timescales in response to tidally modulated vertical displacement of the Filchner-Ronne Ice Shelf (*Gudmundsson*, 2006, 2007; *Murray et al.*, 2007b; *Minchew et al.*, 2017). In addition, passive seismic monitoring has demonstrated increased seismic activity during tidal cycles (*Aðalgeirsdóttir et al.*, 2008). Numerical modelling studies have suggested that the velocity oscillations are transmitted by tidally-forced fluctuations in basal water pressure, that alter the pore pressure of basal sediments and thus effective pressure at the bed (*Thompson et al.*, 2014; *Rosier et al.*, 2015). These observations suggest that the hydrological system beneath the RIS survey site is prone to significant dynamism and reorganisation over short timescales. However, *Minchew et al.* (2017) suggest that weak shear margins are a more dominant factor in the propagation of tidally induced horizontal ice-flow variability compared to fluctuations in basal water pressure.

High-resolution GPS monitoring at several sites along PIG's main trunk showed no tidal signal in ice motion even 55 km upstream from the grounding line (*Scott et al.*, 2009), which lies well downstream of our repeat radar sites R1-R3. The ubiquitous dilated till layer that overlies a relatively flat bed at each of the PIG survey sites provides suitable conditions for a stable, distributed drainage system (*Weertman*, 1972; *Alley*, 1989; *Engelhardt et al.*, 1990; *Engelhardt and Kamb*, 1997) potentially in the form of a canal network as suggested in the upstream catchment of neighbouring Thwaites Glacier (*Schroeder et al.*, 2013), upstream RIS (*King*

et al., 2004) and Whillans Ice Stream (*Engelhardt and Kamb*, 1997). In the absence of a dynamic hydrological system, sediment mobility facilitated by fluvial transport in subglacial sheets or channels (cf. *Weertman*, 1972; *Walder and Fowler*, 1994; *Fowler*, 2010; *Kyrke-Smith and Fowler*, 2014) may be restricted and likely be more stable over time, thereby limiting the rate of erosion and sediment transport detectable within the precision of repeat geophysical measurements.

We therefore consider the possibility that rapid erosion and bed reorganisation on the scale observed beneath RIS is an exception rather than the rule. Surface velocity inversions along PIG's main trunk suggest that most of its bed is subjected to low basal shear stress, except for some discrete "ribs" of high basal traction spanning the trunk downstream from our measurements (*Sergienko and Hindmarsh*, 2013). We suggest therefore that low sediment transport rates might be expected over much of PIG's bed as a consequence of the generally low basal shear stresses at all of our repeat measurement sites, and that future investigation of bed variation needs to be targeted towards an area of high inferred basal traction.

The apparent stability of the bed we observe is also worth considering in the context of debate concerning strain distribution in deforming beds and associated till rheology. The resolution of our data limits the scope of any firm conclusions but may contribute to further discussion on this issue. Field observations and models have argued for viscous (*Boulton and Hindmarsh*, 1987; *Alley et al.*, 1987b; *Hindmarsh*, 1998) and plastic (*Kamb*, 1991; *Tulaczyk et al.*, 2000; *Iverson*, 2010) deformation of subglacial sediments. Subglacial till transport models invoking either viscous or plastic rheology demonstrate that deformation depth increases with effective pressure. Uneven terrains on an ice-stream bed would therefore translate into variable effective pressures and till fluxes, which might facilitate positive feedbacks over bumps and therefore the growth of bedforms (e.g. *Hindmarsh*, 1998; *Fowler*, 2000; *Schoof*, 2007b). However, it remains unclear how rapidly bedforms can evolve, as although some studies have suggested rapid growth (*Smith et al.*, 2007; *Dowling et al.*, 2016) these might represent exceptions and a comprehensive analysis is missing. Such pressure-dependent growth will ultimately be controlled by the depth of deformation. It is also unclear whether bedform growth is always limited: they are typically characterised by a relatively well-defined size-frequency distribution, albeit

positively skewed (e.g. *Fowler et al.*, 2013; *Hillier et al.*, 2016; *Ely et al.*, 2017). In our study area, one would expect that the uneven terrain of the bed would translate into variable effective pressure and till fluxes and that topography would therefore evolve. The lack of morphological change that we have observed at the ice-stream bed could therefore be interpreted as evidence of very shallow deforming sediment, which might translate to a very low pace of bedform growth, not detectable within the relatively short interval of our repeat surveys. Alternatively, it might indicate that the ice-bed system has reached a point of "maturity" where bedform growth is inhibited by other physical factors. It is even possible that the entire PIG system is now experiencing net erosion due to its recent acceleration, yet the rate of such erosion must be very low for us not to be able to detect a lowering of the topography within the six year interval of our observations.

Geophysical surveys of other West Antarctic ice streams (*Alley et al.*, 1986; *Blankenship et al.*, 1986; *Peters et al.*, 2006) have revealed shallow bed gradients and widespread deforming till similar to the surveyed sites on PIG. These characteristics are also evident in offshore records of palaeo-ice stream beds on the outer continental shelf of West Antarctica, where ice streams occupied shallow troughs in the sedimentary basement (*Lowe and Anderson*, 2002; *Wellner et al.*, 2006; *Larter et al.*, 2009; *Graham et al.*, 2010). These offshore regions are characterised by ubiquitous MSGL (*Spagnolo et al.*, 2014) that are also observed in the more extensive grid surveys surrounding our repeat surveys (Figs. 6.2a, 6.3a, 6.h) (*Bingham et al.*, 2017). The uniformity of these bedforms may reflect stable, self-organised bed conditions (cf. *Spagnolo et al.*, 2017).

6.5.2 Implications for subglacial sediment transport and future surveys

The absence of detectable morphological change to the bed over the majority of the $\sim$ 60 km of bed profiles on PIG could be interpreted in three ways: (1) that no sediment erosion/transport/deposition is occurring at the measured sites; (2) that erosion/deposition is occurring but at rates too low to be detected within the vertical range resolution of the radar; or (3) that the subglacial till flux is in a steady state wherein sediment transport is active but is not altering the shape of the bed. The last of these would contradict modelling studies that suggest

that pressure-dependent till fluxes dictate that there can be no steady-state till flux on an uneven basal interface (*Hindmarsh*, 1998; *Fowler*, 2000; *Schoof*, 2007b).

Prior to this study the few repeat geophysical surveys of the ice-bed interface in Alaska and Antarctica yielded subglacial erosion rates of 1000-3900 mm a^{-1} (*Motyka et al.*, 2006; *Smith et al.*, 2007, 2012), far exceeding the 0.01-100 mm a^{-1} range traditionally reported as characteristic of glacial settings using proglacial sediment yields (*Hallet et al.*, 1996; *Koppes and Hallet*, 2006; *Koppes and Montgomery*, 2009; *Cowton et al.*, 2012; *Herman et al.*, 2015) (Fig. 6.6). Consequently, there has been growing consensus that subglacial erosion and transport is likely to be high, i.e. of the order of m a^{-1}, beneath thick, warm-based ice as manifested by polar ice streams. Observations of substantial till deposition at the grounding lines of contemporary and palaeo-ice streams in the West Antarctic support this view (*Anandakrishnan et al.*, 2007; *Batchelor and Dowdeswell*, 2015). The precision of our measurements, essentially defined by the vertical range resolution of the radar, means that the maximum possible erosion rate that could go undetected along our profiles is 500 mm a^{-1}.

Aside from the repeat geophysical studies conducted in Antarctica by *Smith et al.* (2007, 2012), the only other location where this method has been used is southeast Alaska where *Motyka et al.* (2006) found exceptionally high erosion rates of up to 3.9 ± 0.8 m a^{-1} over a period of 14 years (Fig. 6.6). However, this setting is unique and these exceptional erosion rates occurred during short episodes of glacier advance over glaciomarine and outwash sediments driven by ice-sediment dynamics (*Motyka et al.*, 2006; *Brinkerhoff et al.*, 2017). Indeed, erosion rates in southern Alaska are the highest reported for any region. These high erosion rates are associated with high precipitation rates, active tectonic uplift and glaciofluvial evacuation of unlithified sediments (*Hallet et al.*, 1996; *Motyka et al.*, 2006). The equally rapid erosion observed by *Smith et al.* (2007, 2012) therefore evokes a glaciofluvial mechanism. Emerging evidence of subglacial hydrology from West Antarctica shows that meltwater can be stored and released over short timescales through interconnected subglacial lakes and channels (*Wingham et al.*, 2006; *Fricker et al.*, 2007; *Fricker and Scambos*, 2009; *Smith et al.*, 2017a). In our survey area there is no evidence from radar (*Bingham et al.*, 2017) or seismic data (*Brisbourne et al.*, 2017) that indicates the presence of subglacial lakes or concentrated meltwater channels. However,

in Smith et al.'s (2012) repeat seismic measurement over ∼50 years, rapid erosion of 1 m a $^{-1}$ was detected ∼ 25 km downstream of survey R3 (EHT31 in Fig. 6.1b). At this location the bed is also smooth and there is no indication from satellite or geophysical data of rapid meltwater drainage events or channelised meltwater flow (*Smith et al.*, 2012). A possible explanation for the discrepancy between erosion observed at this location and the results of this study is a timescale bias (*Ganti et al.*, 2016). Smith et al.'s (2012) study may have captured intermittent episodes of erosion not captured by our 3-6 year survey intervals.

In Sect. 3, we showed that while the majority of the repeat radar profiles evince negligible morphological change, there is one ∼ 0.5 km section of profile R1 where a possible reorganisation of the bed is expressed as a morphological change in the basal reflector (Fig. 6.5). This region of the bed broadly coincides with a transition from thin ($\leq$ 10 m) sediment overlying a crystalline basement to a deep sedimentary basin imaged in seismic and potential field surveys (*Smith et al.*, 2013). A change in basal drag and ice velocity is also associated with this boundary. It is likely that such boundaries influence subglacial hydrological pathways and, hence, basal ice motion. This exemplifies the importance of the sampling location and periods of measurement to any study attempting to capture subglacial sedimentary processes. For example, the location where *Smith* (2007) monitored deposition (drumlin formation) on RIS between 1997 and 2004 is positioned at the end of a drumlin tail subsequently imaged in a wider radar survey of the region (*King et al.*, 2009, 2016) (Fig. 6.4b). These repeat measurements may have been fortuitously timed to capture the extension of the drumlin tail. The anisotropic morphology of tapering drumlins and MSGL present beneath RIS (*King et al.*, 2016) may not lend itself well to the detection of change from 2-D surveys driven orthogonal to ice flow. Dynamic change in these bedforms may be expressed as downstream migration of a propagating sediment front that would be difficult to detect without more extensive and/or higher-density coverage of repeat surveys over longer timescales.

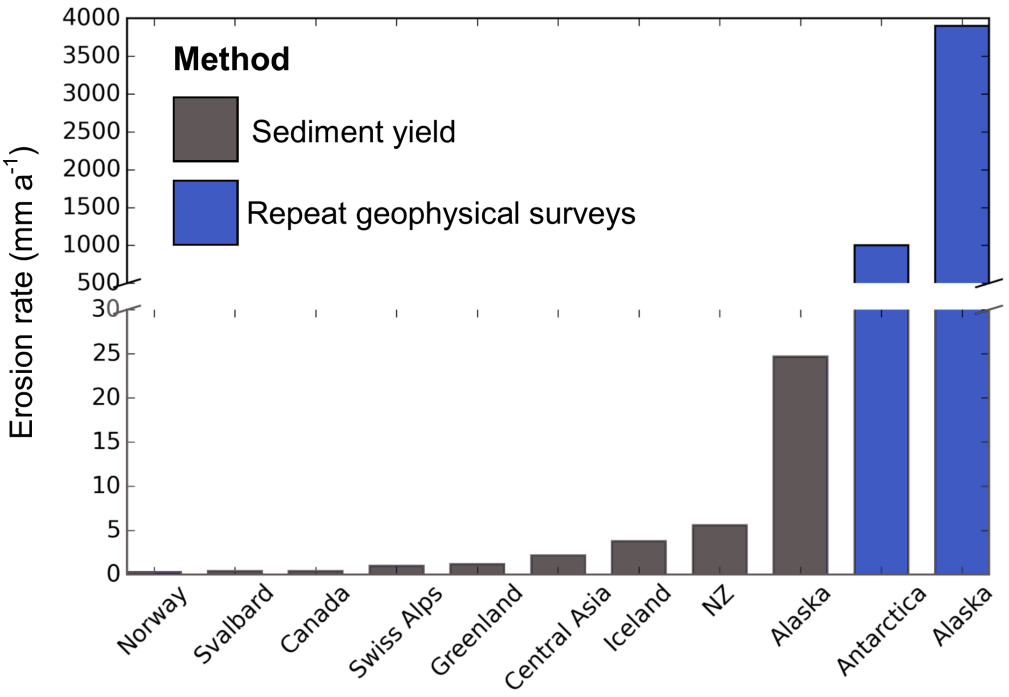

Figure 6.6: Mean erosion rates from previously published literature in a range of locations. Data taken from *Hallet et al.* (1996, and references therein), *Koppes and Hallet* (2006), (*Motyka et al.*, 2006), (*Cowton et al.*, 2012) and *Smith et al.* (2007, 2012).

6.6 Conclusion

We have analysed ∼60 km of repeat radar surveys acquired from Pine Island Glacier, West Antarctica, between austral seasons 2007/2008 and 2013/2014. The results showed that little morphological change occurred at the bed over this period. The absence of large signals of erosion or deposition contrasts with erosion/deposition measured on nearby Rutford Ice Stream between 1991 and 2004 (*Smith et al.*, 2007), and with inferred erosion of ∼1 m a^{-1} at Pine Island Glacier over a half-century (1960-2009; *Smith et al.*, 2012). We attribute the negligible detection of morphological change at the bed of Pine Island Glacier on the sub-decadal timescale to the ubiquitous presence of a deforming till layer, wherein sediment transport is in steady state such that sediment is transported along the basal interface without inducing measurable vertical displacement to the radar-sounded basal interface. Moreover, none of the survey sites on Pine Island Glacier have experienced short-term variations in ice velocity (*Scott et al.*, 2009) diagnostic of active hydrological systems capable of mobilising sediment (*Thompson et al.*, 2014; *Rosier et al.*, 2015). By comparison, the high subglacial erosion and deposition rates reported from Rutford Ice Stream occurred where the ice is overriding a topographic rise 350 m high, there are sharp contrasts in subglacial sediment there are sharp contrasts in subglacial sediment properties, and the subglacial system likely experiences short-term variability influenced by tidal oscillations (*Aðalgeirsdóttir et al.*, 2008; *Thompson et al.*, 2014; *Rosier et al.*, 2015).

The surveys presented in this study have increased the length, by an order or magnitude, of the available records of repeat measurements of Antarctic ice-stream beds. However, these environments remain poorly sampled. The surveys of Pine Island Glacier and Rutford Ice Stream have shown that improved understanding of the dynamism of the ice-sheet bed may best be gained from a multi-method survey approach, involving (1) high-density radar grid surveying to image the subglacial landscape and provide spatial context, (2) seismic survey to discern the physical properties of the basal interface and (3) repeated seismic and/or radar profiles at the same site undertaken over sub-decadal to decadal timescales. Our findings also show the importance of the physical properties of the bed at each site to the sediment erosion and deposition that could be detected, underscoring the requirement to sample sites that, as a

whole, capture a representative range of basal conditions. Models of basal drag inverted from satellite-imaged surface properties (e.g. *Joughin et al.*, 2009; *Arthern et al.*, 2015) offer the best opportunities to guide site selection.

Chapter 7

High-resolution sub-ice-shelf seafloor records of 20th-century ungrounding and retreat of Pine Island Glacier, West Antarctica

In all previous chapters I have considered the properties of the bed of Pine Island Glacier beneath the modern trunk and tributaries. In this chapter I now move to the proglacial environment beneath the modern ice shelf and investigate the geomorphology of the recently deglaciated seafloor. A version of this chapter has been published in the Journal of Geophysical Research: Earth Surface as:

Davies, D., Bingham, R.G., Graham, A.G.C., Spagnolo, M., Dutrieux, P., Vaughan, D.G., Jenkins, A. and Nitsche, F.O., (2017). High-resolution sub-ice-shelf seafloor records of twentieth century ungrounding and retreat of Pine Island Glacier, West Antarctica. *Journal of Geophysical Research: Earth Surface*, 122(9), pp.1698-1714.

I processed and analysed the data, mapped and analysed the metrics of seafloor geomorphology and wrote the manuscript. My co-authors acquired the data in the field and contributed to edits in the writing process.

7.1 Abstract

Pine Island Glacier Ice-Shelf (PIGIS) has been thinning rapidly over recent decades, resulting in a progressive drawdown of the inland ice and an upstream migration of the grounding line. The resultant ice loss from Pine Island Glacier (PIG) and its neighboring ice streams presently contributes an estimated $\sim$10% to global sea-level rise, motivating efforts to constrain better the rate of future ice retreat. One route towards gaining a better understanding of the processes required to underpin physically-based projections is provided by examining assemblages of landforms and sediment exposed over recent decades by the ongoing ungrounding of PIG. Here we present high-resolution bathymetry and sub-bottom-profiler data acquired by autonomous underwater vehicle (AUV) surveys beneath PIGIS in 2009 and 2014 respectively. We identify landforms and sediments associated with grounded-ice flow, proglacial and subglacial sediment transport, overprinting of lightly-grounded ice-shelf keels and stepwise grounding-line retreat. The location of a submarine ridge (Jenkins Ridge) coincides with a transition from exposed crystalline bedrock to abundant sediment cover potentially linked to a thick sedimentary basin extending upstream of the modern grounding line. The capability of acquiring high-resolution data from AUV platforms enable observations of landforms and understanding of processes on a scale that is not possible in standard offshore geophysical surveys.

7.2 Introduction

The ice shelves that surround Antarctica's coast buttress ice flow from the continent's interior to the ocean (*Dupont and Alley*, 2005; *Fürst et al.*, 2016). Over the last 25 years, however, many of the ice shelves along West Antarctica's Amundsen Sea margin have thinned extensively (*Pritchard et al.*, 2012; *Rignot et al.*, 2013; *Paolo et al.*, 2015), leading to progressive acceleration and surface lowering of ice inland (*Rignot et al.*, 2002; *Scott et al.*, 2009; *Wingham et al.*, 2009; *McMillan et al.*, 2014; *Mouginot et al.*, 2014; *Konrad et al.*, 2017), and an inland migration of the grounding line (*Park et al.*, 2013; *Rignot et al.*, 2014). While the ice-shelf thinning has been attributed to sub-shelf melting (*Jacobs et al.*, 1996; *Pritchard et al.*, 2012; *Rignot et al.*, 2013), direct observations of the processes of sub-ice shelf melting and grounding-line

retreat are few, because sub-shelf cavities are one of the Earth's least accessible environments (*Dowdeswell et al.*, 2008b).

Only recently have autonomous underwater vehicles (AUVs) offered an opportunity to access sub-ice regions in Antarctica. Most sub-shelf AUV campaigns conducted to date have prioritized the measurement and characterization of sub-ice-shelf ocean-water properties and ice-shelf bases (*Nicholls et al.*, 2006; *Jenkins et al.*, 2010; *Jacobs et al.*, 2011; *Dutrieux et al.*, 2014a,b). By contrast, comparatively little attention has been given to sounding or imaging seafloor bedforms and sediment properties beneath thinning ice shelves. Such settings, especially where ice has recently been grounded, provide opportunities to investigate "geomorphologically pristine", recently-deglaciated terrains, and to relate these terrains to the processes that created them (e.g. *Domack et al.*, 2005; *Graham et al.*, 2013; *Smith et al.*, 2017b).

In this paper, we present high-resolution bathymetry and sub-bottom-profiler data obtained by the Autosub3 AUV (*McPhail et al.*, 2009) beneath Pine Island Glacier Ice-Shelf (hereafter PIGIS), West Antarctica, during January 2009 and February-March 2014. Using these data we explore the nature of seafloor bedforms and sediment properties, and assess processes associated with retreat from a former pinning point during the mid-20th century. Our results reveal a suite of bedforms created by proglacial sedimentation, grounded ice flow and lightly-grounded ice flow, all reflecting the progressive ungrounding and retreat of Pine Island Glacier from beneath and just in front of the present ice shelf. We demonstrate the necessity to use meter-scale resolution imagery of recently-deglaciated terrains to understand processes of past decadal to centennial retreat.

7.3 Study area and geological context

PIGIS (Figure 1) impounds Pine Island Glacier (PIG), which together with Thwaites Glacier drain ∼20% of the West Antarctic Ice Sheet (WAIS) into Pine Island Bay, the largest embayment of the Amundsen Sea. Since 1973 PIG's flux through PIGIS to the ocean has increased from 78 Gt yr^{-1} to ca. 133 Gt yr^{-1} (*Mouginot et al.*, 2014), an increase in ice transfer to the ocean of >40%. Between 1973 and 2010, the velocity of PIGIS increased by 1.7 km/yr or 75%

and now flows at >4 km/yr (*Mouginot et al.*, 2014). Contemporaneously, the ice has thinned progressively inland, with thinning now measurable at the ice divides (*Wingham et al.*, 2009; *Scott et al.*, 2009; *McMillan et al.*, 2014; *Konrad et al.*, 2017), and the grounding line has retreated 31 km between 1992 and 2011 (*Rignot et al.*, 2014). Collectively, this is the most rapidly retreating region of ice on the planet, and is contributing an estimated ∼5-10% of the currently observed global sea-level rise (*Rignot et al.*, 2008; *Turner et al.*, 2017).

PIG's current retreat is thought to have been triggered by ungrounding from a transverse submarine ridge, Jenkins Ridge (Fig.7.1), that spans the width of PIGIS ∼30 km from the current grounding line (*Jenkins et al.*, 2010; *Smith et al.*, 2017b). Dating of sediments retrieved from the crest and seaward slope of Jenkins Ridge, via hot-water drilling through the ice shelf, suggests that ungrounding was initiated in the 1940s, and became complete by the 1970s (*Smith et al.*, 2017b). Satellite imagery also indicates that contact between the ice shelf and the highest point of Jenkins Ridge persisted in the early 1970s but became ungrounded in subsequent years (*Jenkins et al.*, 2010). This ungrounding and retreat is associated with enhanced melting by incursion of warm Circumpolar Deep Water onto the continental shelf (*Jacobs et al.*, 2011; *Pritchard et al.*, 2012; *Hillenbrand et al.*, 2017). Intermittent grounding of ice-shelf keels on localized bathymetric highs in the central region of PIGIS has also been detected within the last decade (*Joughin et al.*, 2016).

Regional geology is intrinsic to the properties of the seafloor beneath PIGIS. Upstream of the grounding line, relatively low crustal thickness in the PIG catchment observed in aero-gravity data facilitates ice streaming through the presence of thick sedimentary basins and elevated heat flux (*Jordan et al.*, 2009; *Muto et al.*, 2013, 2016). The legacy of continental rifting associated with the formation of the West Antarctic Rift System (*Bingham et al.*, 2012) is a highly varied subglacial environment beneath PIG that exerts topographic controls on ice streaming (*Jordan et al.*, 2009). Seaward of PIGIS this regional topography contrasts between smooth sedimentary strata on the outer continental shelf and rough crystalline bedrock on the inner continental shelf in Pine Island Bay (*Jakobsson et al.*, 2011; *Nitsche et al.*, 2013). Landforms on the outer continental shelf are dominated by mega-scale-glacial lineations (MSGL) associated with ice streaming over deforming sediments and grounding zone wedges (GZW) deposited during

pauses in retreat of the Pine Island-Thwaites paleo-ice stream (*Anderson et al.*, 2002; *Lowe and Anderson*, 2002; *Graham et al.*, 2010; *Jakobsson et al.*, 2011). The inner-continental shelf exhibits a more rugged seafloor charaterized by exposed crystalline bedrock streamlined by ice stream flow with deep (up to 1650 m) basins connected by meltwater channel networks (*Lowe and Anderson*, 2002; *Nitsche et al.*, 2013).

Because of the difficulty of accessing the sub-ice-shelf cavity, comparatively little is known about the detailed properties of the seafloor beneath PIGIS. Aero-geophysical surveys constrained by AUV and radar-soundings have provided broad insights into the sub-ice-shelf bathymetry and sediment distribution (*Studinger et al.*, 2010; *Muto et al.*, 2013, 2016). These studies show that the Jenkins Ridge spans the entire ∼45 km width of PIGIS and rises ∼350-400 m above the seafloor. Landward of Jenkins Ridge lies a sedimentary basin up to ∼800 m thick immediately upstream of the current grounding line, whereas sediments are absent or thin seaward of Jenkins Ridge (*Nitsche et al.*, 2013; *Muto et al.*, 2016).

AUV-mounted geophysical apparatus offers the ability to investigate the seafloor at sub-meter to meter-scale resolution (*Nicholls et al.*, 2006; *Wynn et al.*, 2014; *García et al.*, 2016). Due to the challenging environment beneath Antarctic ice shelves and the operational and logistical limits of AUV operations, the spatial coverage of these data is limited. However, available data from missions beneath PIGIS thus far have provided insights into ocean properties in unprecedented detail (*Jenkins et al.*, 2010; *Jacobs et al.*, 2011; *Dutrieux et al.*, 2014a). Sections of these data have received some geomorphological analysis (*Jenkins et al.*, 2010; *Graham et al.*, 2013), however a detailed study of seafloor geomorphology has not yet been conducted using the entirety of these datasets.

7.4 Data and Methods

7.4.1 Multibeam-swath bathymetry

High-resolution, sub-ice-shelf seafloor bathymetry covering a total distance of ∼110 km (∼3,850 km^2) of the seafloor was obtained from two AUV missions (M433 and M434) beneath PIGIS in January 2009 during Cruise NBP09-01 of the research icebreaker R/V Nathaniel B. Palmer

(tracks marked in Figs.7.1a). Navigation is achieved by dead-reckoning through an Inertial Navigation System (INS), integrated and mechanically coupled with a downward looking Acoustic Doppler Current Profiler (ADCP). Navigational errors are typically between 0.2% and 0.1% of distance travelled (*McPhail*, 2009; *McPhail et al.*, 2009). A Kongsberg EM-2000 multibeam echosounder was operated from the AUV at a nominal height of ∼100 m above the seafloor which provides typical vertical root-mean square errors of <10 cm (*Dowdeswell et al.*, 2008b). Data were processed using MB-System, and a digital elevation model (DEM) was gridded with 2 m cell sizes using a weighted near-neighbor algorithm (*Graham et al.*, 2013; *Dutrieux et al.*, 2014b).

7.4.2 Sub-bottom profiling

Sediment properties were investigated using an Edgetech 2200M sub-bottom profiler mounted on Autosub3. Data were obtained from AUV deployments during the iSTAR research cruise JR294/295 from the RRS James Clark Ross in February and March 2014. The system emits a chirp signal at 2-16 kHz providing shallow penetration images of the seafloor with a resolution of 6-10 cm. Two missions (M447 and M448) covered ∼150 km of the seafloor from ∼20 km seaward of the 2009 ice front across the seaward slope, crest and backslope of Jenkins Ridge and into the ice-shelf cavity (Fig. 7.1a). A bandpass Butterworth filter with lower and upper cut-offs of 1000 and 3500 kHz respectively was applied to the data to remove high-frequency noise. A vertical correction was applied to account for the AUV's flying height. Water depths and sediment thickness were calculated by converting the two-way travel time to meters using acoustic velocities of 1459 m s^{-1} for water and 1500 m s^{-1} for soft unconsolidated sediment respectively. We provide an error margin of ±3% for estimates of sediment thickness as recommended by *Lysså et al.* (2010).

Bathymetric data were not recorded concurrently with the sub-bottom profiler in 2014 due to problems encountered with the EM-2000 multibeam echosounder, and therefore we are unable directly to compare contemporaneous bathymetric and sub-bottom-profiler data. However, survey tracks M447 and M448 closely follow parallel to, and intersect, multibeam survey tracks M433 and M434 (Fig.7.1a).

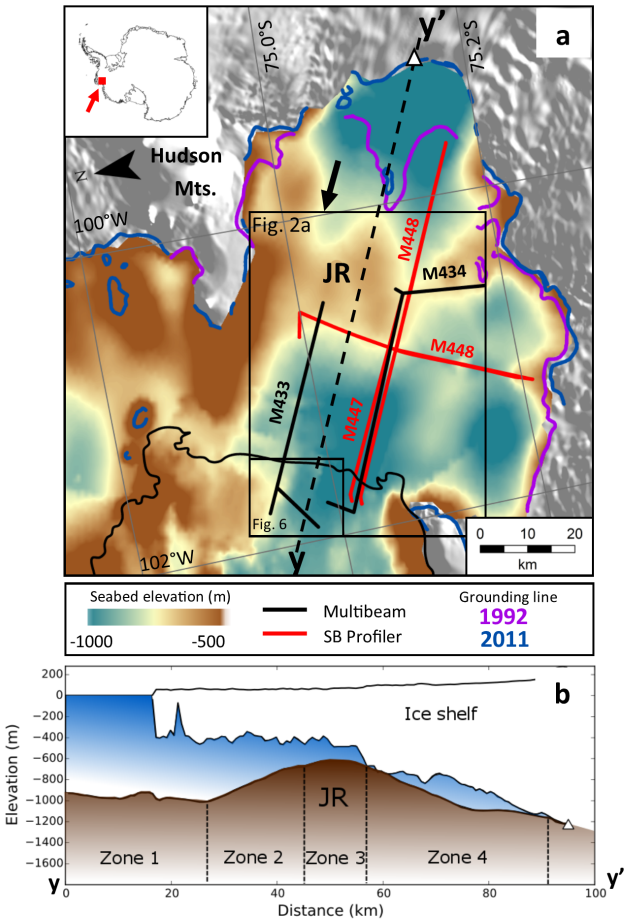

Figure 7.1: Map and locations of Autosub3 sub-ice shelf missions beneath Pine Island Glacier Ice-Shelf (PIGIS). a Sub-ice shelf bathymetry derived from gravity inversion (see supplementary material in *Dutrieux et al.* (2014a) for methodology) showing the location of Jenkins Ridge (JR) and Autosub3 mission tracks. Black line shows the ice-shelf front position in 2009. Boxes show areas covered by figures referred to later in text. Grounding line locations are from the MEaSUREs dataset (*Rignot et al.*, 2011b). **b**, Cross-section of ice and seafloor geometry extracted from profile y-y' (dashed black line) showing geomorphic zones 1-4 (ice draft and bathymetry from *Dutrieux et al.* (2014a); see their supplementary material for methodology). Data for each zone are shown in Figs 7.2-7.4.

7.4.3 Mapping and metrics

Geomorphological features were mapped from bathymetric DEMs in ArcGIS v.10.1. Multiple-illumination azimuths and vertical exaggerations were applied to aid visualization following the methods of *Smith and Clark* (2005). To further aid mapping, subtle geomorphological features were accentuated using a surface-detrending algorithm that fitted a polynomial to the original DEM using a 30 m kernel window to produce a smoothed surface, which was then subtracted from the original DEM (*Hurst et al.*, 2012). Three-dimensional surfaces were produced and visualized in Schlumberger Petrel^{TM}seismic interpretation software.

Linear bedforms were mapped by drawing lines across their crests while azimuths (0-360° from grid North) were extracted using GIS tools. Spacing and amplitude of linear bedforms were calculated by averaging multiple measurements extracted from cross-sectional topographic profiles transverse to bedform crestlines following the method of *Spagnolo et al.* (2014).

7.5 Results and Analysis

In this section we describe the seafloor bedforms and sediment properties imaged below PIGIS, respectively, in 2009 and 2014 using the techniques described above. Figure 7.2 provides an overview of bathymetric data showing relief-shaded DEMs alongside interpretations of landforms. We structure the findings by location relative to Jenkins Ridge, as demarcated on Figure 7.1b: progressively approaching the grounding line the zones can broadly be described as (1) the outer sub-ice-shelf seafloor, (2) the PIG-distal flank of Jenkins Ridge, (3) Jenkins Ridge crest, and (4) the PIGIS submarine cavity (Fig.7.1b). In the following sections we present seafloor bathymetry (Fig. 3) and sub-bottom profiler data (Fig. 4) in turn for each zone with the exception of Zone 4 where only sub-bottom profiler data were acquired.

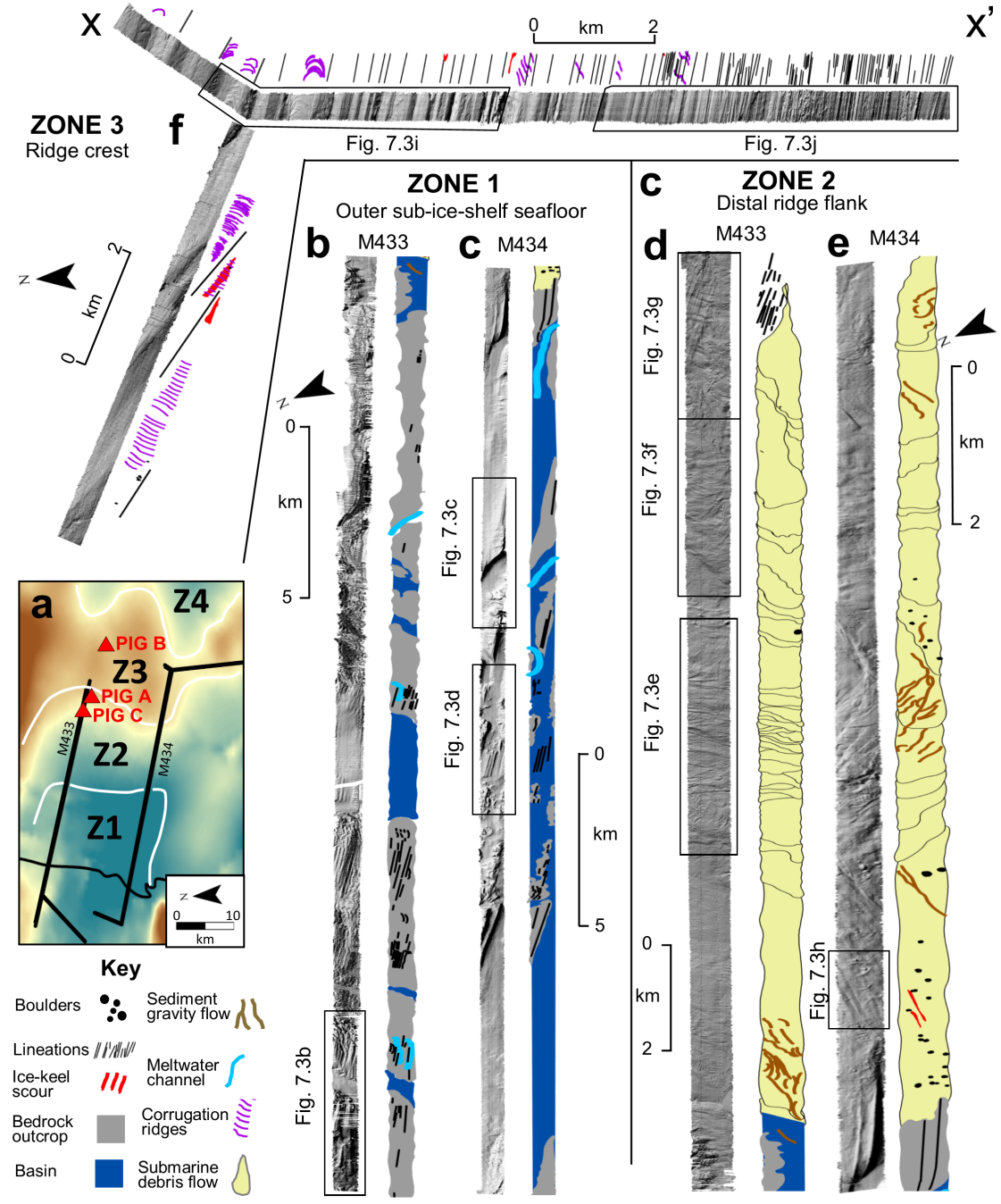

Figure 7.2: Sub-ice-shelf multibeam-bathymetry data and geomorphological interpretation. a, Map of regional bathymetry and location of multibeam surveys M433 and M434. Red triangles show the locations of sediment cores described in (*Smith et al.*, 2017b). Black line shows the ice-shelf front position in 2009. **b-f**, Multi-directional relief-shaded multibeam topography plotted alongside corresponding geomorphological interpretations. Data width have been exaggerated by a factor of two for clarity. Black lines superimposed over debris flows delimit individual debris flow lobes. Black boxes show the location of three-dimensional surface imagery shown in Figure 7.3.

7.5.1 Zone 1:Outer sub-ice-shelf seafloor

Seafloor bathymetry

The regional bathymetry of Zone 1 exhibits rugged topography, likely dominated by outcrops of crystalline bedrock that rise in excess of 40 m above intervening smooth, flat-bottomed basins (Figs. 7.2b, c). The surfaces of outcrops in profile M433 host parallel lineations 2-10 m in amplitude and up to 1.5 km in length orientated along the trough axis (Fig.7.3b). The morphology of these features is consistent with streamlined-bedrock landforms described in offshore-bathymetry datasets in Pine Island Bay and on the inner continental-shelf region of the western Amundsen Sea Embayment (*Lowe and Anderson*, 2002; *Graham et al.*, 2009; *Nitsche et al.*, 2013).

Further south, and traversing an extensive basin, data from profile M434 exhibit lineations and outcrops truncated abruptly by steep-sided channels >200 m wide with curvilinear cross-sectional profiles (Figs. 7.2c; 7.3c,d). A series of irregular depressions up to 3 m deep and 150 m wide punctuates the crest of a lineation in this region (Fig. 7.3f). 6 km downstream from the location of these surface depressions is a chain of flat-topped mounds up to 10 m in height, 300 to 1000 m in width, and up to 2 km in length (Fig. 7.3d). The mounds' long axes generally trend parallel to inferred paleo-ice stream flow.

Sub-bottom profiler

The topography of the seafloor in Zone 1 imaged from the sub-bottom profiler further demonstrates the typical ruggedness of the former ice bed in this region as suggested by the bathymetric surveys (Fig. 7.4b). Regions of elevated seafloor are characterized by a high-amplitude, continuous acoustic reflector, between which some acoustically-stratified topographic depressions are interspersed (Fig. 7.4c). The stratification within each depression is characterized by a series of laterally continuous, parallel reflectors conforming to the underlying seafloor topography. The full sequence of stratified reflectors has a maximum thickness of 7.5 ± 0.2 m (Fig. 7.4c inset).

7.5.2 Zone 2:PIG-distal flank of Jenkins Ridge

Seafloor bathymetry

The transition between Zone 1 and Zone 2 is marked by an abrupt change from rugged to relatively smooth seafloor topography (Fig. 7.2d,e) reflecting an apparent shift to a sediment-dominated regime. Bedforms in Zone 2 broadly display amplitudes an order of magnitude lower than in Zone 1 and, on the whole, show little to no streamlining. Towards the base of Jenkins Ridge flank, on M433, a network of channels and ridges with a dendritic pattern cuts across the slope (Fig. 7.2d; zoom in Fig. 7.3e); individually they vary in size but typically have depths and amplitudes <2 m, and they cover a distance of at least 2800 m ($\sim$980 km^2) of the lower slope of Jenkins Ridge. Further upslope, irregular, undulating surfaces superimposed by lobate ridges (convex downslope) are more common (Fig. 7.2d; zoom in Fig. 7.3f).

Further south on the lower Jenkins Ridge flank (profile M434; Fig. 7.2h) is imaged a series of spherical mounds protruding 1-3 m from the seafloor and with a maximum diameter of $\sim$20 m (profile left of panel 3h). Each mound is fringed by crescent-shaped ridges 1-1.5 m in amplitude. A pair of subtle, parallel, linear scours also occurs in close proximity to these boulders (Fig. 7.3h). They have a mean spacing of 49 m, amplitudes of <1 m, and lengths up to 650 m, and occur at depths of 950-970 m. The scours trend east-west as opposed to the more typical southeast-northwest direction of streamlined-bedform features observed seaward in Zone 1 (rose diagram right of panel h).

Near to the top of Jenkins Ridge's seaward flank, where the headroom between the former ice-shelf base and sea floor narrows, a set of seafloor lineations is also observed, exhibiting orientations in line with modern ice flow vectors (Fig. 7.2d; zoom in Fig. 7.3g). The lineations have spacings of 19-36 m (mean 26 m), amplitudes of <1 m, and lengths up to 600 m. They are located 2.5 km west of sediment cores that date ungrounding of the ice shelf from Jenkins Ridge to 1970 $\pm$4 years (Fig. 7.2a) (*Smith et al.*, 2017b).

Sub-bottom profiler

The transition between Zone 1 and 2 is marked by a change in the character of the seafloor acoustics from a rugged interface with some sub-surface structure to an acoustically-transparent unit with a diffuse seabed reflector (Fig. 7.4d). The seabed within this zone is predominantly smooth with some small-scale lobes or mounds up to ∼3 m in amplitude (Fig.7.4e).

7.5.3 Zone 3: Jenkins Ridge crest

Seafloor bathymetry

Only profile M434 provides data from Zone 3: the AUV imaged data along an ∼8 km long strip broadly along-paleo-ice-flow, and a ∼13 km long strip along the southern half of Jenkins Ridge crest trending broadly orthogonal to current ice-shelf flow (Fig. 7.2f). Along the entire Jenkins Ridge crest the predominant geomorphological feature comprises streamlined lineations oriented parallel to inferred paleo-ice-flow (Figs. 7.3i, j). A change in the metrics of these lineations is clearly evident ∼6 km along the profile (north to south), coinciding with a sharp rise in seafloor elevation from a mean of -730 m to -708 m (Fig. 7.5a). In the northern section, closer to the central flow-axis of PIGIS, the lineations have a mean spacing of 287 m and mean amplitude of 7.3 m; in the southern section they have a mean spacing of 46 m and a mean amplitude of 1.4 m (Fig. 7.5b,c). Furthermore, along the southern section of Jenkins Ridge crest, not all the lineations are parallel to one another, and occasionally they appear to cross-cut or converge (Magnified panel in Fig. 7.3j).

The surface characterized by lineations that we have just described is overprinted by finer-scale features. These include sub-meter-amplitude curvilinear sediment ridges that are convex in the direction of paleo-ice flow and have spacing of 26-90 m (mean 43 m) (left-hand zooms in Fig. 7.3i). The curvilinear ridges initiate at the bases of lineation-troughs and terminate at the apexes of their crests. Curvilinear ridges of this scale and character have not, to our knowledge, been observed elsewhere in glacial settings. Erosional scours with troughs up to 7 m deep also occur at the crests of some lineations and terminate in small-scale asymmetric berms (right-hand zooms in Fig. 7.3i).

Sub-bottom profiler

A 20 km section of profiler data from mission M448 trending southwest to northeast crossed the crest of Jenkins Ridge (Fig. 7.4f). The ridge surface is characterized by an undulating high-amplitude seafloor reflector (Fig. 7.4f). Smaller scale ridges with a mean amplitude of 4 m are superimposed on this surface and have a similar cross-sectional profile to the seabed of survey M434 in Zone 3 (Fig. 7.5a).

7.5.4 Zone 4:PIGIS submarine cavity

Sub-bottom profiler

The morphology and acoustic character of the reverse slope of Jenkins Ridge in the ice-shelf cavity are similar to those of the seaward slope in Zone 2, although there is no evidence for mass-movement deposits on this side of the ridge. At the easternmost limit of the survey, approximately 15 km seaward of the grounding line, a series of ridges with asymmetric cross-sectional profiles, ranging between $\sim$7 and 28 m in amplitude, is imaged (Fig. 7.4i). A series of shorter wavelength, lower amplitude, regularly spaced ridges caps the crest of the largest of these asymmetric ridges (Fig. 7.4i, j).

7.6 Discussion

7.6.1 Interpretation of bedforms and sediment properties

From the combined evidence presented above from beneath PIGIS we identify three distinct components of the sub-ice-shelf landsystem that we associate with 1) grounded ice flow, 2) lightly-grounded ice flow and 3) postglacial deposition. Synthesized maps of bedform interpretations presented alongside the multibeam data in Figure 7.2 provide a useful reference for this discussion.

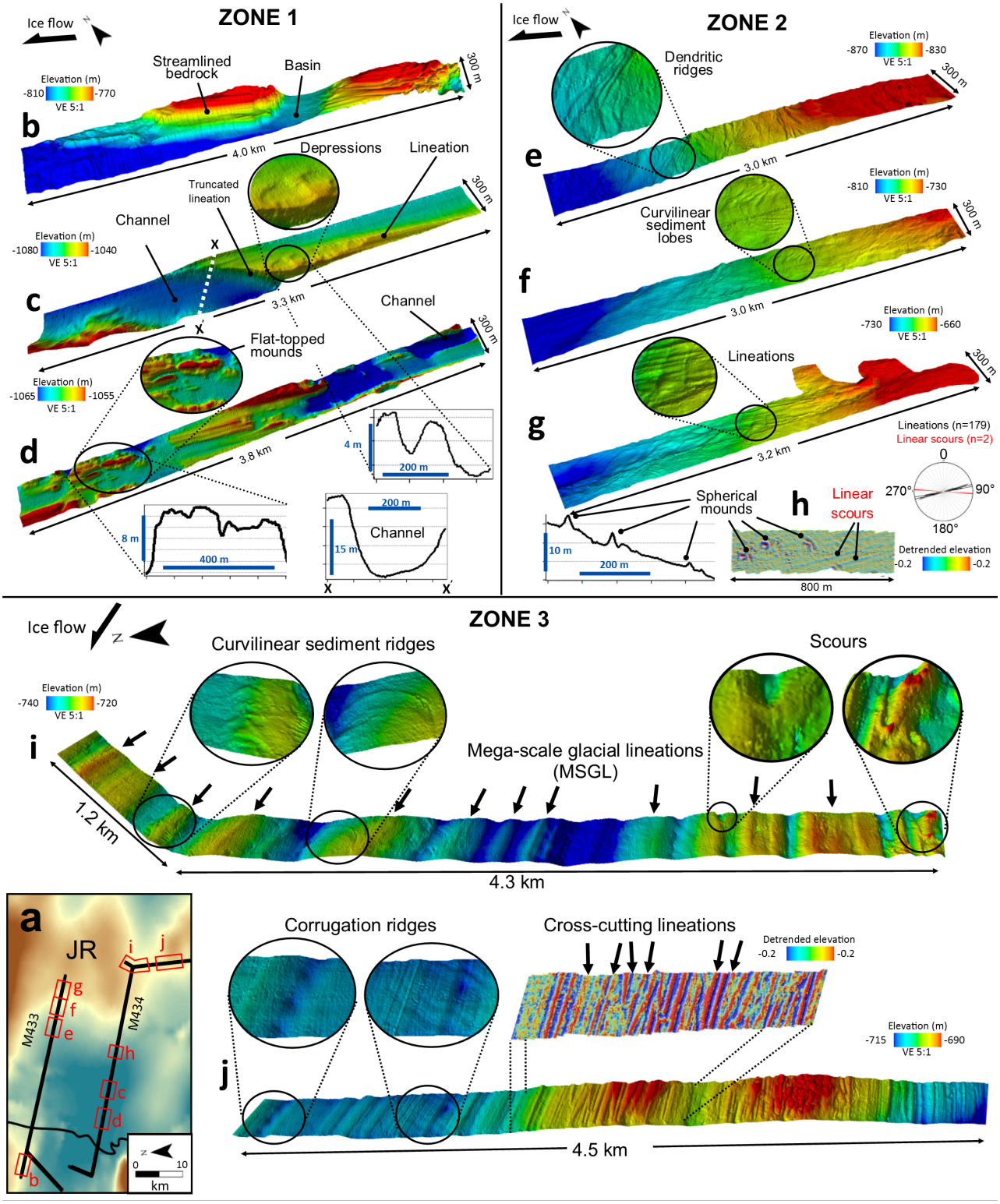

Figure 7.3: Three-dimensional surfaces of multibeam seafloor bathymetry.a, inset map showing the locations of panels **b-j**. Multibeam surface imagery of seafloor topography and extracted topographic profiles in Zone 1 (**b-d**), Zone 2 (**e-h**) and Zone 3 (**i** and **j**). Location of panel **h** is shown in the inset map and Figure 7.2e. Rose diagram next to panel **h** shows the azimuth of lineations sampled from Zones 1-3 compared to linear scours in panel **h**.

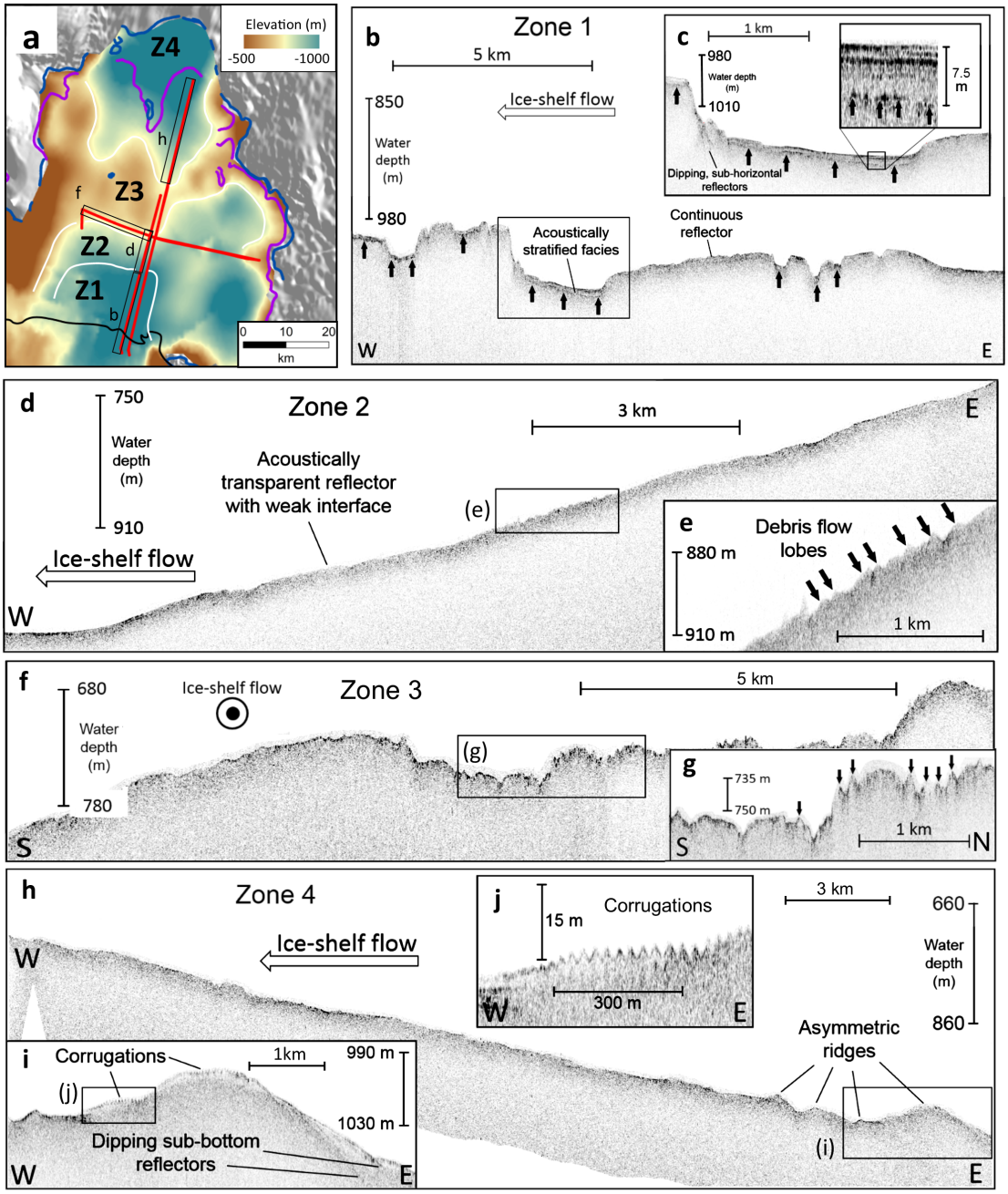

Figure 7.4: Acoustic sub-bottom profiler data. a, Map of regional bathymetry and location of sub-bottom profiler surveys beneath Pine Island Glacier Ice-Shelf. Black boxes denote sections of data shown in the main figure. **b**, Rugged seafloor topography and acoustically stratified basins (black arrows) in Zone 1. **c**, close-up of an acoustically stratified basin showing up to 7.5 m of stratified sediments. Sediment thickness was calculated using an acoustic velocity of 1500 m s^{-1} for sediments. **d**, acoustically transparent seafloor reflector of the seaward flank of Jenkins Ridge. **e**, Close-up showing debris flow lobes (black arrows). **f**, profile across Jenkins Ridge showing a strong surface reflector and undulating seafloor. **g**, Close-up showing mega-scale glacial lineations (black arrows). **h**, acoustically transparent seafloor reflector on the inland slope of Jenkins Ridge. **i**, Close-up view of asymmetric ridges. **j**, Close-up of corrugation ridges overprinting the crest of asymmetric ridges.

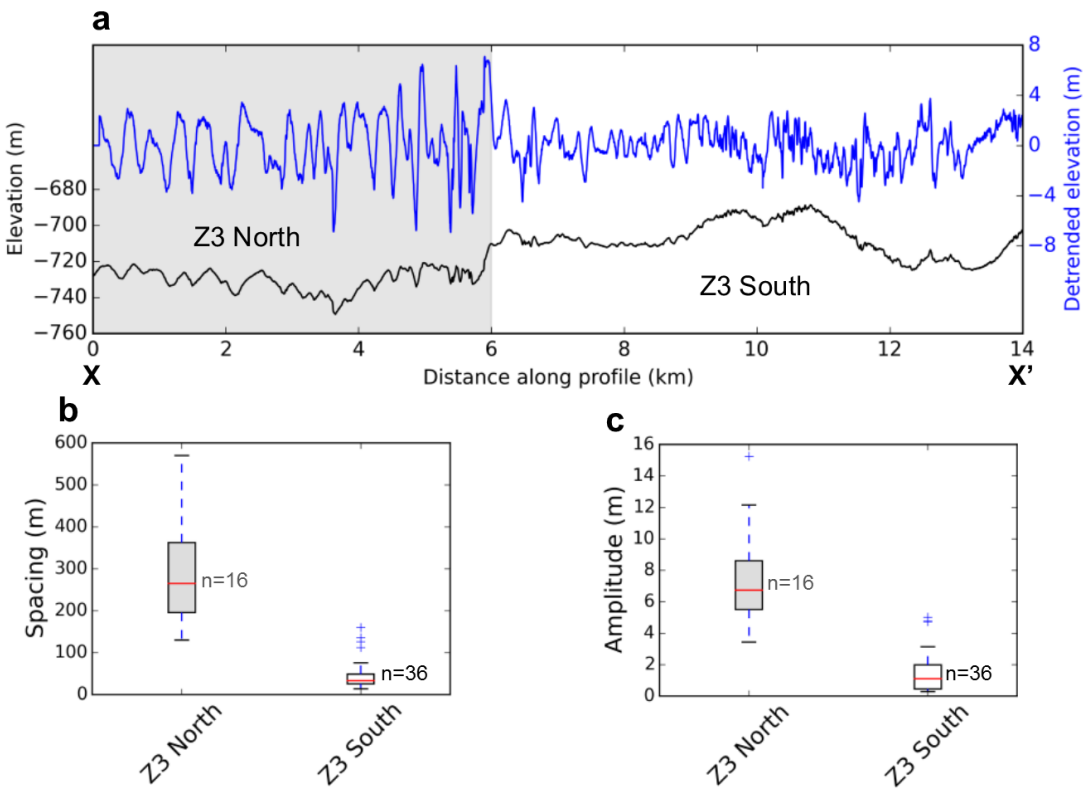

Figure 7.5: Landform metrics of Jenkins Ridge crest. a, Topographic profile of seafloor elevation across the crest of Jenkins Ridge (Zone 3). Blue line shows detrended seafloor topography. Grey shaded area shows the region defined as Z3 North based on a change in landform metrics. **b,c,** Box and whisker plots showing the median, lower and upper quartile and standard deviation of lineation spacing and amplitude of 52 lineations sampled across the ridge crest. A summary of statistics is presented in Table 1 in text.

Grounded-ice bedforms

We interpret a suite of bedforms in Zones 1, 3 and 4 as resulting from subglacial erosion, sediment deposition and meltwater flow beneath grounded ice. Due to their curvilinear cross-sectional profiles, steep-sided channels in Zone 1 (Fig. 7.3c,d) are interpreted as relict subglacial meltwater channels eroded into the substrate when more advanced ice was grounded here during one or more earlier glacial phases (c.f., *Wellner et al.*, 2006; *Nitsche et al.*, 2013). The irregular surface depressions in Figure 7.3c bear resemblance to hill-hole pairs observed in bathymetric data in the Norwegian Channel where they are thought to represent the imprint of sediment slabs that froze onto the glacier sole and were removed/displaced (*Ottesen et al.*, 2016). However, if the surface depressions in Figure 7.3c are similarly interpreted as hill-hole pairs, their estimated volumes are an order of magnitude smaller than those observed in the Norwegian Channel. Flat-topped mounds (Fig. 7.3d), which we interpret as glacitectonic rafts (*Andreassen et al.*, 2004; *Rüther et al.*, 2013; *Rüther et al.*, 2016), are most likely related to a displacing process similar to that which caused the formation of the hill-hole pairs. Because freeze-on is predominantly associated with thin ice (<1 km) close to the glacier margin (*Moran et al.*, 1980; *Alley et al.*, 1997) it is likely that these features were formed when the grounding line was located nearby, and before it became pinned to the crest of Jenkins Ridge.

Ubiquitous lineations on the crest of Jenkins Ridge (Zone 3; Figs. 7.2f and 7.3i, j [multibeam imaging]; and 7.4f [sub-bottom-profiling]) are also the result of formerly-grounded ice flow. To the north, their amplitude and spacing are consistent with dimensions of mega-scale glacial lineations (MSGL) (*Clark*, 1993; *Spagnolo et al.*, 2014) (Table 7.1). Although we are unable to determine the lengths of these individual bedforms from our dataset, a section of bathymetry data along-flow described by *Graham et al.* (2013) captured two lineations with lengths of at least 1800 m. This implies elongation lengths of at least 9:1 and probably greater, a characteristic of elongated streamlined bedforms described beneath paleo- and modern ice streams (*King et al.*, 2009; *Spagnolo et al.*, 2014). Ridges parallel to paleo-ice flow imaged in sub-bottom-profiler data over the crest of Jenkins Ridge (Fig. 7.4g) have comparable amplitudes to ridges observed in the bathymetric data. Although it is not possible to determine their three-dimensional morphology, it is likely they are a continuation of MSGL identified in the northern

Table 7.1: Summary statistics of lineations in Zone 3 compared to previously published metrics of mega-scale glacial lineations and flutes

	Z3 North lineations (this study) n=16	Z3 South lineations (this study) n=36	MSGL [Spagnolo et al., 2014] n=4043	Flutes [Ely et al., 2016] n=88
Spacing (m)				
Minimum	129.8	13.6	-	-
Maximum	569.7	159.8	-	-
Mean	287.2	46.3	458	-
Median	265.0	32.8	330	-
Std. Deviation	121.7	34.8	-	-
Amplitude (m)				
Minimum	3.4	0.2	-	0.02
Maximum	15.2	5.0	-	0.3
Mean	7.3	1.4	4	0.01
Median	6.7	1.0	3	-
Std. Deviation	3.0	1.2	-	0.07

section of Zone 3 (Fig 7.3i).To the south, linear bedforms on Jenkins Ridge have a much shorter wavelength and reduced amplitude intermediate between MSGL and flutes (Table 7.1., Fig. 7.5). We consider this change in metrics to be related to a change in till strength or thickness towards the margin of the ice-stream trough.

Four asymmetric ridges oriented across former flow in Zone 4 with amplitudes of 5-20m (Fig. 7.4h,i) are morphologically similar to small retreat moraines and back-stepping grounding-zone wedges (GZWs) observed on the seafloor in the Ross Sea (*Halberstadt et al.*, 2016; *Simkins et al.*, 2016). Their location close to the modern grounding line suggests that these features were formed in the last 40-70 years through sediment deposition during a series of pauses in grounding-line retreat. Multibeam coverage is needed to verify these observations but, if our interpretation is correct, this indicates the rate of grounding-line retreat has not been constant since ungrounding from Jenkins Ridge. Sub-bottom reflectors dipping at angles greater than the seabed surface slope are also evident on the landward slope of the largest asymmetric ridge, suggesting a sediment history is preserved in the cavity close to the grounding line (Fig. 7.4i).

Lightly-grounded-ice bedforms

On Jenkins Ridge crest, we interpret the ridges and scours that overprint MSGL (zooms in Fig. 7.3i) as forming by sediment squeezing of lightly-grounded ice-shelf keels, modulated by tidal motion as suggested by *Graham et al.* (2013). Some corrugation ridges with amplitudes between 0.5-2 m have been imaged ∼360 km northwest of the grounding line in Pine Island Trough (*Jakobsson et al.*, 2011) and in the Ross Sea (*Shipp et al.*, 1999; *Anderson et al.*, 2014; *Halberstadt et al.*, 2016); the potential corrugation ridges on Jenkins Ridge have amplitudes <1 m with spacing and amplitude varying along the ridge crest (zooms in Fig. 7.3j). This may be related to variable ice-keel morphology as identified by multibeam observations of basal terraces beneath PIGIS (*Dutrieux et al.*, 2014b). However, substantial sub-ice shelf melting since ungrounding from Jenkins Ridge will have altered the basal morphology of the ice shelf compared with the formerly grounded ice keels. This prohibits any direct comparison between corrugation and sub-ice shelf morphology.

The scours (right-hand zooms in 7.3i) are comparable to iceberg ploughmarks observed in water depths in excess of 700 m on the continental shelf and interpreted to have been caused by incision of iceberg keels where they contact the sea floor (*Dowdeswell and Bamber*, 2007; *Gales et al.*, 2016). For iceberg keels to be the mechanism of formation here would require the crest of Jenkins Ridge to have been subject to grounding of free floating icebergs at some point since ungrounding of PIGIS in the 1970s. However, remote sensing imagery shows PIGIS has remained intact throughout this period. We therefore favor forward ploughing of ice-shelf keels as the most likely mechanism for their formation. The alignment of scours parallel to the direction of present ice shelf flow also supports this. Terminal berms associated with these scours (zoom in Fig. 7.3i) are likely to have been created when ice-shelf keels that were last in contact with the crest of Jenkins Ridge became ungrounded.

Postglacial processes

Postglacial deposition is evident in the most distal regions from the current grounding line. In Zone 1, contrasting stratified reflectors in sub-bottom-profiler data are interpreted as alternations between coarse-grained ice-rafted/ice-shelf basal debris and fine-grained hemipelagic sediments from meltwater plumes (c.f. *Damuth*, 1978; *Batchelor et al.*, 2011; *Rebesco et al.*, 2011; *Hogan et al.*, 2012).

Bedforms on the seaward flank of Jenkins Ridge in Zone 2 are dominated by post-glacial slope processes. Dendritic channels and ridges are morphologically characteristic of sediment-gravity flows commonly observed in trough-mouth fan (TMF) and continental-shelf-break settings (*Dowdeswell et al.*, 1998; *Vorren et al.*, 1998; *Dowdeswell et al.*, 2004; *Amblas et al.*, 2006) and on the distal flanks of submarine terminal moraine ridges in fjord settings (*Ottesen and Dowdeswell*, 2006; *Dowdeswell et al.*, 2016). We interpret the lobate, curvilinear ridges on the seaward flank of Jenkins Ridge (zoom in Fig. 7.3f) as submarine debris flows, also observed on continental-margin slopes and ice-distal flanks of submarine moraine ridges, based on the presence of clear depositional sediment fronts and cross-cutting lobes on the flank. Where debris flows are observed, slope angles are very shallow ($<2^{\circ}$), yet they have a run-out distance of over a kilometer. In shallow-slope settings, the ability of debris flows to achieve long run-out distances is considered possible through high-sediment-volume, low-viscosity behavior and excess sediment pore-water pressure (*Laberg and Vorren*, 1996; *Vorren et al.*, 1998). Sediment samples obtained from TMF settings typically contain a range of glacigenic sediments, consisting of muddy diamict, sands and gravels often with low shear strength and high water content. These properties reflect sediment delivery by subglacial deformation, ice-rafting and meltwater deposition in sediment laden plumes (*Kuvaas and Kristoffersen*, 1991; *Hambrey et al.*, 1992; *Laberg and Vorren*, 1996; *Dowdeswell et al.*, 2004). Ice streaming over erodible, soft sedimentary beds has been suggested to be a prerequisite for the formation of TMFs (*Ó Cofaigh et al.*, 2003). High volumes of sediments suggested by debris flow deposits in Zone 2 therefore indicate the presence of a soft bed upstream of Jenkins Ridge.

The spherical mounds imaged in Zone 2 (Fig. 7.3k) are tentatively interpreted as subglacially-

sourced boulders. Their dimensions (1-3 m in height and up to ∼20 m in width) are large but within the upper limit of scales observed and considered theoretically possible to be transported subglacially (*Weertman*, 1958). Crescent-shaped ridges bordering the boulders may have formed either by post-glacial accumulation of sediment during downslope sediment flow or "bulldozing" by the impact of the boulders striking the sea-bed following release from the base of the ice shelf. Adjacent linear scours (Fig. 7.3k) may have formed during debris avalanching down the ridge flank or could also be grounded-ice bedforms partially buried by proglacial sediments.

Bedforms of unknown genesis

The curvilinear ridges superimposed onto MSGLs in Zone 3, (left-hand zoom in Fig. 7.3i) extend transversally for about half the wavelength of the MSGLs, i.e. 300 m, from the trough of a MSGL to its crest. These ridges may be remnants of small-scale recessional moraines or alternatively, they may have formed by the lateral flow of a viscous basal ice layer between MSGL troughs and crests during grounded-ice-flow (*Schoof and Clarke*, 2008), or by post-glacial current reworking of fine-grained surficial sediments.

Interpreting the genesis of the corrugation ridges overprinting the potential GZWs in Zone 4 (Fig. 7.4i) is also challenging. Formation by ephemeral grounding of sub-ice-shelf keels requires corrugation ridges to form on the lee slope of the potential GZW without scouring away its crest. It seems unlikely this would be possible through forward advection of ice keels. Squeezing of sediment ridges during grounding-line retreat could explain their location, but the surfaces of these corrugations have a weak acoustic signal in comparison to acoustic observations of recessional moraines in other studies (e.g. *Halberstadt et al.*, 2016). Another possible mode of formation is through squeezing of sediment by basal crevasses. Regularly-spaced basal crevasses have been observed beneath the Larsen C (*Luckman et al.*, 2012) and Ross Ice shelves (*Jezek and Bentley*, 1983; *Anandakrishnan et al.*, 2007), however they typically have spacings at least an order of magnitude greater than the spacing of corrugations in Zone 3 (Fig. 7.4i). Acquisition of multibeam data in this region would enable a better assessment of their morphology and mode of formation.

7.6.2 Synthesis and implications

Key observations of the sub-ice shelf environment

The data interpreted above provide an unprecedented view of an ice stream bed that has been deglaciated within the past century. Based on our survey of the terrain, a number of important observations can be made that contribute to our wider understanding of these environments and to PIG specifically:

1. Sediment delivery from basal transport has played a key role in shaping each of the zones from the ice-shelf front to the modern grounding line. Our results suggest meltwater plumes and rainout have been important to the accumulation of ice-distal sediments in small basins seaward of the ice shelf. Indeed, observations through Zones 2-4 demonstrate that till deposition and secondary reworking of till (via mass movement to produce debris flows) are the dominant sediment producing and landform-generating processes in this recently deglaciated cavity.
2. Beneath PIGIS, changes in bed properties, specifically contrasting scales of lineations, occur abruptly over limited geographic areas of the bed (Fig. 7.5). This finding supports the relatively small number of ice-stream bed studies that have presented similar evidence for highly variable basal conditions beneath Antarctic ice streams (e.g. *Smith and Murray*, 2009; *Smith et al.*, 2013). However, rather than showing zones of stiff till with no bedforms contrasting with zones of soft till with lineations (*King et al.*, 2009), we are able to show variability in bedforms within a region where sediment cores indicate the presence of deformable sediment (*Smith et al.*, 2017b).
3. Grounding by sub-ice-shelf keels is a process that appears to produce significant features near the grounding zone (e.g. erosional scours). This process may be responsible for the appearance of converging lineations observed in regions of elevated seafloor (e.g., Fig. 7.3j). These variations suggest a more mobile grounding situation in some parts of the ridge, such as might be expected in an ice-plain environment (*Corr et al.*, 2001).
4. Former-ice-flow-oriented lineations on a scale intermediate between MSGL and flutes can form at the grounding zones of major ice streams, and cross-cutting generations at the margins preserve a record of localized flow variability.

5. The presence of glacitectonic rafts and emplaced boulders indicate that till deformation may not be the only sediment transport process in operation under West Antarctic ice streams, and that plucking and rafting of large bedrock/sediment blocks contributes to erosion beneath PIG.
6. The landform mapping presented in this study shows a transition from bedrock outcrops in Zone 1 to sediment bedforms and deposits in Zone 2 broadly coincident with the crystalline to sedimentary bed transition inferred from aerogravity surveys (*Muto et al.*, 2013, 2016). These surveys inferred a thick sedimentary basin extending upstream of the grounding line that would provide an abundant source for sediments deposited as mass flows, MSGL and GZWs in Zones 2-4. These observations indicate that Jenkins Ridge marks a transition between hard, resistant crystalline bedrock to more erodible, soft sedimentary bed upstream of the present-day grounding line. Such transitions have been observed further seaward on the continental shelf and associated with contrasts in the distribution of sediment and character of geomorphic features (*Lowe and Anderson*, 2002; *Wellner et al.*, 2001, 2006; *Graham et al.*, 2009).

Observations of fine-scale bedforms: preservation or data resolution?

High-resolution imaging of the seafloor beneath PIGIS reveals a complex pattern of landforms indicative of a highly dynamic environment. We have identified seldom observed fine-scale submarine landforms, namely curvilinear sediment ridges, intermediate-scale lineations and small-scale hill-hole pairs. With the exception of lineations, these landforms are interpreted as reworked subglacial bedforms, sculpted into their present form by overriding of the ice margin and sub-ice-shelf keels during retreat of the grounding-line. We consider the ability to detect these features is a factor of 1) the youth of the sub-ice-shelf landscape and 2) the high resolution of the data compared to offshore swath bathymetric surveying.

Smith et al. (2017b) calculated sedimentation rates on the crest of Jenkins Ridge (Zone 3) of 0.82-0.95 mm a^{-1}. These rates are too low to have buried the fine-scale features such as curvilinear sediment ridges and sub-metre amplitude lineations since ungrounding from the ridge crest in 1940. Further seaward on the continental shelf, features of this scale may not be

as well preserved having been exposed to marine sedimentation for up to several millennia. However, deep-tow side-scan sonar surveys of the continental shelf have revealed fine-scale landforms such as flutes and corrugations ("washboard pattern") located near the continental shelf break (*Lien et al.*, 1989; *Ship et al.*, 1999; *Shipp et al.*, 2002).

The identification of fine-scale features may therefore be primarily a factor of the ability to image the seafloor at sub-metre to metre-scale resolution. We demonstrate this in Figure 7.6 by conducting a crossover comparison between AUV and ship-based multibeam surveys in Pine Island Bay (*Nitsche et al.*, 2013), just seaward of PIGIS. This analysis reveals intermediate-scale lineations overprinting MSGL, and demonstrates the preservation of fine-scale bedforms $\sim$85 km in front of the modern grounding-line (Fig. 7.6). Our data indicate there is likely a wealth of detailed information of glacial processes not captured by standard offshore marine geophysical surveys. Recent work by *García et al.* (2016) using a remotely-operated underwater vehicle also illustrate the level of detail obtained using these methods. Further targeted AUV/ROV surveys beneath ice shelves and on the continental shelf would provide useful information on bedform preservation and may elucidate processes related to some of the more enigmatic landforms observed beneath PIGIS.

7.7 Conclusions

We have used high-resolution bathymetry and sub-bottom-profiler data obtained by AUV surveys to explore the nature of seafloor bedforms and sediment properties beneath a recently ungrounded Antarctic ice shelf. These data reveal fine-scale landforms in a dynamic environment modified by subglacial erosion, meltwater flow, and sediment deposition, providing an unprecedented view of a recently deglaciated ice-stream bed.

The landscape and sediments we have imaged beneath Pine Island Glacier Ice Shelf record features of direct subglacial erosion and deposition, and postglacial modification by overriding and scouring of ice-shelf keels and gravity-driven slope processes. Seaward of Jenkins Ridge the landscape of streamlined bedrock outcrops is characteristic of direct subglacial erosion with little postglacial modification. In this landscape, ice-rafted boulders, hill-hole pairs and

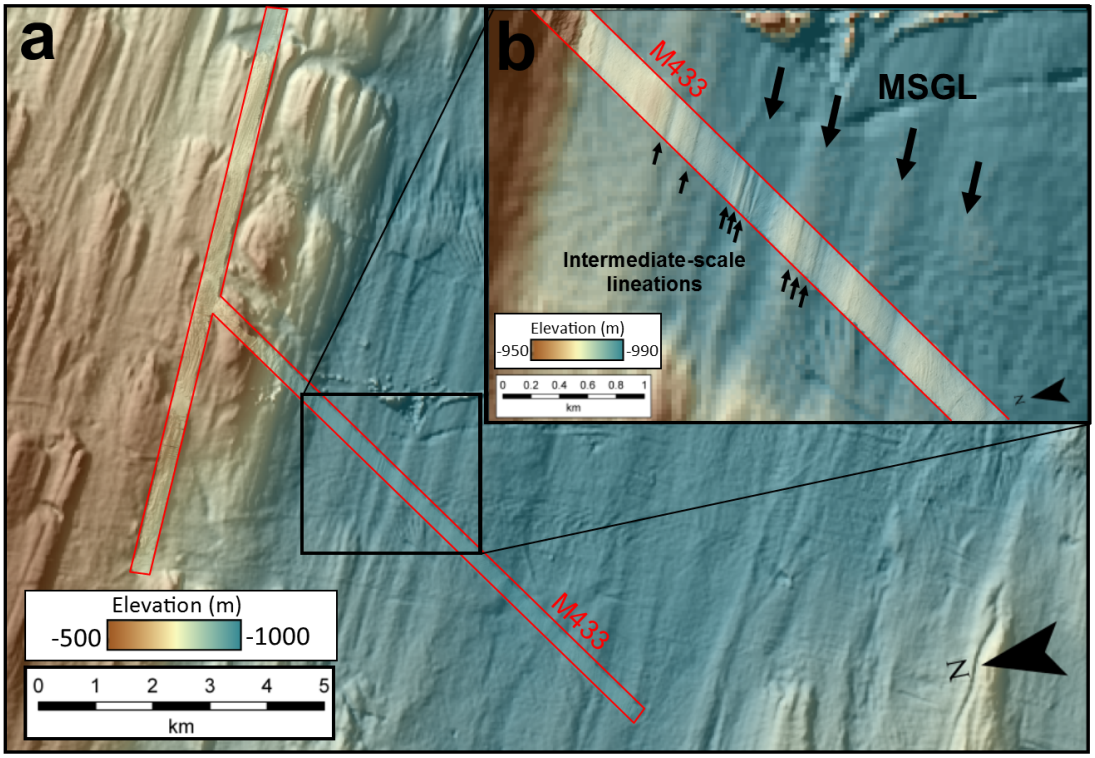

Figure 7.6: Comparison of offshore swath bathymetry and Autosub3 multibeam bathymetry. a, 35 m resolution swath sonar bathymetry of Pine Island Bay acquired offshore seaward of PIGIS (Data from *Nitsche et al.*, 2013) overlain by Autosub3 bathymetry from Mission M433 at 2 m resolution (red polygon). **b**, Magnified image showing the difference in detail between datasets. Large black arrows mark the locations of MSGL visible on both the offshore swath sonar and Autosub3 multibeam bathymetry, small-black arrows denote intermediate-scale lineations only visible on the Autosub3 bathymetry data. Location of data extent is shown in Figure 7.1a.

glacitectonic rafts indicate that freeze-on and plucking of basal material is a significant component of erosion and sediment transport. Upstream over Jenkins Ridge and into the sub-ice-shelf cavity, the landscape is draped by sediments which evince both direct glacial deposition and deformation, and post-glacial modification. This sediment distribution supports Jenkins Ridge having been a stable grounding-line location for a significant period prior to its 20th-century ungrounding.

We have demonstrated the value of imaging recently deglaciated terrain at meter-scale resolution. The insights we have provided through the analysis of fine-scale landforms would not have been achievable without the capability to observe features in recently deglaciated and at meter-scale resolution using an AUV platform. Such landforms are likely to be rapidly modified by postglacial sedimentation or are not readily observable in coarser resolution swath bathymetry datasets.

We recommend further AUV missions to sub-ice shelf cavities to enable a better understanding of recent controls on ice stream retreat and sub-ice shelf processes. Surveys of selected offshore regions previously covered by offshore swath bathymetry surveys would also provide a clearer picture of past ice stream stability and retreat.

Chapter 8

Conclusions

The overall aim of this thesis set out in Chapter 1 was to examine the spatial and temporal characteristics of the bed of Pine Island Glacier (PIG) and the effects this has on local and regional ice flow and stability. This has been motivated by the need to understand the future contribution of the West Antarctic Ice Sheet and Amundsen Sea sector to global sea-level rise.

The work presented in Chapters 3-7 has addressed the four objectives of the thesis (Section 2.7) as follows:

1. Chapter 4 presented high-resolution subglacial topography and demonstrated a diverse subglacial landscape exists beneath the trunk and tributaries of PIG.
2. Chapter 5 investigated the subglacial roughness beneath PIG and explored how the orientation and wavelength of bedforms is correlated with ice flow. It found that along-flow roughness with wavelengths comparable to ice thickness have the greatest correlation with ice flow parameters.
3. Chapter 6 investigated changes in bed morphology beneath PIG and demonstrated no significant changes over a period of 6 years.
4. Chapter 7 presented high-resolution images of the seafloor beneath PIG Ice Shelf and found bedforms modified by subglacial erosion, meltwater flow, sediment deposition and overprinting of lightly-grounded ice-shelf keels.

8.1 Summary of findings

The research presented in Chapter 4 focussed on assessing the effect of short wavelength subglacial topography on ice-stream flow. It found that surveyed areas of the trunk and tributaries of PIG have a varied subglacial topography. The analysis suggested that this variability in short wavelength topography accounts for much of the variability in basal traction calculated from numerical inversions of observable surface parameters (i.e. surface elevation and velocity) (*Arthern et al.*, 2015). This variability is not captured in previous bed products which contain more sparse data points with which to interpolate regional bed elevation. The research highlighted the importance of form drag as a key control on ice dynamics.

Chapter 5 examined the spatial characteristics of short wavelength bed roughness. I found that basal topography in all regions of the bed surveyed is anisotropic (smoother aligned with ice flow than across flow). I also found that along-flow roughness has a stronger influence on ice velocity, modelled basal shear stress and the rate of ice thinning within different tributaries. I demonstrated that beneath ice streams, rough subglacial topography can exhibit the same anisotropic ratio as smooth subglacial topography, thereby highlighting the need for caution when using roughness as an indicator of former high erosion rates under fast ice-stream flow. I also found that subglacial roughness beneath a slow-flowing inter-tributary site displays a ribbed spatial pattern comparable to observed patterns of modelled basal shear stress in other regions of Antarctica. I linked these patterns to transverse ridges beneath PIG, comparable in scale and morphology to similar bedforms observed in palaeo-ice stream beds (*Dunlop and Clark*, 2006; *Greenwood and Kleman*, 2010; *Stokes et al.*, 2016).

In Chapter 6 I analysed repeat radar surveys acquired in the eastern trunk and tributaries of PIG. I found no significant change in the basal topography of the bed over a period of 3-6 years despite acceleration of ice flow and thinning of the ice stream over the same period. I argued that the lack of observable change along with observations of homogeneous basal conditions from seismic reflection surveys suggests a stable bed. I compared these conditions with neighbouring Rutford Ice Stream where rapid sub-decadal erosion has been observed and where bed properties are heterogeneous. These findings suggest that the bed conditions beneath

Rutford may promote a more dynamic system compared to PIG. However it is worth noting that considering the greater spatial context that these data provide, the changes observed beneath Rutford Ice Stream may be isolated and not representative of bed dynamics at a regional scale.

Finally, in Chapter 7 I mapped and interpreted the distribution of bedforms and sediment beneath PIG ice shelf using autonomous underwater vehicle geophysical surveys. Evidence of erosion, deposition, meltwater flow and post-glacial modification was observed in fine detail. The observed distribution of sediment supported previous aerogravity surveys indicating a geological transition coinciding with Jenkins Ridge. I demonstrated that metre-scale resolution images of recently deglaciated ice-stream beds reveals bedforms that are not detectable with traditional offshore bathymetric surveys.

8.2 Synthesis of findings

In this section I provide a synthesis of the key findings of the thesis, addressing the issues inherent to the thesis title, namely the nature and dynamics of ice-stream beds, and implications for ice-sheet stability.

8.2.1 The nature of ice stream-beds: insights from Pine Island Glacier

Topographic constraints on ice-stream flow

This thesis has provided a view of the bed of a modern ice stream in detail that has only previously been achieved in limited regions of Antarctica (*King et al.*, 2009, 2016). Chapter 4 revealed that the network of overdeepened troughs currently occupied by PIG hosts a topographically diverse subglacial landscape. Chapters 4 and 5 further demonstrated that this diversity affects ice velocity through form drag at the glacier bed. This in turn affects observed inland propagation rates of thinning caused by ocean melting of PIG Ice-Shelf (*Konrad et al.*, 2017).

Chapter 7 demonstrated an equally diverse subglacial environment with transitions between rough an smooth topography beneath PIG Ice Shelf. These observations are also consistent

with marine geophysical studies offshore that show transitions between sedimentary strata on the outer continental shelf and crystalline bedrock on the inner shelf in West Antarctica (*Lowe and Anderson*, 2002; *Jakobsson et al.*, 2011; *Nitsche et al.*, 2013). These transitions in bed conditions are likely to have played the same role in affecting the dynamics of PIG in the past, controlling the pace of perturbations leading to retreat from the continental shelf during the Last Glacial Maximum (LGM) (*Graham et al.*, 2010).

The findings of this thesis further demonstrates the interplay between the deep geological history of the Antarctic continent and subsequent Quaternary and modern ice dynamics (c.f. *Jordan et al.*, 2009; *Jamieson et al.*, 2010; *Bingham et al.*, 2012). It is likely that the diversity of subglacial landscapes revealed within PIG's tributaries reflects the geological diversity of West Antarctica as a whole. Therefore, no two catchments can be considered alike in terms of their response to current and future forcing.

Geomorphological evidence presented in Chapters 4, 5 and 7 demonstrate that both rough and smooth regions of the bed have been modified considerably by ice streaming. Striking contrasts in roughness anisotropy between inter-tributary and tributary flow regions suggest that PIG has not experienced major lateral migrations of flow as evinced by some other Antarctic ice streams (c.f. *Echelmeyer and Harrison*, 1999; *Catania et al.*, 2005; *Bingham et al.*, 2015). Future retreat of PIG is therefore likely to be concentrated along the existing trough system, with more rapid retreat directed along the smoother tributaries.

However, the rough topography of the lower tributaries of PIG may not be sufficient to stall retreat of PIG in these regions. Although substantial sediment accumulation on the seaward slope of Jenkins Ridge identified in Chapter 7 indicates a former stable pinning point, equally dramatic topography on the inner continental shelf in Pine Island Bay was not sufficient to halt retreat of PIG during LGM retreat (*Graham et al.*, 2010). Equally rough subglacial topography detected in the present grounding-zone of neighbouring Thwaites Glacier does not appear to be impeding grounding-line retreat and inland propagation of thinning (*Holt et al.*, 2006; *Joughin et al.*, 2014; *Rignot et al.*, 2014). This is likely associated with the relatively small and fractured ice shelf and absence of confined subglacial topography that provides limited back-pressure for inland ice (*Rignot*, 2001; *Parizek et al.*, 2013).

Insights into ice stream geomorphology

Building on previous work by (*King et al.*, 2007b, 2009, 2016), results presented throughout this thesis has provided further evidence for the influence of ice-stream flow on subglacial geomorphology beneath modern ice streams. The ubiquity of mega-scale glacial lineations and streamlined bedforms beneath PIG has added further weight to the substantial body of evidence linking fast ice flow to bedform elongation (*Hart*, 1999; *Stokes and Clark*, 2002; *Briner*, 2007; *King et al.*, 2009). Chapters 4 and 5 also provide the first high-resolution imagery of an inter-tributary region of an ice-stream catchment. Combined with previous evidence from the onset region of Rutford Ice Stream (*King et al.*, 2007b), geophysical observations of bedforms beneath a range of settings now provide convincing evidence to support observations from palaeo-ice stream beds that suggest a subglacial bedform continuum whereby bedform elongation is controlled by ice velocity (*Rose*, 1987; *Ó Cofaigh et al.*, 2002; *Stokes and Clark*, 2002; *Ely et al.*, 2016a)(Fig. 8.1).

Key questions pertaining to the nature of ice-stream beds are how are bedforms created beneath ice streams and on what timescales? Answering these questions is beyond the scope of this thesis, but the research presented in Chapters 6 and 7 has provided further evidence for consideration. Some of this evidence is contradictory. For example, repeat surveys examined in Chapter 6 demonstrate remarkable consistency in the morphology of the bed across $\sim$60 km of surveyed regions of PIG over a period of 6 years. In contrast, previous repeat geophysical measurements by *Smith et al.* (2007) and *Smith et al.* (2012) showed rapid reorganisation of sediment beneath Rutford Ice Stream over a similar time period. Similarly, multibeam imagery of bedforms beneath PIG Ice Shelf (Fig. 7.3) also demonstrated that bedforms undergo modification soon after retreat of the grounding line, indicating a high degree of sediment mobility. This indicates that although subglacial sediments are highly mobile, bedform morphology can remain stable on sub-decadal timescales.

The apparent stability of the subglacial interface observed here beneath one of Antarctica's fastest flowing ice streams indicates decadal stability in the mechanisms of bedform formation, despite the potential for rapid mobilisation of poorly consolidated sediments (*Alley et al.*,

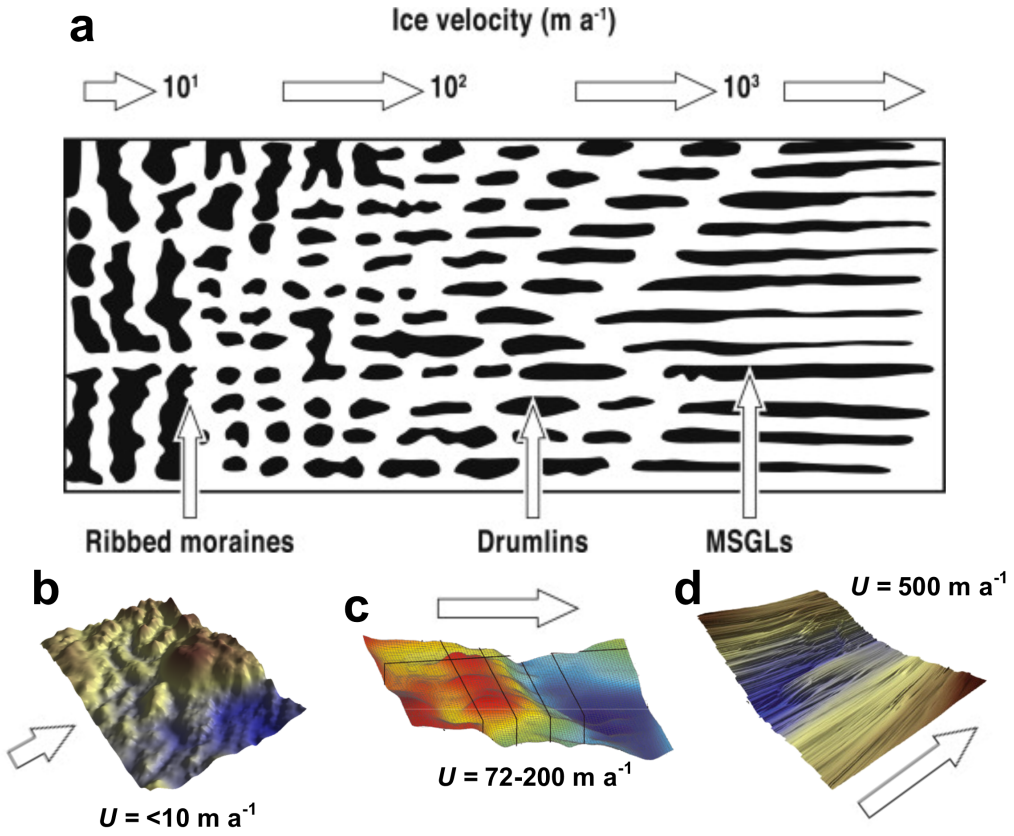

Figure 8.1: Geophysical evidence supporting the subglacial bedform continuum hypothesis. **a** Schematic representation of a subglacial bedform continuum from *Stokes et al.* (2013a).**b** Mega-rib bedforms imaged beneath an inter-tributary region of PIG (see Chapter 4). **c** Drumlins imaged beneath the onset zone of Rutford Ice Stream (*King et al.*, 2007b). **d** MSGL imaged in the main trunk of PIG (see Chapter 4). Ice surface velocities are shown next to images **b-d**.

1997). There are numerous theories for the formation of subglacial bedforms. Instability theory has been adopted as the most popular theory owing to its ability to explain the formation of the diverse range of bedforms observed in ice-stream beds (Fig. 8.1) (*Hindmarsh*, 1998; *Fowler*, 2000, 2010; *Stokes et al.*, 2013b; *Fowler and Chapwanya*, 2014). The theory invokes a mechanism whereby perturbations to the bed, arising from the coupled flow of ice, water and sediment, are amplified, allowing bedforms with a dominant amplitude and wavelength to occur through the localised erosion and accretion (*Stokes et al.*, 2013b). The stability of the bed observed in Chapter 6 indicates that MSGL beneath PIG have achieved a mature state where wavelength and amplitude is not altered on sub-decadal time-scales. These results are also

consistent with formation on millenial timescales as predicted by the instability mechanism of spiral flows in basal ice (*Schoof and Clarke*, 2008).

8.2.2 Bed dynamics of Pine Island Glacier and implications for ice-sheet stability

Another key question that has motivated this research and other studies of ice-stream beds is how sediment is eroded and transported beneath ice streams. This question is important for understanding whether ice streams may in future respond to a change in substrate resulting from erosion of subglacial sediments (*Smith et al.*, 2013). High fluxes of sediment delivered to the ice margin may result in formation of till deltas or grounding-zone wedges that can stabilise retreat by reducing local water depths (*Alley et al.*, 2007; *Batchelor and Dowdeswell*, 2015). Estimates for ice-stream sediment fluxes in Antarctica range from 100 to 1000 m^3 m^{-1} a^{-1} per metre width of ice-stream terminus (*Stokes*, 2017, and references therein). Furthermore, offshore marine sediment records and large accumulations of sediment deposited on continental-shelf slopes ("Trough Mouth Fans") also provide evidence of high volumes of sediment transported beneath ice streams (*Cofaigh et al.*, 2003; *Dowdeswell et al.*, 2006, 2008a; *Hillenbrand et al.*, 2010).

As in the previous section, results from offshore and inland geophysical analyses presented in this thesis throw up some intriguing contradictions. Chapters 6 and 7 showed regions of the bed with dramatic subglacial topography (Fig. 4.7-4.9) comparable to the rugged terrain on the inner continental shelf (*Lowe and Anderson*, 2002; *Nitsche et al.*, 2013) (Fig. 7.3b). Based on geomorphology alone, it is likely that these regions are characterised by hard beds of crystalline bedrock consistent with the geology of the inner continental shelf (*Wellner et al.*, 2001; *Graham et al.*, 2009). However, seismic reflection surveys conducted within these regions of the bed revealed the presence of a deforming till layer with a minimum thickness of 1.5 $\pm$ 0.4 m overlying elevated regions of the bed such as the crag-and-tail bedform in iSTARt1 and the bed elevation high in iSTARt7 (*Brisbourne et al.*, 2017). The presence of sediments here is surprising given the clear geomorphological evidence of erosion evident in the streamlined form of these features. In contrast, sediment is mostly absent from similar terrain in Pine Island Bay (*Nitsche et al.*, 2013).

Chapter 7 also demonstrated abundant sediment cover on the surface and seaward slope of Jenkins Ridge, suggesting high sediment flux delivered to the grounding line when PIG was pinned to the ridge prior to the 1940s (*Smith et al.*, 2017b). These observations have interesting implications for modes of subglacial sediment transport. A number of mechanisms have been suggested by previous researchers. These include deep deformation of viscous till (*Alley et al.*, 1986; *Blankenship et al.*, 1986); shallow deformation of Coulomb-plastic till facilitated by ice-keel ploughing through sediment (*Tulaczyk et al.*, 2001) and entrainment by basal freeze-on (*Bougamont and Tulaczyk*, 2003; *Christoffersen et al.*, 2010; *Bougamont and Christoffersen*, 2012).

The preservation of a till layer observed by *Brisbourne et al.* (2017) is difficult to reconcile with fast ice stream flow over subglacial obstacles. It may be possible that till layers detected by seismic reflection surveys actually represent sediment in basal ice. Basal ice sequences several metres in thickness equivalent to 2.1 ± 0.4 m of frozen sediment have been observed by borehole camera images beneath Kamb Ice Stream in West Antarctica (*Christoffersen et al.*, 2010). These basal ice sequences are thought to transport sediment to the grounding line where they are deposited in till wedges (*Anandakrishnan et al.*, 2007; *Christoffersen et al.*, 2010; *Horgan et al.*, 2013). This could account for the apparent mismatch between inland and offshore geophysical observations. Sediment observed beneath PIG Ice Shelf in Chapter 7 may also have been delivered by this process. Sediment transport by deep deformation (on the order of metres) of viscous till invokes a highly mobile bed with the potential for rapid erosion. The absence of clear morphological change in Chapter 5 is therefore more in line with sediment transport achieved by shallow deformation with only subtle changes in morphology occurring over short time-scales.

In considering the future stability of PIG it is important to think about the system and its history as a whole. Offshore marine geophysical surveys have revealed the ubiquitous presence of sediments and associated bedforms such as MSGL and grounding-zone wedges on the outer continental shelf (*Lowe and Anderson*, 2002; *Graham et al.*, 2010; *Jakobsson et al.*, 2011). On the inner continental shelf, sediment becomes confined to isolated basins and rugged crystalline bedrock with little to no sediment cover (*Lowe and Anderson*, 2002; *Nitsche et al.*,

2013). Beneath PIG Ice Shelf a bedrock-to sediment-rich transition coincides with Jenkins Ridge (Chapter 7) and continues immediately upstream of the present grounding-line (*Muto et al.*, 2016). Inland of the grounding-line, the western tributaries (iSTARt7, it and t9) exhibit rough subglacial topography comparable to the inner continental shelf, yet are underlain by a deforming sediment layer (*Brisbourne et al.*, 2017). The eastern tributaries (iSTARt1, t5 and 56) are much smoother with the widespread presence of MSGL comparable to the outer continental shelf.

This pattern of sediment distribution shows that in the past, PIG has experienced periods of retreat punctuated by stability and high rates of sediment transport evident in grounding-zone wedges (*Jakobsson et al.*, 2012). Recent evidence has also suggested that these periods of stability followed rapid break-up of ice shelves and potentially ice-cliff instability mechanisms leading to rapid retreat (*Jakobsson et al.*, 2011; *Wise et al.*, 2017). This retreat proceeded across rough subglacial topography before a stable pinning-point was reached at Jenkins Ridge depositing high-volumes of sediment from the present inland catchment. Current rapid retreat of PIG initiated in the 1940s (*Smith et al.*, 2017b). It is unclear how fast current inland retreat will progress, although the propagation of inland thinning over the satellite era suggests that the smooth subglacial topography and sediments of the trunk and eastern tributaries will promote rapid retreat in these regions unless sediment transport is sufficient to create stabilising feedbacks (*Alley et al.*, 2007). However there is conflicting evidence of the level of erosion and sediment transport currently taking place beneath PIG (*Smith et al.*, 2012, and Chapter 6). If ice-cliff instabilities were to occur again, retreat may also occur rapidly in the western tributaries leading to a substantial sea-level rise contribution over the coming century (*Pollard and Deconto*, 2016).

8.3 Limitations and future research

This thesis has provided new insights into the nature and dynamics of ice-stream beds. However, more work is required in order to gain sufficient understanding of basal processes to examine their impact on the future dynamic response of ice-sheets to atmospheric and oceanic warming. In this section I will identify some of the key challenges and limitations encountered during the course of this research and identify avenues for future research.

Chapter 4 highlighted the importance of form drag associated with short-wavelength subglacial topography and the challenges for ice-sheet models in accounting for its spatial variability. The data presented in this thesis provides an opportunity for comprehensive modelling experiments to be conducted that will enable an assessment of the importance of accounting for form drag. Such experiments may reveal the requirement for further parameterisation of basal traction associated with short-wavelength topography that can be applied on a regional scale. Recent studies have utilised the high-resolution data presented in this thesis to investigate whether surface observations can be linked to sediment properties derived from active seismic surveys (*Kyrke-Smith et al.*, 2017). Similar work is currently in progress to assess how detailed knowledge of the bed affects inversions of basal friction from surface parameters.

Chapter 5 revealed the importance of grid orientation on spatial pattern and magnitude of subglacial roughness. This work highlights that bias may be introduced in the interpolation of basal topography due to the orientation of geophysical surveys. There is therefore a necessity to capture multiple orientations in future geophysical surveys of ice-stream beds and to develop swath processing techniques to derive more accurate bed elevation data. Chapter 5 demonstrated the potential for the anisotropy of basal topography to be used to characterise distinct geomorphologies beneath ice sheets. Developing algorithms to utilise the high spatial resolution of data presented in this thesis more effectively would provide a more robust approach to quantifying distinct subglacial terrain. This could also be applied to high-resolution DEMs of palaeo-ice stream beds, providing a quantitative approach to addressing key questions about landscape evolution and dynamics.

One of the most challenging components of this PhD was assessing temporal changes at the

ice-bed interface using repeat geophysical methods (Chapter 6). The ability to detect changes at the bed is ultimately controlled by the precision of the instrument and the ability to account for internal ice properties such changes in firn density or englacial temperature that affect the travel-time of radar or seismic wave propagation. Errors associated with these factors can be reduced by increasing the spatial density of measurements. Future repeat measurements should therefore focus on repeating grid surveys such as those conducted for this research that will enable a 3-dimensional assessment of bed change. Selecting sites where more dynamic subglacial environments may exist could also provide information on basal processes. Regions of the bed experiencing rapid acceleration in ice flow or where dynamic subglacial hydrology is known to exist (e.g. connected subglacial lake networks *Wingham et al.*, 2006; *Fricker and Scambos*, 2009; *Smith et al.*, 2017a) may provide the best opportunity to detect changes at the bed. The use of high-precision radar equipment such as the ApRES system that is being widely deployed in Antarctica may allow more reliable measurements of basal change (*Lok et al.*, 2015; *Nicholls et al.*, 2015).

Chapter 7 demonstrated the value of obtaining high-resolution images of recently deglaciated ice streams. These analyses have been applied to terrestrial environments (e.g. *Ely et al.*, 2016b), but have so far been limited for marine-terminating ice streams (*Nicholls et al.*, 2006; *Graham et al.*, 2013; *García et al.*, 2016). A more comprehensive assessment of these environments is limited by the range of Autonomous Underwater Vehicle platforms. Furthermore, due to problems encountered during AUV missions related to this research, sub-bottom profiler and multibeam data could not be acquired simultaneously. This prohibited the ability to link the geomorphology directly to subsurface properties. Future AUV missions should seek to acquire both datasets and link geophysical observations to sediment cores to enable greater understanding of the source and transport history of subglacial sediments beneath ice streams.

8.4 Concluding remarks

An improved understanding of the nature and dynamics of ice-stream beds has previously been hindered by a lack of extensive observations of this environment. Geophysical surveys have offered an opportunity to image the bed beneath ice sheets to gain a more detailed understanding. Prior to this thesis, few studies had conducted surveys that permit the interrogation of sub-kilometre scale topographic features beneath extensive areas of active ice-stream beds. Similarly, the ability to investigate temporal changes in bed properties has been challenging due to the limited extent of repeat geophysical measurements. This thesis has significantly increased the extent of high-resolution spatial and temporal geophysical observations of ice-stream beds. These new data have revealed how this hidden landscape has been shaped by, and influences ice-stream flow. It has also provided a connection between past and present by comparison between modern and palaeo-ice stream settings.

A comprehensive understanding of ice-stream beds requires the acquisition of high-resolution imagery at high spatial and temporal sampling densities linked to direct observations of the bed. This approach is the most effective way to link physical properties of the bed with their geomorphological expression through a clearer understanding of time-dependent basal processes. Achieving this goal is currently hampered by high costs and technological limitations. Considering the progress made in this field of research over the past few decades, it is likely that improvements in geophysical and remote sensing technology in the coming decades will provide equally exciting discoveries with profound implications for our understanding of subglacial environments.

References

Aðalgeirsdóttir, G., A. M. Smith, T. Murray, M. King, K. Makinson, K. W. Nicholls, and A. Behar (2008), Tidal influence on Rutford Ice Stream, West Antarctica: observations of surface flow and basal processes from closely spaced GPS and passive seismic stations, *Journal of Glaciology*, *54*(187), 715–724.

Alley, R. (1989), Water-pressure coupling of sliding and bed deformation: I. Water system, *Journal of Glaciology*, *35*(119), 108–118.

Alley, R. (1993), In search of ice-stream sticky spots, *Journal of Glaciology*, *39*(133), 447–454.

Alley, R., K. Cuffey, E. Evenson, J. Strasser, D. Lawson, and G. Larson (1997), How glaciers entrain and transport basal sediment: Physical constraints, *Quaternary Science Reviews*, *16*(9), 1017 – 1038, doi: http://dx.doi.org/10.1016/S0277-3791(97)00034-6.

Alley, R., D. Lawson, G. Larson, E. Evenson, and G. Baker (2003), Stabilizing feedbacks in glacier-bed erosion, *Nature*, *424*(6950), 758.

Alley, R. B. (1991), Deforming-bed origin for southern laurentide till sheets?, *Journal of Glaciology*, *37*(125), 67–76.

Alley, R. B., D. D. Blankenship, C. R. Bentley, and S. T. Rooney (1986), Deformation of till beneath ice stream B, West Antarctica, *Nature*, *322*, 57–59.

Alley, R. B., D. D. Blankenship, C. R. Bentley, and S. T. Rooney (1987a), Till beneath ice stream B: 3. Till deformation: Evidence and implications, *Journal of Geophysical Research: Solid Earth*, *92*(B9), 8921–8929, doi: 10.1029/JB092iB09p08921.

Alley, R. B., D. D. Blankenship, S. T. Rooney, and C. R. Bentley (1987b), Till beneath ice stream B: 4. A coupled ice-till flow model, *Journal of Geophysical Research: Solid Earth*, *92*(B9), 8931–8940, doi: 10.1029/JB092iB09p08931.

Alley, R. B., D. Blankenship, S. Rooney, and C. Bentley (1987c), Continuous till deformation beneath ice sheets, *The Physical Basis of Ice Sheet Modelling. Proceedings of the Vancouver Symposium, August 1987. IAHS Publications*, *170*, 81–91.

Alley, R. B., S. Anandakrishnan, T. K. Dupont, B. R. Parizek, and D. Pollard (2007), Effect of Sedimentation on Ice-Sheet Grounding-Line Stability, *Science*, *315*(5820), 1838–1841, doi: 10.1126/science.1138396.

Alley, R. B., S. Anandakrishnan, K. Christianson, H. J. Horgan, A. Muto, B. R. Parizek, D. Pollard, and R. T. Walker (2015), Oceanic forcing of ice-sheet retreat: West antarctica and more, *Annual Review of Earth and Planetary Sciences*, *43*(1), 207–231, doi: 10.1146/annurev-earth-060614-105344.

Amblas, D., R. Urgeles, M. Canals, A. M. Calafat, M. Rebesco, A. Camerlenghi, F. Estrada, M. De Batist, and J. E. Hughes-Clarke (2006), Relationship between continental rise development and palaeo-ice sheet dynamics, Northern Antarctic Peninsula Pacific margin, *Quaternary Science Reviews*, *25*(9), 933–944, doi: 10.1016/j.quascirev.2005.07.012.

Anandakrishnan, S., and R. B. Alley (1997), Stagnation of Ice Stream C, West Antarctica by water piracy, *Geophysical Research Letters*, *24*(3), 265–268, doi: 10.1029/96GL04016.

Anandakrishnan, S., D. D. Blankenship, R. B. Alley, and P. L. Stoffa (1998), Influence of subglacial geology on the position of a West Antarctic ice stream from seismic observations, *Nature*, *394*, 62–65.

Anandakrishnan, S., R. B. Alley, R. W. Jacobel, and H. Conway (2001), The flow regime of Ice Stream C and hypotheses concerning its recent stagnation, *The West Antarctic Ice Sheet: Behavior and Environment*, pp. 283–296.

Anandakrishnan, S., G. a. Catania, R. B. Alley, and H. J. Horgan (2007), Discovery of till deposition at the grounding line of Whillans Ice Stream., *Science*, *315*(5820), 1835–1838, doi: 10.1126/science.1138393.

Anderson, J. B., S. S. Shipp, A. L. Lowe, J. S. Wellner, and A. B. Mosola (2002), The Antarctic Ice Sheet during the Last Glacial Maximum and its subsequent retreat history: a review, *Quaternary Science Reviews*, *21*(13), 49–70.

Anderson, J. B., H. Conway, P. J. Bart, A. E. Witus, S. L. Greenwood, R. M. McKay, B. L. Hall, R. P. Ackert, K. Licht, M. Jakobsson, and J. O. Stone (2014), Ross Sea paleo-ice sheet drainage and deglacial history during and since the LGM, *Quaternary Science Reviews*, *100*, 31 – 54, doi: http://dx.doi.org/10.1016/j.quascirev.2013.08.020.

Andreassen, K., L. C. Nilssen, B. Rafaelsen, and L. Kuilman (2004), Three-dimensional seismic data from the Barents Sea margin reveal evidence of past ice streams and their dynamics, *Geology*, *32*(8), 729–732.

Arthern, R. J., and C. R. Williams (2017), The sensitivity of West Antarctica to the submarine melting feedback, *Geophysical Research Letters*, *44*(5), 2352–2359.

Arthern, R. J., R. C. Hindmarsh, and C. R. Williams (2015), Flow speed within the Antarctic ice sheet and its controls inferred from satellite observations, *Journal of Geophysical Research: Earth Surface*, *120*(7), 1171–1188.

Ashmore, D. W., R. G. Bingham, R. C. A. Hindmarsh, H. F. J. Corr, and I. R. Joughin (2014), The relationship between sticky spots and radar reflectivity beneath an active West Antarctic ice stream, *Annals of Glaciology*, *55*(67), 29–38, doi: 10.3189/2014AoG67A052.

Atre, S. R., and C. R. Bentley (1993), Laterally varying basal conditions beneath ice streams B and C, West Antarctica, *Journal of Glaciology*, *39*(133), 507–514.

Bamber, J., J. Gomez-Dans, and J. Griggs (2009a), A new 1 km digital elevation model of the antarctic derived from combined satellite radar and laser data-part 1: Data and methods, *The Cryosphere*, *3*(1), 101.

Bamber, J. L., and W. Aspinall (2013), An expert judgement assessment of future sea level rise from the ice sheets, *Nature Climate Change*, *3*(4), 424–427.

Bamber, J. L., D. G. Vaughan, and I. Joughin (2000), Widespread Complex Flow in the Interior of the Antarctic Ice Sheet, *Science*, *287*(5456), 1248–1250.

Bamber, J. L., R. E. M. Riva, B. L. A. Vermeersen, and A. M. LeBrocq (2009b), Reassessment of the potential sea-level rise from a collapse of the West Antarctic Ice Sheet, *Science*, *324*(5929), 901–903.

Batchelor, C. L., and J. A. Dowdeswell (2015), Ice-sheet grounding-zone wedges (GZWs) on high-latitude continental margins, *Marine Geology*, *363*, 65–92, doi: 10.1016/j.margeo.2015.02.001.

Batchelor, C. L., J. A. Dowdeswell, and K. A. Hogan (2011), Late Quaternary ice flow and sediment delivery through Hinlopen Trough, Northern Svalbard margin: Submarine landforms and depositional fan, *Marine Geology*, *284*(1-4), 13–27, doi: 10.1016/j.margeo.2011.03.005.

Bell, R. E., D. D. Blankenship, C. A. Finn, D. L. Morse, T. A. Scambos, J. M. Brozena, and S. M. Hodge (1998), Influence of subglacial geology on the onset of a West Antarctic ice stream from aerogeophysical observations, *Nature*, *394*, 58–62.

Benn, D., and D. Evans (2010), *Glaciers and Glaciation*, 2nd edition ed., Hodder Education.

Bennett, M. R. (2003), Ice streams as the arteries of an ice sheet: their mechanics, stability and significance, *Earth-Science Reviews*, *61*(3-4), 309–339.

Bentley, C. (1964a), *Research in geophysics, solid earth and interface phenomena*, vol. 2, chap. The strucutre of Antarctica and its ice cover., pp. 335–389, MIT, Cambridge, MA.

Bentley, C., N. Lord, and C. Liu (1998), Radar reflections reveal a wet bed beneath stagnant Ice Stream. C and a frozen bed beneath ridge BC, West Antarctica, *Journal of Glaciology*, *44*(146), 149–156.

Bentley, C. R. (1964b), The structure of Antarctica and its ice cover, in *Research in Geophysics, Volume 2: Solid Earth and Interface Phenomena*, vol. 2, p. 335.

Bentley, C. R., A. P. Crary, N. A. Ostenso, and E. C. Thiel (1960), Structure of West Antarctica, *Science*, *131*(3394), 131–136, doi: 10.1126/science.131.3394.131.

Bindschadler, R., H. Choi, A. Wichlacz, R. Bingham, J. Bohlander, K. Brunt, H. Corr, R. Drews, H. Fricker, M. Hall, et al. (2011), Getting around Antarctica: new high-resolution mappings of the grounded and freely-floating boundaries of the Antarctic ice sheet created for the International Polar Year, *The Cryosphere*.

Bindschadler, R. A. (2002), History of lower Pine Island Glacier, West Antarctica, from Landsat imagery, *Journal of Glaciology*, *48*(163), 536–544.

Bingham, R. G., and M. J. Siegert (2007a), Radio-echo sounding over polar ice masses, *Journal of Environmental and Engineering Geophysics*, *12*(1), 47–62, doi: 10.2113/jeeg12.1.47.

Bingham, R. G., and M. J. Siegert (2007b), Radar-derived bed roughness characterization of Institute and Möller ice streams, West Antarctica, and comparison with Siple Coast ice streams, *Geophysical Research Letters*, *34*(21).

Bingham, R. G., and M. J. Siegert (2009), Quantifying subglacial bed roughness in Antarctica: implications for ice-sheet dynamics and history, *Quaternary Science Reviews*, *28*(3-4), 223–236.

Bingham, R. G., E. C. King, A. M. Smith, and H. D. Pritchard (2010), Glacial geomorphology: Towards a convergence of glaciology and geomorphology, *Progress in Physical Geography*, *34*(3), 327–355.

Bingham, R. G., F. Ferraccioli, E. C. King, R. D. Larter, H. D. Pritchard, A. M. Smith, and D. G. Vaughan (2012), Inland thinning of West Antarctic Ice Sheet steered along subglacial rifts, *Nature*, *487*(7408), 468–471.

Bingham, R. G., D. M. Rippin, N. B. Karlsson, H. F. Corr, F. Ferraccioli, T. A. Jordan, A. M. Le Brocq, K. C. Rose, N. Ross, and M. J. Siegert (2015), Ice-flow structure and ice dynamic changes in the weddell sea sector of west antarctica from radar-imaged internal layering, *Journal of Geophysical Research: Earth Surface*, *120*(4), 655–670.

Bingham, R. G., D. G. Vaughan, E. C. King, D. Davies, S. L. Cornford, A. M. Smith, R. J. Arthern, A. M. Brisbourne, J. De Rydt, A. G. C. Graham, M. Spagnolo, O. J. Marsh, and D. E. Shean (2017), Diverse landscapes beneath Pine Island Glacier influence ice flow, *Nature communications*.

Blankenship, D. D., C. R. Bentley, S. T. Rooney, and R. B. Alley (1986), Seismic measurements reveal a saturated porous layer beneath an active Antarctic ice stream, *Nature*, *322*, 54–57.

Blankenship, D. D., C. R. Bentley, S. T. Rooney, and R. B. Alley (1987), Till beneath Ice Stream B: 1. Properties derived from seismic travel times, *Journal of Geophysical Research: Solid Earth*, *92*(B9), 8903–8911, doi: 10.1029/JB092iB09p08903.

Bo, S., M. J. Siegert, S. M. Mudd, D. Sugden, S. Fujita, C. Xiangbin, J. Yunyun, T. Xueyuan, and L. Yuansheng (2009), The Gamburtsev mountains and the origin and early evolution of the Antarctic Ice Sheet, *Nature*, *459*(7247), 690–693.

Bougamont, M., and P. Christoffersen (2012), Hydrologic forcing of ice stream flow promotes rapid transport of sediment in basal ice, *Geology*, *40*(8), 735–738, doi: 10.1130/G33036.1.

Bougamont, M., and S. Tulaczyk (2003), Glacial erosion beneath ice streams and ice-stream tributaries: constraints on temporal and spatial distribution of erosion from numerical simulations of a West Antarctic ice stream, *Boreas*, *32*(1), 178–190.

Bougamont, M., S. Price, P. Christoffersen, and A. J. Payne (2011), Dynamic patterns of ice stream flow in a 3-D higher-order ice sheet model with plastic bed and simplified hydrology, *Journal of Geophysical Research: Earth Surface*, *116*(F4), 1–13, doi: 10.1029/2011JF002025, f04018.

Boulton, G., and R. C. A. Hindmarsh (1987), Sediment deformation beneath glaciers: rheology and geological consequences, *Journal of Geophysical Research*, *92*(B9), 9059–9082.

Briner, J. P. (2007), Supporting evidence from the New York drumlin field that elongate subglacial bedforms indicate fast ice flow, *Boreas*, *36*(2), 143–147.

Brinkerhoff, D., M. Truffer, and A. Aschwanden (2017), Sediment transport drives tidewater glacier periodicity, *Nature communications*, *8*(1), 90.

Brisbourne, A. M., A. M. Smith, D. G. Vaughan, E. C. King, D. Davies, R. G. Bingham, E. C. Smith, I. J. Nias, and S. H. R. Rosier (2017), Bed conditions of Pine Island Glacier, West Antarctica, *Journal of Geophysical Research: Earth Surface*, *122*(1), 419–433, doi: 10.1002/2016JF004033, 2016JF004033.

Caress, D., and D. Chayes (1995), New software for processing sidescan data from sidescan-capable multibeam sonars, in *OCEANS'95. MTS/IEEE. Challenges of Our Changing Global Environment. Conference Proceedings.*, vol. 2, pp. 997–1000, IEEE.

Catania, G., H. Conway, C. Raymond, and T. Scambos (2005), Surface morphology and internal layer stratigraphy in the downstream end of kamb ice stream, west antarctica, *Journal of Glaciology*, *51*(174), 423–431.

Catania, G., T. Scambos, H. Conway, and C. Raymond (2006), Sequential stagnation of Kamb ice stream, West Antarctica, *Geophysical Research Letters*, *33*(14).

Catania, G. A., H. B. Conway, A. M. Gades, C. F. Raymond, and H. Engelhardt (2003), Bed reflectivity beneath inactive ice streams in West Antarctica, *Annals of Glaciology*, *36*, 287–291, doi: 10.3189/172756403781816310.

Christie, F. D. W., R. G. Bingham, N. Gourmelen, S. F. B. Tett, and A. Muto (2016), Four-decade record of pervasive grounding line retreat along the bellingshausen margin of west antarctica, *Geophysical Research Letters*, *43*(11), 5741–5749, doi: 10.1002/2016GL068972, 2016GL068972.

Christoffersen, P., and S. Tulaczyk (2003), Response of subglacial sediments to basal freeze-on 1. Theory and comparison to observations from beneath the West Antarctic Ice Sheet, *Journal of Geophysical Research: Solid Earth*, *108*(B4).

Christoffersen, P., S. Tulaczyk, and A. Behar (2010), Basal ice sequences in Antarctic ice stream: exposure of past hydrologic conditions and a principal mode of sediment transfer, *Journal of Geophysical Research: Earth Surface*, *115*(F3).

Church, J. A., P. U. Clark, A. Cazenave, J. M. Gregory, S. Jevrejeva, A. Levermann, M. A. Merrifield, G. A. Milne, R. S. Nerem, P. D. Nunn, et al. (2013), Climate change 2013: the physical science basis. Contribution of Working Group I to the Fifth Assessment Report of the Intergovernmental Panel on Climate Change, *Sea level change*, pp. 1137–1216.

Clark, C. D. (1993), Mega-scale glacial lineations and cross-cutting ice-flow landforms, *Earth Surface Processes and Landforms*, *18*(1), 1–29, doi: 10.1002/esp.3290180102.

Clark, C. D., A. L. Hughes, S. L. Greenwood, M. Spagnolo, and F. S. Ng (2009), Size and shape characteristics of drumlins, derived from a large sample, and associated scaling laws, *Quaternary Science Reviews*, *28*(7), 677–692.

Cofaigh, C. ., J. Taylor, J. A. Dowdeswell, and C. J. Pudsey (2003), Palaeo-ice streams, trough mouth fans and high-latitude continental slope sedimentation, *Boreas*, *32*(1), 37–55, doi: 10.1080/03009480310001858.

Conway, H., G. Catania, C. F. Raymond, A. M. Gades, T. A. Scambos, and H. Engelhardt (2002), Switch of flow direction in an Antarctic ice stream, *Nature*, *419*(6906), 465–467.

Cornford, S. L., D. F. Martin, D. T. Graves, D. F. Ranken, A. M. L. Brocq, R. M. Gladstone, A. J. Payne, E. G. Ng, and W. H. Lipscomb (2013), Adaptive mesh, finite volume modeling of marine ice sheets, *Journal of Computational Physics*, *232*(1), 529 – 549, doi: http://dx.doi.org/10.1016/j.jcp.2012.08.037.

Cornford, S. L., D. F. Martin, A. J. Payne, E. G. Ng, A. M. Le Brocq, R. M. Gladstone, T. L. Edwards, S. R. Shannon, C. Agosta, M. R. Van Den Broeke, H. H. Hellmer, G. Krinner, S. R. M. Ligtenberg, R. Timmermann, and D. G. Vaughan (2015), Century-scale simulations of the response of the West Antarctic Ice Sheet to a warming climate, *Cryosphere*, *9*(4), 1579–1600, doi: 10.5194/tc-9-1579-2015.

Corr, H. F. J., C. S. M. Doake, A. Jenkins, and D. G. Vaughan (2001), Investigations of an “ice plain" in the mouth of Pine Island Glacier, Antarctica, *Journal of Glaciology*, *47*(156), 51–57, doi: Doi10.3189/172756501781832395.

Cowton, T., P. Nienow, I. Bartholomew, A. Sole, and D. Mair (2012), Rapid erosion beneath the Greenland ice sheet, *Geology*, *40*(4), 343–346, doi: 10.1130/G32687.1.

Cuffey, K., and R. B. Alley (1996), Is erosion by deforming subglacial sediments significant?(Toward till continuity), *Annals of Glaciology*, *22*, 17–24.

Damsgaard, A., D. L. Egholm, J. A. Piotrowski, S. Tulaczyk, N. K. Larsen, and K. Tylmann (2013), Discrete element modeling of subglacial sediment deformation, *Journal of Geophysical Research: Earth Surface*, *118*(4), 2230–2242.

Damsgaard, A., D. L. Egholm, L. H. Beem, S. Tulaczyk, N. K. Larsen, J. A. Piotrowski, and M. R. Siegfried (2016), Ice flow dynamics forced by water pressure variations in subglacial granular beds, *Geophysical Research Letters*, *43*(23).

Damuth, J. E. (1978), Echo character of the Norwegian-Greenland Sea: Relationship to Quaternary sedimentation, *Marine Geology*, *28*(1-2), 1–36, doi: 10.1016/0025-3227(78)90094-4.

Domack, E., D. Duran, A. Leventer, S. Ishman, et al. (2005), Stability of the larsen b ice shelf on the antarctic peninsula during the holocene epoch, *Nature*, *436*(7051), 681.

Dowdeswell, J., and J. Bamber (2007), Keel depths of modern Antarctic icebergs and implications for sea-floor scouring in the geological record, *Marine Geology*, *243*(1), 120 – 131, doi: http://dx.doi.org/10.1016/j.margeo.2007.04.008.

Dowdeswell, J., A. Elverhøi, and R. Spielhagen (1998), Glacimarine sedimentary processes and facies on the polar North Atlantic margins., *Quaternary Science Reviews*, *17*(1), 243–272, doi: 10.1016/S0277-3791(97)00071-1.

Dowdeswell, J., C. Ó Cofaigh, and C. Pudsey (2004), Continental slope morphology and sedimentary processes at the mouth of an Antarctic palaeo-ice stream, *Marine Geology*, *204*(1), 203–214, doi: 10.1016/S0025-3227(03)00338-4.

Dowdeswell, J., J. Evans, C. Ó Cofaigh, and J. Anderson (2006), Morphology and sedimentary processes on the continental slope off Pine Island Bay, Amundsen Sea, West Antarctica, *GSA Bulletin*, *118*(5-6), 606, doi: 10.1130/B25791.1.

Dowdeswell, J., C. Cofaigh, R. Noormets, R. Larter, C.-D. Hillenbrand, S. Benetti, J. Evans, and C. Pudsey (2008a), A major trough-mouth fan on the continental margin of the Bellingshausen Sea, West Antarctica: The Belgica Fan, *Marine Geology*, *252*(3), 129 – 140, doi: http://dx.doi.org/10.1016/j.margeo.2008.03.017.

Dowdeswell, J. A., J. Evans, R. Mugford, G. Griffiths, S. McPhail, N. Millard, P. Stevenson, M. A. Brandon, C. Banks, K. J. Heywood, M. R. Price, P. A. Dodd, A. Jenkins, K. W. Nicholls, D. Hayes, E. P. Abrahamsen, P. Tyler, B. Bett, D. Jones, P. Wadhams, J. P. Wilkinson, K. Stansfield, and S. Ackley (2008b), Autonomous underwater vehicles (AUVs) and investigations of the ice-ocean interface in Antarctic and Arctic waters, *Journal of Glaciology*, *54*(187), 661–672, doi: 10.3189/002214308786570773.

Dowdeswell, J. A., D. Ottesen, and L. Plassen (2016), Debris-flow lobes on the distal flanks of terminal moraines in spitsbergen fjords, *Geological Society, London, Memoirs*, *46*(1), 77–78, doi: 10.1144/M46.97.

Dowling, T. P., P. Möller, and M. Spagnolo (2016), Rapid subglacial streamlined bedform formation at a calving bay margin, *Journal of Quaternary Science*, *31*(8), 879–892.

Drewry, D. (1983), *Antarctica: Glaciological and Geophysical Folio*, Cambridge University Press, Cambridge, UK.

Drewry, D. J. (1975), Radio echo sounding map of Antarctica, (90°-180°), *Polar Record*, *17*(109), 359–374.

Dunlop, P., and C. D. Clark (2006), The morphological characteristics of ribbed moraine, *Quaternary Science Reviews*, *25*(13-14), 1668–1691.

Dupont, T. K., and R. B. Alley (2005), Assessment of the importance of ice-shelf buttressing to ice-sheet flow, *Geophysical Research Letters*, *32*(4), n/a–n/a, doi: 10.1029/2004GL022024, l04503.

Durand, G., O. Gagliardini, L. Favier, T. Zwinger, and E. Le Meur (2011), Impact of bedrock description on modeling ice sheet dynamics, *Geophysical Research Letters*, *38*(20).

Dutrieux, P., J. De Rydt, A. Jenkins, P. R. Holland, H. K. Ha, S. H. Lee, E. J. Steig, Q. Ding, E. P. Abrahamsen, and M. Schröder (2014a), Strong sensitivity of Pine Island ice-shelf melting to climatic variability, *Science*, *343*(6167), 174–178.

Dutrieux, P., C. Stewart, A. Jenkins, K. W. Nicholls, H. F. J. Corr, E. Rignot, and K. Steffen (2014b), Basal terraces on melting ice shelves, *Geophysical Research Letters*, *41*(15), 5506–5513, doi: 10.1002/2014GL060618, 2014GL060618.

Echelmeyer, K., and W. Harrison (1999), Ongoing margin migration of ice stream b, antarctica, *Journal of Glaciology*, *45*(150), 361–369.

Ely, J. C., C. D. Clark, M. Spagnolo, C. R. Stokes, S. L. Greenwood, A. L. Hughes, P. Dunlop, and D. Hess (2016a), Do subglacial bedforms comprise a size and shape continuum?, *Geomorphology*, *257*, 108 – 119, doi: http://dx.doi.org/10.1016/j.geomorph.2016.01.001.

Ely, J. C., C. Graham, I. D. Barr, B. R. Rea, M. Spagnolo, and J. Evans (2016b), Using uav acquired photography and structure from motion techniques for studying glacier landforms: application to the glacial flutes at isfallsglaciären, *Earth Surface Processes and Landforms*, pp. n/a–n/a, doi: 10.1002/esp.4044, eSP-16-0084.R2.

Ely, J. C., C. D. Clark, M. Spagnolo, A. L. Hughes, and C. R. Stokes (2017), Using the size and position of drumlins to understand how they grow, interact and evolve, *Earth Surface Processes and Landforms*.

Engelhardt, H., and B. Kamb (1997), Basal hydraulic system of a West Antarctic ice stream: constraints from borehole observations, *Journal of Glaciology*, *43*(144), 207–230.

Engelhardt, H., and B. Kamb (1998), Basal sliding of Ice Stream B, West Antarctica, *Journal of Glaciology*, *44*(147), 223–230.

Engelhardt, H., N. Humphrey, B. Kamb, and M. Fahnestock (1990), Physical conditions at the base of a fast moving Antarctic ice stream, *Science*, *248*(4951), pp. 57–59.

Evans, J., J. A. Dowdeswell, C. Ó Cofaigh, T. J. Benham, and J. B. Anderson (2006), Extent and dynamics of the West Antarctic Ice Sheet on the outer continental shelf of Pine Island Bay during the last glaciation, *Marine Geology*, *230*(1-2), 53–72.

Favier, L., G. Durand, S. L. Cornford, G. H. Gudmundsson, O. Gagliardini, F. Gillet-Chaulet, T. Zwinger, A. J. Payne, and A. M. Le Brocq (2014), Retreat of Pine Island Glacier controlled by marine ice-sheet instability, *Nature Clim. Change*, *4*, 117–121.

Fowler, A. (1979), A mathematical approach to the theory of glacier sliding, *Journal of Glaciology*, *23*(89), 131–141.

Fowler, A., M. Spagnolo, C. Clark, C. Stokes, A. Hughes, and P. Dunlop (2013), On the size and shape of drumlins, *GEM-International Journal on Geomathematics*, *4*(2), 155–165.

Fowler, A. C. (2000), An instability mechanism for drumlin formation, *Geological Society, London, Special Publications*, *176*(1), 307–319, doi: 10.1144/GSL.SP.2000.176.01.23.

Fowler, A. C. (2010), The formation of subglacial streams and mega-scale glacial lineations, *Proceedings of the Royal Society A: Mathematical, Physical and Engineering Sciences*, *466*(2123), 3181–3201.

Fowler, A. C., and M. Chapwanya (2014), An instability theory for the formation of ribbed moraine, drumlins and mega-scale glacial lineations, in *Proceedings of the Royal Society of London A: Mathematical, Physical and Engineering Sciences*, vol. 470, p. 20140185, The Royal Society.

Fretwell, P., H. D. Pritchard, D. G. Vaughan, J. L. Bamber, N. E. Barrand, R. Bell, C. Bianchi, R. G. Bingham, D. D. Blankenship, G. Casassa, G. Catania, D. Callens, H. Conway, A. J. Cook, H. F. J. Corr, D. Damaske, V. Damm, F. Ferraccioli, R. Forsberg, S. Fujita, Y. Gim, P. Gogineni, J. A. Griggs, R. C. A. Hindmarsh, P. Holmlund, J. W. Holt, R. W. Jacobel, A. Jenkins, W. Jokat, T. Jordan, E. C. King, J. Kohler, W. Krabill, M. Riger-Kusk, K. A. Langley, G. Leitchenkov, C. Leuschen, B. P. Luyendyk, K. Matsuoka, J. Mouginot, F. O. Nitsche, Y. Nogi, O. A. Nost, S. V. Popov, E. Rignot, D. M. Rippin, A. Rivera, J. Roberts, N. Ross, M. J. Siegert, A. M. Smith, D. Steinhage, M. Studinger, B. Sun, B. K. Tinto, B. C. Welch, D. Wilson, D. A. Young, C. Xiangbin, and A. Zirizzotti (2013), Bedmap2: improved ice bed, surface and thickness datasets for antarctica, *The Cryosphere*, *7*(1), 375–393, doi: 10.5194/tc-7-375-2013.

Fricker, H. A., and T. Scambos (2009), Connected subglacial lake activity on lower Mercer and Whillans ice streams, West Antarctica, 2003-2008, *Journal of Glaciology*, *55*(190), 303–315.

Fricker, H. A., T. Scambos, R. Bindschadler, and L. Padman (2007), An active subglacial water system in west antarctica mapped from space, *Science*, *315*(5818), 1544–1548, doi: 10.1126/science.1136897.

Fürst, J. J., G. Durand, F. Gillet-chaulet, L. Tavard, M. Rankl, M. Braun, and O. Gagliardini (2016), The safety band of Antarctic ice shelves, *Nature Clim. Change*, *6*(May), 2014–2017, doi: 10.1038/NCLIMATE2912.

Gades, A. (1998), Spatial and temporal variations of basal conditions beneath glaciers and ice sheets inferred from radio echo soundings, Ph.D. thesis, University of Washington.

Gades, A. M., C. F. Raymond, H. Conway, and R. W. Jacobel (2000), Bed properties of Siple Dome and adjacent ice streams, West Antarctica, inferred from radio-echo sounding measurements, *Journal of Glaciology*, *46*(152), 88–94, doi: 10.3189/172756500781833467.

Gales, J. A., R. D. Larter, and P. T. Leat (2016), Iceberg ploughmarks and associated sediment ridges on the southern weddell sea margin, *Geological Society, London, Memoirs*, *46*(1), 289–290, doi: 10.1144/M46.11.

Ganti, V., C. von Hagke, D. Scherler, M. P. Lamb, W. W. Fischer, and J.-P. Avouac (2016), Time scale bias in erosion rates of glaciated landscapes, *Science Advances*, *2*(10), doi: 10.1126/sciadv.1600204.

García, M., J. A. Dowdeswell, R. Noormets, K. Hogan, J. Evans, C. Ó. Cofaigh, and R. D. Larter (2016), Geomorphic and shallow-acoustic investigation of an antarctic peninsula fjord system using high-resolution rov and shipboard geophysical observations: Ice dynamics and behaviour since the last glacial maximum, *Quaternary Science Reviews*, *153*, 122–138.

Gasson, E., R. DeConto, and D. Pollard (2015), Antarctic bedrock topography uncertainty and ice sheet stability, *Geophysical Research Letters*, *42*(13), 5372–5377.

Gladstone, R. M., V. Lee, J. Rougier, A. J. Payne, H. Hellmer, A. Le Brocq, A. Shepherd, T. L. Edwards, J. Gregory, and S. L. Cornford (2012), Calibrated prediction of Pine Island Glacier retreat during the 21st and 22nd centuries with a coupled flowline model, *Earth and Planetary Science Letters*, *333-334*, 191–199, doi: 10.1016/j.epsl.2012.04.022.

Graham, A. G. C., R. D. Larter, K. Gohl, C.-D. Hillenbrand, J. A. Smith, and G. Kuhn (2009), Bedform signature of a West Antarctic palaeo-ice stream reveals a multi-temporal record of flow and substrate control, *Quaternary Science Reviews*, *28*(25-26), 2774–2793.

Graham, A. G. C., R. D. Larter, K. Gohl, J. A. Dowdeswell, C.-D. Hillenbrand, J. A. Smith, J. Evans, G. Kuhn, and T. Deen (2010), Flow and retreat of the Late Quaternary Pine Island-Thwaites palaeo-ice stream, West Antarctica, *Journal of Geophysical Research*, *115*(F3).

Graham, A. G. C., P. Dutrieux, D. G. Vaughan, F. O. Nitsche, R. Gyllencreutz, S. L. Greenwood, R. D. Larter, and A. Jenkins (2013), Seabed corrugations beneath an Antarctic ice shelf revealed by autonomous underwater vehicle survey: Origin and implications for the history of Pine Island Glacier, *Journal of Geophysical Research: Earth Surface*, *118*(3), 1356–1366, doi: 10.1002/jgrf.20087.

Greenwood, S. L., and J. Kleman (2010), Glacial landforms of extreme size in the Keewatin sector of the Laurentide Ice Sheet, *Quaternary Science Reviews*, *29*(15), 1894–1910.

Gudlaugsson, E., A. Humbert, M. Winsborrow, and K. Andreassen (2013), Subglacial roughness of the former Barents Sea ice sheet, *Journal of Geophysical Research: Earth Surface*, *118*(4), 2546–2556.

Gudmundsson, G. H. (2006), Fortnightly variations in the flow velocity of Rutford Ice Stream, West Antarctica, *Nature*, *444*(7122), 1063–1064.

Gudmundsson, G. H. (2007), Tides and the flow of Rutford Ice Stream, West Antarctica, *Journal of Geophysical Research: Earth Surface*, *112*(4), 1063–1064, doi: 10.1029/2006JF000731.

Gudmundsson, G. H., C. F. Raymond, and R. Bindschadler (1998), The origin and longevity of flow stripes on Antarctic ice streams, *Annals of Glaciology*, *27*(1), 145–152.

Halberstadt, A. R. W., L. M. Simkins, S. L. Greenwood, and J. B. Anderson (2016), Past ice-sheet behaviour: Retreat scenarios and changing controls in the Ross Sea, Antarctica, *Cryosphere*, *10*(3), 1003–1020, doi: 10.5194/tc-10-1003-2016.

Hallet, B., L. Hunter, and J. Bogen (1996), Rates of erosion and sediment evacuation by glaciers: A review of field data and their implications, *Global and Planetary Change*, *12*(1-4), 213 – 235, doi: http://dx.doi.org/10.1016/0921-8181(95)00021-6.

Hambrey, M. J., W. U. Ehrmann, and B. Larsen (1992), *Cenozoic glacial record of the Prydz Bay continental shelf, East Antarctica*, Geological Survey in Denmark.

Hanna, E., F. J. Navarro, F. Pattyn, C. M. Domingues, X. Fettweis, E. R. Ivins, R. J. Nicholls, C. Ritz, B. Smith, S. Tulaczyk, P. L. Whitehouse, and H. J. Zwally (2013), Ice-sheet mass balance and climate change, *Nature*, *498*(7452), 51–59.

Hart, J. K. (1999), Identifying fast ice flow from landform assemblages in the geological record: a discussion, *Annals of Glaciology*, *28*(1), 59–66.

Herman, F., F. Beaud, J.-D. Champagnac, J.-M. Lemieux, and P. Sternai (2011), Glacial hydrology and erosion patterns: A mechanism for carving glacial valleys, *Earth and Planetary Science Letters*, *310*(3), 498 – 508, doi: http://dx.doi.org/10.1016/j.epsl.2011.08.022.

Herman, F., O. Beyssac, M. Brughelli, S. N. Lane, S. Leprince, T. Adatte, J. Y. Y. Lin, J.-P. Avouac, and S. C. Cox (2015), Erosion by an alpine glacier, *Science*, *350*(6257), 193–195, doi: 10.1126/science.aab2386.

Hillenbrand, C. D., R. D. Larter, J. A. Dowdeswell, W. Ehrmann, C. Ó Cofaigh, S. Benetti, A. G. C. Graham, and H. Grobe (2010), The sedimentary legacy of a palaeo-ice stream on the shelf of the southern Bellingshausen Sea: Clues to West Antarctic glacial history during the Late Quaternary, *Quaternary Science Reviews*, *29*(19-20), 2741–2763.

Hillenbrand, C.-D., J. A. Smith, D. A. Hodell, M. Greaves, C. R. Poole, S. Kender, M. Williams, T. J. Andersen, P. E. Jernas, H. Elderfield, et al. (2017), West antarctic ice sheet retreat driven by holocene warm water incursions, *Nature*, *547*(7661), 43–48.

Hillier, J. K., M. J. Smith, C. D. Clark, C. R. Stokes, and M. Spagnolo (2013), Sizes and shapes of subglacial bedforms reveal an exponential size-frequency distribution, in *EGU General Assembly Conference Abstracts*, vol. 15.

Hillier, J. K., I. A. Kougioumtzoglou, C. R. Stokes, M. J. Smith, C. D. Clark, and M. S. Spagnolo (2016), Exploring explanations of subglacial bedform sizes using statistical models, *PloS one*, *11*(7), e0159,489.

Hindmarsh, R. C. A. (1998), Drumlinization and drumlin-forming instabilities : viscous till mechanisms, *Journal of Glaciology*, *44*(147), 293–314.

Hogan, K. A., J. A. Dowdeswell, and C. Ó Cofaigh (2012), Glacimarine sedimentary processes and depositional environments in an embayment fed by West Greenland ice streams, *Marine Geology*, *311-314*, 1–16, doi: 10.1016/j.margeo.2012.04.006.

Hogg, A. E., A. Shepherd, S. L. Cornford, K. H. Briggs, N. Gourmelen, J. A. Graham, I. Joughin, J. Mouginot, T. Nagler, A. J. Payne, et al. (2017), Increased ice flow in Western Palmer Land linked to ocean melting, *Geophysical Research Letters*, *44*(9), 4159–4167.

Holt, J. W., D. D. Blankenship, D. L. Morse, D. A. Young, M. E. Peters, S. D. Kempf, T. G. Richter, D. G. Vaughan, and H. F. J. Corr (2006), New boundary conditions for the West Antarctic Ice Sheet: Subglacial topography of the Thwaites and Smith glacier catchments, *Geophysical Research Letters*, *33*(9).

Horgan, H. J., K. Christianson, R. W. Jacobel, S. Anandakrishnan, and R. B. Alley (2013), Sediment deposition at the modern grounding zone of Whillans Ice Stream, West Antarctica, *Geophysical Research Letters*, *40*(15), 3934–3939, doi: 10.1002/grl.50712.

Hubbard, B., M. J. Siegert, and D. McCarroll (2000), Spectral roughness of glaciated bedrock geomorphic surfaces: implications for glacier sliding, *Journal of Geophysical Research: Solid Earth*, *105*(B9), 21,295–21,303.

Hughes, T. (1973), Is the west antarctic ice sheet disintegrating?, *Journal of Geophysical Research*, *78*(33), 7884–7910, doi: 10.1029/JC078i033p07884.

Hughes, T. J. (1981), The weak underbelly of the West Antarcic Ice Sheet, *Journal of Glaciology*, *27*, 518–525.

Hurst, M. D., S. M. Mudd, R. Walcott, M. Attal, and K. Yoo (2012), Using hilltop curvature to derive the spatial distribution of erosion rates, *Journal of Geophysical Research: Earth Surface*, *117*(F2), n/a–n/a, doi: 10.1029/2011JF002057, f02017.

Iverson, N. R. (2010), Shear resistance and continuity of subglacial till: hydrology rules, *Journal of Glaciology*, *56*(200), 1104–1114.

Iverson, N. R., and R. M. Iverson (2001), Distributed shear of subglacial till due to Coulomb slip, *Journal of Glaciology*, *47*(158), 481–488.

Iverson, N. R., and L. K. Zoet (2015), Experiments on the dynamics and sedimentary products of glacier slip, *Geomorphology*, *244*, 121–134.

Jacobel, R. W., B. C. Welch, D. Osterhouse, R. Pettersson, and J. A. MacGregor (2009), Spatial variation of radar-derived basal conditions on Kamb Ice Stream, West Antarctica, *Annals of Glaciology*, *50*(51), 10–16.

Jacobs, S. S., H. H. Hellmer, and A. Jenkins (1996), Antarctic ice sheet melting in the southeast Pacific, *Geophysical Research Letters*, *23*(9), 957–960, doi: 10.1029/96GL00723.

Jacobs, S. S., A. Jenkins, C. F. Giulivi, and P. Dutrieux (2011), Stronger ocean circulation and increased melting under Pine Island Glacier ice shelf, *Nature Geosci*, *4*, 519–523.

Jakobsson, M., J. B. Anderson, F. O. Nitsche, J. A. Dowdeswell, R. Gyllencreutz, N. Kirchner, R. Mohammad, M. O'Regan, R. B. Alley, S. Anandakrishnan, B. Eriksson, A. Kirshner, R. Fernandez, T. Stolldorf, R. Minzoni, and W. Majewski (2011), Geological record of ice shelf break-up and grounding line retreat, Pine Island Bay, West Antarctica, *Geology*, *39*(7), 691–694, doi: 10.1130/G32153.1.

Jakobsson, M., J. B. Anderson, F. O. Nitsche, R. Gyllencreutz, A. E. Kirshner, N. Kirchner, M. O'Regan, R. Mohammad, and B. Eriksson (2012), Ice sheet retreat dynamics inferred from glacial morphology of the central Pine Island Bay Trough, West Antarctica, *Quaternary Science Reviews*, *38*, 1–10.

Jamieson, S. S. R., D. E. Sugden, and N. R. J. Hulton (2010), The evolution of the subglacial landscape of Antarctica, *Earth and Planetary Science Letters*, *293*(1-2), 1–27.

Jenkins, A., D. G. Vaughan, S. S. Jacobs, H. H. Hellmer, and J. R. Keys (1997), Glaciological and oceanographic evidence of high melt rates beneath Pine Island Glacier, West Antarctica, *Journal of Glaciology*, *4*(143), 114–121.

Jenkins, A., P. Dutrieux, S. S. Jacobs, S. D. McPhail, J. R. Perrett, A. T. Webb, and D. White (2010), Observations beneath Pine Island Glacier in West Antarctica and implications for its retreat, *Nature Geosci*, *3*, 468–472.

Jenson, J. W., P. U. Clark, D. R. MacAyeal, C. Ho, and J. C. Vela (1995), Numerical modeling of advective transport of saturated deforming sediment beneath the lake michigan lobe, laurentide ice sheet, *Geomorphology*, *14*(2), 157 – 166, doi: http://dx.doi.org/10.1016/0169-555X(95)00056-0.

Jezek, K. C., and C. R. Bentley (1983), Field studies of bottom crevasses in the Ross Ice Shelf, Antarctica, *Journal of Glaciology*, *29*(101), 118–126.

Jordan, T. A., F. Ferraccioli, D. G. Vaughan, J. W. Holt, H. Corr, D. D. Blankenship, and T. M. Diehl (2009), Aerogravity evidence for major crustal thinning under the Pine Island Glacier region (West Antarctica), *Geological Society of America Bulletin*, *122*(5-6), 714–726.

Joughin, I. (2003), Timing of Recent Accelerations of Pine Island Glacier, Antarctica, *Geophysical Research Letters*, *30*(13).

Joughin, I., D. R. MacAyeal, and S. Tulaczyk (2004), Basal shear stress of the Ross ice streams from control method inversions, *Journal of Geophysical Research: Solid Earth*, *109*(B9).

Joughin, I., S. Tulaczyk, J. L. Bamber, D. Blankenship, J. W. Holt, T. Scambos, and D. G. Vaughan (2009), Basal conditions for Pine Island and Thwaites Glaciers, West Antarctica, determined using satellite and airborne data, *Journal of Glaciology*, *55*(190), 245–257.

Joughin, I., B. E. Smith, and D. M. Holland (2010), Sensitivity of 21st century sea level to ocean-induced thinning of Pine Island Glacier, Antarctica, *Geophysical Research Letters*, *37*(20), doi: 10.1029/2010GL044819.

Joughin, I., B. E. Smith, and B. Medley (2014), Marine Ice Sheet collapse potentially under way for the Thwaites Glacier Basin, West Antarctica, *Science*, *344*(6185), 735–738, doi: 10.1126/science.1249055.

Joughin, I., D. E. Shean, B. E. Smith, and P. Dutrieux (2016), Grounding line variability and subglacial lake drainage on Pine Island Glacier, Antarctica, *Geophysical Research Letters*, *43*(17), 9093–9102, doi: 10.1002/2016GL070259, 2016GL070259.

Kamb, B. (1991), Rheological nonlinearity and flow instability in the deforming bed mechanism of ice stream motion, *Journal of Geophysical Research: Solid Earth*, *96*(B10), 16,585–16,595.

Karlsson, N. B., D. M. Rippin, R. G. Bingham, and D. G. Vaughan (2012), A continuity-index for assessing ice-sheet dynamics from radar-sounded internal layers, *Earth and Planetary Science Letters*, *335-336*, 88–94.

King, E. (2011), Generating 3d images of sub-glacial landscapes: Three antarctic case studies, in *AGU Fall Meeting Abstracts*.

King, E. C., J. Woodward, and A. M. Smith (2004), Seismic evidence for a water-filled canal in deforming till beneath Rutford Ice Stream, West Antarctica, *Geophysical Research Letters*, *31*(20), doi: 10.1029/2004GL020379.

King, E. C., J. Woodward, and A. M. Smith (2007a), Seismic and radar observations of subglacial bed forms beneath the onset zone of Rutford Ice Stream, Antarctica, *Journal of Glaciology*, *53*(183), 665–672.

King, E. C., J. Woodward, and A. M. Smith (2007b), Seismic and radar observations of subglacial bed forms beneath the onset zone of Rutford Ice Stream, Antarctica, *Journal of Glaciology*, *53*(183), 665–672, doi: 10.3189/002214307784409216.

King, E. C., R. C. A. Hindmarsh, and C. R. Stokes (2009), Formation of mega-scale glacial lineations observed beneath a West Antarctic ice stream, *Nature Geosci*, *2*, 585–588.

King, E. C., H. Pritchard, and A. Smith (2016), Subglacial landforms beneath rutford ice stream, antarctica: detailed bed topography from ice-penetrating radar., *Earth System Science Data*, *8*, 913–934, doi: 10.5194/essdd-8-913-2015.

Konrad, H., L. Gilbert, S. L. Cornford, A. Payne, A. Hogg, A. Muir, and A. Shepherd (2017), Uneven onset and pace of ice-dynamical imbalance in the Amundsen Sea Embayment, West Antarctica, *Geophysical Research Letters*, pp. 910–918, doi: 10.1002/2016GL070733, 2016GL070733.

Koppes, M., and B. Hallet (2006), Erosion rates during rapid deglaciation in Icy Bay, Alaska, *Journal of Geophysical Research: Earth Surface*, *111*(F2).

Koppes, M. N., and D. R. Montgomery (2009), The relative efficacy of fluvial and glacial erosion over modern to orogenic timescales, *Nature Geoscience*, *2*(9), 644–647.

Kuvaas, B., and Y. Kristoffersen (1991), The Crary Fan: a trough-mouth fan on the Weddell Sea continental margin, Antarctica, *Marine Geology*, *97*(3-4), 345–362.

Kyrke-Smith, T., and A. Fowler (2014), Subglacial swamps, in *Proceedings of the Royal Society of London A: Mathematical, Physical and Engineering Sciences*, vol. 470, p. 20140340, The Royal Society.

Kyrke-Smith, T. M., G. H. Gudmundsson, and P. E. Farrell (2017), Can seismic observations of bed conditions on ice streams help constrain parameters in ice flow models?, *Journal of Geophysical Research: Earth Surface*.

Laberg, J., and T. O. Vorren (1996), Late Weichselian submarine debris flow deposits on the Bear Island Trough Mouth Fan, *Oceanographic Literature Review*, *43*(4), 368.

Larter, R. D., A. G. C. Graham, K. Gohl, G. Kuhn, C. D. Hillenbrand, J. A. Smith, T. J. Deen, R. A. Livermore, and H. W. Schenke (2009), Subglacial bedforms reveal complex basal regime in a zone of paleo-ice stream convergence, Amundsen Sea embayment, West Antarctica, *Geology*, *37*(5), 411–414.

Li, X., B. Sun, M. J. Siegert, R. G. Bingham, X. Tang, D. Zhang, X. Cui, and X. Zhang (2010), Characterization of subglacial landscapes by a two-parameter roughness index, *Journal of Glaciology*, *56*(199), 831–836.

Lien, R., A. Solheim, A. Elverhøi, and K. Rokoengen (1989), Iceberg scouring and sea bed morphology on the eastern weddell sea shelf, antarctica, *Polar Research*, *7*(1), 43–57, doi: 10.1111/j.1751-8369.1989.tb00603.x.

Limpert, E., W. A. Stahel, and M. Abbt (2001), Log-normal Distributions across the Sciences: Keys and Clues: On the charms of statistics, and how mechanical models resembling gambling machines offer a link to a handy way to characterize log-normal distributions, which can provide deeper insight into variability and probabilityŮnormal or log-normal: That is the question, *AIBS Bulletin*, *51*(5), 341–352.

Livingstone, S. J., C. Ó Cofaigh, C. R. Stokes, C.-D. Hillenbrand, A. Vieli, and S. S. R. Jamieson (2012), Antarctic palaeo-ice streams, *Earth-Science Reviews*, *111*(1-2), 90–128.

Lok, L., P. Brennan, M. Ash, and K. Nicholls (2015), Autonomous phase-sensitive radio echo sounder for monitoring and imaging antarctic ice shelves, in *Advanced Ground Penetrating Radar (IWAGPR), 2015 8th International Workshop on*, pp. 1–4, IEEE.

Lowe, A. L., and J. B. Anderson (2002), Reconstruction of the West Antarctic Ice Sheet in Pine Island Bay during the Last Glacial Maximum and its subsequent retreat history, *Quaternary Science Reviews*, *21*(16), 1879 – 1897.

Luckman, A., D. Jansen, B. Kulessa, E. C. King, P. Sammonds, and D. I. Benn (2012), The Cryosphere Basal crevasses in Larsen C Ice Shelf and implications for their global abundance, *The Cryosphere*, pp. 113–123, doi: 10.5194/tc-6-113-2012.

Lysså, A., B. Hjelstuen, and E. Larsen (2010), Fjord infill in a high-relief area: Rapid deposition influenced by deglaciation dynamics, glacio-isostatic rebound and gravitational activity, *Boreas*, *39*(1), 39–55, doi: 10.1111/j.1502-3885.2009.00117.x.

Lythe, M. B., and D. G. Vaughan (2001), BEDMAP: A new ice thickness and subglacial topographic model of Antarctica, *Journal of Geophysical Research: Solid Earth*, *106*(B6), 11,335–11,351, doi: 10.1029/2000JB900449.

MacAyeal, D. (1987), Ice-shelf backpressure: form drag versus dynamic drag., in *Glaciology and Quaternary Geology*, edited by C. Van der Veen, pp. 141–160, Reidel, Dordrecht.

MacAyeal, D. R. (1992), The basal stress distribution of Ice Stream E, Antarctica, inferred by control methods, *Journal of Geophysical Research: Solid Earth*, *97*(B1), 595–603, doi: 10.1029/91JB02454.

Macayeal, D. R., R. A. Bindschadler, and T. A. Scambos (1995), Basal friction of ice stream E, West Antarctica, *Journal of Glaciology*, *41*(138), 247–262.

Matsuoka, K. (2011), Pitfalls in radar diagnosis of ice-sheet bed conditions: Lessons from englacial attenuation models, *Geophysical Research Letters*, *38*(5).

Matsuoka, K., D. Morse, and C. F. Raymond (2010), Estimating englacial radar attenuation using depth profiles of the returned power, central West Antarctica, *Journal of Geophysical Research*, *115*(F2).

Matsuoka, K., J. A. MacGregor, and F. Pattyn (2012), Predicting radar attenuation within the Antarctic ice sheet, *Earth and Planetary Science Letters*, *359-360*, 173–183.

McCarroll, D., and A. Nesje (1996), Rock surface roughness as an indicator of degree of rock surface weathering, *Earth Surface Processes and Landforms*, *21*(10), 963–977.

McMillan, M., A. Shepherd, A. Sundal, K. Briggs, A. Muir, A. Ridout, A. Hogg, and D. Wingham (2014), Increased ice losses from Antarctica detected by CryoSat-2, *Geophysical Research Letters*, *41*(11), 3899–3905, doi: 10.1002/2014GL060111, 2014GL060111.

McPhail, S. (2009), Autosub6000: A Deep Diving Long Range AUV, *Journal of Bionic Engineering*, *6*(1), 55 – 62, doi: http://dx.doi.org/10.1016/S1672-6529(08)60095-5.

McPhail, S. D., M. E. Furlong, M. Pebody, J. R. Perrett, P. Stevenson, A. Webb, and D. White (2009), Exploring beneath the PIG Ice Shelf with the Autosub3 AUV, in *OCEANS 2009-EUROPE*, pp. 1–8, doi: 10.1109/OCEANSE.2009.5278170.

Meinshausen, M., S. J. Smith, K. Calvin, J. S. Daniel, M. L. T. Kainuma, J.-F. Lamarque, K. Matsumoto, S. A. Montzka, S. C. B. Raper, K. Riahi, A. Thomson, G. J. M. Velders, and D. P. van Vuuren (2011), The RCP greenhouse gas concentrations and their extensions from 1765 to 2300, *Climatic Change*, *109*(1), 213, doi: 10.1007/s10584-011-0156-z.

Mercer, J. H. (1978), West Antarctic ice sheet and CO2 greenhouse effect: a threat of disaster, *Nature*, *271*(5643), 321–325, doi: 10.1038/271321a0.

Minchew, B., M. Simons, B. Riel, and P. Milillo (2017), Tidally induced variations in vertical and horizontal motion on Rutford Ice Stream, West Antarctica, inferred from remotely sensed observations, *Journal of Geophysical Research: Earth Surface*, *122*(1), 167–190.

Moran, S., L. Clayton, R. Hooke, M. Fenton, and L. Andriashek (1980), Glacier-bed landforms of the prairie region of North America., *Journal of Glaciology*, *25*(93), 457–476, cited By 92.

Morlighem, M., E. Rignot, H. Seroussi, E. Larour, H. Ben Dhia, and D. Aubry (2010), Spatial patterns of basal drag inferred using control methods from a full-Stokes and simpler models for Pine Island Glacier, West Antarctica, *Geophysical Research Letters*, *37*(14), n/a–n/a.

Motyka, R. J., M. Truffer, E. M. Kuriger, and A. K. Bucki (2006), Rapid erosion of soft sediments by tidewater glacier advance: Taku Glacier, Alaska, USA, *Geophysical Research Letters*, *33*(24), n/a–n/a, doi: 10.1029/2006GL028467, l24504.

Mouginot, J., E. Rignot, and B. Scheuchl (2014), Sustained increase in ice discharge from the Amundsen Sea Embayment, West Antarctica, from 1973 to 2013, *Geophysical Research Letters*, *41*(5), 1576–1584.

Murray, T., A. Booth, and D. M. Rippin (2007a), Water-content of glacier-ice: Limitations on estimates from velocity analysis of surface ground-penetrating radar surveys, *Journal of Environmental & Engineering Geophysics*, *12*(1), 87–99.

Murray, T., A. Smith, M. King, and G. Weedon (2007b), Ice flow modulated by tides at up to annual periods at Rutford Ice Stream, West Antarctica, *Geophysical Research Letters*, *34*(18).

Muto, A., S. Anandakrishnan, and R. B. Alley (2013), Subglacial bathymetry and sediment layer distribution beneath the Pine Island Glacier ice shelf, West Antarctica, modeled using aerogravity and autonomous underwater vehicle data, *Annals of Glaciology*, *54*(64), 27–32, doi: 10.3189/2013AoG64A110.

Muto, A., L. E. Peters, K. Gohl, I. Sasgen, R. B. Alley, S. Anandakrishnan, and K. L. Riverman (2016), Subglacial bathymetry and sediment distribution beneath Pine Island Glacier ice shelf modeled using aerogravity and in situ geophysical data: New results, *Earth and Planetary Science Letters*, *433*, 63–75, doi: 10.1016/j.epsl.2015.10.037.

Ng, F., and H. Conway (2004), Fast-flow signature in the stagnated Kamb Ice Stream, West Antarctica, *Geology*, *32*(6), 481–484.

Nias, I. J., S. L. Cornford, and A. J. Payne (2016), Contrasting the Modelled sensitivity of the Amundsen Sea Embayment ice streams, *Journal of Glaciology*, *62*(233), 552–562, doi: 10.1017/jog.2016.40.

Nicholls, K. W., E. P. Abrahamsen, J. J. H. Buck, P. A. Dodd, C. Goldblatt, G. Griffiths, K. J. Heywood, N. E. Hughes, A. Kaletzky, G. F. Lane-Serff, S. D. McPhail, N. W. Millard, K. I. C. Oliver, J. Perrett, M. R. Price, C. J. Pudsey, K. Saw, K. Stansfield, M. J. Stott, P. Wadhams, A. T. Webb, and J. P. Wilkinson (2006), Measurements beneath an Antarctic ice shelf using an autonomous underwater vehicle, *Geophysical Research Letters*, *33*(8), n/a–n/a, doi: 10.1029/2006GL025998, l08612.

Nicholls, K. W., H. F. Corr, C. L. Stewart, L. B. Lok, P. V. Brennan, and D. G. Vaughan (2015), A ground-based radar for measuring vertical strain rates and time-varying basal melt rates in ice sheets and shelves, *Journal of Glaciology*, *61*(230), 1079–1087.

Nitsche, F. O., K. Gohl, R. D. Larter, C. D. Hillenbrand, G. Kuhn, J. A. Smith, S. Jacobs, J. B. Anderson, and M. Jakobsson (2013), Paleo ice flow and subglacial meltwater dynamics in Pine Island Bay, West Antarctica, *The Cryosphere*, *7*(1), 249–262.

Ó Cofaigh, C., C. J. Pudsey, J. A. Dowdeswell, and P. Morris (2002), Evolution of subglacial bedforms along a paleo-ice stream, Antarctic Peninsula continental shelf, *Geophysical Research Letters*, *29*(8), 41–1–41–4, doi: 10.1029/2001GL014488.

Ó Cofaigh, C. Ã., J. Taylor, J. A. Dowdeswell, and C. J. Pudsey (2003), Palaeo-ice streams, trough mouth fans and high-latitude continental slope sedimentation, *Boreas*, *32*(1), 37–55.

Oran Brigham, E. (1988), The Fast Fourier Transform and its applications, *UK: Prentice Hall*.

Ottesen, D., and J. Dowdeswell (2006), Assemblages of submarine landforms produced by tidewater glaciers in svalbard, *Journal of Geophysical Research: Earth Surface*, *111*(F1).

Ottesen, D., C. R. Stokes, R. Bøe, L. Rise, O. Longva, T. Thorsnes, O. Olesen, T. Bugge, A. Lepland, and O. B. Hestvik (2016), Landform assemblages and sedimentary processes along the Norwegian Channel Ice Stream, *Sedimentary Geology*, *338*, 115 – 137, doi: http://dx.doi.org/10.1016/j.sedgeo.2016.01.024.

Paolo, F. S., H. A. Fricker, and L. Padman (2015), Volume loss from Antarctic ice shelves is accelerating, *Science*, *348*(6232), 327–331, doi: 10.1126/science.aaa0940.

Parizek, B. R., K. Christianson, S. Anandakrishnan, R. B. Alley, R. T. Walker, R. A. Edwards, D. S. Wolfe, G. T. Bertini, S. K. Rinehart, R. A. Bindschadler, and S. M. J. Nowicki (2013), Dynamic (in)stability of Thwaites Glacier, West Antarctica, *Journal of Geophysical Research: Earth Surface*, *118*(2), 638–655, doi: 10.1002/jgrf.20044.

Park, J. W., N. Gourmelen, A. Shepherd, S. W. Kim, D. G. Vaughan, and D. J. Wingham (2013), Sustained retreat of the Pine Island Glacier, *Geophysical Research Letters*, *40*(10), 2137–2142.

Pattyn, F., L. Perichon, G. Durand, L. Favier, O. Gagliardini, R. C. Hindmarsh, T. Zwinger, T. Albrecht, S. Cornford, D. Docquier, et al. (2013), Grounding-line migration in plan-view marine ice-sheet models: results of the ice2sea MISMIP3d intercomparison, *Journal of Glaciology*, *59*(215), 410–422.

Payne, A. J. (2004), Recent dramatic thinning of largest West Antarctic ice stream triggered by oceans, *Geophysical Research Letters*, *31*(23).

Payne, A. J., P. R. Holland, A. P. Shepherd, I. C. Rutt, A. Jenkins, and I. Joughin (2007), Numerical modeling of ocean-ice interactions under Pine Island Bay's ice shelf, *Journal of Geophysical Research*, *112*(C10).

Peters, L. E., S. Anandakrishnan, R. B. Alley, J. P. Winberry, D. E. Voigt, A. M. Smith, and D. L. Morse (2006), Subglacial sediments as a control on the onset and location of two Siple Coast ice streams, West Antarctica, *Journal of Geophysical Research*, *111*(B1).

Peters, L. E., S. Anandakrishnan, R. B. Alley, and A. M. Smith (2007), Extensive storage of basal meltwater in the onset region of a major West Antarctic ice stream, *Geology*, *35*(3), 251.

Pollard, D., and R. DeConto (2012), A simple inverse method for the distribution of basal sliding coefficients under ice sheets, applied to antarctica, *The Cryosphere*, *6*(5), 953.

Pollard, D., and R. M. Deconto (2016), Contribution of Antarctica to past and future sea-level rise, *Nature*, *531*(7596), 591–597, doi: 10.1038/nature17145.

Pritchard, H. D., R. J. Arthern, D. G. Vaughan, and L. A. Edwards (2009), Extensive dynamic thinning on the margins of the Greenland and Antarctic ice sheets, *Nature*, *461*(7266), 971–5.

Pritchard, H. D., S. R. Ligtenberg, H. A. Fricker, D. G. Vaughan, M. R. van den Broeke, and L. Padman (2012), Antarctic ice-sheet loss driven by basal melting of ice shelves, *Nature*, *484*(7395), 502–5.

Raiswell, R., M. Tranter, L. G. Benning, M. Siegert, R. De'ath, P. Huybrechts, and T. Payne (2006), Contributions from glacially derived sediment to the global iron (oxyhydr)oxide cycle: Implications for iron delivery to the oceans, *Geochimica et Cosmochimica Acta*, *70*(11), 2765 – 2780, doi: http://dx.doi.org/10.1016/j.gca.2005.12.027.

Raymond, M. J., and G. H. Gudmundsson (2005), On the relationship between surface and basal properties on glaciers, ice sheets, and ice streams, *Journal of Geophysical Research: Solid Earth*, *110*(B8).

Rebesco, M., Y. Liu, A. Camerlenghi, M. Winsborrow, J. S. Laberg, A. Caburlotto, P. Diviacco, D. Accettella, C. Sauli, N. Wardell, and I. Tomini (2011), Deglaciation of the western margin of the Barents Sea Ice Sheet. A swath bathymetric and sub-bottom seismic study from the Kveithola Trough, *Marine Geology*, *279*(1-4), 141–147.

Rignot, E. (2001), Evidence for rapid retreat and mass loss of Thwaites Glacier, West Antarctica, *Journal of Glaciology*, *47*(157), 213–222.

Rignot, E. (2008), Changes in West Antarctic ice stream dynamics observed with ALOS PALSAR data, *Geophysical Research Letters*, *35*(12).

Rignot, E., D. G. Vaughan, M. Schmeltz, T. Dupont, and D. MacAyeal (2002), Acceleration of Pine Island and Thwaites Glaciers, West Antarctica, *Annals of Glaciology*, *34*, 189–194, doi: 10.3189/172756402781817950.

Rignot, E., J. L. Bamber, M. R. van den Broeke, C. Davis, Y. Li, W. J. van de Berg, and E. van Meijgaard (2008), Recent Antarctic ice mass loss from radar interferometry and regional climate modelling, *Nature Geoscience*, *1*(2), 106–110.

Rignot, E., J. Mouginot, and B. Scheuchl (2011a), Ice flow of the Antarctic ice sheet, *Science*, *333*(6048), 1427–30.

Rignot, E., I. Velicogna, M. R. van den Broeke, A. Monaghan, and J. T. M. Lenaerts (2011b), Acceleration of the contribution of the Greenland and Antarctic ice sheets to sea level rise, *Geophysical Research Letters*, *38*(5), n/a–n/a, doi: 10.1029/2011GL046583.

Rignot, E., S. Jacobs, J. Mouginot, and B. Scheuchl (2013), Ice-shelf melting around Antarctica, *Science*, *341*(6143), 266–270, doi: 10.1126/science.1235798.

Rignot, E., J. Mouginot, M. Morlighem, H. Seroussi, and B. Scheuchl (2014), Widespread, rapid grounding line retreat of Pine Island, Thwaites, Smith, and Kohler glaciers, West Antarctica, from 1992 to 2011, *Geophysical Research Letters*, *41*(10), 3502–3509.

Rignot, E. J. (1998), Fast recession of a west antarctic glacier, *Science*, *281*(5376), 549–551, doi: 10.1126/science.281.5376.549.

Rippin, D., J. Bamber, M. Siegert, D. Vaughan, and H. Corr (2006), Basal conditions beneath enhanced-flow tributaries of Slessor Glacier, East Antarctica, *Journal of Glaciology*, *52*(179), 481–490.

Rippin, D., D. Vaughan, and H. Corr (2011), The basal roughness of Pine Island Glacier, West Antarctica, *Journal of Glaciology*, *57*(201), 67–76.

Rippin, D., R. Bingham, T. Jordan, A. Wright, N. Ross, H. Corr, F. Ferraccioli, A. Le Brocq, K. Rose, and M. Siegert (2014), Basal roughness of the Institute and Möller Ice Streams, West Antarctica: Process determination and landscape interpretation, *Geomorphology*, *214*, 139–147.

Ritz, C., T. L. Edwards, G. Durand, A. J. Payne, V. Peyaud, and R. C. Hindmarsh (2015), Potential sea-level rise from Antarctic ice-sheet instability constrained by observations, *Nature*, *528*(7580), 115–118.

Robin, G. D. Q., D. J. Drewry, and D. T. Meldrum (1977), International Studies of Ice Sheet and Bedrock, *Philosophical Transactions of the Royal Society B: Biological Sciences*, *279*(963), 185–196.

Rooney, S. T., D. D. Blankenship, R. B. Alley, and C. R. Bentley (1987), Till beneath ice stream B: 2. Structure and continuity, *Journal of Geophysical Research: Solid Earth*, *92*(B9), 8913–8920, doi: 10.1029/JB092iB09p08913.

Rose, J. (1987), Drumlins as part of a glacier bedform continuum, in *Drumlin Symposium*, edited by J. Menzies and J. Rose, pp. 103–116, Balkema, Rotterdam.

Rosier, S. H., G. H. Gudmundsson, and J. M. Green (2015), Temporal variations in the flow of a large Antarctic ice stream controlled by tidally induced changes in the subglacial water system, *The Cryosphere*, *9*(4), 1649–1661.

Rüther, D., K. Andreassen, and M. Spagnolo (2013), Aligned glaciotectonic rafts on the central Barents Sea seafloor revealing extensive glacitectonic erosion during the last deglaciation, *Geophysical Research Letters*, *40*(24), 6351–6355, doi: 10.1002/2013GL058413, 2013GL058413.

Rüther, D. C., K. Andreassen, and M. Spagnolo (2016), Aligned glacitectonic rafts on the floor of the central Barents Sea, *Geological Society, London, Memoirs*, *46*(1), 189 LP – 190.

Rydt, J. D., G. H. Gudmundsson, H. Corr, and P. Christoffersen (2013), Surface undulations of antarctic ice streams tightly controlled by bedrock topography, *The Cryosphere*, *7*(2), 407–417.

Schoof, C. (2002), Basal perturbations under ice streams: form drag and surface expression, *Journal of Glaciology*, *48*(162), 407–416.

Schoof, C. (2007a), Ice sheet grounding line dynamics: Steady states, stability, and hysteresis, *Journal of Geophysical Research: Earth Surface*, *112*(F3), 1–19, doi: 10.1029/2006JF000664.

Schoof, C. (2007b), Cavitation on deformable glacier beds, *SIAM Journal on Applied Mathematics*, *67*(6), 1633–1653.

Schoof, C. G., and G. K. C. Clarke (2008), A model for spiral flows in basal ice and the formation of subglacial flutes based on a Reiner-Rivlin rheology for glacial ice, *Journal of Geophysical Research*, *113*(B5).

Schroeder, D. M., D. D. Blankenship, and D. A. Young (2013), Evidence for a water system transition beneath Thwaites Glacier, West Antarctica, *Proceedings of the National Academy of Sciences*, *110*(30), 12,225–12,228.

Scott, J. B. T., G. H. Gudmundsson, A. M. Smith, R. G. Bingham, H. D. Pritchard, and D. G. Vaughan (2009), Increased rate of acceleration on Pine Island Glacier strongly coupled to changes in gravitational driving stress, *The Cryosphere*, *3*, 125–131, doi: doi: 10.5194/tc-3-125-2009.

Sergienko, O., T. T. Creyts, and R. Hindmarsh (2014), Similarity of organized patterns in driving and basal stresses of Antarctic and Greenland ice sheets beneath extensive areas of basal sliding, *Geophysical Research Letters*, *41*(11), 3925–3932.

Sergienko, O. V., and R. C. A. Hindmarsh (2013), Regular patterns in frictional resistance of ice-stream beds seen by surface data inversion, *Science*, *342*(6162), 1086–1089, doi: 10. 1126/science.1243903.

Seroussi, H., M. Morlighem, E. Rignot, J. Mouginot, E. Larour, M. Schodlok, and A. Khazendar (2014a), Sensitivity of the dynamics of Pine Island Glacier, West Antarctica, to climate forcing for the next 50 years, doi: 10.5194/tc-8-1699-2014.

Seroussi, H., M. Morlighem, E. Rignot, J. Mouginot, E. Larour, M. Schodlok, and A. Khazendar (2014b), Sensitivity of the dynamics of Pine Island Glacier, West Antarctica, to climate forcing for the next 50 years, *Cryosphere*, *8*(5).

Shackleton, N. J., and N. D. Opdyke (1973), Oxygen isotope and palaeomagnetic stratigraphy of Equatorial Pacific core V28-238: Oxygen isotope temperatures and ice volumes on a 105 year and 106 year scale, *Quaternary Research*, *3*(1), 39 – 55, doi: http://dx.doi.org/10.1016/0033-5894(73)90052-5.

Shean, D. E., O. Alexandrov, Z. M. Moratto, B. E. Smith, I. R. Joughin, C. Porter, and P. Morin (2016), An automated, open-source pipeline for mass production of digital elevation models (DEMs) from very-high-resolution commercial stereo satellite imagery., *ISPRS Journal of Photogrammetry and Remote Sensing*, *116*, 101–117.

Shepard, M. K., B. A. Campbell, M. H. Bulmer, T. G. Farr, L. R. Gaddis, and J. J. Plaut (2001), The roughness of natural terrain: A planetary and remote sensing perspective, *Journal of Geophysical Research: Planets*, *106*(E12), 32,777–32,795.

Shepherd, A. (2004), Warm ocean is eroding West Antarctic Ice Sheet, *Geophysical Research Letters*, *31*(23).

Shepherd, A., and D. Wingham (2007), Recent sea-level contributions of the Antarctic and Greenland ice sheets, *Science*, *315*(5818), 1529–32, doi: 10.1126/science.1136776.

Shepherd, A., D. J. Wingham, J. A. Mansley, and H. F. Corr (2001), Inland thinning of Pine Island Glacier, West Antarctica, *Science*, *291*(5505), 862–4.

Shepherd, A., D. J. Wingham, and J. A. Mansley (2002), Inland thinning of the Amundsen Sea sector, West Antarctica, *Geophysical Research Letters*, *29*(10).

Shepherd, A., E. R. Ivins, G. A, V. R. Barletta, M. J. Bentley, S. Bettadpur, K. H. Briggs, D. H. Bromwich, R. Forsberg, N. Galin, M. Horwath, S. Jacobs, I. Joughin, M. A. King, J. T. Lenaerts, J. Li, S. R. Ligtenberg, A. Luckman, S. B. Luthcke, M. McMillan, R. Meister, G. Milne, J. Mouginot, A. Muir, J. P. Nicolas, J. Paden, A. J. Payne, H. Pritchard, E. Rignot, H. Rott, L. S. Sorensen, T. A. Scambos, B. Scheuchl, E. J. Schrama, B. Smith, A. V. Sundal, J. H. van Angelen, W. J. van de Berg, M. R. van den Broeke, D. G. Vaughan, I. Velicogna, J. Wahr, P. L. Whitehouse, D. J. Wingham, D. Yi, D. Young, and H. J. Zwally (2012), A reconciled estimate of ice-sheet mass balance, *Science*, *338*(6111), 1183–9.

Ship, S., J. Anderson, and E. Domack (1999), Late Pleistocene–Holocene retreat of the West Antarctic Ice-Sheet system in the Ross Sea: part 1Ůgeophysical results, *Geological Society of America Bulletin*, *111*(10), 1486–1516.

Shipp, S., J. Anderson, and E. Domack (1999), Late Pleistocene-Holocene retreat of the West Antarctic Ice-Sheet system in the Ross Sea: Part 1 - geophysical results, *Bulletin of the Geological Society of America*, *111*(10), 1486–1516, cited By 241.

Shipp, S. S., J. S. Wellner, and J. B. Anderson (2002), Retreat signature of a polar ice stream: sub-glacial geomorphic features and sediments from the Ross Sea, Antarctica, *Geological Society, London, Special Publications*, *203*(1), 277–304, doi: 10.1144/GSL.SP.2002.203.01.15.

Siegert, M. J. (2008), Antarctic subglacial topography and ice-sheet evolution, *Earth Surface Processes and Landforms*, *33*(4), 646–660.

Siegert, M. J., J. Taylor, A. J. Payne, and B. Hubbard (2004), Macro-scale bed roughness of the Siple Coast ice streams in West Antarctica, *Earth Surface Processes and Landforms*, *29*(13), 1591–1596, 883WK Times Cited:19 Cited References Count:20.

Siegert, M. J., M. Pokar, J. A. Dowdeswell, and T. Benham (2005a), Radio-echo layering in West Antarctica: a spreadsheet dataset, *Earth Surface Processes and Landforms*, *30*(12), 1583–1591.

Siegert, M. J., J. Taylor, and A. J. Payne (2005b), Spectral roughness of subglacial topography and implications for former ice-sheet dynamics in East Antarctica, *Global and Planetary Change*, *45*(1), 249–263.

Simkins, L. M., J. B. Anderson, and S. L. Greenwood (2016), Glacial landform assemblage reveals complex retreat of grounded ice in the ross sea, antarctica, *Geological Society, London, Memoirs*, *46*(1), 353–356, doi: 10.1144/M46.168.

Smith, A. (1997a), Variations in basal conditions on Rutford Ice Stream, West Antarctica, *Journal of Glaciology*, *43*(144), 251–261.

Smith, A. (1997b), Basal conditions on Rutford ice stream, West Antarctica, from seismic observations, *Journal of Geophysical Research: Solid Earth*, *102*(B1), 543–552.

Smith, A. M. (1997c), Basal conditions on Rutford Ice Stream, West Antarctica, from seismic observations, *Journal of Geophysical Research: Solid Earth*, *102*(B1), 543–552, doi: 10.1029/96JB02933.

Smith, A. M. (2007), Subglacial bed properties from normal-incidence seismic reflection data, *Journal of Environmental and Engineering Geophysics*, *12*(1), 3–13, doi: 10.2113/JEEG12.1.3.

Smith, A. M., and T. Murray (2009), Bedform topography and basal conditions beneath a fast-flowing West Antarctic ice stream, *Quaternary Science Reviews*, *28*(7-8), 584–596.

Smith, A. M., T. Murray, K. W. Nicholls, K. Makinson, G. Adalgeirsdóttir, A. E. Behar, and D. G. Vaughan (2007), Rapid erosion, drumlin formation, and changing hydrology beneath an Antarctic ice stream, *Geology*, *35*(2), 127.

Smith, A. M., C. R. Bentley, R. G. Bingham, and T. A. Jordan (2012), Rapid subglacial erosion beneath Pine Island Glacier, West Antarctica, *Geophysical Research Letters*, *39*(12).

Smith, A. M., T. A. Jordan, F. Ferraccioli, and R. G. Bingham (2013), Influence of subglacial conditions on ice stream dynamics: Seismic and potential field data from Pine Island Glacier, West Antarctica, *Journal of Geophysical Research: Solid Earth*, *118*(4), 1471–1482.

Smith, B. E., C. F. Raymond, and T. Scambos (2006), Anisotropic texture of ice sheet surfaces, *Journal of Geophysical Research*, *111*(F1).

Smith, B. E., N. Gourmelen, A. Huth, and I. Joughin (2017a), Connected subglacial lake drainage beneath Thwaites Glacier, West Antarctica, *The Cryosphere*, *11*(1), 451–467, doi: 10.5194/tc-11-451-2017.

Smith, E., A. Smith, R. White, A. Brisbourne, and H. Pritchard (2015), Mapping the ice-bed interface characteristics of Rutford Ice Stream, West Antarctica, using microseismicity, *Journal of Geophysical Research: Earth Surface*, *120*(9), 1881–1894.

Smith, J. A., T. J. Andersen, M. Shortt, A. M. Gaffney, M. Truffer, T. P. Stanton, R. Bindschadler, P. Dutrieux, A. Jenkins, C. Hillenbrand, W. Ehrmann, H. F. J. Corr, N. Farley, S. Crowhurst, and D. G. Vaughan (2017b), Sub-ice-shelf sediments record history of twentieth-century retreat of Pine Island Glacier, *Nature*, *541*(7635), 77–80, doi: 10.1038/nature20136.

Smith, M. J., and C. D. Clark (2005), Methods for the visualization of digital elevation models for landform mapping, *Earth Surface Processes and Landforms*, *30*(7), 885–900.

Smith, M. W. (2014), Roughness in the earth sciences, *Earth-Science Reviews*, *136*, 202–225.

Spagnolo, M., C. D. Clark, J. C. Ely, C. R. Stokes, J. B. Anderson, K. Andreassen, A. G. C. Graham, and E. C. King (2014), Size, shape and spatial arrangement of mega-scale glacial lineations from a large and diverse dataset, *Earth Surface Processes and Landforms*, *39*(11), 1432–1448, doi: 10.1002/esp.3532.

Spagnolo, M., E. Phillips, J. A. Piotrowski, B. R. Rea, C. D. Clark, C. R. Stokes, S. J. Carr, J. C. Ely, A. Ribolini, W. Wysota, and I. Szuman (2016), Ice stream motion facilitated by a shallow-deforming and accreting bed, *Nature Communications*, *7*(10723), 1–11.

Spagnolo, M., T. C. Bartholomaus, C. D. Clark, C. R. Stokes, N. Atkinson, J. A. Dowdeswell, J. C. Ely, A. G. Graham, K. A. Hogan, E. C. King, et al. (2017), The periodic topography of ice stream beds: insights from the Fourier spectra of mega-scale glacial lineations, *Journal of geophysical research: earth surface*.

Stenoien, M. D., and C. R. Bentley (2000), Pine Island Glacier, Antarctica: A study of the catchment using interferometric synthetic aperture radar measurements and radar altimetry, *Journal of Geophysical Research: Solid Earth*, *105*(B9), 21,761–21,779.

Stokes, C., and C. Clark (2001), Palaeo-ice streams, *Quaternary Science Reviews*, *20*(13), 1437 – 1457.

Stokes, C., M. Spagnolo, C. Clark, C. . Cofaigh, O. Lian, and R. Dunstone (2013a), Formation of mega-scale glacial lineations on the dubawnt lake ice stream bed: 1. size, shape and spacing from a large remote sensing dataset, *Quaternary Science Reviews*, *77*, 190 – 209, doi: http://dx.doi.org/10.1016/j.quascirev.2013.06.003.

Stokes, C. R. (2017), Geomorphology under ice streams: Moving from form to process, *Earth Surface Processes and Landforms*.

Stokes, C. R., and C. D. Clark (1999), Geomorphological criteria for identifying Pleistocene ice streams, *Annals of Glaciology*, *28*(1), 67–74.

Stokes, C. R., and C. D. Clark (2002), Are long subglacial bedforms indicative of fast ice flow?, *Boreas*, *31*(3), 239–249, doi: 10.1111/j.1502-3885.2002.tb01070.x.

Stokes, C. R., C. D. Clark, O. B. Lian, and S. Tulaczyk (2007), Ice stream sticky spots: A review of their identification and influence beneath contemporary and palaeo-ice streams, *Earth-Science Reviews*, *81*(3-4), 217–249.

Stokes, C. R., O. B. Lian, S. Tulaczyk, and C. D. Clark (2008), Superimposition of ribbed moraines on a palaeo-ice-stream bed: implications for ice stream dynamics and shutdown, *Earth Surface Processes and Landforms*, *33*(4), 593–609.

Stokes, C. R., A. C. Fowler, C. D. Clark, R. C. Hindmarsh, and M. Spagnolo (2013b), The instability theory of drumlin formation and its explanation of their varied composition and internal structure, *Quaternary Science Reviews*, *62*, 77–96.

Stokes, C. R., M. Margold, and T. T. Creyts (2016), Ribbed bedforms on palaeo-ice stream beds resemble regular patterns of basal shear stress ('traction ribs') inferred from modern ice streams, *Journal of Glaciology*, *62*(234), 696–713.

Studinger, M., C. Allen, W. Blake, L. Shi, S. Elieff, W. Krabill, J. Sonntag, S. Martin, P. Dutrieux, A. Jenkins, et al. (2010), Mapping pine island glacier's sub-ice cavity with airborne gravimetry, in *AGU Fall Meeting Abstracts*.

Sugden, D., and B. John (1976), *Glaciers and Landscape*, Edward Arnold.

Sugden, D. E., D. R. Marchant, and G. H. Denton (1993), The Case for a Stable East Antarctic Ice Sheet: The Background, *Geografiska Annaler. Series A, Physical Geography*, *75*(4), 151–154.

Sun, S., S. L. Cornford, Y. Liu, and J. C. Moore (2014), Dynamic response of Antarctic ice shelves to bedrock uncertainty, *The Cryosphere*, *8*(4), 1561–1576, doi: 10.5194/tc-8-1561-2014.

Taylor, J., M. J. Siegert, A. J. Payne, and B. Hubbard (2004), Regional-scale bed roughness beneath ice masses: measurement and analysis, *Computers & Geosciences*, *30*(8), 899–908.

Thomas, R. H., and C. R. Bentley (1978), A model for Holocene retreat of the West Antarctic ice sheet, *Quaternary Research*, *10*(2), 150–170.

Thompson, J., M. Simons, and V. C. Tsai (2014), Modeling the elastic transmission of tidal stresses to great distances inland in channelized ice streams, *Cryosphere*, *8*(6), 2007–2029.

Truffer, M., W. D. Harrison, and K. A. Echelmeyer (2000), Glacier motion dominated by processes deep in underlying till, *Journal of Glaciology*, *46*(153), 213–221.

Tulaczyk, S., W. B. Kamb, and H. F. Engelhardt (2000), Basal mechanics of Ice Stream B, west Antarctica: 1. Till mechanics, *Journal of Geophysical Research: Solid Earth*, *105*(B1), 463–481, doi: 10.1029/1999JB900329.

Tulaczyk, S. M., R. P. Scherer, and C. D. Clark (2001), A ploughing model for the origin of weak tills beneath ice streams: a qualitative treatment, *Quaternary International*, *86*(1), 59–70.

Turner, J., A. Orr, G. H. Gudmundsson, A. Jenkins, R. G. Bingham, C.-D. Hillenbrand, and T. J. Bracegirdle (2017), Atmosphere-ocean-ice interactions in the Amundsen Sea Embayment, West Antarctica, *Reviews of Geophysics*, pp. n/a–n/a, doi: 10.1002/2016RG000532, 2016RG000532.

Vaughan, D. G. (2008), West Antarctic Ice Sheet collapse the fall and rise of a paradigm, *Climatic Change*, *91*(1-2), 65–79.

Vaughan, D. G., H. F. J. Corr, F. Ferraccioli, N. Frearson, A. O'Hare, D. Mach, J. W. Holt, D. D. Blankenship, D. L. Morse, and D. A. Young (2006), New boundary conditions for the West Antarctic ice sheet: Subglacial topography beneath Pine Island Glacier, *Geophysical Research Letters*, *33*(9).

Vaughan, D. G., H. F. J. Corr, A. M. Smith, H. D. Pritchard, and A. Shepherd (2008), Flow-switching and water piracy between Rutford ice stream and Carlson inlet, West Antarctica, *Journal of Glaciology*, *54*(184), 41–48, doi: 10.3189/002214308784409125.

Vorren, T. O., J. S. Laberg, F. Blaume, J. A. Dowdeswell, N. H. Kenyon, J. Mienert, J. Rumohr, and F. Werner (1998), The Norwegian–Greenland Sea continental margins: morphology and late Quaternary sedimentary processes and environment., *Quaternary Science Reviews*, *17*(1-3), 273–302.

Walder, J. S., and A. Fowler (1994), Channelized subglacial drainage over a deformable bed, *Journal of Glaciology*, *40*(134), 3–15.

Wang, Z., S. Gogineni, F. Rodriguez-Morales, J.-B. Yan, J. Paden, C. Leuschen, R. D. Hale, J. Li, C. L. Carabajal, D. Gomez-Garcia, et al. (2016), Multichannel Wideband Synthetic Aperture Radar for Ice Sheet Remote Sensing: Development and the First Deployment in Antarctica, *IEEE Journal of Selected Topics in Applied Earth Observations and Remote Sensing*, *9*(3), 980–993.

Weertman, J. (1958), Transport of boulders by glaciers and ice sheets, *International Association of Scientific Hydrology Bulletin*, *3*(2), 44–44, doi: 10.1080/02626665809493102.

Weertman, J. (1972), General theory of water flow at the base of a glacier or ice sheet, *Reviews of Geophysics*, *10*(1), 287–333.

Weertman, J. (1974), Stability of the junction of an ice sheet and an ice shelf, *Journal of Glaciology*, *13*(67), 3–11.

Welch, B. C., and R. W. Jacobel (2003), Analysis of deep-penetrating radar surveys of West Antarctica, US-ITASE 2001, *Geophysical Research Letters*, *30*(8).

Wellner, J., A. Lowe, S. Shipp, and J. Anderson (2001), Distribution of glacial geomorphic features on the Antarctic continental shelf and correlation with substrate: implications for ice behavior, *Journal of Glaciology*, *47*(158), 397–411, doi: doi:10.3189/172756501781832043.

Wellner, J., D. Heroy, and J. Anderson (2006), The death mask of the antarctic ice sheet: Comparison of glacial geomorphic features across the continental shelf, *Geomorphology*, *75*(1âĂŞ2), 157 – 171, doi: http://dx.doi.org/10.1016/j.geomorph.2005.05.015.

Wingham, D., M. Siegert, A. Shepherd, and A. Muir (2006), Rapid discharge connects antarctic subglacial lakes, *Nature*, *440*, 1033–1036.

Wingham, D. J. (1998), Antarctic Elevation Change from 1992 to 1996, *Science*, *282*(5388), 456–458.

Wingham, D. J., D. W. Wallis, and A. Shepherd (2009), Spatial and temporal evolution of Pine Island Glacier thinning, 1995-2006, *Geophysical Research Letters*, *36*(17), doi: 10.1029/2009GL039126, l17501.

Winsborrow, M. C. M., C. D. Clark, and C. R. Stokes (2010), What controls the location of ice streams?, *Earth-Science Reviews*, *103*(1-2), 45–59.

Wise, M. G., J. A. Dowdeswell, M. Jakobsson, and R. D. Larter (2017), Evidence of marine ice-cliff instability in Pine Island Bay from iceberg-keel plough marks, *Nature*, *550*(7677), 506–510.

Wynn, R. B., V. A. I. Huvenne, T. P. Le Bas, B. J. Murton, D. P. Connelly, B. J. Bett, H. A. Ruhl, K. J. Morris, J. Peakall, D. R. Parsons, E. J. Sumner, S. E. Darby, R. M. Dorrell, and J. E. Hunt (2014), Autonomous Underwater Vehicles (AUVs): Their past, present and future contributions to the advancement of marine geoscience, *Marine Geology*, *352*, 451–468, doi: 10.1016/j.margeo.2014.03.012.

Zachos, J., M. Pagani, L. Sloan, E. Thomas, and K. Billups (2001), Trends, rhythms, and aberrations in global climate 65 ma to present, *Science*, *292*(5517), 686–693, doi: 10.1126/science.1059412.

Zwally, H. J., M. B. Giovinetto, M. A. Beckley, and J. L. Saba (2012), Antarctic and greenland drainage systems, *GSFC Cryospheric Sciences Laboratory*.

Appendix A

Bingham *et al.* 2017 (Nature Communications)

nature COMMUNICATIONS

ARTICLE

DOI: 10.1038/s41467-017-01597-y OPEN

Diverse landscapes beneath Pine Island Glacier influence ice flow

Robert G. Bingham[1], David G. Vaughan[2], Edward C. King[2], Damon Davies[1], Stephen L. Cornford[3], Andrew M. Smith[2], Robert J. Arthern[2], Alex M. Brisbourne[2], Jan De Rydt[2], Alastair G.C. Graham[4], Matteo Spagnolo[5,6], Oliver J. Marsh[7] & David E. Shean[8]

The retreating Pine Island Glacier (PIG), West Antarctica, presently contributes ~5–10% of global sea-level rise. PIG's retreat rate has increased in recent decades with associated thinning migrating upstream into tributaries feeding the main glacier trunk. To project future change requires modelling that includes robust parameterisation of basal traction, the resistance to ice flow at the bed. However, most ice-sheet models estimate basal traction from satellite-derived surface velocity, without a priori knowledge of the key processes from which it is derived, namely friction at the ice-bed interface and form drag, and the resistance to ice flow that arises as ice deforms to negotiate bed topography. Here, we present high-resolution maps, acquired using ice-penetrating radar, of the bed topography across parts of PIG. Contrary to lower-resolution data currently used for ice-sheet models, these data show a contrasting topography across the ice-bed interface. We show that these diverse subglacial landscapes have an impact on ice flow, and present a challenge for modelling ice-sheet evolution and projecting global sea-level rise from ice-sheet loss.

[1] School of GeoSciences, University of Edinburgh, Edinburgh, EH8 9XP, UK. [2] British Antarctic Survey, Cambridge, CB3 0ET, UK. [3] Department of Geography, College of Science, Swansea University, Swansea, SA2 8PP, UK. [4] College of Life and Environmental Sciences, University of Exeter, Exeter, EX4 4RJ, UK. [5] School of Geosciences, University of Aberdeen, Aberdeen, AB24 3UF, UK. [6] Department of Earth and Planetary Science, University of California, Berkeley, CA 94720-4767, USA. [7] Gateway Antarctica, University of Canterbury, Christchurch 8140, New Zealand. [8] Applied Physics Laboratory, University of Washington, Seattle, WA 98105-6698, USA. Correspondence and requests for materials should be addressed to R.G.B. (email: r.bingham@ed.ac.uk)

Over 40 years of satellite observations, the West Antarctic Ice Sheet (WAIS) has consistently lost ice and contributed up to a 10th of the observed rise in global sea levels[1–6]. The potential for this contribution to accelerate further as a consequence of the ice sheet's dynamical instability[7, 8] poses a threat to the long-term security and prosperity of the planet's coastal populations and infrastructure[1]. However, despite advances in Earth-system modelling to constrain future change, recent projections of the Antarctic Ice Sheet's future global sea-level contribution still have a significant uncertainty[9, 10]. One of the greatest sources of this uncertainty is the parameterisation of basal boundary conditions in the ice-sheet models used for projection[11, 12]. This is most acute for the fast-flowing ice streams that discharge >90% of ice from Antarctica. A particular challenge for these models is the simulation of the basal traction generated by ice flow over its bed, which is the primary restraint on ice flow[11–15]. Few observational data exist beneath Antarctic ice streams at the sub-km scale required to parameterise this complex, but crucial, interaction.

Here, we present high-resolution images of the topography underlying West Antarctica's Pine Island Glacier (PIG; Fig. 1). This glacier has undergone sustained retreat since at least the 1940s[16], with thinning having propagated progressively upstream from the floating ice shelf, along the main trunk and into its tributaries over the interior basin[6]. Several modelling studies have projected that the retreat and progressive upstream thinning of PIG will continue in the coming decades, potentially increasing its contributions to global sea-level rise[7, 17–20]. However, the magnitude and rate of the projected contribution critically depend on the pace at which the retreat may propagate into the interior basin, which is largely controlled by the poorly constrained basal boundary conditions[12, 14, 17, 21].

Our results reveal that PIG is underlain by a diverse landscape, and that the roughness of the landscape at the short wavelengths revealed by our observations impacts directly upon the ice flow. This demonstrates the predominance of form drag on ice flow, which presents a challenge for modelling the future retreat of the ice and, in turn, projecting global sea-level rise from ice-sheet loss.

Results

High-resolution images of Pine Island Glacier bed. Our data comprise the first set of radar surveys that captures sub-kilometre-scale basal topography across an Antarctic glacial catchment, with a total coverage of ~1500 km^2, or ~15%, of PIG's main trunk and tributaries (defined as surface ice flow >200 m a^{-1}). The data, obtained by 1–3 MHz over-snow radar during three austral field seasons (2007/08, 2010/11 and 2013/14), were typically acquired in 10 × 15-km patches. The data comprise a total of nine patches imaged at 40 m (cross-flow) × 100 m (along-flow) grid resolution (Fig. 1d–l) and, as a complete set, constitute by far the largest and most spatially detailed observational data set of a contemporary subglacial landscape ever acquired. Full details of the radar data acquisition and processing, and generation of these images, are given in the Methods.

The data reveal diverse subglacial environments across PIG that contrast with the smooth interpolated bed from prior airborne radar surveys (Fig. 2), and which has been used to define the boundary condition in most ice-sheet modelling of the last decade[20, 22–24]. All but one of the sites displays lineated bedforms aligned with the current ice flow, which are typical of features found on palaeo-ice-stream beds[25–30](Fig. 2). The exception is in the inter-tributary slow-flowing area (Fig. 1k), where no streamlined topography is seen. Broadly, these observations confirm previous assertions that the pattern of PIG's ice-flow configuration has not changed significantly for thousands of years, despite variations in ice discharge[22, 31]. Between the different patches, however, the character and dimensions of the lineations vary (Table 1). Beneath the main trunk, subglacial lineations have vertical heights of ~2–10 m (measured trough-to-crest) and typical widths of 2–400 m redolent of 'Mega-Scale Glacial Lineations' (MSGL) moulded into subglacial sediments[25–28] (Figs. 1c, d, f, g and 2b, c; Table 1). Beneath the southern tributaries, much larger lineated bedforms are present, with vertical heights of ~25–80 m and widths of 300–1000 m (Fig. 1j, l; Table 1). In some locations, the smaller lineations are superimposed over larger basal features, for instance in the main trunk where an ~5-km-wide, ~400-m-high subglacial protuberance projects upwards from an otherwise flat bed (Fig. 1e) and in the southeastern tributary t5 where ~1-km-wavelength MSGL are superimposed over, and sometimes oblique to, a set of along-flow lineations with an ~5-km spacing (Fig. 1g).

The observed heterogeneity in sub-kilometre subglacial topography likely results from a combination of glacial activity and the inherited underlying geology. Seismic surveys have revealed that soft, deformed subglacial sediments are ubiquitous beneath the ice in all of our surveyed regions[32, 33], regardless of the amplitude of the radar-imaged subglacial features. The vertically subtle MSGL present in most of our patches have dimensions consistent with MSGLs from other settings that have been interpreted as the topographic expression of ice flow over deformable beds[27, 30, 34, 35] (Fig. 2). The larger features in the subglacial landscape, such as the ~400-m-high protuberance within the central trunk (Fig. 1e), the >300-m cliff which basal ice overrides in one southern tributary (Fig. 1j) and the >100-m-high ridges that are seen within both southern tributaries (Fig. 1j, l), all have amplitudes far exceeding those of MSGL recorded from any deglaciated setting[30], and probably express components of the underlying geology, draped by deforming sediments a few 10 s of metres thick[33]. PIG's trunk is bounded to the south by gravity anomalies indicative of a thicker crust, often associated with a harder subglacial bedrock[36], and one explanation for the rougher basal topography observed in PIG's southern tributaries (Fig. 1h–j) is that the substrate here is substantially tougher to erode and the subglacial landscape is less mature.

Implications for ice-sheet modelling projections. The magnitude of ice flow through much of PIG dictates that the major component must result from basal motion, being a combination of sliding of ice over its bed, and deformation of the uppermost layers of that bed[37]. Under such conditions, the resistive force exerted by the bed on the overlying ice sheet involves two processes: basal friction at the ice/bed interface and/or in a layer of deforming basal sediments[38]; and form drag, the resistance to ice flow as ice deforms across and around basal obstacles[39]. A fully three-dimensional ice-sheet model might naturally simulate form drag arising from basal features longer than its horizontal resolution, but cannot be expected to simulate form drag not represented in the subglacial topographic model on which it rests nor, indeed, due to features of wavelengths shorter than it can resolve. Since neither basal friction nor form drag can currently be predicted from observable parameters, most models are initialised by an inversion which yields a field of basal traction (a.k.a. slipperiness) that allows the model to match the observed ice-surface velocity and/or elevation changes[11–15, 24, 37]. It is clear that the short-wavelength bed roughness shown in our data can explain much of the variability in the traction coefficient (β in Fig. 1d–l; Table 1) derived by the initialisation inversion in one model[37] (Fig. 3a). Given that seismic data indicate broadly similar

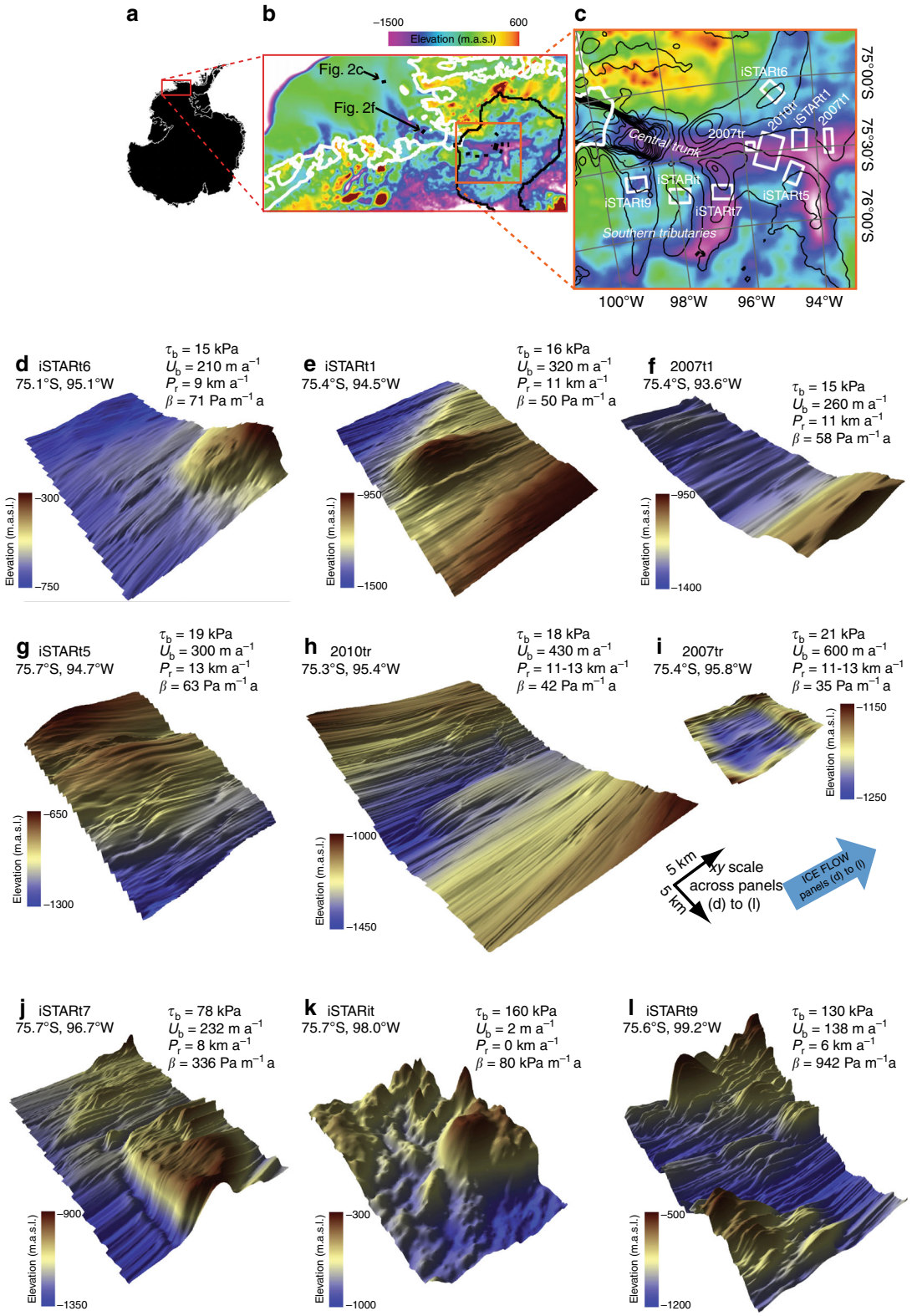

Fig. 1 High-resolution images of the bed across Pine Island Glacier. **a** Location and context. In **b**, the colourmap shows regional bed topography from Bedmap2[23], the black line is the ice divide, the white line is the grounding line[51], and high-resolution survey patches are shown as black rectangles. Locations of offshore bathymetry shown in Fig. 2c, f are marked. **c** uses the same schema but demarcating survey patches with white rectangles, labelled by season of data acquisition (2007/08, 2010/11 and 'iSTAR' = 2013/14) and an end label denoting the location (where 'tr' = trunk; 'it' = intertributary and 't1, t5…' denotes tributaries numbered after ref. [52]. Surface ice velocities[53] contoured at 100-m intervals are also shown. **d**–**l** Perspective views of the bed beneath Pine Island Glacier, together with parameters of ice flow. Vertical exaggeration in all images = 10. τ_b and U_b are the mean basal shear stress (kPa) and mean basal ice velocity (m a^{-1}) from model inversion[37]; P_r is the measured upstream propagation rate of ice thinning per ice-stream tributary from 1992 to 2015 using a thinning/non-thinning threshold of 1.0 m a^{-1} [6] and β is the inverted basal traction coefficient equal to τ_b/U_b

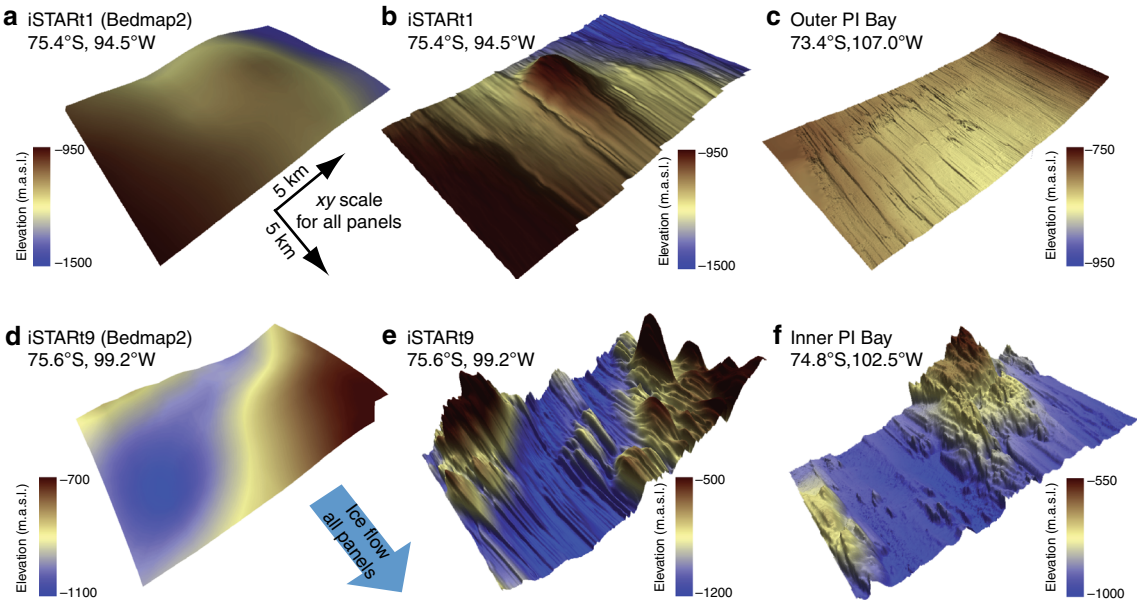

Fig. 2 Comparison of surveyed beds beneath Pine Island Glacier with those used in ice-sheet modelling and imaged in selected palaeo-ice-streams. **a** Bed topography at site iSTARt1 (location in Fig. 1) from previous knowledge[23]. **b** New bed topography (alternative perspective view to Fig. 1e). **c** Analogous subsample of bed topography from outer Pine Island Bay imaged from data presented in ref. [27]; patch location marked on Fig. 1b. **d** Bed topography at site iSTARt9 (location in Fig. 1) from previous knowledge[23]. **e** New bed topography (alternative perspective view to Fig. 1l). **f** Analogous subsample of bed topography from inner Pine Island Bay imaged from data presented in ref. [29]; patch location marked in Fig. 1b

properties in subglacial sediments across the PIG catchment[32, 33], we conclude that much of the variability in the basal traction must be related to unresolved bed topography.

Discussion

Many state-of-the-art Antarctic ice-sheet models use the 'Bedmap2' basal topography[23] or derivations thereof[40]. This topography was derived from unevenly distributed ice-bed elevation measurements spaced between tracks by many ice thicknesses, and interpolated onto a regular 5-km grid and, although supplied at 1-km resolution, only 17% of 5-km cells in Bedmap2 contained measurements[23]. Thus, Bedmap2 contains limited information on bed roughness, even for length scales >10 times the ice thickness. Our data thus show that significant, and potentially influential, bed topography occurs throughout PIG (and presumably other ice streams) on length scales of ~5–50% of the ice thickness.

The issue of the degree to which basal traction arises from friction or form drag becomes more significant when models are used for projection. To achieve projections, most models are run from the initialised condition with an unchanging field of traction coefficient varying according to a heuristic parameterisation of bed rheology, ranging from linear viscous to plastic. The choice of this parameterisation has a substantial impact on the timing and magnitude of ice loss[12]. However, while basal friction is likely to be a highly dynamic field, evolving as water melts, flows and refreezes, and subglacial till is mobilised and refrozen[41], form drag is likely to be considerably more static, defined primarily by the size and orientation of bedrock undulations and protuberances. Recent changes in PIG already indicate the potential importance of this factor, in as much as satellite data have shown that the rate of upstream propagation of ice thinning on PIG varies considerably between the tributaries, the southerly tributaries with rough beds showing 2–3 times slower propagation than the smoother tributaries[6] (Table 1; Fig. 3b). In summary, the new data show that the basal traction (hence ice flow) of Pine Island Glacier is much more heavily influenced by form drag, i.e., as opposed to basal friction, than has previously been shown to be the case.

Our data provide insight into the topographic diversity that exists even within one subglacial basin, let alone the entire ice sheet, which cannot adequately be represented in ice-sheet models. Given that the basal boundary is already identified as a major source of uncertainty in model projections[17, 21], they expose an urgent need to develop techniques for efficient measurement or more intelligent indirect estimation of short-wavelength subglacial topography beneath other vulnerable ice streams. One prospect for recovering short-wavelength subglacial topography may be provided by airborne swath–radar techniques that are currently under development[42]. Until such independent evaluation of form drag and basal friction is integrated into models, the current generation of ice-sheet models will be hampered in establishing projections of ice loss and sea-level rise. As an immediate step, the new data now make it possible to run data-informed experiments to develop adequate parameterisations of short-wave form drag on large outlet glaciers and ice streams, and in doing so expand our theoretical knowledge of its effects on ice flow, building upon existing idealised treatments[43, 44].

The issues that we highlight will be particularly acute in PIG's neighbour, Thwaites Glacier, which holds the potential for rapid and irreversible retreat, and a considerable contribution to sea-level rise[8]. Thwaites Glacier's lower reaches appear to exhibit a similarly high basal traction to the roughest of our patches[11, 37], and may thus contain a similarly dramatic basal topography, but apparently already show a more rapid inland propagation of thinning than even the smoothest tributaries on PIG[6]. Here, the significance of the interplays between basal topography, which may be sufficient to pause the retreat of the grounding line, and the static and dynamic contributions to basal traction, have yet to be explored.

Table 1 Parameters pertaining to ice flow and basal topography across each survey patch

	Mean basal shear stress (τ_b)/kPa	Mean basal ice velocity (U_b)/m a^{-1}	Measured upstream propagation of thinning (P_r)/km a^{-1}	Inverted basal traction coefficient (β)	Dominant vertical height of topography/m	Typical width of streamlined features/m	Normalised across-flow roughness using a 2-km moving window	Normalised along-flow roughness using a 2-km moving window
iSTARt6	15	210	9	71	2–6	450–550	0.08 (new)0.10 (BM2)	0.001 (new)0.04 (BM2)
iSTARt1	16	320	11	50	2–3	100–300	0.77 (new)0.24 (BM2)	0.72 (new)0.04 (BM2)
2007t1	15	260	11	58	2–6	200–400	0.28 (new)0.09 (BM2)	0.04 (new)0.002 (BM2)
iSTARt5	19	300	13	63	3–6 (MSGL) 100 (larger features)	500–800 (MSGL) 5000 (larger features)	0.43 (new)0.24 (BM2)	0.07 (new)0.16 (BM2)
2010tr	18	430	12	42	5–10	300–400	0.18 (new)0.14 (BM2)	0.07 (new)0.08 (BM2)
2007tr	21	600	12	35	2–6	200–300	0.05 (new)0.08 (BM2)	0.04 (new)0 (BM2)
iSTARt7	78	232	8	336	5–10 (MSGL) 25–50(larger features)	300–500 (MSGL) 700–900 (larger features)	0.13 (new/upstream) 0.27 (new/downstream)0.22 (BM2)	0.02 (new)0.05 (BM2)
iSTARit	160	2	0	80,000	n/a	n/a	0.59 (new)0.17 (BM2)	0.90 (new)0.21 (BM2)
iSTARt9	130	138	6	942	5–12 (MSGL) 50–80 (larger features)	300–600 (MSGL) 600–1000 (larger features)	1 (new) 0.22 (BM2)	0.67 (new)0.12 (BM2)

FFT fast Fourier transform
τ_b and U_b are the mean basal shear stress (kPa) and mean basal ice velocity (m a^{-1}) from model inversion[37]; P_r is the measured upstream propagation rate of ice thinning per ice-stream tributary from 1992 to 2015 using a thinning/non-thinning threshold of 1.0 m a^{-1} [6] and β is the inverted basal traction coefficient equal to τ_b/U_b. Columns 6 and 7, respectively, list the dominant vertical heights (measured trough-to-crest) and typical widths of streamlined features; in the cases of patches iSTARt5, iSTARt7 and iSTARt9, two sets are listed, where the smaller values pertain to likely MSGL and the larger values pertain to the longer-wavelength lineations over which the MSGL are superimposed. Most lineations continue beyond the patch boundaries rendering us unable to provide typical lengths. Columns 8 and 9 list normalised FFT-derived roughness values retrieved from profiles taken across and along flow, respectively, using 2-km moving windows—see Methods summary for more details. For iSTARt7, two across-flow profiles were measured, one across the relatively flat upstream region and one across the higher elevation, rougher downstream portion

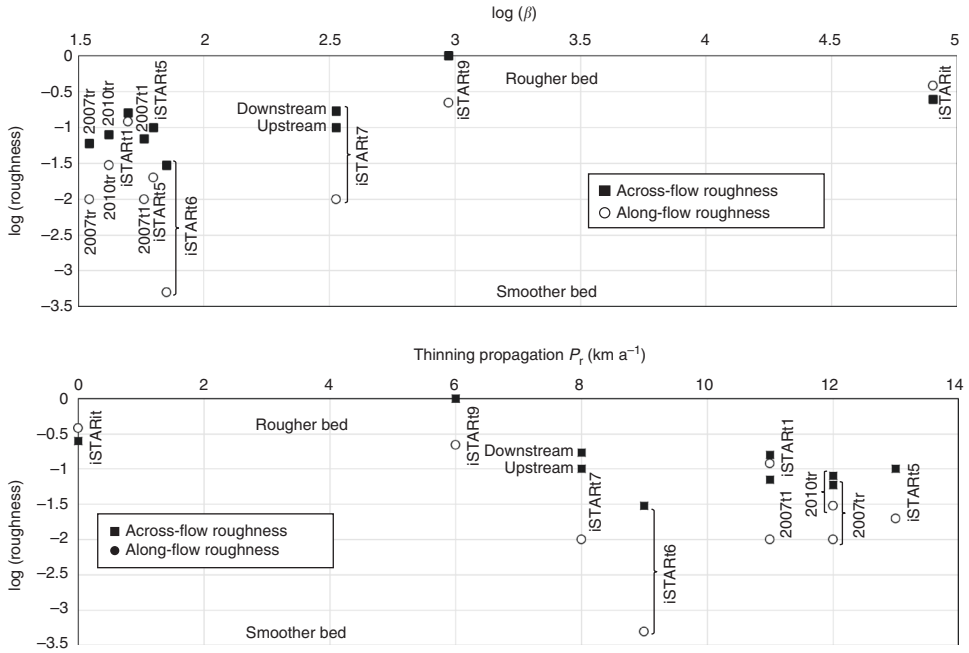

Fig. 3 Influence of bed roughness on inverted basal traction and inland propagation of ice-stream thinning. Table 1 caption describes the derivation of basal traction β and inland propagation of thinning P_r. Basal roughness has been measured across and along flow at each patch in 2-km moving windows. In all cases except site iSTARit, the along-flow profiles are smoother than across-flow profiles, as expected in locations of streamlining

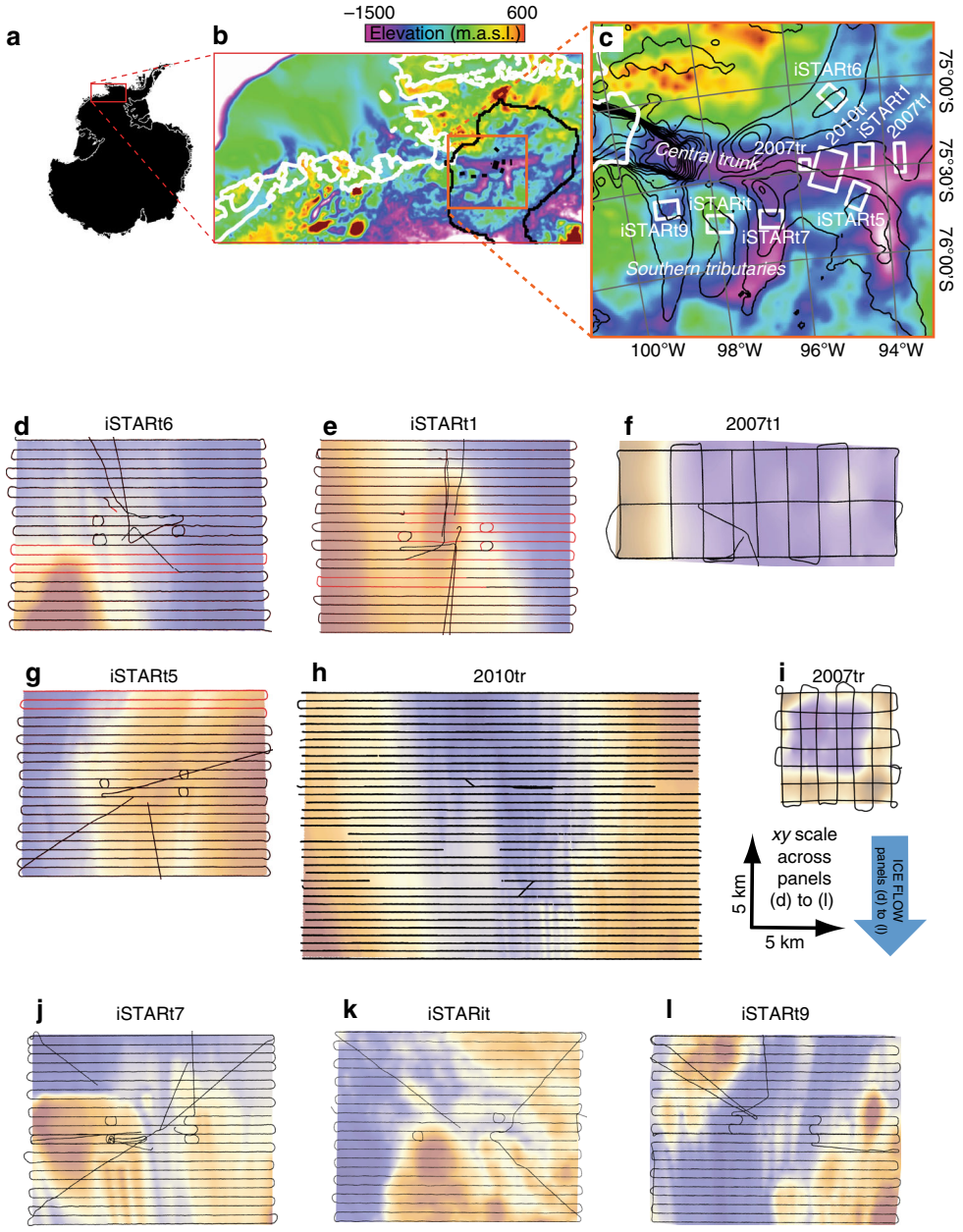

Fig. 4 Radar coverage. **a** Location and context. In **b**, the colourmap shows regional bed topography from Bedmap2[23], the black line is the ice divide, the white line is the grounding line[51] and high-resolution survey patches are shown as black rectangles. Locations of offshore bathymetry shown in Fig. 2c, f are marked. **c** uses the same schema but demarcating survey patches with white rectangles, labelled by season of data acquisition (2007/08, 2010/11 and 'iSTAR' = 2013/14) and an end label denoting the location (where 'tr' = trunk; 'it' = intertributary and 't1, t5...' denote tributaries numbered after ref. [52]. Also shown are surface ice velocities[53] contoured at 100-m intervals. **d**–**l** Plan views of each radar-survey patch across PIG. The colourmap shows bed elevation (scales in Fig. 1). Black lines depict radar tracks with dual-frequency GPS navigation. Red lines in **d**, **e**, **g** depict traverses where the dual-frequency GPS failed and navigation was recovered as described in the Methods summary

Methods

Radar data acquisition. All the radar data were collected with British Antarctic Survey DEep-LOoking Radio Echo Sounder (DELORES) monopulse radars towed by snowmobiles operated at a constant speed of $12 \pm 2\,km\,h^{-1}$. Each system has a transmitter that fires a ±2500-V pulse into resistively loaded dipole antennae at a firing rate between 1 and 5 kHz, and a receiver that registers the returned signals at identical dipole antennae and records them on a ruggedised computer equipped with oscilloscope software. A dual-frequency GPS was used to record the *x*, *y*, *z* coordinates of the centre point between the transmitter and receiver; from 2010, an additional single-frequency GPS was integrated into the system to collect duplicate *x*, *y*, *z* information primarily to facilitate rapid field quality control checks and also to store back-up navigation in the event of dual-frequency GPS failure.

Data from 2007/08 were acquired with 40-m half-dipole antennae, giving a centre frequency of ~1 MHz, and the transmitter was fired at a pulse-repetition rate of 3 kHz. Data from 2010/11 and 2013/14 were acquired with 20-m half-dipole antennae, giving a centre frequency of ~3 MHz, with the transmitter fired at 1-kHz repetition rate. In all years, however, multiple radar returns were first stacked in the oscilloscope buffer to reduce the signal-to-noise ratio, so that each trace of the final record was built up of the data acquired over an along-track distance of ~4–6 m.

The digital oscilloscope used in 2007/8 and 2010/11 had a sampling rate of 100 MHz, giving a time resolution of 10 ns, equivalent to 1.68-m vertical resolution on ice. The sample rate in 2013/14 was 250 MHz, giving a 4-ns time resolution equivalent to 0.67-m vertical resolution. The system was therefore capable of detecting a change in ice thickness from trace to trace of <2 m when a high-amplitude bed reflection was present.

Table 2 Radar-track crossover statistics

	Number of crossovers analysed	Mean ice-thickness difference/m	Standard deviation of ice-thickness difference/m	% age of crossovers where along-flow elevation <across-flow elevation
iSTARt6	11	2.1	1.1	100
iSTARt1	36	9.0	7.1	84
2007t1	9	6.1	2.7	89
iSTARt5	22	2.7	2.6	100
2010tr	1	7.2	n/a	n/a
2007tr	30	8.3	3.7	100
iSTARt7	27	3.2	2.8	52
iSTARit	18	8.7	8.2	44
iSTARt9	15	15.2	7.2	80

Crossover locations as depicted in Fig. 4. The largest discrepancies (6–15 m) occur at the patches with greater topographic variability at the crossover locations (iSTARt1, iSTARit and iSTARt9) or acquired in the earlier seasons (2007t1, 2007tr and 2010tr), when the radar oscilloscope had a lower sampling rate as described in the Methods summary. In all cases except the non-streamlined intertributary patch iSTARit, the majority of ice-thickness measurements acquired when driving orthogonal to flow exceeded those acquired when driving along flow. This is an expected result over streamlined topography as the radar footprint will capture the flanks of adjacent ridges (e.g., MSGL crests) when driven along tracks paralleling ridges, and will be more pronounced where the amplitude of streamlined topography is greater

For all radar surveys in 2010/11 and 2013/14, the radars were driven along pre-planned lines oriented orthogonal to the ice flow, spaced 500-m apart, following the practice previously applied to surveys on Rutford Ice Stream[34, 45] and Carlson Inlet[46]. In each of the survey 'patches', extra radar profiles acquired at different orientations (usually acquired opportunistically in transit between a camp and starting a new cross-flow radar profile) were used as an additional check for consistency in data acquisition across the patch (Fig. 4; Table 2). The radar surveys acquired in 2007/08 had sparser line spacing (1 km for 2007tr, 3 km for 2007t1) but benefitted from multiple along-flow profiles (Fig. 4).

Before radar processing, the dual-frequency GPS data collected during each survey were processed using the Canadian Spatial Reference System (CSRS) Precise Point Positioning (PPP) service (Canadian Geodetic Survey; https://webapp.geod.nrcan.gc.ca/geod/tools-outils/ppp.php). This is an online service that uses the precise GNSS satellite orbit ephemerides to produce corrected x, y, z coordinates of a constant 'absolute' accuracy. We submitted all data in RINEX format, and processed them in kinematic mode in the International Terrestrial Reference Frame. Each output was provided in WGS84 coordinates, with z values given with respect to the WGS84 ellipsoid.

For a few radar profiles acquired in 2013/14, comprising small proportions of the data collected across three of the survey patches (iSTARt1, iSTARt5 and iSTARt6), dual-frequency GPS files were not collected or were overwritten due to a GPS software malfunction. For the affected radar profiles (marked on Fig. 4), we used x, y coordinates acquired by the single-frequency GPS during the same drive. Cross-checking between dual- and single-frequency GPS-acquired coordinates for all other profiles where both the dual- and single-frequency systems were working showed that the single-frequency GPS-acquired x, y coordinates were broadly comparable with the dual-frequency GPS data and had an accuracy of <1 m (confirming their usability) but that the single-frequency GPS z coordinates had a vertical accuracy of ±10 m (confirming their non-usability). For the affected radar profiles, we therefore recovered z from surface elevation data generated from DigitalGlobe WorldView-1 and WorldView-2 along-track stereo image data[47]. For each of iSTARt1, iSTARt5 and iSTARt6, we first generated two DEMs: one a weighted average of WorldView-generated DEMs from 2010 to 2015 (hence spanning our 2013/14 survey), and the other a 50-m-resolution gridded output of the CSRS-PPP-processed surface elevation data generated from the radar profiles where the dual-frequency GPS had worked (which was the majority of radar profiles for each survey patch). From these two products for each survey patch, which showed a maximum elevation difference of 3 m but usually ~1 m, we generated difference maps from which we recovered z coordinates to fit to the single-frequency x, y coordinates for the affected radar profiles.

Radar data processing. All the radar data were processed using ReflexW software (Sandmeier Geophysical Research). We first assigned positioning information to every recorded radar trace from the CSRS-PPP output (or its substitute data from WorldView DEMs) as described above. We suppressed noise induced by the arrival of the direct wave using an average filter, and then used a band-pass filter to increase the signal-to-noise ratio. The data were then given an amplitude-scaling proportional to the two-way travel time to compensate for spherical spreading of the radar wavefront with depth, and were migrated using the Kirchoff function to reassign energy back to source points. Finally, a further band-pass filter removed processing-induced noise. The data were archived in SEG-Y format.

To pick the ice-bed interface and to generate the DEMs for each radar-survey patch, the SEG-Y files were imported into the Schlumberger Petrel interpretation software suite. The travel times of each reflection from the ice-bed interface were picked on the radar profiles using a semi-automatic picker that followed the onset of the bed-reflection wavelet from trace to trace. In every radar trace collected for this study, the bed-reflection wavelet had a significantly higher reflection amplitude than nearby internal layers and with a negligible signal below, and because the radar-acquisition strategy involved the interpretation of multiple parallel radar tracks, consistency in identifying the bed could be checked profile by profile: for both of these reasons, we are confident that the bed returns could be picked with high precision, and were not affected by the quarter-wavelength criteria that control the resolution between two adjacent reflectors of similar amplitude. The procedure created a raw data set of x, y, t coordinates, where x and y were the coordinates in South Pole stereographic projection, and t was the two-way travel time. We converted t into depth h using a single value of radiowave speed through ice of 0.168 m ns^{-1}, and adding 10 m to correct for propagation of the radiowaves through a layer of firn at the surface, based on prior experience[34, 45]. The elevation values for the bed at each radar trace were then calculated by subtracting h from the surface elevation, giving bed elevations with an estimated vertical precision of ±3 m. We acknowledge that using the single value for radiowave propagation is a standard simplification that neglects possible, but unquantifiable, variability in attenuation at each survey patch, which may arise due to variations in ice temperature or chemistry; however, we argue that making such an assumption is reasonable over the relatively local areas covered by each survey patch. Varying the radiowave speed across a range of 0.167–0.170 m ns^{-1}, a plausible range based on reported values across Antarctica[48, 49], has the effect of varying ice thickness (hence bed elevation) across a range of ~35 m for ice between 1.5 and 2-km thick. This does not have an impact on the essential shapes of the bed topography maps per survey patch, and affects the trough-crest heights of MSGL (Table 1) by <10%. Our use of a single firn correction value is also adopted because we cannot quantify variations in firn properties along each radar track: this is a possible source of error in the absolute values of bed elevation data that we report. However, because our data collection strategy involved acquiring multiple parallel profiles, so that consistency of radar returns between adjacent profiles could be ascertained, we argue that any such firn-derived errors most likely affect adjacent tracks consistently, and therefore do not affect the main findings of our study.

Deriving digital elevation models and bed roughness. To produce the images of the bed for Figs. 1 and 2 of this paper, we interpolated the measured x, y, z bed elevations onto a 40 m (cross-flow) × 100 m (along-flow) grid oriented orthogonal to the profile lines using a natural neighbour algorithm with a 5:1 anisotropy ratio aligned along the ice flow direction. This interpolation scheme preserves the continuity of the features that are elongate in the ice-flow direction while preserving some of the high spatial sampling along the cross-flow radar tracks.

Bed roughness for Table 1 and Fig. 3 was calculated using a forward fast Fourier transform (FFT) technique described in ref. [50]. The code enables the derivation of roughness along 2D tracks using moving windows of predefined length. We applied the code along 2-km moving windows, which are sufficiently long to capture multiple streamlined landforms when applied across flow, yet small enough to capture roughness variability within each of the survey patches.

Data availability. All the data in this paper are available from the lead author by request and will be made available on the NERC/iSTAR GIS site, http://gis.istar.ac.uk/.

Received: 6 April 2017 Accepted: 2 October 2017
Published online: 20 November 2017

References

1. Church, M. A. et al. in *Climate Change 2013: The Physical Science Basis. Contribution of Working Group I to the Fifth Assessment Report of the Intergovernmental Panel on Climate Change* (eds Stocker, T. et al) 1137–1216 (Cambridge University Press, Cambridge, 2013).
2. Mouginot, J., Rignot, E. & Scheuchl, B. Sustained increase in ice discharge from the Amundsen Sea Embayment, West Antarctica, from 1973 to 2013. *Geophys. Res. Lett.* **41**, 1576–1584 (2014).
3. Turner, J. et al. Atmosphere-ocean-ice interactions in the Amundsen Sea Embayment. *Rev. Geophys.* **55**, 235–276 (2017).
4. Rignot, E., Mouginot, J., Morlighem, M. & Seroussi, H. Widespread, rapid grounding line retreat of Pine Island, Thwaites, Smith, and Kohler glaciers, West Antarctica, from 1992 to 2011. *Geophys. Res. Lett.* **41**, 3502–3509 (2014).
5. Christie, F. D. W., Bingham, R. G., Gourmelen, N., Tett, S. F. B. & Muto, A. Four-decade record of pervasive grounding line retreat along the Bellingshausen margin of West Antarctica. *Geophys. Res. Lett.* **43**, 5741–5749 (2016).
6. Konrad, H. et al. Uneven onset and pace of ice-dynamical imbalance in the Amundsen Sea Embayment, West Antarctica. *Geophys. Res. Lett.* **44**, 910–918 (2017).
7. Cornford, S. L. et al. Century-scale simulations of the response of the West Antarctic Ice Sheet to a warming climate. *Cryosphere* **9**, 1579–1600 (2015).
8. Alley, R. B. et al. Oceanic forcing of ice-sheet retreat: West Antarctica and more. *Ann. Rev. Earth Planet. Sci.* **43**, 207–231 (2015).
9. Shepherd, A. et al. A reconciled estimate of ice-sheet mass balance. *Science* **338**, 1183–1189 (2012).
10. Bamber, J. L. & Aspinall, W. P. An expert judgement assessment of future sea level rise from the ice sheets. *Nat. Clim. Change* **3**, 424–427 (2013).
11. Joughin, I. et al. Basal conditions for Pine Island and Thwaites Glaciers, West Antarctica, determined using satellite and airborne data. *J. Glaciol.* **55**, 245–257 (2009).
12. Ritz, C. et al. Potential sea-level rise from Antarctic ice-sheet instability constrained by observations. *Nature* **528**, 115–118 (2015).
13. Morlighem, M. et al. Spatial patterns of basal drag inferred using control methods from a full-Stokes and simpler models for Pine Island Glacier, West Antarctica. *Geophys. Res. Lett.* **37**, L043853 (2010).
14. Durand, G., Gagliardini, O., Favier, L., Zwinger, T. & Le Meur, E. Impact of bedrock description on modeling ice sheet dynamics. *Geophys. Res. Lett.* **38**, L048892 (2011).
15. Pollard, D. & DeConto, R. M. A simple inverse method for the distribution of basal sliding coefficients under ice sheets, applied to Antarctica. *Cryosphere* **6**, 953–971 (2012).
16. Smith, J. A. et al. Sub-ice-shelf sediments record history of twentieth-century retreat of Pine Island Glacier. *Nature* **541**, 77–80 (2017).
17. Nias, I. J., Cornford, S. L. & Payne, A. J. Contrasting the modelled sensitivity of the Amundsen Sea Embayment ice streams. *J. Glaciol.* **62**, 552–562 (2016).
18. Favier, L. et al. Retreat of Pine Island Glacier controlled by marine ice-sheet instability. *Nat. Clim. Change* **4**, 117–121 (2014).
19. Seroussi, H. et al. Sensitivity of the dynamics of Pine Island Glacier, West Antarctica, to climate forcing for the next 50 years. *Cryosphere* **8**, 1699–1710 (2014).
20. Arthern, R. J. & Williams, C. R. The sensitivity of West Antarctica to the submarine melting feedback. *Geophys. Res. Lett.* **44**, 2352–2359 (2017).
21. Gasson, E., DeConto, R. & Pollard, D. Antarctic bedrock topography uncertainty and ice sheet stability. *Geophys. Res. Lett.* **42**, 5372–5377 (2015).
22. Vaughan, D. G. et al. New boundary conditions for the West Antarctic Ice Sheet: subglacial topography beneath Pine Island Glacier. *Geophys. Res. Lett.* **33**, L09501 (2006).
23. Fretwell, P. et al. Bedmap2: improved ice bed, surface and thickness datasets for Antarctica. *Cryosphere* **7**, 375–393 (2013).
24. Pattyn, F. et al. Grounding-line migration in plan-view marine ice-sheet models: results of the ice2sea MISMIP3d intercomparison. *J. Glaciol.* **59**, 410–422 (2013).
25. Clark, C. D. Mega-scale glacial lineations and cross-cutting ice-flow landforms. *Earth Surf. Proc. Land.* **18**, 1–29 (1993).
26. Stokes, C. R. & Clark, C. D. Palaeo-ice streams. *Quat. Sci. Rev.* **20**, 1437–1457 (2001).
27. Jakobsson, M. et al. Ice sheet retreat dynamics inferred from glacial morphology of the central Pine Island Bay Trough, West Antarctica. *Quat. Sci. Rev.* **38**, 1–10 (2012).
28. Livingstone, S. L. et al. Antarctic paleo-ice streams. *Earth Sci. Rev.* **111**, 90–128 (2012).
29. Nitsche, F. O. et al. Paleo ice flow and subglacial meltwater dynamics in Pine Island Bay, West Antarctica. *Cryosphere* **7**, 249–262 (2013).
30. Spagnolo, M. et al. Size, shape and spatial arrangement of mega-scale glacial lineations from a large and diverse dataset. *Earth Surf. Proc. Land.* **39**, 1432–1448 (2014).
31. Karlsson, N. B., Rippin, D. M., Bingham, R. G. & Vaughan, D. G. A 'continuity-index' for assessing ice-sheet dynamics from radar-sounded internal layers. *Earth Planet. Sci. Lett.* **335-6**, 88–94 (2012).
32. Smith, A. M., Jordan, T. A., Ferraccioli, F. & Bingham, R. G. Influence of subglacial conditions on ice stream dynamics: seismic and potential field data from Pine Island Glacier, West Antarctica. *J. Geophys. Res.* **118**, B009582 (2013).
33. Brisbourne, A. M. et al. Bed conditions of Pine Island Glacier, West Antarctica. *J. Geophys. Res.* **122**, 419–433 (2017).
34. King, E. C., Hindmarsh, R. C. A. & Stokes, C. R. Formation of mega-scale glacial lineations observed beneath a West Antarctic ice stream. *Nat. Geosci.* **2**, 585–588 (2009).
35. Spagnolo, M. et al. Ice stream motion facilitated by a shallow-deforming and accreting bed. *Nat. Commun.* **7**, 10723 (2016).
36. Jordan, T. A. et al. Aerogravity evidence for major crustal thinning under the Pine Island Glacier region (West Antarctica). *Geol. Soc. Am. Bull.* **122**, 714–726 (2010).
37. Arthern, R. J., Hindmarsh, R. C. A. & Williams, C. R. Flow speed within the Antarctic ice sheet and its controls inferred from satellite observations. *J. Geophys. Res.* **120**, 1171–1188 (2015).
38. Zoet, L. K. & Iverson, N. R. Experiments on the dynamics and sedimentary products of glacier slip. *Geomorphology* **244**, 121–134 (2015).
39. MacAyeal, D. R. in *Glaciology and Quaternary Geology* (ed. Van der Veen, C. J.) 141–160 (Reidel, Dordrecht, 1987).
40. Rignot, E., Mouginot, J., Morlighem, M., Seroussi, H. & Scheuchl, B. Widespread, rapid grounding line retreat of Pine Island, Thwaites, Smith and Kohler Glaciers, West Antarctica, from 1992 to 2011. *Geophys. Res. Lett.* **41**, 3502–3509 (2014).
41. Christoffersen, P. & Tulaczyk, S. Response of subglacial sediments to basal freeze-on. 1. Theory and comparison to observations beneath the West Antarctic Ice Sheet. *J. Geophys. Res.* **108**, 2222 (2003).
42. Wang, Z. B. et al. Multichannel wideband synthetic aperture radar for ice-sheet remote sensing: development and the first deployment in Antarctica. *IEEE J. Sel. Top. Appl. Earth Observ. Remote Sens.* **9**, 980–993 (2016).
43. Fowler, A. C. A mathematical approach to the theory of glacier sliding. *J. Glaciol.* **23**, 131–141 (1979).
44. Schoof, C. S. Basal perturbations under ice streams: form drag and surface expression. *J. Glaciol.* **48**, 407–416 (2002).
45. King, E. C., Pritchard, H. D. & Smith, A. M. Subglacial landforms beneath Rutford Ice Stream, Antarctica: detailed bed topography from ice-penetrating radar. *Earth Syst. Sci. Data* **8**, 151–158 (2016).
46. King, E. C. Ice stream or not? Radio-echo sounding of Carlson Inlet, West Antarctica. *Cryosphere* **5**, 907–916 (2011).
47. Shean, D. E. et al. An automated, open-source pipeline for mass production of digital elevation models (DEMs) from very-high-resolution commercial stereo satellite imagery. *ISPRS J. Photogramm. Remote Sens.* **116**, 101–117 (2016).
48. Fujita, S., Matsuoka, T., Ishida, T., Matsuoka, K. & Mae, S. in *Physics of Ice Core Records* (ed. Hondoh, T.) 185–212 (Hokkaido University Press, Hokkaido, 2000).
49. Popov, S. et al. Velocity of radio-wave propagation in ice at Vostok station, Antarctica. *J. Glaciol.* **49**, 179–183 (2003).
50. Bingham, R. G. & Siegert, M. J. Radar-derived bed roughness characterization of Institute and Möller Ice Streams, West Antarctica, and comparison with Siple Coast ice streams. *Geophys. Res. Lett.* **34**, L21504 (2007).
51. Bindschadler, R. A. et al. Getting around Antarctica: new high-resolution mappings of the grounded and freely-floating boundaries of the Antarctic ice sheet created for the International Polar Year. *Cryosphere* **5**, 569–588 (2011).
52. Stenoien, M. D. & Bentley, C. R. Pine Island Glacier, Antarctica: a study of the catchment using interferometric synthetic aperture radar measurements and radar altimetry. *J. Geophys. Res.* **105**, 21761–21779 (2000).
53. Rignot, E., Mouginot, J. & Scheuchl, B. Ice flow of the Antarctic Ice Sheet. *Science* **333**, 1427–1430 (2011).

Acknowledgements

This work was supported by funding from the UK Natural Environment Research Council (NERC) iSTAR Programme (Grants NE/J005665 and NE/K011189), NERC grants NE/B502287/1 and NE/J004766/1 and the British Antarctic Survey (BAS) Polar Science for Planet Earth Programme. D.E.S. was supported by a NASA NESSF fellowship (NNX12AN36H). Bathymetric data used for Fig. 2c and f were sourced from the Bolin Centre Database Oden Mapping Data (cruise OSO 0910; http://oden.geo.su.se/oso0910) and NSF/IEDA Marine Geoscience Data System (http://www.marine-geo.org/tools/search/Files.php?data_set_uid=20080) respectively, and we thank the lead authors M. Jakobsson and F.O. Nitsche for their lodging. All fieldwork was supported by the staff at BAS's Rothera Research Station and members of the iSTAR Traverse. In particular, we thank James Wake, Tim Gee, Jonny Yates (2013/14), David Routledge (2010/11) and Feargal Buckley, Chris Griffiths and Julian Scott (2007/08) for their help with data

acquisition. We thank three anonymous referees for thorough and constructive reviews, which improved the final form of the manuscript.

Author contributions

R.G.B. and D.G.V. designed the research and wrote the paper. Data from 2013/14 were acquired by D.D., D.G.V., S.L.C., R.G.B., A.M.S. and J.D.R. Data from 2007/08 to 2010/11 were acquired by R.G.B. and E.C.K., respectively, under research programmes led by A.M.S. All radar data were processed by R.G.B., D.D. and E.C.K.; O.J.M. contributed to processing of radar data from 2007/08; and D.E.S. provided high-resolution surface ice DEMs to calibrate data acquired in 2013/14. All authors contributed ideas and edits to the manuscript.

Additional information

Supplementary Information accompanies this paper at doi:10.1038/s41467-017-01597-y.

Competing interests: The authors declare no competing financial interests.

Reprints and permission information is available online at http://npg.nature.com/reprintsandpermissions/

Publisher's note: Springer Nature remains neutral with regard to jurisdictional claims in published maps and institutional affiliations.

Open Access This article is licensed under a Creative Commons Attribution 4.0 International License, which permits use, sharing, adaptation, distribution and reproduction in any medium or format, as long as you give appropriate credit to the original author(s) and the source, provide a link to the Creative Commons license, and indicate if changes were made. The images or other third party material in this article are included in the article's Creative Commons license, unless indicated otherwise in a credit line to the material. If material is not included in the article's Creative Commons license and your intended use is not permitted by statutory regulation or exceeds the permitted use, you will need to obtain permission directly from the copyright holder. To view a copy of this license, visit http://creativecommons.org/licenses/by/4.0/.

© The Author(s) 2017

Appendix B

Davies *et al.* 2018 (The Cryosphere)

The Cryosphere, 12, 1615–1628, 2018
https://doi.org/10.5194/tc-12-1615-2018
© Author(s) 2018. This work is distributed under
the Creative Commons Attribution 4.0 License.

The Cryosphere Open Access EGU

How dynamic are ice-stream beds?

Damon Davies[1], Robert G. Bingham[1], Edward C. King[2], Andrew M. Smith[2], Alex M. Brisbourne[2], Matteo Spagnolo[3], Alastair G. C. Graham[4], Anna E. Hogg[5], and David G. Vaughan[2]

[1]School of GeoSciences, University of Edinburgh, Edinburgh, EH8 9XP, UK
[2]NERC British Antarctic Survey, Cambridge, CB3 0ET, UK
[3]School of Geosciences, University of Aberdeen, Aberdeen, AB24 3UF, UK
[4]College of Life and Environmental Sciences, University of Exeter, Exeter, EX4 4RJ, UK
[5]Centre for Polar Observation and Modelling, School of Earth and Environment, University of Leeds, Leeds, LS2 9JT, UK

Correspondence: Robert G. Bingham (r.bingham@ed.ac.uk)

Received: 27 September 2017 – Discussion started: 13 October 2017
Revised: 8 March 2018 – Accepted: 12 March 2018 – Published: 4 May 2018

Abstract. Projections of sea-level rise contributions from West Antarctica's dynamically thinning ice streams contain high uncertainty because some of the key processes involved are extremely challenging to observe. An especially poorly observed parameter is sub-decadal stability of ice-stream beds, which may be important for subglacial traction, till continuity and landform development. Only two previous studies have made repeated geophysical measurements of ice-stream beds at the same locations in different years, but both studies were limited in spatial extent. Here, we present the results from repeat radar measurements of the bed of Pine Island Glacier, West Antarctica, conducted 3–6 years apart, along a cumulative ~ 60 km of profiles. Analysis of the correlation of bed picks between repeat surveys shows that 90 % of the bed displays no significant change despite the glacier increasing in speed by up to 40 % over the last decade. We attribute the negligible detection of morphological change at the bed of Pine Island Glacier to the ubiquitous presence of a deforming till layer, wherein sediment transport is in steady state, such that sediment is transported along the basal interface without inducing morphological change to the radar-sounded basal interface. Given the precision of our measurements, the upper limit of subglacial erosion observed here is 500 mm a^{-1}, far exceeding erosion rates reported for glacial settings from proglacial sediment yields, but substantially below subglacial erosion rates of 1.0 m a^{-1} previously reported from repeat geophysical surveys in West Antarctica.

1 Introduction

Glaciological studies over the past three decades have revealed that the West Antarctic Ice Sheet (WAIS) is losing mass at an accelerating rate, raising concerns over its potential future contribution to global sea level (Shepherd et al., 2012; DeConto and Pollard, 2016). Between 2010 and 2013, around 33 % of the ice sheet's net mass loss came from Pine Island Glacier (hereafter PIG), a major ice stream draining to the Amundsen Sea Embayment (McMillan et al., 2014). There, from satellite altimetry observations, mass loss was first expressed at the grounding zone in the mid-1990s, and has now propagated all the way up to the divides (McMillan et al., 2014) by a set of processes broadly termed dynamic thinning (Shepherd et al., 2001; Pritchard et al., 2009). At PIG the dynamic thinning has incorporated an upstream expansion of regions both of accelerating ice (e.g. Scott et al., 2009; Mouginot et al., 2014) and ice-surface lowering (e.g. Konrad et al., 2017), and upstream migration, by several 10s of km, of the grounding line (e.g. Park et al., 2013; Rignot et al., 2014), prompting suggestions that PIG is in runaway retreat (Joughin et al., 2014). However, the detailed processes by which dynamic thinning works, especially upstream from the grounding zone, are not well constrained. Particularly unclear is how the coupling between basal ice and the bed may evolve or vary over time and whether this needs to be accounted for in models projecting future ice response. For example, previous studies have theorised that high subglacial till fluxes can lead to the rapid formation of grounding-zone

wedges, potentially stabilising ice streams against sea-level rise (e.g. Alley et al., 1989, 2003; Alley et al., 2007).

Monitoring the beds of ice streams is also important for understanding processes of erosion and sediment transport that can provide information on landscape evolution (e.g. Jamieson et al., 2010; Herman et al., 2011), basal processes (Cuffey and Alley, 1996; Alley et al., 1997; Alley, 2000) and the supply of nutrients to polar oceans (Raiswell et al., 2006). Furthermore, knowledge of till flux and associated till properties is key to an improved understanding of glacier physics and ice-stream stability (Blankenship et al., 1986; Boulton and Hindmarsh, 1987; Alley, 1989; Jenson et al., 1995; Engelhardt and Kamb, 1998; Truffer et al., 2000; Iverson and Iverson, 2001; Nygård et al., 2007; Damsgaard et al., 201, 2016). A review of previously published erosion rates for hard-bedded glaciers (Hallet et al., 1996) indicates low erosion rates in polar settings ($0.01\,\mathrm{mm\,a^{-1}}$) contrasting with relatively high rates beneath temperate alpine glaciers ($10–100\,\mathrm{mm\,a^{-1}}$). However, more recent studies have identified far more rapid erosion rates of $4.8\,\mathrm{mm\,a^{-1}}$ in Greenland (Cowton et al., 2012) and as much as $1\,\mathrm{m\,a^{-1}}$ or more in soft-bedded glaciers in Alaska (Motyka et al., 2006) and Antarctica (Smith et al., 2007; 2012). Critically, measurements of erosion rates in Antarctica are limited both temporally and spatially, making it difficult to assess whether such high rates of erosion are typical or exceptional.

A significant difficulty in assessing temporal changes to the beds of WAIS ice streams is lack of direct access. Theoretical and geophysical constraints have shown that ice streams typically achieve fast flow by overriding dilated till that provides low basal drag (Alley et al., 1986; Bentley et al., 1998). It has been inferred that even relatively small fluctuations to hydrological conditions in these locations can induce significant changes to basal drag, in the most extreme circumstances causing ice streams to switch on or off (e.g. Anandakrishnan and Alley, 1997; Conway et al., 2002; Vaughan et al., 2008). However, to our knowledge, only two studies have attempted directly to capture temporal changes to ice-stream bed conditions over decadal to sub-decadal timescales commensurate with available satellite records of surface elevation and velocity change. The first was a single-location repeat measurement of ice thickness and surface elevation on PIG (location, Fig. 1) made firstly in 1960 and remeasured in 2009 (Smith et al., 2012). That study found surface lowering with no significant change in ice thickness, suggesting that mean erosion of the ice-stream bed of up to $1\,\mathrm{m\,a^{-1}}$ took place during the study period (Smith et al., 2012). This rate is well above the range reported elsewhere (Hallet et al., 1996). The second, more detailed study, consisted of three repeat seismic surveys of the bed of Rutford Ice Stream (hereafter RIS; Fig. 1c) obtained in 1991, 1997 and 2004 (Smith et al., 2007). There, across a ~ 0.5 km width of the bed, 6 m of sediment were removed from the ice bed between 1991 and 1997 followed by the appearance of a drumlin 10 m high and 100 m wide between 1997 and 2004. Both of the studies from West Antarctica therefore implied that active sediment erosion or deposition at rates $\sim 1–1.4\,\mathrm{m\,a^{-1}}$, and landform evolution, are possible beneath ice streams on decadal to sub-decadal timescales.

In this paper, we present and analyse results from three repeat surveys of the bed of PIG, whereby we geophysically surveyed co-located profiles of PIG's bed in different years along a cumulative ~ 60 km of traverses. Our principal aim was to ascertain whether erosion or deposition, and any morphological changes, were detectable at the bed of PIG over intervals of 3–7 years, periods over which PIG (from satellite monitoring) has undergone considerable ice-surface lowering and ice acceleration (McMillan et al., 2014; Mouginot et al., 2014).

2 Methods

Our data consist of three repeat radar surveys of PIG's bed acquired with a low frequency ice-penetrating radar system in austral seasons 2007/2008 and 2013/2014 (two profiles of 18 and 16 km long separated by ~ 6 years) and 2010/2011 and 2013/2014 (one 25 km profile separated by ~ 3 years) (Fig. 1a, b). The 18 km profile, R1, was acquired 3 km downstream and parallel to an 18 km seismic survey acquired in austral season 2007/2008 (Smith et al., 2013), 5 km of which was resurveyed in austral season 2014/2015 (Brisbourne et al., 2017) (profiles $S1_{2007}$ and $S1_{2014}$ on Fig. 1b respectively). Each of the repeat survey locations on PIG experienced significant ice-surface lowering and acceleration over the encompassing period (Table 1). In our analysis we consider our findings from PIG against the results from Smith et al.'s (2007) repeat seismic surveys of the bed of RIS (profile C1 in Fig. 1c), where ice flow has remained relatively stable over decadal timescales and negligible surface lowering has been observed (Table 1).

2.1 Data acquisition

All radar profiles were acquired with the British Antarctic Survey's "DELORES" (Deep-Look Radio-Echo Sounder) system, a skidoo-towed monopulse array (see King et al., 2016, for general specifications). During the 2007/2008 field season, the system operated using 40 m half-dipole antennae, resulting in a centre frequency of 1.2 MHz. In 2010/2011 and 2013/2014, 20 m half-dipole antennae were used, giving a centre frequency of 3 MHz. Along-track traces were sampled at < 1 m intervals, stacked for noise reduction to produce data points at ~ 5 m spacing, and georeferenced with a dual-frequency differential GPS mounted on the radar system.

The repeat radar surveys on PIG were each acquired approximately orthogonal to ice flow at sites 150, 120 and 115 km upstream from the 2011 grounding line (Park et al., 2013) (R1, R2 and R3 respectively in Fig. 1b), in each case

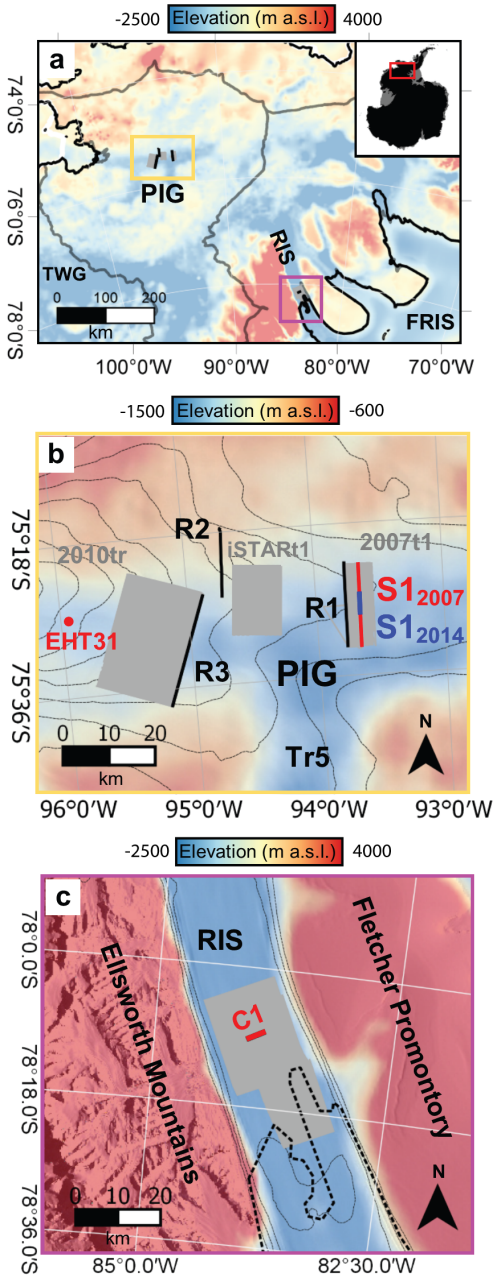

Figure 1. Location maps of the study area. Colour scale shows BEDMAP2 bed elevation (Fretwell et al., 2013). **(a)** Map of the Pine Island Glacier (PIG) and Rutford Ice Stream (RIS) catchments. Grey lines show drainage boundaries (Zwally et al., 2012). **(b)** Location of PIG surveys. Grey contours are 100 m a^{-1} ice surface velocity contours (Rignot et al., 2011). Grey shaded boxes show the locations of radar grid DEMs in Figs. 2a, 3a and 3f, black lines are repeat radar surveys. $S1_{2007}$ is a seismic survey presented in Smith et al. (2013) and $S1_{2014}$ is a section of this profile resurveyed in 2014 (presented in Brisbourne et al., 2017). EHT31 is a single point repeat survey presented in Smith et al. (2012). **(c)** Location of RIS surveys. Thick dashed line represents the MODIS grounding line. Grey contours are 100 m a^{-1} velocity contours (Rignot et al., 2011). Grey shaded box is the area of the radar grid DEM in Fig. 5a.

close to, or forming part of, more extensive radar surveys of patches of the ice bed conducted in the three field seasons (Bingham et al., 2017). Repeat radar profile R1 comprises a traverse ∼ 18 km in length, first surveyed in January 2008 and then again in December 2013. The January 2008 profile also represents the most downstream traverse of a more extensive set of radar profiles used to image a 108 km^2 patch of PIG's bed in January 2008 surrounding the 18 km seismic profile acquired in the same season (patch 2007t1 and seismic profile $S1_{2007}$ in Fig. 1b). Profile R2 is derived from a 16 km traverse first driven in December 2007 and then again in December 2013; this profile lies ∼ 2 km downstream of an extensive survey of 150 km^2 of PIG's bed also surveyed in December 2013 (patch iSTARt1 in Fig. 1b). Profile R3, ∼ 25 km in length, was first surveyed in January 2011 as the upstream profile of multiple transects used to image a 425 km^2 patch of PIG's bed (patch 2010tr in Fig. 1b), and then again in December 2013 to yield a survey gap of ∼ 3 years.

2.2 Data processing

Radar data were processed using ReflexW seismic processing software (Sandmeier Scientific Software). A data processing flow was applied which included a gain function to improve the strength of reflections at greater depth, and bandpass and 2-D median filters to reduce data noise. Finite-difference (FD) migration was used to contract diffraction hyperbolae and to recover the correct locations of individual reflectors. The onset time of the bed reflector was determined at 5 m horizontal intervals at the peak in the amplitude of the bed reflector using a semi-automated "phase follower" picking procedure that allows automatic assignment of picks to a selected phase. These picks were checked and edited using manual picking where necessary. Bed picks were then converted to depth using a radar wave speed of 0.168 m ns^{-1} and no additional firn correction. We smoothed bed picks by applying a moving average over a 50 m window to all bed picks to remove high-frequency noise.

To assess changes at the bed, we focus on comparing the morphological character of the picked bed along repeat profiles rather than deriving changes in absolute bed elevation between surveys. This is for two reasons. Firstly, we do not have the data to assess whether firn properties, that impact upon radar wave speed, changed over the periods between repeat surveys. However we do not expect firn properties to have varied spatially on the scale of our surveys. For this reason we make no firn correction to our derived ice thicknesses. Secondly, differences in the triggering mechanism of the radar system between survey years meant that we could not directly match the onset waveforms between repeat surveys. In both cases, the effects preclude recovery of absolute ice thickness or bed elevation. Therefore we compare relative bed profiles by applying a static correction to a common bed datum (0 m) for both surveys.

Table 1. Mean velocities and surface elevation change for each repeat radar survey profile 2007–2017.

Survey	Velocity ($m\,a^{-1}$) 2007–2009 (MEaSUREs)	Velocity ($m\,a^{-1}$) 2017[a]	Velocity change ($m\,a^{-1}$)	Mean surface elevation change (m)[b]
C1 (RIS)	370	407	37	–
R1 (PIG)	287	361	74	−8.2
R2 (PIG)	384	523	139	−8.0
R3 (PIG)	435	609	174	–

[a] Velocities derived from Sentinel-1 image pairs obtained in April 2017. Details of processing methodology are provided in Hogg et al. (2017). [b] Surface elevation change derived from differential GPS measurements. No GPS data were available for surveys C1 and R3.

The seismic surveys $S1_{2007}$ and $S1_{2014}$ in the vicinity of R1 were processed and analysed by Smith et al. (2013; 2007/2008 profile only) and Brisbourne et al. (2017; both profiles). Brisbourne et al. (2017) primarily report on the calculation of acoustic impedance at the bed from both profiles, which we will consider in our discussion below. For this paper, we also investigated the possibility of directly picking the bed for the repeated 5 km section in an analogous manner to the radar picking described above. However, low signal-noise ratios along large parts of the bed, resulting from the similarity of ice and bed acoustic impedance (Brisbourne et al., 2017), precluded the recovery of results with sufficiently low picking errors to have confidence in identifying any change or lack thereof.

2.3 Errors

For each profile R1–R3, the ability to detect changes in bed morphology is largely determined by the precision with which the bed reflector can be picked, and the degree to which the second radar profile of a repeat survey follows or diverges slightly from the path driven by the first profile.

The signal-to-noise ratio in all our radar profiles is high and the strength of the basal reflector produces a clearly discernible, high-amplitude wavelet (e.g. radargrams in Figs. 2–5) that requires little user interaction during the semi-automatic picking procedure. With such clear data, the uncertainty with which the bed reflection can be picked is determined primarily by the system rise-time of $250\,V\,ns^{-1}$, the recording-system bandwidth of 50 MHz and the digitisation interval of 10 ns. Also, considering the uncertainty in our GPS-derived elevations, we estimate that our radar data have a vertical range precision of ±3 m.

As we are unable to recover absolute elevation change, in this study the horizontal resolution is more important than the vertical range precision. Differences in the morphology of the basal reflector need to be considered along with consideration of the different frequencies used in repeat surveys (1.2 and 3 MHz). This is best illustrated using commonly adopted resolution limits. For a circular wavefront, features at the bed with a width less than $\sqrt{2d\lambda + \frac{\lambda^2}{4}}$ will appear as point diffractors. For a bed at a depth of 2000 m, a 1.2 MHz ($\lambda_{ice} = 250$ m) wavelet will image features with a width < 1008 m and a 3 MHz ($\lambda_{ice} = 100$ m) wavelet will image features with a width < 634 m. These differences may affect the appearance of the basal reflector depending on the roughness of the bed. For these reasons we express caution when considering subtle changes in basal morphology.

Table 2. Analysis of navigational divergence and associated variability in bed elevation.

Repeat survey line	R1	R2	R3
Repeat survey divergence (m)			
Maximum	45.1	54.0	35.0
Mean	23.7	13.7	20.0
Standard deviation	±10.3	±12.0	±8.0

Survey lines were repeated by following a route programmed into a dashboard GPS unit mounted on the radar skidoo. Due to the higher accuracy and precision of the dual-frequency GPS compared to the dashboard units, and the challenges of navigating in featureless terrain, navigational divergences were registered. These divergences were mostly < 50 m (Table 2); however, where bed topography is rough, even small navigational divergences may lead to incorrect interpretation of bed change. In order to visually assess whether navigational divergence affects observed bed change we have provided plots of minimum horizontal distance between repeat surveys alongside bed elevation profiles in Figs. 2 and 3.

3 Results

Bed picks for the repeat geophysical surveys from PIG are shown in Figs. 2 and 3 alongside associated geophysical images. A visual inspection of the radar/seismic images and bed picks (Figs. 2 and 3) shows that there is remarkable consistency in the morphology of the bed at all three of the repeat survey sites. This qualitative impression is confirmed by calculating the Pearson correlation coefficient (r) of each repeat

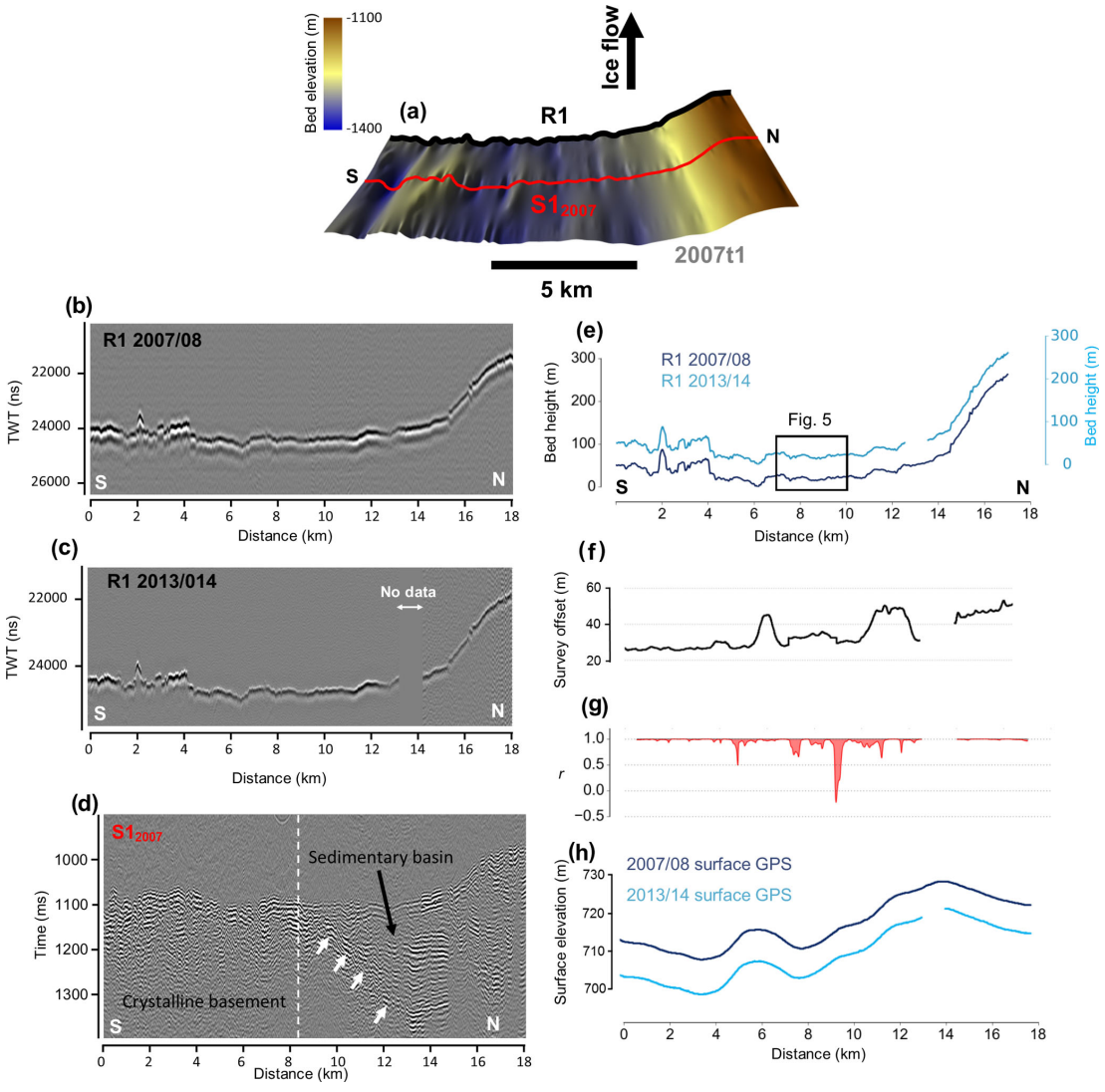

Figure 2. Geophysical data and bed picks from PIG. **(a)** Radar derived DEM from PIG showing the location of radar (black line) and seismic survey (red line). **(b, c)** processed radargrams of repeat radar surveys. **(d)** Processed seismic section of S1 (Smith et al., 2013). White arrows denote a dipping reflector demarcating a sedimentary basin. **(e)** Bed picks from repeat radar survey R1. **(f)** Plot showing the survey divergence between radar profiles in 2007/2008 and 2013/2014. **(g)** Correlation coefficient of repeat bed picks between 2008/2009 and 2013/2014 across a 500 m moving window. **(h)** Plot of surface elevation profiles derived from differential GPS measurements.

profile's bed picks across 500 m moving windows (Figs. 2 and 3). For 90 % of the repeat radar tracks $r > 0.9$, underscoring that there has been negligible morphological change for much of the surveys. For context, we performed the same correlation routine for the bed picks of repeat seismic survey data acquired in 1991, 1997 and 2004 along the 3.5 km profile C1 of RIS previously reported by Smith et al. (2007) (these results are shown in Fig. 4e). At C1, the ~ 0.5 km section of track for which Smith et al. (2007) reported basal erosion between 1991 and 1997 yields $r \sim 0.5$, and the ~ 100 m length of profile interpreted as hosting the growth of a drumlin between 1997 and 2004 returns $r \sim -0.2$.

There is only one location on PIG where r is considerably lower than 0.9; this occurs between 8.5 and 9 km along profile R1 where r spikes around a value of -0.2 (Fig. 2). Closer inspection of this location reveals a subtle change in the morphology of the bed picks between 2007/2008 and 2013/2014 (Fig. 5). At this site two bumps of ~ 1–2 m height in 2007/2008 are replaced in 2013/2014 by a central ridge with two troughs ~ 3 m in depth. However, it is possible that this change is caused by the aforementioned differences in horizontal resolution of the radar systems between surveys. We are therefore cautious to interpret this as a genuine change in bed morphology resulting from erosion and deposition.

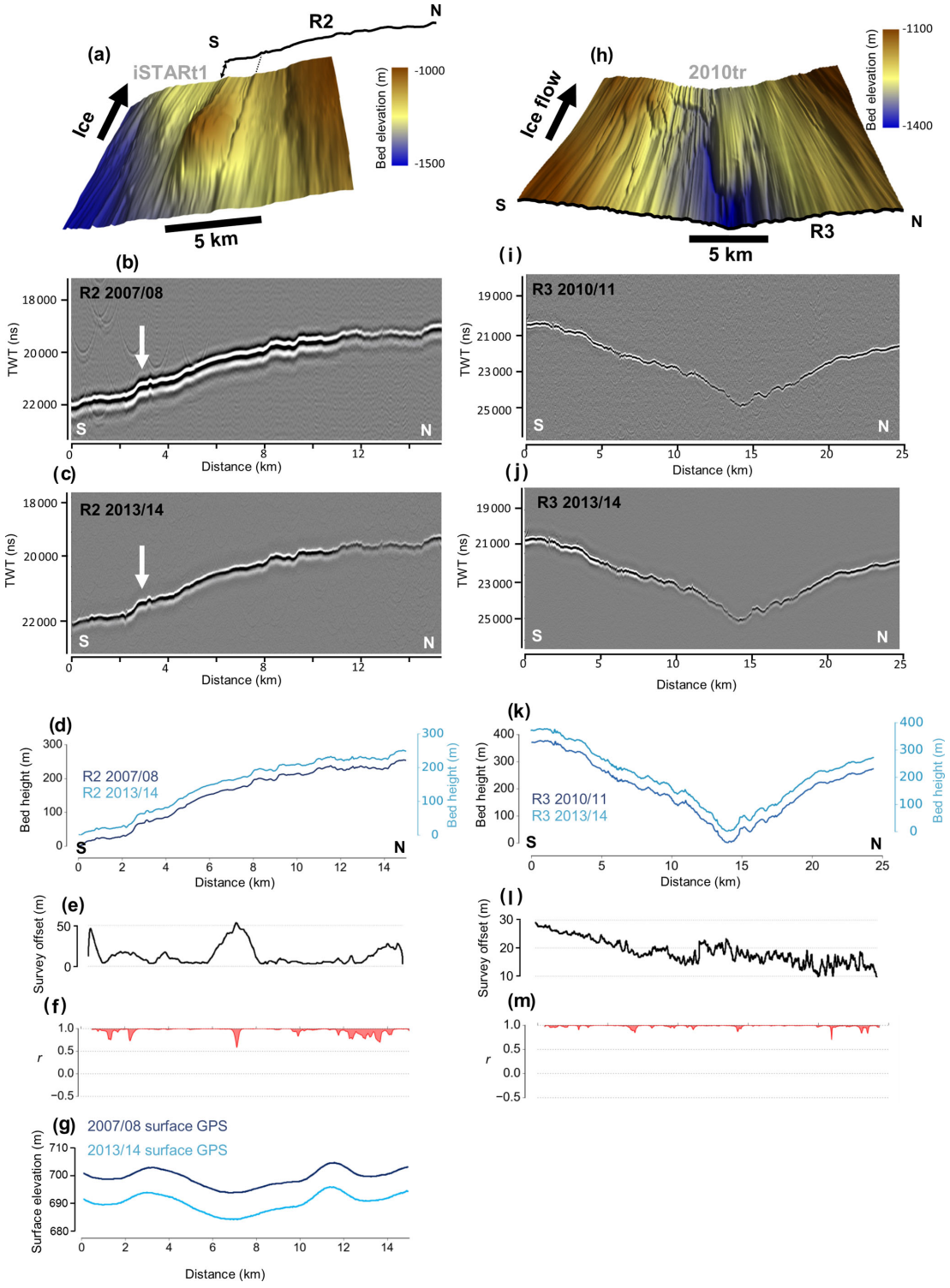

Figure 3. Geophysical data and bed picks from PIG. **(a)** Radar derived bed DEM (Bingham et al., 2017) showing the location of survey R2 2 km downstream. **(b, c)** Processed radargrams of repeat radar surveys. **(d)** Bed picks from repeat radar survey R2. **(e)** Plot showing the survey divergence between radar profiles in 2007/2008 and 2013/2014. **(f)** Correlation coefficient of repeat bed picks between 2008/2009 and 2013/2014 across a 500 m moving window. **(g)** Plot of surface elevation profiles derived from differential GPS measurements. **(h)** Radar derived bed DEM (Bingham et al., 2017) showing the location of survey R3 at the upstream limit of the radar grid. **(i, j)** Processed radargrams of repeat radar surveys. **(k)** Bed picks from repeat radar survey R3. **(l)** Plot showing the survey divergence between radar profiles in 2007/2008 and 2013/2014. **(m)** Correlation coefficient of repeat bed picks between 2010/2011 and 2013/2014 across a 500 m moving window.

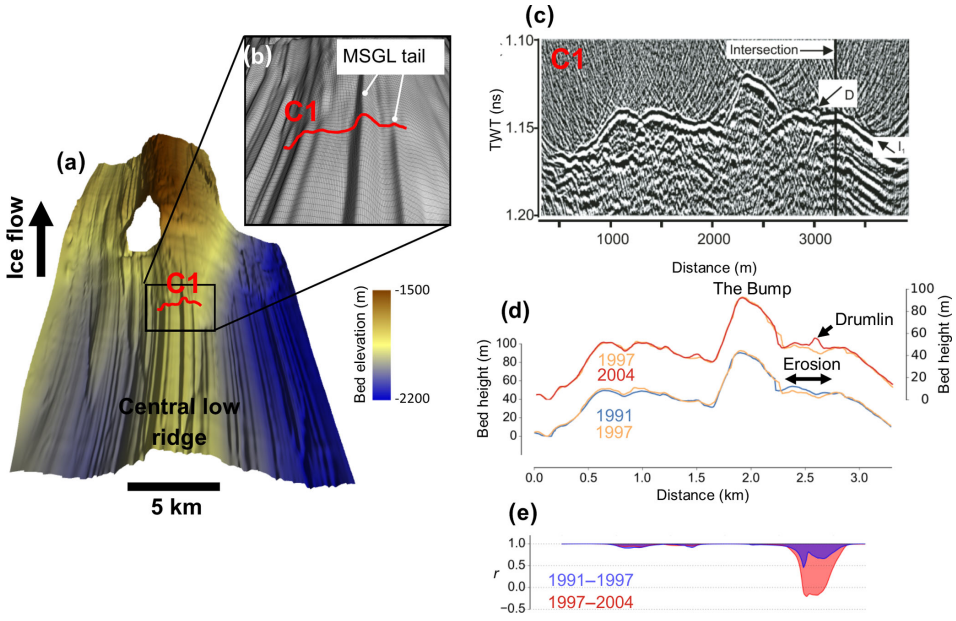

Figure 4. Geophysical data and bed picks from RIS **(a)** Radar derived bed DEM for RIS (King et al., 2016) showing geomorphology of the bed and the location of survey C1. **(b)** Close-up of the location of survey C1 showing the three-dimensional character of the bed. **(c)** Processed seismic section of survey C1. **(d)** Bed picks from repeat seismic surveys showing erosion and drumlin formation between 1991 and 2004 (Smith et al., 2007). **(e)** Correlation coefficient of repeat bed picks between 1991 and 2004 across a 500 m moving window.

4 Discussion

The prevailing picture that emerges from our 58 km of repeat surveys of PIG's bed is one of little measurable change having been effected to the ice stream's basal topography and morphology over the 3–7 year timescale. This is despite significant changes occurring to ice-flow speeds and ice-surface elevations over the same periods (Table 1), and the observations of active erosion and deposition made over similar timescales at RIS (Fig. 4); at RIS ice has experienced little to no dynamic thinning and ice flow is essentially stable (Table 1). In the following discussion we firstly consider how these apparently different behaviours between the ice beds of PIG and RIS can be reconciled (Sect. 4.1). We then turn to the implications of our results for the understanding of processes of sediment erosion, transport and deposition beneath ice streams and implications for future monitoring of the bed (Sect. 4.2).

4.1 Are ice-stream beds dynamic?

The only precedent for the measurements obtained here from PIG in terms of repeat geophysical survey over comparable timescales is that from RIS where erosion and deposition on the order of $\sim 1\,\mathrm{m\,a^{-1}}$ were observed in association with morphological changes at the bed (Smith et al., 2007). Here we assess whether the lack of comparable changes observed at PIG can be explained by contrasting glaciological, hydrological and basal characteristics to the RIS survey site, and whether either is likely to be more representative of wider changes occurring at the beds of Antarctic ice streams.

The first notable difference between PIG and RIS is the broad subglacial topography. Each of the repeat surveys on PIG was conducted across the 30 km-wide, ~ 2000 m deep, main ice-stream trunk where, at the multi-km wavelength, the bed is largely flat along and across flow (Vaughan et al., 2006). By contrast, the repeat survey location on RIS, though also traversing the ice-stream trunk, overlies a notable topographic ridge ("Central low ridge") that abuts ~ 350 m vertically upwards into the central ~ 5 km width of the ~ 30 km-wide, ~ 2000 m deep ice-stream trunk (Fig. 4a). There is, therefore, a clear contrast in the gross topographic shape of the cross-sectional bed profile between the PIG and RIS repeat survey sites; and we note that the flat-bedded trough of PIG is more characteristic of the majority of ice streams in West Antarctica (Fretwell et al., 2013). Turning to the finer, sub-km morphological character of each site, detailed ground-based radar surveys of PIG's trunk (Figs. 2 and 3, and see further imagery in Bingham et al., 2017) have depicted ubiquitous mega-scale glacial lineations (MSGL) across all regions of PIG's trunk, indicative of the widespread presence of deforming sediment (Clark, 1993; Stokes and Clark, 2001; Spagnolo et al., 2016). MSGL with mean amplitudes ~ 10 m and a mode spacing of 300–400 m are also pervasive surrounding the RIS repeat survey site (Fig. 4a) but, unlike PIG, within the MSGL themselves linear features with much higher amplitudes (up to 70 m) are observed; King et al. (2016) termed these features "tapering drumlins".

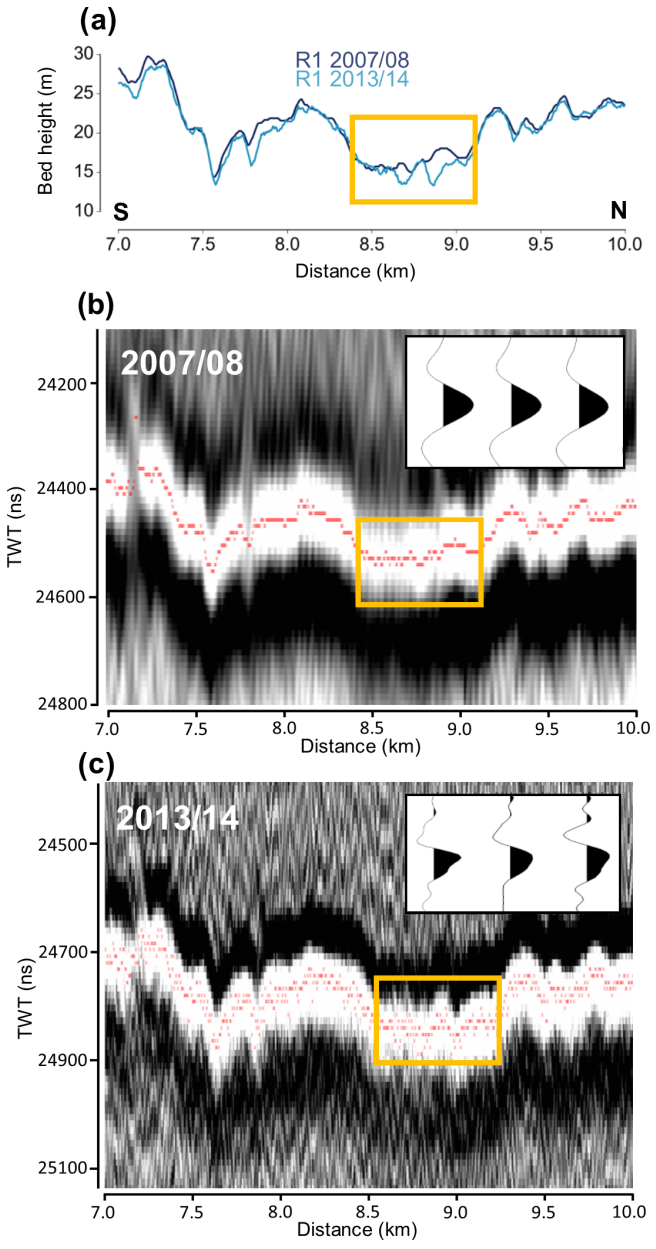

Figure 5. Close-up view of change in bed morphology between 2007/2008 and 2013/2014 identified in survey R1. Yellow boxes outline the area of change identified as having a low correlation ($r = -0.2$). **(a)** Smoothed bed picks from radar data. **(b, c)** Raw bed picks (red dots) of the basal reflector in 2007/2008 and 2013/2014. Inset plots show representative traces sampled from the bed reflector.

The physical properties of the bed between PIG and RIS also differ. Seismic reflection surveying of several sites along PIG's trunk, including upstream and downstream of our repeat survey sites, has confirmed that the bed immediately below the ice pervasively consists of dilated sediments, which are at least several metres thick (Smith et al., 2013; Brisbourne et al., 2017). Along seismic profile $S1_{2007}$ potential-field data indicate that a transition from sedimentary to crystalline bedrock lies beneath the cap of deformable sediments (at position 9 km on Fig. 2d) (Smith et al., 2013), but the repeat survey of S1 in 2014/2015 ($S1_{2014}$) exhibited no change to acoustic impedance anywhere along this profile (Brisbourne et al., 2017), reinforcing the notion of a relatively stable basal environment despite the transition in geology below the deforming till layer. By contrast, the bed around RIS profile site C1 is characterised by a "patchwork" of soft, deforming sediments contrasting with regions of basal sliding indicative of more consolidated sediments (Smith and Murray, 2009; Smith et al., 2015). Notably, the areas of deforming sediment coincide with topographic highs such as the feature known as "The Bump" (Smith, 1997) (Fig. 4c). Changes in acoustic impedance were detected for parts of the RIS repeat profile between 1997 and 2004, and were interpreted as changes in hydrological conditions within subglacial sediments affecting till porosity (Smith et al., 2007).

A third key difference between the PIG and RIS repeat survey sites is the degree to which the survey sites are affected by tidal influences, and the potential effects this can have on subglacial hydrology. High temporal resolution GPS monitoring of ice motion at RIS site C1, 10 km upstream of the grounding line, has shown that horizontal ice velocity varies by $\sim 20\,\%$ on fortnightly timescales in response to tidally modulated vertical displacement of the Filchner–Ronne Ice Shelf (Gudmundsson, 2006, 2007; Murray et al., 2007; Minchew et al., 2017). In addition, passive seismic monitoring has demonstrated increased seismic activity during tidal cycles (Aðalgeirsdóttir et al., 2008). Numerical modelling studies have suggested that the velocity oscillations are transmitted by tidally-forced fluctuations in basal water pressure, that alter the pore pressure of basal sediments and thus effective pressure at the bed (Thompson et al., 2014; Rosier et al., 2015). These observations suggest that the hydrological system beneath the RIS survey site is prone to significant dynamism and reorganisation over short timescales. However, Minchew et al. (2017) suggest that weak shear margins are a more dominant factor in the propagation of tidally induced horizontal ice-flow variability compared to fluctuations in basal water pressure.

High resolution GPS monitoring at several sites along PIG's main trunk showed no tidal signal in ice motion even 55 km upstream from the grounding line (Scott et al., 2009), which lies well downstream of our repeat radar sites R1–R3. The ubiquitous dilated till layer that overlies a relatively flat bed at each of the PIG survey sites provides suitable conditions for a stable, distributed drainage system (Weertman, 1972; Alley, 1989; Engelhardt et al., 1990; Engelhardt and Kamb, 1997) potentially in the form of a canal network as suggested in the upstream catchment of neighbouring Thwaites Glacier (Schroeder et al., 2013), upstream RIS (King et al., 2004) and Whillans Ice Stream (Engelhardt and Kamb, 1997). In the absence of a dynamic hydrological system, sediment mobility facilitated by fluvial transport in sub-

glacial sheets or channels (cf. Weertman, 1972; Walder and Fowler, 1994; Fowler, 2010; Kyrke-Smith and Fowler, 2014) may be restricted and likely be more stable over time, thereby limiting the rate of erosion and sediment transport detectable within the precision of repeat geophysical measurements.

We therefore consider the possibility that rapid erosion and bed reorganisation on the scale observed beneath RIS is an exception rather than the rule. Surface velocity inversions along PIG's main trunk suggest that most of its bed is subjected to low basal shear stress, except for some discrete "ribs" of high basal traction spanning the trunk downstream from our measurements (Sergienko and Hindmarsh, 2013). We suggest therefore that low sediment transport rates might be expected over much of PIG's bed as a consequence of the generally low basal shear stresses at all of our repeat measurement sites, and that future investigation of bed variation needs to be targeted towards an area of high inferred basal traction.

The apparent stability of the bed we observe is also worth considering in the context of debate concerning strain distribution in deforming beds and associated till rheology. The resolution of our data limits the scope of any firm conclusions but may contribute to further discussion on this issue. Field observations and models have argued for viscous (Boulton and Hindmarsh, 1987; Alley et al., 1987; Hindmarsh, 1998) and plastic (Kamb, 1991; Tulaczyk et al., 2000; Iverson, 2010) deformation of subglacial sediments. Subglacial till transport models invoking either viscous or plastic rheology demonstrate that deformation depth increases with effective pressure. Uneven terrains on an ice-stream bed would therefore translate into variable effective pressures and till fluxes, which might facilitate positive feedbacks over bumps and therefore the growth of bedforms (e.g. Hindmarsh, 1998; Fowler, 2000; Schoof, 2007). However, it remains unclear how rapidly bedforms can evolve, as although some studies have suggested rapid growth (Smith et al., 2007; Dowling et al., 2016) these might represent exceptions and a comprehensive analysis is missing. Such pressure-dependent growth will ultimately be controlled by the depth of deformation. It is also unclear whether bedform growth is always limited: they are typically characterised by a relatively well-defined size–frequency distribution, albeit positively skewed (e.g. Fowler et al., 2013; Hillier et al., 2016; Ely et al., 2018). In our study area, one would expect that the uneven terrain of the bed would translate into variable effective pressure and till fluxes and that topography would therefore evolve. The lack of morphological change that we have observed at the ice-stream bed could therefore be interpreted as evidence of very shallow deforming sediment, which might translate to a very low pace of bedform growth, not detectable within the relatively short interval of our repeat surveys. Alternatively, it might indicate that the ice-bed system has reached a point of "maturity" where bedform growth is inhibited by other physical factors. It is even possible that the entire PIG system is now experiencing net erosion due to its recent acceleration,

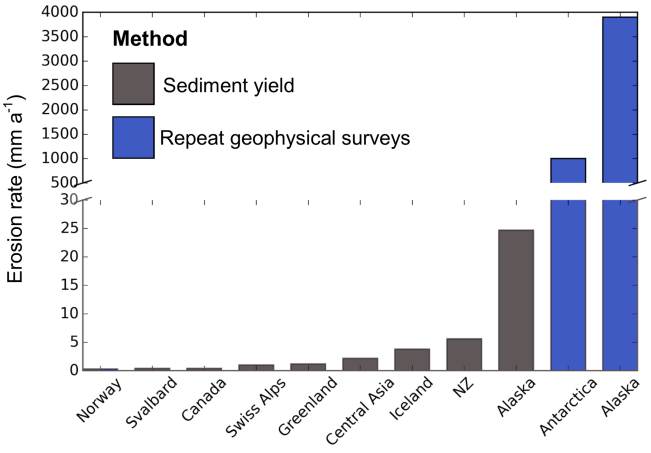

Figure 6. Mean erosion rates from previously published literature in a range of locations. Data taken from Hallet et al. (1996, and references therein), Koppes and Hallet (2006), Motyka et al. (2006), Cowton et al. (2012) and Smith et al. (2007, 2012).

yet the rate of such erosion must be very low for us not to be able to detect a lowering of the topography within the six year interval of our observations.

Geophysical surveys of other West Antarctic ice streams (Alley et al., 1986, Blankenship et al., 1986; Peters et al., 2006) have revealed shallow bed gradients and widespread deforming till similar to the surveyed sites on PIG. These characteristics are also evident in offshore records of palaeo-ice stream beds on the outer continental shelf of West Antarctica, where ice streams occupied shallow troughs in the sedimentary basement (Lowe and Anderson, 2002; Wellner et al., 2006; Larter et al., 2009; Graham et al., 2010). These offshore regions are characterised by ubiquitous MSGL (Spagnolo et al., 2014) that are also observed in the more extensive grid surveys surrounding our repeat surveys (Figs. 2a, 3a, h) (Bingham et al., 2017). The uniformity of these bedforms may reflect stable, self-organised bed conditions (cf. Spagnolo et al., 2017).

4.2 Implications for subglacial sediment transport and future surveys

The absence of detectable morphological change to the bed over the majority of the $\sim$60 km of bed profiles on PIG could be interpreted in three ways: (1) that no sediment erosion/transport/deposition is occurring at the measured sites; (2) that erosion /deposition is occurring but at rates too low to be detected within the vertical range resolution of the radar; or (3) that the subglacial till flux is in a steady state wherein sediment transport is active but is not altering the shape of the bed. The last of these would contradict modelling studies that suggest that pressure-dependent till fluxes dictate that there can be no steady-state till flux on an uneven basal interface (Hindmarsh, 1998; Fowler, 2000; Schoof, 2007).

Prior to this study the few repeat geophysical surveys of the ice-bed interface in Alaska and Antarctica yielded subglacial erosion rates of 1000–3900 mm a^{-1} (Motyka et al., 2006; Smith et al., 2007, 2012), far exceeding the 0.01–100 mm a^{-1} range traditionally reported as characteristic of glacial settings using proglacial sediment yields (Hallet et al., 1996; Koppes and Hallet, 2006; Koppes and Montgomery, 2009; Cowton et al., 2012; Herman et al., 2015) (Fig. 6). Consequently, there has been growing consensus that subglacial erosion and transport is likely to be high, i.e. of the order of m a^{-1}, beneath thick, warm-based ice as manifested by polar ice streams. Observations of substantial till deposition at the grounding lines of contemporary and palaeo-ice streams in the West Antarctic support this view (Anandakrishnan et al., 2007; Batchelor and Dowdeswell, 2015). The precision of our measurements, essentially defined by the vertical range resolution of the radar, means that the maximum possible erosion rate that could go undetected along our profiles is 500 mm a^{-1}.

Aside from the repeat geophysical studies conducted in Antarctica by Smith et al. (2007, 2012), the only other location where this method has been used is southeast Alaska where Motyka et al. (2006) found exceptionally high erosion rates of up to 3.9 ± 0.8 m a^{-1} over a period of 14 years (Fig. 6). However, this setting is unique and these exceptional erosion rates occurred during short episodes of glacier advance over glaciomarine and outwash sediments driven by ice–sediment dynamics (Motyka et al., 2006; Brinkerhoff et al., 2017). Indeed, erosion rates in southern Alaska are the highest reported for any region. These high erosion rates are associated with high precipitation rates, active tectonic uplift and glaciofluvial evacuation of unlithified sediments (Hallet et al., 1996; Motyka et al., 2006). The equally rapid erosion observed by Smith et al. (2007, 2012) therefore evokes a glaciofluvial mechanism. Emerging evidence of subglacial hydrology from West Antarctica shows that meltwater can be stored and released over short timescales through interconnected subglacial lakes and channels (Wingham et al., 2006; Fricker et al., 2007; Fricker and Scambos, 2009; Smith et al., 2017). In our survey area there is no evidence from radar (Bingham et al., 2017) or seismic data (Brisbourne et al., 2017) that indicates the presence of subglacial lakes or concentrated meltwater channels. However, in Smith et al.'s (2012) repeat seismic measurement over ~ 50 years, rapid erosion of 1 m a^{-1} was detected ~ 25 km downstream of survey R3 (EHT31 in Fig. 1b). At this location the bed is also smooth and there is no indication from satellite or geophysical data of rapid meltwater drainage events or channelised meltwater flow (Smith et al., 2012). A possible explanation for the discrepancy between erosion observed at this location and the results of this study is a timescale bias (Ganti et al., 2016). Smith et al.'s (2012) study may have captured intermittent episodes of erosion not captured by our 3–6 year survey intervals.

In Sect. 3, we showed that while the majority of the repeat radar profiles evince negligible morphological change, there is one ~ 0.5 km section of profile R1 where a possible reorganisation of the bed is expressed as a morphological change in the basal reflector (Fig. 5). This region of the bed broadly coincides with a transition from thin (≤ 10 m) sediment overlying a crystalline basement to a deep sedimentary basin imaged in seismic and potential field surveys (Smith et al., 2013). A change in basal drag and ice velocity is also associated with this boundary. It is likely that such boundaries influence subglacial hydrological pathways and, hence, basal ice motion. This exemplifies the importance of the sampling location and periods of measurement to any study attempting to capture subglacial sedimentary processes. For example, the location where Smith et al. (2007) monitored deposition (drumlin formation) on RIS between 1997 and 2004 is positioned at the end of a drumlin tail subsequently imaged in a wider radar survey of the region (King et al., 2009, 2016) (Fig. 4b). These repeat measurements may have been fortuitously timed to capture the extension of the drumlin tail. The anisotropic morphology of tapering drumlins and MSGL present beneath RIS (King et al., 2016) may not lend itself well to the detection of change from 2-D surveys driven orthogonal to ice flow. Dynamic change in these bedforms may be expressed as downstream migration of a propagating sediment front that would be difficult to detect without more extensive and/or higher-density coverage of repeat surveys over longer timescales.

5 Conclusions

We have analysed ~ 60 km of repeat radar surveys acquired from Pine Island Glacier, West Antarctica, between austral seasons 2007/2008 and 2013/2014. The results showed that little morphological change occurred at the bed over this period. The absence of large signals of erosion or deposition contrasts with erosion/deposition measured on nearby Rutford Ice Stream between 1991 and 2004 (Smith et al., 2007), and with inferred erosion of ~ 1 m a^{-1} at Pine Island Glacier over a half century (1960–2009; Smith et al., 2012). We attribute the negligible detection of morphological change at the bed of Pine Island Glacier on the sub-decadal timescale to the ubiquitous presence of a deforming till layer, wherein sediment transport is in steady state such that sediment is transported along the basal interface without inducing measurable vertical displacement to the radar-sounded basal interface. Moreover, none of the survey sites on Pine Island Glacier have experienced short-term variations in ice velocity (Scott et al., 2009) diagnostic of active hydrological systems capable of mobilising sediment (Thompson et al., 2014; Rosier et al., 2015). By comparison, the high subglacial erosion and deposition rates reported from Rutford Ice Stream occurred where the ice is overriding a topographic rise 350 m high, there are sharp contrasts in subglacial sediment proper-

ties, and the subglacial system likely experiences short-term variability influenced by tidal oscillations (Aðalgeirsdóttir et al., 2008; Thompson et al., 2014; Rosier et al., 2015).

The surveys presented in this study have increased the length, by an order or magnitude, of the available records of repeat measurements of Antarctic ice-stream beds. However, these environments remain poorly sampled. The surveys of Pine Island Glacier and Rutford Ice Stream have shown that improved understanding of the dynamism of the ice-sheet bed may best be gained from a multi-method survey approach, involving (1) high-density radar grid surveying to image the subglacial landscape and provide spatial context, (2) seismic survey to discern the physical properties of the basal interface and (3) repeated seismic and/or radar profiles at the same site undertaken over sub-decadal to decadal timescales. Our findings also show the importance of the physical properties of the bed at each site to the sediment erosion and deposition that could be detected, underscoring the requirement to sample sites that, as a whole, capture a representative range of basal conditions. Models of basal drag inverted from satellite-imaged surface properties (e.g. Joughin et al., 2009; Arthern et al., 2015) offer the best opportunities to guide site selection.

Data availability. All the data in this paper are available from the lead author by request and will be made available on the NERC/iSTAR GIS site, http://gis.istar.ac.uk/.

Author contributions. Radar and seismic data from 2007/2008 were acquired by RGB; radar data from 2010/2011 by ECK; radar data from 2013/2014 by DD, RGB, AMS and DGV; and seismic data from 2014/2015 by AMB, AMS and DD. Radar data were processed by DD, RGB and ECK and seismic data by AMB and AMS. Sentinel-1 velocity estimates for each geophysical site were produced by AEH. DD analysed the data and wrote the paper. All authors contributed edits to the final manuscript.

Competing interests. The authors declare that they have no conflict of interest.

Acknowledgements. Damon Davies was supported by the NERC Training Grant NE/K011189/1 awarded to Robert Bingham. All fieldwork was supported by funding from the UK Natural Environment Research Council (NERC) iSTAR Programme Grants NE/J005665 (RGB/ECK/AMS/AMB/DGV) and NE/J005681 (AEH), NERC grants NE/B502287 (ECK/AMS) and NE/J004766 (MS), and the British Antarctic Survey (BAS) *Polar Science for Planet Earth* Programme. Anna E. Hogg was supported by an independent research fellowship (no. 4000112797/15/I-SBo) jointly funded by the European Space Agency, the University of Leeds and the British Antarctic Survey. We would like to thank all members of the iSTAR traverses of Pine Island Glacier for assistance with field data acquisition in 2013/2014 and 2014/2015; Mark Baird, Tim Gee, James Wake and Jonny Yates for field operational support during iSTAR; Feargal Buckley, Chris Griffiths and Julian Scott for field assistance in 2007/2008 and David Routledge for field assistance in 2010/2011. We are especially grateful for the dedicated and professional support of BAS Operations and Logistics without whom this study would not have been possible. Finally we are grateful to Anders Damsgaard and Huw Horgan for their insightful comments in reviewing this work which has led to a much improved manuscript.

Edited by: Chris R. Stokes
Reviewed by: Huw Horgan and Anders Damsgaard

References

Aðalgeirsdóttir, G., Smith, A. M., Murray, T., King, M. A., Makinson, K., Nicholls, K. W., and Behar, A. E.: Tidal influence on Rutford Ice Stream, West Antarctica: observations of surface flow and basal processes from closely spaced GPS and passive seismic stations, J. Glaciol., 54, 715–724, 2008.

Alley, R.: Water-pressure coupling of sliding and bed deformation: I. Water system, J. Glaciol., 35, 108–118, 1989.

Alley, R., Cuffey, K., Evenson, E., Strasser, J., Lawson, D., and Larson, G.: How glaciers entrain and transport basal sediment: physical constraints, Quaternary Sci. Rev., 16, 1017–1038, 1997.

Alley, R. B.: Continuity comes first: recent progress in understanding subglacial deformation, Geol. Soc. SP, 176, 171–179, 2000.

Alley, R. B., Blankenship, D. D., Bentley, C. R. and Rooney, S. T.: Deformation of till beneath ice stream B, West Antarctica, Nature, 322, 57–59, 1986.

Alley, R. B., Blankenship, D. D., Rooney, S. T., and Bentley, C. R.: Till beneath ice stream B: 4. A coupled ice-till flow model, J. Geophys. Res.-Sol.-Ea., 92, 8931–8940, 1987.

Alley, R. B., Blankenship, D. D., Rooney, S. T., and Bentley, C. R.: Sedimentation beneath ice shelves – the view from ice stream, B. Mar. Geol., 85, 101–120, 1989.

Alley, R. B., Lawson, D. E., Larson, G. J., Evenson, E. B., and Baker, G. S.: Stabilizing feedbacks in glacier-bed erosion, Nature, 424, 758–760, 2003.

Alley, R. B., Anandakrishnan, S., Dupont, T. K., Parizek, B. R., and Pollard, D.: Effect of sedimentation on ice-sheet grounding-line stability, Science, 315, 1838–1841, 2007.

Anandakrishnan, S. and Alley, R.: Stagnation of Ice Stream C, West Antarctica by water piracy, Geophys. Res. Lett., 24, 265–268, https://doi.org/10.1029/96GL04016, 1997.

Anandakrishnan, S., Catania, G. A., Alley, R. B., and Horgan, H. J.: Discovery of till deposition at the grounding line of Whillans Ice Stream, Science, 315, 1835–1838, https://doi.org/10.1126/science.1138393, 2007.

Arthern, R. J., Hindmarsh, R. C. A., and Williams, C. R.: Flow speed within the Antarctic ice sheet and its controls inferred from satellite observations, J. Geophys. Res., 120, 1171–1188, 2015.

Batchelor, C. L. and Dowdeswell, J. A.: Ice-sheet grounding-zone wedges (GZWs) on high-latitude continental margins, Mar. Geol., 363, 65–92, https://doi.org/10.1016/j.margeo.2015.02.001, 2015.

Bentley, C., Lord, N., and Liu, C.: Radar reflections reveal a wet bed beneath stagnant Ice Stream. C and a frozen bed beneath ridge BC, West Antarctica, J. Glaciol., 44, 149–156, 1998.

Bingham, R. G., Vaughan, D. G., King, E. C., Davies, D., Cornford, S. L., Smith, A. M., Arthern, R. J., Brisbourne, A. M., De Rydt, J., Graham, A. G. C., Spagnolo, M., Marsh, O. J., and Shean, D. E.: Diverse landscapes beneath Pine Island Glacier influence ice flow, Nat. Commun., 8, 1618, https://doi.org/10.1038/s41467-017-01597-y, 2017.

Blankenship, D. D., Bentley, C. R., Rooney, S. T., and Alley, R. B.: Seismic measurements reveal a saturated porous layer beneath an active Antarctic ice stream, Nature, 322, 54–57, 1986.

Boulton, G. S. and Hindmarsh, R. C. A., Sediment deformation beneath glaciers: rheology and geological consequences, J. Geophys. Res., 92, 9059–9082, 1987.

Brinkerhoff, D., Truffer, M., and Aschwanden, A.: Sediment transport drives tidewater glacier periodicity, Nat. Commun., 8, p. 90, https://doi.org/10.1038/s41467-017-00095-5, 2017.

Brisbourne, A. M., Smith, A. M., Vaughan, D. G., King, E. C., Davies, D., Bingham, R. G., Smith, E. C., Nias, I. J., and Rosier, S. H. R.: Bed conditions of Pine Island Glacier, West Antarctica, J. Geophys. Res.-Earth, 122, 419–433, https://doi.org/10.1002/2016JF004033, 2017.

Clark, C. D.: Mega-scale glacial lineations and cross-cutting ice-flow landforms, Earth Surf. Proc. Land., 18, 1–29, https://doi.org/10.1002/esp.3290180102, 1993.

Conway, H., Catania, G., Raymond, C. F., Gades, A. M., Scambos, T. A., and Engelhardt, H.: Switch of flow direction in an Antarctic ice stream, Nature, 419, 465–467, 2002.

Cowton, T., Nienow, P., Bartholomew, I., Sole, A., and Mair, D.: Rapid erosion beneath the Greenland ice sheet, Geology, 40, 343–346, 2012.

Cuffey, K. and Alley, R. B.: Is erosion by deforming subglacial sediments significant? (Toward till continuity), Ann. Glaciol., 22, 17–24, 1996.

Damsgaard, A., Egholm, D. L., Piotrowski, J. A., Tulaczyk, S., Larsen, N. K., and Tylmann, K.: Discrete element modelling of subglacial sediment deformation, J. Geophys. Res.-Earth, 118, 2230–2242, 2013.

Damsgaard, A., Egholm, D. L., Beem, L. H., Tulaczyk, S., Larsen, N. K., Piotrowski, J. A., and Siegfried, M. R.: Ice flow dynamics forced by water pressure variations in subglacial granular beds, Geophys. Res. Lett., 43, 12165–12173, 2016.

DeConto, R. M. and Pollard, D.: Contribution of Antarctica to past and future sea-level rise, Nature, 531, 591–597, 2016.

Dowling, T. P. F., Moller, P., and Spagnolo, M.: Rapid subglacial streamlined bedform formation at a calving bay margin, J. Quaternary Sci., 31, 879–892, https://doi.org/10.1002/jqs.2912, 2016.

Ely, J. C., Clark, C. D., Ng, F., Spagnolo, M., Hughes, A. L. C., and Stokes, C. R.: Using the size and position of drumlins to understand how they grow, interact and evolve, Earth Surf. Proc. Land., 43, 1073–1087, https://doi.org/10.1002/esp.4241, 2018.

Engelhardt, H. and Kamb, B.: Basal hydraulic system of a West Antarctic ice stream: constraints from borehole observations, J. Glaciol., 43, 207–229, 1997.

Engelhardt, H. and Kamb, B.: Basal sliding of Ice Stream B, West Antarctica, J. Glaciol., 44, 223–230, 1998.

Engelhardt, H., Humphrey, N., Kamb, B., and Fahnestock, M., Physical conditions at the base of a fast moving Antarctic ice stream, Science, 248, 57–59, 1990.

Fowler, A. C.: The formation of subglacial streams and mega-scale glacial lineations, P. R. Soc. Lond. A Mat., 466, 3181–3201, 2010.

Fowler, A. C., Spagnolo, M., Clark, C. D., Stokes, C. R., Hughes, A. L. C., and Dunlop, P.: On the size and shape of drumlins, International Journal on Geomathematics, 4, 155–165, 2013.

Fretwell, P., Pritchard, H. D., Vaughan, D. G., Bamber, J. L., Barrand, N. E., Bell, R., Bianchi, C., Bingham, R. G., Blankenship, D. D., Casassa, G., Catania, G., Callens, D., Conway, H., Cook, A. J., Corr, H. F. J., Damaske, D., Damm, V., Ferraccioli, F., Forsberg, R., Fujita, S., Gim, Y., Gogineni, P., Griggs, J. A., Hindmarsh, R. C. A., Holmlund, P., Holt, J. W., Jacobel, R. W., Jenkins, A., Jokat, W., Jordan, T., King, E. C., Kohler, J., Krabill, W., Riger-Kusk, M., Langley, K. A., Leitchenkov, G., Leuschen, C., Luyendyk, B. P., Matsuoka, K., Mouginot, J., Nitsche, F. O., Nogi, Y., Nost, O. A., Popov, S. V., Rignot, E., Rippin, D. M., Rivera, A., Roberts, J., Ross, N., Siegert, M. J., Smith, A. M., Steinhage, D., Studinger, M., Sun, B., Tinto, B. K., Welch, B. C., Wilson, D., Young, D. A., Xiangbin, C., and Zirizzotti, A.: Bedmap2: improved ice bed, surface and thickness datasets for Antarctica, The Cryosphere, 7, 375–393, https://doi.org/10.5194/tc-7-375-2013, 2013.

Fricker, H. A. and Scambos, T., Connected subglacial lake activity on lower Mercer and Whillans ice streams, West Antarctica, 2003–2008, J. Glaciol., 55, 303–315, 2009.

Fricker, H. A., Scambos, T., Bindschadler, R., and Padman, L.: An active subglacial water system in West Antarctica mapped from space, Science, 315, 1544–1548, https://doi.org/10.1126/science.1136897, 2007.

Ganti, V., Hagke, C. V., Scherler, D., Lamb, M. P., Fischer, W. W., and Avouac J.-P.: Time scale bias in erosion rates of glaciated landscapes, Science Advances, 2, e1600204, https://doi.org/10.1126/sciadv.1600204, 2016.

Graham, A. G. C., Larter, R. D., Gohl, K., Dowdeswell, J. A., Hillenbrand, C.-D., Smith, J. A., Evans, J., Kuhn, G., and Deen, T.: Flow and retreat of the Late Quaternary Pine Island-Thwaites palaeo-ice stream, West Antarctica, J. Geophys. Res., 115, F03025, https://doi.org/10/1029/2009JF001482, 2010.

Gudmundsson, G. H.: Fortnightly variations in the flow velocity of Rutford Ice Stream, West Antarctica, Nature, 444, 1063–1064, 2006.

Gudmundsson, G. H.: Tides and the flow of Rutford Ice Stream, West Antarctica, J. Geophys. Res.-Earth, 112, 1063–1064, https://doi.org/10.1029/2006JF000731, 2007.

Hallet, B., Hunter, L., and Bogen, J.: Rates of erosion and sediment evacuation by glaciers: A review of field data and their implications, Global Planet. Change, 12, 213–235, 1996.

Herman, F., Beaud, F. Champagnac, J.-D. Lemieux, J.-M., and Sternai, P.: Glacial hydrology and erosion patterns: a mechanism for carving glacial valleys, Earth Planet. Sc. Lett., 310, 498–508, 2011.

Herman, F., Beyssac, O., Brughelli, M., Lane, S. N., Leprince, S., Adatte, T., Lin, J. Y. Y., Avouac, J.-P., and Cox, S. C.: Erosion by an alpine glacier, Science, 350, 193–195, https://doi.org/10.1126/science.aab2386, 2015.

Hillier, J. K., Kougioumtzoglou, I. A., Stokes, C. R., Smith, M. J., Clark, C. D., and Spagnolo, M.: Exploring explanations of subglacial bedform sizes using statistical models, PloS ONE, 11, e0159489, https://doi.org/10.1371/journal.pone.0159489, 2016.

Hindmarsh, R. C.: The stability of a viscous till sheet coupled with ice flow, considered at wavelengths less than the ice thickness, J. Glaciol., 44, 285–292, 1998.

Hogg, A., Shepherd, A., Cornford, S. L., Briggs, K. H., Gourmelen, N., Graham, J. A., Joughin, I., Mouginot, J., Nagler, T., Payne, A. J., Rignot, E., and Wuite, J.: Increased ice flow in Western Palmer Land linked to ocean melting, Geophys. Res. Lett., 9, 4159–4167, 2017.

Iverson, N. R.: Shear resistance and continuity of subglacial till: hydrology rules, J. Glaciol., 56, 1104–1114, 2010.

Iverson, N. R. and Iverson, R. M.: Distributed shear of subglacial till due to Coulomb slip, J. Glaciol., 47, 481–488, 2001.

Jamieson, S. S. R., Sugden, D. E., and Hulton, N. R. J.: The evolution of the subglacial landscape of Antarctica, Earth Planet. Sc. Lett., 293, 1–27, 2010.

Jenson, J. W., Clark, P. U., MacAyeal, D. R., Ho, C., and Vela, J. C.: Numerical modelling of advective transport of saturated deforming sediment beneath the Lake Michigan Lobe, Laurentide Ice Sheet, Geomorphology, 14, 157–166, 1995.

Joughin, I., Tulaczyk, S., Bamber, J. L., Blankenship, D., Holt, J. W., Scambos, T., and Vaughan, D. G.: Basal conditions for Pine Island and Thwaites Glaciers, West Antarctica, determined using satellite and airborne data, J. Glaciol., 55, 245–257, 2009.

Joughin, I., Smith, B. E., and Medley, B.: Marine ice sheet collapse potentially under way for the Thwaites Glacier basin, West Antarctica, Science, 344, 735–738, 2014.

Kamb, B.: Rheological nonlinearity and flow instability in the deforming bed mechanism of ice stream motion, J. Geophys. Res.-Sol. Ea., 96, 16585–16595, 1991.

King, E. C., Woodward, J., and Smith, A. M.: Seismic evidence for a water-filled canal in deforming till beneath Rutford Ice Stream, West Antarctica, Geophys. Res. Lett., 31, https://doi.org/10.1029/2004GL020379, 2004.

King, E. C., Hindmarsh, R. C. A., and Stokes, C. R.: Formation of mega-scale glacial lineations observed beneath a West Antarctic ice stream, Nat. Geosci., 2, 585–588, https://doi.org/10.1038/NGEO581, 2009.

King, E. C., Pritchard, H. D., and Smith, A. M.: Subglacial landforms beneath Rutford Ice Stream, Antarctica: detailed bed topography from ice-penetrating radar, Earth Syst. Sci. Data, 8, 151–158, https://doi.org/10.5194/essd-8-151-2016, 2016.

Konrad, H., Gilbert, L., Cornford, S. L., Payne, A., Hogg, A., Muir, A., and Shepherd, A.: Uneven onset and pace of ice-dynamical imbalance in the Amundsen Sea Embayment, West Antarctica, Geophys. Res. Lett., 44, 910–918, 2017.

Koppes, M. and Hallet, B.: Erosion rates during rapid deglaciation in Icy Bay, Alaska, J. Geophys. Res., 111, https://doi.org/10.1029/2005JF000349, 2006.

Koppes, M. N. and Montgomery, D. R.: The relative efficacy of fluvial and glacial erosion over modern to orogenic timescales, Nat. Geosci., 2, 644–647, 2009.

Kyrke-Smith, T. M. and Fowler, A. C.: November, Subglacial swamps, P. Roy. Soc. Lond. A Mat., 470, 20140340, https://doi.org/10.1098/rspa.2014.0340, 2014.

Larter, R. D., Graham, A. G. C., Gohl, K., Kuhn, G., Hillenbrand, C. D., Smith, J. A., Deen, T. J., Livermore, R. A., and Schenke, H. W.: Subglacial bedforms reveal complex basal regime in a zone of paleo-ice stream convergence, Amundsen Sea embayment, West Antarctica, Geology, 37, 411–414, 2009.

Lowe, A. L. and Anderson, J. B.: Reconstruction of the West Antarctic Ice Sheet in Pine Island Bay during the Last Glacial Maximum and its subsequent retreat history, Quaternary Sci. Rev., 21, 1879–1897, 2002.

McMillan, M., Shepherd, A., Sundal, A., Briggs, K., Muir, A., Ridout, A., Hogg, A., and Wingham, D.: Increased ice losses from Antarctica detected by CryoSat-2, Geophys. Res. Lett., 41, 3899–3905, 2014.

Minchew, B., Simons, M., Riel, B., and Milillo, P.: Tidally induced variations in vertical and horizontal motion on Rutford Ice Stream, West Antarctica, inferred from remotely sensed observations, J. Geophys. Res.-Earth, 122, 167–190, 2017.

Motyka, R. J., Truffer, M., Kuriger, E. M., and Bucki, A. K.: Rapid erosion of soft sediments by tidewater glacier advance: Taku Glacier, Alaska, USA, Geophys. Res. Lett., 33, L24504, https://doi.org/10.1029/2006GL028467, 2006.

Mouginot, J., Rignot, E., and Scheuchl, B.: Sustained increase in ice discharge from the Amundsen Sea Embayment, West Antarctica, from 1973 to 2013, Geophys. Res. Lett., 41, 1576–1584, 2014.

Murray, T., Smith, A. M., King, M. A., and Weedon, G. P.: Ice flow modulated by tides at up to annual periods at Rutford Ice Stream, West Antarctica, Geophys. Res. Lett., 34, L18503, https://doi.org/10.1029/2007GL031207, 2007.

Nygård, A., Sejrup, H. P., Haflidason, H., Lekens, W. A. H., Clark, C. D. and Bigg, G. R.: Extreme sediment and ice discharge from marine-based ice streams: New evidence from the North Sea, Geology, 35, 395–398, 2007.

Park, J. W., Gourmelen, N., Shepherd, A., Kim, S. W., Vaughan, D. G., and Wingham, D. J.: Sustained retreat of the Pine Island Glacier, Geophys. Res. Lett., 40, 2137–2142, 2013.

Peters, L. E., Anandakrishnan, S., Alley, R. B., Winberry, J. P., Voigt, D. E., Smith, A. M., and Morse, D. L.: Subglacial sediments as a control on the onset and location of two Siple Coast ice streams, West Antarctica, J. Geophys. Res.-Sol. Ea., 111, B01302, https://doi.org/10.1029/2005JB003766, 2006.

Pritchard, H. D., Arthern, R. J., Vaughan, D. G., and Edwards, L. A.: Extensive dynamic thinning on the margins of the Greenland and Antarctic ice sheets, Nature, 461, 971–975, 2009.

Raiswell, R., Tranter, M., Benning, L. G., Siegert, M., De'Ath, R., Huybrechts, P., and Payne, T.: Contributions from glacially derived sediment to the global iron (oxyhydr)oxide cycle: implications for iron delivery to the oceans, Geochim. Cosmochim. Ac., 70, 2765–2780, 2006.

Rignot, E., Mouginot, J., and Scheuchl, B.: Ice flow of the Antarctic Ice Sheet, Science, 333, 1427–1430, 2011.

Rignot, E., Mouginot, J., Morlighem, M., Seroussi, H., and Scheuchl, B.: Widespread, rapid grounding line retreat of Pine Island, Thwaites, Smith, and Kohler glaciers, West Antarctica, from 1992 to 2011, Geophys. Res. Lett., 41, 3502–3509, 2014.

Rosier, S. H. R., Gudmundsson, G. H., and Green, J. A. M.: Temporal variations in the flow of a large Antarctic ice stream controlled by tidally induced changes in the subglacial water system, The Cryosphere, 9, 1649–1661, https://doi.org/10.5194/tc-9-1649-2015, 2015.

Schoof C.: Cavitation on deformable glacier beds, SIAM J. Appl. Math., 67, 1633–1653, 2007.

Schroeder, D. M., Blankenship, D. D., and Young, D. A.: Evidence for a water system transition beneath Thwaites Glacier, West Antarctica, P. Natl. Acad. Sci. USA, 110, 12225–12228, 2013.

Scott, J. B. T., Gudmundsson, G. H., Smith, A. M., Bingham, R. G., Pritchard, H. D., and Vaughan, D. G.: Increased rate of acceleration on Pine Island Glacier strongly coupled to changes in gravitational driving stress, The Cryosphere, 3, 125–131, https://doi.org/10.5194/tc-3-125-2009, 2009.

Sergienko, O. V. and Hindmarsh, R. C. A.: Regular patterns in frictional resistance of ice-stream beds seen by surface data inversion, Science, 342, 1086–1089, 2013.

Shepherd, A., Wingham, D. J., Mansley, J. A. D., and Corr, H. F. J.: Inland thinning of Pine Island Glacier, West Antarctica, Science, 291, 862–864, 2001.

Shepherd, A., Ivins, E. R., Geruo, A., Barletta, V. R., Bentley, M. J., Bettadpur, S., Briggs, K. H., Bromwich, D. H., Forsberg, R., Galin, N., Horwath, M., Jacobs, S., Joughin, I., King, M. A., Lenaerts, J. T. M., Li, J., Ligtenberg, S. R. M., Luckman, A., Luthcke, S. B., McMillan, M., Meister, R., Milne, G., Mouginot, J., Muir, A., Nicolas, J. P., Paden, J., Payne, A. J., Pritchard, H., Rignot, E., Rott, H., Sørensen, L. S., Scambos, T. A., Scheuchl, B., Schrama, E. J. O., Smith, B., Sundal, A. V., van Angelen, J. H., van de Berg,W. J., van den Broeke, M. R., Vaughan, D. G., Velicogna, I.,Wahr, J., Whitehouse, P. L.,Wingham, D. J., Yi, D., Young, D., and Zwally, H. J.: A reconciled estimate of ice-sheet mass balance, Science, 338, 1183–1189, 2012.

Smith, A. M.: Basal conditions on Rutford Ice Stream, West Antarctica, from seismic observations, J. Geophys. Res.-Sol. Ea., 102, 543–552, 1997.

Smith, A. M. and Murray, T.: Bedform topography and basal conditions beneath a fast-flowing West Antarctic ice stream, Quaternary Sci. Rev., 28, 584–596, 2009.

Smith, A. M., Murray, T., Nicholls, K. W., Makinson, K., Aðalgeirsdóttir, G., Behar, A. E., and Vaughan, D. G.: Rapid erosion, drumlin formation, and changing hydrology beneath an Antarctic ice stream, Geology, 35, 127–130, 2007.

Smith, A. M., Bentley, C. R., Bingham, R. G., and Jordan, T. A.: Rapid subglacial erosion beneath Pine Island Glacier, West Antarctica, Geophys. Res. Lett., 39, L12501, https://doi.org/10.1029/2012GL051651, 2012.

Smith, A. M., Jordan, T. A., Ferraccioli, F., and Bingham, R. G.: Influence of subglacial conditions on ice stream dynamics: Seismic and potential field data from Pine Island Glacier, West Antarctica, J. Geophys. Res.-Sol. Ea., 118, 1471–1482, 2013.

Smith, B. E., Gourmelen, N., Huth, A., and Joughin, I.: Connected subglacial lake drainage beneath Thwaites Glacier, West Antarctica, The Cryosphere, 11, 451–467, https://doi.org/10.5194/tc-11-451-2017, 2017.

Smith, E. C., Smith, A. M., White, R. S., Brisbourne, A. M., and Pritchard, H. D.: Mapping the ice-bed interface characteristics of Rutford Ice Stream,West Antarctica, using microseismicity, J. Geophys. Res.-Earth, 120, 1881–1894, 2015.

Spagnolo, M., Clark, C. D., Ely, J. C., Stokes, C. R., Anderson, J. B., Andreassen, K., Graham, A. G. C., and King, E. C.: Size, shape and spatial arrangement of mega-scale glacial lineations from a large and diverse dataset, Earth Surf. Proc. Land., 39, 1432–1448, https://doi.org/10.1002/esp.3532, 2014.

Spagnolo, M., Phillips, E., Piotrowski, J., Rea, B. R., Clark, C. D., Stokes, C. R., Carr, S., Ely, J. C., Ribolini, A., Wysota, W., and Szuman, I.: Ice stream motion facilitated by a shallow-deforming and accreting bed, Nat. Commun., 7, 10723, https://doi.org/10.1038/ncomms10723, 2016.

Spagnolo, M., Bartholomaus, T. C., Clark, C. D., Stokes, C. R., Atkinson, N., Dowdeswell, J. A., Ely, J. C., Graham, A. G. C., Hogan, K. A., King, E. C., Larter, R. D., Livingstone, S. J., and Pritchard, H. D.: The periodic topography of ice stream beds: Insights from the Fourier spectra of mega-scale glacial lineations, J. Geophys. Res., 122, 1355–1373, 2017.

Stokes, C. and Clark, C.: Palaeo-ice streams, Quaternary Sci. Rev., 20, 1437–1457, 2001.

Thompson, J., Simons, M., and Tsai, V. C.: Modeling the elastic transmission of tidal stresses to great distances inland in channelized ice streams, The Cryosphere, 8, 2007–2029, https://doi.org/10.5194/tc-8-2007-2014, 2014.

Truffer, M., Harrison, W. D., and Echelmeyer, K. A., Glacier motion dominated by processes deep in underlying till, J. Glaciol., 46, 213–221, https://doi.org/10.3189/172756500781832909.6, 2000.

Tulaczyk, S., Kamb, W. B., and Engelhardt, H. F.: Basal mechanics of ice stream B, West Antarctica: 1. Till mechanics, J. Geophys. Res.-Sol. Ea., 105, 463–481, 2000.

Vaughan, D. G., Corr, H. F. J., Ferraccioli, F., Frearson, N., O'Hare, A., Mach, D., Holt, J. W., Blankenship, D. D., Morse, D. L., and Young, D. A.: New boundary conditions for the West Antarctic ice sheet: Subglacial topography beneath Pine Island Glacier, Geophys. Res. Lett., 33, L09501, https://doi.org/10.1029/2005GL025588, 2006.

Vaughan, D. G., Corr, H. F., Smith, A. M., Pritchard, H. D., and Shepherd, A.: Flow switching and water piracy between Rutford ice stream and Carlson inlet, West Antarctica, J. Glaciol., 54, 41–48, https://doi.org/10.3189/002214308784409125, 2008.

Walder, J. S. and Fowler, A.: Channelized subglacial drainage over a deformable bed, J. Glaciol., 40, 3–15, 1994.

Weertman, J.: General theory of water flow at the base of a glacier or ice sheet, Rev. Geophys., 10, 287–333, 1972.

Wellner, J., Heroy, D., and Anderson, J.: The death mask of the Antarctic ice sheet: Comparison of glacial geomorphic features across the continental shelf, Geomorphology, 75, 157–171, https://doi.org/10.1016/j.geomorph.2005.05.015, 2006.

Wingham, D. J., Siegert, M. J., Shepherd, A., and Muir, A. S.: Rapid discharge connects Antarctic subglacial lakes, Nature, 440, 1033–1036, 2006.

Zwally, H. J., Giovinetto, M., Beckley, B. A., and Saba, J. L.: Antarctic and Greenland drainage systems, GSFC Cryospheric Sciences Laboratory, available at: https://icesat4.gsfc.nasa.gov/cryo_data/ant_grn_drainage_systems.php, 2012.

Appendix C

Davies *et al.* 2017 (JGR-Earth Surface)

AGU PUBLICATIONS

JGR

Journal of Geophysical Research: Earth Surface

RESEARCH ARTICLE
10.1002/2017JF004311

Key Points:
- Ungrounding of Pine Island Glacier Ice Shelf from submarine ridge in 1940s left imprint of recent (de)glaciation on seafloor
- Sub-ice-shelf bathymetric and sub-bottom profiling shows transition in bed properties across submarine ridge
- AUVs offer capability to image submerged deglaciated settings at resolution required for improved process understanding

Correspondence to:
D. Davies,
D.Davies@ed.ac.uk

Citation:
Davies, D., R. G. Bingham, A. G. C. Graham, M. Spagnolo, P. Dutrieux, D. G. Vaughan, A. Jenkins, and F. O. Nitsche (2017), High-resolution sub-ice-shelf seafloor records of twentieth century ungrounding and retreat of Pine Island Glacier, West Antarctica, *J. Geophys. Res. Earth Surf.*, *122*, 1698–1714, doi:10.1002/2017JF004311.

Received 7 APR 2017
Accepted 27 JUL 2017
Accepted article online 11 AUG 2017
Published online 20 SEP 2017

©2017. The Authors.
This is an open access article under the terms of the Creative Commons Attribution License, which permits use, distribution and reproduction in any medium, provided the original work is properly cited.

High-resolution sub-ice-shelf seafloor records of twentieth century ungrounding and retreat of Pine Island Glacier, West Antarctica

D. Davies[1], R. G. Bingham[1], A. G. C. Graham[2], M. Spagnolo[3,4], P. Dutrieux[5], D. G. Vaughan[6], A. Jenkins[6], and F. O. Nitsche[5]

[1]School of GeoSciences, University of Edinburgh, Edinburgh, UK, [2]College of Life and Environmental Sciences, University of Exeter, Exeter, UK, [3]School of Geosciences, University of Aberdeen, Aberdeen, UK, [4]Earth and Planetary Science Department, University of California, Berkeley, California, USA, [5]Lamont-Doherty Earth Observatory, Columbia University, Palisades, New York, USA, [6]British Antarctic Survey, Cambridge, UK

Abstract Pine Island Glacier Ice Shelf (PIGIS) has been thinning rapidly over recent decades, resulting in a progressive drawdown of the inland ice and an upstream migration of the grounding line. The resultant ice loss from Pine Island Glacier (PIG) and its neighboring ice streams presently contributes an estimated ~10% to global sea level rise, motivating efforts to constrain better the rate of future ice retreat. One route toward gaining a better understanding of the processes required to underpin physically based projections is provided by examining assemblages of landforms and sediment exposed over recent decades by the ongoing ungrounding of PIG. Here we present high-resolution bathymetry and sub-bottom-profiler data acquired by autonomous underwater vehicle (AUV) surveys beneath PIGIS in 2009 and 2014, respectively. We identify landforms and sediments associated with grounded ice flow, proglacial and subglacial sediment transport, overprinting of lightly grounded ice-shelf keels, and stepwise grounding line retreat. The location of a submarine ridge (Jenkins Ridge) coincides with a transition from exposed crystalline bedrock to abundant sediment cover potentially linked to a thick sedimentary basin extending upstream of the modern grounding line. The capability of acquiring high-resolution data from AUV platforms enables observations of landforms and understanding of processes on a scale that is not possible in standard offshore geophysical surveys.

1. Introduction

The ice shelves that surround Antarctica's coast buttress ice flow from the continent's interior to the ocean [*Dupont and Alley*, 2005; *Fürst et al.*, 2016]. Over the last 25 years, however, many of the ice shelves along West Antarctica's Amundsen Sea margin have thinned extensively [*Pritchard et al.*, 2012; *Rignot et al.*, 2013; *Paolo et al.*, 2015], leading to progressive acceleration and surface lowering of ice inland [*Rignot et al.*, 2002; *Scott et al.*, 2009; *Wingham et al.*, 2009; *McMillan et al.*, 2014; *Mouginot et al.*, 2014; *Konrad et al.*, 2017], and an inland migration of the grounding line [*Park et al.*, 2013; *Rignot et al.*, 2014]. While the ice-shelf thinning has been attributed to sub-ice-shelf melting [*Jacobs et al.*, 1996; *Pritchard et al.*, 2012; *Rignot et al.*, 2013], direct observations of the processes of sub-ice-shelf melting and grounding-line retreat are few, because sub-ice-shelf cavities are one of the Earth's least accessible environments [*Dowdeswell et al.*, 2008].

Only recently have autonomous underwater vehicles (AUVs) offered an opportunity to access sub-ice-shelf regions in Antarctica. Most sub-ice-shelf AUV campaigns conducted to date have prioritized the measurement and characterization of ocean-water properties and ice-shelf bases [*Nicholls et al.*, 2006; *Jenkins et al.*, 2010; *Jacobs et al.*, 2011; *Dutrieux et al.*, 2014a, 2014b]. By contrast, comparatively little attention has been given to sounding or imaging seafloor bedforms and sediment properties beneath thinning ice shelves. Such settings, especially where ice has recently been grounded, provide opportunities to investigate "geomorphologically pristine," recently deglaciated terrains, and to relate these terrains to the processes that created them [e.g., *Domack et al.*, 2005; *Graham et al.*, 2013; *Smith et al.*, 2017].

In this paper, we present high-resolution bathymetry and sub-bottom-profiler data obtained by the Autosub3 AUV [*McPhail et al.*, 2009] beneath Pine Island Glacier Ice Shelf (hereafter PIGIS), West Antarctica,

during January 2009 and February–March 2014. Using these data, we explore the nature of seafloor bedforms and sediment properties and assess processes associated with retreat from a former pinning point during the mid-twentieth century. Our results reveal a suite of bedforms created by proglacial sedimentation, grounded ice flow, and lightly grounded ice flow, all reflecting the progressive ungrounding and retreat of Pine Island Glacier from beneath and just in front of the present ice shelf. We demonstrate the necessity to use meter-scale resolution imagery of recently deglaciated terrains to understand processes of past decadal to centennial retreat.

2. Study Area and Geological Context

PIGIS (Figure 1) impounds Pine Island Glacier (PIG) which, together with Thwaites Glacier, drains ~20% of the West Antarctic Ice Sheet (WAIS) into Pine Island Bay, the largest embayment of the Amundsen Sea. Since 1973 PIG's flux through PIGIS to the ocean increased from 78 ± 7 Gt yr^{-1} to 133 ± 4 Gt yr^{-1} [*Mouginot et al.*, 2014], an increase in ice transfer to the ocean of >40%. Between 1973 and 2010, the velocity of PIGIS increased by 1.7 km/yr or 75% and now flows at >4 km/yr [*Mouginot et al.*, 2014]. Contemporaneously, the ice thinned progressively inland, with thinning now measurable at the ice divides [*Wingham et al.*, 2009; *Scott et al.*, 2009; *McMillan et al.*, 2014; *Konrad et al.*, 2017], and the grounding line retreated 31 km between 1992 and 2011 [*Rignot et al.*, 2014]. Collectively, this is the most rapidly retreating region of ice on the planet and is contributing an estimated ~5–10% of the currently observed global sea level rise [*Rignot et al.*, 2008; *Turner et al.*, 2017].

PIG's current retreat is thought to have been triggered by ungrounding from a transverse submarine ridge, Jenkins Ridge (Figure 1), that spans the width of PIGIS ~30 km from the current grounding line [*Jenkins et al.*, 2010; *Smith et al.*, 2017]. Dating of sediments retrieved from the crest and seaward slope of Jenkins Ridge, via hot-water drilling through the ice shelf, suggests that ungrounding was initiated in the 1940s and became complete by the 1970s [*Smith et al.*, 2017]. Satellite imagery also indicates that contact between the ice shelf and the highest point of Jenkins Ridge persisted in the early 1970s but became ungrounded in subsequent years [*Jenkins et al.*, 2010]. This ungrounding and retreat is associated with enhanced melting by incursion of warm Circumpolar Deep Water onto the continental shelf [*Jacobs et al.*, 2011; *Pritchard et al.*, 2012; *Hillenbrand et al.*, 2017]. Intermittent grounding of ice-shelf keels on localized bathymetric highs in the central region of PIGIS has also been detected within the last decade [*Joughin et al.*, 2016].

Regional geology is intrinsic to the properties of the seafloor beneath PIGIS. Upstream of the grounding line, relatively low crustal thickness in the PIG catchment observed in aerogravity data facilitates ice streaming through the presence of thick sedimentary basins and elevated heat flux [*Jordan et al.*, 2009; *Muto et al.*, 2013, 2016]. The legacy of continental rifting associated with the formation of the West Antarctic Rift System [*Bingham et al.*, 2012] is a highly varied subglacial environment beneath PIG that exerts topographic controls on ice streaming [*Jordan et al.*, 2009]. Seaward of PIGIS this regional topography contrasts between smooth sedimentary strata on the outer continental shelf and rough crystalline bedrock on the inner continental shelf in Pine Island Bay [*Jakobsson et al.*, 2011; *Nitsche et al.*, 2013]. Landforms on the outer continental shelf are dominated by mega-scale glacial lineations (MSGL) associated with ice streaming over deforming sediments and grounding zone wedges (GZW) deposited during pauses in retreat of the Pine Island-Thwaites paleo-ice stream [*Anderson et al.*, 2002; *Lowe and Anderson*, 2002; *Graham et al.*, 2010; *Jakobsson et al.*, 2011]. The inner continental shelf exhibits a more rugged seafloor characterized by exposed crystalline bedrock streamlined by ice-stream flow with deep (up to 1650 m) basins connected by meltwater-channel networks [*Lowe and Anderson*, 2002; *Nitsche et al.*, 2013].

Because of the difficulty of accessing the sub-ice-shelf cavity, comparatively little is known about the detailed properties of the seafloor beneath PIGIS. Aerogeophysical surveys constrained by AUV and radar soundings have provided broad insights into the sub-ice-shelf bathymetry and sediment distribution [*Studinger et al.*, 2010; *Muto et al.*, 2013, 2016]. These studies show that Jenkins Ridge spans the entire ~45 km width of PIGIS and rises ~350–400 m above the seafloor. Landward of Jenkins Ridge lies a sedimentary basin up to ~800 m thick immediately upstream of the current grounding line, whereas sediments are absent or thin seaward of Jenkins Ridge [*Nitsche et al.*, 2013; *Muto et al.*, 2016].

AUV-mounted geophysical apparatus offers the ability to investigate the seafloor at submeter to meter-scale resolution [*Nicholls et al.*, 2006; *Wynn et al.*, 2014; *García et al.*, 2016]. Due to the challenging environment

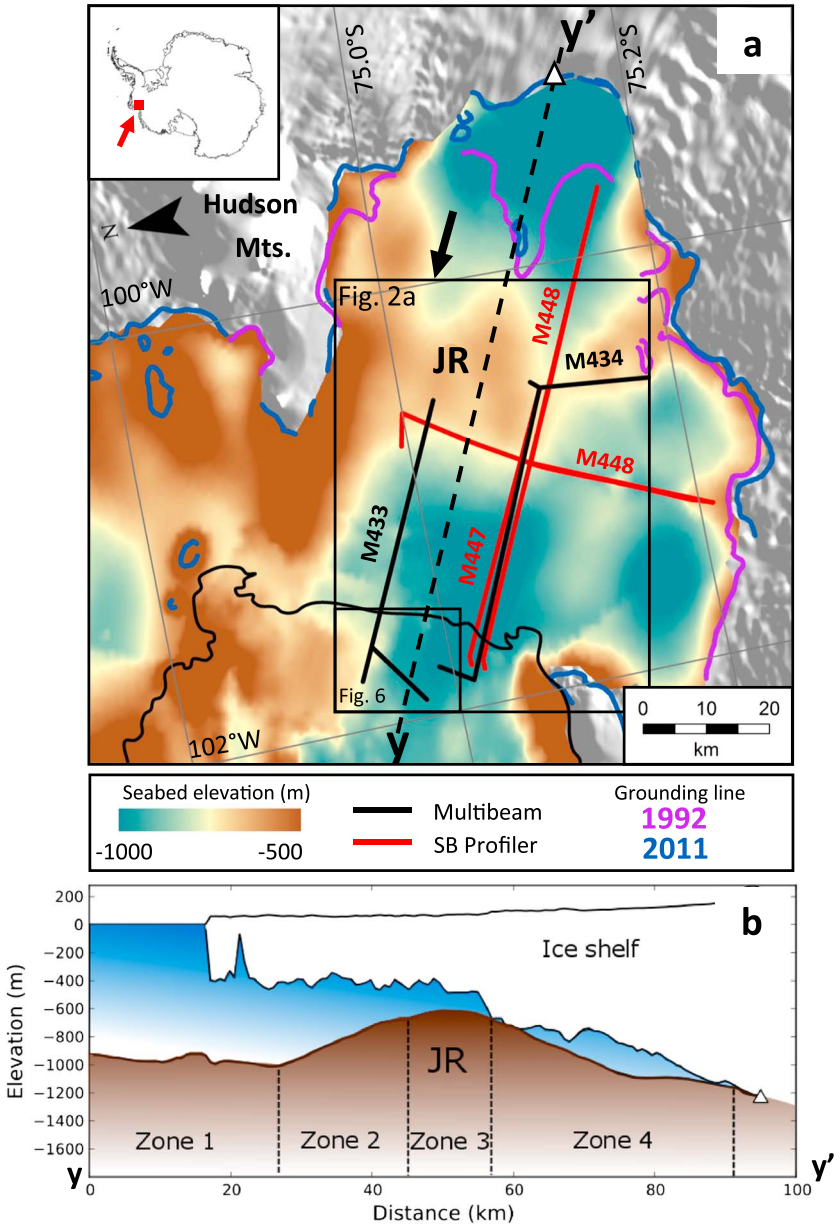

Figure 1. Map and locations of Autosub3 sub-ice-shelf missions beneath Pine Island Glacier Ice Shelf (PIGIS). (a) Sub-ice-shelf bathymetry derived from gravity inversion (see supporting information in *Dutrieux et al.* [2014a] for methodology) showing the location of Jenkins Ridge (JR) and Autosub3 mission tracks. Black line shows the ice-shelf front position in 2009. Boxes show areas covered by figures referred to later in text. Grounding line locations are from the MEaSUREs data set [*Rignot et al.*, 2011]. (b) Cross section of ice and seafloor geometry extracted from profile *y*-*y*′ (dashed black line) showing geomorphic zones 1–4 (ice draft and bathymetry from *Dutrieux et al.* [2014a]; see their supporting information for methodology). Data for each zone are shown in Figures 2–4.

beneath Antarctic ice shelves and the operational and logistical limits of AUV operations, the spatial coverage of these data is limited. However, available data from missions beneath PIGIS thus far have provided insights into ocean properties in unprecedented detail [*Jenkins et al.*, 2010; *Jacobs et al.*, 2011; *Dutrieux et al.*, 2014a]. Sections of these data have received some geomorphological analysis [*Jenkins et al.*, 2010; *Graham et al.*, 2013]; however, a detailed study of seafloor geomorphology has not yet been conducted using the entirety of these data sets.

3. Data and Methods

3.1. Multibeam-Swath Bathymetry

High-resolution, sub-ice-shelf seafloor bathymetry covering a total distance of ~110 km (~3850 km^2) of the seafloor was obtained from two AUV missions (M433 and M434) beneath PIGIS in January 2009 during Cruise NBP09-01 of the research icebreaker R/V *Nathaniel B. Palmer* (tracks marked in Figure 1a). Navigation was achieved by dead reckoning through an Inertial Navigation System (INS), integrated and mechanically coupled with a downward looking Acoustic Doppler Current Profiler (ADCP). Navigational errors are typically between 0.2% and 0.1% of distance traveled [*McPhail*, 2009; *McPhail et al.*, 2009]. A Kongsberg EM-2000 multibeam echosounder was operated from the AUV at a nominal height of ~100 m above the seafloor which provides typical vertical root mean square errors of <10 cm [*Dowdeswell et al.*, 2008]. Data were processed using MB-System, and a digital elevation model (DEM) was gridded with 2 m cell sizes using a weighted near-neighbor algorithm [*Graham et al.*, 2013; *Dutrieux et al.*, 2014b].

3.2. Sub-Bottom Profiling

Sediment properties were investigated using an Edgetech 2200 M sub-bottom profiler mounted on Autosub3. Data were obtained from AUV deployments during the iSTAR research cruise JR294/295 from the RRS *James Clark Ross* in February and March 2014. The system emits a chirp signal at 2–16 kHz providing shallow penetration images of the seafloor with a resolution of 6–10 cm. Two missions (M447 and M448) covered ~150 km of the seafloor from ~20 km seaward of the 2009 ice front across the seaward slope, crest and backslope of Jenkins Ridge, and into the sub-ice-shelf cavity (Figure 1a). A band-pass Butterworth filter with lower and upper cutoffs of 1000 and 3500 kHz, respectively, was applied to the data to remove high-frequency noise. A vertical correction was applied to account for the AUV's flying height. Water depths and sediment thickness were calculated by converting the two-way travel time to meters using acoustic velocities of 1459 m s^{-1} for water and 1500 m s^{-1} for soft unconsolidated sediment, respectively. We provide an error margin of ±3% for estimates of sediment thickness as recommended by *Lysså et al.* [2010].

Bathymetric data were not recorded concurrently with the sub-bottom profiler in 2014 due to problems encountered with the EM-2000 multibeam echosounder, so therefore we are unable directly to compare contemporaneous bathymetric and sub-bottom-profiler data. However, survey tracks M447 and M448 closely follow parallel to, and intersect, multibeam survey tracks M433 and M434 (Figure 1a).

3.3. Mapping and Metrics

Geomorphological features were mapped from bathymetric DEMs in ArcGIS v.10.1. Multiple-illumination azimuths and vertical exaggerations were applied to aid visualization following the methods of *Smith and Clark* [2005]. To aid mapping further, subtle geomorphological features were accentuated using a surface-detrending algorithm that fitted a polynomial to the original DEM using a 30 m kernel window to produce a smoothed surface, which was then subtracted from the original DEM [*Hurst et al.*, 2012]. Three-dimensional surfaces were produced and visualized in Schlumberger Petrel™ seismic interpretation software.

Linear bedforms were mapped by drawing lines across their crests while azimuths (0–360° from grid North) were extracted using GIS tools. Spacing and amplitude of linear bedforms were calculated by averaging multiple measurements extracted from cross-sectional topographic profiles transverse to bed form crestlines following the method of *Spagnolo et al.* [2014].

4. Results and Analysis

In this section we describe the seafloor bedforms and sediment properties imaged below PIGIS, respectively, in 2009 and 2014 using the techniques described above. Figure 2 provides an overview of bathymetric data showing relief-shaded DEMs alongside interpretations of landforms. We structure the findings by location relative to Jenkins Ridge, as demarcated on Figure 1b: progressively approaching the grounding line the zones can broadly be described as (1) the outer sub-ice-shelf seafloor, (2) the PIG-distal flank of Jenkins Ridge, (3) Jenkins Ridge crest, and (4) the PIGIS sub-ice-shelf cavity (Figure 1b). In the following sections we present seafloor bathymetry (Figure 3) and sub-bottom profiler data (Figure 4) in turn for each zone with the exception of Zone 4 where only sub-bottom profiler data were acquired.

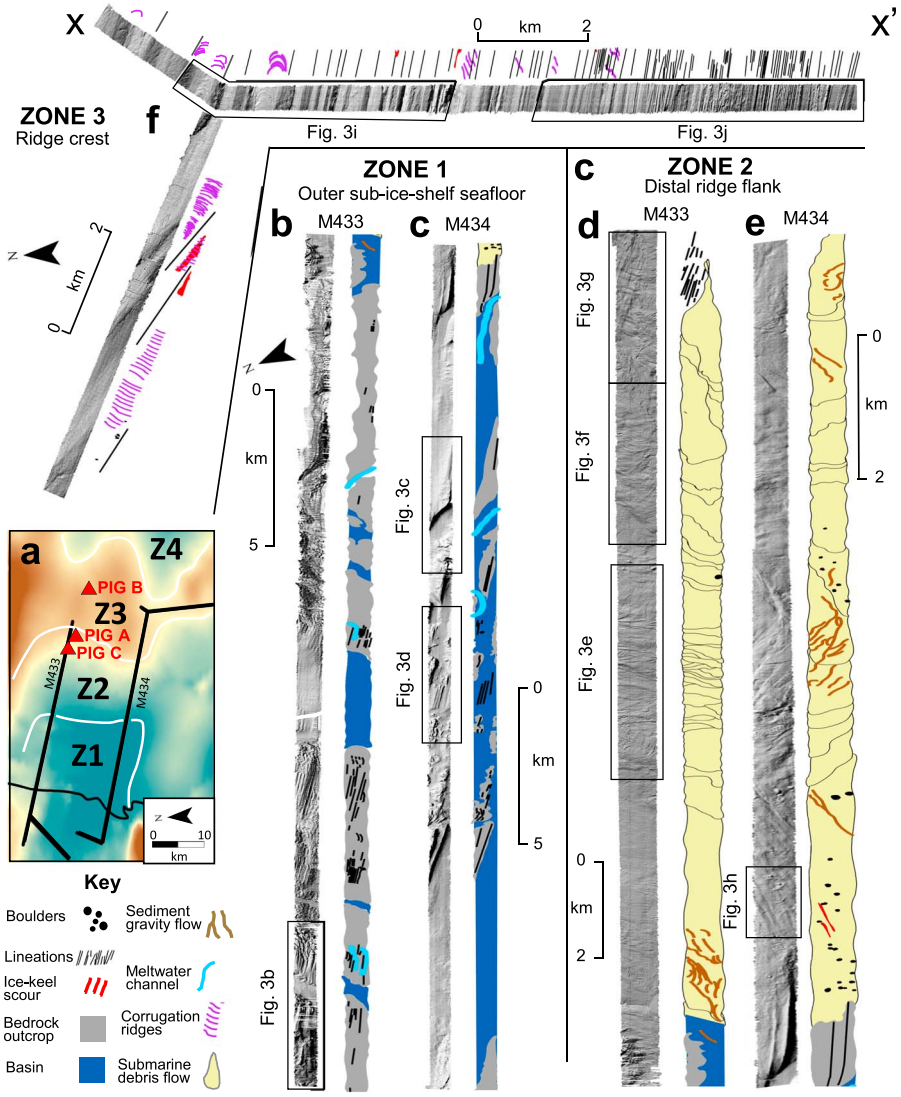

Figure 2. Sub-ice-shelf multibeam bathymetry data and geomorphological interpretation. (a) Map of regional bathymetry and location of multibeam surveys M433 and M434. Red triangles show the locations of sediment cores described in *Smith et al.* [2017]. Black line shows the ice-shelf front position in 2009. (b–f) Multidirectional relief-shaded multibeam topography plotted alongside corresponding geomorphological interpretations. Data width has been exaggerated by a factor of 2 for clarity. Black lines superimposed over debris flows delimit individual debris flow lobes. Black boxes show the location of three-dimensional surface imagery shown in Figure 3.

4.1. Zone 1: Outer Sub-Ice-Shelf Seafloor

4.1.1. Seafloor Bathymetry

The regional bathymetry of Zone 1 exhibits rugged topography, likely dominated by outcrops of crystalline bedrock that rise in excess of 40 m above intervening smooth, flat-bottomed basins (Figures 2b and 2c). The surfaces of outcrops in profile M433 host parallel lineations 2–10 m in amplitude and up to 1.5 km in length orientated along the trough axis (Figure 3b). The morphology of these features is consistent with streamlined bedrock landforms described in offshore-bathymetry data sets in Pine Island Bay and on the inner continental-shelf region of the western Amundsen Sea Embayment [*Lowe and Anderson*, 2002; *Graham et al.*, 2009; *Nitsche et al.*, 2013].

Farther south, and traversing an extensive basin, data from profile M434 exhibit lineations and outcrops truncated abruptly by steep-sided channels >200 m wide with curvilinear cross-sectional profiles (Figures 2c, and 3c and 3d). A series of irregular depressions up to 3 m deep and 150 m wide punctuates the crest of a lineation in this region (Figure 3f). Six kilometers downstream from the location of these surface depressions is a chain

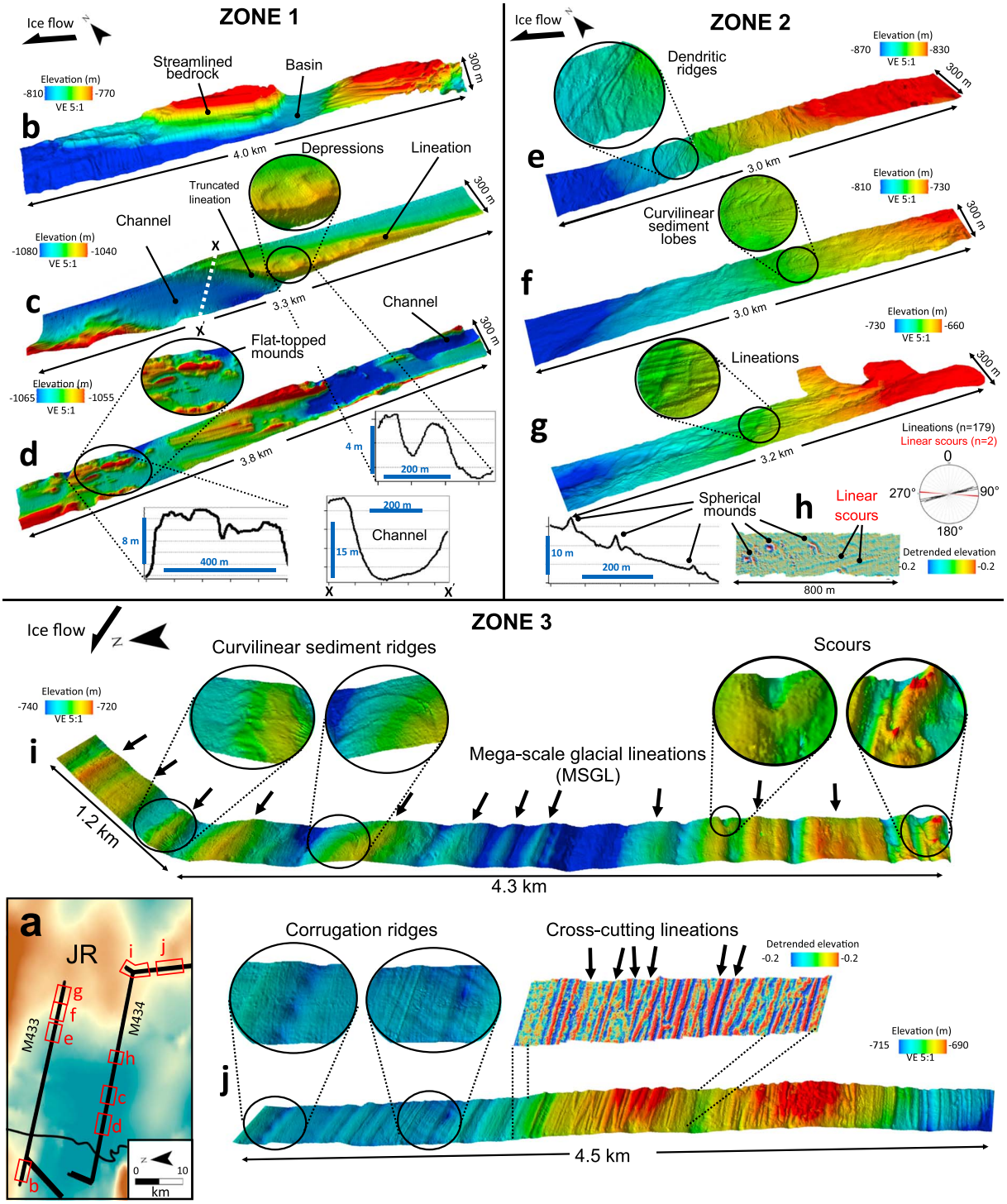

Figure 3. Three-dimensional surfaces of multibeam seafloor bathymetry. (a) Inset map showing the locations of Figures 3b–3j. Multibeam surface imagery of seafloor topography and extracted topographic profiles in (b–d) Zone 1, (e–h) Zone 2, and (i and j) Zone 3. Location of Figure 3h is shown in the inset map and Figure 2e. Rose diagram next to Figure 3h shows the azimuth of lineations sampled from Zones 1–3 compared to linear scours in Figure 3h.

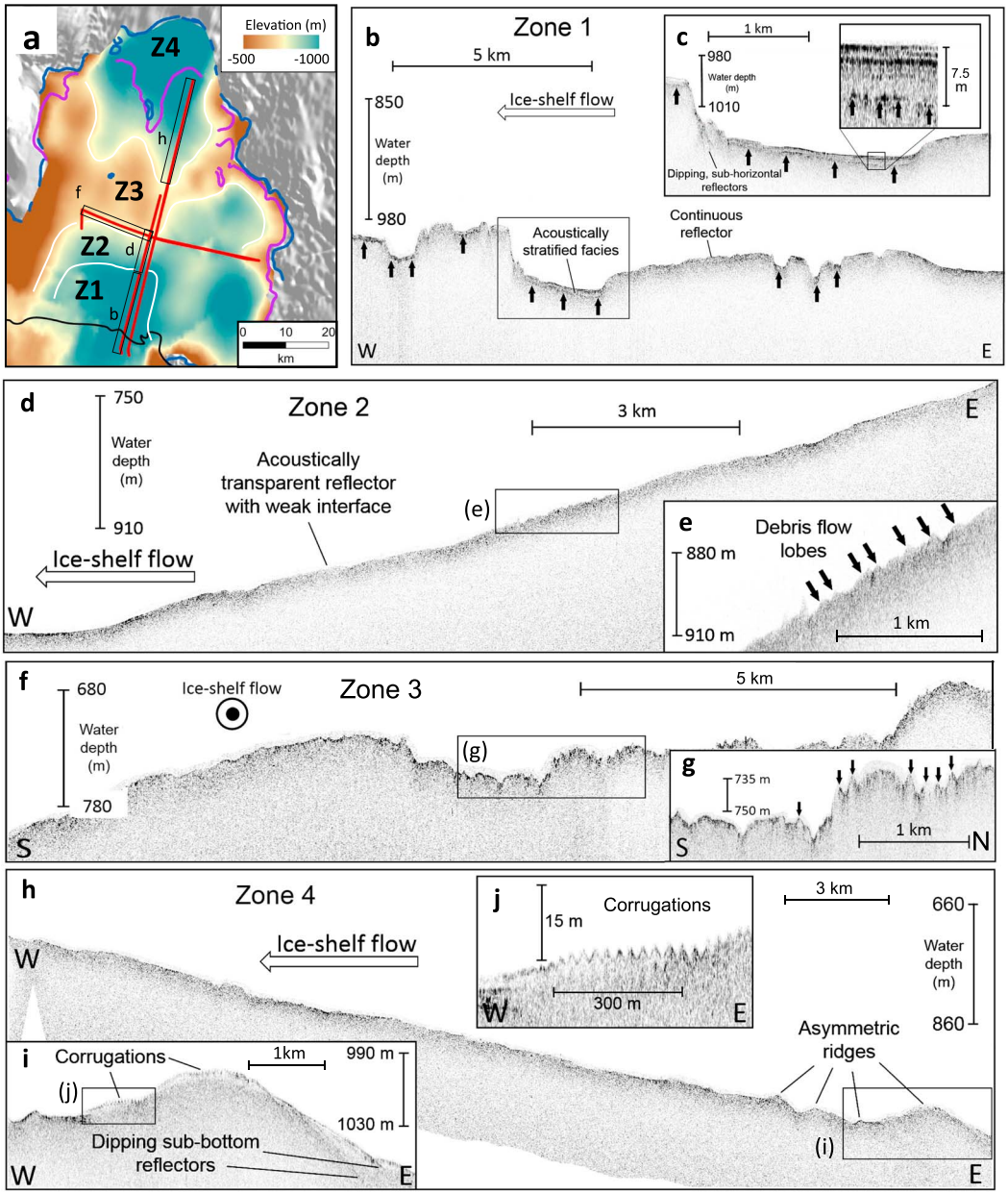

Figure 4. Acoustic sub-bottom profiler data. (a) Map of regional bathymetry and location of sub-bottom profiler surveys beneath Pine Island Glacier Ice Shelf. Black boxes denote sections of data shown in the main figure. (b) Rugged seafloor topography and acoustically stratified basins (black arrows) in Zone 1. (c) Close-up of an acoustically stratified basin showing up to 7.5 m of stratified sediments. Sediment thickness was calculated using an acoustic velocity of 1500 m s^{-1} for sediments. (d) Acoustically transparent seafloor reflector of the seaward flank of Jenkins Ridge. (e) Close-up showing debris flow lobes (black arrows). (f) Profile across Jenkins Ridge showing a strong surface reflector and undulating seafloor. (g) Close-up showing mega-scale glacial lineations (black arrows). (h) Acoustically transparent seafloor reflector on the inland slope of Jenkins Ridge. (i) Close-up view of asymmetric ridges. (j) Close-up of corrugation ridges overprinting the crest of asymmetric ridges.

of flat-topped mounds up to 10 m in height, 300 to 1000 m in width, and up to 2 km in length (Figure 3d). The mounds' long axes generally trend parallel to inferred paleo-ice-stream flow.

4.1.2. Sub-Bottom Profiler

The topography of the seafloor in Zone 1 imaged from the sub-bottom profiler further demonstrates the typical ruggedness of the former ice bed in this region as suggested by the bathymetric surveys (Figure 4b). Regions of elevated seafloor are characterized by a high-amplitude, continuous acoustic reflector,

between which some acoustically stratified topographic depressions are interspersed (Figure 4c). The stratification within each depression is characterized by a series of laterally continuous, parallel reflectors conforming to the underlying seafloor topography. The full sequence of stratified reflectors has a maximum thickness of 7.5 ± 0.2 m (Figure 4c, inset).

4.2. Zone 2: PIG-Distal Flank of Jenkins Ridge

4.2.1. Seafloor Bathymetry

The transition between Zone 1 and Zone 2 is marked by an abrupt change from rugged to relatively smooth seafloor topography (Figures 2d and 2e) reflecting an apparent shift to a sediment-dominated regime. Bedforms in Zone 2 broadly display amplitudes an order of magnitude lower than in Zone 1 and, on the whole, show little to no streamlining. Toward the base of Jenkins Ridge flank, on M433, a network of channels and ridges with a dendritic pattern cuts across the slope (Figure 2d and zoom in Figure 3e); individually, they vary in size but typically have depths and amplitudes <2 m, and they cover a distance of at least 2800 m (~980 km^2) of the lower slope of Jenkins Ridge. Further upslope, irregular, undulating surfaces superimposed by lobate ridges (convex downslope) are more common (Figure 2d and zoom in Figure 3f).

Farther south on the lower Jenkins Ridge flank (profile M434; Figure 2h) is imaged a series of spherical mounds protruding 1–3 m from the seafloor and with a maximum diameter of ~20 m (profile left of Figure 3h). Each mound is fringed by crescent-shaped ridges 1–1.5 m in amplitude. A pair of subtle, parallel, linear scours also occurs in close proximity to these boulders (Figure 3h). They have a mean spacing of 49 m, amplitudes of <1 m, and lengths up to 650 m, and occur at depths of 950–970 m. The scours trend east-west as opposed to the more typical southeast-northwest direction of streamlined bedform features observed seaward in Zone 1 (rose diagram right of Figure 3h).

Near to the top of Jenkins Ridge's seaward flank, where the headroom between the former ice-shelf base and seafloor narrows, a set of seafloor lineations is also observed, exhibiting orientations in line with modern ice flow vectors (Figure 2d and zoom in Figure 3g). The lineations have spacings of 19–36 m (mean 26 m), amplitudes of <1 m, and lengths up to 600 m. They are located 2.5 km west of sediment cores that date ungrounding of the ice shelf from Jenkins Ridge to 1970 ± 4 years (Figure 2a) [*Smith et al.*, 2017].

4.2.2. Sub-Bottom Profiler

The transition between Zones 1 and 2 is marked by a change in the character of the seafloor acoustics from a rugged interface with some subsurface structure to an acoustically transparent unit with a diffuse seabed reflector (Figure 4d). The seabed within this zone is predominantly smooth with some small-scale lobes or mounds up to ~3 m in amplitude (Figure 4e).

4.3. Zone 3: Jenkins Ridge Crest

4.3.1. Seafloor Bathymetry

Only profile M434 provides data from Zone 3: the AUV imaged data along an ~8 km long strip broadly along paleo-ice flow, and a ~13 km long strip along the southern half of Jenkins Ridge crest trending broadly orthogonal to current ice-shelf flow (Figure 2f). Along the entire Jenkins Ridge crest the predominant geomorphological feature comprises streamlined lineations oriented parallel to inferred paleo-ice flow (Figures 3i and 3j). A change in the metrics of these lineations is clearly evident ~6 km along the profile (north to south), coinciding with a sharp rise in seafloor elevation from a mean of −730 m to −708 m (Figure 5a). In the northern section, closer to the central flow axis of PIGIS, the lineations have a mean spacing of 287 m and mean amplitude of 7.3 m; in the southern section they have a mean spacing of 46 m and a mean amplitude of 1.4 m (Figures 5b and 5c). Furthermore, along the southern section of Jenkins Ridge crest, not all the lineations are parallel to one another, and occasionally, they appear to crosscut or converge (magnified panel in Figure 3j).

The surface characterized by lineations that we have just described is overprinted by finer-scale features. These include submeter amplitude curvilinear sediment ridges that are convex in the direction of paleo-ice flow and have spacing of 26–90 m (mean 43 m) (left-hand zooms in Figure 3i). The curvilinear ridges initiate at the bases of lineation troughs and terminate at the apexes of their crests. Curvilinear ridges of this scale and character have not, to our knowledge, been observed elsewhere in glacial settings. Erosional scours with troughs up to 7 m deep also occur at the crests of some lineations and terminate in small-scale asymmetric berms (right-hand zooms in Figure 3i).

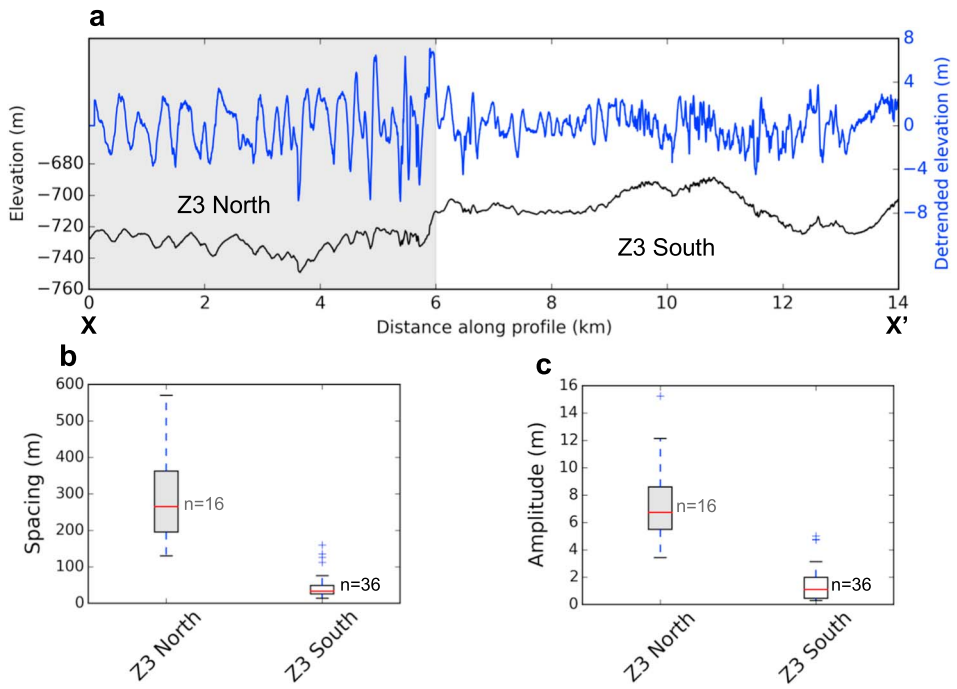

Figure 5. Landform metrics of Jenkins Ridge crest. (a) Topographic profile of seafloor elevation across the crest of Jenkins Ridge (Zone 3). Blue line shows detrended seafloor topography. Grey shaded area shows the region defined as Z3 north based on a change in landform metrics. (b, c) Box and whisker plots showing the median, lower and upper quartiles, and standard deviation of lineation spacing and amplitude of 52 lineations sampled across the ridge crest. A summary of statistics is presented in Table 1 in text.

4.3.2. Sub-Bottom Profiler

A 20 km section of profiler data from mission M448 trending southwest to northeast crossed the crest of Jenkins Ridge (Figure 4f). The ridge surface is characterized by an undulating high-amplitude seafloor reflector (Figure 4f). Smaller-scale ridges with a mean amplitude of 4 m are superimposed on this surface and have a similar cross-sectional profile to the seabed of survey M434 in Zone 3 (Figure 5a).

4.4. Zone 4: PIGIS Sub-Ice-Shelf Cavity

4.4.1. Sub-Bottom Profiler

The morphology and acoustic character of the reverse slope of Jenkins Ridge in the sub-ice-shelf cavity are similar to those of the seaward slope in Zone 2, although there is no evidence for mass movement deposits on this side of the ridge. At the easternmost limit of the survey, approximately 15 km seaward of the grounding line, a series of ridges with asymmetric cross-sectional profiles, ranging between ~7 and 28 m in amplitude, are imaged (Figure 4i). A series of shorter wavelength, lower amplitude, regularly spaced ridges caps the crest of the largest of these asymmetric ridges (Figures 4i and 4j).

5. Discussion

5.1. Interpretation of Bedforms and Sediment Properties

From the combined evidence presented above from beneath PIGIS, we identify three distinct components of the sub-ice-shelf landsystem that we associate with (1) grounded ice flow, (2) lightly grounded ice flow, and (3) postglacial deposition. Synthesized maps of bed form interpretations presented alongside the multibeam data in Figure 2 provide a useful reference for this discussion.

5.1.1. Grounded Ice Bedforms

We interpret a suite of bedforms in Zones 1, 3, and 4 as resulting from subglacial erosion, sediment deposition, and meltwater flow beneath grounded ice. Due to their curvilinear cross-sectional profiles, steep-sided channels in Zone 1 (Figures 3c and 3d) are interpreted as relict subglacial meltwater channels eroded into the substrate when more advanced ice was grounded here during one or more earlier glacial phases [cf. *Wellner et al.*, 2006; *Nitsche et al.*, 2013]. The irregular surface depressions in Figure 3c bear resemblance to hill-hole

Table 1. Summary Statistics of Lineations in Zone 3 Compared to Previously Published Metrics of Mega-Scale Glacial Lineations and Flutes

	Z3 North Lineations (This Study) $n = 16$	Z3 South Lineations (This Study) $n = 36$	MSGL [*Spagnolo et al.*, 2014] $n = 4043$	Flutes [*Ely et al.*, 2017] $n = 88$
		Spacing (m)		
Minimum	129.8	13.6	-	-
Maximum	569.7	159.8	-	-
Mean	287.2	46.3	458	-
Median	265.0	32.8	330	-
Standard Deviation	121.7	34.8	-	-
		Amplitude (m)		
Minimum	3.4	0.2	-	0.02
Maximum	15.2	5.0	-	0.3
Mean	7.3	1.4	4	0.01
Median	6.7	1.0	3	-
Standard Deviation	3.0	1.2	-	0.07

pairs observed in bathymetric data in the Norwegian Channel where they are thought to represent the imprint of sediment slabs that froze onto the glacier sole and were removed/displaced [*Ottesen et al.*, 2016]. However, if the surface depressions in Figure 3c are similarly interpreted as hill-hole pairs, their estimated volumes are an order of magnitude smaller than those observed in the Norwegian Channel. Flat-topped mounds (Figure 3d), which we interpret as glacitectonic rafts [*Andreassen et al.*, 2004; *Rüther et al.*, 2013, 2016], are most likely related to a displacing process similar to that which caused the formation of the hill-hole pairs. Because freeze-on is predominantly associated with thin ice (<1 km) close to the glacier margin [*Moran et al.*, 1980; *Alley et al.*, 1997], it is likely that these features were formed when the grounding line was located nearby, and before it became pinned to the crest of Jenkins Ridge.

Ubiquitous lineations on the crest of Jenkins Ridge (Zone 3; Figures 2f, and 3i and 3j (multibeam imaging) and 4f (sub-bottom profiling)) are also the result of formerly grounded ice flow. To the north, their amplitude and spacing are consistent with dimensions of mega-scale glacial lineations (MSGL) [*Clark*, 1993; *Spagnolo et al.*, 2014] (Table 1). Although we are unable to determine the lengths of these individual bedforms from our data set, a section of bathymetry data along flow described by *Graham et al.* [2013] captured two lineations with lengths of at least 1800 m. This implies elongation lengths of at least 9:1 and probably greater, a characteristic of elongated streamlined bedforms described beneath both paleo and modern ice streams [*King et al.*, 2009; *Spagnolo et al.*, 2014]. Ridges parallel to paleo-ice flow imaged in sub-bottom-profiler data over the crest of Jenkins Ridge (Figure 4g) have comparable amplitudes to ridges observed in the bathymetric data. Although it is not possible to determine their three-dimensional morphology, it is likely they are a continuation of MSGL identified in the northern section of Zone 3 (Figure 3i). To the south, linear bedforms on Jenkins Ridge have a much shorter wavelength and reduced amplitude intermediate between MSGL and flutes (Table 1 and Figure 5). We consider this change in metrics to be related to a change in till strength or thickness toward the margin of the ice stream trough.

Four asymmetric ridges oriented across former flow in Zone 4 with amplitudes of 5–20 m (Figures 4h and 4i) are morphologically similar to small retreat moraines and back-stepping grounding zone wedges (GZWs) observed on the seafloor in the Ross Sea [*Halberstadt et al.*, 2016; *Simkins et al.*, 2016]. Their location close to the modern grounding line suggests that these features were formed in the last 40–70 years through sediment deposition during a series of pauses in grounding-line retreat. Multibeam coverage is needed to verify these observations, but, if our interpretation is correct, this indicates the rate of grounding-line retreat has not been constant since ungrounding from Jenkins Ridge. Sub-bottom reflectors dipping at angles greater than the seabed surface slope are also evident on the landward slope of the largest asymmetric ridge, suggesting a sediment history is preserved in the cavity close to the grounding line (Figure 4i).

5.1.2. Lightly Grounded Ice Bedforms

On Jenkins Ridge crest, we interpret the ridges and scours that overprint MSGL (zooms in Figure 3i) as forming by sediment squeezing of lightly grounded ice-shelf keels, modulated by tidal motion as suggested by *Graham et al.* [2013]. Some corrugation ridges with amplitudes between 0.5 and 2 m have been imaged ~360 km northwest of the grounding line in Pine Island Trough [*Jakobsson et al.*, 2011] and in the Ross Sea [*Shipp et al.*, 1999; *Anderson et al.*, 2014; *Halberstadt et al.*, 2016]; the potential corrugation ridges on Jenkins Ridge have amplitudes <1 m with spacing and amplitude varying along the ridge crest (zooms in Figure 3j). This may be related to variable ice-keel morphology as identified by multibeam observations of basal terraces beneath PIGIS [*Dutrieux et al.*, 2014b]. However, substantial sub-ice-shelf melting since ungrounding from Jenkins Ridge will have altered the basal morphology of the ice shelf compared with the formerly grounded ice keels. This prohibits any direct comparison between corrugation and sub-ice shelf morphology.

The scours (right-hand zooms in 3i) are comparable to iceberg plow marks observed in water depths in excess of 700 m on the continental shelf and interpreted to have been caused by incision of iceberg keels where they contact the sea floor [*Dowdeswell and Bamber*, 2007; *Gales et al.*, 2016]. For iceberg keels to be the mechanism of formation here would require the crest of Jenkins Ridge to have been subjected to grounding of free floating icebergs at some point since ungrounding of PIGIS in the 1970s. However, remote sensing imagery shows PIGIS has remained intact throughout this period. We therefore favor forward plowing of ice-shelf keels as the most likely mechanism for their formation. The alignment of scours parallel to the direction of present ice-shelf flow also supports this. Terminal berms associated with these scours (zoom in Figure 3i) are likely to have been created when ice-shelf keels that were last in contact with the crest of Jenkins Ridge became ungrounded.

5.1.3. Postglacial Processes

Postglacial deposition is evident in the most distal regions from the current grounding line. In Zone 1, contrasting stratified reflectors in sub-bottom-profiler data are interpreted as alternations between coarse-grained ice-rafted/ice-shelf basal debris and fine-grained hemipelagic sediments from meltwater plumes [cf. *Damuth*, 1978; *Batchelor et al.*, 2011; *Rebesco et al.*, 2011; *Hogan et al.*, 2012].

Bedforms on the seaward flank of Jenkins Ridge in Zone 2 are dominated by postglacial slope processes. Dendritic channels and ridges are morphologically characteristic of sediment-gravity flows commonly observed in trough-mouth fan (TMF) and continental-shelf break settings [*Dowdeswell et al.*, 1998; *Vorren et al.*, 1998; *Dowdeswell et al.*, 2004; *Amblas et al.*, 2006] and on the distal flanks of submarine terminal moraine ridges in fjord settings [*Ottesen and Dowdeswell*, 2006; *Dowdeswell et al.*, 2016]. We interpret the lobate, curvilinear ridges on the seaward flank of Jenkins Ridge (zoom in Figure 3f) as submarine debris flows, also observed on continental margin slopes and ice-distal flanks of submarine moraine ridges, based on the presence of clear depositional sediment fronts and crosscutting lobes on the flank. Where debris flows are observed, slope angles are very shallow (<2°), yet they have a runout distance of over a kilometer. In shallow-slope settings, the ability of debris flows to achieve long runout distances is considered possible through high-sediment-volume, low-viscosity behavior and excess sediment pore water pressure [*Laberg and Vorren*, 1996; *Vorren et al.*, 1998]. Sediment samples obtained from TMF settings typically contain a range of glacigenic sediments, consisting of muddy diamict, sands, and gravels often with low shear strength and high water content. These properties reflect sediment delivery by subglacial deformation, ice rafting, and meltwater deposition in sediment-laden plumes [*Kuvaas and Kristoffersen*, 1991; *Hambrey et al.*, 1992; *Laberg and Vorren*, 1996; *Dowdeswell et al.*, 2004]. Ice streaming over erodible, soft sedimentary beds has been suggested to be a prerequisite for the formation of TMFs [*Cofaigh et al.*, 2003]. High volumes of sediments suggested by debris flow deposits in Zone 2 therefore indicate the presence of a soft bed upstream of Jenkins Ridge.

The spherical mounds imaged in Zone 2 (Figure 3k) are tentatively interpreted as subglacially sourced boulders. Their dimensions (1–3 m in height and up to ~20 m in width) are large but within the upper limit of scales observed and considered theoretically possible to be transported subglacially [*Weertman*, 1958]. Crescent-shaped ridges bordering the boulders may have formed either by postglacial accumulation of sediment during downslope sediment flow or "bulldozing" by the impact of the boulders striking the seabed following release from the base of the ice shelf. Adjacent linear scours (Figure 3k) may have formed during debris avalanching down the ridge flank or could also be grounded ice bedforms partially buried by proglacial sediments.

5.1.4. Bedforms of Unknown Genesis

The curvilinear ridges superimposed onto MSGLs in Zone 3 (left-hand zoom in Figure 3i) extend transversally for about half the wavelength of the MSGLs, i.e., 300 m, from the trough of a MSGL to its crest. These ridges may be remnants of small-scale recessional moraines or, alternatively, they may have formed by the lateral flow of a viscous basal-ice layer between MSGL troughs and crests during grounded-ice flow [*Schoof and Clarke*, 2008], or by postglacial current reworking of fine-grained surficial sediments.

Interpreting the genesis of the corrugation ridges overprinting the potential GZWs in Zone 4 (Figure 4i) is also challenging. Formation by ephemeral grounding of sub-ice-shelf keels requires corrugation ridges to form on the lee slope of the potential GZW without scouring away its crest. It seems unlikely this would be possible through forward advection of ice keels. Squeezing of sediment ridges during grounding-line retreat could explain their location, but the surfaces of these corrugations have a weak acoustic signal in comparison to acoustic observations of recessional moraines in other studies [e.g., *Halberstadt et al.*, 2016]. Another possible mode of formation is through squeezing of sediment by basal crevasses. Regularly spaced basal crevasses have been observed beneath the Larsen C [*Luckman et al.*, 2012] and Ross Ice Shelves [*Jezek and Bentley*, 1983; *Anandakrishnan et al.*, 2007]; however, they typically have spacings at least an order of magnitude greater than the spacing of corrugations in Zone 3 (Figure 4i). Acquisition of multibeam data in this region would enable a better assessment of their morphology and mode of formation.

5.2. Synthesis and Implications

5.2.1. Key Observations of the Sub-Ice-Shelf Environment

The data interpreted above provide an unprecedented view of an ice-stream bed that has been deglaciated within the past century. Based on our survey of the terrain, a number of important observations can be made that contribute to our wider understanding of these environments and to PIG specifically:

1. Sediment delivery from basal transport has played a key role in shaping each of the zones from the ice-shelf front to the modern grounding line. Our results suggest meltwater plumes and rainout have been important to the accumulation of ice-distal sediments in small basins seaward of the ice shelf. Indeed, observations through Zones 2–4 demonstrate that till deposition and secondary reworking of till (via mass movement to produce debris flows) are the dominant sediment-producing and landform-generating processes in this recently deglaciated cavity.
2. Beneath PIGIS, changes in bed properties, specifically contrasting scales of lineations, occur abruptly over limited geographic areas of the bed (Figure 5). This finding supports the relatively small number of ice-stream bed studies that have presented similar evidence for highly variable basal conditions beneath Antarctic ice streams [e.g., *Smith and Murray*, 2009; *Smith et al.*, 2013]. However, rather than showing zones of stiff till with no bedforms contrasting with zones of soft till with lineations [*King et al.*, 2009], we are able to show variability in bedforms within a region where sediment cores indicate the presence of deformable sediment [*Smith et al.*, 2017].
3. Grounding by sub-ice-shelf keels is a process that appears to produce significant features near the grounding zone (e.g., erosional scours). This process may be responsible for the appearance of converging lineations observed in regions of elevated seafloor (e.g., Figure 3j). These variations suggest a more mobile grounding situation in some parts of the ridge, such as might be expected in an ice-plain environment [*Corr et al.*, 2001].
4. Former ice-flow-oriented lineations on a scale intermediate between MSGL and flutes can form at the grounding zones of major ice streams and crosscutting generations at the margins preserve a record of localized flow variability.
5. The presence of glacitectonic rafts and emplaced boulders indicate that till deformation may not be the only sediment transport process in operation under West Antarctic ice streams and that plucking and rafting of large bedrock/sediment blocks contributes to erosion beneath PIG.
6. The landform mapping presented in this study shows a transition from bedrock outcrops in Zone 1 to sediment bedforms and deposits in Zone 2 broadly coincident with the crystalline to sedimentary bed transition inferred from aerogravity surveys [*Muto et al.*, 2013, 2016]. These surveys inferred a thick sedimentary basin extending upstream of the grounding line that would provide an abundant source for sediments deposited as mass flows, MSGL, and GZWs in Zones 2–4. These observations indicate that Jenkins Ridge marks a transition between hard, resistant crystalline bedrock to more erodible, soft sedimentary bed upstream of the present-day grounding line [*Brisbourne et al.*, 2017]. Such transitions have been observed farther seaward

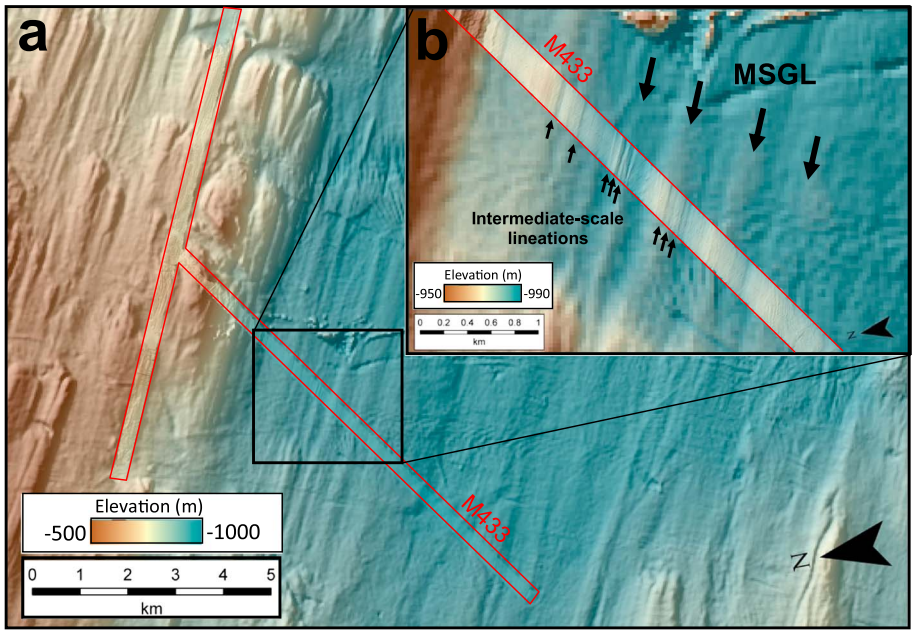

Figure 6. Comparison of offshore swath bathymetry and Autosub3 multibeam bathymetry. (a) The 35 m resolution swath sonar bathymetry of Pine Island Bay acquired offshore seaward of PIGIS (data from *Nitsche et al.* [2013]) overlain by Autosub3 bathymetry from Mission M433 at 2 m resolution (red polygon). (b) Magnified image showing the difference in detail between data sets. Large black arrows mark the locations of MSGL visible on both the offshore swath sonar and Autosub3 multibeam bathymetry, and small black arrows denote intermediate-scale lineations only visible on the Autosub3 bathymetry data. Location of data extent is shown in Figure 1a.

on the continental shelf and associated with contrasts in the distribution of sediment and character of geomorphic features [*Lowe and Anderson*, 2002; *Wellner et al.*, 2001, 2006; *Graham et al.*, 2009].

5.2.2. Observations of Fine-Scale Bedforms: Preservation or Data Resolution?

High-resolution imaging of the seafloor beneath PIGIS reveals a complex pattern of landforms indicative of a highly dynamic environment. We have identified seldom observed fine-scale submarine landforms, namely, curvilinear sediment ridges, intermediate-scale lineations, and small-scale hill-hole pairs. With the exception of lineations, these landforms are interpreted as reworked subglacial bedforms, sculpted into their present form by overriding of the ice margin and sub-ice-shelf keels during retreat of the grounding line. We consider the ability to detect these features is a factor of (1) the youth of the sub-ice-shelf landscape and (2) the high resolution of the data compared to offshore swath bathymetric surveying.

Smith et al. [2017] calculated sedimentation rates on the crest of Jenkins Ridge (Zone 3) of 0.82–0.95 mm a^{-1}. These rates are too low to have buried the fine-scale features such as curvilinear sediment ridges and submeter-amplitude lineations since ungrounding from the ridge crest in 1940. Farther seaward on the continental shelf, features of this scale may not be as well preserved having been exposed to marine sedimentation for up to several millennia. However, deep-tow side-scan sonar surveys of the continental shelf have revealed fine-scale landforms such as flutes and corrugations ("washboard pattern") located near the continental-shelf break [*Lien et al.*, 1989; *Ship et al.*, 1999; *Shipp et al.*, 2002].

The identification of fine-scale features may therefore be primarily a factor of the ability to image the seafloor at submeter to meter-scale resolution. We demonstrate this in Figure 6 by conducting a crossover comparison between AUV and ship-based multibeam surveys in Pine Island Bay [*Nitsche et al.*, 2013], just seaward of PIGIS. This analysis reveals intermediate-scale lineations overprinting MSGL and demonstrates the preservation of fine-scale bedforms ~85 km in front of the modern grounding line (Figure 6). Our data indicate that there is likely a wealth of detailed information of glacial processes not captured by standard offshore marine geophysical surveys. Recent work by *García et al.* [2016] using a remotely operated underwater vehicle also illustrates the level of detail obtained using these methods. Further targeted AUV/ROV surveys beneath ice shelves and on the continental shelf would provide useful information on bedform preservation and may elucidate processes related to some of the more enigmatic landforms observed beneath PIGIS.

6. Conclusions

We have used high-resolution bathymetry and sub-bottom-profiler data obtained by AUV surveys to explore the nature of seafloor bedforms and sediment properties beneath a recently ungrounded Antarctic ice shelf. These data reveal fine-scale landforms in a dynamic environment modified by subglacial erosion, meltwater flow, and sediment deposition, providing an unprecedented view of a recently deglaciated ice-stream bed.

The landscape and sediments we have imaged beneath Pine Island Glacier Ice Shelf record features of direct subglacial erosion and deposition, and postglacial modification by overriding and scouring of ice-shelf keels and gravity-driven slope processes. Seaward of Jenkins Ridge the landscape of streamlined bedrock outcrops is characteristic of direct subglacial erosion with little postglacial modification. In this landscape, ice-rafted boulders, hill-hole pairs, and glacitectonic rafts indicate that freeze-on and plucking of basal material is a significant component of erosion and sediment transport. Upstream over Jenkins Ridge and into the sub-ice-shelf cavity, the landscape is draped by sediments which evince both direct glacial deposition and deformation, and postglacial modification. This sediment distribution supports Jenkins Ridge having been a stable grounding line location for a significant period prior to its twentieth-century ungrounding.

We have demonstrated the value of imaging recently deglaciated terrain at meter-scale resolution. The insights we have provided through the analysis of fine-scale landforms would not have been achievable without the capability to observe features in recently deglaciated terrain at meter-scale resolution using an AUV platform. Such landforms are likely to be rapidly modified by postglacial sedimentation or are not readily observable in coarser resolution swath bathymetry data sets.

We recommend further AUV missions to sub-ice-shelf cavities to enable a better understanding of recent controls on ice stream retreat and sub-ice-shelf processes. Surveys of selected offshore regions previously covered by offshore swath bathymetry surveys would also provide a clearer picture of past ice-stream stability and retreat.

Acknowledgments

This work was supported by funding from the UK Natural Environment Research Council (NERC) iSTAR Programme grants NE/J005665/2 and NE/J005770/1 and NERC grant NE/G001367/1. D.D. was supported by NERC Training grant NE/K011189/1. F.O.N. was supported by NSF grant ANT-838735. M.S. was supported by NERC grant NE/J004766/1. We thank the Autosub technical teams led by Steve McPhail and the Captain and cruise participants of RRS *James Clark Ross* cruise JR294/295 and RVIB *Nathaniel B. Palmer* cruise NBP09-01 for conducting the AUV operations. We thank Julian Dowdeswell and two anonymous reviewers for constructive reviews which improved the clarity of the manuscript. Data used in this article can be obtained from the UK Polar Data Centre and the iSTAR programme web-GIS repository gis.istar.ac.uk.

References

Alley, R., K. Cuffey, E. Evenson, J. Strasser, D. Lawson, and G. Larson (1997), How glaciers entrain and transport basal sediment: Physical constraints, *Quat. Sci. Rev.*, *16*(9), 1017–1038, doi:10.1016/S0277-3791(97)00034-6.

Amblas, D., R. Urgeles, M. Canals, A. M. Calafat, M. Rebesco, A. Camerlenghi, F. Estrada, M. De Batist, and J. E. Hughes-Clarke (2006), Relationship between continental rise development and palaeo-ice sheet dynamics, Northern Antarctic Peninsula Pacific margin, *Quat. Sci. Rev.*, *25*(9), 933–944, doi:10.1016/j.quascirev.2005.07.012.

Anandakrishnan, S., G. a. Catania, R. B. Alley, and H. J. Horgan (2007), Discovery of till deposition at the grounding line of Whillans Ice Stream, *Science*, *315*(5820), 1835–1838, doi:10.1126/science.1138393.

Anderson, J. B., S. S. Shipp, A. L. Lowe, J. S. Wellner, and A. B. Mosola (2002), The Antarctic ice sheet during the Last Glacial Maximum and its subsequent retreat history: A review, *Quat. Sci. Rev.*, *21*(1–3), 49–70.

Anderson, J. B., et al. (2014), Ross Sea paleo-ice sheet drainage and deglacial history during and since the LGM, *Quat. Sci. Rev.*, *100*, 31–54, doi:10.1016/j.quascirev.2013.08.020.

Andreassen, K., L. C. Nilssen, B. Rafaelsen, and L. Kuilman (2004), Three-dimensional seismic data from the Barents Sea margin reveal evidence of past ice streams and their dynamics, *Geology*, *32*(8), 729–732.

Batchelor, C. L., J. A. Dowdeswell, and K. A. Hogan (2011), Late Quaternary ice flow and sediment delivery through Hinlopen Trough, Northern Svalbard margin: Submarine landforms and depositional fan, *Mar. Geol.*, *284*(1–4), 13–27, doi:10.1016/j.margeo.2011.03.005.

Bingham, R. G., F. Ferraccioli, E. C. King, R. D. Larter, H. D. Pritchard, A. M. Smith, and D. G. Vaughan (2012), Inland thinning of West Antarctic ice sheet steered along subglacial rifts, *Nature*, *487*(7408), 468–471.

Brisbourne, A. M., A. M. Smith, D. G. Vaughan, E. C. King, D. Davies, R. G. Bingham, E. C. Smith, I. J. Nias, and S. H. R. Rosier (2017), Bed conditions of Pine Island Glacier, West Antarctica, *J. Geophys. Res. Earth Surf.*, *122*, 419–433, doi:10.1002/2016JF004033.

Clark, C. D. (1993), Mega-scale glacial lineations and cross-cutting ice-flow landforms, *Earth Surf. Processes Landforms*, *18*(1), 1–29, doi:10.1002/esp.3290180102.

Corr, H. F. J., C. S. M. Doake, A. Jenkins, and D. G. Vaughan (2001), Investigations of an "ice plain" in the mouth of Pine Island Glacier, Antarctica, *J. Glaciol.*, *47*(156), 51–57, doi:10.3189/172756501781832395.

Damuth, J. E. (1978), Echo character of the Norwegian-Greenland Sea: Relationship to quaternary sedimentation, *Mar. Geol.*, *28*(1–2), 1–36, doi:10.1016/0025-3227(78)90094-4.

Domack, E., et al. (2005), Stability of the Larsen B ice shelf on the Antarctic Peninsula during the Holocene Epoch, *Nature*, *436*(7051), 681–685.

Dowdeswell, J., and J. Bamber (2007), Keel depths of modern Antarctic icebergs and implications for sea-floor scouring in the geological record, *Mar. Geol.*, *243*(1–4), 120–131, doi:10.1016/j.margeo.2007.04.008.

Dowdeswell, J., A. Elverhøi, and R. Spielhagen (1998), Glacimarine sedimentary processes and facies on the polar North Atlantic margins, *Quat. Sci. Rev.*, *17*(1), 243–272, doi:10.1016/S0277-3791(97)00071-1.

Dowdeswell, J., C. Ó. Cofaigh, and C. Pudsey (2004), Continental slope morphology and sedimentary processes at the mouth of an Antarctic palaeo-ice stream, *Mar. Geol.*, *204*(1), 203–214, doi:10.1016/S0025-3227(03)00338-4.

Dowdeswell, J. A., et al. (2008), Autonomous underwater vehicles (AUVs) and investigations of the ice-ocean interface in Antarctic and Arctic waters, *J. Glaciol.*, *54*(187), 661–672, doi:10.3189/002214308786570773.

Dowdeswell, J. A., D. Ottesen, and L. Plassen (2016), Debris-flow lobes on the distal flanks of terminal moraines in Spitsbergen fjords, *Geol. Soc. London Mem.*, *46*(1), 77–78, doi:10.1144/M46.97.

Dupont, T. K., and R. B. Alley (2005), Assessment of the importance of ice-shelf buttressing to ice-sheet flow, *Geophys. Res. Lett.*, *32*, L04503, doi:10.1029/2004GL022024.
Dutrieux, P., J. De Rydt, A. Jenkins, P. R. Holland, H. K. Ha, S. H. Lee, E. J. Steig, Q. Ding, E. P. Abrahamsen, and M. Schröder (2014a), Strong sensitivity of Pine Island ice-shelf melting to climatic variability, *Science*, *343*(6167), 174–178.
Dutrieux, P., C. Stewart, A. Jenkins, K. W. Nicholls, H. F. J. Corr, E. Rignot, and K. Steffen (2014b), Basal terraces on melting ice shelves, *Geophys. Res. Lett.*, *41*, 5506–5513, doi:10.1002/2014GL060618.
Ely, J. C., C. Graham, I. D. Barr, B. R. Rea, M. Spagnolo, and J. Evans (2017), Using UAV acquired photography and structure from motion techniques for studying glacier landforms: Application to the glacial flutes at Isfallsglaciären, *Earth Surf. Process. Landforms*, *42*, 877–888, doi:10.1002/esp.4044.
Fürst, J. J., G. Durand, F. Gillet-chaulet, L. Tavard, M. Rankl, M. Braun, and O. Gagliardini (2016), The safety band of Antarctic ice shelves, *6*(May), 2014–2017, doi:10.1038/NCLIMATE2912.
Gales, J. A., R. D. Larter, and P. T. Leat (2016), Iceberg ploughmarks and associated sediment ridges on the southern Weddell Sea margin, *Geol. Soc. London Mem.*, *46*(1), 289–290, doi:10.1144/M46.11.
García, M., J. A. Dowdeswell, R. Noormets, K. Hogan, J. Evans, C. Ó. Cofaigh, and R. D. Larter (2016), Geomorphic and shallow-acoustic investigation of an Antarctic Peninsula fjord system using high-resolution ROV and shipboard geophysical observations: Ice dynamics and behaviour since the Last Glacial Maximum, *Quat. Sci. Rev.*, *153*, 122–138.
Graham, A. G. C., R. D. Larter, K. Gohl, C.-D. Hillenbrand, J. A. Smith, and G. Kuhn (2009), Bedform signature of a West Antarctic palaeo-ice stream reveals a multi-temporal record of flow and substrate control, *Quat. Sci. Rev.*, *28*(25-26), 2774–2793.
Graham, A. G. C., R. D. Larter, K. Gohl, J. A. Dowdeswell, C.-D. Hillenbrand, J. A. Smith, J. Evans, G. Kuhn, and T. Deen (2010), Flow and retreat of the Late Quaternary Pine Island-Thwaites palaeo-ice stream, West Antarctica, *J. Geophys. Res.*, *115*, F03025, doi:10.1029/2009JF001482.
Graham, A. G. C., P. Dutrieux, D. G. Vaughan, F. O. Nitsche, R. Gyllencreutz, S. L. Greenwood, R. D. Larter, and A. Jenkins (2013), Seabed corrugations beneath an Antarctic ice shelf revealed by autonomous underwater vehicle survey: Origin and implications for the history of Pine Island Glacier, *J. Geophys. Res. Earth Surf.*, *118*, 1356–1366, doi:10.1002/jgrf.20087.
Halberstadt, A. R. W., L. M. Simkins, S. L. Greenwood, and J. B. Anderson (2016), Past ice-sheet behaviour: Retreat scenarios and changing controls in the Ross Sea, Antarctica, *Cryosphere*, *10*(3), 1003–1020, doi:10.5194/tc-10-1003-2016.
Hambrey, M. J., W. U. Ehrmann, and B. Larsen (1992), *Cenozoic Glacial Record of the Prydz Bay Continental Shelf, East Antarctica*, Geological Survey in Denmark.
Hillenbrand, C.-D., et al. (2017), West Antarctic Ice Sheet retreat driven by Holocene warm water incursions, *Nature*, *547*(7661), 43–48.
Hogan, K. A., J. A. Dowdeswell, and C. Ó. Cofaigh (2012), Glacimarine sedimentary processes and depositional environments in an embayment fed by West Greenland ice streams, *Mar. Geol.*, *311–314*, 1–16, doi:10.1016/j.margeo.2012.04.006.
Hurst, M. D., S. M. Mudd, R. Walcott, M. Attal, and K. Yoo (2012), Using hilltop curvature to derive the spatial distribution of erosion rates, *J. Geophys. Res.*, *117*, F02017, doi:10.1029/2011JF002057.
Jacobs, S. S., H. H. Hellmer, and A. Jenkins (1996), Antarctic ice sheet melting in the southeast Pacific, *Geophys. Res. Lett.*, *23*(9), 957–960, doi:10.1029/96GL00723.
Jacobs, S. S., A. Jenkins, C. F. Giulivi, and P. Dutrieux (2011), Stronger ocean circulation and increased melting under Pine Island Glacier ice shelf, *Nat. Geosci.*, *4*, 519–523.
Jakobsson, M., et al. (2011), Geological record of ice shelf break-up and grounding line retreat, Pine Island Bay, West Antarctica, *Geology*, *39*(7), 691–694, doi:10.1130/G32153.1.
Jenkins, A., P. Dutrieux, S. S. Jacobs, S. D. McPhail, J. R. Perrett, A. T. Webb, and D. White (2010), Observations beneath Pine Island Glacier in West Antarctica and implications for its retreat, *Nat. Geosci.*, *3*, 468–472.
Jezek, K. C., and C. R. Bentley (1983), Field studies of bottom crevasses in the Ross Ice Shelf, Antarctica, *J. Glaciol.*, *29*(101), 118–126.
Jordan, T. A., F. Ferraccioli, D. G. Vaughan, J. W. Holt, H. Corr, D. D. Blankenship, and T. M. Diehl (2009), Aerogravity evidence for major crustal thinning under the Pine Island Glacier region (West Antarctica), *Geol. Soc. Am. Bull.*, *122*(5–6), 714–726.
Joughin, I., D. E. Shean, B. E. Smith, and P. Dutrieux (2016), Grounding line variability and subglacial lake drainage on Pine Island Glacier, Antarctica, *Geophys. Res. Lett.*, *43*, 9093–9102, doi:10.1002/2016GL070259.
King, E. C., R. C. A. Hindmarsh, and C. R. Stokes (2009), Formation of mega-scale glacial lineations observed beneath a West Antarctic ice stream, *Nat. Geosci.*, *2*, 585–588.
Konrad, H., L. Gilbert, S. L. Cornford, A. Payne, A. Hogg, A. Muir, and A. Shepherd (2017), Uneven onset and pace of ice-dynamical imbalance in the Amundsen Sea Embayment, West Antarctica, *Geophys. Res. Lett.*, *44*, 910–918, doi:10.1002/2016GL070733.
Kuvaas, B., and Y. Kristoffersen (1991), The Crary Fan: A trough-mouth fan on the Weddell Sea continental margin, Antarctica, *Mar. Geol.*, *97*(3–4), 345–362.
Laberg, J., and T. O. Vorren (1996), Late Weichselian submarine debris flow deposits on the Bear Island Trough Mouth Fan, *Oceanogr. Lit. Rev.*, *43*(4), 368.
Lien, R., A. Solheim, A. Elverhøi, and K. Rokoengen (1989), Iceberg scouring and sea bed morphology on the eastern Weddell Sea shelf, Antarctica, *Polar Res.*, *7*(1), 43–57, doi:10.1111/j.1751-8369.1989.tb00603.x.
Lowe, A. L., and J. B. Anderson (2002), Reconstruction of the West Antarctic Ice Sheet in Pine Island Bay during the Last Glacial Maximum and its subsequent retreat history, *Quat. Sci. Rev.*, *21*(16–17), 1879–1897.
Luckman, A., D. Jansen, B. Kulessa, E. C. King, P. Sammonds, and D. I. Benn (2012), Basal crevasses in Larsen C Ice Shelf and implications for their global abundance, *The Cryosphere*, 113–123, doi:10.5194/tc-6-113-2012.
Lysså, A., B. Hjelstuen, and E. Larsen (2010), Fjord infill in a high-relief area: Rapid deposition influenced by deglaciation dynamics, glacio-isostatic rebound and gravitational activity, *Boreas*, *39*(1), 39–55, doi:10.1111/j.1502-3885.2009.00117.x.
McMillan, M., A. Shepherd, A. Sundal, K. Briggs, A. Muir, A. Ridout, A. Hogg, and D. Wingham (2014), Increased ice losses from Antarctica detected by CryoSat-2, *Geophys. Res. Lett.*, *41*, 3899–3905, doi:10.1002/2014GL060111.
McPhail, S. (2009), Autosub6000: A deep diving long range AUV, *J. Bionic Eng.*, *6*(1), 55–62, doi:10.1016/S1672-6529(08)60095-5.
McPhail, S. D., M. E. Furlong, M. Pebody, J. R. Perrett, P. Stevenson, A. Webb, and D. White (2009), *Exploring Beneath the PIG Ice Shelf With the Autosub3 AUV*, paper presented at Oceans 09–Europe, pp. 1–8, Bremen, Germany. doi:10.1109/OCEANSE.2009.5278170.
Moran, S., L. Clayton, R. Hooke, M. Fenton, and L. Andriashek (1980), Glacier-bed landforms of the prairie region of North America, *J. Glaciol.*, *25*(93), 457–476.
Mouginot, J., E. Rignot, and B. Scheuchl (2014), Sustained increase in ice discharge from the Amundsen Sea Embayment, West Antarctica, from 1973 to 2013, *Geophys. Res. Lett.*, *41*, 1576–1584, doi:10.1002/2013GL059069.
Muto, A., S. Anandakrishnan, and R. B. Alley (2013), Subglacial bathymetry and sediment layer distribution beneath the Pine Island Glacier ice shelf, West Antarctica, modeled using aerogravity and autonomous underwater vehicle data, *Ann. Glaciol.*, *54*(64), 27–32, doi:10.3189/2013AoG64A110.

Muto, A., L. E. Peters, K. Gohl, I. Sasgen, R. B. Alley, S. Anandakrishnan, and K. L. Riverman (2016), Subglacial bathymetry and sediment distribution beneath Pine Island Glacier ice shelf modeled using aerogravity and in situ geophysical data: New results, *Earth Planet. Sci. Lett.*, *433*, 63–75, doi:10.1016/j.epsl.2015.10.037.

Nicholls, K. W., et al. (2006), Measurements beneath an Antarctic ice shelf using an autonomous underwater vehicle, *Geophys. Res. Lett.*, *33*, L08612, doi:10.1029/2006GL025998.

Nitsche, F. O., K. Gohl, R. D. Larter, C.-D. Hillenbrand, G. Kuhn, J. A. Smith, S. Jacobs, J. B. Anderson, and M. Jakobsson (2013), Paleo ice flow and subglacial meltwater dynamics in Pine Island Bay, West Antarctica, *The Cryosphere*, *7*(1), 249–262.

Cofaigh, C. Ó., J. Taylor, J. A. Dowdeswell, and C. J. Pudsey (2003), Palaeo-ice streams, trough mouth fans and high-latitude continental slope sedimentation, *Boreas*, *32*(1), 37–55.

Ottesen, D., and J. Dowdeswell (2006), Assemblages of submarine landforms produced by tidewater glaciers in Svalbard, *J. Geophys. Res.*, *111*, F01016, doi:10.1029/2005JF000330.

Ottesen, D., C. R. Stokes, R. Bøe, L. Rise, O. Longva, T. Thorsnes, O. Olesen, T. Bugge, A. Lepland, and O. B. Hestvik (2016), Landform assemblages and sedimentary processes along the Norwegian Channel Ice Stream, *Sediment. Geol.*, *338*, 115–137, doi:10.1016/j.sedgeo.2016.01.024.

Paolo, F. S., H. A. Fricker, and L. Padman (2015), Volume loss from Antarctic ice shelves is accelerating, *Science*, *348*(6232), 327–331, doi:10.1126/science.aaa0940.

Park, J. W., N. Gourmelen, A. Shepherd, S. W. Kim, D. G. Vaughan, and D. J. Wingham (2013), Sustained retreat of the Pine Island Glacier, *Geophys. Res. Lett.*, *40*(10), 2137–2142, doi:10.1002/grl.50379.

Pritchard, H. D., S. R. Ligtenberg, H. A. Fricker, D. G. Vaughan, M. R. van den Broeke, and L. Padman (2012), Antarctic ice-sheet loss driven by basal melting of ice shelves, *Nature*, *484*(7395), 502–5.

Rebesco, M., et al. (2011), Deglaciation of the western margin of the Barents Sea Ice Sheet. A swath bathymetric and sub-bottom seismic study from the Kveithola Trough, *Mar. Geol.*, *279*(1-4), 141–147.

Rignot, E., D. G. Vaughan, M. Schmeltz, T. Dupont, and D. MacAyeal (2002), Acceleration of Pine Island and Thwaites Glaciers, West Antarctica, *Ann. Glaciol.*, *34*, 189–194, doi:10.3189/172756402781817950.

Rignot, E., J. L. Bamber, M. R. van den Broeke, C. Davis, Y. Li, W. J. van de Berg, and E. van Meijgaard (2008), Recent Antarctic ice mass loss from radar interferometry and regional climate modelling, *Nat. Geosci.*, *1*(2), 106–110.

Rignot, E., I. Velicogna, M. R. van den Broeke, A. Monaghan, and J. T. M. Lenaerts (2011), Acceleration of the contribution of the Greenland and Antarctic ice sheets to sea level rise, *Geophys. Res. Lett.*, *38*, L05503, doi:10.1029/2011GL046583.

Rignot, E., S. Jacobs, J. Mouginot, and B. Scheuchl (2013), Ice-shelf melting around Antarctica, *Science*, *341*(6143), 266–270, doi:10.1126/science.1235798.

Rignot, E., J. Mouginot, M. Morlighem, H. Seroussi, and B. Scheuchl (2014), Widespread, rapid grounding line retreat of Pine Island, Thwaites, Smith, and Kohler glaciers, West Antarctica, from 1992 to 2011, *Geophys. Res. Lett.*, *41*, 3502–3509, doi:10.1002/2014GL060140.

Rüther, D., K. Andreassen, and M. Spagnolo (2013), Aligned glaciotectonic rafts on the central Barents Sea seafloor revealing extensive glacitectonic erosion during the last deglaciation, *Geophys. Res. Lett.*, *40*, 6351–6355, doi:10.1002/2013GL058413.

Rüther, D. C., K. Andreassen, and M. Spagnolo (2016), Aligned glacitectonic rafts on the floor of the central Barents Sea, *Geol. Soc. London Mem.*, *46*(1), 189–190.

Schoof, C. G., and G. K. C. Clarke (2008), A model for spiral flows in basal ice and the formation of subglacial flutes based on a Reiner-Rivlin rheology for glacial ice, *J. Geophys. Res.*, *113*, B05204, doi:10.1029/2007JB004957.

Scott, J. B. T., G. H. Gudmundsson, A. M. Smith, R. G. Bingham, H. D. Pritchard, and D. G. Vaughan (2009), Increased rate of acceleration on Pine Island Glacier strongly coupled to changes in gravitational driving stress, *The Cryosphere*, *3*, 125–131, doi:10.5194/tc-3-125-2009.

Ship, S., J. Anderson, and E. Domack (1999), Late Pleistocene–Holocene retreat of the West Antarctic Ice-Sheet system in the Ross Sea: Part 1—Geophysical results, *Geol. Soc. Am. Bull.*, *111*(10), 1486–1516.

Shipp, S., J. Anderson, and E. Domack (1999), Late Pleistocene-Holocene retreat of the West Antarctic Ice-Sheet system in the Ross Sea: Part 1—Geophysical results, *Geol. Soc. Am. Bull.*, *111*(10), 1486–1516.

Shipp, S. S., J. S. Wellner, and J. B. Anderson (2002), Retreat signature of a polar ice stream: Sub-glacial geomorphic features and sediments from the Ross Sea, Antarctica, *Geol. Soc. Spec. Publ.*, *203*(1), 277–304, doi:10.1144/GSL.SP.2002.203.01.15.

Simkins, L. M., J. B. Anderson, and S. L. Greenwood (2016), Glacial landform assemblage reveals complex retreat of grounded ice in the Ross Sea, Antarctica, *Geol. Soc. London Mem.*, *46*(1), 353–356, doi:10.1144/M46.168.

Smith, A. M., and T. Murray (2009), Bedform topography and basal conditions beneath a fast-flowing West Antarctic ice stream, *Quat. Sci. Rev.*, *28*(7–8), 584–596.

Smith, A. M., T. A. Jordan, F. Ferraccioli, and R. G. Bingham (2013), Influence of subglacial conditions on ice stream dynamics: Seismic and potential field data from Pine Island Glacier, West Antarctica, *J. Geophys. Res. Solid Earth*, *118*, 1471–1482, doi:10.1029/2012JB009582.

Smith, J. A., et al. (2017), Sub-ice-shelf sediments record history of twentieth-century retreat of Pine Island Glacier, *Nature*, *541*(7635), 77–80, doi:10.1038/nature20136.

Smith, M. J., and C. D. Clark (2005), Methods for the visualization of digital elevation models for landform mapping, *Earth Surf. Processes Landforms*, *30*(7), 885–900.

Spagnolo, M., C. D. Clark, J. C. Ely, C. R. Stokes, J. B. Anderson, K. Andreassen, A. G. C. Graham, and E. C. King (2014), Size, shape and spatial arrangement of mega-scale glacial lineations from a large and diverse dataset, *Earth Surf. Processes Landforms*, *39*(11), 1432–1448, doi:10.1002/esp.3532.

Studinger, M., et al. (2010), Mapping pine island glacier's sub-ice cavity with airborne gravimetry, in *Fall Meeting Abstracts*, AGU, San Francisco, Calif.

Turner, J., A. Orr, G. H. Gudmundsson, A. Jenkins, R. G. Bingham, C.-D. Hillenbrand, and T. J. Bracegirdle (2017), Atmosphere-ocean-ice interactions in the Amundsen Sea Embayment, West Antarctica, *Rev. Geophys.*, *55*, 235–276, doi:10.1002/2016RG000532.

Vorren, T. O., J. S. Laberg, F. Blaume, J. A. Dowdeswell, N. H. Kenyon, J. Mienert, J. Rumohr, and F. Werner (1998), The Norwegian-Greenland Sea continental margins: Morphology and Late Quaternary sedimentary processes and environment, *Quat. Sci. Rev.*, *17*(1), 273–302, doi:10.1016/S0277-3791(97)00072-3.

Weertman, J. (1958), Transport of boulders by glaciers and ice sheets, *Int. Assoc. Sci. Hydrol. Bull.*, *3*(2), 44–44, doi:10.1080/02626665809493102.

Wellner, J., A. Lowe, S. Shipp, and J. Anderson (2001), Distribution of glacial geomorphic features on the Antarctic continental shelf and correlation with substrate: Implications for ice behavior, *J. Glaciol.*, *47*(158), 397–411, doi:10.3189/172756501781832043.

Wellner, J., D. Heroy, and J. Anderson (2006), The death mask of the Antarctic Ice Sheet: Comparison of glacial geomorphic features across the continental shelf, *Geomorphology*, *75*(1–2), 157–171, doi:10.1016/j.geomorph.2005.05.015.

Wingham, D. J., D. W. Wallis, and A. Shepherd (2009), Spatial and temporal evolution of Pine Island Glacier thinning, 1995–2006, *Geophys. Res. Lett.*, *36*, L17501, doi:10.1029/2009GL039126.

Wynn, R. B., et al. (2014), Autonomous underwater vehicles (AUVs): Their past, present and future contributions to the advancement of marine geoscience, *Mar. Geol.*, *352*, 451–468, doi:10.1016/j.margeo.2014.03.012.

Appendix D

Brisbourne *et al.* 2017 (JGR-Earth Surface)

AGU PUBLICATIONS

JGR

Journal of Geophysical Research: Earth Surface

RESEARCH ARTICLE
10.1002/2016JF004033

Key Points:
- Results from an extensive new seismic survey of the bed of Pine Island Glacier are presented
- Tributaries of Pine Island Glacier are underlain by widespread low-porosity dilated sediments
- Deep older deposits provide an abundant supply of sediment across the basin

Correspondence to:
A. M. Brisbourne,
aleisb@bas.ac.uk

Citation:
Brisbourne, A. M., A. M. Smith, D. G. Vaughan, E. C. King, D. Davies, R. G. Bingham, E. C. Smith, I. J. Nias, and S. H. R. Rosier (2017), Bed conditions of Pine Island Glacier, West Antarctica, *J. Geophys. Res. Earth Surf.*, *122*, 419–433, doi:10.1002/2016JF004033.

Received 21 JUL 2016
Accepted 18 NOV 2016
Accepted article online 22 NOV 2016
Published online 26 JAN 2017

©2016. American Geophysical Union. All Rights Reserved.

Bed conditions of Pine Island Glacier, West Antarctica

A. M. Brisbourne[1], A. M. Smith[1], D. G. Vaughan[1], E. C. King[1], D. Davies[2], R. G. Bingham[2], E. C. Smith[1], I. J. Nias[3], and S. H. R. Rosier[1]

[1]British Antarctic Survey, Natural Environment Research Council, Cambridge, UK, [2]School of GeoSciences, University of Edinburgh, Edinburgh, UK, [3]School of Geographical Sciences, University of Bristol, Bristol, UK

Abstract Although 90% of Antarctica's discharge occurs via its fast-flowing ice streams, our ability to project future ice sheet response has been limited by poor observational constraints on the ice-bed conditions used in numerical models to determine basal slip. We have helped address this observational deficit by acquiring and analyzing a series of seismic reflection profiles to determine basal conditions beneath the main trunk and tributaries of Pine Island Glacier (PIG), West Antarctica. Seismic profiles indicate large-scale sedimentary deposits. Combined with seismic reflection images, measured acoustic impedance values indicate relatively uniform bed conditions directly beneath the main trunk and tributaries, comprising a widespread reworked sediment layer with a dilated sediment lid of minimum thickness 1.5 ± 0.4 m. Beneath a slow-moving intertributary region, a discrete low-porosity sediment layer of 7 ± 3 m thickness is imaged. Despite considerable basal topography, seismic observations indicate that a till layer at the ice base is ubiquitous beneath PIG, which requires a highly mobile sediment body to maintain an abundant supply. These results are compatible with existing ice sheet models used to invert for basal shear stress: existing basal conditions upstream will not inhibit further rapid retreat of PIG if the high-friction region currently restraining flow, directly upstream of the grounding line, is breached. However, small changes in the pressure regime at the bed, as a result of stress reorganization following retreat, may result in a less-readily deformable bed and conditions which are less likely to maintain high ice-flow rates.

1. Introduction

Net mass loss from the Antarctic Ice Sheet is concentrated in the Amundsen Sea Embayment in West Antarctica [*Rignot et al.*, 2011b; *Shepherd et al.*, 2012]. Within this region lies Pine Island Glacier (PIG, Figure 1a), currently the largest single contributor to sea level rise in Antarctica [*Shepherd et al.*, 2012]. Thinning of PIG has been accelerating since the 1980s, and as a result it is currently responsible for 20% of ice discharge from the West Antarctic Ice Sheet (WAIS) and contributes ~0.12 mm yr^{-1} to sea level rise [*Medley et al.*, 2014; *Rignot et al.*, 2011b; *Wingham et al.*, 2009]. Ice-flow velocity at the grounding line increased by 34% between 1996 and 2006 [*Rignot et al.*, 2008]. Inland thinning rates are an order of magnitude lower than at the grounding line [*Wingham et al.*, 2009] although the response of the tributaries is not uniform [*McMillan et al.*, 2014; *Wingham et al.*, 2009].

The rapid changes in the ice streams of the Amundsen Sea Embayment are widely attributed to oceanographic perturbations. Incursion of relatively warm Circumpolar Deep Water beneath the ice shelves is held responsible for ice shelf thinning through melting of their undersides, in turn reducing the buttressing of upstream grounded ice and facilitating retreat of the grounding line [see *Alley et al.*, 2015, and references therein]. Analysis of a 28 year record of Landsat images by *Bindschadler* [2002] indicated that significant migration of the margins in the lower sections of PIG, and ice shelf thinning, was already underway in 1973. Retreat in the early 1970s to behind a submarine sill (Jenkins Ridge) has left the main trunk of PIG resting on a reverse-slope bed [*Jenkins et al.*, 2010]. The stability of this configuration may be critically dependent on buttressing, bedrock topography, and friction at the bed [*Nias et al.*, 2016; *Ritz et al.*, 2015]. Improved constraints on basal properties are therefore imperative to understand the future evolution of PIG. Similarly, the reliability of projections of the future response of PIG is governed in part by a better understanding of the nonuniform behavior of its tributaries. This variation is not simply determined by the gross basal topography; the main trunk of PIG and two of its tributaries lie in deep troughs, whereas ice flow in the remainder of the tributaries is less strongly correlated with bed topography (Figure 1b). As summarized by *Peters et al.* [2006],

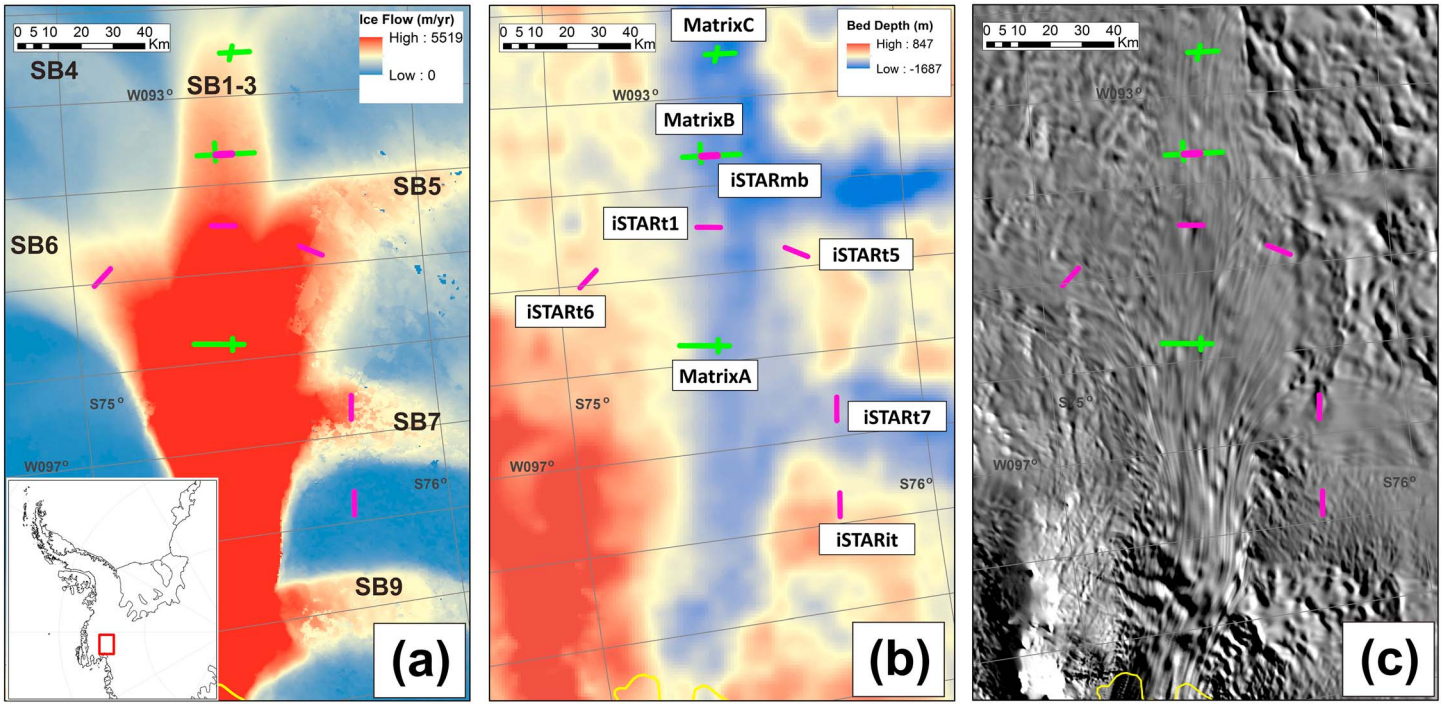

Figure 1. Location of seismic profiles across Pine Island Glacier used in this study. The inset in Figure 1a shows the location of the detailed maps of PIG within West Antarctica (red box). (a) Ice-flow speed in m yr^{-1} from interferometric synthetic aperture radar (InSAR) measurements [*Rignot et al*., 2011b]. The "SBx" annotation refers to the tributary nomenclature of *Stenoien and Bentley* [2000]. (b) Bedmap2 bed elevation [*Fretwell et al*., 2013]. iSTAR seismic lines (acquired 2014/2015) are in magenta, and Matrix lines (acquired 2006–2008) are in green. (c) Moderate Resolution Imaging Spectroradiometer (MODIS) image [*Scambos et al*., 2007].

where subdued bed topography exerts less influence on flow, basal conditions, and more specifically the presence, distribution, and water content of subglacial sediments, can have fundamental control over the extent and rate of ice streaming, as exemplified by the Ross Ice Streams across the Siple Coast region of Antarctica [e.g., *Blankenship et al*., 1986; *Engelhardt and Kamb*, 1998; *Tulaczyk et al*., 1998].

Ice sheet models, constrained by satellite and airborne observations, have been used to invert for basal conditions across the entire PIG basin and indicate the presence of a weak sediment beneath the downstream sector and a more "mixed" region of both weak sediment and bedrock further upstream [*Joughin et al*., 2009]. *Smith et al*. [2013], using both seismic data and airborne potential field data, also inferred the presence of both weak and stiff sediment on the main tributary. Offshore, Pine Island Bay is characterized by regions of thick sediments close to the ice shelf. These sediments become more unevenly distributed farther offshore, resulting in exposed bedrock in places [*Muto et al*., 2016; *Nitsche et al*., 2013]. At least part of the region of WAIS currently beneath grounded ice is likely to have been deglaciated in the Pliocene or Pleistocene [*Pollard and DeConto*, 2009], and as such the presence of considerable amounts of sediments beneath the present-day ice stream is expected. *Rippin et al*. [2011] calculated basal roughness from airborne radar measurements of bed topography. They attribute a smooth bed beneath the main trunk and two tributaries of PIG to the presence of sufficient sediment to allow bed deformation and erosion.

Seismic reflection techniques can be used to distinguish softer deforming sediments from harder nondeforming or consolidated sediments [*Smith*, 1997a, 1997b, 2007]. Previous results have demonstrated a high degree of variability in basal properties. For example, beneath Rutford Ice Stream, *Smith* [1997a] discriminated areas of both dilated and lodged till along a seismic line a few kilometers in length. Also in the Weddell Sea region, *Vaughan et al*. [2003] determined a range of basal conditions both across individual ice streams (Rutford and Talutis Inlet) and between adjacent ice streams (Evans and Carlson Inlet). Similarly, inferred till porosity, or till stiffness, varies significantly across Whillans Ice Stream, dependent on the likely hydrological conditions of the area in question, e.g., comparing areas of smooth deformable bed investigated by *Blankenship et al*. [1986] with the "sticky spot" site of *Luthra et al*. [2016].

Table 1. Details of the Seismic Profiles Used in This Study

Seismic Experiment	Data Acquisition Field Season	Line Length (Across/Along Flow)	Sensor
MatrixA	2006/2007	16/5 km	100 Hz geophone
MatrixB	2007/2008	18/5 km	100 Hz geophone
MatrixC	2007/2008	10/5 km	100 Hz geophone
iSTAR	2014/2015	5 or 7 n/a	40 Hz georod

In this study we present results from a series of seismic reflection lines across PIG. Seismic imaging and the strength of reflections from the ice stream bed are here used to constrain subglacial bed properties. Seismic results are consistent with a widespread dilated sediment layer at the bed which would enable rapid ice flow. We demonstrate the presence of this readily deformable layer, even over topographic highs, where the scouring of any sediment to expose the more flow-resistive bedrock may have been expected. In contrast, the bed beneath an intertributary area of slow-moving ice is shown to be underlain by much lower porosity or frozen sediments. We show that these results corroborate previous studies which used remotely sensed observations to infer basal shear stress.

2. Data and Methods

The data used for this study consist of a series of seismic reflection profiles acquired across PIG and its tributaries over three field seasons (Figure 1). Profiles acquired in 2006/2007 and August 2007/2008 are collectively termed "Matrix"; profiles acquired in austral summer 2014/2015 are labeled "iSTAR". Where necessary, we have assigned individual seismic profile names following the tributary nomenclature of *Stenoien and Bentley* [2000] (see Table 1 and Figure 1a). Although acquired over three different field seasons, the field methods were consistent throughout each of the field campaigns and all data were processed in a similar manner to maintain consistency. Any differences are specified in the text below.

2.1. Data Acquisition

The seismic source used for the reflection profiles was 300 g of high explosive, placed in holes of 20 m depth, backfilled with snow. A shot interval of 240 m and receiver interval of 10 m with 30 m offset was used throughout to produce single-fold normal-incidence ($<10°$ incidence angle) data with a midpoint interval of 5 m. A 48 channel Geode seismic system recorded 2 s record lengths at 8000 Hz sample rate. The only marked difference in acquisition hardware between seasons was the use of 100 Hz geophones on the Matrix lines and 40 Hz georods [*Voigt et al.*, 2013] on the iSTAR lines, which demonstrably improves the signal to noise ratio. The method of determining the absolute reflection coefficient of the bed relies on the calibration of the primary bed reflection with a coincident multiple reflection [see *Roethlisberger*, 1972; *Smith*, 1997a; *Holland and Anandakrishnan*, 2009]. Where multiple bed returns are not available on the primary seismic reflection line data, larger shots were used with a longer record length to capture the multiple.

2.1.1. iSTAR Seismic Data

Locations for seismic profiling in 2014/2015 were identified using radar data that were acquired at each of the sites in the previous season. The radar data were acquired in a series of 15×10 km "patches" wherein radar processing revealed the presence of a range of subglacial regimes and bedforms underlying the ice at each of the survey sites [*Bingham et al.*, 2014]. Seismic reflection profiles 7.2 km in length were acquired at each site, with the specific selection of profiles at each site designed overall to sample a range of bed features characteristic of the entire basin. With the exception of line iSTARit, which is on a slow-moving intertributary bed elevation high, all iSTAR seismic lines were acquired on fast-flowing tributaries. All iSTAR lines were acquired "across flow," i.e., orthogonal to the overall ice-flow direction, with the aim of sampling a wider range of bed conditions than would likely be achieved along flow due to the linear nature of the bed forms along flow.

2.1.2. Matrix Seismic Data

The Matrix lines, acquired in 2006/2007 and 2007/2008, were located on the main trunk of PIG and farther up the main tributary (Figure 1b). Long lines were acquired across ice flow, and intersecting shorter lines were acquired along flow (Table 1). One additional seismic line was acquired in 2014/2015, iSTARmb, and is a repeat survey of a 5 km section of the MatrixB line (Figure 1b).

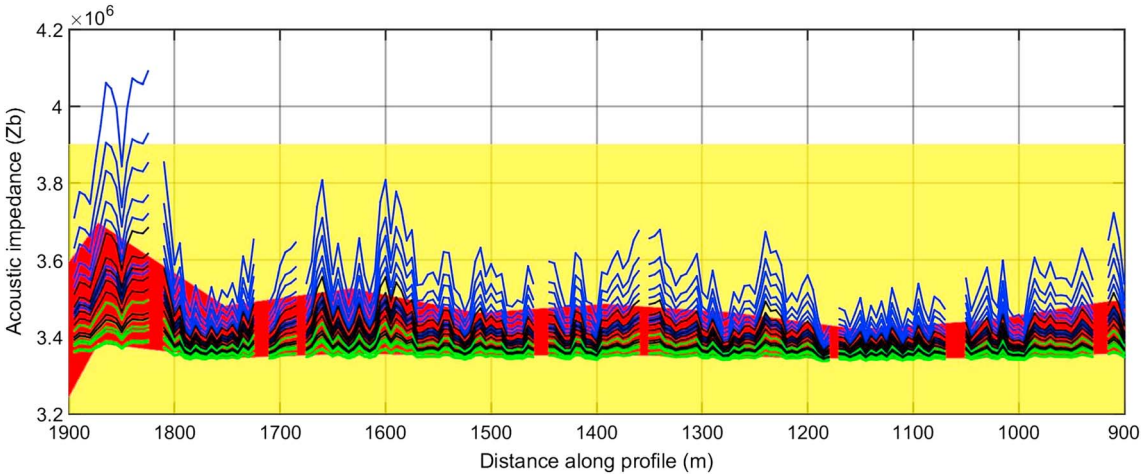

Figure 2. Raw bed acoustic impedance values in kg m^{-2} s^{-1} over a 1 km section of iSTARt7 demonstrating the spatial variability of raw data and the smoothing effects of binning. Colored lines represent acoustic impedance values calculated using all applicable multiple reflections for this seismic profile: black lines, assumed parameters; green lines, minimum possible values calculated with measurement and assumed parameter uncertainties; and blue lines, maximum possible values calculated with uncertainties. The red band is the first standard deviation of the binned values of the acoustic impedance as described in the text. The yellow band indicates the likely acoustic impedance values of dilated sediments generally associated with the deformation of bed material [*Atre and Bentley*, 1993]. The ice-flow direction is into the page.

2.2. Data Processing and Calculation of Bed Acoustic Impedance

The absolute reflection coefficient of the bed was determined following the method of *Smith* [1997a], using the ratio of the energy of the primary and multiple bed reflections. This method requires reliable amplitude recovery from the data. As such, data processing is kept to a minimum, with only normal moveout and static corrections being applied prior to time domain migration. Ice thickness is determined from seismic traveltimes, corrected for the reduced velocity in the firn which is derived from shallow seismic refraction experiments [*Kirchner and Bentley*, 1990]. Seismic attenuation in the ice of $2 \pm 1 \times 10^{-4}$ m^{-1} is assumed, based on the likely temperature profile of the ice column [*Bentley and Kohnen*, 1976]. Derivation of the acoustic impedance of the bed material from the calibrated reflection coefficient requires the acoustic impedance of the basal ice to be assumed. A value of $3.33 \pm 0.04 \times 10^6$ kg m^{-2} s^{-1} is used here, based on the likely basal-ice conditions [*Atre and Bentley*, 1993]. From the calculated acoustic impedance measurements of the base, inferences about likely bed materials can be drawn and are discussed below.

Bed picks are made at the first-arriving energy of the primary and multiple bed reflections in the seismic section and 5 ms time windows exported to encapsulate the Ricker wavelet of the first arrival. The sum of the square of the amplitudes is then used to determine the energy of the ice-base reflection and multiple. A calibrated bed reflection coefficient can be determined at the site of the bed multiple and then extrapolated along the entire line using the energy of the primary bed reflection. Unlike previous studies, e.g., *Smith et al.* [2013], where a single multiple reflection per line has been used, the calculations are carried out separately for every applicable multiple recorded, allowing verification of the result and quantification of the uncertainty resulting from shot-to-shot variability and any lateral variation in ice properties.

2.3. Uncertainties in Acoustic Impedance Measurements

For each trace along the seismic line where a bed pick can be made, the measured, minimum, and maximum acoustic impedance values are calculated, determined using the uncertainties in the measurements and assumed parameters as described above. The calculation is repeated at each bed pick for every multiple applicable to that line to produce a population range including all likely maximum and minimum acoustic impedance values. This population is then used to determine the standard deviation of possible measured values at each point to describe the likely range of values. Measured acoustic impedance values and uncertainties are then averaged over 24 channels, or 120 m bed interval bins, equivalent to the first Fresnel zone of the unmigrated data (150 Hz center frequency and 1600 m depth). This averaging reduces the effects of laterally varying thin bed layers, migration artifacts, and non-2D structure, and also indicates variance in the observations allowing quantification of the uncertainty. Figure 2 demonstrates the effect of uncertainties

and smoothing along a 1 km section of iSTARt7. Black lines represent the raw acoustic impedance values calculated using measured amplitude values and assumed parameters without uncertainties. The green and blue lines represent the minimum and maximum raw acoustic impedance values calculated using uncertainties. The nonlinear effect of the uncertainties is demonstrated by the increased spread of measurements away from the reference acoustic impedance value of ice (3.33×10^6 kg m^{-2} s^{-1}) and also in the asymmetry of the first standard deviation of the measurement population.

For lines where no multiple bed returns were recorded, data from adjacent lines are used to calibrate the reflection coefficient. Consistency in acquisition procedures and an assumption of laterally consistent ice properties are required for this step. Testing this assumption is possible on a line where multiples are available, such as iSTARt5: the mean difference in basal acoustic impedance along this line between the analysis using multiples from iSTARt5 itself and that using multiples from the adjacent iSTARt7 line is $<1\%$. This indicates good consistency in the acquisition procedures and little lateral variation in ice properties.

Seismic attenuation in ice is controlled primarily by ice temperature [*Peters et al.*, 2012, and references therein]. Therefore, the attenuation coefficient value used is based on previous studies in regions with a similar temperature range [*Smith et al.*, 2013]. Uncertainties in seismic attenuation of 1×10^{-4} m^{-1} encapsulate the likely temperature range and uncertainty in previous attenuation measurements and are included in the variance of the final acoustic impedance observations presented here. Where multiples from adjacent lines are used to calibrate the reflection coefficient, the range of possible seismic attenuation values is doubled to accommodate variation in the ice column due to advection from different locations. We attempted to minimize shot-to-shot variability at the data acquisition stage by ensuring a consistent field methodology to achieve uniform shot and receiver coupling. The most difficult aspect of the field acquisition to repeat uniformly is the backfilling of shot holes: A funnel with a coarse grating was therefore placed over the shot hole and only cold and dry snow used. However, shot-to-shot variation in the amplitude of direct-path energy is still observed, indicative of a variation in source amplitude, assuming that variation in seismic attenuation is negligible over distances of a few hundred meters [*Holland and Anandakrishnan*, 2009]. We therefore correct for variability in shot coupling by quantifying the energy in the ground roll or direct-wave surface noise. Shot gathers are normalized for shot-to-shot variability according to the energy recorded at each receiver during a 200 ms window of data following the first arrival. In most cases, the correction for shot-to-shot variability has little effect on the acoustic impedance results. However, data from MatrixB show appreciable shot-to-shot variation in the ground roll energy, such that the correction cannot be applied without skewing the data beyond physically realistic limits. Though we do not know the exact cause of this, we note that the ice at MatrixB was under extremely high tension during the period of seismic-data acquisition [*Scott et al.*, 2010], and we hypothesize that microfractures may have been present beneath the surface which would have affected the lateral propagation of seismic energy. As such, no shot-to-shot correction is made. The results for MatrixB are therefore regarded as less-well constrained than the other lines. However, as the seismic energy of the bed reflections is vertically propagating, the impact of surface cracks on the bed reflections is less significant than on the ground roll, and it is likely that the MatrixB data are comparable to the other lines.

The effect of the change in hardware from 100 Hz geophones on the Matrix lines to 40 Hz georods on the iSTAR lines was tested. To emulate the geophone data of the Matrix lines, a 100 Hz high-pass filter was applied to the raw seismic data from line iSTARt6, where the highest number of coincident multiple reflections for calibration was observed. The mean difference in the calculated acoustic impedance results between the filtered and unfiltered data is less than 0.3% and therefore deemed negligible.

3. Seismic Observations and Interpretation

3.1. Seismic Profiles

The large range of bed topography across the tributaries is indicated by an obvious ice-base reflection in all seismic sections and is in agreement with coincident radar-derived bed topography [*Bingham et al.*, 2014], with changes of a few hundred meters vertically over a few kilometers laterally on a number of profiles. Example seismic sections illustrating key features are presented in Figure 3. Seismic reflections consistent with deeper sedimentary layering are observed at up to 100 ms two-way traveltime beneath the ice-bed interface at a number of sites, e.g., iSTARt1 (Figure 3a) and iSTARt5 (Figure 3b). The sedimentary structures

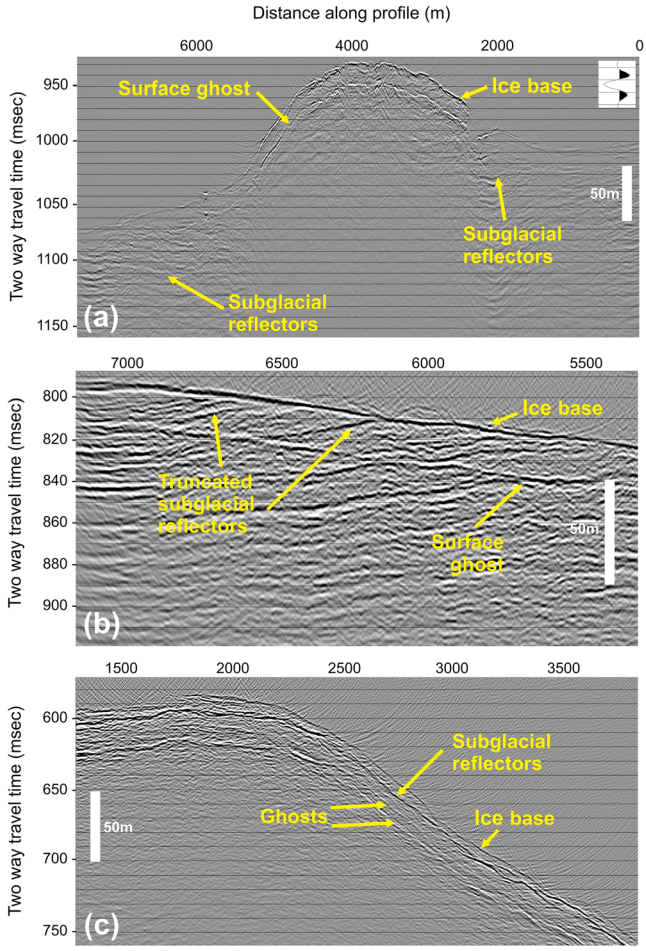

Figure 3. Example of migrated seismic sections (a) iSTARt1: a clear ice-base reflector is observed along the entire profile beneath >1600 m of ice. Sub-bed reflectors are visible at the margins of the topographic high only. Inset: An example of Ricker wavelet from a relatively low acoustic impedance subglacial bed (i.e., high-porosity dilated sediment) to highlight the polarity convention; (b) iSTARt5: illustrating details of stratigraphic structure beneath the ice-bed interface of a tributary. Reflectors within the bed are truncated by a thin layer at the interface but maintain coherency close to the interface; (c) iSTARit: illustrating details of stratigraphic structure beneath the ice of the intertributary profile. Vertical scale bars represent thickness beneath the ice base assuming a *P* wave velocity in sediment of 2000 m s^{-1}. Distance along profile values refers directly to Figure 4a. The ice-flow direction is into the page.

imaged in the seismic profiles, such as dipping reflectors truncated by the ice base, indicate that these are older sediments which must predate the current glacial cycle. Assuming a typical seismic velocity in consolidated sediments of 2000 m s^{-1} [*Smith et al.*, 2013], these observations are consistent with >100 m thick sedimentary sequences, indicating deep sedimentary deposits immediately beneath the ice base. In general, we do not observe these preexisting sedimentary features beneath topographic highs of the bed. Along profile iSTARit, between tributaries, we observe continuous seismic reflections almost parallel to the bed, consistent with a discernible basal sediment layer of variable thickness (Figure 3c). Similar but less continuous reflections are observed along short sections of profiles iSTARt1 and iSTARt7.

With the exception of iSTARit, and possibly short sections of the Matrix profiles, the bed reflections on all the seismic lines are either negative or weak and positive. The polarity of the bed reflection is in itself diagnostic [*Atre and Bentley*, 1993]; the acoustic impedance of ice is very similar to that of dilated sediment, and therefore, a small change in the acoustic impedance across this threshold results in a polarity change of the bed reflection which is observed: Rapid reversals in polarity may indicate a basal acoustic impedance value close to that of ice with only slight variation. A negative reflection coefficient can be unambiguously interpreted as high-porosity sediment or water: a positive reflection coefficient is more ambiguous, indicating high-porosity sediment if the reflection is weak, or else harder material if the reflection is strong. Where the reflection is very weak the polarity becomes harder to discriminate unambiguously. However, as the acoustic impedance value remains close to that of ice the interpretation is still valid.

3.2. Acoustic Impedance of the Bed Material

The acoustic impedance measurements of the bed along all seismic profiles are shown in Figures 4a and 4b, with the uncertainty to one standard deviation plotted. Likely basal materials can be determined by comparison of measured acoustic impedance values with those typical of dilated sediment, stiff sediment, or lithified sediment, a frozen bed or crystalline bedrock [*Smith*, 1997a]. For reference, the acoustic impedance values of water and basal ice are plotted. The yellow band highlights the approximate range of acoustic impedance values expected for a dilated sediment associated with bed deformation, which would exhibit a porosity in

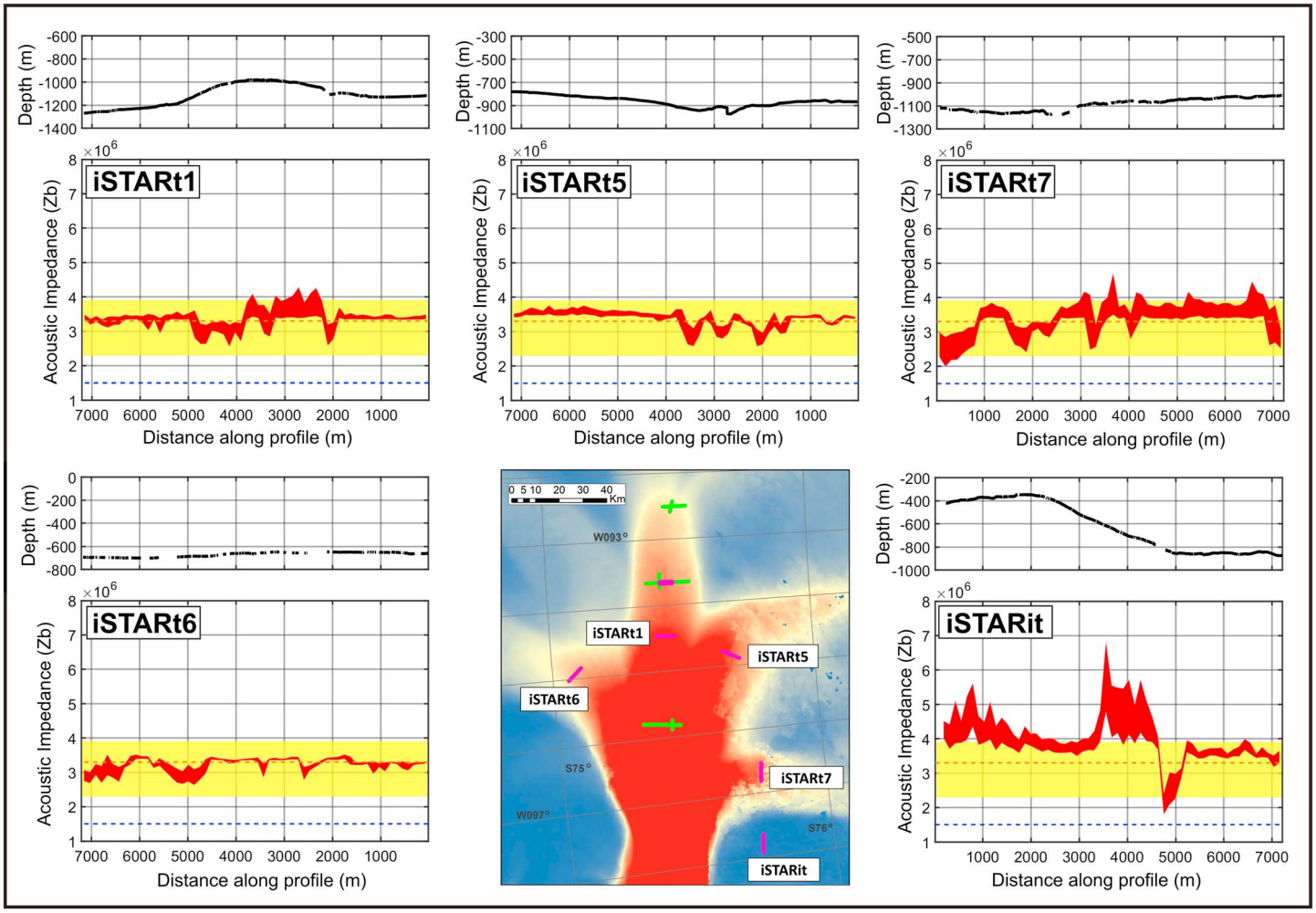

Figure 4a. Bed elevation in meters (upper plots) and bed acoustic impedance in kg m^{-2} s^{-1} (lower plots) measured along iSTAR seismic profiles. The blue dashed line indicates the acoustic impedance value of water; the brown dashed line indicates the acoustic impedance value of ice; the yellow band indicates the likely acoustic impedance values of dilated sediments generally associated with the deformation of bed material [*Atre and Bentley*, 1993]. The ice-flow direction is into the page.

the range of 30–45% [*Atre and Bentley*, 1993]. Acoustic impedance values above this range are consistent with a lodged till with porosity ≤30%, poorly lithified sedimentary rock, or, at even higher values, a frozen bed [*Smith*, 1997a].

Across all surveyed tributaries, the mean acoustic impedance value of the bed immediately beneath the ice base is $3.0 \pm 0.2 \times 10^6$ kg m^{-2} s^{-1}, consistent with a dilated sediment of 35–45% porosity [*Atre and Bentley*, 1993]. In contrast, the mean acoustic impedance along profile iSTARit, between tributaries, is $3.9 \pm 0.3 \times 10^6$ kg m^{-2} s^{-1}, consistent with stiffer lower porosity sediment, increasing to a mean of $4.7 \pm 0.6 \times 10^6$ kg m^{-2} s^{-1} along the middle section of the line.

The most striking feature of the acoustic impedance results is their consistency across a range of basal topography. The Matrix lines (located along the central trunk and upstream main tributary) indicate a greater variation than the iSTAR lines (more widely spread around the basin), but this also encompasses a greater uncertainty in the results, most likely due to the use of geophones rather than georods [*Voigt et al.*, 2013], as well as the surface fractures noted at MatrixB. This is evident in the iSTARmb data which are coincident with the MatrixB results. The iSTARmb line is a repeat of a section of the MatrixB line (Figures 1b and 4b) and would therefore be expected to reproduce the earlier results with any temporal changes superimposed. Although the results are consistent, the significantly higher uncertainties assigned to the

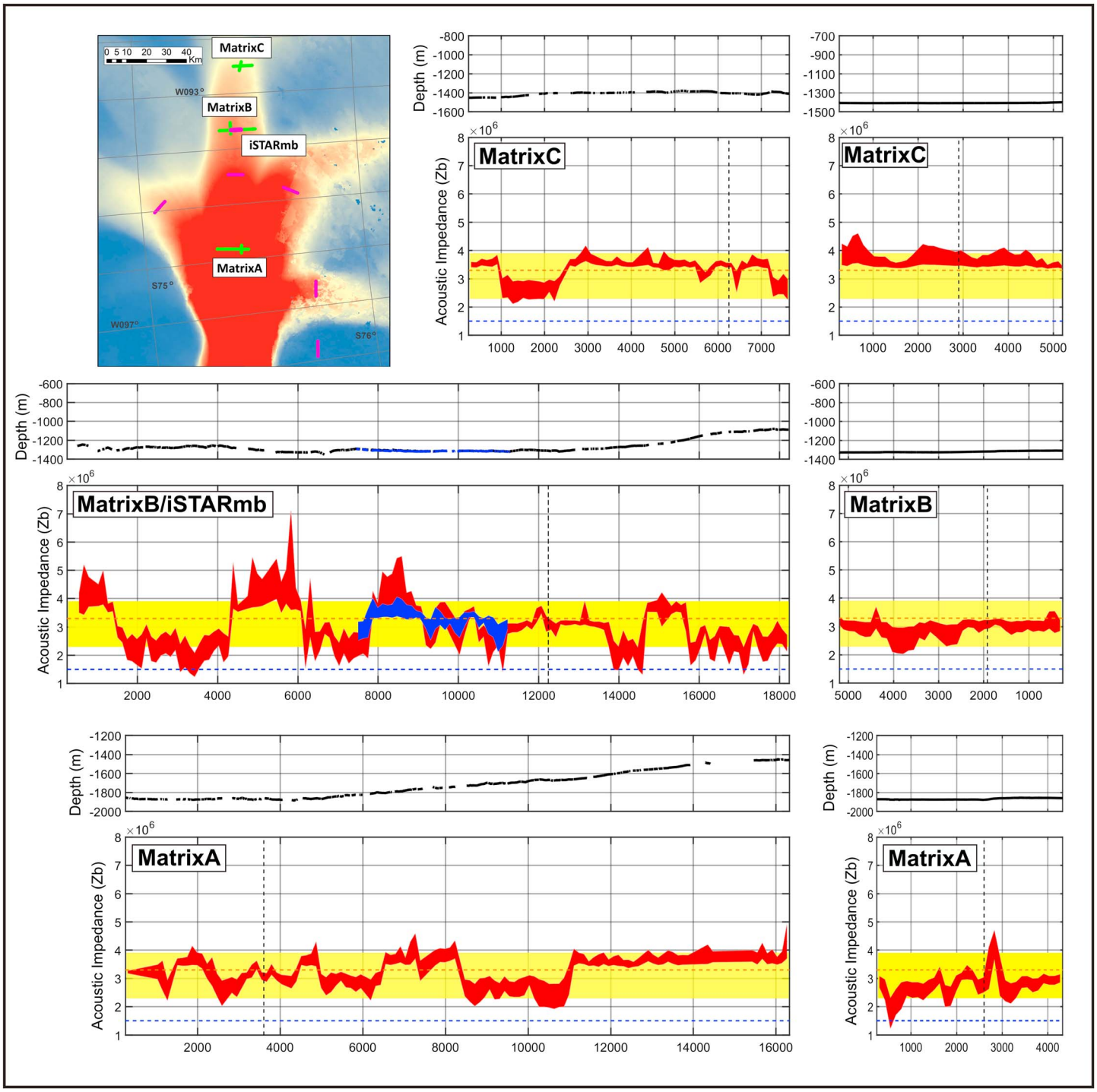

Figure 4b. Bed elevation in meters (upper plots) and bed acoustic impedance in kg m^{-2} s^{-1} (lower plots) measured along Matrix seismic profiles as per Figure 4a. Across-flow profiles are to the left, along-flow plots are to the right. The crossing locations of the Matrix along- and across-flow lines are highlighted with the black dashed line. iSTARmb results are overlain in blue on the MatrixB results. iSTARmb results are consistent with the MatrixB results within uncertainties but highlight the lower uncertainties in the more recent data acquisition. The ice-flow direction is into the page across flow and left to right along flow.

MatrixB data are clearly demonstrated. An earlier analysis of the MatrixB data by *Smith et al.* [2013] interpreted a basal sediment layer with lateral variation between soft and hard sediment. However, the more recent iSTARmb data, with lower uncertainties, and the higher uncertainties assigned here to the earlier MatrixB data, preclude such an interpretation along the repeated sections of seismic lines and

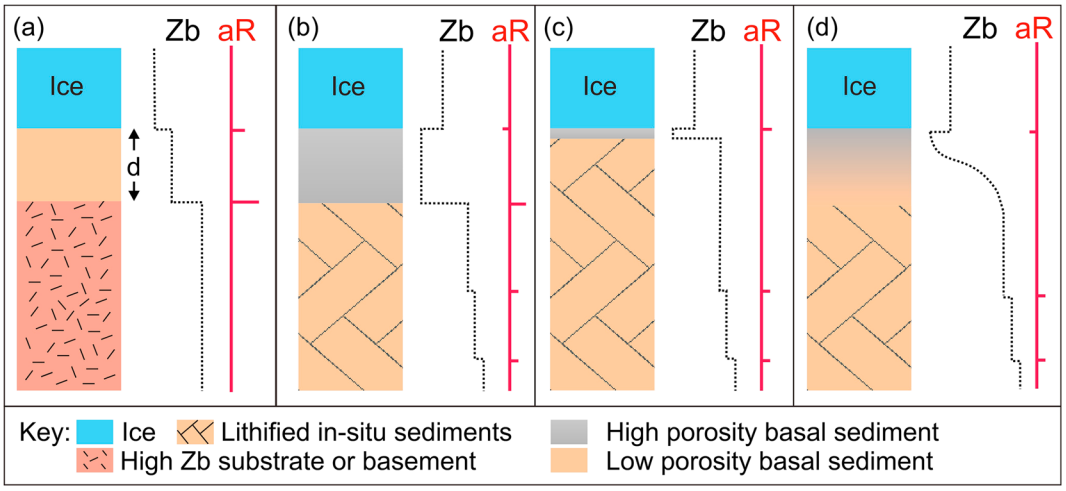

Figure 5. Schematic of possible basal structures directly beneath the ice with respective acoustic impedance values (Zb) and apparent reflection coefficients (aR). (a) The likely conditions beneath the intertributary line and (b–d) likely conditions beneath the tributaries. Thick ($d>\lambda/4$) low-porosity basal sediment layer directly overlying a substrate of different lithology (Figure 5a); thick ($d>\lambda/4$) high-porosity basal sediment layer over in situ sediments with sharp acoustic impedance contrast (Figure 5b); thin ($d<\lambda/4$) high-porosity basal sediment layer over in situ sediments with sharp acoustic impedance contrast resulting in a reverse polarity in the apparent reflectivity (Figure 5c); and thick ($d>\lambda/4$) reworked basal sediment layer with acoustic impedance gradient to deeper sediment, resulting in aweak negative reflection coefficient at the ice base (Figure 5d).

therefore reduce confidence in the MatrixB data elsewhere. Segments of the intertributary line, with acoustic impedance measurements above that of dilated sediments, are the only indication of either a stiff low-porosity sediment or frozen bed. These results are consistent with inferred basal temperature models [*Joughin et al.*, 2009].

3.3. Constraining the Nature and Thickness of the Basal Sediment Layers

We constrain basal sediment layer thickness by combining seismic imaging, measured acoustic impedance values, and assumed seismic velocity values from previous studies appropriate to the measured acoustic impedance contrast at the ice base.

3.3.1. Constraining the Thickness of the Intertributary Basal Layer

Along profile iSTARit, acquired on slow-moving ice between tributaries 7 and 9, a clear reflection is observed directly after the ice-base reflection (Figure 3c), indicating a discrete subglacial sediment layer (Figure 5a). The layer thickness varies laterally. The strong positive reflection from the base of this layer indicates a substrate of relatively high acoustic impedance directly beneath the ice. Similar reflectors are reported elsewhere [e.g., *Horgan et al.*, 2013; *Luthra et al.*, 2016; *Rooney et al.*, 1987] and associated with a deforming sediment layer. Where a clear reflection from the base of the subglacial layer is recorded we can estimate layer thickness directly. Assuming a seismic velocity in this layer of $2120 \pm 200\,\mathrm{m\,s^{-1}}$ [*Luthra et al.*, 2016], consistent with the positive ice-base reflection coefficient and relatively high acoustic impedance substrate compared to the tributaries, we can constrain the mean thickness to 7 ± 3 m with a maximum thickness of 13 m. The highest acoustic impedance values at the ice base are observed along the intertributary line iSTARit and are coincident with the absence of the basal sediment layer and may represent the in situ material. In general, beneath sections of the profiles where clear reflections from basal layers are present, no sedimentary features are observed. We therefore infer that this layer at the ice base is a discrete sediment layer overlying a substrate of different lithology (Figure 5a). Although the layer thickness is similar to that observed beneath Whillans Ice Stream [*Rooney et al.*, 1987], the acoustic impedance measurements do not infer an actively deforming layer beneath the intertributary ice. The origin of the layer may be similar, perhaps having formed previously during a period of faster ice flow, but now likely represents a stiff nondeforming till.

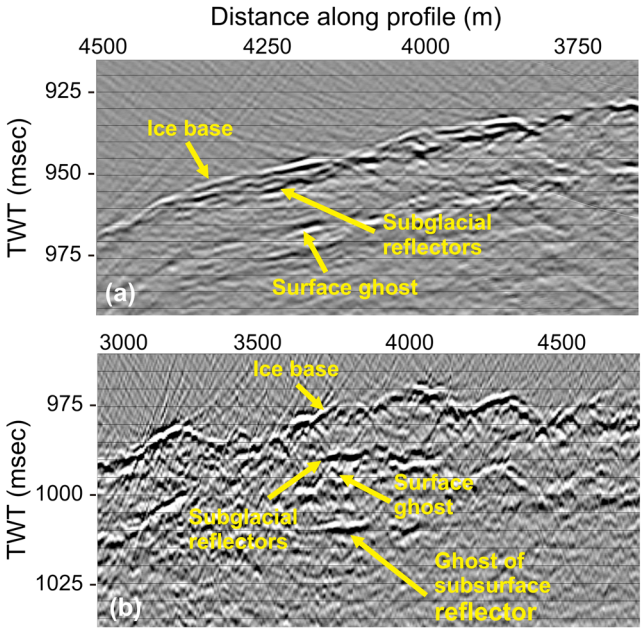

Figure 6. Details of migrated seismic sections highlighting the discontinuous seismic reflectors directly beneath the ice base of the tributaries (a) iSTARt1 and (b) iSTARt7. Distance along profile values refer directly to Figure 4a. The ice-flow direction is into the page.

3.3.2. Constraining the Nature of the Basal Layer Beneath the Tributaries

In contrast to the intertributary measurements, the acoustic impedance measurements along the fast-flowing tributaries indicate high-porosity dilated sediments at the ice base, with either a negative or weak-positive ice-base reflection, consistent with a subglacial till [*Blankenship et al.*, 1986; *Engelhardt and Kamb*, 1998; *Tulaczyk et al.*, 2000a]. The presence of deeper reflectors in the seismic sections confirms that sufficient energy is propagating beneath the ice base reflector to allow discrimination of the base of the till layer if sufficiently thick and of sufficiently high acoustic impedance contrast to its substrate (Figure 5b). However, the seismic profiles along the tributaries do not indicate extensive, consistent, or unambiguous bed-parallel reflections as observed on the intertributary profile. The absence of bed-parallel reflections does not preclude the presence of a basal till layer: the till layer may be too thin to be resolved by the seismic wavelength of our data (Figure 5c), in which case the reflections from the upper and lower interfaces of the till layer form a composite wavelet [*Booth et al.*, 2012], resulting in an apparent acoustic impedance contrast (aR) which may not be representative; or the lower boundary of the basal layer may be seismically transparent due to an acoustic impedance gradient rather than a sharp contrast at its base (Figure 5d), indicative of a reworked sediment layer.

In the absence of a till-base reflection we can infer the likely thickness range of the layer by assuming ranges of acoustic impedance values consistent with previous studies [*Atre and Bentley*, 1993]. Observations of preexisting sedimentary stratigraphy beneath the till layer (Figure 3b) are consistent with a more consolidated or lithified substrate, implying material with an acoustic impedance of $5.5 \pm 1.0 \times 10^6$ kg m^{-2} s^{-1} [*Smith et al.*, 2013].

3.3.3. Constraining the Thickness of the Basal Layer Beneath the Tributaries

As stated above, in general, no seismic reflection is visible from the base of the high-porosity sediment layer at the bed of the fast-flowing tributaries. However, this dilated lid must be of sufficient thickness to result in a negative reflection coefficient measurement, as observed along large segments of the profiles. Below a layer thickness of $\lambda/4$ (one quarter of the seismic wavelength in the layer), the reflection coefficient becomes a composite of the upper and lower boundaries, the negative polarity of the reflection becomes increasingly difficult to identify above the background noise, and the apparent reflection coefficient switches polarity to reflect the higher acoustic impedance sediments imaged directly beneath. We therefore use this limit to assign a minimum lid thickness of 1.5 ± 0.4 m, constrained by the measured maximum peak frequency of 260 Hz and seismic velocity in the high porosity till of 1600 ± 100 m s^{-1} [*Blankenship et al.*, 1986]. To account for the likely presence of an acoustic impedance gradient beneath this layer, rather than a sharp impedance contrast, we assign a large uncertainty.

The absence of a continuous seismic reflection from the base of this layer beneath the tributaries prevents direct measurement of maximum layer thickness except in a few localized sections of profiles iSTARt1 and iSTARt7 (Figure 6), where a layer thickness range of 6 to 10 m is calculated assuming a high-porosity till velocity of 1600 ± 100 m s^{-1}, compatible with the negative reflection coefficient at the ice base [*Blankenship et al.*, 1986]. Also, where we observe the truncation of dipping reflectors (e.g., iSTARt5; Figure 3b) we can infer that

the thickness of the reworked layer may be as low as the tuning thickness of the layer, equivalent to one quarter of a wavelength, or ~2 m (assuming 1600 m s^{-1} for high-porosity sediment). We therefore do not assign a maximum thickness to the reworked sediment layer other than to state that it is laterally variable, and the thickness has been measured at up to 6 to 10 m.

The absence of a basal reflection from a layer greater than the tuning thickness, as is likely to be the case here between the derived end-member thickness measurements, requires that the increase in acoustic impedance with depth within this layer must be gradational, from that of high porosity sediment at the top to more consolidated sediments at the base. This interpretation is consistent with a layer formed by the reworking of existing sediments, as outlined in Figure 5d.

Our preferred model therefore consists of an upper layer of dilated till with minimum thickness 1.5 ± 0.4 m immediately at the ice base, which forms the lid of a reworked sediment layer of variable thickness. Where a positive reflection coefficient is measured, this dilated lid layer must be too thin to be resolved or at the lower end of the proposed porosity range, but always distinct from the deeper sediments with a higher acoustic impedance. We summarize the likely basal conditions in the tributaries in Figure 5.

4. Discussion

Across both the main trunk of PIG and all surveyed tributaries acoustic impedance results indicate widespread dilated sediment of relatively high porosity (30–45%) at the ice base. This layer is most likely formed of reworked sediments and includes a high-porosity lid of minimum thickness 1.5 ± 0.4 m. The thickness of the reworked layer is, in general, poorly constrained due to the seismically transparent base or thin nature, although in places is measured at 6 to 10 m. Although such high-porosity sediment is generally associated with active deformation [*Alley et al*., 1987], the resolution of the seismic data does not allow us to discriminate whether deformation of the basal till is by deep ploughing [*Brown et al*., 1987], sliding on discrete planes, or pervasive with depth within the layer. The dilated sediment lid thickness estimated here is greater than the few decimeters of actively deforming till layers observed on glaciers flowing at more moderate rates [*Cuffey and Paterson*, 2010, Table 7.4, and references therein]. It is possible that deformation is localized to the top of the sediment, and this layer allows pathways for water drainage at the interface with the thawed bed, as observed on the Siple Coast of the WAIS [*Kamb*, 2001]. Although sparse, these thickness estimates are comparable to the 6–8 m till layer observed beneath Whillans Ice Stream [*Blankenship et al*., 1987; *Luthra et al*., 2016; *Rooney et al*., 1987], which flows at a similar rate to the tributaries of PIG. Again, in a similar manner, the actively deforming till layer beneath Whillans Ice Stream unconformably overlies older sedimentary rocks [*Luthra et al*., 2016].

Beneath slow-moving ice, between tributaries, a well-defined basal sediment layer of thickness 7 ± 3 m is observed. Acoustic impedance measurements indicate lower porosities than those observed beneath the fast-flowing tributaries, with the basal layer overlying material of higher acoustic impedance. Seismic reflections are not observed beneath this layer and may therefore indicate massive homogeneous sediment or a crystalline basement.

The seismic observations indicate widespread sediments, and as such imply that the system is not supply limited and likely to be in a steady state rather than transitional. This conclusion is supported by the presence of deep sequences of older sediment in the seismic profiles. However, the high-porosity sediment cover is thin in places, e.g., iSTARt5 between 6000 and 6500 m (Figure 3b), indicating a complex regime of erosion, transport, and deposition controlled by bed geometry, the stress regime in the ice and sediment rheology. Scouring of subglacial sediment at prominent topographic features would generally be expected across the highly variable basal topography of the surveyed sites [*Nitsche et al*., 2013]. Both *Lowe and Anderson* [2003] and *Nitsche et al*. [2013] describe a range of seabed morphologies offshore of PIG, from thin or absent sediment cover and exposed bedrock in the central region to thick sedimentary strata immediately offshore of the ice shelf. The results of *Muto et al*. [2016], from the inversion of airborne gravity data, indicate an 800 m deep sedimentary basin immediately offshore of the grounding line of PIG with either thin sediment cover or exposed crystalline basement beyond the Jenkins Ridge. These offshore observations are consistent with the likely onshore subglacial regimes presented here: widespread sediment cover is viable due to an abundant supply from older sedimentary sequences; topographic highs at the bed are a result of more resistant

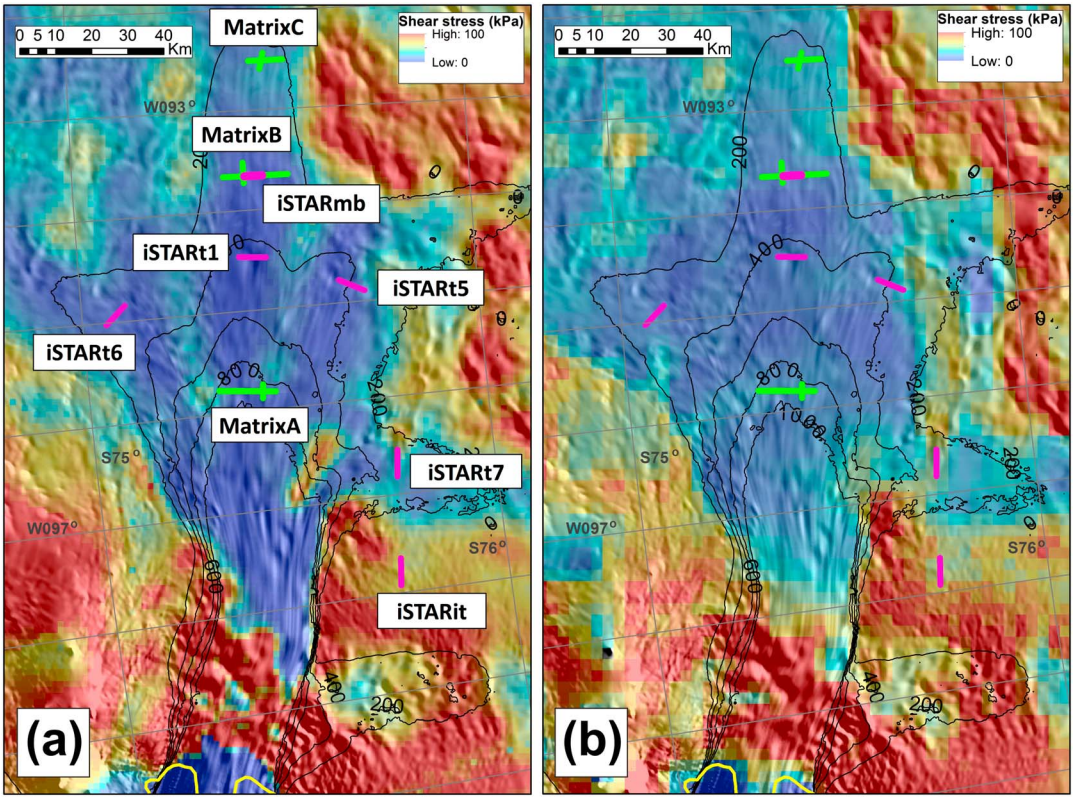

Figure 7. Location of seismic profiles (iSTAR, magenta; Matrix, green) with respect to basal shear stress derived from ice sheet models: (a) *Joughin et al.* [2009] and (b) *Arthern et al.* [2015]. Ice flow speed from Differential InSAR [*Rignot et al.*, 2011b] is contoured from 200 to 1000 m yr^{-1} at 200 m yr^{-1} intervals. The grounding line in 1999/2000 from MEaSUREs [*Rignot et al.*, 2011a, 2011b] is represented by the yellow line. The MODIS Mosaic [*Scambos et al.*, 2007] showing mean surface morphology is underlain.

lithologies, possibly massive sediments or crystalline basement, with a widespread but thin sediment cover; and a temperature-pressure regime exists beneath the tributaries which ensures bed materials remain unfrozen and deformable or mobile.

The seismic observations presented here constrain basal conditions at a scale which is significantly smaller than those previously inferred with numerical basal shear inversions. Likewise, the comparison of observational results at the small scale with models at a large scale does not provide validation. However, with the ultimate aim in mind of using field-based geophysical observations to constrain large-scale numerical inversions it is useful to compare the broader patterns of the relatively small-scale features determined here with the basin-scale features derived from satellite observations and numerical inversions. *Joughin et al.* [2009] used ice velocity, surface elevation, and bed elevation data to derive basal conditions of PIG and Thwaites Glacier. Although they find strong basal melting in areas upstream of the grounding line, farther inland a "mixed" bed is inferred, with extensive areas of both bedrock and weak sediment. This observation is not consistent with the results presented. Our observations are dominated by the widespread dilated sediment at the ice base. However, projection of the locations of the seismic lines on to these basal shear stress results (Figure 7a) indicates that the seismic profile locations map to areas of relatively low basal shear stress, consistent with the sediment drape results presented here. Similar conclusions can be drawn by comparison to the results of *Arthern et al.* [2015] in Figure 7b. Both of these models indicate a region of higher friction immediately upstream of the grounding line which is currently preventing further rapid retreat of PIG to the upstream region where low basal stress is currently exhibited and areas of low topographic restraint exist [*Joughin et al.*, 2009].

Similarly, *Smith et al.* [2013] presented the data from MatrixB, alongside airborne potential field data, and interpreted the lateral variation in acoustic impedance as being consistent with the results of *Joughin et al.* [2009].

The uncertainties allocated here to the MatrixB data are higher than those assigned by *Smith et al*. [2013] due to the inclusion of shot-to-shot variability. Unlike *Smith et al*. [2013], higher uncertainties attributed to these data reduce our confidence in any interpretation of significant lateral variations in basal properties. However, the overall interpretation remains unchanged, the acoustic impedance measurements are consistent with the basal shear calculations. Beneath Whillans Ice Stream, on the Siple Coast of West Antarctica, the presence of a deforming sediment layer [*Alley et al*., 1987; *Blankenship et al*., 1987] results in low basal resistance which allows high ice-flow velocities by basal slip. The acoustic impedance measurements here are consistent with this model being applicable to PIG, and as such indicate that basal conditions upstream will not inhibit further rapid retreat of PIG if the high-friction region directly upstream of the grounding line, currently restraining flow, is breached. Furthermore, there is no evidence of "sticky spots" which increase basal drag, as observed, for example, beneath Rutford [*Smith et al*., 2015] or Kamb Ice Streams [*Anandakrishnan and Alley*, 1994].

Topographic features at the bed can reach heights of a few hundred meters over a few kilometers laterally and are comparable to those observed elsewhere beneath ice streams of West Antarctica [*Horgan et al*., 2011]. The scale of these features is much greater than is normally attributed to drumlins [e.g., *Boulton*, 1987] or even mega-scale glacial lineations [*Clark*, 1993] and likely reflects deeper geological structure: features of this scale are unlikely to be formed purely by deforming sediment and there is likely to be a harder core over which sediment is draped, termed a "fixed core" when applied to drumlins [*Boulton*, 1987]. Although we are unable to determine the nature of this core, the discrete till layer on profile iSTARit between tributaries is consistent with a sediment layer overlying a more consolidated substrate. No sedimentary features are observed within the large basal topographic highs, indicating either massive homogeneous sedimentary sequences or a crystalline origin: Where the basal till layer is inferred to be absent (iSTARit, 3500 m, Figure 3a), higher acoustic impedance values indicate a well consolidated or lithified sediment, perhaps suggesting the former interpretation is more likely. Although features of this scale will oppose ice flow through form drag, the presence of dilated sediment at the bed will result in basal drag lower than that of an exposed hard bed [*Cuffey and Paterson*, 2010]. Similarly, invariant acoustic impedance measurements across a range of topographic features indicate that water pressures are not reduced locally, as might be expected, and as such stronger till does not always result over basal highs.

Although high-porosity subglacial till provides a readily deformable bed, and as such facilitates sliding, small changes in porosity can have a large influence on the degree of lubrication provided by the bed [*Tulaczyk et al*., 2000b]. Both the Kamb and Whillans Ice Streams have shown significant reduction in flow rate and subsequent ice stream thickening [*Engelhardt and Kamb*, 2013; *Joughin et al*., 2005] which has been attributed to changes at the bed [*Anandakrishnan and Alley*, 1997; *Winberry et al*., 2014]. As such, minor reorganization of the stress regime or hydrological potential gradient beneath PIG, with subsequent effective pressure changes at the bed resulting from water pressure variation, may alter the effectiveness of the till to facilitate flow. However, the abundant supply and widespread distribution of sediments imply that the existing basal conditions will likely persist until a significant external forcing or internal reorganization takes place, perhaps as a result of retreat beyond the high-friction region upstream of the grounding line.

5. Conclusions

Seismic reflection profiles were collected across the main trunk and tributaries of Pine Island Glacier to constrain bed properties. Newly acquired profiles, combined with existing data, have been used to derive the calibrated reflection coefficient of the bed from the relative strength of the primary and multiple bed returns. This has been used to determine the acoustic impedance of the bed material which, combined with the seismic images, can be used to infer basal material and conditions. Variance in the results has been constrained by utilizing all available bed-multiple arrivals, along with uncertainties in all measured and assumed parameters.

Seismic profiles indicate older sedimentary deposits, providing sufficient material to maintain a widespread till layer at the ice base, despite considerable topographic variation. Combined with seismic reflection images, the measured acoustic impedance values indicate relatively uniform bed conditions beneath the main trunk and tributaries, with a widespread reworked sediment layer measured at up to 10 m thick in places with a dilated sediment lid of minimum thickness 1.5 ± 0.4 m. Both radar and seismic surveys indicate considerable basal topography; seismic observations indicate that sediment is draped over these features. Beneath the intertributary ice, a discrete till layer of 7 ± 3 m thickness is observed, of lower porosity than beneath the

fast-flowing tributaries. These combined results point to a highly mobile sediment body at the base of the ice with an abundant supply. We recognize that other interpretations of these data are feasible, although we believe the models presented here represent the most likely scenario and have taken care not to overinterpret variation in the observations. Subsequent targeted seismic amplitude-versus-angle or drilling campaigns would allow more definitive interpretations to be reached and a number of our assumptions to be tested.

Sediments of high porosity, as inferred here, provide a weak, readily deformable substrate which reduces basal drag and facilitates fast ice flow. This result is consistent with the results of the inversion of satellite data for shear stress at the bed. Both *Joughin et al*. [2009] and *Arthern et al*. [2015] infer relatively low shear stress values at the locations of all the seismic profiles with the exception of the site on slow-moving ice between two tributaries. The uniform bed conditions and nonuniform response of the individual tributaries discount any direct control by the basal material on the response of the individual tributaries to ice shelf thinning and grounding line retreat.

These measurements, in combination with detailed bed topography and digital elevation models of the surface, will allow detailed modeling of the subglacial regime to help better understand the hydrological system beneath the tributaries and the contribution this may make to the response of PIG to grounding line retreat.

Acknowledgments

This work was supported by funding from the UK Natural Environment Research Council's iSTAR Programme, NERC grant NE/J005754/1 and from NERC grant NE/B502287/1. All fieldwork was supported by staff at the British Antarctic Survey's Rothera Research Station and members of the iSTAR Traverse. In particular, we thank Alex Taylor, James Wake, Tim Gee, Jonny Yates, Mark Baird, Julian Scott, Rob Smith, Roger Stilwell, Feargal Buckley, and Chris Griffiths for help with data acquisition. Data are available from the NERC Polar Data Centre (www.bas.ac.uk/data/uk-pdc/). This manuscript was greatly improved with constructive comments from Hugh Horgan, one anonymous reviewer, and the Associate Editor, Olga Sergienko.

References

Alley, R. B., D. D. Blankenship, C. R. Bentley, and S. T. Rooney (1987), Till beneath ice stream-B 3. Till deformation—Evidence and implications, *J. Geophys. Res.*, *92*(B9), 8921–8929, doi:10.1029/JB092ib09p08921.

Alley, R. B., S. Anandakrishnan, K. Christianson, H. J. Horgan, A. Muto, B. R. Parizek, D. Pollard, and R. T. Walker (2015), Oceanic forcing of ice-sheet retreat: West Antarctica and more, *Annu. Rev. Earth Planet. Sci.*, *43*, 207–231, doi:10.1146/annurev-earth-060614-105344.

Anandakrishnan, S., and R. B. Alley (1994), Ice stream C, Antarctica, sticky spots detected by microearthquake monitoring, *Ann. Glaciol.*, *20*, 183–186.

Anandakrishnan, S., and R. B. Alley (1997), Stagnation of ice stream C, West Antarctica by water piracy, *Geophys. Res. Lett.*, *24*, 265–268, doi:10.1029/96GL04016.

Arthern, R. J., R. C. A. Hindmarsh, and C. R. Williams (2015), Flow speed within the Antarctic ice sheet and its controls inferred from satellite observations, *J. Geophys. Res. Earth Surf.*, *120*, 1171–1188, doi:10.1002/2014JF003239.

Atre, S., and C. R. Bentley (1993), Laterally varying basal conditions beneath ice streams B and C, West Antarctica, *J. Glaciol.*, *39*(133), 507–514.

Bentley, C. R., and H. Kohnen (1976), Seismic refraction measurements of internal friction in Antarctic ice, *J. Geophys. Res.*, *81*(8), 1519–1526, doi:10.1029/JB081i008p01519.

Bindschadler, R. A. (2002), History of lower Pine Island Glacier, West Antarctica, from Landsat imagery, *J. Glaciol.*, *48*(163), 536–544.

Bingham, R. G., D. Davies, E. C. King, S. L. Cornford, D. G. Vaughan, J. D. Rydt, and A. M. Smith (2014), The nature and dynamics of the bed beneath Pine Island Glacier, Antarctica, paper presented at WAIS meeting, Julian, Calif.

Blankenship, D. D., C. R. Bentley, S. T. Rooney, and R. B. Alley (1986), Seismic measurements reveal a saturated porous layer beneath an active Antarctic ice stream, *Nature*, *322*(6074), 54–57, doi:10.1038/322054a0.

Blankenship, D. D., C. R. Bentley, S. T. Rooney, and R. B. Alley (1987), Till beneath ice stream-B 1. Properties derived from seismic travel-times, *J. Geophys. Res.*, *92*(B9), 8903–8911, doi:10.1029/JB092ib09p08903.

Booth, A. D., R. A. Clark, B. Kulessa, T. Murray, J. Carter, S. Doyle, and A. Hubbard (2012), Thin-layer effects in glaciological seismic amplitude-versus-angle (AVA) analysis: Implications for characterising a subglacial till unit, Russell Glacier, West Greenland, *Cryosphere*, *6*(4), 909–922, doi:10.5194/tc-6-909-2012.

Boulton, G. S. (1987), A theory of drumlin formation by subglacial sediment deformation, in *Drumlin Symposium*, edited by J. Menzies and J. Rose, pp. 25–80, Balkema, Rotterdam, Netherlands.

Brown, N. E., B. Hallet, and D. B. Booth (1987), Rapid soft bed sliding of the Puget Glacial Lobe, *J. Geophys. Res.*, *92*(B9), 8985–8997, doi:10.1029/JB092iB09p08985.

Clark, C. D. (1993), Mega-scale glacial lineations and cross-cutting ice-flow landforms, *Earth Surf. Process. Landf.*, *18*(1), 1–29, doi:10.1002/esp.3290180102.

Cuffey, K. M., and W. S. B. Paterson (2010), *The Physics of Glaciers*, Acad. Press, New York.

Engelhardt, H., and B. Kamb (1998), Basal sliding of ice stream B, West Antarctica, *J. Glaciol.*, *44*(147), 223–230.

Engelhardt, H., and B. Kamb (2013), Kamb ice stream flow history and surge potential, *Ann. Glaciol.*, *54*(63), 287–298, doi:10.3189/2013AoG63A535.

Fretwell, P., et al. (2013), Bedmap2: Improved ice bed, surface and thickness datasets for Antarctica, *Cryosphere*, *7*(1), 375–393, doi:10.5194/tc-7-375-2013.

Holland, C. W., and S. Anandakrishnan (2009), Subglacial seismic reflection strategies when source amplitude and medium attenuation are poorly known, *J. Glaciol.*, *55*(193), 931–937.

Horgan, H. J., S. Anandakrishnan, R. B. Alley, P. G. Burkett, and L. E. Peters (2011), Englacial seismic reflectivity: Imaging crystal-orientation fabric in West Antarctica, *J. Glaciol.*, *57*(204), 639–650.

Horgan, H. J., K. Christianson, R. W. Jacobel, S. Anandakrishnan, and R. B. Alley (2013), Sediment deposition at the modern grounding zone of Whillans Ice Stream, West Antarctica, *Geophys. Res. Lett.*, *40*, 3934–3939, doi:10.1002/grl.50712.

Jenkins, A., P. Dutrieux, S. S. Jacobs, S. D. McPhail, J. R. Perrett, A. T. Webb, and D. White (2010), Observations beneath Pine Island Glacier in West Antarctica and implications for its retreat, *Nat. Geosci.*, *3*(7), 468–472, doi:10.1038/ngeo890.

Joughin, I., et al. (2005), Continued deceleration of Whillans Ice Stream, West Antarctica, *Geophys. Res. Lett.*, *32*, L22501, doi:10.1029/2005GL024319.

Joughin, I., S. Tulaczyk, J. L. Bamber, D. Blankenship, J. W. Holt, T. Scambos, and D. G. Vaughan (2009), Basal conditions for Pine Island and Thwaites Glaciers, West Antarctica, determined using satellite and airborne data, *J. Glaciol.*, *55*(190), 245–257, doi:10.3189/002214309788608705.

Kamb, B. (2001), Basal zone of the West Antarctic ice streams and its role in lubrication of their rapid motion, in *The West Antarctic Ice Sheet: Behavior and Environment*, edited by R. B. Alley and R. A. Bindschadler, pp. 157–199, AGU, Washington, D. C., doi:10.1029/AR077p0157.

Kirchner, J. F., and C. R. Bentley (1990), RIGGS III: Seismic short-refraction studies using an analytical curve-fitting technique, *Ant. Res. Series*, *42*, 109–126.

Lowe, A. L., and J. B. Anderson (2003), Evidence for abundant subglacial meltwater beneath the paleo-ice sheet in Pine Island Bay, Antarctica, *J. Glaciol.*, *49*, 125–138, doi:10.3189/172756503781830971.

Luthra, T., S. Anandakrishnan, J. P. Winberry, R. B. Alley, and N. Holschuh (2016), Basal characteristics of the main sticky spot on the ice plain of Whillans Ice Stream, Antarctica, *Ear. Planet. Sci. Let.*, *440*, 12–19, doi:10.1016/j.epsl.2016.01.035.

McMillan, M., A. Shepherd, A. Sundal, K. Briggs, A. Muir, A. Ridout, A. Hogg, and D. Wingham (2014), Increased ice losses from Antarctica detected by CryoSat-2, *Geophys. Res. Lett.*, *41*, 3899–3905, doi:10.1002/2014GL060111.

Medley, B., et al. (2014), Constraining the recent mass balance of Pine Island and Thwaites glaciers, West Antarctica, with airborne observations of snow accumulation, *Cryosphere*, *8*(4), 1375–1392, doi:10.5194/tc-8-1375-2014.

Muto, A., L. E. Peters, K. Gohl, I. Sasgen, R. B. Alley, S. Anandakrishnan, and K. L. Riverman (2016), Subglacial bathymetry and sediment distribution beneath Pine Island Glacier ice shelf modeled using aerogravity and in situ geophysical data: New results, *Ear. Planet. Sci. Let.*, *433*, 63–75.

Nias, I. J., S. L. Cornford, and A. J. Payne (2016), Contrasting the modelled sensitivity of the Amundsen Sea Embayment ice streams, *J. Glaciol.*, *62*(233), 552–562, doi:10.1017/jog.2016.40.

Nitsche, F. O., K. Gohl, R. D. Larter, C. D. Hillenbrand, G. Kuhn, J. A. Smith, S. Jacobs, J. B. Anderson, and M. Jakobsson (2013), Paleo ice flow and subglacial meltwater dynamics in Pine Island Bay, West Antarctica, *Cryosphere*, *7*(1), 249–262, doi:10.5194/tc-7-249-2013.

Peters, L. E., S. Anandakrishnan, R. B. Alley, J. P. Winberry, D. E. Voigt, A. M. Smith, and D. L. Morse (2006), Subglacial sediments as a control on the onset and location of two Siple Coast ice streams, West Antarctica, *J. Geophys. Res.*, *111*, B01302, doi:10.1029/2005JB003766.

Peters, L. E., S. Anandakrishnan, R. B. Alley, and D. E. Voigt (2012), Seismic attenuation in glacial ice: A proxy for englacial temperature, *J. Geophys. Res.*, *117*, F02008, doi:10.1029/2011JF002201.

Pollard, D., and R. M. DeConto (2009), Modelling West Antarctic ice sheet growth and collapse through the past five million years, *Nature*, *458*(7236), 329–333, doi:10.1038/nature07809.

Rignot, E., J. L. Bamber, M. R. Van Den Broeke, C. Davis, Y. H. Li, W. J. Van De Berg, and E. Van Meijgaard (2008), Recent Antarctic ice mass loss from radar interferometry and regional climate modelling, *Nat. Geosci.*, *1*(2), 106–110, doi:10.1038/ngeo102.

Rignot, E., J. Mouginot, and B. Scheuchl (2011a), *MEaSUREs Antarctic Grounding Line From Differential Satellite Radar Interferometry*, NASA EOSDIS Distributed Active Archive Center at NSIDC, Boulder, Colo., Accessed on 17 June 2016.

Rignot, E., I. Velicogna, M. R. van den Broeke, A. Monaghan, and J. Lenaerts (2011b), Acceleration of the contribution of the Greenland and Antarctic ice sheets to sea level rise, *Geophys. Res. Lett.*, *38*, L05503, doi:10.1029/2011GL046583.

Rippin, D. M., D. G. Vaughan, and H. F. J. Corr (2011), The basal roughness of Pine Island Glacier, West Antarctica, *J. Glaciol.*, *57*(201), 67–76, doi:10.3189/002214311795306574.

Ritz, C., T. L. Edwards, G. Durand, A. J. Payne, V. Peyaud, and R. C. Hindmarsh (2015), Potential sea-level rise from Antarctic ice-sheet instability constrained by observations, *Nature*, *528*(7580), 115–118, doi:10.1038/nature16147.

Roethlisberger, H. (1972), *Seismic Exploration in Cold Regions*, *Rep. Monogr. II A2a*, 153 pp., U.S. Army Cold Reg. Res. and Eng. Lab., Hanover, N. H.

Rooney, S. T., D. D. Blankenship, R. B. Alley, and C. R. Bentley (1987), Till beneath ice stream-B2. Structure and Continuity, *J. Geophys. Res.*, *92*(B9), 8913–8920, doi:10.1029/JB092iB09p08913.

Scambos, T. A., T. M. Haran, M. A. Fahnestock, T. H. Painter, and J. Bohlander (2007), MODIS-based Mosaic of Antarctica (MOA) data sets: Continent-wide surface morphology and snow grain size, *Remote Sens. Environ.*, *111*(2–3), 242–257, doi:10.1016/j.rse.2006.12.020.

Scott, J. B. T., A. M. Smith, R. G. Bingham, and D. G. Vaughan (2010), Crevasses triggered on Pine Island Glacier, West Antarctica, by drilling through an exceptional melt layer, *Ann. Glaciol.*, *51*(55), 65–70, doi:10.3189/172756410791392763.

Shepherd, A., et al. (2012), A reconciled estimate of ice-sheet mass balance, *Science*, *338*(6111), 1183–1189, doi:10.1126/science.1228102.

Smith, A. M. (1997a), Basal conditions on Rutford Ice Stream, West Antarctica, from seismic observations, *J. Geophys. Res.*, *102*, 543–552, doi:10.1029/96JB02933.

Smith, A. M. (1997b), Variations in basal conditions on Rutford Ice Stream, West Antarctica, *J. Glaciol.*, *43*(144), 245–255.

Smith, A. M. (2007), Seismic reflection and subglacial conditions, *J. Env. Eng. Geophys.*, *12*(1), 3–13.

Smith, A. M., T. A. Jordan, F. Ferraccioli, and R. G. Bingham (2013), Influence of subglacial conditions on ice stream dynamics: Seismic and potential field data from Pine Island Glacier, West Antarctica, *J. Geophys. Res.-Solid Earth*, *118*(4), 1471–1482, doi:10.1029/2012JB009582.

Smith, E. C., A. M. Smith, R. S. White, A. M. Brisbourne, and H. D. Pritchard (2015), Mapping the ice-bed interface characteristics of Rutford Ice Stream, West Antarctica, using microseismicity, *J. Geophys. Res.-Earth Surf.*, *120*, 1881–1894, doi:10.1002/2015JF003587.

Stenoien, M. D., and C. R. Bentley (2000), Pine Island Glacier, Antarctica: A study of the catchment using interferometric synthetic aperture radar measurements and radar altimetry, *J. Geophys. Res.*, *105*(B9), 21,761–21,779, doi:10.1029/2000JB900151.

Tulaczyk, S., B. Kamb, R. P. Scherer, and H. F. Engelhardt (1998), Sedimentary processes at the base of a West Antarctic ice stream: Constraints from textural and compositional properties of subglacial debris, *J. Sedim. Res.*, *68*(3), 487–496.

Tulaczyk, S., W. B. Kamb, and H. F. Engelhardt (2000a), Basal mechanics of ice stream B, West Antarctica 1. Till mechanics, *J. Geophys. Res.*, *105*(B1), 463–481, doi:10.1029/1999JB900329.

Tulaczyk, S., W. B. Kamb, and H. F. Engelhardt (2000b), Basal mechanics of ice stream B, West Antarctica: 2. Undrained plastic bed model, *J. Geophys. Res.*, *105*(B1), 483–494, doi:10.1029/1999JB900328.

Vaughan, D. G., A. M. Smith, P. C. Nath, and E. Le Meur (2003), Acoustic impedance and basal shear stress beneath four Antarctic ice streams, *Ann. Glaciol.*, *36*, 225–232.

Voigt, D., L. E. Peters, and S. Anandakrishnan (2013), 'Georods': The development of a four-element geophone for improved seismic imaging of glaciers and ice sheets, *Ann. Glaciol.*, *54*(64), 142–148.

Winberry, J. P., S. Anandakrishnan, R. B. Alley, D. A. Wiens, and M. J. Pratt (2014), Tidal pacing, skipped slips and the slowdown of Whillans Ice Stream, Antarctica, *J. Glaciol.*, *60*(222), 795–807, doi:10.3189/2014JoG14J038.

Wingham, D. J., D. W. Wallis, and A. Shepherd (2009), Spatial and temporal evolution of Pine Island Glacier thinning, 1995–2006, *Geophys. Res. Lett.*, *36*, L17501, doi:10.1029/2009GL039126.

Appendix E

Morris *et al.,* 2017 (JGR-Earth Surface)

AGU PUBLICATIONS

JGR

Journal of Geophysical Research: Earth Surface

RESEARCH ARTICLE
10.1002/2017JF004357

Snow Densification and Recent Accumulation Along the iSTAR Traverse, Pine Island Glacier, Antarctica

E. M. Morris[1], R. Mulvaney[2], R. J. Arthern[2], D. Davies[3], R. J. Gurney[1], P. Lambert[1], J. De Rydt[2], A. M. Smith[2], R. J. Tuckwell[2], and M. Winstrup[4]

[1]Department of Meteorology, University of Reading, Reading, UK, [2]British Antarctic Survey, Cambridge, UK, [3]School of Geosciences, University of Edinburgh, Edinburgh, UK, [4]Centre for Ice and Climate, Niels Bohr Institute, University of Copenhagen, Copenhagen, Denmark

Abstract Neutron probe measurements of snow density from 22 sites in the Pine Island Glacier basin have been used to determine mean annual accumulation using an automatic annual layer identification routine. A mean density profile which can be used to convert radar two-way travel times to depth has been derived, and the effect of annual fluctuations in density on estimates of the depth of radar reflectors is shown to be insignificant, except very near the surface. Vertical densification rates have been derived from the neutron probe density profiles and from deeper firn core density profiles available at 9 of the sites. These rates are consistent with the rates predicted by the Herron and Langway model for stage 1 densification (by grain-boundary sliding, grain growth and intracrystalline deformation) and stage 2 densification (predominantly by sintering), except in a transition zone extending from ≈8 to ≈13 m from the surface in which 10–14% of the compaction occurs. Profiles of volumetric strain rate at each site show that in this transition zone the rates are consistent with the Arthern densification model. Comparison of the vertical densification rates and volumetric strain rates indicates that the expected relation to mean annual accumulation breaks down at high accumulation rates even when corrections are made for horizontal ice velocity divergence.

Key Points:
- Accumulation rates have been derived from snow density profiles by automatic layer identification
- The mean density profile may be used to estimate the depth of radar reflectors
- A significant transition region has been found between stage 1 and stage 2 densification

Supporting Information:
- Supporting Information S1

Correspondence to:
E. M. Morris,
emm36@cam.ac.uk

Citation:
Morris, E. M., Mulvaney, R., Arthern, R. J., Davies, D., Gurney, R. J., Lambert, P., … Winstrup, M. (2017). Snow densification and recent accumulation along the iSTAR traverse, Pine Island Glacier, Antarctica. *Journal of Geophysical Research: Earth Surface*, *122*. https://doi.org/10.1002/2017JF004357

Received 10 MAY 2017
Accepted 2 NOV 2017
Accepted article online 8 NOV 2017

©2017. The Authors.
This is an open access article under the terms of the Creative Commons Attribution License, which permits use, distribution and reproduction in any medium, provided the original work is properly cited.

1. Introduction

Better estimates of the contribution to sea level rise from Antarctica require an improvement in the meteorological and snow densification models used to interpret satellite measurements of elevation change. The UK Natural Environment Research Council (NERC) research program iSTAR provided an opportunity to collect data from the Pine Island Glacier (PIG) basin to verify these models and hence provide an improved estimate of sea level rise from this sector of Antarctica.

In this paper we focus on the analysis of snow density profiles collected using a neutron probe at 22 sites along an 890 km traverse of the basin and repeat measurements made a year later. These allow recent accumulation to be determined from the snow stratigraphy and profiles of volumetric strain rate to be calculated.

Accumulation has been successfully determined from neutron probe density profiles in the dry snow area of Greenland (Morris & Wingham, 2011, 2014, 2015), but in the PIG basin the method faces a new challenge: complex meteorological conditions which do not always produce a clear annual variation in snow density. New techniques of analysis have therefore had to be developed.

The PIG strain rate profiles are of particular interest because they come from sites with a wide range of mean annual accumulation and relatively high surface density. The transition density between stage 1 and stage 2 densification in the Herron and Langway (1980) model (and many others, see section 3) is reached about halfway down the profile, so that the transition region can be examined in some detail. We are also able to consider the effect of horizontal velocity divergence on densification using data from mid-ice stream sites.

In this paper we compare direct measurements of the change in density with time with the rates inferred indirectly from density profiles, assuming steady state conditions. This indirect method is based on an early suggestion made by Robin (1958) that in a natural snow cover the increase in overburden stress is linearly related to the proportional decrease in air volume in the mean density profile. Much of the existing data

on strain rates in polar snow is derived from profiles using the Robin hypothesis. We show that at the high accumulation sites in the PIG basin this method does not produce good estimates in the transition region between stage 1 and stage 2 densification.

This is important because, as we shall show in section 6, in the PIG basin ≈31% of compaction occurs in the surface layer and stage 1 region, 10–14% in the transition region, and 37–33% in the stage 2 region. Thus, compaction in the transition region is a significant proportion of the total compaction as the surface snow turns to ice.

2. The iSTAR Traverse

The iSTAR traverse route (Figure 1) crosses the Pine Island Glacier basin from site 1 at the northeast upstream boundary to site 22 near the grounding line in Pine Island Bay to the west. The positions and climatological characteristics of the sites are given in Table 1, which gives values for the mean annual accumulation derived from airborne radar survey data (Medley et al., 2014) over the period 1985–2009 and the regional atmospheric climate model RACMO 2.3 (van Wessem et al., 2014) over the period 1979–2013. The RACMO2.3 values for the iSTAR sites have been determined by interpolation between model grid points. For convenience the table also includes the mean annual temperatures (from 10 m temperatures measured during the traverses), accumulation rates for the period between traverses and mean annual accumulation rates derived from iSTAR traverse data in section 4.2. The latter cover periods of 8 to 29 years up to and including 2012.

Mean annual temperature only varies by a few degrees over the traverse, but the accumulation increases significantly in the southwest of the basin. Satellite altimeter observations show elevation change rates also vary considerably over the basin, with the greatest thinning rates in areas of high ice velocity (Shepherd et al., 2001). In order to distinguish between dynamic thinning and the effect of changes in accumulation on elevation, the traverse route was chosen to pass through sites with low accumulation and low thinning (sites 2 and 10), low accumulation and high thinning (sites 7 and 13), high accumulation and low thinning (site 22), and high accumulation and high thinning (site 18).

In the austral summer of 2013/2014 (T1) the route was traversed from site 1 to site 22; in 2014/2015 (T2) the traverse began at site 22. Snow density profiles were measured at all sites during T1 using a neutron probe deployed in 13 m deep access holes. During T2 repeat measurements were made in the same access holes, and new profiles were measured nearby in order to record the density of the snow accumulated since T1. At sites 7, 8, 13, 15, 17, and 18 density profiles were collected over a nested grid to establish local spatial variability on the 1 m to 1 km scale. During T1 ground penetrating radar (GPR) and very high bandwidth radar (pRES) surveys were conducted between sites, and during T2 firn cores to 50 m depth were collected at sites 1, 4, 6, 7, 8, 10, 13, 15, 18, and 20. Airborne surveys using the ASIRAS radar in December 2014 covered the traverse from site 7 to site 22. Other airborne survey tracks covered areas north of site 9, south of site 15 and passed between sites 4 and 5 on a north-south line.

The neutron probe profiles serve to supplement the firn core data and provide the density data needed to derive accumulation from the various radar measurements of snow layering. This work will be reported elsewhere; in this paper we focus on the derivation of densification and accumulation rates directly from the neutron probe profiles. The densification analysis requires an estimate of the horizontal velocity divergence at each site. Direct measurements of this divergence are available from the repeat measurement of strain networks during T1 and T2 at sites 6 to 9 and 13 to 19. Estimates can also be made from velocity maps for the PIG basin derived from satellite data.

3. Theory

3.1. The Steady State Approximation

Snow densification models need to provide a constitutive law to describe the dependence of volumetric strain rate, $\dot{\varepsilon}$, on the applied stress, σ, and on the strength of the snow, characterized by its bulk density, temperature, and sometimes by other variables such as grain size, coordination number, and impurity concentration. The material-following densification rate is related to $\dot{\varepsilon}$ by the definition

$$\dot{\varepsilon} = -\frac{1}{\rho}\frac{D\rho}{Dt} \tag{1}$$

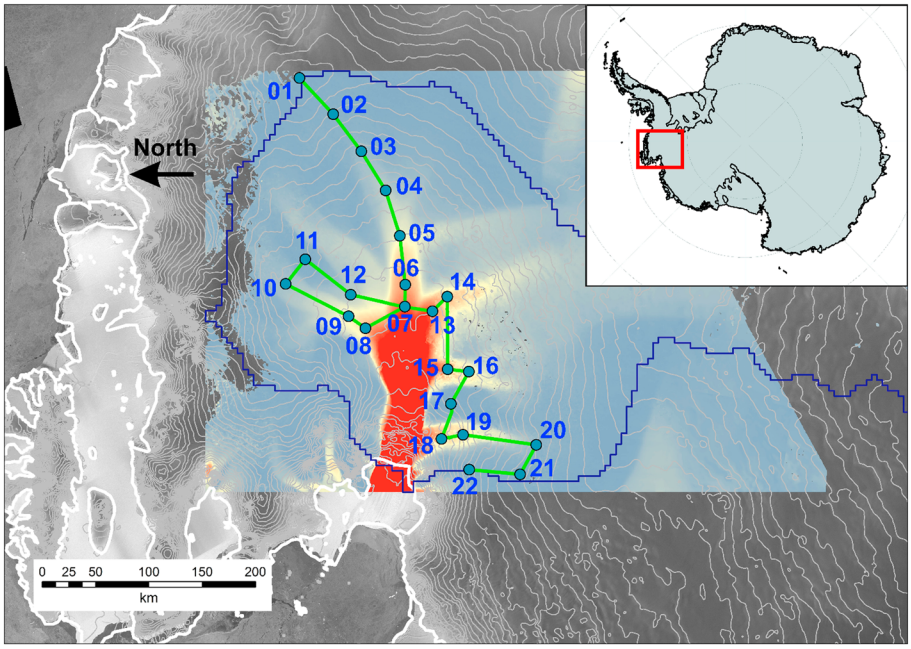

Figure 1. Route of the Pine Island Glacier (PIG) traverses in the austral summers of 2013/2014 (T1) and 2014/2015 (T2) with the 22 sites of neutron probe measurements shown as blue dots. Contours are shown at 50 m intervals (Bamber et al., 2009), the background color shows surface velocity (Rignot et al., 2011) and the basin boundary is shown as a blue solid line.

Table 1
Climatological Conditions at the iSTAR Traverse Sites

Site	x (km)	Latitude (deg)	Longitude (deg)	Elevation (mae)	T_m^* (°C)	$a_{(2014)}$ (mwe a^{-1})	$\bar{a}^{(1)}$ (mwe a^{-1})	$\bar{a}^{(2)}$ (mwe a^{-1})	$\bar{a}^{(3)}$ (mwe a^{-1})	N (a)
1	0	−74.565	−86.913	1,362	−25.5	0.41		0.36	0.35 (−0.04) (+0.02)	17
2	47	−74.865	−88.030	1,195	−25.3	0.14	0.276 ± 0.025	0.30	0.34 (−0.02) (0.00)	19
3	91	−74.111	−89.224	1,032	−24.3	0.39	0.300 ± 0.010	0.38	0.43 (−0.03) (+0.03)	14
4	135	−75.319	−90.524	860	−23.6	0.56	0.365 ± 0.008	0.47	0.58 (−0.05) (+0.05)	10
5	180	−75.431	−92.060	798	−23.1	0.22	0.459 ± 0.018	0.54	0.45 (−0.03) (+0.08)	18
6	226	−75.456	−93.718	708	−22.6	0.45	0.466 ± 0.024	0.53	0.45 (0.00) (+0.07)	13
7	247	−75.440	−94.460	679	−22.6	0.53	0.444 ± 0.027	0.53	0.33 (−0.04) (+0.06)	20
8	290	−75.090	−95.070	708	−22.2	0.40	0.367 ± 0.016	0.48	0.32 (−0.05) (+0.05)	17
9	310	−74.956	−94.631	733	−22.2	0.29	0.354 ± 0.009	0.46	0.37 (−0.04) (+0.02)	18
10	377	−74.442	−93.448	867	−21.5	0.24	0.336 ± 0.020	0.33	0.23 (−0.04) (+0.01)	27
11	407	−74.620	−92.700	909	−21.9	0.16	0.297 ± 0.015	0.35	0.23 (−0.02) (+0.02)	29
12	461	−74.998	−93.930	762	−22.2	0.28	0.346 ± 0.007	0.47	0.28 (−0.02) (+0.02)	24
13	540	−75.670	−94.690	691	−22.4	0.50	0.504 ± 0.027	0.57	0.43 (−0.03) (0.00)	15
14	560	−75.805	−94.231	749	−22.4	0.44	0.550 ± 0.020	0.57	0.47 (0.00) (+0.04)	14
15	629	−75.750	−96.730	712	−21.9	0.81	0.618 ± 0.010	0.59	0.80 (−0.04) (0.00)	8
16	649	−75.926	−96.898	763	−21.9	0.66	0.667 ± 0.014	0.61	0.51 (0.00) (0.00)	13
17	684	−75.740	−97.930	716	−21.2	0.42	0.678 ± 0.014	0.71	0.52 (0.00) (+0.04)	11
18	719	−75.617	−99.073	527	−19.6	0.71	0.639 ± 0.012	0.82	0.69 (0.00) (0.00)	9
19	739	−75.803	−99.048	704	−20.2	0.44	0.757 ± 0.009	0.79	0.69 (0.00) (0.00)	9
20	810	−76.404	−99.828	1,096	−22.8	0.83	0.687 ± 0.004	0.62	0.64 (0.00) (+0.09)	10
21	842	−76.224	−100.770	1,075	−22.3	0.78	0.690 ± 0.005	0.69	0.75 (−0.08) (0.00)	9
22	890	−75.804	−100.280	819	−20.1	0.75	0.806 ± 0.014	0.88	0.78 (−0.06) (0.00)	8

Note. x is the distance along the traverse, T_m^* is the mean annual temperature in degrees Celsius (Mulvaney & Smith, 2017), $a_{(2014)}$ is the accumulation rate between Traverse 1 and Traverse 2, and $\bar{a}$ is the mean annual accumulation rate estimated using (1) airborne radar data (Medley et al., 2014), (2) the regional atmospheric climate model RACMO 2.3 (van Wessem et al., 2014), and (3) the iSTAR density profiles (see section 4.2). N is the number of years over which $\bar{a}^{(3)}$ is averaged.

The variable ρ is the snow density and t time. In polar firn there are density fluctuations on an annual or subannual scale about a vertically smoothed density ρ_0, which monotonically increases with depth. In the upper layer of the snow, densification is enhanced by annual and subannual temperature variations, but below ≈2–3 m depth the effect of these variations is sufficiently diminished for it to be possible to assume a constant temperature to a first approximation. The steady state approximation applies below the surface layer for constant mean annual temperature T_m and constant accumulation rate $\bar{a}$.

The Robin hypothesis (Robin, 1958) introduced in section 1 is equivalent to writing

$$\dot{\varepsilon} = c\left(\frac{\rho_i - \rho_0}{\rho_0}\right) \tag{2}$$

where ρ_i is the density of ice and c is a site-specific constant. Hidden within this formulation is an assumption that the overburden stress σ, which increases with water equivalent depth, is offset by a corresponding increase in snow strength because of some other factor that also increases with depth, such as the time since deposition, τ. Hence, at a given site, the volumetric strain rate depends only on the mean density and c can be interpreted as a constant density-corrected volumetric strain rate.

In the one-dimensional case when the horizontal velocity divergence $\dot{\varepsilon}_H$ is negligible $\dot{\varepsilon} = \dot{\varepsilon}_{zz}$ where

$$\dot{\varepsilon}_{zz} = \frac{\partial w}{\partial z} \tag{3}$$

We define a coordinate system in which vertical distance, z, velocity, w, and water equivalent height, q, are positive upward. In this system density *decreases* with increasing z and q. Given a constant accumulation rate $\bar{a} = -\rho_0 w$, equations (2) and (3) give

$$\begin{aligned} c &= \frac{\bar{a}}{\rho_0(\rho_i - \rho_0)}\frac{\mathrm{d}\rho_0}{\mathrm{d}z} \\ &= \frac{\bar{a}}{\rho_i}\frac{\mathrm{d}}{\mathrm{d}z}\left(\ln\left(\frac{\rho_0}{(\rho_i - \rho_0)}\right)\right) \end{aligned} \tag{4}$$

The value of c can be estimated from a single steady state profile $\rho_0(z)$ by plotting the best fit straight line through $\ln(\rho_0/(\rho_i - \rho_0)$ as a function of z over a section of the profile, say from the point z where the water equivalent height is q to the point $z + Z$ where the water equivalent height is $q + Q$. Writing the (negative) gradient of this line as $-k\rho_i$ we obtain

$$c = -\bar{a}k \tag{5}$$

where k is a positive constant. To emphasis the point that k is derived from the rate of change of density with the vertical coordinate z, we shall refer to it as the "vertical densification rate."

Equation (5) shows that, if we accept the Robin hypothesis, in the 1-D, steady state case the density-corrected volumetric strain rate c may be calculated from the vertical densification rate if the (constant) accumulation rate is known. A similar calculation could be made given any other specified density function, of course, but the Robin hypothesis leads to a particularly simple transformation.

3.2. Time-Varying Conditions

Suppose that in a natural firn layer, built up under time-varying conditions, the effect of density on strain rate is given by a factor $(\rho_i - \rho)/\rho$ by analogy with equation (2), that is, the Robin hypothesis still holds. Then given measurements of density $\rho_1(q)$ for a material element at time t and $\rho_2(q)$ for the same element at time $t + \Delta t$, we may calculate a density-corrected volumetric strain rate as

$$\begin{aligned} F(q) &= \frac{1}{\Delta t}\int_t^{t+\Delta T}\left(\frac{\rho}{\rho_i - \rho}\right)\dot{\varepsilon}\,\mathrm{d}t \\ &= -\frac{1}{\Delta t}\int_t^{t+\Delta T}\left(\frac{1}{\rho_i - \rho}\right)\frac{D\rho}{Dt}\mathrm{d}t \\ &= \frac{1}{\Delta t}\ln\left(\frac{\rho_i - \rho_2}{\rho_i - \rho_1}\right) \end{aligned} \tag{6}$$

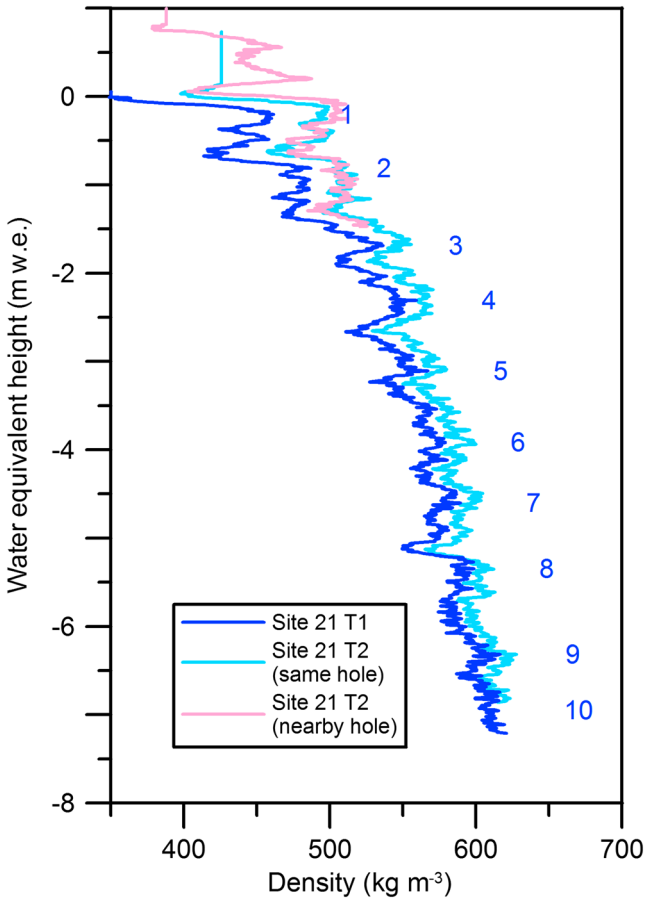

Figure 2. Density at site 21 measured at 1 cm intervals and smoothed with a three-point running mean. Peak 1 marks the 2013 austral winter (c. July 2013). During T2, the T1 access hole was reopened by digging through the accumulated snow and reprofiled. An overlapping profile from a nearby hole extends this profile to the T2 surface and shows two 2014 austral winter peaks.

To minimize the effect of density fluctuations we calculate an average value of F over a section of the profile from q to $q + Q$ where Q is several years of accumulation. Then

$$\bar{F} = \frac{1}{Q\Delta t}\int_{q}^{q+Q} \ln\left(\frac{\rho_i - \rho_2}{\rho_i - \rho_1}\right) dq \tag{7}$$

Let $-k\rho_i$ now be the gradient of the best straight line through a plot of $\ln(\rho_1/(\rho_i - \rho_1)$ as a function of z over the section of the profile from q to $q + Q$ and let $\bar{a}$ be the mean annual accumulation over this section. The indirect method of estimating strain rate from a single profile is based on the assumption that

$$\bar{F} \approx -\bar{a}k \tag{8}$$

by analogy with the steady state case (equation (5)). In this paper we determine $\bar{F}$, $\bar{a}$, and k separately to see how far this assumption holds.

3.3. Stage 1 and Stage 2 Densification

Herron and Langway (1980) proposed different densification rates for snow with $\rho < 550$ kg m^{-3} and 550 kg m$^{-3} \leq \rho \leq 800$ kg m^{-3}. Other authors have followed suit. This implies a sharp transition between "stage 1 densification" for the lower densities, in which grain boundary sliding and grain growth are thought to be the dominant mechanisms and "stage 2 densification" for the higher densities in which sintering is the primary mechanism. The proposed transition density is the maximum packing density of uniform spheres of ice. However, in natural snow, with a range of grain sizes, high-resolution measurements of density profiles (Hörhold et al., 2011) suggest that the transition density varies between sites and that the transition may be gradual. For this reason it is useful to define a transition region between the stages 1 and 2 regions and to use the subscripts 0, t, and 1 to distinguish values of the vertical densification rate k. (This has the advantage of being a simple and consistent notation, but means that our symbol k_1 is not the same as the k_1 used by Herron & Langway, 1980 for stage 2 densification). We envisage the transition as a gradual change in the balance of densification processes from those dominant in stage 1 to those dominant in stage 2.

In this paper we shall allocate densities greater than 550 kg m^{-3} from depths greater than 15 m below the surface to the stage 2 region. Densities greater than 550 kg m^{-3} from depths that are less than 15 m below the surface will be regarded as potentially transitional. Note that this choice of how to bin the data does not imply that there are "hard" boundaries to the transition region in reality; it is a convenience for the sake of data analysis.

Herron and Langway (1980) suggest an Arrhenius expression

$$k_0 = k_0^* \exp\left(\frac{-E_0}{RT_m}\right) \tag{9}$$

for the local (site-specific) stage 1 vertical densification rate k_0. Here R = 8.314 J mol^{-1} K^{-1} is the gas constant, $E_0 = (10.16 \pm 0.94)$ kJ mol^{-1} is the stage 1 activation energy, T_m mean annual temperature in degrees Kelvin and $k_0^* = 11(+6, -4)$ (metre water equivalent (mwe)) $^{-1}$ is a constant global stage 1 vertical densification rate. Equation (9) does not necessarily apply in the near-surface layer with strongly varying temperature. For stage 2 densification, Herron and Langway (1980) propose

$$k_1 = (\bar{a})^{-1/2} k_1^* \exp\left(\frac{-E_1}{RT_m}\right) \tag{10}$$

where $E_1 = 21.40$ kJ mol^{-1} is the stage 2 activation energy and the constant $k_1^* = 575$ mwe$^{-1/2}$ a$^{-1/2}$.

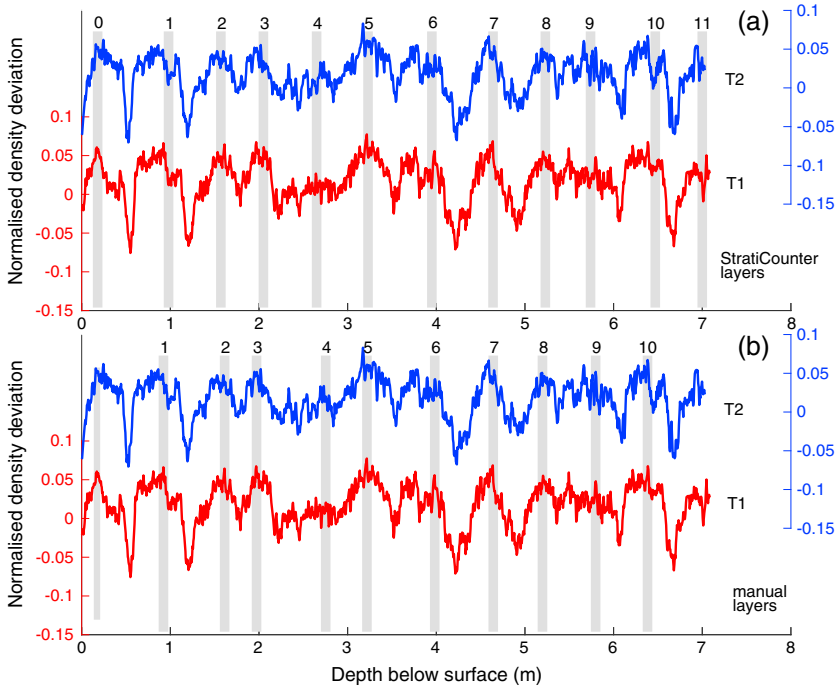

Figure 3. Normalized density profiles r_1 and r_2 from site 4. The ordinate for r_1 (T1 profile, red) is shown to the left and that for r_2 (T2 repeat profile, blue) to the right. (a) The annual layers picked by *StratiCounter* delineated with grey vertical lines; (b) the manually picked layers used as input. Note that *StratiCounter* plots increasing depth ($-z$) from left to right.

If $\bar{F} = F_0$ in the stage 1 region and F_1 in the stage 2 region, the Robin hypothesis implies

$$F_0 \exp\left(\frac{E_0}{RT_m}\right) \approx -k_0^* \bar{a} \tag{11}$$

and

$$F_1 \exp\left(\frac{E_1}{RT_m}\right) \approx -k_1^* (\bar{a})^{1/2} \tag{12}$$

Other authors have suggested modifications to the Herron and Langway (1980) model. For example, Arthern et al. (2010) suggest that both k_0 and k_1 are independent of $\bar{a}$ from consideration of the physics and find a good fit to Antarctic strain rate data from sites with $\bar{a} = 0.13 - 1.04$ mwe a^{-1} using

$$k_0 = 686.7\,\text{mwe}^{-1} \exp\left(\frac{-17.6\,\text{kJ mol}^{-1}}{RT_m}\right) \tag{13}$$

for stage 1 and

$$k_1 = 294.3\,\text{mwe}^{-1} \exp\left(\frac{-17.6\,\text{kJ mol}^{-1}}{RT_m}\right) \tag{14}$$

for stage 2. All the iSTAR sites lie within this mean annual accumulation range. Ligtenberg et al. (2011) found it necessary to add empirical tuning parameters containing $\bar{a}$ to the Arthern model in order to match profiles from Antarctica over a wider range of accumulation. They suggest multiplying the right-hand side (RHS) of equation (13) by the ratio

$$\text{MO} = 1.435 - 0.151 \ln\left[\left(10^3 \text{mwe}^{-1}\text{a}\right)\,\bar{a}\right] \tag{15}$$

and the RHS of equation (14) by

$$\text{MO} = 2.366 - 0.293 \ln\left[\left(10^3 \text{mwe}^{-1}\text{a}\right)\,\bar{a}\right]. \tag{16}$$

Since these tuning parameters have been derived using data from a wider range of climatological conditions than the data used to derive the Arthern model itself, there is an element of extrapolation involved.

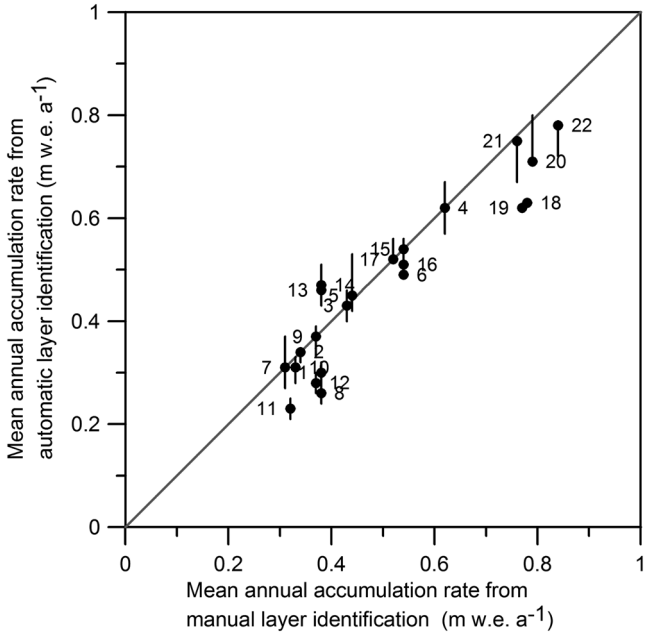

Figure 4. Estimates of mean annual accumulation rate given by the automatic layer identification routine *StratiCounter* as a function of the estimates derived by manual layer identification alone. Points lying below the 1:1 line arise when *StratiCounter* detects a layer missed by the manual method, which is used to provide initial estimates of the annual layering. The vertical bars show the uncertainty in the mean annual accumulation arising from the uncertainty in the number of layers determined by *StratiCounter*.

3.4. The Effect of Horizontal Velocity Divergence

We now consider the densification of snow above a horizontal ice surface subject to strain. At the ice/snow boundary

$$\dot{\varepsilon}_H = -\dot{\varepsilon}_{zz} \tag{17}$$

since the ice is incompressible. This horizontal velocity divergence is imposed upon the overlying snow and is constant with depth in the snow layer. If the main density peaks lie initially at water equivalent heights $q_1(i)$ and, after time interval Δt, at depths $q_2(i)$ conservation of mass in a snow column initially of unit area gives

$$q_1(i) \approx \left(1 + \dot{\varepsilon}_H \Delta t\right) q_2(i) \tag{18}$$

Given a suitable choice of origin for q_2 the gradient of the best straight line fitted through the points $q_1(i) - q_2(i)$, $q_2(i)\Delta t$ can be used to estimate the horizontal velocity divergence from the neutron probe data albeit with an uncertainty which, for the iSTAR sites, is mostly of the same order as $\dot{\varepsilon}_H$. Fortunately, for the PIG basin more precise estimates are available, either from direct measurement of strain networks or from velocity maps derived by remote sensing. Horizontal velocity divergences range from −36.7 to $+89 \cdot 10^{-4}$ a^{-1}.

In the presence of horizontal velocity divergence the accumulation in an annual layer τ years old is reduced by the factor $1/(1 + \dot{\varepsilon}_H \tau)$. This factor is not significant for the time scale of the neutron probe data, but the deeper firn core annual accumulation rates do need to be corrected.

The density-corrected vertical strain rate, F_z, may be estimated by subtracting a correction for the effect of $\dot{\varepsilon}_H$:

$$F_z(\rho) \approx F(\rho) - \left(\frac{\rho_m}{\rho_i - \rho_m}\right) \dot{\varepsilon}_H \,, \tag{19}$$

where ρ_m is the mean density over time Δt. That is, for a given density change the vertical compression of a volume element increases in magnitude if there is horizontal loss of mass from the element.

In the steady state case the constant accumulation rate $\bar{a} \approx -\rho_0 w(1 + \dot{\varepsilon}_H \tau)$ and substitution for w in equation (3) no longer leads to equation (4). We, therefore, do not necessarily expect that $\bar{F}_z$ can be estimated from $-\bar{a}k(\rho_1)$ unless τ is sufficiently small. For example, given a horizontal divergence of 0.01 a^{-1}, for $\dot{\varepsilon}_H \tau$ to be an order of magnitude less than 1, τ must be less than 10 years.

3.5. Errors

Since neutron emission is a random process, there is a random error in density measured using the neutron probe, which in our case is $\sigma_\rho \approx 0.02\rho$. From the neutron probe calibration equation, the relative systematic errors in ρ_2 and q_2, which arise if the nominal value R for the access hole radius has a systematic error, σ_R^* can be estimated as

$$\frac{\sigma_\rho^*}{\rho_2} \equiv \frac{\sigma_q^*}{q_2} \approx -0.4\frac{\sigma_R^*}{R} \tag{20}$$

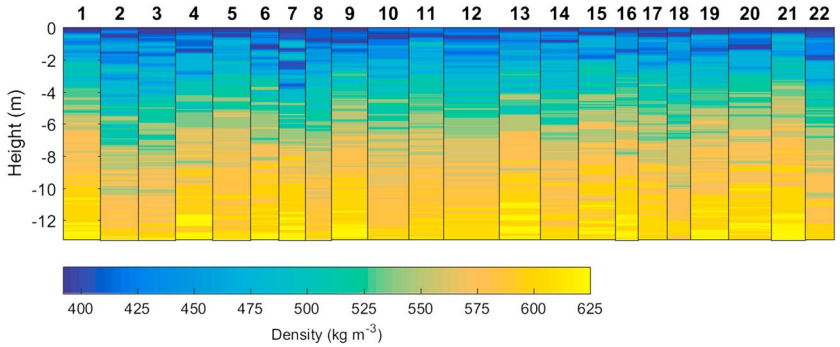

Figure 5. Density variation over the iSTAR traverse in T1.

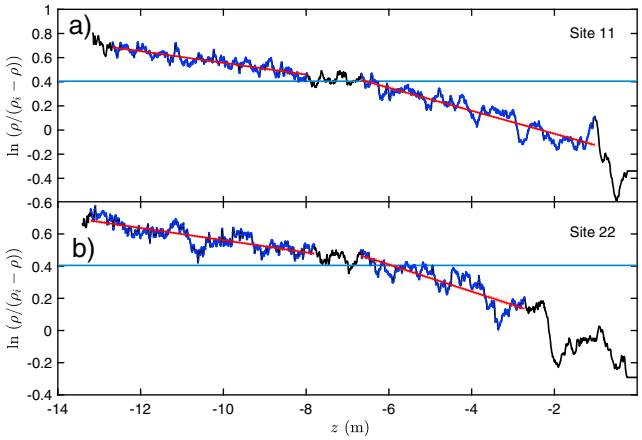

Figure 6. Profile of $\ln(\rho/(\rho_i - \rho))$ as a function of z for (a) site 11 (low accumulation) and (b) site 22 (high accumulation). The data are shown at intervals of 1 cm of water equivalent. Red lines show the best linear fits to the data shown in blue. These data are either continuously above, or continuously below, the horizontal line $\ln(\rho/(\rho_i - \rho)) = 0.424$ (ρ = 550 kg m^{-3}). The start and end points of the fits are at density peaks. Data excluded from the fits are shown in black.

If the radius of the access hole changes over time Δt because of horizontal velocity divergence

$$\frac{\sigma_R^*}{R} \approx \dot{\varepsilon}_H \Delta t \tag{21}$$

For $\dot{\varepsilon}_H \approx 10^{-3}$ a^{-1} and $\Delta t \approx 1$ a, the relative systematic error in density and water equivalent height arising from horizontal velocity divergence is $\approx 4 \cdot 10^{-4}$, that is, very much smaller than the random error. However, larger systematic errors can arise if the access hole becomes enlarged by careless drilling or if the probe does not remain resting against the sidewall of the hole.

$\bar{F}$ has a random error, σ_F, which arises from the fluctuations in F, and a systematic error

$$\sigma_F^* = -\frac{1}{\Delta t}\left(\frac{\rho_2}{\rho_i - \rho_2}\right)\left(\frac{\sigma_\rho^*}{\rho_2}\right) \tag{22}$$

which is ≈0.6 $\dot{\varepsilon}_H$ for a representative value of ρ_2 of 550 kg m^{-3}. Using this value the potential systematic errors are of the same order as the random errors for $\bar{F}$. The random error in $\dot{\varepsilon}_H$ is unknown so we simply set $\sigma_{Fz} = \sigma_F$.

4. Methods

As an example of the data obtained using the neutron probe, Figure 2 shows profiles of density at site 21 as a function of water equivalent height. The techniques involved have been described in a series of papers (Morris & Cooper, 2003; Morris, 2008; Morris & Wingham, 2011, 2014, 2015) so will not be repeated here. Very near the surface both snow and atmosphere are included in the measurement volume, so the apparent snow density decreases. Missing near-surface data are represented in the profiles by a constant density (vertical line).

4.1. Accumulation Rates in 2014

At a given site, the water equivalent Δq of snow accumulated over the time between measurements can be determined from the short T2 record, using the T1 record to help identify the position of the T1 surface. An error of order ± 0.01 mwe may arise because of the missing near-surface data and will be more significant at low accumulations.

4.2. Annual Accumulation Series

The stratigraphic method of determining annual accumulation series depends on the identification of an annual variation in the physical properties of the surface snow. Benson (1962) singles out the "fall (autumn) sequence" of coarse-grained, low-density snow, often containing hoar crystals, overlain by a finer-grained, harder layer of higher density and uses this discontinuity to mark the boundary of annual layers in dry snow areas of the Greenland Ice Sheet. Lister (1959) also uses a “criterion” layer of depth hoar as the annual marker in Antarctic snow, but finds that this is not present in some years while in others there are hoar layers both above and below a hard summer layer. He stresses the importance of examining the cyclical structure of the data as a whole, rather than relying on a single marker. Alley et al. (1997) comment that Benson’s simple fall sequence is not always found in Greenland snow. There may be a series of depth hoar/surface hoar complexes formed during the summer, separated by finer-grained, denser snow. These authors therefore suggest that the annual marker should be taken at the center of the hoar complexes, that is, at the midsummer rather than fall surface.

Where there is a clear annual variation in density, as at site 21 (Figure 2), the density peaks can be selected for use as annual markers without too much difficulty (Morris & Wingham, 2011). Here late summer/autumn low-density hoar layers alternate with winter snow which has densified under the influence of warm summer temperatures and the mass between peaks is an estimate of accumulation from mid-winter (June/July) to mid-winter. However, at some sites along the iSTAR traverse, for example, at site 7, the stratigraphy is quite complex and difficult to interpret, possibly because there are competing coastal influences from east and west. In an attempt to improve the manual estimates of annual layering we used an automatic method to help ensure the criteria for layer identification were applied consistently.

Table 2
Vertical Densification Rates and Density-Corrected Strain Rates Along the iSTAR Traverse

Site	k_0 (10^{-4} mwe^{-1})	k_t (10^{-4} mwe^{-1})	k_1 (10^{-4} mwe^{-1})	$\dot{\varepsilon}_H$ (10^{-4} a^{-1})	$F_0 \pm \sigma_F$ (10^{-4} a^{-1})	$F_{z0} \pm \sigma_{Fz}$ (10^{-4} a^{-1})	$F_t \pm \sigma_F$ (10^{-4} a^{-1})	$F_{zt} \pm \sigma_{Fz}$ (10^{-4} a^{-1})	σ_F^* (10^{-4} a^{-1})
1	1,027 ± 17	474 ± 12	300 ± 7	6.06	−313 ± 13	−321 ± 13	−176 ± 5	−187 ± 5	4
2	833 ± 29	439 ± 22		0.44	−168 ± 15	−236 ± 15	−91 ± 7	−188 ± 7	0
3	909 ± 22	417 ± 14		1.08	−357 ± 15	−359 ± 15	−234 ± 5	−236 ± 5	1
4	843 ± 33	456 ± 15	302 ± 6	−28.86	−549 ± 26	−511 ± 26	−286 ± 6	−235 ± 6	−17
5	1,234 ± 49	372 ± 12		7.87	−360 ± 18	−369 ± 18	−175 ± 5	−189 ± 5	5
6	840 ± 43	464 ± 12	314 ± 8	**9.3**	−482 ± 17	−494 ± 17	−359 ± 6	−376 ± 6	6
7	1,094 ± 39	504 ± 13	314 ± 8	**−36.7**	−324 ± 14	−281 ± 14	−212 ± 6	−148 ± 6	−22
8	1,063 ± 13	414 ± 12	370 ± 10	**12.1**	−370 ± 14	−384 ± 14	−208 ± 5	−230 ± 5	7
9	1,000 ± 20	493 ± 14		**26.1**	−325 ± 16	−358 ± 16	−162 ± 5	−209 ± 5	16
10	1,009 ± 42	501 ± 22	458 ± 14	1.58	−222 ± 15	−224 ± 15	−145 ± 5	−148 ± 5	1
11	1,039 ± 17	527 ± 13		13.52	−270 ± 14	−286 ± 14	−154 ± 5	−179 ± 5	8
12	1,143 ± 20	533 ± 9		23.53	−304 ± 18	−332 ± 18	−174 ± 5	−217 ± 5	14
13	894 ± 43	494 ± 15		**25.1**	−329 ± 18	−362 ± 18	−237 ± 6	−282 ± 6	15
14	856 ± 22	380 ± 12		**68.6**	−349 ± 12	−433 ± 12	−316 ± 6	−440 ± 6	41
15	949 ± 55	304 ± 16	280 ± 12	**43.6**	−802 ± 48	−862 ± 48	−412 ± 8	−489 ± 8	26
16	947 ± 23	446 ± 15		**51.2**	−582 ± 24	−649 ± 24	−303 ± 6	−398 ± 6	31
17	704 ± 32	444 ± 18		**10.7**	−511 ± 27	−525 ± 27	−284 ± 6	−303 ± 6	6
18	755 ± 34	518 ± 16	274 ± 11	**43.7**	−710 ± 25	−771 ± 25	−497 ± 7	−576 ± 7	26
19	1,021 ± 39	541 ± 18		**89**	−574 ± 20	−695 ± 20	−552 ± 7	−724 ± 7	53
20	884 ± 24	508 ± 17	257 ± 8	7.50	−588 ± 20	−598 ± 20	−378 ± 6	−391 ± 6	5
21	934 ± 23	426 ± 13		2.53	−724 ± 20	−727 ± 20	−535 ± 8	−539 ± 8	2
22	914 ± 27	413 ± 13		−13.38	−628 ± 23	−647 ± 23	−422 ± 7	−446 ± 7	8

Note. The parameters k_0 and k_t are stage 1 and transitional vertical densification rates derived from T1 neutron probe profiles; k_1 is the stage 2 vertical densification rate derived from T2 firn core density profiles. $\dot{\varepsilon}_H$ is the horizontal divergence derived from velocity maps or strain networks (in bold). F_0 and F_t are means of the density-corrected volumetric strain rate and F_{z0}, F_{zt} are means of the density-corrected vertical strain rate, with their errors, and σ_F^* the systematic error arising from $\dot{\varepsilon}_H$.

4.2.1. StratiCounter

The layer counting algorithm *StratiCounter* (release date 30/4/2015) was developed for ice core analysis (Winstrup et al., 2012; Winstrup, 2016) and allows a variety of data records (e.g., chemical species, isotopic ratios, and stratigraphy) on a common depth scale to be used together to determine the annual layering in a core. Some preprocessing of the density data is required before it can be used. We fit a fourth-order polynomial ρ_{0n} to each of the n available profiles from a given site and then normalize so that the density peaks are not damped with depth. This produces n data series of the form

$$r_n = \frac{\rho_n - \rho_{0n}}{\rho_i - \rho_{0n}} \tag{23}$$

which are input to *StratiCounter*.

The manual peak picks are read in as a first estimate of the layering and have a strong influence on the outcome. This is because *StratiCounter* looks for repeated patterns, not single peaks; it is up to the user to decide whether a typical annual layer should have a single peak or a more complex density variation. There is then an iteration process to determine the best positions of the annual markers. The standard deviation of the log-normal distribution of annual accumulation, σ_a, is held constant during iteration, usually at the value determined from the manual peak picks.

As an example of the output from *StratiCounter*, Figure 3 shows the annual layers inferred by *StratiCounter* for site 4. Two normalized density profiles are available for this site, from T1 and T2. The first estimate of annual layering was made by identifying peaks in the T1 profile. The standard deviation in layer thickness is $\sigma_a = 0.24$,

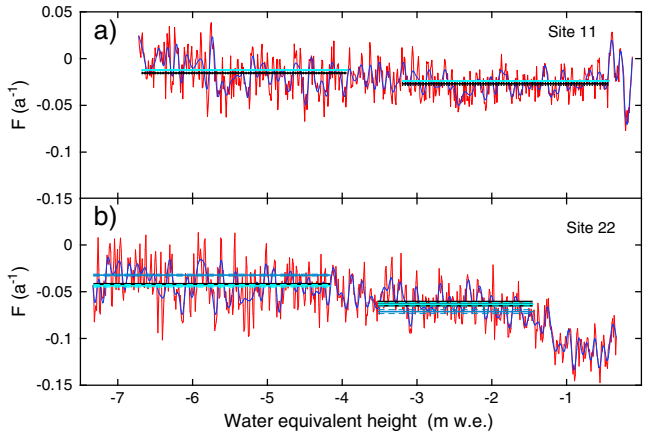

Figure 7. Profile of F with water equivalent height q for (a) site 11 (low accumulation) and (b) site 22 (high accumulation). The red curve shows data at intervals of 1 cm of water equivalent; the blue curve shows these data smoothed over ≈3 cmwe. The black lines show mean values of F above and below the nominal transition density of $\rho = 550$ kg m^{-3}. At site 22 the near-surface layer affected by the annual temperature variation extends to a greater depth than at site 11.

within the expected range for annual accumulation determined from chemical species (0.15–0.3). The upper part of the figure shows the same curves, with the annual layering determined automatically by giving equal weight to each density profile. One extra layer has been identified at the bottom of the profile, and the position of some of the annual markers has changed to reflect peaks in the T2 record.

Site 4 is moderately difficult to interpret because of the multiple density peaks in some winters; it requires experience to recognize these by eye. At sites where density peaks have not formed in some years, it is even harder to determine a good manual estimate of layering from the density profile alone. Given a range of possible initial estimates *StratiCounter* may converge on different solutions for the layering. In this case further information from neighboring sites must be used to fix the number of layers expected between the surface and a recognizable peak at a given depth. This is akin to layer tracing in an accumulation radar return or identification of volcanic horizons in ice cores. *StratiCounter* is designed to be able to include such tie points in automatic analysis of ice cores, but the neutron probe density records are much shorter, so the extra information is simply used to select from competing solutions. This was necessary only at sites 4 and 7, where we also used the ice core chemistry to guide the initial estimate of annual layering.

The great advantages of the automatic method are that missed or spurious layers can be identified using a rigorous statistical method and that the uncertainty in the number of annual layers is defined. Hence, errors can be attached to the mean annual accumulation rates derived using *StratiCounter*. Note that layers are "missed" in the sense that a consistent criterion for layer selection has not been applied at the manual stage and *StratiCounter* has been able to detect this and rectify it by adding a layer. The converse is the situation in which *StratiCounter* subtracts a "spurious" layer to rectify an inconsistency. Using *StratiCounter* improves the internal logical consistency of the stratigraphic method but does not, of course, guarantee that the annual layers have been correctly identified. For this ice core data, ideally from more than one chemical species, are required.

Figure 4 shows that the automatic rates are generally slightly less than those derived by manual peak picking, an indication that missed layers have been found. An uncertainty of one layer is, of course, more important at higher accumulations where the number of annual layers in the 13 m profile is smaller. However, this is offset by the fact that the higher accumulation regions have less complex stratigraphy and are easier to interpret. Hence, there is no correlation between the percentage error (+ or −) derived using *StratiCounter* and mean annual accumulation.

5. Results

5.1. Spatial Variation of Density

Figure 5 shows the large-scale variation of density with distance along the iSTAR traverse. Each density column (derived from a single profile) is centered over a site and covers the distance between the midpoints with

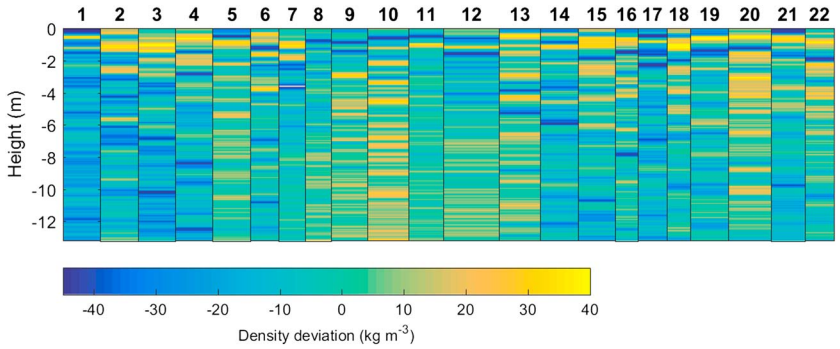

Figure 8. Deviation from the global mean density profile over the iSTAR traverse.

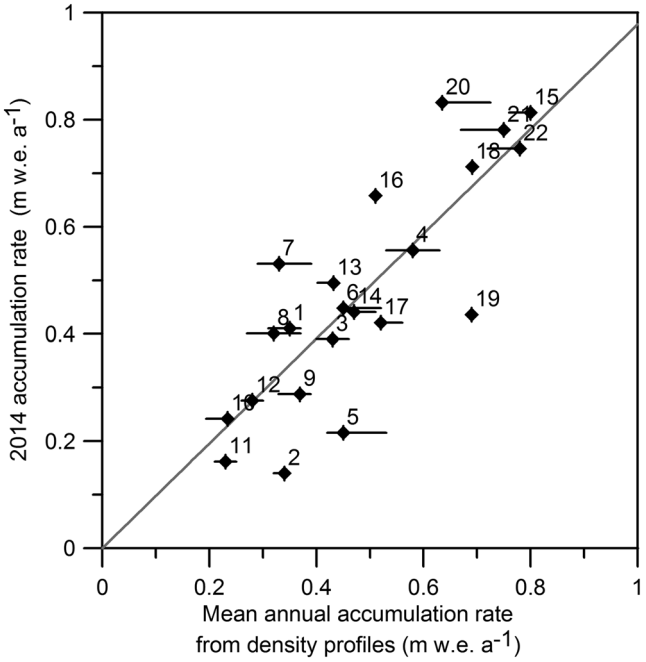

Figure 9. The 2014 annual accumulation rate as a function of mean annual accumulation rate derived from the density profiles. The solid line shows the best linear fit.

neighboring sites. Note that there are loops in the traverse path so that, for example, sites 8 and 12 are quite close together. Some of the annual layers can be traced between nearby sites, but there is no obvious feature that can be traced along the traverse. The nominal density for the transition between stages 1 and 2 is reached at 7–9 m below the surface and the density at the bottom of the profile ($z = -13$ m) varies from 600 to 625 kg m^{-3}.

5.2. Accumulation

We derive annual accumulation series for each profile by retaining the manual peak positions but adding or subtracting peaks to conform with the number of layers determined using *StratiCounter*. This allows us to retain a common definition of the annual marker between sites. The mean value over the profile is shown in Table 1 as is the 2014 accumulation rate $a_{(2014)} \approx \Delta q/\Delta t$.

5.3. Vertical Densification Rates, k

At most sites neutron probe profiles were obtained to around 13 m depth. We also have some firn core density profiles to 50 m. Local vertical densification rates k_0, k_t, and k_1 are given by the gradients of linear fits to profiles of $\ln(\rho/(\rho_i - \rho))$, where we write k_t for the possibly transitional value obtained from the lower part of the neutron probe profiles and k_1 for the Stage 2 value obtained from the firn cores. As an example, Figure 6 shows the fits for the neutron probe profiles for two sites with similar mean annual temperature but contrasting mean annual accumulation. Data from the upper part of each profile have been excluded from the Stage 1 fit, because here densification has been enhanced by warm summer temperatures. Each section to be fitted runs from density peak to density peak, to avoid skewing the gradient. However, there is clearly a potential for a systematic error in k_0 and k_t, since the annual fluctuations in density are not regular and are relatively large compared to the range of the ordinate. The fits for all sites are shown in the supporting information as Figures S1 to S3.

Values of k are given in Table 2 with random errors derived by minimizing the sum of the deviations from the best straight line. Stage 1 values range from $(704 \pm 32) \cdot 10^{-4}$ mwe^{-1} at site 17 to $(1{,}234 \pm 49) \cdot 10^{-4}$ mwe^{-1} at site 5. Transitional values range from $(372 \pm 12) \cdot 10^{-4}$ mwe^{-1} at site 5 to $(541 \pm 18) \cdot 10^{-4}$ mwe^{-1} at site 19. Stage 2 values are lower still, ranging from $(257 \pm 8) \cdot 10^{-4}$ mwe^{-1} at site 20 to $(458 \pm 14) \cdot 10^{-4}$ mwe^{-1} at site 10.

5.4. Density-Corrected Volumetric Strain Rates, *F*

Figure 7 shows an example of the variation of F with water equivalent height for sites 11 and 22. The mean values F_0 and F_t are calculated from peak to peak, over exactly the same ranges of water equivalent as used in the calculation of k_0 and k_t. There is no obvious step change between the two values. Table 2 shows that mean values of F_0 range from -0.080 a^{-1} at site 15 to -0.022 a^{-1} at site 10. Transitional vales F_t range from -0.055 a^{-1} at site 19 to -0.015 a^{-1} at site 10. The low values at site 2 may be inaccurate because this was the only site where ρ_2 does not come from the same access hole as ρ_1. F_{z0} is significantly different from F_0 at sites 4, 7, 9, 12, 14, 16, 18, and 19 (higher horizontal velocity divergence) and site 2 where there is a possible systematic error in R. F_{zt} is significantly different from F_t at more sites (1, 4, 5, 6, 7, 8, 9, 11, 12, 13, 14, 15, 16, 17, 18, 19, and 2), because the random error σ_F decreases with depth and the fluctuations in density are attenuated.

6. Discussion

6.1. Spatial Variation of Density

In order to analyze radar returns from continuous tracks across a basin, a single global density profile is often used (see, for example, Richardson et al., 1997). Such a profile, derived from the neutron probe profiles from sites 6 to 22, has been used to calculate two-way travel (twt) times for iSTAR GPR data (H. Konrad, personal communication). Fitting a third-order polynomial to this profile gives the global density profile

$$\rho_G = (385 \text{ kg m}^{-3}) - (39.8 \text{ kg m}^{-4})\, z - (2.91 \text{ kg m}^{-5})\, z^2 - (9.01\, 10^{-2} \text{kg m}^{-6})\, z^3 \quad (24)$$

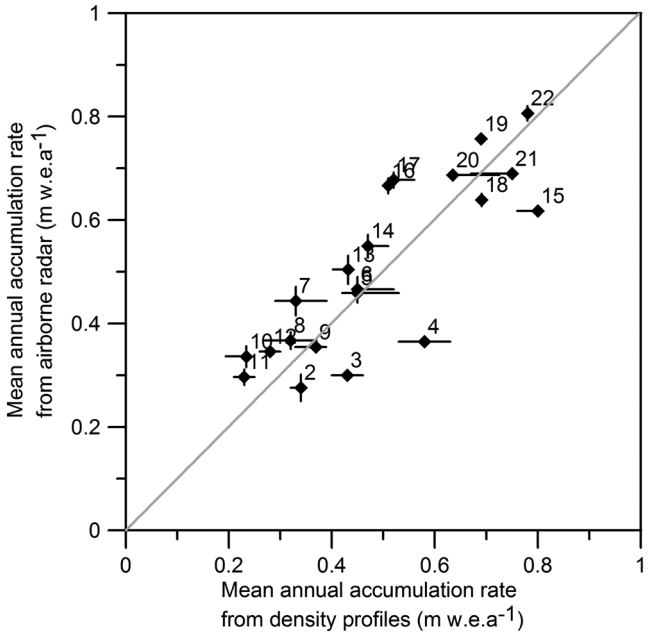

Figure 10. Mean annual accumulation rate derived from airborne radar data (Medley et al., 2014) as a function of mean annual accumulation rate from the density profiles. The solid line shows the best linear fit through the origin.

Figure 8 shows the deviation from ρ_G at each site. Sites 1–5 are not noticeably different from the sites used to produce ρ_G. The annual and subannual fluctuations in density are up to ±8%. However, the cumulative effect of these fluctuations with depth is much smaller. Using the polynomial leads to a maximum underestimate of twt of 0.44 ns, that is, ≈5 cm in depth for any of the 22 sites. This is significant only for location of reflections very near the surface.

Taking $\rho_G = 385\ \mathrm{kg\ m^{-3}}$ at $z = 0$ as an estimate of the density of the surface snow, we may now calculate the percentage of total compaction that takes place in the surface layer and stage 1 (i.e., to $\rho \leq 550\ \mathrm{kg\ m^{-3}}$) as 31% and in stage 3 (i.e., $\rho \geq 800\ \mathrm{kg\ m^{-3}}$) as 22%. Hence, stage 2 and transitional compaction form 47% of the whole. For practical reasons we have allocated neutron probe data with $z > -15$ m to the transitional region and firn core data with $z \leq -15$ m to stage 2; the division occurs at $\rho = 600$–$625\ \mathrm{kg\ m^{-3}}$. This leads to an estimate of 10–14% compaction in the transitional zone and 37–33% in stage 2.

Throughout the traverse the spatial variation is complex and it is clear that mean annual temperature and accumulation are not the only factors controlling it. For example, sites 10 and 11 have similar values of T_m and $\bar{a}$ (Table 1) but at site 10 (mid-ice stream valley) the density is greater than that at site 11 (interstream ridge). Similarly, 20 and 21 have similar T_m and $\bar{a}$ and again the valley site 20 has denser snow than the ridge site 21. In a multiple linear regression analysis of 40 measurements of surface snow density, Kaspers et al. (2004) found that T_m contributed ≈70% to the surface density, $\bar{a} \approx 2.5\%$, and the annual average wind speed at 10 m ≈7.5%. If the iSTAR valley sites have an increased surface density because of higher (katabatic) wind speeds, the difference in these profiles can be explained.

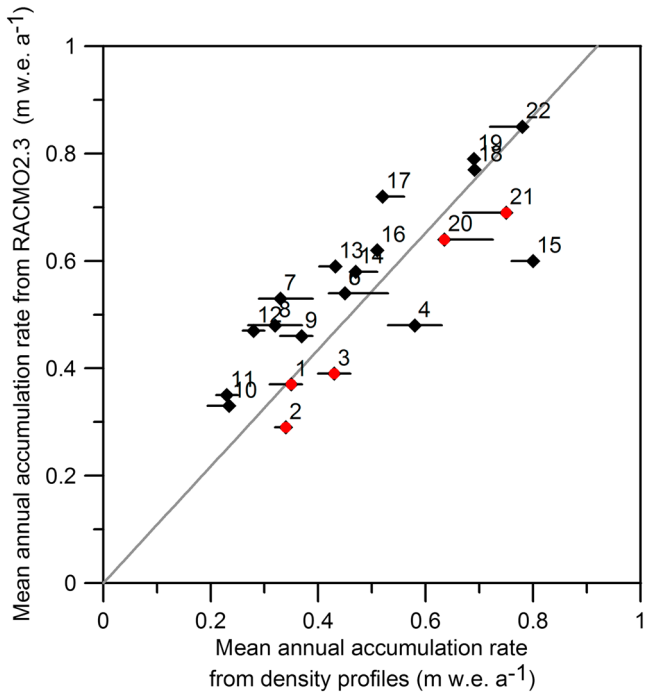

Figure 11. Mean annual accumulation rate derived from RACMO 2.3 data (van Wessem et al., 2014) compared to mean annual accumulation rate from the density profiles. The gradient of the best linear fit through the origin for all sites is 1.08 ± 0.05 ($r^2 = 0.96$). Sites above 1,000 m above sea level (asl) are shown in red.

Although we do not have measurements of surface density from the probe, an approximate value of ρ_S can be obtained for each site from third-order polynomial fits to the density profiles $\rho(z)$. The regression equation

$$\rho_S = (1620 \pm 460\ \mathrm{kg\ m^{-3}}) - (5 \pm 1.8\ \mathrm{kg\ m^{-3}\ K^{-1}})\, T_m + (68 \pm 14\ \mathrm{kg\ m^{-3}\ mwe^{-1}a})\, \bar{a} \qquad r^2 = 0.58 \tag{25}$$

shows a sensitivity to $\bar{a}$ similar to the 67 kg m^{-3}mwe^{-1} a found by Kaspers et al. (2004) who used measured values of ρ_S. However, the range of T_m over the traverse is small, and the (unknown) wind speed cannot be explicitly included in the regression, so we do not put too much weight on this equation.

6.2. Accumulation

The accumulation values derived from the density profiles will in due course be used with radar and core data to produce an accumulation map of the PIG basin. At that stage it will be appropriate to discuss the spatial and temporal variability of accumulation over the basin and make a full comparison with meteorological model data. In this section we need only to establish that the point values of accumulation at the sites where we have measured densification rates are reliable. This will allow us to proceed to test models of densification that use mean annual accumulation rate as a parameter.

Figure 9 shows the directly measured 2014 rates $a_{(2014)}$ as a function of the mean annual accumulation rates $\bar{a}^{(3)}$. The best linear fit is

$$a_{(2014)} = (0.99 \pm 0.15)\, \bar{a}^{(3)} - (0.00 \pm 0.08) \qquad r^2 = 0.68 \tag{26}$$

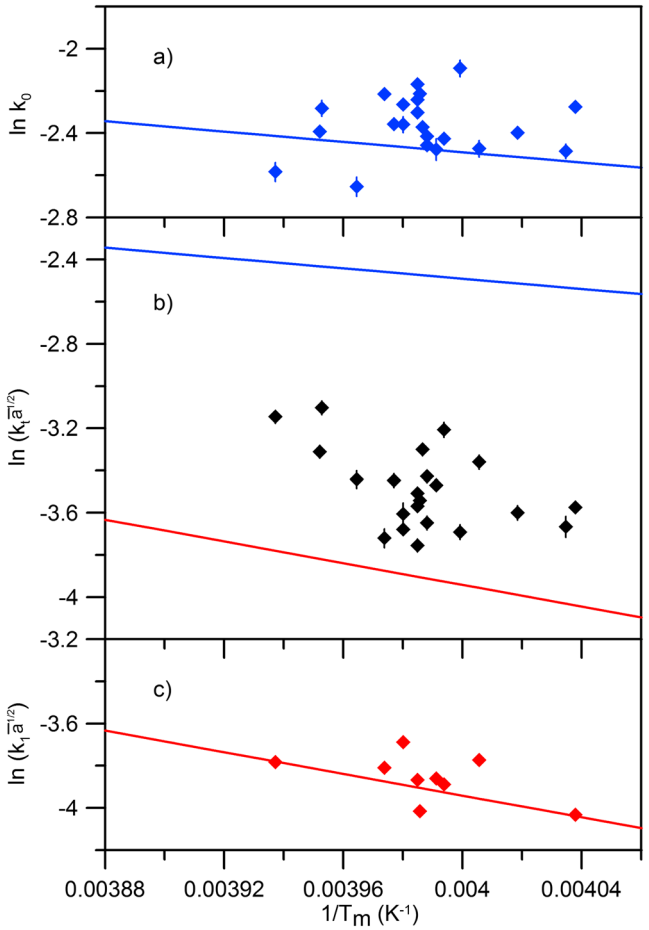

Figure 12. Vertical densification rates as a function of mean annual temperature, T_m: (a) stage 1 rates, k_0, estimated from neutron probe data with $\rho \leq 550$ kg m^{-3}, (b) transitional rates, k_t, estimated from neutron probe data with $\rho \geq 550$ kg m^{-3} and -13 m $\leq z \leq -8$ m and corrected for accumulation by a factor $\bar{a}^{1/2}$, and (c) stage 2 rates, k_1, estimated from firn core density data with 800 kg m$^{-3} > \rho > 550$ kg m^{-3} and $z \geq -8$ m, also corrected for accumulation by the factor $\bar{a}^{1/2}$. Straight lines show the Herron and Langway (1980) densification rates for stages 1 (blue) and 2 (red).

Hence, over the traverse as a whole the accumulation rate in 2014 is not significantly different from the mean. Bearing in mind that the accumulation rates are point values, it is not surprising that there is a fair amount of scatter. However, no one point stands out as anomalous. This is a useful independent check of the stratigraphic estimates of mean annual accumulation.

Figure 10 shows values $\bar{a}^{(1)}$ of mean annual accumulation rate over the period 1985–2009 derived from airborne radar data by Medley et al. (2014) as a function of rates $\bar{a}^{(3)}$ derived from the density profiles, which cover periods of 8 to 29 years up to 2012. The best linear fit is

$$\bar{a}^{(1)} = (0.79 \pm 0.12)\,\bar{a}^{(3)} + (0.12 \pm 0.06)\text{mwe a}^{-1} \qquad r^2 = 0.69. \tag{27}$$

A nonzero intercept suggests a constant (absolute) difference between $\bar{a}^{(1)}$ and $\bar{a}^{(3)}$. If we discount this, the best linear fit through the origin is

$$\bar{a}^{(1)} = (1.00 \pm 0.04)\,\bar{a}^{(3)} \qquad r*^2 = 0.96. \tag{28}$$

(Note that the coefficients of determination r^2 and $r*^2$ are not calculated in the same way for regression with nonzero and zero intercept and so are not strictly comparable). Equation (27) is preferable on purely statistical grounds. However, on physical grounds equation (28) is perhaps more realistic. In either case there are no obvious outliers, so that comparison with the radar data is again a useful check of the stratigraphic accumulation rates.

Finally, we compare the mean annual accumulation rates $\bar{a}^{(2)}$ for the period 1979–2013 given by a regional atmospheric climate model, RACMO 2.3 (van Wessem et al., 2014) to the accumulation rates $\bar{a}^{(3)}$ over N years up to and including 2012. The best linear fit through the origin is

$$\bar{a}^{(2)} = (1.09 \pm 0.05)\,\bar{a}^{(3)} \qquad r*^2 = 0.96. \tag{29}$$

suggesting either that the model slightly overestimates accumulation over the whole traverse or that accumulation was higher over the more recent period. Recalculating $\bar{a}^{(2)}$ over N years for each site, that is, matching the averaging period for model and field data, produces essentially the same gradient (Figure 11). This suggests that the model estimates may indeed be a little too high, at least at some sites. We note that Medley et al. (2013) have shown that for the neighboring Thwaites Glacier basin, radar and RACMO2 mean annual accumulations are very close for the elevation range 1,000–1,400 m above sea level (asl). Restricting the fit to this range gives

$$\bar{a}^{(2)} = (0.95 \pm 0.03)\,\bar{a}^{(3)} \qquad r*^2 = 1.00. \tag{30}$$

so that the model values for the higher-elevation sites 1, 2, 3, 20, and 21 are slightly too low. Overall, the model values support the stratigraphic values and there are no obvious outliers.

Having established reliable point values of accumulation at the iSTAR sites, we can now use our data to test various densification models. We first compare the iSTAR vertical densification rates with the predictions of the Herron and Langway (1980) model. This model has parameters derived by fitting vertical densification rates derived from firn core profiles so we may think of it as a "k model." We then compare the iSTAR volumetric strain rates with the Arthern et al. (2010) model, which has parameters derived by fitting strain rates (an "F model") and the Ligtenberg et al. (2011) model which adds further empirical parameters to the Arthern model. Since these parameters are derived by fitting the depth to transition densities in firn core profiles, this becomes a "hybrid model."

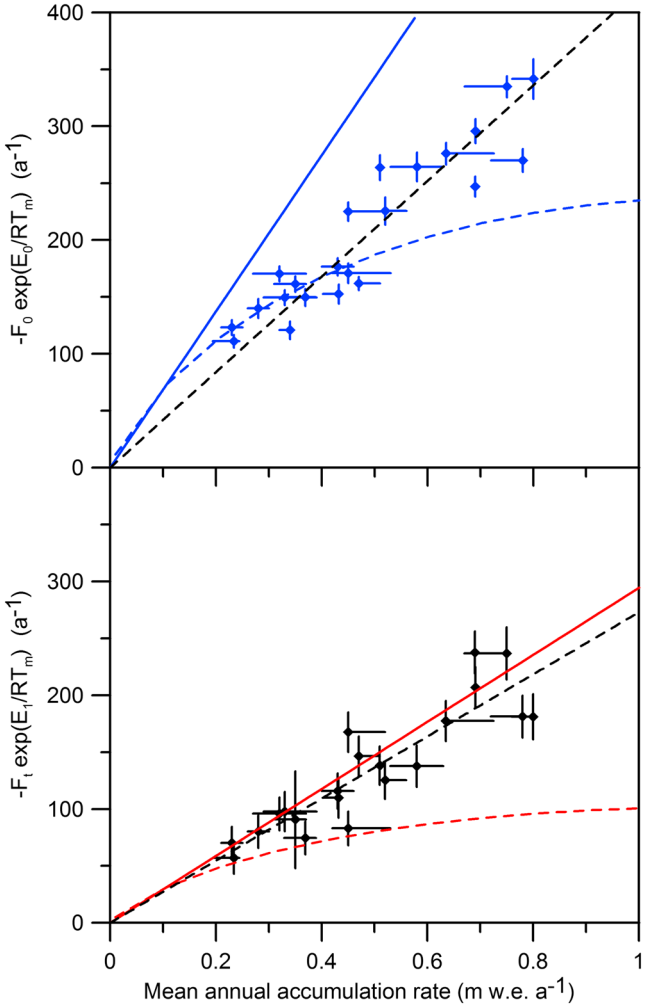

Figure 13. (top) $-F_0 \exp(E_0/RT_m)$ and (bottom) $-F_t \exp(E_1/RT_m)$ as a function of mean annual accumulation rate. The activation energies are set to the Arthern value $E_0 = E_1 = 17.6$ kJ mol^{-1}. The blue and red solid lines show the curves expected for stages 1 and 2 from the Arthern model and the blue and red dashed lines the curves expected from the Ligtenberg model. Black dashed lines show the best fit to the data through the origin.

6.3. Vertical Densification Rates

We can test whether the local vertical densification rates from the iSTAR sites given in Table 2 are consistent with the Herron and Langway (1980) model by plotting $\ln(k_0)$ as a function of $1/T_m$ (see equation (9) for stage 1 and $\ln(k_1)\bar{a}^{1/2}$ as a function of $1/T_m$ for stage 2 (see equation (10)). In the Herron and Langway (1980) model our transitional region is treated as stage 2 so we plot $\ln(k_t)\bar{a}^{1/2}$ as a function of $1/T_m$.

Figure 12a shows that iSTAR values of $\ln(k_0)$ are consistent with the Herron and Langway (1980) stage 1 curve. The temperature range is too narrow, and the scatter too great, for independent values of k_0^* and E_0 to be determined from these data alone. However, it is worth noting that site 4 and sites 15–22 do not have anomalous values of k_0, suggesting that the model can be used for sites with mean annual accumulations outside the 0.02–0.50 mwe a^{-1} range for which it was derived.

Figure 12c shows that the values of $\ln(k_1)\bar{a}^{1/2}$ derived from the firn cores are consistent with the Herron and Langway (1980) stage 2 curve and are less scattered, as might be expected as the length of the profile from which the values are derived is nearly 10 times greater than for stage 1. Again, the high accumulation sites do not have anomalous values. The values of $\ln(k_t)\bar{a}^{1/2}$ (Figure 12b) lie between the stage 1 and stage 2 curves; hence, our description of these as transitional.

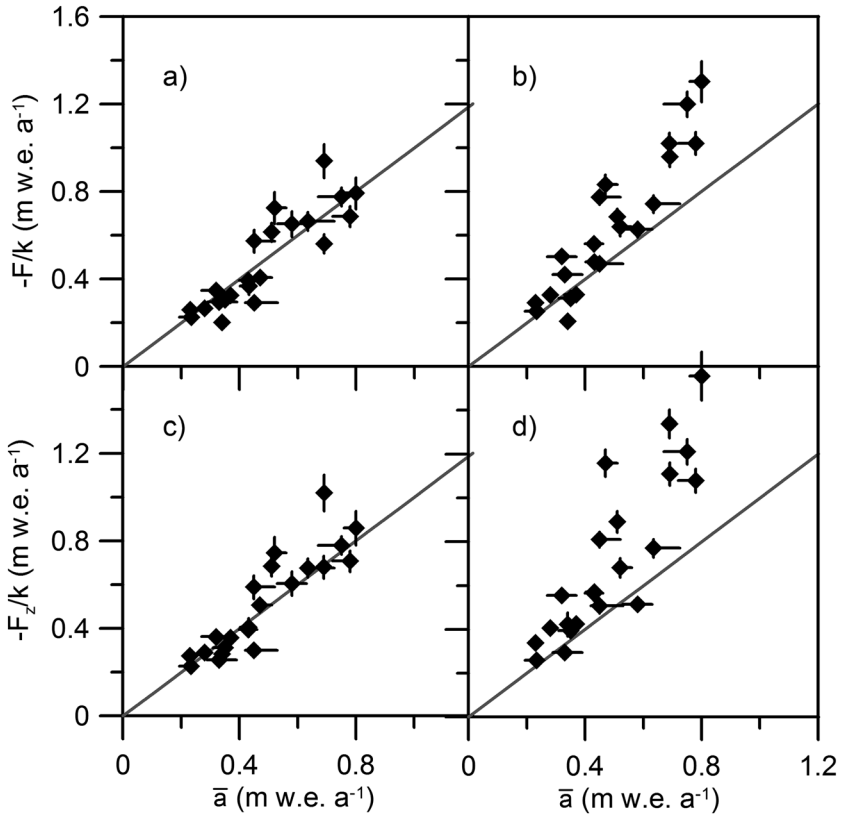

Figure 14. Variation of the ratio of measured density-corrected strain rates to the vertical densification rate inferred from profiles for stage 1 and transitional densification. (a) $-F_0/k_0$, (b) $-F_t/k_t$, (c) $-F_{z0}/k_0$, and (d) $-F_{zt}/k_t$ as a function of mean annual accumulation rate $\bar{a}$. The grey lines show the 1:1 curve in each plot.

6.4. Volumetric Strain Rates

The Arthern et al. (2010) model implies an activation energy of 17.6 kJ mol^{-1} for both stages 1 and 2 once $T \approx T_m$. We test whether the iSTAR strain rates are consistent with this model by plotting $-F_0 \exp\left(\frac{E_0}{RT_m}\right)$ and $-F_t \exp\left(\frac{E_1}{RT_m}\right)$, with $E_0 = E_1 = 17.6$ kJ mol^{-1}, as a function of $\bar{a}$ for all sites except site 2 (Figure 13) for which the data are not reliable. The best linear fit through the origin for the PIG data in stage 1 has a gradient of 421 ± 12 mwe^{-1} with $r^2 = 0.98$, whereas the gradient expected from the model is 687 mwe^{-1} . That is, the Arthern model overpredicts the strain rate in stage 1. This is not unexpected as the Arthern model was tuned using data which included the surface snow layer, in which temperature varies and densification is enhanced, within the nominal stage 1. The best linear fit through the origin for the PIG data in the transition stage has a gradient of 273 ± 10 mwe^{-1} with $r^2 = 0.97$. This is close to the gradient of 294 mwe^{-1} expected from the Arthern model. This is nominally a stage 2 value, but was derived from strain rates in snow with 550 kg m^{-3} $< \rho \lessapprox 700$ kg m^{-3}, that is, from data covering the transitional densification region and only part of the stage 2 region. This may be why the model fits the PIG transitional data so well.

In order to simulate the two nominal transition depths at which $\rho = 550$ and 800 kg m^{-3} in firn cores, Ligtenberg et al. (2011) found it necessary to supplement the Arthern model with functions depending on mean annual accumulation (equations (15) and (16)). In stage 1, at low accumulation rates, the Ligtenberg correction improves the fit to the PIG data. At higher accumulation rates in stage 1, and in the transition region, the strain rate is underpredicted. These differences can be explained by examining the data used to derive the Ligtenberg corrections. The depth at which $\rho = 550$ kg m^{-3} depends on densification both in the surface layer and in stage 1 (as we define it), with the relative importance of enhanced densification in the surface layer dependent on $\bar{a}$. Similarly the depth range between $\rho = 550$ and 800 kg m^{-3} covers the whole of stage 2 and the transition region, with the relative importance of higher densification in the transition region dependent on $\bar{a}$. It is therefore physically reasonable that there should be correction factors to the Arthern model, which depend on the accumulation rate. However, since the Arthern model has been derived for sites

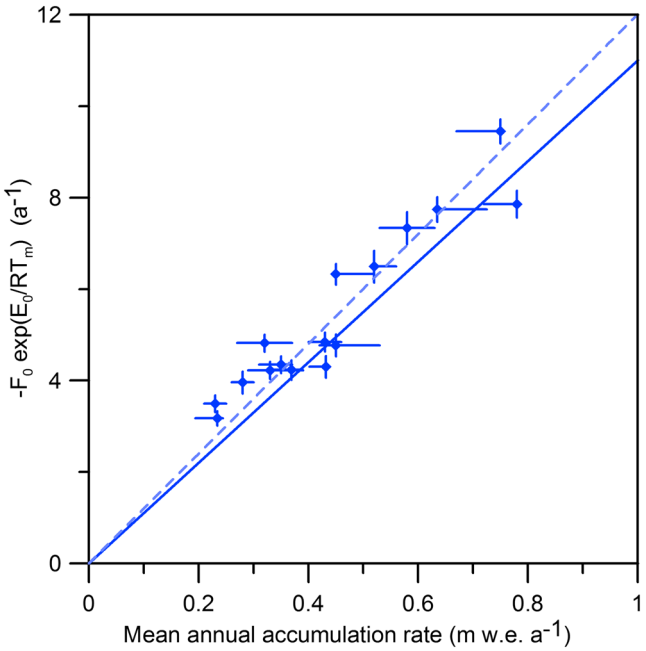

Figure 15. $-F_0 \exp(E_0/RT_m)$ as a function of mean annual accumulation rate. The activation energy is set to the Herron and Langway stage 1 value $E_0 = 10.16$ kJ mol^{-1}. The solid line is the curve expected for stage 1 from the Herron and Langway model and the dashed line the best fit to the data through the origin.

with $\bar{a} = 0.13–1.04$ mwe a^{-1}, ice core data from sites with $\bar{a}$ outside this range cannot necessarily be used in the determination of these correction factors.

6.5. *F/k*

Finally, we test whether the negative ratio of the density-corrected volumetric strain rate F to the vertical densification rate k is approximately equal to the mean annual accumulation rate $\bar{a}$, as we expect for steady state conditions when horizontal flow divergence can be neglected (equation (8)). Figure 14a shows this is the case for stage 1 (where the mean value $\bar{F} = F_0$ and $k = k_0$), but Figure 14b shows that transitional values of $-F/k$ (with $\bar{F} = F_t$ and $k = k_t$) clearly deviate from the 1:1 curve for higher accumulations. Figures 14c and 14d show the ratio of the density-corrected vertical strain rate F_z to the vertical densification rate k as a function of $\bar{a}$. At low accumulations in stage 1, $-F_{z0}/k_0$ is slightly closer than $-F_0/k_0$ to $\bar{a}$; at high accumulations in the transitional stage the opposite is true and $-F_t/k_t$ is slightly closer than $-F_{zt}/k_t$ to $\bar{a}$. For some high accumulation sites (14, 15, and 16), $\tau\dot{\varepsilon}_H > 0.05$ and we would not expect $-F_z/k$ to give an improved approximation to $\bar{a}$ (see section 3.4) . However, $-F_t/k \neq \bar{a}$ for higher accumulation rates even when $\dot{\varepsilon}_H$ is negligible. We must conclude that the Robin hypothesis, which leads to equation (8), is the source of the problem. If the effect of bulk density on the strain rate is not well described by the term $(\rho_i - \rho)/\rho$ over a certain range, then $\bar{F} \neq -\bar{a}k$ for that range.

The consequence is, therefore, that it is only in the case of stage 1 densification with negligible horizontal divergence that the Herron and Langway (1980) vertical densification model can be transformed to a strain rate model using $\bar{a}$. We test whether the iSTAR data are consistent with such a transformed model by plotting $-F_0 \exp\left(\frac{E_0}{RT_m}\right)$ against the accumulation rate $\bar{a}$ for each site except site 2, 15, 16, 18, and 19 where $\dot{\varepsilon}_H$ is high (Figure 15). E_0 is fixed at 10.16 kJ mol^{-1}. The gradient of the best linear fit through the origin is 12.0 ± 0.4 mwe^{-1} ($r^2 = 0.98$); the expected value is $k_0^* = 11(+6, -4)$ mwe^{-1}.

7. Conclusion

Deriving accumulation rates from snow density profiles in the PIG basin has proved challenging, but by introducing the automatic layer identification routine *Straticounter* (Winstrup et al., 2012) we have been able to produce estimates of mean annual accumulation which are consistent with previous airborne measurements (Medley et al., 2014) and with direct measurements of accumulation over 1 year. Chemical analysis of ice core samples remains the most accurate way to determine annual layering, especially when information from several different species can be combined. However, the stratigraphic method does have some advantages: high-resolution density profiles can be collected relatively easily using the neutron probe and can be analyzed in situ. In the overall iSTAR project they have an important role to play in extending the accumulation data set to sites where ice core data were not collected. The density profiles also provide information needed to derive accumulation from radar returns. We have derived a mean density profile which can be used to convert two-way travel times to depth and have shown that the effect of annual fluctuations in density on depth estimates is insignificant, except very near the surface.

Other members of the iSTAR team will construct an accumulation map for the PIG basin using the radar data to extend the site measurements and will make a detailed comparison of measured climatological variables with those derived from meteorological models. In this paper we have made a limited comparison of our accumulation rates with surface mass balance given by the RACMO2.3 model (van Wessem et al., 2014). Although there is good agreement for sites above 1,000 m a.s.l., the model results for most of the iSTAR traverse sites have to be regarded with some caution. Hence, in this paper, we discuss densification in terms of the measured mean climatological parameters T_m and $\bar{a}$ alone. A further study using time-varying meteorological input data will be undertaken when suitable meteorological models have been properly assessed against the limited in situ meteorological data available from the PIG basin.

Our analysis of neutron probe and core density profiles shows that the established Herron and Langway (1980) model gives good predictions for the vertical densification rate when $\rho \leq 550$ kg m^{-3} (excluding the surface layer) and when $\rho \geq 600-625$ kg m^{-3}. However, between these values the vertical densification rate is up to twice that expected from the Herron and Langway model. We therefore define a transitional region between the Herron and Langway stages 1 and 2 for which a new model equation is required. Our analysis of strain rate profiles shows that the Arthern et al. (2010) equation for stage 2 densification produces good predictions of iSTAR transitional strain rates, so this is a potential candidate. The problem is that the Arthern model, like the Herron and Langway model, is based on the Robin hypothesis (equation (2)) and we have shown that this does not hold in the transitional region.

In the longer term a better approach to empirical modeling of snow densification might be to accept that strain rate is dependent on a more complex function of density than that proposed by Robin. This would allow a gradual change in densification rate with depth, as the relative importance of grain-boundary sliding, grain growth and sintering changes. However, for the moment, since the Herron and Langway model and its derivatives have been so widely accepted, adding a transitional stage is the most practical option. In any case, some modification to existing models is required; since we have found that over the iSTAR traverse some 10–14% of total compaction occurs in the transitional region, it is important that the rate at which this occurs is correctly estimated.

Notation

a_{2014} Accumulation rate between traverses, mwe a^{-1}.
$\bar{a}$ Mean annual accumulation rate, mwe a^{-1}.
c Steady state density-corrected volumetric strain rate, a^{-1}.
E Activation energy, J mol^{-1}.
F Density-corrected volumetric strain rate, a^{-1}.
F_z Density-corrected vertical strain rate, a^{-1}.
i Peak number.
k Local vertical densification rate, mwe^{-1}.
k^* Global vertical densification rate, mwe^{-1}.
n Profile number.
N Number of years in the annual accumulation series from neutron probe density profiles
q Water equivalent, mwe
Q Mass of section of profile, mwe
r Normalized density deviation.
R Radius of access hole, m.
R Gas constant, 8.314 J mol^{-1} K^{-1}
t Time, a.
T_m Mean annual temperature, K.
T_m^* Mean annual temperature, °C.
w Vertical velocity, m a^{-1}.
x Horizontal coordinate, along traverse, m or km.
y Horizontal coordinate, across traverse, m.
z Vertical coordinate, m.
Z Length of section of profile, m.
Δq Accumulation between measurements at a given site, mwe
Δt Time between measurements at a given site, a.
$\dot{\varepsilon}$ Volumetric strain rate, a^{-1}.
$\dot{\varepsilon}_H$ Horizontal velocity divergence, a^{-1}.
$\dot{\varepsilon}_{zz}$ Vertical strain rate, a^{-1}.
ρ Density, kg m^{-3}.
ρ_G Global density profile, kg m^{-3}.
ρ_i Density of ice, 912 kg m^{-3}.
ρ_0 Vertically smoothed density, kg m^{-3}.
ρ_m Temporal mean density, kg m^{-3}.
ρ_S Site-specific surface snow density, kg m^{-3}.

σ Stress, Pa.
σ_ρ Random error in density measurement, kg m^{-3}.
σ^*_ρ Systematic error in density measurement, kg m^{-3}.
σ_F Random error in density-corrected volumetric strain rate, a^{-1}.
σ^*_F Systematic error in density-corrected volumetric strain rate, a^{-1}.
σ^*_q Systematic error in mass measurement, mwe
σ^*_R Systematic error in access hole radius, m.
σ_a Standard deviation of log-normal distribution of annual accumulation.
τ Time since deposition of snow, a.

Acknowledgments
This work was supported by funding from the UK Natural Environment Research Council's iSTAR program and NERC grant [10.13039/501100000270] (NE/J005797/1). We thank the BAS logistics team and iSTAR colleagues for support in the field, B. Medley for accumulation data, and R. Jones for RACMO output at the iSTAR sites. RACMO data were provided by the Institute for Marine and Atmospheric Research, University of Utrecht. The NERC Geophysical Equipment Facility provided GPS receivers (Loan 998). Data are archived at the NERC Polar Data Centre and are available from the first author, pending open access via the iSTAR Geographical Information System (http://gis.istar.ac.uk).

References

Alley, R. B., Shuman, C. A., Meese, D. A., Gow, A. J., Taylor, K. C., Cuffey, K. M., … Elder, B. (1997). Visual-stratigraphic dating of the GISP2 ice core: Basis, reproducibility, and application. *Journal of Geophysical Research*, *102*(C12), 26,367–26,381.

Arthern, R. J., Vaughan, D. G., Rankin, A. M., Mulvaney, R., & Thomas, E. R. (2010). In situ measurements of Antarctic snow compaction compared with predictions of models. *Journal of Geophysical Research*, *115*, F03011. https://doi.org/10.1029/2009JF001306

Bamber, J. L., Gomez-Dans, J. L., & Griggs, J. A. (2009). A new 1 km digital elevation model of the Antarctic derived from combined satellite radar and laser data—Part 1: Data and methods. *The Cryosphere*, *3*, 101–111.

Benson, C. S. (1962). Stratigraphic studies in the snow and firn of the Greenland ice sheet (*Tech. Rep. 70*). Wilmette, IL: U.S Army Snow Ice and Permafrost Research Establishment.

Herron, M. M., & Langway, C. C. (1980). Firn densification: An empirical model. *Journal of Glaciology*, *25*(93), 373–385.

Hörhold, M. W., Kipfstuhl, S., Wilhelms, F., Freitag, J., & Frenzel, A. (2011). The densification of layered polar firn. *Journal of Geophysical Research*, *116*, F01001. https://doi.org/10.1029/2009JF001630

Kaspers, K., van de Wal, R. S. W., Van den Broeke, M. R., Schwander, J., Lipzig, N., & Brennenkmeijer, C. (2004). Model calculations of the age of firn air across the Antarctic continent. *Atmospheric Chemistry and Physics*, *4*, 1365–1380.

Ligtenberg, S. R. M., Helsen, M. M., & van den Broeke, M. R. (2011). An improved semi-empirical model for the densification of Antarctic firn. *The Cryosphere*, *5*(4), 809–819.

Lister, H. (1959). Geophysical investigations of the Commonwealth Trans-Antarctic Expedition.1. The climate and ice mass balance. *Geographical Journal*, *125*(3–4), 343–354.

Medley, B., Joughin, I., Das, S. B., Steig, E. J., Conway, H., Gogineni, S., … Nicolas, J. P. (2013). Airborne-radar and ice-core observations of annual snow accumulation over Thwaites Glacier, West Antarctica confirm the spatiotemporal variability of global and regional atmospheric models. *Geophysical Research Letters*, *40*, 3649–3654. https://doi.org/10.1002/grl.50706

Medley, B., Joughin, I., Smith, B. E., Das, S. B., Steig, E. J., Conway, H., … Leuschen, C. (2014). Constraining the recent mass balance of Pine Island and Thwaites glaciers, West Antarctica, with airborne observations of snow accumulation. *The Cryosphere*, *8*(4), 1375–1392.

Morris, E., & Wingham, D. J. (2011). The effect of fluctuations in surface density, accumulation and compaction on elevation change rates along the EGIG line, central Greenland. *Journal of Glaciology*, *57*(203), 416–430.

Morris, E. M. (2008). A theoretical analysis of the neutron scattering method of measuring snow and ice density. *Journal of Geophysical Research*, *113*, F03019. https://doi.org/10.1029/2007JF000,962

Morris, E. M., & Cooper, J. D. (2003). Density measurements in ice boreholes using neutron scattering. *Journal of Glaciology*, *49*(167), 599–604.

Morris, E. M., & Wingham, D. J. (2014). Densification of polar snow: Measurements, modeling, and implications for altimetry. *JGR Earth Surfaces*, *119*, 349–365.

Morris, E. M., & Wingham, D. J. (2015). Uncertainty in mass balance trends derived from altimetry; a case study along the EGIG line, Central Greenland. *Journal of Glaciology*, *61*(226), 345–356.

Mulvaney, R., & Smith, A. M. (2017). *Borehole derived Pine Island glacier mean annual temperatures—Collected 2014/2015*. Cambridge, UK: NERC Polar Data Centre. https://doi.org/10.5285/eae547d0-9668-4bal-9fc4-67929382395f

Richardson, C., Aarholt, E., Hamran, S. E., Holmlund, P., & Isaksson, E. (1997). Spatial distribution of snow in western Dronning Maud Land, East Antarctica, mapped by a ground-based snow radar. *Journal of Geophysical Research*, *102*(B9), 20,343–20,353.

Rignot, E., Mouginot, J., & Scheuchl, B. (2011). MEaSUREs Antarctic grounding line from differential satellite radar interferometry.

Robin, G. d. Q. (1958). Glaciology III: Seismic shooting and related investigations, *Norwegian-British-Swedish Antarctic Expedition, 1949-52. Scientific Results* (Vol. 5, pp. 134). Oslo: Norsk Polarinstitutt.

Shepherd, A., Wingham, D. J., Mansley, J. A. D., & Corr, H. F. J. (2001). Inland thinning of Pine Island Glacier, West Antarctica. *Science*, *291*, 862–864.

van Wessem, J. M., Reijmer, C. H., Morlighem, M., Mouginot, J., Rignot, E., Medley, B., … van Meijgaard, E. (2014). Improved representation of East Antarctic surface mass balance in a regional atmospheric climate model. *Journal of Glaciology*, *60*(222), 761–770.

Winstrup, M. (2016). A hidden Markov model approach to infer timescales for high-resolution climate archives. In *Proceedings of the 30th AAAI Conference on Artificial Intelligence and the 28th Innovative Applications of Artificial Intelligence Conference, February 12–17, 2016* (*Vol. VI, 4053*, pp. 8). Phoenix, Arizona USA.

Winstrup, M., Svensson, A. M., Rasmussen, S. O., Winther, O., Steig, E. J., & Axelrod, A. E. (2012). An automated approach for annual layer counting in ice cores. *Climate of the Past*, *8*(6), 1881–1895.